RESIDUAL STRESSES IN COLD-FORMED STEEL SECTIONS AND THEIR EFFECT ON COLUMN BEHAVIOUR

by

Wai Meng QUACH

A thesis

Submitted to the
Department of Civil and Structural Engineering
in partial fulfilment of the requirements
for the Degree of

Doctor of Philosophy

THE HONG KONG
POLYTECHNIC UNIVERSITY
香港理工大學

August 2005

CERTIFICATE OF ORIGINALITY

I hereby declare that this thesis is my own work and that, to the best of my knowledge and belief, it reproduces no material previously published or written, nor material that has been accepted for the award of any other degree or diploma, except where due acknowledgement has been made in the text.

_____ (Signed)

Wai Meng QUACH (Name of Student)

ABSTRACT

The cold-bending operations required in manufacturing cold-formed steel columns have a significant effect on their structural behaviour. This effect has traditionally been assessed using idealized residual stress distributions based on limited laboratory measurements in conjunction with separate specifications of mechanical properties for the flat portions and the corner regions, or using whole section mechanical properties obtained from stub column tests. These conventional approaches are highly empirical and do not provide an accurate description of the co-existent residual stresses and strain hardening of the material arising from the manufacturing process.

This thesis is concerned with the theoretical modelling of the manufacturing process of press-braked carbon and stainless steel sections for the prediction of the resulting residual stresses and equivalent plastic strains. The residual stresses in such cold-formed sections are derived from two sources: the coiling, uncoiling and flattening process (referred to simply as the coiling-uncoiling process) and the cold-forming process. A series of analytical solutions are presented in this thesis to predict the residual stresses and the associated equivalent plastic strains in steel sheets as a result of cold bending, covering both processes. These solutions are verified using finite element simulations of cold bending of steel sheets. For the modelling of cold bending of stainless steel sheets, a new stress-strain relationship was established to overcome significant deficiencies of existing stress-strain relationships.

On the basis of these analytical solutions, two alternative approaches for the prediction of residual stresses and equivalent plastic strains in press-braked sections

are presented and verified: (a) a finite element-based method in which a finite element simulation of the cold-forming process is carried out with its initial state being defined by an analytical solution for the coiling-uncoiling process; and (b) a complete analytical model in which the residual stresses and equivalent plastic strains from both processes are given by analytical solutions. A parametric study employing the finite element-based method was conducted to study the effect of forming parameters on the resulting residual stresses in cold-formed sections. The complete analytical model provides an attractive approach for defining the initial state of a section in a column nonlinear buckling analysis.

The thesis next presents an advanced numerical approach to predict the buckling behaviour of cold-formed columns in which the effect of the manufacturing process is explicitly and accurately accounted for. In this approach, the complete analytical model for residual stresses is employed together with an appropriate imperfection model. Using this finite element method, the effect of cold work on buckling behaviour was examined.

Based on results from the present study, it can be concluded that the through-thickness variation of residual stresses in cold-formed sections is nonlinear, and thus the traditional assumption of linear variation is inappropriate. The distributions of residual stresses in the flat portions of a cold-formed section are highly dependent on the initial coil diameter of the metal sheet used for fabrication, so very different residual stresses can arise in the flat portions of otherwise identical cold-formed sections as a result of different initial coil diameters, which are unknown to designers and users of these sections. This may have been a major factor responsible for the

significant scatter in test load capacities of cold-formed members. It is also shown that whether the buckling strength of a cold-formed column can be enhanced or reduced by cold work is a result of the combined effect of the residual stresses and the equivalent plastic strains in the member, and this effect varies depending on the initial material properties and the forming parameters.

PREFACE

This thesis is submitted to The Hong Kong Polytechnic University, Hong Kong SAR, PR China, for the degree of Doctor of Philosophy. The work described herein was performed by the author in the Department of Civil and Structural Engineering, The Hong Kong Polytechnic University. The period of candidature was from September 1999 to August 2005, on a part-time basis. The author was supervised by his chief supervisor, Dr. Jin-Guang Teng, Chair Professor of Structural Engineering; and his co-supervisor, Dr. Kwok-Fai Chung, Professor in the Department of Civil and Structural Engineering.

The following papers, based on the work presented in this thesis, were written in collaboration with Professor Teng and Professor Chung:

Journal Papers

Quach, W. M., Teng, J. G. and Chung, K. F. (2004). Residual stresses in steel sheets due to coiling and uncoiling: A closed-form analytical solution. *Engineering Structures*, **26**, 1249-1259.

Conference Papers

Quach, W. M., Teng, J. G. and Chung, K. F. (2003). Finite element predictions of residual stresses in cold-formed sections. *Advances in Structures: Proceedings of the*

International Conference on Advances in Structures (ASSCCA'03), Sydney, Australia, 22-25 June 2003, A.A. Balkema, 325-331.

Quach, W. M., Teng, J. G. and Chung, K. F. (2004). Residual stresses in steel sheets due to coiling and uncoiling. *Progress in Structural Engineering, Mechanics and Computation: Proceedings of the Second International Conference on Structural Engineering, Mechanics and Computation*, 5-7 July 2004, Cape Town, South Africa, A.A. Balkema, 270.

ACKNOWLEDGEMENTS

I truly thank my chief supervisor, Professor Jin-Guang Teng, for all his help during my candidature, and for introducing me to scientific research of thin-walled structures. He has provided continuous encouragement, expert advice and useful discussions throughout the period of my study. I would also like to thank my co-supervisor, Professor Kwok-Fai Chung, for sharing his practical experience and expertise on issues related to cold-formed structures. I also benefited from the useful discussions with him. The efforts from both my supervisors have made me a better researcher and engineer. I am also grateful to Professor Jan-Ming Ko for introducing me to Professor Teng, so that I can have the opportunity to do research with him.

I would like to acknowledge the financial support provided by The Hong Kong Polytechnic University (Project No. G-V864) and the Research Grants Council of the Hong Kong S.A.R. (Project No. PolyU5056/02E). Thanks should go to the University of Macau for providing me an academic post and meanwhile allowing me to complete my PhD study on a part-time basis at The Hong Kong Polytechnic University. The University of Macau has also provided financial support to cover the expenses of transportation, reference books and photocopying during my PhD study.

I would like to thank my postgraduate colleagues: Xiang Lin, Chang-Yong Song, Hon-Ting Wong and Jian Yao, for their friendship and help during my time on the campus. Most of them have completed their PhD degrees and continued their academic career at other universities. Thanks also go to Dr. Scott Smith, Dr. Zeng-Chun Wang and Dr. Xing-Fei Yuan who were doing their post-doctoral research in

the department and have now left the university. All of them are good researchers and good people. Thanks are also due to the technical staff, especially Mr. Qiu, in the Heavy Structures Laboratory.

Finally, I would like to thank all my friends who shine my life with their love and support. They always share their joy with me. I am grateful to my family for their tolerance towards my absence from them in many ways during the period of my study.

TABLE OF CONTENTS

LIST OF TABLES

LIST OF FIGURES

Chapter 1

INTRODUCTION

1.1 BACKGROUND

Cold-formed thin-walled structural members used in building construction have various cross-sectional shapes, and are fabricated from metallic sheets, strips and plates. Carbon steel and stainless steel are two common materials used in the production of cold-formed members.

The use of cold-formed carbon steel members in building construction began in about 1850s in both the United States and Great Britain (Yu 2000). However, cold-formed carbon steel structural members did not become widely used in buildings until the issuance of the first design specification developed by the American Iron and steel Institute (AISI) in 1946.

Cold-formed stainless steel members are often used architecturally in building construction because of their pleasing appearance and superior corrosion resistance. Since the mechanical properties of stainless steel alloys are significantly different from those of carbon steels, the design rules for cold-formed carbon steel structural members cannot be directly adopted for the structural design of stainless steel members without any modification. The use of cold-formed stainless steel members in structural applications had thus been limited until the first design specification for

cold-formed stainless steel structural members (AISI 1968) was issued by the AISI in 1968. The first design rules for stainless steel structural members were developed on the basis of the experience accumulated in the design of cold-formed carbon steel structural members and the research work on stainless steel structural members (Johnson 1966, Johnson and Winter 1966).

Cold-formed members are usually manufactured by either roll forming (see Figure 1.1) or press braking (see Figure 1.2). Roll forming is widely used for a high production capacity. The roll forming machine forms a steel strip into the final required shape of a cold-rolled section by feeding the strip from a coil continuously through successive pairs of rollers which act as male and female dies. The completed element is cut to required lengths by an automatic cut-off tool. The press braking is commonly used for sections of simple configurations and a limited quantity of production. In a press-braking operation, flat sheets or short lengths of strips cut from a coil are fed into a press brake and a complete fold is produced along the full length of a section. The complete forming process of a section generally requires the press-braking operation to be repeated several times.

In both roll forming and press braking, before the cold-forming process is applied to the flat strip, the flat strip has already experienced the coiling, uncoiling and flattening process which is here referred to simply as the coiling-uncoiling process. That is, cold-rolled strips are first coiled into rolls for storage. They are subsequently uncoiled from the roll and forced to become flat before cold-forming forces are applied.

The manufacturing process of cold-formed sections can modify the mechanical properties of the sheet material, and induce residual stresses in the cold-formed sections. This modification depends on the type of material and the history of cold work throughout the forming process. Different cold-forming processes can bring about different cold work effects into a section, and result in different residual stresses and different changes in the mechanical properties of the material in various parts of the section. Consequently, the structural behaviour of the produced member is also affected, and may not be predicted accurately on the basis of the mechanical properties of the virgin material. However, in most current design codes, the effect of cold work from forming is considered in design only for the corner regions of fully effective sections (compact sections). The effect of cold work from the cold-forming process on the load-carrying capacity of a member is not accounted for explicitly and properly. Against this background, the research work presented in this thesis was carried out to model the cold work in cold-formed sections induced by the manufacturing process and to simulate the structural behaviour of members possessing such sections.

1.2 OBJECTIVES AND LAYOUT OF THE THESIS

1.2.1 Objectives

The main objectives of the research work are: (a) to develop an advanced numerical approach to the modelling of the structural behaviour of cold-formed members, in which the consequences of the manufacturing process, including the strain-hardening

of the material, residual stresses in the section and geometric imperfections, are explicitly accounted for, and (b) to study the effects of these factors on the buckling behaviour of cold-formed steel columns under axial compression using this new approach. This new approach will provide a useful tool in optimizing the forming parameters of cold-formed steel sections and will greatly reduce the need for laboratory testing in the development of design rules for them. The study is concerned only with press-braked carbon steel and stainless steel sections.

1.2.2 Layout

Chapter 1 gives a brief introduction to cold-formed members and cold-forming processes as well as the motivation to initiate this research work. The chapter also presents the outline of this thesis.

Chapter 2 provides a review of the literature on topics relevant to the modelling of the structural response of cold-formed members. It includes a review of the existing research on the modelling of material behaviour for flats and corners, residual stresses, and initial geometrical imperfections. Some of the available literature is reviewed and discussed in other parts of the thesis.

Chapter 3 describes the development of a new stress-strain relationship for stainless steel alloys, which is capable of accurate predictions over the full ranges of both tensile and compressive strains. A complete comparison of its predictions with experimental stress-strain curves is shown in Appendix A.

Chapter 4 presents a general analytical solution to predict residual stresses and equivalent plastic strains in steel sheets arising from the coiling-uncoiling process. Based on this general analytical solution, separate solutions are formulated for four common types of sheet steels: (1) elastic-perfectly plastic steels, (2) elastic-linear strain-hardening steels, (3) elastic-nonlinear strain-hardening steels, and (4) nonlinear strain-hardening steels, such as stainless steel alloys with negligible material anisotropy. As residual stresses and equivalent plastic strains are the two defining parameters of the effect of cold work, the cold work effect of the coiling-uncoiling process is captured by this analytical solution.

The aforementioned analytical solution for the coiling-uncoiling process is based on the plane strain assumption which is invalid for a narrow zone along each longitudinal edge of a wide plate of finite width. The validity and limitation of this plane strain assumption are examined and discussed in Appendices B and C.

Chapter 5 presents a finite element-based method to predict residual stresses in press-braked carbon steel sections. In this chapter, comparisons between numerical results from this method and laboratory measurements are given to demonstrate the validity and accuracy of the method.

Chapter 6 presents a general analytical solution for predicting residual stresses and equivalent plastic strains due to cold bending at corners of press-braked sections. To obtain this analytical solution, the formulation for small-curvature pure bending involved in the coiling-uncoiling process presented in Chapter 4 is extended to deal

with large-curvature bending involved in the cold bending of an uncoiled sheet into a corner of a cold-formed section. Based on this general analytical solution, separate solutions are formulated for three common types of sheet steels: (1) elastic-linear strain-hardening steels, (2) elastic-nonlinear strain-hardening steels, and (3) nonlinear strain-hardening steels, such as stainless steel alloys.

Chapter 7 is concerned with the analytical prediction of residual stresses and equivalent plastic strains in press-braked stainless steel sections, in which material anisotropy is taken into account. Two distinct analytical solutions are presented for the coiling-uncoiling process and the press-braking operation respectively. On the basis of these two analytical solutions, a complete analytical model is proposed to predict residual stresses and equivalent plastic strains in press-braked sections. The predictions from this complete analytical model are compared with results obtained from the finite element-based method presented in Chapter 5, in order to demonstrate the accuracy of the complete analytical model. The validity of the simplifying assumptions made for this complete analytical model and their effect on the column behaviour are examined in Appendix C.

Chapter 8 presents results from parametric studies of residual stresses in press-braked carbon steel sections and stainless steel sections on the basis of the analytical solutions and the finite element-based method presented in the earlier chapters. In this chapter, a study on the effect of die size is also presented.

Chapter 9 presents an advanced finite element approach to the modelling of the structural behaviour of press-braked carbon steel columns and stainless steel columns.

In this advanced finite element approach, the effect of cold work from the manufacturing process is taken into account using the analytical solutions of residual stresses and equivalent plastic strains presented in the earlier chapters.

In Chapter 10, important findings and conclusions from this research are summarized. Suggestions for further work are also given.

1.3 REFERENCES

AISI (1968). *Specification for the Design of Light Gage Cold-Formed Stainless Steel Structural Members*, 1968 edition, American Iron and Steel Institute, Washington, D.C.

Johnson, A. L. (1966). *The Structural Performance of Austenitic Stainless Steel Members, Report No. 327*, Department of Structural Engineering, Cornell University, Nov. 1966.

Johnson, A. L. and Winter, G. (1966). Behaviour of stainless steel columns and beams. *Journal of the Structural Division, ASCE*, **92:ST5**, 97-118.

Walker, A. C. (1975). *Design and Analysis of Cold-Formed Sections*, International Textbook Company.

Yu, W. W. (2000). *Cold-Formed Steel Design*, 3rd. edition, John Wiley & Sons, United States.

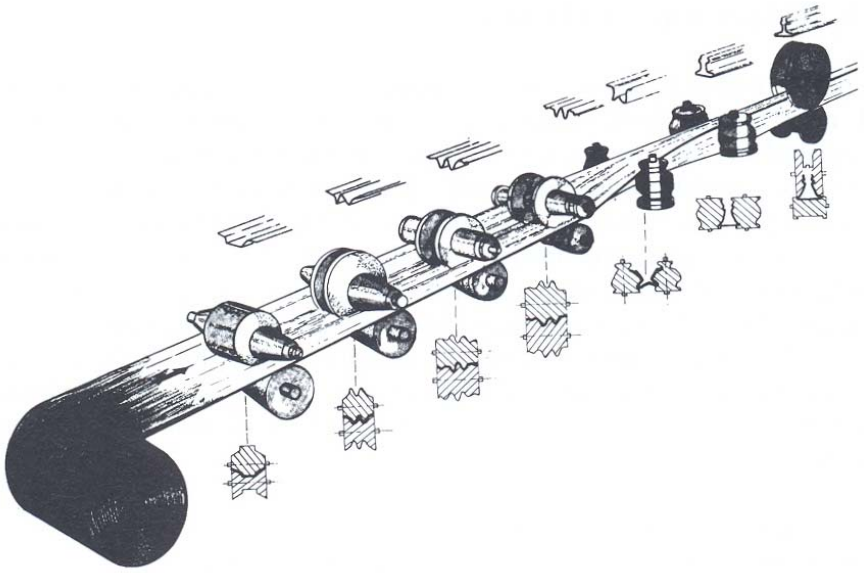

Figure 1.1 Manufacturing process of cold-rolled sections (reproduced from Walker 1975).

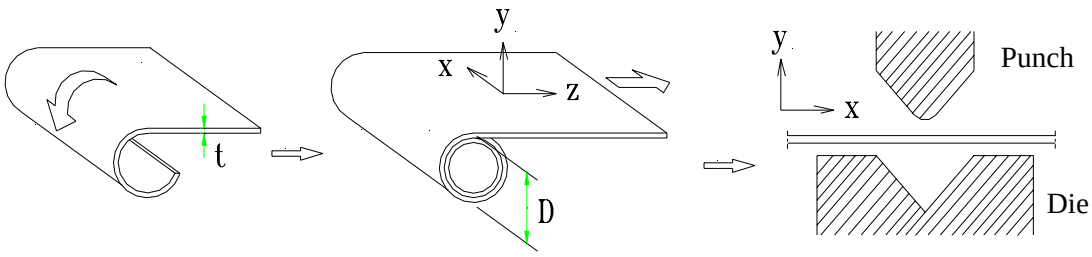

(a) Coiling (b) Uncoiling including flattening (c) Press braking

Figure 1.2 Manufacturing process of press-braked sections.

Chapter 2

LITERATURE REVIEW

2.1 GENERAL

Numerical methods such as the finite element method and the finite strip method have provided powerful tools to simulate the structural behaviour of cold-formed thin-walled structural members experiencing geometrical and material nonlinearities. As these numerical techniques have been developed to a mature and reliable stage, the accuracy of nonlinear numerical simulations of structural responses is highly dependent on the validity of input parameters used for characterizing the behaviour of structural members. These input parameters need to describe the mechanical response of the material, and define the initial state of the member. Hence, sound knowledge of these input parameters is essential for accurate numerical simulations of member behaviour.

Stress-strain relationships, residual stresses, and initial geometrical imperfections are the three basic components needed for the accurate numerical modelling of the structural behaviour of cold-formed members (Key and Hancock 1993, Abdel-Rahman and Sivakumaran 1997, Pi and Trahair 1997, Pi *et al*. 1998, Narayanan and Mahendran 2003, Gardner and Nethercot 2004a, Telue and Mahendran 2004a and 2004b), although, in some cases, researchers (Dubina and Ungureanu 2002, Wilkinson and Hancock 2002, Young and Yan 2002a and 2002b, Young 2004) have

chosen to ignore the effect of residual stresses. Among these studies, various methods have been established or adopted to characterize these three components (i.e. stress-strain relationships, residual stresses, and initial geometrical imperfections), but up until now, the effect of cold work of the manufacturing process has not been modelled explicitly.

In this chapter, existing techniques for the modelling of material behaviour, residual stresses, initial geometrical imperfection and structure behaviour of cold-formed members are reviewed. They are relevant to the development of a new numerical approach to the modelling of press-braked structural members presented in the subsequent chapters of the thesis.

2.2 MATERIAL MODELLING

2.2.1 Carbon steel sections

The existing research on material modelling can be classified into two categories: (1) determination of corner properties, and (2) establishment of stress-strain relationships. The aim of research work in category (1) is to determine the cold-worked corner properties in terms of the basic mechanical properties (i.e. yield strength and ultimate strength) of the virgin material or the flat material (material of flat portions). The basic mechanical properties are conventionally obtained from coupon tests. The aim of research in category (2) is to define the mechanical response of material which is generally needed in numerical modelling.

2.2.1.1 Corner properties

The earliest experimental work for determining the corner properties was done by Karren (1967). Karren (1967) carried out a series of coupon tests on the virgin materials and the corners to investigate the influence of various cold-forming methods on the mechanical properties of corners in cold-formed sections. He concluded that cold working could significantly increase the yield strength, but the increase of ultimate strength was considerably less than that of yield strength. He also found that cold working in corners could cause the original sharp yielding behaviour to become gradual yielding, and the method of cold forming had only little influence on the material properties of corners.

Karren (1967) realized the significant effect of corner radius on the corner strength. By describing the stress-strain relationship with the power function, a semi-empirical equation was derived to define the yield strength F_{yc} of corners as

$$F_{yc} = \frac{B_c}{(R/t)^m} F_{yv} \tag{2.1a}$$

in which

$$B_c = 3.69\frac{F_{uv}}{F_{yv}} - 0.819\left(\frac{F_{uv}}{F_{yv}}\right)^2 - 1.79 \tag{2.1b}$$

$$m = 0.192\frac{F_{uv}}{F_{yv}} - 0.068 \tag{2.1c}$$

where F_{yv} and F_{uv} are the yield strength and the ultimate tensile strength of the virgin material respectively, R is the inside bend radius, and t is the sheet thickness.

Subsequently, Karren and Winter (1967) examined the influence of cold-forming methods on the mechanical properties of flat portions of open sections. They found that the roll-forming method produced the larger increase in the yield strength of flats than the press-braking method. They also concluded that, in the roll-forming process, strength increases in the flats may be attributed mainly to the rolling pressure on the flat portions as well as the strain hardening and aging of carbon steel sheets. For press-braked sections, the strain hardening and aging of carbon steel sheets was considered as the only factor that contributes significantly to the enhancement of yield strength in flats, and the press-braking operation itself was found to cause no effect on flat portions. For practical purposes, Karren and Winter (1967) suggested taking the yield strength in the flats of press-braked sections as the virgin value. They also proposed the use of Eq. (2.2) to calculate the full-section tensile yield strength F_{ya} for both press-braked sections and roll-formed sections:

$$F_{ya} = CF_{yc} + (1-C)F_{yf} \tag{2.2}$$

where C is the ratio of corner area to the total cross-sectional area, F_{yc} is the average tensile yield strength of corners and its value can be given by Eq. (2.1), and F_{yf} is the average tensile yield strength of flats and its value can be given conservatively by the yield strength of the virgin material in cases that tests are not conducted.

Eqs. (2.1) and (2.2) have been adopted by the AISI (1996) Specification and the Australian/New Zealand Standard AS/NZS 4600 (AS/NZS 1996) to determine the full-section yield strength (or average yield strength in AS/NZS 4600 Standard) for fully effective carbon steel sections. To account for the enhanced strength due to cold work in the corners of a cold-formed steel section, Part 1.3 of Eurocode 3, ENV 1993-1-3 (CEN 1996), provides the following expression for the average yield strength f_{ya} of the section:

$$f_{ya} = f_{yb} + \frac{knt^2}{A_g}\left(f_u - f_{yb}\right), \text{ but } \quad f_{ya} \le \frac{f_u + f_{yb}}{2} \tag{2.3}$$

where f_{yb} is the nominal yield strength of steel, f_u is the nominal ultimate tensile strength of steel, A_g is the gross cross-sectional area, t is the thickness of steel sheet before cold forming, n is the number of 90° bends in the cross-section with an internal radius $r \le 5t$ (fractions of 90° bends should be counted as fractions of n), and k is a numerical coefficient that depends on the type of forming as follows: $k = 7$ for cold rolling and $k = 5$ for other methods of forming.

Part 5 of British Standard BS5950 (BSI 1998) also uses the same expression (Eq. (2.3)) as Eurocode 3, ENV 1993-1-3 (CEN 1996), for the average yield strength, but uses $k = 5$ in Eq. (2.3) regardless of the methods of forming. According to the provisions of both design standards, the use of Eq. (2.3) in design is limited only to fully effective sections.

2.2.1.2 Stress-strain relationships

The yield strengths for corners and full sections are insufficient to describe the mechanical response of a material which is needed in nonlinear numerical analysis. Hence, the stress-strain relationship has also been studied by many researchers. Some efforts have been made to model stress-strain relationships for both flat portions and corner regions, and they are reviewed below.

Key and Hancock (1993) incorporated stress-strain models with elastic-perfectly plastic and Ramberg-Osgood stress-strain relationships (see Figure 2.1(b)) for flat portions and corner regions respectively in their finite strip analyses of cold-rolled square hollow section columns. Similar stress-strain models were also employed by other researchers from University of Sydney in nonlinear finite element analyses (Pi and Trahair 1997, Pi *et al*. 1998), but in these later studies, a tri-linear elastic-plastic strain-hardening relationship was used to replace the elastic-perfectly plastic stress-strain relationship for flat portions (see Figure 2.1(a)).

Abdel-Rahman and Sivakumaran (1997) proposed to divide a cold-rolled lipped channel section into a flat zone and a corner zone (the corner zone includes cross-section areas of curved corners, lips, and equivalent flat areas on both sides of each curved corner). They took the yield-strength increase in the corner zone as 60 % of that predicted by Karren's second corner model (Karren 1967), and the flat zone of the cold-rolled section was assumed to have the same yield strength as the virgin material. An idealized elastic-plastic stress-strain model with multi-linear isotropic strain hardening as shown in Figure 2.2 was used. In the idealized model, the elastic

behaviour was represented by a linear segment up to a proportional limit stress F_p which was taken as 75 % of the yield strength F_y.

These stress-strain relationships for flat portions used in the above studies are suitable only for sections cold-formed from hot-rolled carbon steel sheets and cold-reduced and annealed carbon steel sheets. When cold-rolled carbon steel sheets are used to form cold-formed sections, the stress-strain curves for both flats and corners are always of the gradual-yielding type (or the so-called roundhouse type) and should be defined by the Ramberg-Osgood relationship (Rasmussen and Rondal 1997 and 1998).

2.2.2 Stainless steel sections

Stainless steel is characterized by a considerable strain-hardening capability, material anisotropy, and different mechanical properties in tension and compression. These characteristics of stainless steel lead to differences in material modelling, in comparison with carbon steel.

2.2.2.1 Corner properties

Due to the great extent of strain hardening of stainless steel alloys, the strength enhancement in corners of cold-formed stainless steel sections has interested many researchers. The first investigation on the effect of cold work on the strength of cold-formed stainless steel sections was carried out by Coetsee *et al*. (1990). Press-braked lipped channel sections in three different grades of stainless steel were studied. By

comparing the stress-strain curve of the virgin sheet with the weighted average stress-strain curve obtained from the tests of the coupons cut from various parts of the section, Coetsee *et al*. (1990) demonstrated the increase of strength in corners due to the cold work of forming.

In analogy with Karren's corner model (Karren 1967) for the corner strength of carbon steel sections, Van den Berg and Van der Merwe (1992) proposed an equation (see Eq. (2.4)) for the prediction of corner 0.2% proof strength F_{yc} for stainless steel alloys. The equation was developed based on the test results from the corner and flat specimens of four different stainless steel grades:

$$F_{yc} = \frac{B_c}{(R/t)^m} F_{yv} \tag{2.4a}$$

in which

$$B_c = 3.289\frac{F_{uv}}{F_{yv}} - 0.861\left(\frac{F_{uv}}{F_{yv}}\right)^2 - 1.34 \tag{2.4b}$$

$$m = 0.06\frac{F_{uv}}{F_{yv}} + 0.031 \tag{2.4c}$$

In the Australian/New Zealand Standard AS/NZS 4673 (AS/NZS 2001) for cold-formed stainless steel structures, it is permitted to account for the increase of the 0.2% proof strength in corners of sections formed from ferritic alloys using the average yield strength (0.2% proof strength) for full sections defined by Eq. (2.2). In using Eq. (2.2) for sections of ferritic alloys, the average tensile yield strength (0.2% proof strength) F_{yc} of corners is given by

$$F_{yc} = \frac{B_c}{(R/t)^m} F_{yv} \tag{2.5a}$$

in which

$$B_c = 1.486 \frac{F_{uv}}{F_{yv}} - 0.210 \left(\frac{F_{uv}}{F_{yv}} \right)^2 - 0.128 \tag{2.5b}$$

$$m = 0.123 \frac{F_{uv}}{F_{yv}} - 0.068 \tag{2.5c}$$

This equation is also based on Karren's methodology. The enhanced strength calculated by Eqs. (2.2) and (2.5) can only be utilized in the design of fully effective sections, and is applicable only to ferritic alloys. The use of enhanced strength is also permitted in design for other stainless alloys, provided that the enhanced strength is determined by a rational method or by tests.

Recently, a research team (Gardner 2002, Ashraf *et al*. 2005) at the Imperial College, London carried out an extensive study on the corner properties of cold-formed stainless steel sections. Based on the collected test data for different cold-forming processes, four expressions were developed to model strength enhancements from forming processes. A simplified expression was first developed by Gardner (2002) to predict the corner 0.2% proof strength $\sigma_{0.2,c}$ in roll-formed sections from the ultimate tensile strength $\sigma_{u,f}$ of the flat material. The expression was then recalibrated against all available test data for roll-formed sections by Ashraf *et al*. (2005), which yielded the final simplified expression Eq. (2.6), which is applicable only to roll-formed stainless steel sections:

$$\sigma_{0.2,c} = 0.82\sigma_{u,f} \tag{2.6}$$

Since the mechanical properties such as $\sigma_{u,f}$ of the flat material are not always available, Ashraf *et al*. (2005) proposed two power function modes to predict the corner 0.2% proof strength $\sigma_{0.2,c}$ from the 0.2% proof strength $\sigma_{0.2,v}$ and the ultimate tensile strength $\sigma_{u,v}$ of the virgin material. These two models also follow the methodology of Karren (1967) and are given by

$$\sigma_{0.2,c} = \frac{1.881}{(R/t)^{0.194}}\sigma_{0.2,v} \tag{2.7}$$

and

$$\sigma_{0.2,c} = \frac{C_1}{(R/t)^{C_2}}\sigma_{u,v} \tag{2.8a}$$

with

$$C_1 = -0.382\left(\frac{\sigma_{u,v}}{\sigma_{0.2,v}}\right) + 1.711 \tag{2.8b}$$

$$C_2 = 0.176\left(\frac{\sigma_{u,v}}{\sigma_{0.2,v}}\right) - 0.1496 \tag{2.8b}$$

In order to obtain a full picture of the changes of the material properties at corners, besides the corner 0.2% proof strength $\sigma_{0.2,c}$, the ultimate strength $\sigma_{u,c}$ of corners should also be known. Hence, Ashraf *et al*. (2005) proposed an expression to predict the ultimate corner strength $\sigma_{u,c}$ from the corner 0.2% proof strength $\sigma_{0.2,c}$ and the properties of the virgin material:

$$\sigma_{u,c} = 0.75\sigma_{0.2,c}\left(\frac{\sigma_{u,v}}{\sigma_{0.2,v}}\right) \tag{2.9}$$

2.2.2.2 Stress-strain relationships

The nonlinear stress-strain behaviour of stainless steel alloys is of the "roundhouse" type and is commonly described by the Ramberg-Osgood relationship (see Eq. (2.10)). This relationship is generally defined by the initial Young's modulus E_0, the 0.2% proof stress $\sigma_{0.2}$ and the strain-hardening exponent n:

$$\varepsilon = \frac{\sigma}{E_0} + 0.002\left(\frac{\sigma}{\sigma_{0.2}}\right)^n \tag{2.10a}$$

in which

$$n = \frac{\ln(20)}{\ln(\sigma_{0.2}/\sigma_{0.01})} \tag{2.10b}$$

where E_0 is the initial Young's modulus, $\sigma_{0.01}$ and $\sigma_{0.2}$ are the 0.01% and 0.2% proof stresses respectively.

In practice, the definition of the strain-hardening exponent *n* requires the Ramberg-Osgood curve to match the measured stress-strain curve exactly at the 0.01% proof stress $\sigma_{0.01}$ and the 0.2% proof stress $\sigma_{0.2}$, so that the Ramberg-Osgood expression can closely approximate the measured stress-strain curve up to the 0.2% proof stress $\sigma_{0.2}$. However, the use of the Ramberg-Osgood expression for higher strains can lead

to overestimation of stress with serious inaccuracy as indicated by numerous previous studies (Macdonald *et al*. 2000, Rasmussen 2003, Gardner and Nethercot 2004b).

A number of studies (Macdonald *et al*. 2000, Mirambell and Real 2000, Olsson 2001, Rasmussen 2003, Gardner and Nethercot 2004b) have recently been conducted on the modelling of the stress-strain behaviour of stainless steel for higher strains. Although a number of stress-strain relationships have resulted from these studies, each of them is capable of accurate predictions either for a limited strain range or for the tensile stress-strain behaviour only. Moreover, most of them (Macdonald *et al*. 2000, Mirambell and Real 2000, Olsson 2001, Gardner and Nethercot 2004b) require the knowledge of not only the basic Ramberg-Osgood parameters (E_0, $\sigma_{0.2}$ and n), but also some additional parameters which are generally not specified in existing design codes (AS/NZS 2001, ASCE 2002) and need to be found from measured stress-strain curves. The limitations of these recent approaches are examined in detail below.

Macdonald *et al*. (2000) realized that higher values of the strain-hardening exponent n should be used for higher strains, and thus modified the Ramberg-Osgood expression such that the exponent n becomes a function of stress. The function was obtained by curve-fitting the overall measured stress-strain curve for each individual coupon test. The modified expression was found to give accurate predictions but its application is limited to a particular specimen for which a suitable value for n has been found.

Olsson (2001) observed that the true stress-nominal strain curve converted from the measured stress-strain curve approaches a straight line at high strains, and proposed

that the true stress-nominal strain curve can be approximated by the Ramberg-Osgood expression for strains up to the total strain $\varepsilon_{2.0}$ at the 2% proof stress (or the so-called the 2% total strain) and a straight line from this point onwards as an average fit to the stress-strain curve. The straight line was not required to pass through the point of the true ultimate tensile strength σ_{tu} at the nominal ultimate total strain ε_u. However, in his proposed curve, the parameter n was determined by use of the 0.2% and 1% proof stresses, and inaccuracy may arise in the important strain range $\varepsilon < \varepsilon_{0.2}$ (where $\varepsilon_{0.2}$ is the total strain at the 0.2% proof stress $\sigma_{0.2}$).

Another attempt to model the nominal stress-strain behaviour at high strains was made by Mirambell and Real (2000), who proposed the use of the basic Ramberg-Osgood relationship (Eq. (2.10)) up to the 0.2% proof stress and a modified Ramberg-Osgood expression, given by Eq. (2.11), between the 0.2% proof stress and the ultimate stress:

$$\varepsilon = \frac{\sigma - \sigma_{0.2}}{E_{0.2}} + \varepsilon_{pu}\left(\frac{\sigma - \sigma_{0.2}}{\sigma_u - \sigma_{0.2}}\right)^{n'_{0.2,u}} + \varepsilon_{0.2}, \qquad \sigma > \sigma_{0.2} \tag{2.11}$$

where $E_{0.2}$ is the tangent modulus at the 0.2% proof stress, σ_u and ε_{pu} are the ultimate strength and the plastic strain at ultimate strength respectively, $n'_{0.2,u}$ is a strain-hardening exponent that can be determined from the ultimate strength and an intermediate stress. The values of σ_u, ε_{pu} and $n'_{0.2,u}$ cannot be determined from the basic Ramberg-Osgood parameters, and need to be obtained from experimental stress-strain curves.

Similar to Mirambell and Real's approach, Rasmussen (2003) proposed a full-range stress-strain expression, in which the Ramberg-Osgood expression (Eq. (2.10)) is used for the range up to the 0.2% proof stress and a new expression, given by Eq. (2.12), is used for higher strains:

$$\varepsilon = \frac{\sigma - \sigma_{0.2}}{E_{0.2}} + \varepsilon_u \left(\frac{\sigma - \sigma_{0.2}}{\sigma_u - \sigma_{0.2}} \right)^m + \varepsilon_{0.2}, \qquad \sigma > \sigma_{0.2} \tag{2.12a}$$

in which

$$e = \frac{\sigma_{0.2}}{E_0} \tag{2.12b}$$

$$\varepsilon_{0.2} = \frac{\sigma_{0.2}}{E_0} + 0.002 \tag{2.12c}$$

$$E_{0.2} = \frac{E_0}{1 + 0.002n/e} \tag{2.12d}$$

$$\frac{\sigma_u}{\sigma_{0.2}} = \frac{1}{0.2 + 185e} \quad \text{for austenitic and duplex alloys} \tag{2.12e}$$

$$\frac{\sigma_u}{\sigma_{0.2}} = \frac{1 - 0.0375(n-5)}{0.2 + 185e} \quad \text{for all alloys} \tag{2.12f}$$

$$\varepsilon_u = 1 - \frac{\sigma_{0.2}}{\sigma_u} \tag{2.12g}$$

$$m = 1 + 3.5 \left(\frac{\sigma_{0.2}}{\sigma_u} \right) \tag{2.12h}$$

where e is the non-dimensional 0.2% proof stress, σ_u and ε_u are the ultimate stress and the total strain at ultimate stress (or the so-called ultimate strain) respectively. In the above full-range stress-strain curve, Eq. (2.12f) is less accurate than Eq. (2.12e)

for austenitic and duplex alloys, but is more generally applicable for all alloys as Eq. (2.12f) takes into account the influence of n.

While Mirambell and Real's approach requires the knowledge of not only the Ramberg-Osgood parameters (E_0, $\sigma_{0.2}$ and n) but also the additional parameters σ_u, ε_{pu} and $n'_{0.2,u}$ which need to be determined from measured stress-strain curves, Rasmussen's full-range stress-strain model can provide the nominal stress-strain relationship for different alloys over the full strain range with the needs of the basic Ramberg-Osgood parameters (E_0, $\sigma_{0.2}$ and n) only. Nevertheless, as shown later in Chapter 3, Rasmussen's mode can generally provide excellent predictions for tensile coupon tests but underestimates the stresses at strains $\varepsilon > \varepsilon_{0.2}$ for most compression coupon tests.

Gardner and Nethercot (2004b) recognized that Mirambell and Real's approach is not applicable to compressive stress-strain behaviour as the ultimate stress in compression cannot be obtained from the compression tests of flat coupons. They also realized that the strain at σ_u is far higher than those strains concurrent with general structural response and the use of the strain at σ_u in Eq. (2.11) can result in greater differences between the measured and the modelled material behaviour than if a lower strain is used. They thus proposed to use the 1% proof stress $\sigma_{1.0}$ in place of the ultimate stress σ_u in Eq. (2.11), leading to Eq. (2.13), and to use the Ramberg-Osgood relationship given by Eq. (2.10) for stresses up to $\sigma_{0.2}$:

$$\varepsilon = \frac{\sigma - \sigma_{0.2}}{E_{0.2}} + \left(0.008 - \frac{\sigma_{1.0} - \sigma_{0.2}}{E_{0.2}} \right) \left(\frac{\sigma - \sigma_{0.2}}{\sigma_{1.0} - \sigma_{0.2}} \right)^{n'_{0.2,1.0}} + \varepsilon_{0.2}, \qquad \sigma > \sigma_{0.2} \qquad (2.13)$$

where $n'_{0.2,1.0}$ is a strain-hardening exponent representing a curve that passes through $\sigma_{0.2}$ and $\sigma_{1.0}$, and its value can be determined from measured stress-strain curves. Gardner and Nethercot (2004b) found that Eq. (2.13) gave results in excellent agreement with experimental stress-strain data, in both tension and compression, up to strains of approximately 10% (of about 2% for compression coupon tests, since compression coupon tests were carried out up to about a 2% compressive strain). However, their model cannot provide predictions over full ranges of strains and the values of $\sigma_{1.0}$ and $n'_{0.2,1.0}$ in their model cannot be simply determined by the basic Ramberg-Osgood parameters.

Due to various limitations of existing stress-strain models, there is a need to develop a new more accurate stress-strain relationship for stainless steel alloys, to fulfil the requirement needed by the advanced numerical modelling of cold-formed structural members presented in this thesis. The development of such a stress-strain relationship is described in Chapter 3 of the thesis.

2.3 RESIDUAL STRESSES

2.3.1 Experimental studies

Residual stresses in cold-formed sections may play a significant role in determining their behaviour and strength, so they have often been measured in the laboratory and idealized on the basis of experimental findings. Most existing experimental studies on residual stresses have been focused on cold-formed carbon steel sections. Residual stresses in cold-formed stainless steel sections have received very little attention, and the only reported measurement of residual stresses was carried out on stainless steel tubular sections by Rasmussen and Hancock (1993). As Rasmussen and Hancock's study did not lead to any idealized model for residual stresses in stainless steel sections, only the experimental studies of residual stresses in carbon steel sections are reviewed below.

Batista and Rodrigues (1992) measured the distributions of longitudinal residual stresses in both roll-formed and press-braked channel sections with the same cross-sectional geometry by the sectioning method, and concluded that residual stresses in roll-formed sections were larger than those in press-braked sections. Their observation indicates that the magnitude of residual stresses depends on the amount of cold work. Weng and Peköz (1990) measured longitudinal residual stresses in cold-formed channel sections and found that residual stresses in corner regions were higher than those in flat portions (webs, flanges and lips). They also noted that the inner surface of the section was subject to compressive residual stresses while the outer surface was subject to tensile residual stresses. Similar observations were also made

by Abdel-Rahman and Sivakumaran (1997). Abdel-Rahman and Sivakumaran (1997) suggested ignoring transverse residual stresses due to their small magnitudes measured on the sheet surface, and only longitudinal residual stresses were considered to be important. Therefore, most existing studies on the modelling of residual stresses have been focused on the characterization of longitudinal residual stresses.

Based on experimental results, Weng and Peköz (1990) and Abdel-Rahman and Sivakumaran (1997) respectively proposed two different idealized distributions for longitudinal residual stresses in channel sections. These two idealized models were based on the same assumption for the through-thickness variations of residual stresses, but with different treatments for the magnitudes and distributions of residual stresses along the perimeter of the section. In both studies, the longitudinal residual stress was assumed to vary linearly across the plate thickness, reaching its maximum tensile value on the outer surface and its maximum compressive value on the inner surface of the section. Moreover, the longitudinal residual stress was assumed to consist of the bending component only with the membrane component being neglected, so that the magnitudes of the tensile and compressive surface residual stresses were assumed to be the same.

In Weng and Peköz's idealized model, longitudinal residual stresses are assumed to be uniformly distributed along the perimeter of the section by neglecting the increase of residual stresses at corners, and the maximum longitudinal residual stress is taken to be 50% of the yield stress of the flat material. In Abdel-Rahman and Sivakumaran's model, a cold-rolled channel section is divided into two zones: a flat zone and a corner zone (the corner zone includes cross-section areas of curved

corners, lips, and equivalent flat areas on both sides of each curved corner). The magnitude of the longitudinal surface residual stress in the corner zone is taken to be 40% of the yield stress of the flat material, and the longitudinal surface residual stress in the flat zone is assumed to have a magnitude varying from 12% to 18% of the yield stress of the flat material depending on steel grades.

Using the common assumption (i.e. linear through-thickness variations of residual stresses) made by Weng and Peköz (1990) and Abdel-Rahman and Sivakumaran (1997), Schafer and Peköz (1998) idealized longitudinal residual stresses across the plate thickness as a summation of a bending component and a membrane component. Schafer and Peköz (1998) collected and studied the available experimental data of residual stresses in various cross sections formed by both the roll-forming and the press-braking methods. Based on the statistical results for both the bending and membrane components as summarized in Tables 2.1 and 2.2, they proposed that the magnitudes of longitudinal residual stresses in various parts of a cold-formed section can be modelled by the corresponding statistical means. They also suggested that the membrane component can be ignored provided that the increase of yield strength due to the cold work of forming is not modelled. As an alterative approach, a method of using a cumulative distribution function was proposed to approximate the magnitudes of residual stresses.

In existing experimental studies on cold-formed channel sections (Weng and Peköz 1990, Batista and Rodrigues 1992, Abdel-Rahman and Sivakumaran 1997), only surface residual stresses were measured due to the small plate thickness, with the variations across the plate thickness being assumed to be linear. Through-thickness

variations of residual stresses are difficult to examine experimentally for thin sections, but have been measured in thick plates by Weng and White (1990a, 1990b) and in thick steel tubes by Key and Hancock (1993).

Key and Hancock (1993) carried out an experimental study on residual stresses in thick cold-rolled square hollow sections (SHS), and proposed idealized distributions of both longitudinal and transverse residual stresses in the section. Due to a greater plate thickness of these SHS sections, their measurements were able to show the complex through-thickness residual stress variations. They concluded that both longitudinal and transverse residual stresses in SHS sections consisted of three components: (1) membrane, (2) bending and (3) layering components. Their proposed idealized distributions of these three components are shown in Figure 2.3.

Existing experimental studies have shown the existence of residual stresses in cold-formed sections due to the cold work of forming. However, there are large variations in the magnitudes of measured residual stresses. For example, Kwon and Hancock (1992) as well as Young and Rasmussen (1995) found negligible residual stresses in the flat portion of their lipped channels, while Weng and Peköz (1990) found residual strains in the flat portion of their channel sections to be up to about 40% of the yield strain. It is worth noting that this difference in residual stresses in flat portions may be attributed to certain cold-forming parameters which may vary during the manufacturing process.

2.3.2 Theoretical predictions

Various methods for residual stress measurements are available and each has its own limitations (Rowlands 1993). Laboratory measurements of residual stresses in cold-formed thin-walled sections are time-consuming, difficult and with limited accuracy. For example, due to the thinness of cold-formed sections, variations of residual stresses across the plate thickness generally cannot be obtained. Indeed, residual stresses measured in thicker plates (Weng and White 1990a and 1990b, Key and Hancock 1993) have shown that they vary across the plate thickness in a complex manner. Moreover, clear relationships between residual stresses and various steps of the fabrication process cannot be established by an examination of the measurement results.

Accurate theoretical predictions of residual stresses in cold-formed sections require the modelling of the cold-forming process and are not yet available. Nevertheless, a limited amount of effort has been made in modelling residual stresses due to cold bending (Ingvarsson 1975, Kato and Aoki 1978, Rondal 1987). Ingvarsson (1975) and Kato and Aoki (1978) modelled the pure plastic bending of a wide plate as a plane strain problem by means of an incremental numerical process, with the steel assumed to obey the von Mises yield criterion and the Prandtl-Reuss flow rule. Rondal (1987) presented a similar numerical analysis of the pure plastic bending of wide plates, and then proposed an approximate approach of deriving residual stresses in channel sections based on the results from his pure bending analysis. Numerical results from all three studies also showed complex residual stress variations through the plate thickness.

To accurately predict residual stresses in cold-formed members, their manufacturing process needs to be closely modelled. Cold-formed members are usually manufactured by either roll forming or press braking. In both roll forming and press braking, before the cold-forming process is applied to the flat sheet, the flat sheet has already experienced the coiling, uncoiling and flattening process (see Chapter 1). The residual stresses in a cold-formed section are therefore derived from two sources: the coiling, uncoiling and flattening process (referred to simply as the coiling-uncoiling process) and the cold-forming process. Such a two-stage fabrication process is illustrated in Figure 1.2 (refer to Chapter 1) for the press-braking method. Predictions of residual stresses in press-braked sections can thus be separated into two tasks: the prediction of residual stresses from the coiling and uncoiling process involving pure bending of the steel sheet and the prediction of residual stresses from the cold-bending process. Chapters 4, 6 and 7 of this thesis are concerned with both tasks by presenting accurate analytical solutions for the pure bending of wide plates with different amounts of straining in the two orthogonal directions respectively.

The pure bending of wide plates into the plastic range has been studied by many researchers (Ingvarsson 1975, Kato and Aoki 1978, Johnson and Yu 1981, Rondal 1987, Tan *et al.* 1994 and 1995, Pourboghrat and Chu 1995, Guggenberger 1996, Zhang and Hu 1998, Chakrabarty *et al.* 2000 and 2001). Among these existing studies, several were based on the deformation theory of plasticity (Johnson and Yu 1981, Tan *et al.* 1994, Pourboghrat and Chu 1995) so that the effect of deformation history on residual stresses was ignored. This effect was shown to be important by Zhang and Hu (1998), so for accurate predictions, the flow theory of plasticity should be used.

The studies based on the flow theory (Ingvarsson 1975, Kato and Aoki 1978, Rondal 1987, Tan *et al.* 1995, Guggenberger 1996, Chakrabarty *et al.* 2000 and 2001) have all been numerical, and some of them (Ingvarsson 1975, Rondal 1987, Tan *et al.* 1995) ignored part of the elastic deformation which is important for the coiling and uncoiling process of steel sheets where the curvature involved is not so large. Moreover, some of these studies based on the flow theory (Tan *et al.* 1995, Chakrabarty *et al.* 2000 and 2001) were only concerned with moment-curvature relationships. Therefore, in this thesis, accurate analytical solutions are presented for both the coiling-uncoiling process and the cold-bending process modelled as plane strain pure bending problems with all factors appropriately included.

2.4 GEOMETRICAL IMPERFECTIONS

The existing work on the modelling of geometrical imperfections can be classified into three categories, according to their purposes: (1) modelling of geometrical imperfections in isolated plate elements of cold-formed sections, (2) modelling of geometrical imperfections in cold-formed columns, and (3) modelling of geometrical imperfections in cold-formed beams. The modelling techniques for these three categories are summarized in Tables 2.3~2.5 respectively, and are briefly reviewed in this section.

The early attempts (Dawson and Walker 1972, Walker 1975) to model geometrical imperfections in isolated plate elements resulted in some generalized expressions by

fitting the available test data. Dawson and Walker (1972) studied three different forms to express the imperfection amplitude for simply supported plates:

$$\delta_o = \alpha\ t \tag{2.14a}$$

$$\delta_o = \beta\left(\sigma_y / \sigma_{cr}\right)^{0.5} t \tag{2.14b}$$

$$\delta_o = \gamma\left(\sigma_y / \sigma_{cr}\right)\ t \tag{2.14c}$$

where δ_o is the local imperfection amplitude, t is the plate thickness, σ_y is the yield stress, σ_{cr} is the plate critical buckling stress, and α, β and γ are constants. They found that α = 0.2, β = 0.2 and γ = 0.2 can provide the reasonably conservative fit to test data for cold-rolled carbon steel sections, and they concluded that the expression $\delta_o = \gamma\left(\sigma_y / \sigma_{cr}\right)\ t$ with a value of γ = 0.2 was the most suitable expression for simply supported plates and square hollow sections. To take account of the variation of edge restraints for various cross-sectional geometries of cold-formed steel members, Walker (1975) recommended the use of the expression $\delta_o = \beta\left(\sigma_y / \sigma_{cr}\right)^{0.5} t$ with a value of β = 0.3. Dawson and Walker's work has formed the basis for the later research on the characterization of local imperfections in cold-formed sections. For example, Gardner and Nethercot (2004a) recently adopted Dawson and Walker's expression $\delta_o = \gamma\left(\sigma_y / \sigma_{cr}\right)\ t$ to define local imperfection amplitudes for cold-rolled stainless steel rectangular hollow sections, but proposed the use of a new value of γ = 0.023 to achieve the best fit to the measurement data of local imperfection magnitudes and replaced the yield stress σ_y in the expression with the 0.2% proof stress $\sigma_{0.2}$.

The above early studies on geometrical imperfections in isolated plate elements were focused only on the modelling of imperfection amplitudes. More attention has been paid to the characterization of both imperfection shapes and magnitudes of plate elements, since the study by Schafer and Peköz (1998). Schafer and Peköz (1998) proposed both simple rules of thumb and a probabilistic treatment for determining the imperfection magnitudes for local and distortional modes. They also made use of the imperfection spectrum to generate artificial imperfections (or the so-called generalized imperfections) and to determine modal imperfection magnitudes. These proposals for the modelling of geometrical imperfections in isolated plate elements have often been adopted by researchers to characterize local and/or distortional mode imperfections in cold-formed members.

As summarized in Table 2.4, there have been many attempts to model geometrical imperfections in cold-formed columns (Dubina and Ungureanu 2002, Kaitila 2002, Young and Yan 2002a and 2002b, Narayanan and Mahendran 2003, Gardner and Nethercot 2004a, Telue and Mahendran 2004a and 2004b, Yan and Young 2004, Yang *et al*. 2004). Most of them (Dubina and Ungureanu 2002, Kaitila 2002, Gardner and Nethercot 2004a, Telue and Mahendran 2004a and 2004b, Yan and Young 2004, Yang *et al*. 2004) introduced both the global and the local (or distortional) geometrical imperfections into their numerical models to take account of the interaction between the global buckling mode and a local (or distortional) buckling mode. Some researchers (Kaitila 2002) even introduced multiple local modes to consider the possible additional interaction among the global mode and the multiple local modes.

In the above attempts, the local imperfection was often assumed to be affine with the lowest local eigenmode, and the global imperfection was usually assumed to be the same as either the scaled shape of the lowest global eigenmode or a prescribed sinusoidal imperfection. The local imperfection amplitude was usually given by the magnitude determined for isolated plate elements in compression (see Table 2.3). The global imperfection amplitude was usually given by the calibrated magnitude for the best prediction of member strength, or the maximum allowable initial out-of-straightness of 1/1000 times the member length (Bjorhovde 1992).

Concerning the modelling of geometrical imperfections for cold-formed beams, only a limited amount of work has been conducted (Pi and Trahair 1997, Pi *et al*. 1998, Avery *et al*. 2000, Wilkinson and Hancock 2002, Dubina and Ungureanu 2002), and these studies are summarized in Table 2.5. It can be seen that local imperfections were often not introduced in numerical models for beams. The global imperfection was usually modelled by the prescribed sinusoidal initial crookedness and the initial twist with the amplitudes consistent with the design code requirements for hot-rolled steel beams (e.g. AS4100 (AS 1990)). In comparison with the modelling of geometrical imperfections in columns, less attention has been paid to the characterization of local imperfections in beams. This difference may be possibly due to the fact that the interaction between the local modes and the global mode is more pronounced in columns than in beams. It has also been shown by Dubina and Ungureanu (2002) that the influence of local-sectional imperfections on lateral-torsional buckling is low, but global imperfections such as initial twists combined with initial deflections can affect the ultimate strength considerably.

2.5 MODELLING OF STRUCTURAL BEHAVIOUR

The load-carrying capacity of a cold-formed member is generally affected by geometrical and material imperfections. Material imperfections refer to residual stresses and different material properties for different parts of a cold-formed section, and result from the cold work of the manufacturing process. Modelling techniques for the material behaviour, residual stresses and geometrical imperfections have been reviewed in the preceding sections. For the accurate numerical modelling of the structural behaviour of cold-formed members, these modelling techniques need to be properly incorporated into the analysis.

There have been many studies (Ingvarsson 1975, Weng 1991, Weng and Lin 1992, Key and Hancock 1993, Abdel-Rahman and Sivakumaran 1997, Pi and Trahair 1997, Pi *et al*. 1998, Sivakumaran and Abdel-Rahman 1998, Dubina and Ungureanu 2002, Wilkinson and Hancock 2002, Young and Yan 2002a and 2002b, Narayanan and Mahendran 2003, Young 2004, Gardner and Nethercot 2004a) to model the structural behaviour of cold-formed members. In these studies, initial geometrical imperfections were often characterized by the imperfection measurement data or using the modelling techniques reviewed in the preceding section. To account for the cold work effect of the manufacturing process, many researchers (Ingvarsson 1975, Weng and Lin 1992, Key and Hancock 1993, Abdel-Rahman and Sivakumaran 1997, Pi and Trahair 1997, Pi *et al*. 1998, Sivakumaran and Abdel-Rahman 1998, Wilkinson and Hancock 2002, Gardner and Nethercot 2004a) used two different stress-strain curves respectively for the flat portions and the corner regions of cold-formed sections, together with the idealized residual stress distribution (Weng and Peköz 1990, Key

and Hancock 1993, Abdel-Rahman and Sivakumaran 1997, Schafer and Peköz 1998) interpreted from measured residual stresses.

Considering that corners usually form only a small proportion of the overall cross-sectional area of a cold-formed section, some researchers (Weng 1991, Dubina and Ungureanu 2002, Young and Yan 2002a and 2002b, Narayanan and Mahendran 2003, Young 2004) ignored the difference in the stress-strain behaviour between the flat portions and the corner regions, and also ignored the curvature of the rounded corners. Such omission may not be appropriate for cold-formed sections with greater corner areas, and the effect of cold work (e.g. strength enhancement) in the corners on the structural performance cannot be identified.

2.6 CONCLUSIONS

Based on the review of existing literature presented in this chapter, the following conclusions can be drawn:

(a) In existing design codes, the utilization of the enhanced material strength due to the cold work of the forming process is permitted only for fully effective sections.

(b) In a cold-formed channel section, the inner surface of the section is subject to compressive residual stresses while the outer surface is subject to tensile residual stresses. There are large variations in the magnitude of residual stresses in the flat portions.

(c) In the flat portions of a cold-formed channel section, longitudinal residual stresses are greater than transverse residual stresses. The latter are thus generally considered to be insignificant.

(d) In the modelling of residual stresses in cold-formed channel sections, the through-thickness variation of residual stresses has generally been assumed to be linear, and residual stresses have been assumed to consist of a bending component and a membrane component.

(e) In cold-formed square hollow sections, residual stresses across the thickness have been found to consist of three components: (1) the bending component, (2) the membrane component, and (3) the layering component.

(f) In the modelling of geometrical imperfections in cold-formed members in compression, both local and global imperfections are generally considered to take account of the interaction between local and global buckling modes. The lowest local eigenmode and the lowest global eigenmode are often used to define the shapes of local and global imperfections.

(g) In the modelling of geometrical imperfections in cold-formed members in bending, local imperfections are not always considered, as the influence of local-sectional imperfections on lateral-torsional buckling is small. Global imperfections are usually modelled by prescribed sinusoidal initial crookedness and initial twist with their amplitudes being consistent with design code requirements for hot-rolled steel beams.

(h) In the modelling of the structural behaviour of cold-formed members, two different stress-strain curves for the flat portions and the corner regions respectively are often used together with the idealized residual stress distribution to account for the cold work effect of the manufacturing process.

2.7 REFERENCES

Abdel-Rahman, N. and Sivakumaran, K. S. (1997). Material properties models for analysis of cold-formed steel members. *Journal of Structural Engineering, ASCE,* **123:9,** 1135-1143.

AISI (1996). *Cold-Formed Steel Design Manual*, 1996 edition, American Iron and Steel Institute, Washington, D.C.

AS (1990). *Steel Structures, AS 4100-1990*, Australian Standard, Standards Association of Australia, Sydney.

ASCE (2002). *Specification for the Design of Cold-Formed Stainless Steel Structural Members, SEI/ASCE 8-02*, American Society of Civil Engineers, New York.

Ashraf, M., Gardner, L. and Nethercot, D. A. (2005). Strength enhancement of the corner regions of stainless steel cross-sections. *Journal of Constructional Steel Research*, **61**, 37-52.

AS/NZS (1996). *Cold-Formed Steel Structures, AS/NZS 4600:1996*, Australian/New Zealand Standard, Standards Australia, Sydney.

AS/NZS (2001). *Cold-Formed Stainless Steel Structures, AS/NZS 4673:2001*, Australian/New Zealand Standard, Standards Australia, Sydney.

Avery, P., Mahendran, M. and Nasir, A. (2000). Flexural capacity of hollow flange beams. *Journal of Constructional Steel Research*, **53**, 201-223.

Batista, E. M. and Rodrigues, F. C. (1992). Residual stresses measurements on cold-formed profiles. *Experimental Techniques*, **Sept./Oct.,** 25-29.

Bjorhovde, R. (1992). Compression members. *Constructional Steel Design: An International Guide*, edited by Dowling, P. J., Harding, J. E. and Bjorhovde, R., Elsevier Science Ltd., United Kingdom.

BSI (1998). *Structural Use of Steelwork in Building – Part 5. Code of Practice for Design of Cold Formed Thin Gauge Sections, BS5950-5:1998*, British Standards Institution, London.

CEN (1996). *Eurocode 3: Design of Steel Structures – Part 1.3: General Rules – Supplementary Rules for Cold-Formed Thin Gauge Members and Sheeting, ENV 1993-1-3*, European Committee for Standardisation.

Chakrabarty, J., Lee, W. B. and Chan, K. C. (2000). An analysis of the plan-strain bending of an orthotropic sheet in the elastic/plastic range. *Journal of Materials Processing Technology*, **104,** 48-52.

Chakrabarty, J., Lee, W. B. and Chan, K. C. (2001). An exact solution for the elastic/plastic bending of anisotropic sheet metal under conditions of plane strain. *International Journal of Mechanical Sciences*, **43,** 1871-1880.

Coetsee, J. S., Van den Berg, G. J. and Van der Merwe, P. (1990). The effect of work hardening and residual stresses due to cold work of forming on the strength of cold-formed stainless steel lipped channel sections. *Proceedings of the Tenth International Specialty Conference on Cold-Formed Steel Structures*, St. Louis, Missouri, United States, October 23-24, 505-523.

Dawson, R. G. and Walker, A. C. (1972). Post-buckling of geometrically imperfect plates. *Journal of the Structural Division, ASCE*, **98:ST1**, 75-94.

Dempsey, R. I. (1993). *Hollow Flange Beam Member Design Manual*, Palmer Tube Mills Pty Ltd., Australia.

Dubina, D. and Ungureanu, V. (2002). Effect of imperfections on numerical simulation of instability behaviour of cold-formed steel members. *Thin-Walled Structures*, **40**, 239-262.

Gardner, L. (2002). *A New Approach to Structural Stainless Steel Design*, PhD Thesis, Department of Civil and Environmental Engineering, Imperial College, London, U.K.

Gardner, L. and Nethercot, D. A. (2004a). Numerical modelling of stainless steel structural components – A consistent approach. *Journal of Structural Engineering, ASCE*, **130:10,** 1586-1601.

Gardner, L. and Nethercot, D. A. (2004b). Experiments on stainless steel hollow sections – Part 1: Material and cross-sectional behaviour. *Journal of Constructional Steel Research*, **60**, 1291-1318.

Guggenberger, W. (1996). Effect of geometric imperfections taking into account the fabrication process and consistent residual stress fields of cylinders under local axial loads. *Imperfections in metal silos workshop,* Lyon, France, 19th April 1996, 219-231.

Ingvarsson, L. (1975). Cold-forming residual stresses – Effect on buckling. *Proceedings of the Third International Specialty Conference on Cold-Formed Steel Structures,* University of Missouri-Rolla, United States, Nov., 1975, 85-119.

Johnson, W. and Yu, T. X. (1981). Springback after the biaxial elastic-plastic pure bending of a rectangular plate – I. *International Journal of Mechanical Sciences,* **23:10,** 619-630.

Kaitila, O. (2002). Imperfection sensitivity analysis of lipped channel columns at high temperatures. *Journal of Constructional Steel Research*, **58**, 333-351.

Karren, K. W. (1967). Material properties models for analysis of cold-formed steel members. *Journal of the Structural Division, ASCE*, **93:ST1,** 401-432.

Karren, K. W. and Winter, G. (1967). Effect of cold-forming on light-gage steel members. *Journal of the Structural Division, ASCE*, **93:ST1,** 433-469.

Kato, B. and Aoki, H. (1978). Residual stresses in cold-formed tubes. *Journal of Strain analysis*, **13:4**, 193-204.

Key, P. W. and Hancock, G. J. (1993). A theoretical investigation of the column behaviour of cold- formed square hollow sections. *Thin-Walled Structures*, **16**, 31-64.

Kwon, Y. B. and Hancock, G. J., (1992). Tests of cold-formed channels with local and distortional buckling. *Journal of Structural Engineering, ASCE,* **117:7,** 1787-1803.

Macdonald, M., Rhodes, J. and Taylor, G. T. (2000). Mechanical properties of stainless steel lipped channels. *Proceedings of the Fifteenth International Specialty Conference on Cold-Formed Steel Structures*, St. Louis, Missouri, United States, October 19-20, 673-686.

Mirambell, E. and Real, E. (2000). On the calculation of deflections in structural stainless steel beams: An experimental and numerical investigation. *Journal of Constructional Steel Research*, **54**, 109-133.

Narayanan, R. and Chow, F. Y. (1984). Ultimate capacity of uniaxially compressed perforated plates. *Thin-Walled Structures*, **2**, 241-264.

Narayanan, S. and Mahendran, M. (2003). Ultimate capacity of innovative cold-formed steel columns. *Journal of Constructional Steel Research*, **59**, 489-508.

Olsson, A. (2001). *Stainless Steel Plasticity – Material Modelling and Structural Applications*, Doctoral Thesis, Division of Steel Structures, Department of Civil and Mining Engineering, Luleå University of Technology, Sweden.

Pi, Y. L. and Trahair, N. S. (1997). Lateral-distortional buckling of hollow flange beams. *Journal of Structural Engineering, ASCE*, **123:6,** 695-702.

Pi, Y. L., Put, B. M. and Trahair, N. S. (1998). Lateral buckling strengths of cold-formed channel section beams. *Journal of Structural Engineering, ASCE,* **124:10,** 1182-1191.

Pourboghrat, F. and Chu, E. (1995). Springback in plane strain stretch/draw sheet forming. *International Journal of Mechanical Sciences,* **36:3,** 327-341.

Rasmussen, K. J. R. (2003). Full-range stress-strain curves for stainless steel alloys. *Journal of Constructional Steel Research*, **59**, 47-61.

Rasmussen, K. J. R. and Hancock, G. J. (1993). Design of cold-formed stainless steel tubular members, I: Columns. *Journal of Structural Engineering, ASCE*, **119:8,** 2349-2367.

Rasmussen, K. J. R. and Rondal, J. (1997). Strength curves for metal columns. *Journal of Structural Engineering, ASCE*, **123:6**, 721-728.

Rasmussen, K. J. R. and Rondal, J. (1998). Explicit approach to design of stainless steel columns. *Journal of Structural Engineering, ASCE*, **123:7**, 857-863.

Rondal, J. (1987). Residual stresses in cold-rolled profiles. *Construction & Building Materials*, **1:3,** 150-164.

Rowlands, R. E. (1993). Residual stress. *Handbook on Experimental Mechanics*, 2nd revised edition, edited by Kobayashi, A. S., VCH publisher, New York, 785-828.

Schafer, B. W. and Peköz, T. (1998). Computational modelling of cold-Formed steel: Characterizing geometric imperfections and residual stresses. *Journal of Constructional Steel Research*, **47**, 193-210.

Sivakumaran, K. S. and Abdel-Rahman, N. (1998). A finite element analysis model for the behaviour of cold-formed steel members. *Thin-Walled Structures,* **31,** 305-324.

Tan, Z., Li, W. B. and Persson, B. (1994). On analysis and measurement of residual stresses in the bending of sheet metals. *International Journal of Mechanical Sciences,* **36:5,** 483-491.

Tan, Z., Persson, B. and Magnusson, C. (1995). Plastic bending of anisotropic sheet metals. *International Journal of Mechanical Sciences*, **37:4**, 405-421.

Telue, Y. and Mahendran, M. (2004a). Numerical modelling and design of unlined cold-formed steel wall frames. *Journal of Constructional Steel Research*, **60:8**, 1241-1256.

Telue, Y. and Mahendran, M. (2004b). Behaviour and design of cold-formed steel wall frames lined with plasterboard on both sides. *Engineering Structures*, **26**, 567-579.

Van den Berg, G. J. and Van der Merwe, P. (1992). Prediction of corner mechanical properties for stainless steels due to cold forming. *Proceedings of the Eleventh International Specialty Conference on Cold-Formed Steel Structures*, St. Louis, Missouri, United States, October 20-21, 571-586.

Walker, A. C. (1975). *Design and Analysis of Cold-Formed Sections*, International Textbook Company.

Weng, C. C. (1991). Effect of residual stress on cold-formed steel column strength. *Journal of Structural Engineering, ASCE*, **117:6,** 1622-1640.

Weng, C. C. and Lin, C. P. (1992). Study of maximum strength of cold-formed steel columns. *Journal of Structural Engineering, ASCE*, **118:1,** 128-146.

Weng, C. C. and Peköz, T. (1990). Residual stresses in cold-formed steel members. *Journal of Structural Engineering, ASCE*, **116:6,** 1611-1625.

Weng, C. C. and White, R. N. (1990a). Residual stresses in cold-bent thick steel plates. *Journal of Structural Engineering, ASCE*, **116:1**, 24-39.

Weng, C. C. and White, R. N. (1990b). Cold-bending of thick high-strength steel plates. *Journal of Structural Engineering, ASCE*, **116:1**, 40-54.

Wilkinson, T. and Hancock, G. J. (2002). Predicting the rotation capacity of cold-formed RHS beams using finite element analysis. *Journal of Constructional Steel Research*, **58**, 1455-1471.

Yan, J. and Young, B. (2004). Numerical investigation of channel columns with complex stiffeners – Part I: Test verification. *Thin-Walled Structures*, **42:6,** 883-893.

Yang, D., Hancock, G. J. and Rasmussen, K. J. R. (2004). Compression tests of cold-reduced high strength steel sections. II: Long columns. *Journal of Structural Engineering, ASCE*, **130:11**, 1782-1789.

Young, B. (2004). Design of channel columns with inclined edge stiffeners. *Journal of Constructional Steel Research*, **60**, 183-197.

Young B., and Rasmussen, K. J. R. (1995). *Compression Tests of Fixed-Ended and Pin-Ended Cold-Formed Lipped Channels, Research Report No. R715*, School of Civil and Mining Engineering, University of Sydney, Australia.

Young, B. and Yan, J. (2002a). Finite element analysis and design of fixed-ended plain channel columns. *Finite Elements in Analysis and Design*, **38**, 549-566.

Young, B. and Yan, J. (2002b). Channel columns undergoing local, distortional, and overall buckling. *Journal of Structural Engineering, ASCE*, **128:6,** 728-736.

Zhang, Z. T. and Hu, S. J. (1998). Stress and residual stress distributions in plane strain bending. *International Journal of Mechanical Sciences*, **40:6,** 533-534.

Table 2.1 Bending residual stresses as percentages of yield stress σ_y (reproduced from Schafer and Peköz 1998).

Element	Roll-formed steel sections		Press-braked steel sections	
	Mean	Variance	Mean	Variance
Corners	26.8	5.0	32.7	3.3
Edge stiffened elements (i.e. Flanges)	23.5	1.0	8.0	2.5
Lips	6.7	6.4	56.0*	11.6
Stiffened elements (i.e. Webs)	38.9	6.2	16.9	4.5
Note: *Some lips are flame-cut, thus distorting this value.				

Table 2.2 Membrane residual stresses as percentages of yield stress σ_y (reproduced from Schafer and Peköz 1998).

Element	Roll-formed steel sections		Press-braked steel sections	
	Mean	Variance	Mean	Variance
Corners	6.8	1.1	5.2	0.4
Edge stiffened elements (i.e. Flanges)	3.9	1.0	0.9	1.0
Lips	7.9	1.5	0.2	0.3
Stiffened elements (i.e. Webs)	-1.7	1.2	0.9	0.1

Table 2.3 Summary of modelling techniques for geometrical imperfections in isolated plate elements of cold-formed sections.

Approach	Shape	Amplitude	Remarks
Dawson and Walker (1972)	General shape	Given by any one of the following: (1) $0.2\,t$, (2) $0.2\sqrt{\sigma_y/\sigma_{cr}}\,t$, (3) $0.2(\sigma_y/\sigma_{cr})\,t$	Amplitude expression (3) is more rational than the other two expressions, and is recommended as the most suitable expression for simply supported plates and square hollow carbon steel sections.
Schafer and Peköz (1998)	Single eigenmode, or superposition of multiple eigenmodes (local and distortional modes)	Given by any one of the following: (1) Rules of thumb (2) Probabilistic approach using the observed imperfection magnitude data (3) Modal imperfection magnitude from the imperfection spectrum	Only the geometrical imperfections of isolated plate elements (i.e. stiffened webs, lipped or unstiffened flanges) were modelled.
Schafer and Peköz (1998)	Normalized artificial imperfection signals generated by the imperfection spectrum	Given by probabilistic approach using the observed imperfection magnitude data	Only the geometrical imperfections of isolated plate elements were modelled.
Sivakumaran and Abdel-Rahman (1998)	Double sine-wave imperfection for webs of cold-rolled channel sections. No prescription for the flanges and lips.	Maximum allowable imperfection magnitude for compression steel plates, from the British Steel Design Code*	The stub-column behaviour of lipped channel sections was considered, and only the webs were imposed with local geometrical imperfections.
Walker (1975)	General shape	$0.3\sqrt{P_y/P_{cr}}\,t$	The imperfection amplitude expression took into account variations of edge restraints for various geometries of cold-formed sections.

Note: L = column length, h = height of web, t = plate thickness, σ_y = yield stress, σ_{cr} = plate critical buckling stress.

* The maximum imperfection magnitude for plates in compression, suggested by the British Steel Design Code (Narayanan and Chow 1984): $\delta_o = 0.145(w/t)\sqrt{\sigma_y/E}\,t$, in which w = width of plate and E = elastic modulus.

Table 2.4 Summary of modelling techniques for geometrical imperfections in cold-formed columns.

Approach	Local and/or distortional imperfections		Global imperfections		Remarks
	Shape	Amplitude	Shape	Amplitude	
Dubina and Ungureanu (2002)	Selected local or distortional mode	Given by Schafer and Peköz's rules of thumb	Global sinusoidal flexural imperfection about the minor axis	L/1000	Influence of the shape of local-sectional imperfection on the interaction between the local-sectional mode and the global mode was studied.
Gardner and Nethercot (2004)	Lowest local eigenmode	*Square and rectangular hollow sections:* $0.023(\sigma_{0.2}/\sigma_{cr})\ t$ *Circular hollow sections:* $0.2t$	Lowest global eigenmode	L/2000	Pin-ended stainless steel hollow section columns were modelled.
Kaitila (2002)	Superposition of two or more closely spaced local eigenmodes (e.g. the combination of the 20th and 21st eigenmodes)	h/200 for the combined mode	Global flexural eigenmode about the major axis	L/500	An imperfection sensitivity study was carried out on a pin-ended lipped channel column attached to wall panels at each flange, loaded at high temperature.
Narayanan and Mahendran (2003)	Lowest eigenmode	*Local modes*: (1) Given by Schafer and Peköz's rules of thumb, or (2) Maximum allowable imperfection magnitude suggested by the British Steel Design Code * *Distortional modes*: Given by Schafer and Peköz's rules of thumb	Null	Null	Distortional buckling behaviour of a series of 1-m long innovative cold-formed columns was studied.

Table 2.4 Summary of modelling techniques for geometrical imperfections in cold-formed columns (continued).

Approach	Local and/or distortional imperfections		Global imperfections		Remarks
	Shape	Amplitude	Shape	Amplitude	
Telue and Mahendran (2004a, 2004b)	Local eigenmode and distortional eigenmode	Given by Schafer and Peköz's rules of thumb	Global flexural eigenmode about the minor axis	L/700 for 75-mm deep stud, L/1000 for 200-mm deep stud	Stud wall frame systems made of plain channels were modelled.
Yan and Young (2004)	First eigenmode (generally local buckling mode)	Not mentioned	Half-wave sinusoidal flexural imperfection about the minor axis	Measured magnitude at mid-length	Fixed-ended cold-formed steel channels with complex stiffeners were modelled.
Yang *et al*. (2004)	Lowest local eigenmode	Given by Walker (1975) **	Global imperfection represented by load eccentricity	L/1000	Pin-ended cold-reduced high strength steel columns of lipped-box sections were modelled.
Young and Yan (2002a, 2002b)	Lowest eigenmode (only if it is a local buckling mode), or null	$0.25t$ ***	Lowest eigenmode (only if it is a global buckling mode), or null	$0.25t$ ***	Fixed-ended plain channels and lipped channels were modelled.

Note: L = column length, h = height of web, t = plate thickness, $\sigma_{0.2}$ = 0.2% proof stress, σ_{cr} = plate critical buckling stress.

* The maximum imperfection magnitude for plates in compression, suggested by the British Steel Design Code (Narayanan and Chow 1984): $\delta_o = 0.145(w/t)\sqrt{\sigma_y / E}\ t$, in which w = width of plate, σ_y = yield stress, and E = elastic modulus.

** The imperfection amplitude for stiffened plate elements of cold-formed sections suggested by Walker (1975): $\delta_o = 0.3\sqrt{P_y / P_{cr}}\ t$, in which P_y = yield load, and P_{cr} = critical buckling load.

*** The magnitude of $0.25t$ was shown to provide good predictions for the test series, in terms of both the mean value and coefficient of variation (COV) for both column strengths and axial shortenings.

Table 2.5 Summary of modelling techniques for geometrical imperfections in cold-formed beams.

Approach	Local and/or distortional imperfections		Global imperfections		Remarks
	Shape	Amplitude	Shape	Amplitude	
Avery *et al*. (2000)	Any possible local buckling mode	Given by fabrication tolerances specified in Dempsey (1993)	Lateral distortional buckling mode	(1) L/1000 (which was based on the AS4100 fabrication tolerance for compression members), or (2) Measurement data	Cross-section distortions of hollow flange I beams were included by means of imperfections in lateral distortional buckling modes.
Dubina and Ungureanu (2002)	Selected shapes of local-sectional imperfection	Given by Schafer and Peköz's rules of thumb	Sinusoidal flexural imperfection about the minor axis and initial twist	Magnitudes of initial crookedness and twist for hot-rolled I beams given by AS4100 (AS 1990)	Influence of local-sectional imperfections on the interaction between the local-sectional mode and the global mode was studied.
Pi and Trahair (1997)	Null	Null	Sinusoidal initial crookedness and initial twist	Magnitudes of initial crookedness and twist consistent with AS4100 (AS 1990) for hot-rolled steel beams	Web distortions of hollow flange I beams were not considered.
Pi *et al*. (1998)	Null	Null	Sinusoidal initial crookedness and initial twist	Magnitudes of initial crookedness and twist consistent with AS4100 (AS 1990) for hot-rolled steel beams	Web distortions of lipped channel beams were also considered.
Wilkinson and Hancock (2001)	Sinusoidal bow-out imperfection on each face of a rectangular hollow section	Element width /500	Null	Null	The imperfection magnitude and the half-wavelength of the sinusoidal imperfection were adjusted to achieve a good match between the predicted moment-rotation curve and the experiment curve.

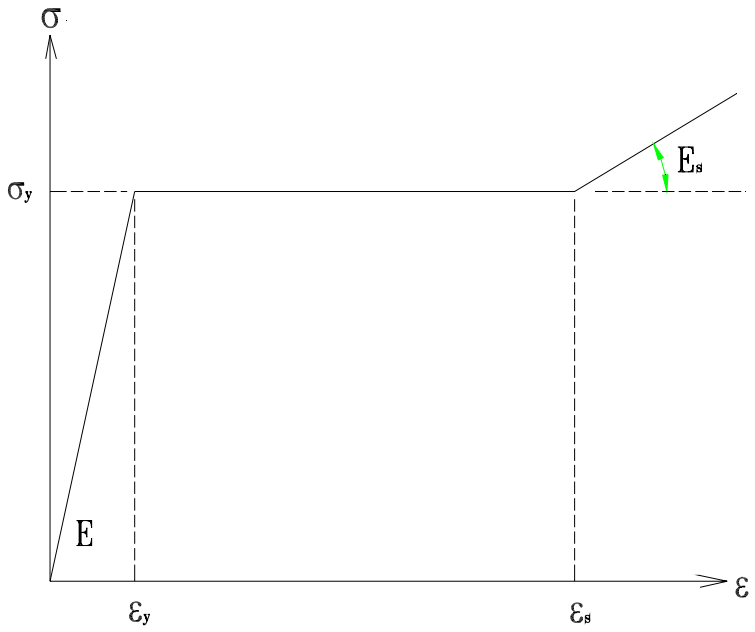

(a) Tri-linear elastic-plastic strain-hardening relationship for flat portions

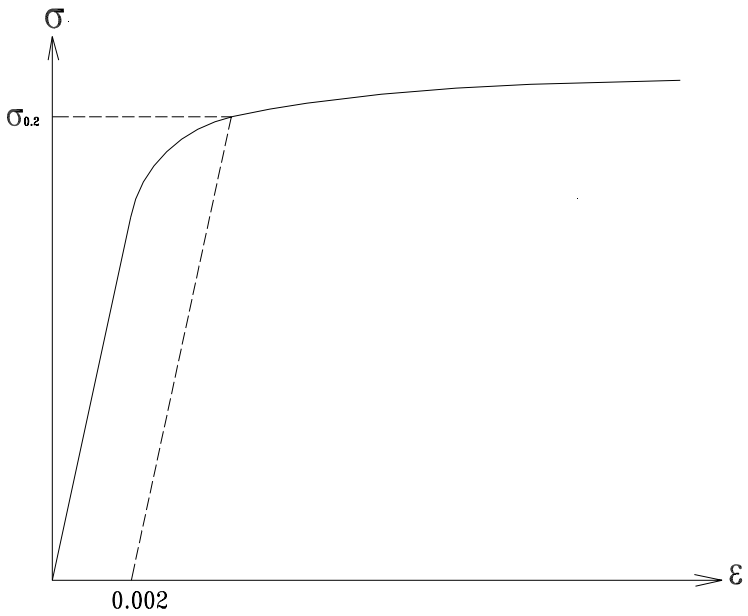

(b) Ramberg-Osgood relationship for corner regions

Figure 2.1 Stress-strain curves (reproduced from Pi and Trahair 1997, Pi *et al*. 1998).

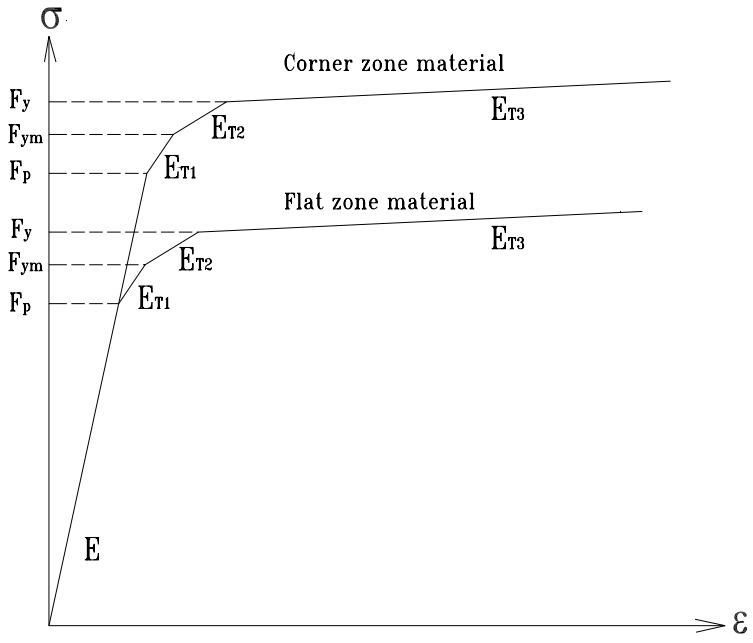

Figure 2.2 Multi-linear stress-strain curves (reproduced from Abdel-Rahman and Sivakumaran 1997).

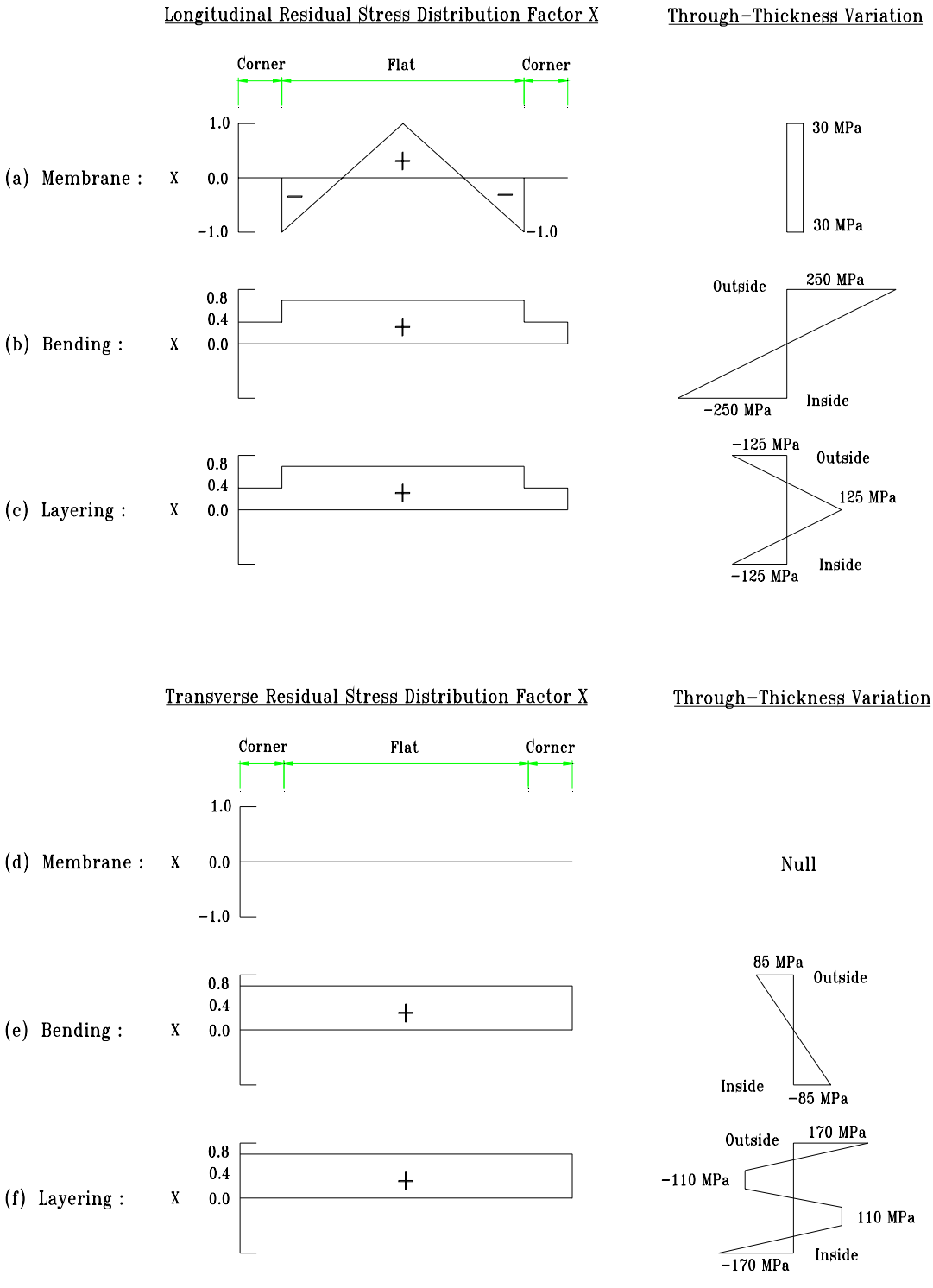

Figure 2.3 Idealized residual stress distributions in cold-formed steel square hollow sections (reproduced from Key and Hancock 1993).

Chapter 3

STRESS-STRAIN MODEL FOR STAINLESS STEEL

3.1 INTRODUCTION

In addition to material anisotropy, stainless steel is characterized by nonlinear stress-strain behaviour and different mechanical properties in tension and compression. A number of stress-strain models (Macdonald *et al*. 2000, Mirambell and Real 2000, Olsson 2001, Rasmussen 2003, Gardner and Nethercot 2004) have been developed to describe the nonlinear stress-strain behaviour of stainless steel alloys, but each of them is subjected to various limitations (see Chapter 2). This chapter is concerned with the development of a new stress-strain relationship for stainless steel alloys, which is capable of accurate predictions over full ranges of both tensile and compressive strains. The new stress-strain relationship is defined by the basic Ramberg-Osgood parameters (E_0 , $\sigma_{0.2}$ and n) only and is based on a careful interpretation of existing experimental data.

The work presented in this chapter was conducted to provide an accurate stress-strain model for use in the finite element simulation of the manufacturing process and in the subsequent buckling analysis of cold-formed stainless steel members. This advanced finite element analysis of cold-formed stainless steel sections requires a stress-strain relationship that is accurate for small and intermediate strains in the regime of general structural response under loading, as well as for large strains in the regime of cold

bending during the manufacturing process. The new stress-strain relationship was developed to fulfil these requirements, which are not met by existing stress-strain models (refer to Chapter 2).

3.2 RECENT APPROACHES

Recent approaches to the modelling of stress-strain relationships (Macdonald *et al*. 2000, Mirambell and Real 2000, Olsson 2001, Rasmussen 2003, Gardner and Nethercot 2004) have been reviewed in Chapter 2. Among the reviewed approaches, most of them (Macdonald *et al*. 2000, Mirambell and Real 2000, Olsson 2001) are incapable of predicting the compressive stress-strain relationship over the full range of strains. Gardner and Nethercot (2004) presented an accurate expression for the nominal stress-strain relationships for both tension and compression, up to relatively high strains (of about 10% for tension and of about 2% for compression), but their expression may not be capable of accurate predictions for higher strains associated with the plastic straining of cold bending at corners of cold-formed stainless steel sections. Therefore, Gardner and Nethercot's expression was adopted in this study as the basis for further development to arrive at a stress-strain relationship that covers the entire ranges of both tensile and compressive strains.

It is highly desirable that a stress-strain relationship for stainless steel alloys over full ranges of strains is defined in terms of the Ramberg-Osgood parameters (E_0, $\sigma_{0.2}$ and n) only, since these parameters are generally available in the current design codes (AS/NZS 2001, ASCE 2002). Except the full-range stress-strain model of

Rasmussen (2003), all the reviewed stress-strain models for wide strain ranges cannot be simply described by the basic Ramberg-Osgood parameters (E_0, $\sigma_{0.2}$ and n) only. Rasmussen's approach is attractive as the stress-strain curve can be constructed over the entire strain range by the basic Ramberg-Osgood parameters and is regarded as applicable to all alloys in both tension and compression. The agreement between test curves (mostly from tension coupon tests) and the full-range stress-strain relationship of Rasmussen (2003) was shown to be generally excellent. However, the expressions for σ_u and ε_u (Eqs. (2.12e) and (2.12f)) were developed by interpreting the test data of tension coupons and the expression for the strain-hardening exponent *m* (Eq. (2.12g)) was obtained by trial and error using stress-strain curves which were mostly from tension coupon tests. Hence, the applicability of this full-range model to stainless steel in compression has not been properly demonstrated.

Indeed, when the full-range stress-strain curves from Rasmussen (2003) are compared with the measured stress-strain curves (see Figures 3.1~3.8) from the existing literature (Korvink *et al*. 1995, Macdonald *et al*. 2000, Rasmussen *et al*. 2002 and 2003, Gardner and Nethercot 2004), it can be found that the full-range model of Rasmussen (2003) can generally provide excellent predictions for tension coupon tests but underestimates the stresses at strains $\varepsilon > \varepsilon_{0.2}$ for most compression coupon tests; the difference between the experimental and the modelled stress-strain curves increases with the strain. For this reason, Rasmussen's full-range stress-strain model was not adopted in this study.

3.3 3-STAGE FULL-RANGE STRESS-STRAIN MODEL

3.3.1 Expression for stress-strain relationships

The observation made by Olsson (2001) suggests that the true stress-nominal strain curve can be modelled as a straight line for strains exceeding $\varepsilon_{2.0}$. Olsson's approach possesses the simplicity in treating the stress-strain relationship for high strains, but its drawback is the compromised accuracy in the important strain range of $\varepsilon < \varepsilon_{0.2}$. Hence, in the present study, Gardner and Nethercot's approach (see Eqs. (2.10) and (2.13)) was adopted to model the nominal stress-strain relationship up to $\varepsilon_{2.0}$, as they (Gardner and Nethercot 2004) have already shown that their model can provide excellent predictions up to approximately a tensile strain of 10% and about a compressive strain of 2%. It can be found that the curve defined by the Eq. (2.13) does not pass through the point of the 1% proof stress $\sigma_{1.0}$ exactly at the corresponding total strain $\varepsilon_{1.0}$. However, the errors induced are negligible. To maintain consistency, Eq. (2.13) is thus rewritten for the strain range $\varepsilon_{0.2} < \varepsilon < \varepsilon_{2.0}$ as

$$\varepsilon = \frac{\sigma - \sigma_{0.2}}{E_{0.2}} + \left[0.008 + \left(\sigma_{1.0} - \sigma_{0.2}\right)\left(\frac{1}{E_0} - \frac{1}{E_{0.2}}\right)\right]\left(\frac{\sigma - \sigma_{0.2}}{\sigma_{1.0} - \sigma_{0.2}}\right)^{n'_{0.2,1.0}} + \varepsilon_{0.2}, \quad \sigma_{0.2} < \sigma < \sigma_{2.0} \tag{3.1}$$

By taking advantage of Olsson's simplified treatment for $\varepsilon > \varepsilon_{2.0}$, the nominal stress-strain relationship for nominal strains $\varepsilon > \varepsilon_{2.0}$ is modelled by assuming that the corresponding true stress-nominal strain curve is a straight line passing through the

points of the 2% proof stress at $\varepsilon_{2.0}$ and the ultimate strength at ε_u. Since the slope of the true stress-nominal strain curve over the strain range $\varepsilon_{2.0} < \varepsilon < \varepsilon_u$ does not show much variation as indicated by Olsson's observation, this assumption is acceptable. In particular, within the context of the present study, the stress-strain relationship for $\varepsilon > \varepsilon_{2.0}$ was needed only in the numerical simulation of the manufacturing process (i.e. cold bending at corners). Small inaccuracies of the stress-strain relationship in such numerical simulations produce negligible errors.

The true stress-nominal strain relationship for $\varepsilon > \varepsilon_{2.0}$ can then be formulated as

$$\sigma_t = a + b\varepsilon \tag{3.2}$$

in which σ_t is the true stress, ε is the nominal strain, a and b are constants which can be obtained from values at the boundary points $(\sigma_{t2.0}, \varepsilon_{2.0})$ and $(\sigma_{tu}, \varepsilon_u)$. $\sigma_{t2.0}$ and σ_{tu} are the 2% true proof stress and the true ultimate strength, while $\varepsilon_{2.0}$ and ε_u are the 2% nominal total strain and the nominal ultimate strain. The true stress σ_t and the true strain ε_t can be converted to the nominal stress σ and the nominal strain ε by following relationships for both tension and compression tests (Chakrabarty 2000):

$$\sigma_t = \sigma(1 \pm \varepsilon) \tag{3.3a}$$

$$\varepsilon_t = \pm \ln(1 \pm \varepsilon) \tag{3.3b}$$

where the upper sign corresponds to tension, the lower sign to compression, and σ, ε, σ_t and ε_t are absolute values for both tension and compression tests.

By substituting Eq. (3.3a) into Eq. (3.2) and using the boundary values of stresses and strains, the constants a and b can be determined:

$$a = \sigma_{2.0}\left(1 \pm \varepsilon_{2.0}\right) - b\varepsilon_{2.0} \tag{3.4a}$$

$$b = \frac{\sigma_u\left(1 \pm \varepsilon_u\right) - \sigma_{2.0}\left(1 \pm \varepsilon_{2.0}\right)}{\varepsilon_u - \varepsilon_{2.0}} \tag{3.4b}$$

with

$$\varepsilon_{2.0} = \frac{\sigma_{2.0}}{E_0} + 0.02 \tag{3.4c}$$

where the upper sign corresponds to tension, and the lower sign to compression.

Making use of Eqs. (3.2) and (3.3a), the nominal stress-strain relationship can be obtained as

$$\sigma = \frac{a + b\varepsilon}{1 \pm \varepsilon}, \qquad \varepsilon > \varepsilon_{2.0} \tag{3.5a}$$

or

$$\varepsilon = \frac{\sigma - a}{b \mp \sigma}, \qquad \sigma > \sigma_{2.0} \tag{3.5b}$$

in which the upper sign corresponds to tension, and the lower sign to compression.

Finally, the 3-stage nominal stress-strain model can be written over the full ranges of both tensile and compressive strains as

$$\varepsilon = \begin{cases} \dfrac{\sigma}{E_0} + 0.002\left(\dfrac{\sigma}{\sigma_{0.2}}\right)^n, & \sigma \le \sigma_{0.2} \\ \dfrac{\sigma-\sigma_{0.2}}{E_{0.2}} + \left[0.008 + \left(\sigma_{1.0}-\sigma_{0.2}\right)\left(\dfrac{1}{E_0}-\dfrac{1}{E_{0.2}}\right)\right]\left(\dfrac{\sigma-\sigma_{0.2}}{\sigma_{1.0}-\sigma_{0.2}}\right)^{n'_{0.2,1.0}} + \varepsilon_{0.2}, & \sigma_{0.2} < \sigma \le \sigma_{2.0} \\ \dfrac{\sigma-a}{b \mp \sigma}, & \sigma > \sigma_{2.0} \end{cases} \tag{3.6}$$

It is desirable to characterize the above full-range stress-strain relationship using only the basic Ramberg-Osgood parameters (E_0, $\sigma_{0.2}$ and n), since the values of other parameters including $\sigma_{1.0}$, $\sigma_{2.0}$, $n'_{0.2,1.0}$, σ_u and ε_u are not always available in existing design codes, especially those for the compressive stress-strain behaviour. Therefore, these additional parameters in Eq. (3.6) need to be expressed in terms of the basic Ramberg-Osgood parameters (E_0, $\sigma_{0.2}$ and n) or ($e = \sigma_{0.2}/E_0$ and n). Expressions for these parameters in terms of the basic Ramberg-Osgood parameters are presented below.

3.3.2 Expression for $\sigma_{2.0}$

As Gardner and Nethercot's model has been adopted for strains up to $\varepsilon_{2.0}$, the 2% proof stress $\sigma_{2.0}$ can be determined by setting the boundary values (σ, ε) to $(\sigma_{2.0}, \varepsilon_{2.0})$ in Eq. (3.1), which leads to the following expression:

$$\sigma_{2.0} = \sigma_{0.2} + (\sigma_{1.0} - \sigma_{0.2}) A^{1/n'_{0.2,1.0}} \left[1 - \frac{(1/E_{0.2} - 1/E_0)\sigma_{2.0}}{B} \right]^{1/n'_{0.2,1.0}} \tag{3.7a}$$

with

$$A = \frac{B}{0.008 + e(\sigma_{1.0}/\sigma_{0.2} - 1)(1 - E_0/E_{0.2})} \tag{3.7b}$$

$$B = 0.018 + e\left(\frac{E_0}{E_{0.2}} - 1 \right) \tag{3.7c}$$

Since $\sigma_{2.0}$ exists on both sides of Eq. (3.7a), an explicit expression for $\sigma_{2.0}$ cannot be obtained from Eq. (3.7a). An approximation of $\sigma_{2.0}$ by an explicit expression is thus desirable. As $\left|(1/E_{0.2} - 1/E_0)\sigma_{2.0}/B\right| < 1$ and $n'_{0.2,1.0} > 1$ for the typical ranges of the basic parameters (e , n), the binomial expansion of the term $\left[1 - (1/E_{0.2} - 1/E_0)\sigma_{2.0}/B\right]^{1/n'_{0.2,1.0}}$ in Eq. (3.7a) results in an infinite convergent series:

$$\begin{aligned} \left[1 - \frac{(1/E_{0.2} - 1/E_0)\sigma_{2.0}}{B} \right]^{1/n'_{0.2,1.0}} &= 1 - \left(\frac{1}{n'_{0.2,1.0}} \right) \frac{(1/E_{0.2} - 1/E_0)\sigma_{2.0}}{B} \\ &\quad + \frac{1}{2} \left(\frac{1}{n'_{0.2,1.0}} \right) \left(\frac{1}{n'_{0.2,1.0}} - 1 \right) \frac{(1/E_{0.2} - 1/E_0)^2 \sigma_{2.0}^2}{B^2} - \cdots \end{aligned} \tag{3.8}$$

By keeping the first two terms of the infinite series in Eq. (3.8) and then substituting it into Eq. (3.7a), an approximation of $\sigma_{2.0}$ can be obtained as

$$\sigma_{2.0} \cong \frac{1 + (\sigma_{1.0}/\sigma_{0.2} - 1) A^{1/n'_{0.2,1.0}}}{1 + e(E_0/E_{0.2} - 1)(\sigma_{1.0}/\sigma_{0.2} - 1) \dfrac{A^{1/n'_{0.2,1.0}}}{n'_{0.2,1.0} B}} \sigma_{0.2} \tag{3.9}$$

in which $E_{0.2}/E_0 = 1/(1+0.002n/e)$, $\sigma_{1.0}/\sigma_{0.2}$ and $n'_{0.2,1.0}$ are given by Eqs. (3.11) and (3.12) presented later.

The relative error in $\sigma_{2.0}$ due to the approximation given by Eq. (3.9) tends to increase, as n increases and e decreases. According to existing design codes, the values of e typically vary from 0.001 to 0.003, and the values of n vary from 3 to 10 for austenitic and duplex alloys and can reach 16 for ferritic alloys. Within these ranges, the maximum relative error due to this approximation is about 3% for austenitic and duplex alloys and about 5% for ferritic alloys. Such small errors can be considered as negligible. If higher accuracy is desired, a more accurate value of $\sigma_{2.0}$ can be determined by substituting the approximation obtained from Eq. (3.9), into the right-hand side of Eq. (3.7a).

3.3.3 Expressions for $\sigma_{1.0}$ and $n'_{0.2,1.0}$

In order to establish the expressions for $\sigma_{1.0}$ and $n'_{0.2,1.0}$ in terms of the parameters e and n, experimental data from coupons tests were analysed for their relationships. Among the available test data, only the test data of austenitic and duplex alloys reported by the Steel Construction Institute (SCI 1991) and Gardner and Nethercot (2004) contain values of both the 1% proof stress $\sigma_{1.0}$ and the basic Ramberg-Osgood parameters (E_0, $\sigma_{0.2}$ and n), and only the test data of austenitic alloys reported by Gardner and Nethercot (2004) contain values of $n'_{0.2,1.0}$. Hence, the test data from the

Steel Construction Institute (SCI 1991) and Gardner and Nethercot (2004) were used to develop the expression for $\sigma_{1.0}$, while the test data from Gardner and Nethercot (2004) were used to develop the expression for $n'_{0.2,1.0}$.

Both the Steel Construction Institute (SCI 1991) and Gardner and Nethercot (2004) did not report the complete stress-strain curves. The Steel Construction Institute's report includes test data for 112 tension and 117 compression coupon tests in both the longitudinal and transverse directions, on austenitic (equivalent to grades UNS30403 and UNS31603 in accordance with ASTM E527-83 (ASTM 2003)) and duplex (equivalent to grade UNS31803) alloys of various thicknesses (from 2 mm to 12 mm). Gardner and Nethercot (2004) tested 54 tension coupons and 56 compression coupons cut from the flat portion of each face of SHS and RHS members in grade 1.4301 austenitic stainless steel in accordance with European material standard BS EN 10088-1 (BSI 1995) (equivalent to grade UNS30400 in accordance with ASTM E527-83 (ASTM 2003)), but only the weighted average properties for each section were reported, leading to a total of 15 sets of test data for tension coupons and 16 sets for compression coupons. They also reported the test results of 5 additional tension coupons taken from corner regions, which are not discussed here.

A total of 127 sets of test data for tension coupons and 133 sets for compression coupons on austenitic and duplex alloys were analysed to develop an expression for $\sigma_{1.0}$. For these test data, the values of n range from 2.9 to 13.7, and the values of the non-dimensional proof stress e $(=\sigma_{0.2}/E_0)$ range from 0.0011 to 0.0032. As the 1% proof stress $\sigma_{1.0}$ can be considered to depend on the basic parameters e and n, the

correlation between $\sigma_{1.0}/\sigma_{0.2}$ and e and n should exist and can be studied by means of the correlation coefficient $\rho_{X,Y}$. By treating $\sigma_{1.0}/\sigma_{0.2}$ and $1/n$ (or e) as discrete random variables X and Y, the correlation coefficient $\rho_{X,Y}$ can be calculated from Eq. (3.10):

$$\rho_{X,Y} = \frac{E(XY) - \mu_X \mu_Y}{\sigma_X \cdot \sigma_Y} \tag{3.10a}$$

with

$$E(XY) = \sum_{all\ x_i} \sum_{all\ y_j} x_i y_j p_{X,Y}(x_i, y_j) \tag{3.10b}$$

where μ_X and μ_Y are the means of the discrete random variables X and Y respectively, σ_X and σ_Y are the standard deviations of X and Y respectively, each combination of x_i and y_j represents the values of X and Y for one sampling point (or one data point), and $p_{X,Y}(x_i, y_j)$ is the joint probability mass function (PMF) and equals to $1/N$ for each of N sampling points (or N sets of test data) in which all sampling points are assumed to be equally likely. The correlation coefficient $\rho_{X,Y}$ represents the degree of linear dependence between two random variables X and Y. Values of $\rho_{X,Y}$ vary between –1 and +1. Negative values of $\rho_{X,Y}$ indicate a negative relationship between X and Y. It is suggested that two random variables X and Y can be considered to be uncorrelated or to possess some form of nonlinear relationship if $|\rho_{X,Y}| < 0.3$; they can be considered to be perfectly correlated if $|\rho_{X,Y}| > 0.9$ (Haldar and Mahadevan 2000).

By analysing the test data, it can be found that the data points for tension coupons and those for compression coupons vary in two different ways, but the test data for both longitudinal and transverse coupons vary in the same trend. Hence, the test data for tension coupons and those for compression coupons were treated separately. The correlation coefficients of $\sigma_{1.0}/\sigma_{0.2}$ and $1/n$ (or e) for both tension and compression coupons are shown in Table 3.1. It can be seen that for both tension and compression coupons, the correlation coefficients of $\sigma_{1.0}/\sigma_{0.2}$ and e are quite small, and their absolute values $|\rho_{X,Y}|$ are much smaller than 0.3. The correlation coefficient of $\sigma_{1.0}/\sigma_{0.2}$ and $1/n$ is quite large (= 0.82) for compression coupons, but smaller (= 0.62) for tension coupons. These results imply that linear relationships between $\sigma_{1.0}/\sigma_{0.2}$ and $1/n$ could be established for tension and compression coupons with different degrees of adequacy. By linear regression (see Figure 3.8), the following expressions were obtained:

$$\frac{\sigma_{1.0}}{\sigma_{0.2}} = 0.542\frac{1}{n} + 1.072 \quad \text{for tension coupons} \tag{3.11a}$$

$$\frac{\sigma_{1.0}}{\sigma_{0.2}} = 0.662\frac{1}{n} + 1.085 \quad \text{for compression coupons} \tag{3.11b}$$

As indicated in Figure 3.8, the above expressions for $\sigma_{1.0}/\sigma_{0.2}$ can provide predictions with maximum deviations from the test data being about $\pm 6\%$ for both tension and compression coupons.

To establish the expression for $n'_{0.2,1.0}$, 15 sets of test data for tension coupons and 16 sets for compression coupons of austenitic alloys were analysed. For these test data, the values of *n* range from 3.5 to 11.5, while the values of *e* range from 0.0013 to 0.0032. The strain-hardening exponent $n'_{0.2,1.0}$ controls the shape of the nominal stress-strain curve passing through $\sigma_{0.2}$ and $\sigma_{1.0}$, and can be considered to depend on the tangent modulus $E_{0.2}$ at the 0.2% proof stress and the value of the 1% proof stress $\sigma_{1.0}$ relative to the 0.2% proof stress $\sigma_{0.2}$. Their correlations can be studied by treating $n'_{0.2,1.0}$, $E_{0.2}/E_0$ [$=1/(1+0.002n/e)$] and $\sigma_{1.0}/\sigma_{0.2}$ as discrete random variables. As shown in Table 3.2, the correlation coefficients of $n'_{0.2,1.0}$ and $E_{0.2}/E_0$ for both tension and compression coupons are greater than 0.9, which implies that $n'_{0.2,1.0}$ and $E_{0.2}/E_0$ are perfectly correlated by a linear relationship. The correlation coefficient of $n'_{0.2,1.0}$ and $\sigma_{1.0}/\sigma_{0.2}$ for compression coupons is also quite large (= 0.81), but its value for tension coupons is relatively small (= 0.41). Nevertheless, positive correlations do exist between $n'_{0.2,1.0}$ and $E_{0.2}/E_0$, and between $n'_{0.2,1.0}$ and $\sigma_{1.0}/\sigma_{0.2}$.

Physically, $n'_{0.2,1.0}$ should not depend on either $E_{0.2}/E_0$ or $\sigma_{1.0}/\sigma_{0.2}$ alone. It should depend on both $E_{0.2}/E_0$ and $\sigma_{1.0}/\sigma_{0.2}$, even though $n'_{0.2,1.0}$ has been shown to be perfectly correlated to $E_{0.2}/E_0$. Therefore, the correlation coefficient of $n'_{0.2,1.0}$ and $(E_{0.2}/E_0)(\sigma_{1.0}/\sigma_{0.2})$ also needs to be studied and its values for both tension and compression coupons are greater than 0.9 as shown in Table 3.2. This implies that $n'_{0.2,1.0}$ and $(E_{0.2}/E_0)(\sigma_{1.0}/\sigma_{0.2})$ are also perfectly correlated. As indicated above, it is

more desirable to establish a linear relationship between $n'_{0.2,1.0}$ and $(E_{0.2}/E_0)(\sigma_{1.0}/\sigma_{0.2})$. By linear regression (see Figure 3.2), their relationship is obtained as

$$n'_{0.2,1.0} = 12.255\left(\frac{E_{0.2}}{E_0}\right)\left(\frac{\sigma_{1.0}}{\sigma_{0.2}}\right) + 1.037 \quad \text{for tension coupons} \tag{3.12a}$$

$$n'_{0.2,1.0} = 6.399\left(\frac{E_{0.2}}{E_0}\right)\left(\frac{\sigma_{1.0}}{\sigma_{0.2}}\right) + 1.145 \quad \text{for compression coupons} \tag{3.12b}$$

in which $E_{0.2}/E_0 = 1/(1+0.002\,n/e)$ and $\sigma_{1.0}/\sigma_{0.2}$ is given by Eq. (3.11). As indicated in Figure 3.9, the above expressions for $n'_{0.2,1.0}$ can provide predictions with the maximum deviations from the test data being about $\pm 10\%$ for both tension and compression coupons.

Ferritic alloys are characterized by n values which are generally larger than those for austenitic and duplex alloys, varying from about 6.5 to 16 according to AS/NZS 4673 (AS/NZS 2001). Although the database used for developing Eq. (3.11) covers only austenitic and duplex alloys, the n values of the test data range from 2.9 to 13.7, which also cover the major practical range of the n values for ferritic alloys. Hence, Eq. (3.11) can be considered to be applicable to ferritic alloys with acceptable accuracy.

Similarly, though the database used for developing Eq. (3.12) covers only austenitic alloys, the n values of the test data range from 3.5 to 11.5, which also cover the major practical range of n values for duplex and ferritic alloys. Hence, Eq. (3.12) can

also be considered to be applicable to duplex and ferritic alloys with reasonable accuracy.

3.3.4 Expressions for σ_u and ε_u

The empirical expressions for σ_u and ε_u proposed by Rasmussen (2003), in terms of the basic parameters e and n, are considered to be applicable to tension coupon tests but the use of them for compression coupon tests is not justifiable, since these expressions were developed by interpreting the test data of tension coupons, which also included test data from the Steel Construction Institute (SCI 1991). Therefore, in this study, Rasmussen's expressions for σ_u and ε_u are adopted only for tensile strains:

$$\frac{\sigma_u^{ten}}{\sigma_{0.2}^{ten}} = \frac{1}{0.2 + 185e^{ten}} \quad \text{for austenitic and duplex alloys} \qquad (3.13a)$$

$$\frac{\sigma_u^{ten}}{\sigma_{0.2}^{ten}} = \frac{1 - 0.0375\left(n^{ten} - 5\right)}{0.2 + 185e^{ten}} \quad \text{for all alloys} \qquad (3.13b)$$

$$\varepsilon_u^{ten} = 1 - \frac{\sigma_{0.2}^{ten}}{\sigma_u^{ten}} \qquad (3.13c)$$

in which the superscript "*ten*" indicates tension, σ_u^{ten} and ε_u^{ten} are the nominal ultimate tensile stress and the nominal ultimate tensile strain, e^{ten} and n^{ten} are the basic parameters e and n, and $\sigma_{0.2}^{ten}$ is the 0.2% nominal proof stress.

There is sufficient experimental evidence to suggest that the macroscopic stress-strain curve of metal in simple compression coincides with that in simple tension when the true stress is plotted against the true strain (Cottrell 1964, Kalpakjian 1991, Chakrabarty 2000). The supporting experimental evidence was generally obtained by careful testing of solid cylindrical specimens and comparing the true stress-true strain data in tension and compression for high strains, e.g. greater than 2% approximately (Cottrell 1964). Although stainless steel alloys are characterized by different stress-strain responses under tension and compression, this difference in material behaviour has been observed on the basis of comparisons of nominal stress-strain data up to strains of about 2% only, since test data from compression tests on flat coupons are normally available only up to a 2% compressive strain.

Therefore, it is reasonable to assume that the true stress-strain curve of a stainless steel alloy in uniaxial compression coincides with that in uniaxial tension at sufficiently large strains such as the ultimate tensile strain. This assumption means that the true ultimate compressive strength σ_{tu}^{com} and the true ultimate compressive strain ε_{tu}^{com} could be approximated by the corresponding true ultimate tensile strength σ_{tu}^{ten} and true ultimate tensile strain ε_{tu}^{ten}:

$$\sigma_{tu}^{com} \cong \sigma_{tu}^{ten} = \sigma_{u}^{ten}\left(1+\varepsilon_{u}^{ten}\right) \tag{3.14a}$$

$$\varepsilon_{tu}^{com} \cong \varepsilon_{tu}^{ten} = \ln\left(1+\varepsilon_{u}^{ten}\right) \tag{3.14b}$$

in which the superscripts "*ten*" and "*com*" indicate tension and compression respectively. It should be noted that ductile materials, such as stainless steels, do not

possess a definite ultimate compressive strength. Instead, the compressive strength is an arbitrary value dependent on the degree of deformation (Davis *et al*. 1982). Hence, the true ultimate compressive strength σ_{tu}^{com} and the true ultimate compressive strain ε_{tu}^{com} in Eq. (3.14), represent an artificially defined point located on the compressive stress-strain curve, rather than an ultimate point corresponding to material rupture.

By combining Eqs. (3.3) and (3.14), the nominal ultimate compressive stress σ_u^{com} and the nominal ultimate compressive strain ε_u^{com} can be obtained as

$$\sigma_u^{com} \cong \sigma_u^{ten}\left(1+\varepsilon_u^{ten}\right)^2 \tag{3.15a}$$

$$\varepsilon_u^{com} \cong 1-\frac{1}{1+\varepsilon_u^{ten}} \tag{3.15b}$$

in which σ_u^{ten} and ε_u^{ten} are given by Eq. (3.13). Finally, the parameters σ_u and ε_u in Eq. (3.4) are given by σ_u^{ten} and ε_u^{ten} (Eq. (3.13)) for tensile strains and by σ_u^{com} and ε_u^{com} (Eqs. (3.13) and (3.15)) for compressive strains, which eventually leads to values of the constants a and b in the 3-stage stress-strain curve (see Eqs. (3.4) and (3.6)).

3.4 COMPARISON WITH TEST DATA

Totally 39 experimental stress-strain curves available in the existing literature were used to assess the accuracy of the proposed 3-stage stress-strain model. The test data

include results from both tension and compression coupon tests on different alloys: 31 tests on austenitic alloys, 4 tests on duplex alloys and 4 tests on ferritic alloys. The measured values of the basic Ramberg-Osgood parameters for these 39 tests are summarized in Table 3.3. Although some other test data have been reported in Mirambell and Real (2000) and Olsson (2001), which also contain the experimental stress-strain curves, the values of n reported in these studies were calculated in accordance with different definitions. Therefore, their test data have not been included for comparison.

Gardner and Nethercot (2004) only reported the weighted averages of measured material properties for each hollow section, rather than the complete stress-strain curves, and they concluded that their proposed stress-strain model could provide excellent predictions of the experimental data up to about a 10% tensile strain and a 2% compressive strain. For this reason, the “experimental” stress-strain curves shown in Figures 3.2 and 3.3 for their tests were re-produced using their proposed model and the measured material properties for tensile strains up to 10% and compressive strains up to 2%. The measured values of all parameters needed by their proposed model (see Eq. (2.13)) can be found in Gardner and Nethercot (2004).

In obtaining stress-strain curves using the proposed 3-stage stress-strain model for comparison, the values of the basic Ramberg-Osgood parameters shown in Table 3.3 were used. Furthermore, Eq. (3.13a) was used to determine the ultimate stress for austenitic and duplex alloys, while Eq. (3.13b) was used for ferritic alloys. Representative comparisons between the proposed stress-strain model and the experimental stress-strain curves were shown in Figures 3.1~3.7. The whole set of

comparisons can be found in Appendix A. The proposed stress-strain model is generally in good agreement with the experimental stress-strain curves over wide ranges of both tensile and compressive strains. Typical nominal stress-strain curves for stainless steel defined by the proposed stress-strain model (Eq. (3.6)) are shown in Figure 3.10 for the full ranges of tensile and compressive strains, while the corresponding true stress-strain curves are shown in Figure 3.11.

3.5 CONCLUSIONS

The effect of cold work on the load resistance of cold-formed stainless steel members can be studied using advanced finite element analysis which includes the numerical simulation of the manufacturing process and the subsequent buckling analysis of the cold-formed member. Numerical simulation of the manufacturing process (i.e. cold bending at corners) requires the knowledge of the stress-strain relationship up to very high strains, while the subsequent buckling analysis of cold-formed members needs the precise definition of the stress-strain relationship at low and intermediate strains (i.e. $\varepsilon < \varepsilon_{2.0}$, $\varepsilon_{2.0}$ is the total strain at the 2% proof stress). This chapter has presented a new full-range stress-strain relationship for stainless steel alloys, which is capable of accurate predictions over the full ranges of both tensile and compressive strains, as is needed by the above-mentioned advanced finite element analysis.

The stress-strain relationships of stainless steel over full ranges of strains need to be characterized not only by the basic Ramberg-Osgood parameters (E_0, $\sigma_{0.2}$ and n), but also by certain additional parameters which may not be available in existing

design codes or cannot be obtained from tests due to experimental limitations (e.g. ultimate compressive strengths). In this chapter, expressions for these additional parameters in terms of the basic Ramberg-Osgood parameters have been presented. These expressions have been developed by careful interpretations of existing experimental data, such that the new full-range stress-strain model can be defined by the basic Ramberg-Osgood parameters alone. The proposed stress-strain model has been compared with available experimental stress-strain curves, and good agreement has generally been found over wide ranges of both tensile and compressive strains.

3.6 REFERENCES

ASCE (2002). *Specification for the Design of Cold-Formed Stainless Steel Structural Members, SEI/ASCE 8-02*, American Society of Civil Engineers, New York.

AS/NZS (2001). *Cold-Formed Stainless Steel Structures, AS/NZS 4673:2001*, Australian/New Zealand Standard, Standards Australia, Sydney.

ASTM (2003). *Standard Practice for Numbering Metals and Alloys (UNS), ASTM E527-83*, American Society for Testing and Materials, United States.

BSI (1995). *Stainless Steels – Part 1: List of Stainless Steels, BS EN 10088-1*, British Standards Institution, United Kingdom.

Chakrabarty, J. (2000). *Applied Plasticity*, Springer-Verlag, Inc., New York.

Cottrell, A.H. (1964). *The Mechanical Properties of Matter*, Wiley, New York.

Davis, H. E., Troxell, G. E. and Hauck, G. F. W. (1982). *The Testing of Engineering Materials*, 4th edition, McGraw-Hill, Inc., New York.

Gardner, L. and Nethercot, D. A. (2004). Experiments on stainless steel hollow sections – Part 1: Material and cross-sectional behaviour. *Journal of Constructional Steel Research,* **60**, 1291-1318.

Haldar, A. and Mahadevan, S. (2000). *Probability, Reliability and Statistical Methods in Engineering Design*, John Wiley & Sons, Inc., New York.

Kalpakjian, S. (1991). *Manufacturing Processes for Engineering Materials*, 2nd edition, Addison-Wesley, Inc., United States.

Korvink, S. A., Van den Berg, G. J. and Van der Merwe, P. (1995). Web crippling of stainless steel cold-formed beams. *Journal of Constructional Steel Research,* **34**, 225-248.

Macdonald, M., Rhodes, J. and Taylor, G. T. (2000). Mechanical properties of stainless steel lipped channels. *Proceedings of the Fifteenth International Specialty Conference on Cold-Formed Steel Structures*, St. Louis, Missouri, United States, 19-20 Oct., 673-686.

Mirambell, E. and Real, E. (2000). On the calculation of deflections in structural stainless steel beams: an experimental and numerical investigation. *Journal of Constructional Steel Research,* **54**, 109-133.

Olsson, A. (2001). *Stainless Steel Plasticity – Material Modelling and Structural Applications*, Doctoral Thesis, Division of Steel Structures, Department of Civil and Mining Engineering, Luleå University of Technology, Sweden.

Rasmussen, K. J. R. (2003). Full-range stress-strain curves for stainless steel alloys. *Journal of Constructional Steel Research*, **59**, 47-61.

Rasmussen, K. J. R., Burns, T., Bezkorovainy, P. and Bambach, M. R. (2002). *Numerical Modelling of Stainless Steel Plates in Compression, Research Report No. R813*, March 2002, Department of Civil Engineering, University of Sydney, Sydney.

Rasmussen, K. J. R., Burns, T., Bezkorovainy, P. and Bambach, M. R. (2003). Numerical modelling of stainless steel plates in compression. *Journal of Constructional Steel Research*, **59**, 1345-1362.

SCI (1991). *Tests on Stainless Steel Materials, Report No. SCI-RT-251*, Steel Construction Institute, London.

Table 3.1 Correlation coefficients $\rho_{X,Y}$ of $\sigma_{1.0}/\sigma_{0.2}$ and the basic parameters.

X / Y	$\sigma_{1.0}/\sigma_{0.2}$	
	Tension Coupons	Compression Coupons
$1/n$	0.62	0.82
e	-0.03	0.17

Table 3.2 Correlation coefficients $\rho_{X,Y}$ of $n'_{0.2,1.0}$ and other key parameters.

X / Y	$n'_{0.2,1.0}$	
	Tension Coupons	Compression Coupons
$E_{0.2}/E_0$	0.97	0.94
$\sigma_{1.0}/\sigma_{0.2}$	0.41	0.81
$(E_{0.2}/E_0)(\sigma_{1.0}/\sigma_{0.2})$	0.97	0.94

Table 3.3 Material properties of stainless steel alloys used for comparison.

Source[a]	Alloy[b]	Specimen[c]	Coupon[e]	E_0 (MPa)	$\sigma_{0.2}$ (MPa)	n
1	UNS30400	W	W3	180,000	460	4.7
2	UNS30400	SHS 80×80×4	TF	186,600	457	5.0
2	UNS30400	SHS 80×80×4	CF	203,200	416	3.5
2	UNS30400	SHS 100×100×2	TF	201,300	382	6.6
2	UNS30400	SHS 100×100×2	CF	207,100	370	4.7
2	UNS30400	SHS 100×100×3	TF	195,800	388	5.6
2	UNS30400	SHS 100×100×3	CF	208,800	379	3.8
2	UNS30400	SHS 100×100×4	TF	191,300	465	5.7
2	UNS30400	SHS 100×100×4	CF	203,400	437	3.9
2	UNS30400	SHS 100×100×6	TF	198,400	501	5.2
2	UNS30400	SHS 100×100×6	CF	197,900	473	4.4
2	UNS30400	SHS 100×100×8	TF	202,400	328	6.4
2	UNS30400	SHS 100×100×8	CF	205,200	330	6.4
2	UNS30400	SHS 150×150×4	TF	206,000	314	6.8
2	UNS30400	SHS 150×150×4	CF	195,400	294	4.5
2	UNS30400	RHS 60×40×4	TF	192,800	489	3.9
2	UNS30400	RHS 60×40×4	CF	193,100	469	3.6
2	UNS30400	RHS 120×80×3	TF	209,300	419	4.1
2	UNS30400	RHS 120×80×3	CF	197,300	429	4.2
2	UNS30400	RHS 120×80×6	TF	194,500	509	5.3
2	UNS30400	RHS 120×80×6	CF	192,300	466	4.4
2	UNS30400	RHS 150×100×4	TF	205,800	297	8.0
2	UNS30400	RHS 150×100×4	CF	200,300	319	4.7
2	UNS30400	RHS 100×50×2	TF	208,000	403	6.9
2	UNS30400	RHS 100×50×2	CF	205,900	370	5.2
2	UNS30400	RHS 100×50×3	TF	203,600	479	4.2
2	UNS30400	RHS 100×50×3	CF	200,900	455	4.1
2	UNS30400	RHS 100×50×4	TF	208,000	471	5.2
2	UNS30400	RHS 100×50×4	CF	203,900	439	3.8
2	UNS30400	RHS 100×50×6	TF	187,200	605	5.7
2	UNS30400	RHS 100×50×6	CF	206,300	494	4.0
3	UNS31803	Plate	LT	200,000	575	4.8
3	UNS31803	Plate	LC	181,650	527	4.6
3	UNS31803	Plate	TT	215,250	635	7.7
3	UNS31803	Plate	TC	210,000	617	6.2
4	UNS43000	Plate[d]	LT	190,930	308	9.5
4	UNS43000	Plate[d]	LC	186,040	312	7.0
4	UNS43000	Plate[d]	TT	212,510	334	15.0
4	UNS43000	Plate[d]	TC	214,720	344	10.7

Table 3.3 Material properties of stainless steel alloys used for comparison (continued).

Note:

a. 1: Macdonald *et al*. (2000)
   2: Gardner and Nethercot (2004)
   3: Rasmussen *et al*. (2002)
   4: Korvink *et al*. (1995)

b. UNS30400: austenitic alloys
   UNS31803: duplex alloys
   UNS43000: ferritic alloys

c. W: thick lipped channel section
   SHS: square hollow section
   RHS: rectangular hollow section
   Plate: plate or sheet

d. Virgin stainless steel sheet from which lipped channel sections were press-braked

e. LT: longitudinal tension coupon
   LC: longitudinal compression coupon
   TT: transverse tension coupon
   TC: transverse compression coupon
   TF: tension coupon cut from flat portion
   CF: compression coupon cut from flat portion
   W3: tension coupon cut from web of a thick lipped channel section

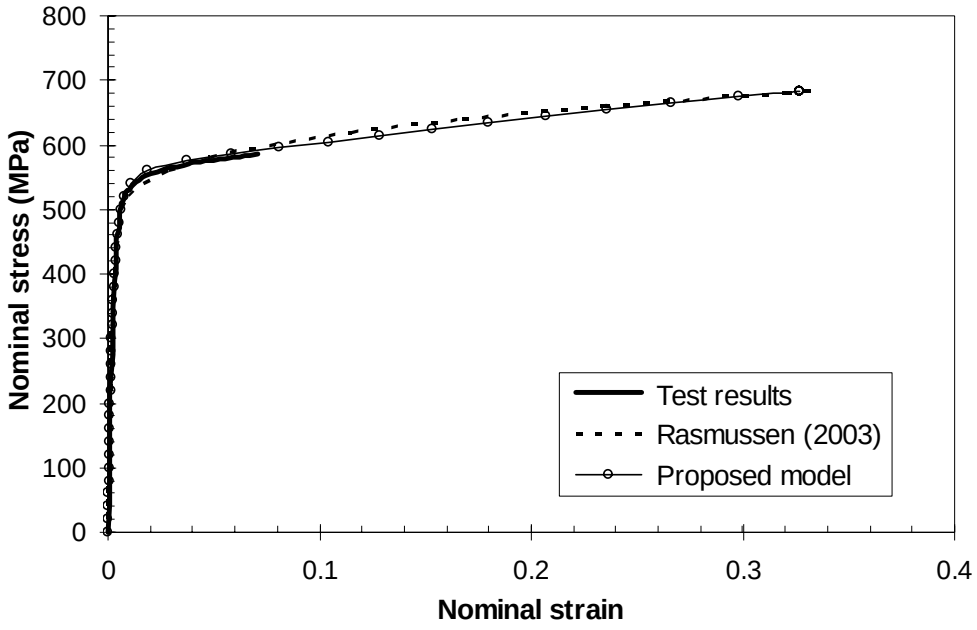

(a) Full stress-strain curves

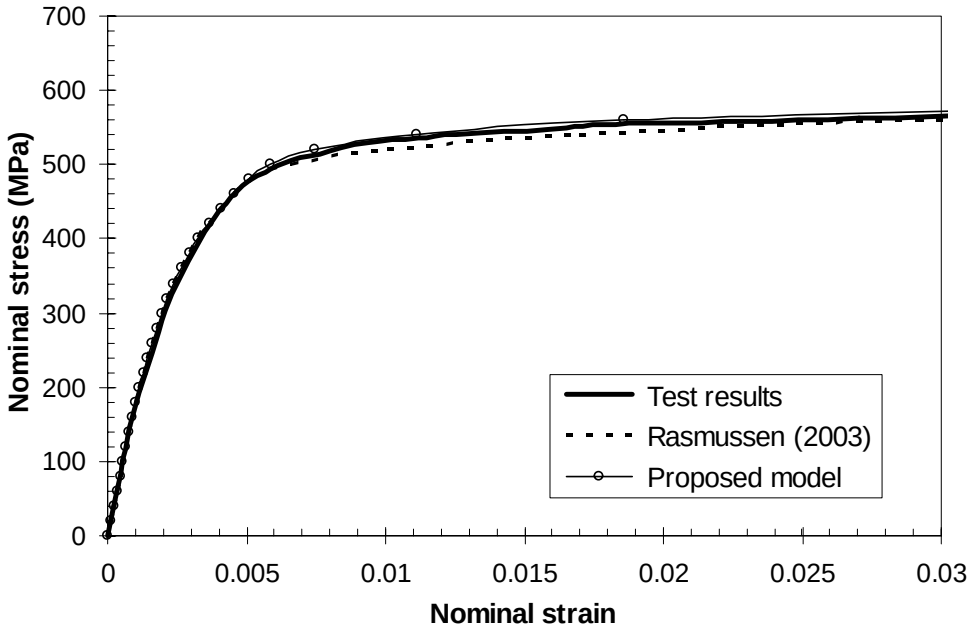

(b) Initial stress-strain curves

Figure 3.1 Nominal stress-strain curves for the tension coupon cut from the thick lipped channel section tested by Macdonald *et al*. (2000).

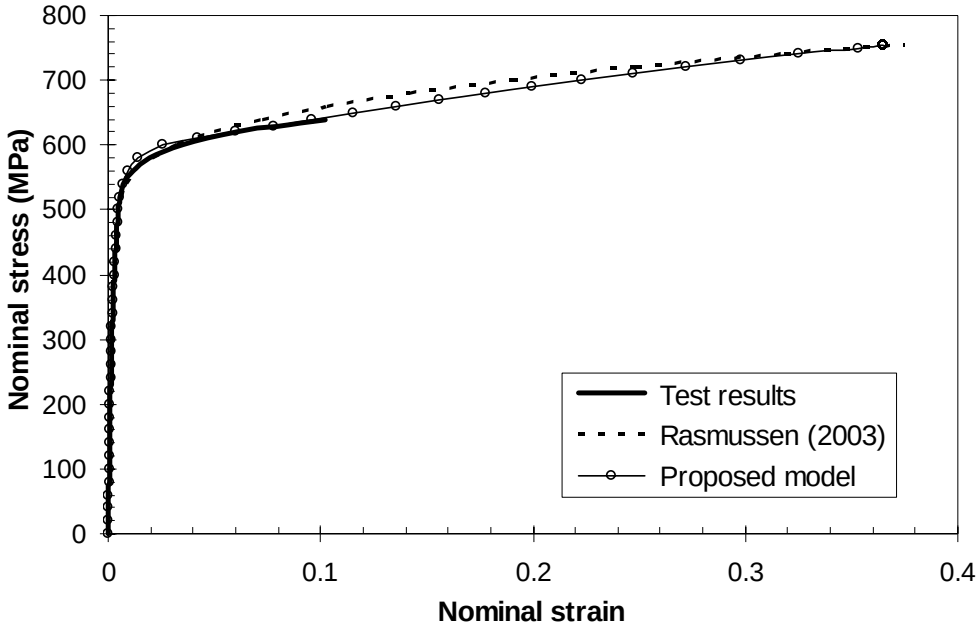

(a) Full stress-strain curves

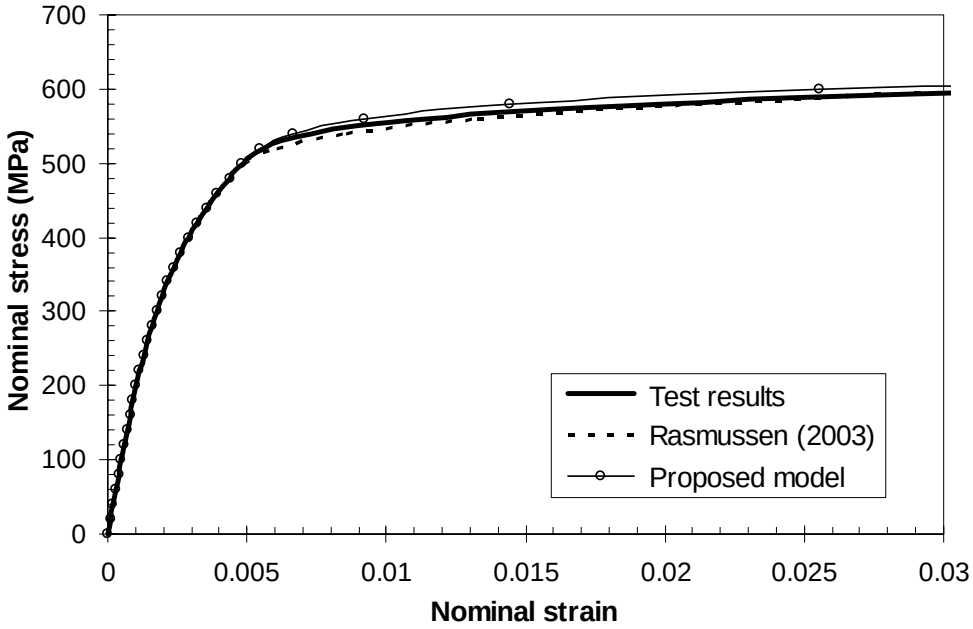

(b) Initial stress-strain curves

Figure 3.2 Nominal stress-strain curves for the flat tension coupon cut from section RHS 100×50×3 by Gardner and Nethercot (2004).

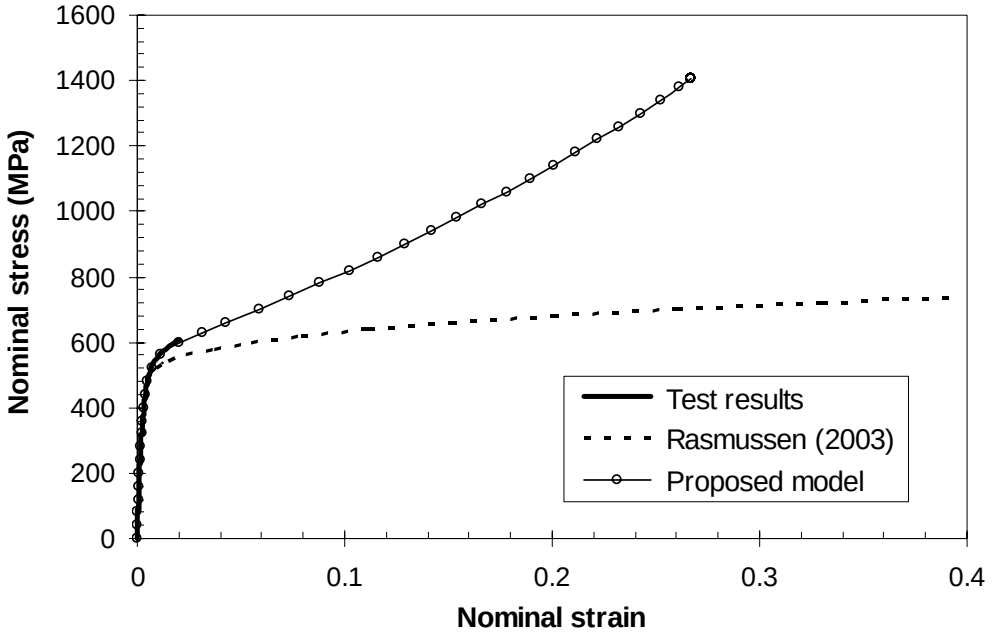

(a) Full stress-strain curves

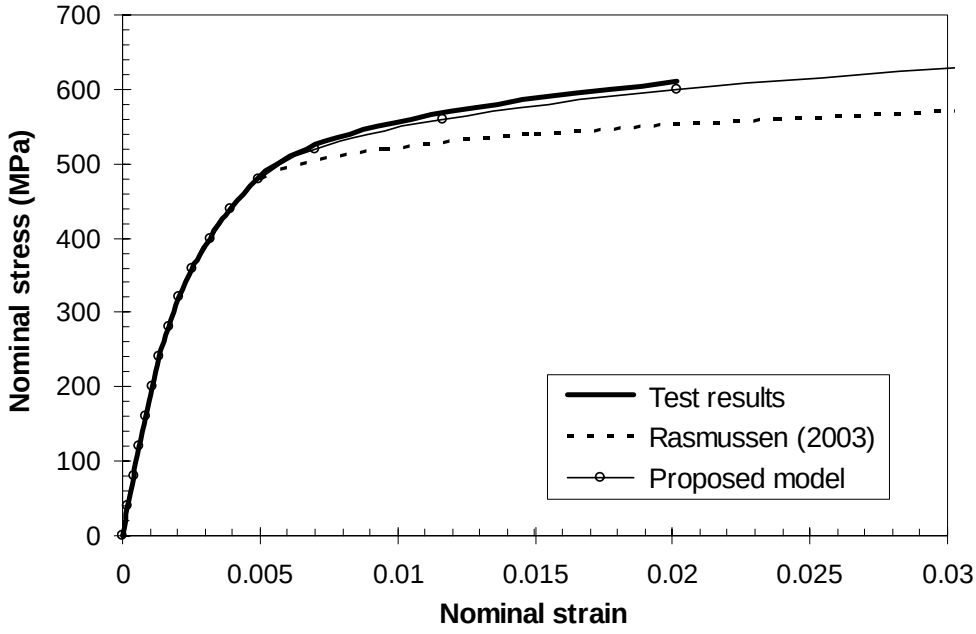

(b) Initial stress-strain curves

Figure 3.3 Nominal stress-strain curves for the flat compression coupon cut from section RHS 100×50×3 by Gardner and Nethercot (2004).

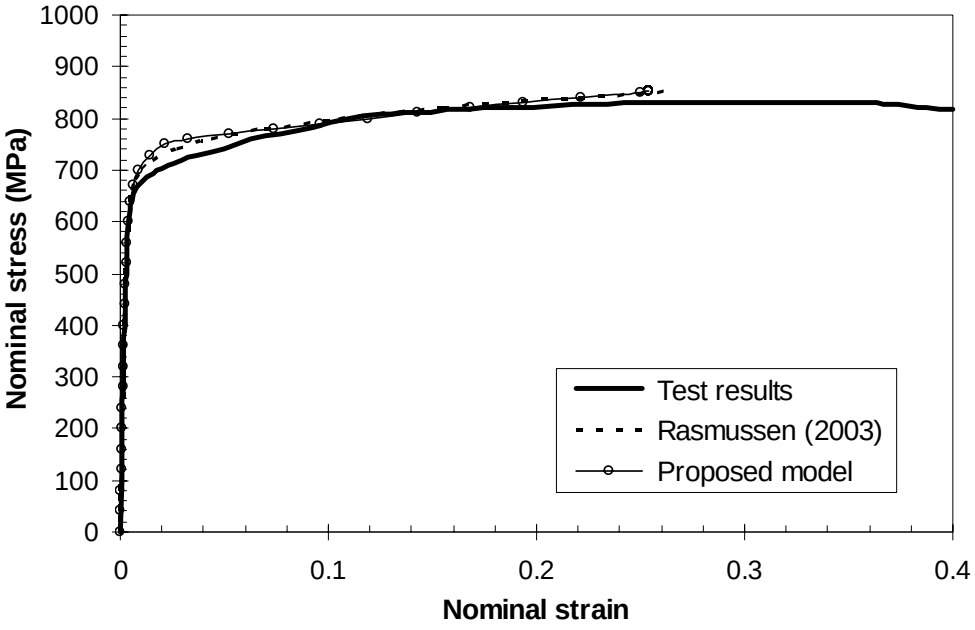

(a) Full stress-strain curves

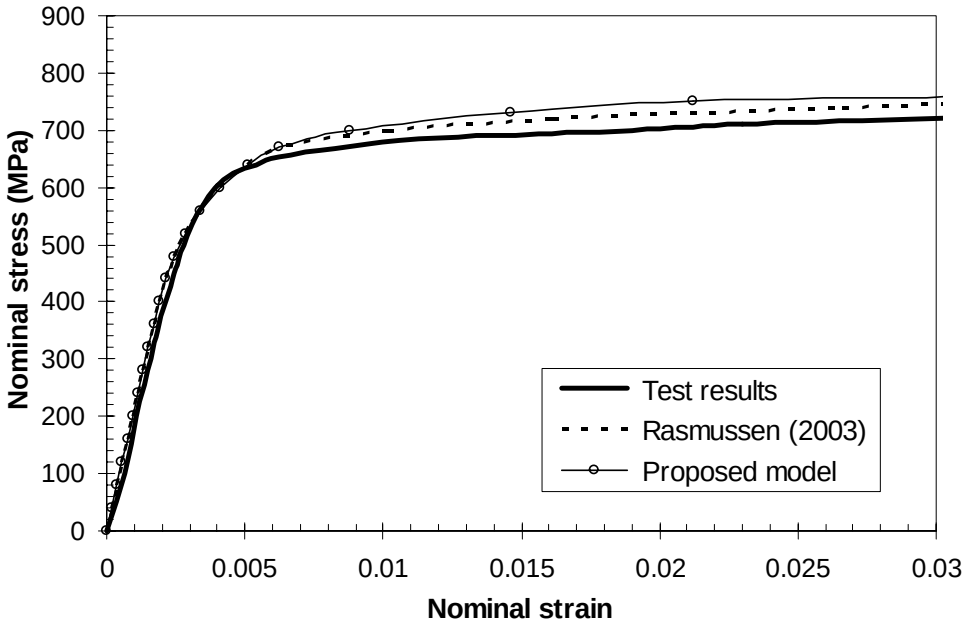

(b) Initial stress-strain curves

Figure 3.4 Nominal stress-strain curves for the transverse tension coupon cut from the duplex stainless steel plate tested by Rasmussen *et al*. (2002).

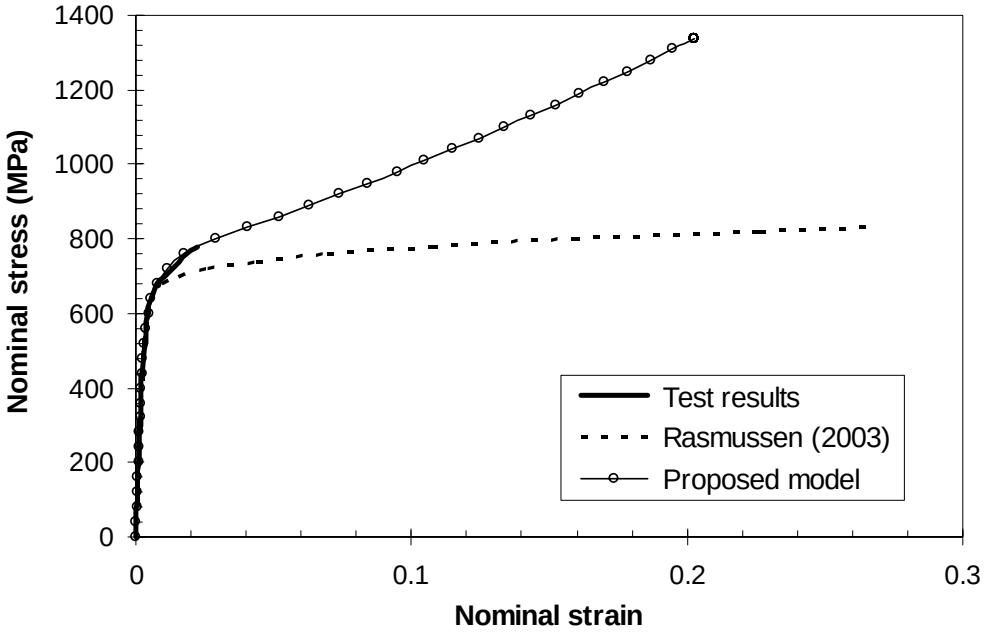

(a) Full stress-strain curves

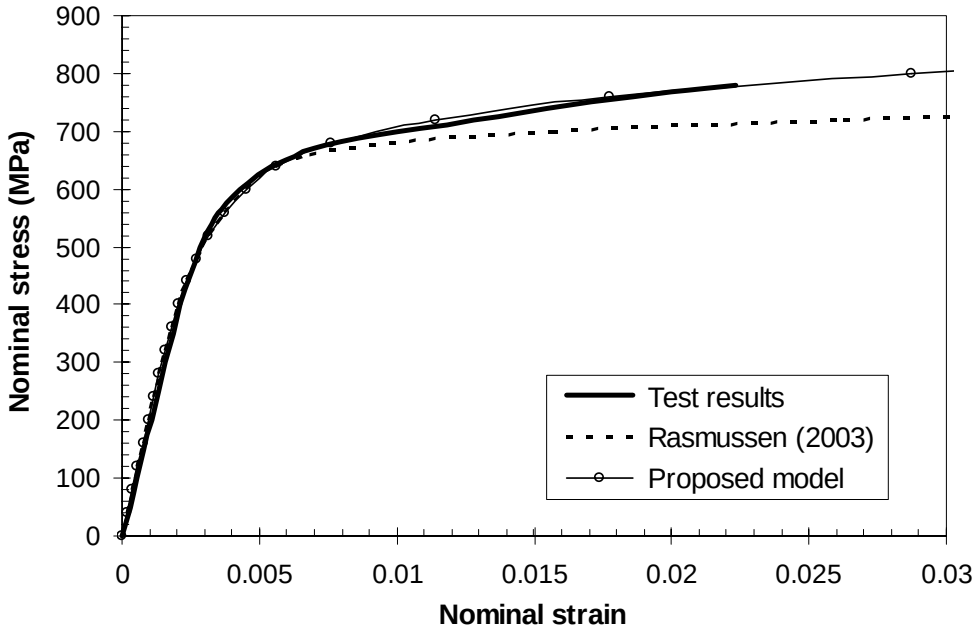

(b) Initial stress-strain curves

Figure 3.5 Nominal stress-strain curves for the transverse compression coupon cut from the duplex stainless steel plate tested by Rasmussen *et al*. (2002).

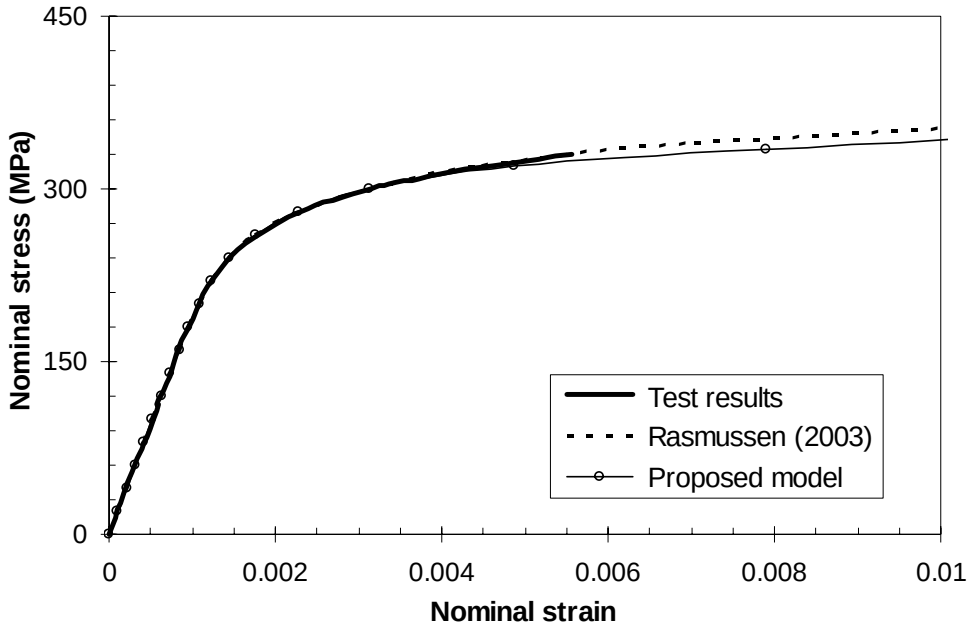

Figure 3.6 Nominal stress-strain curves for the longitudinal tension coupon cut from the ferritic stainless steel plate tested by Korvink *et al*. (1995).

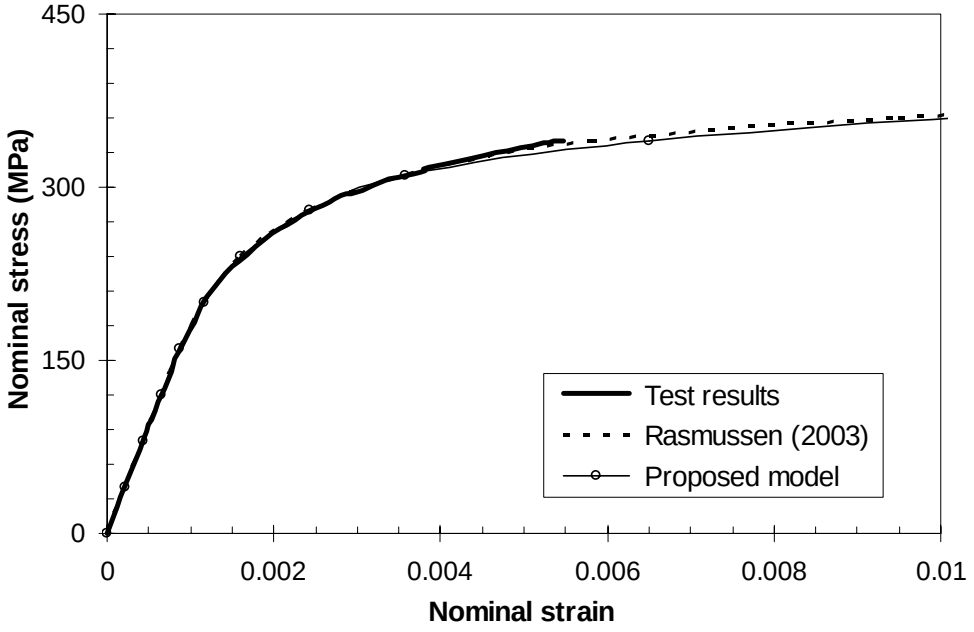

Figure 3.7 Nominal stress-strain curves for the longitudinal compression coupon cut from the ferritic stainless steel plate tested by Korvink *et al*. (1995).

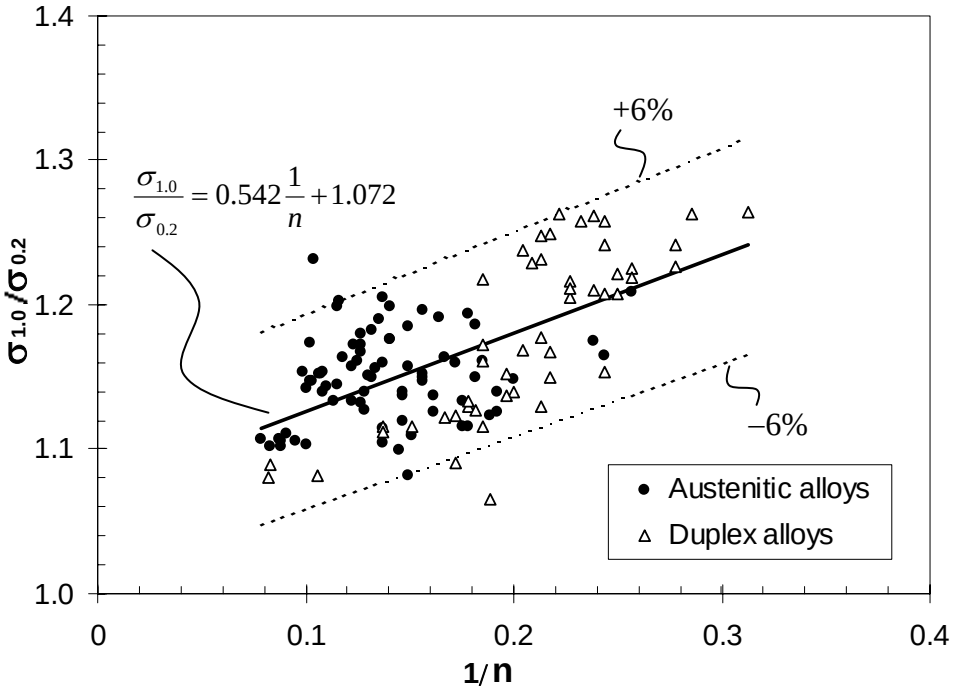

(a) Tension coupons

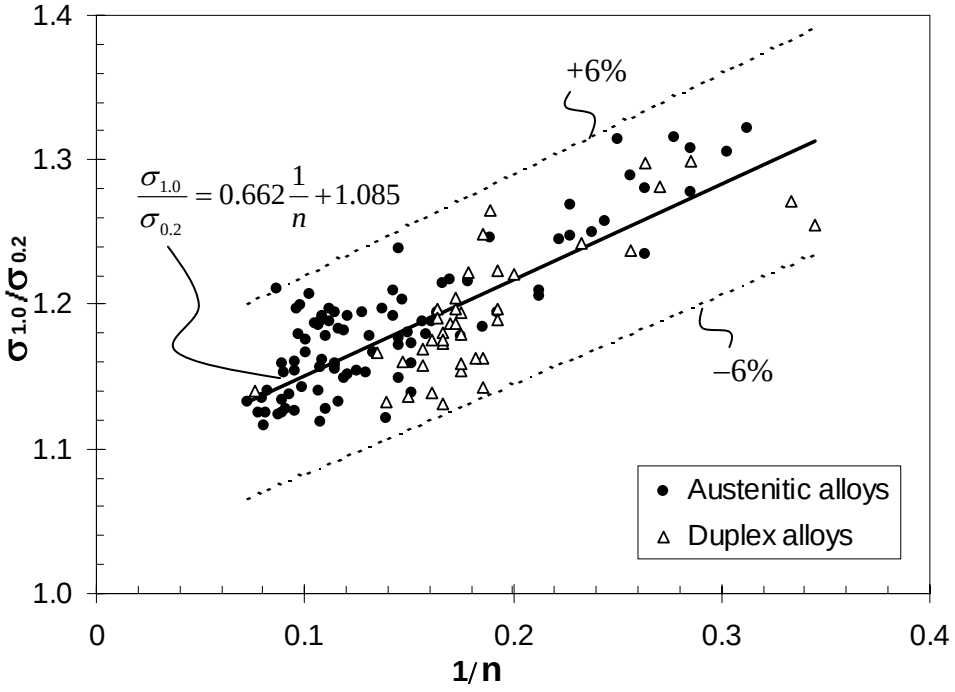

(b) Compression coupons

Figure 3.8 Relationship between $\sigma_{1.0}/\sigma_{0.2}$ and $1/n$.

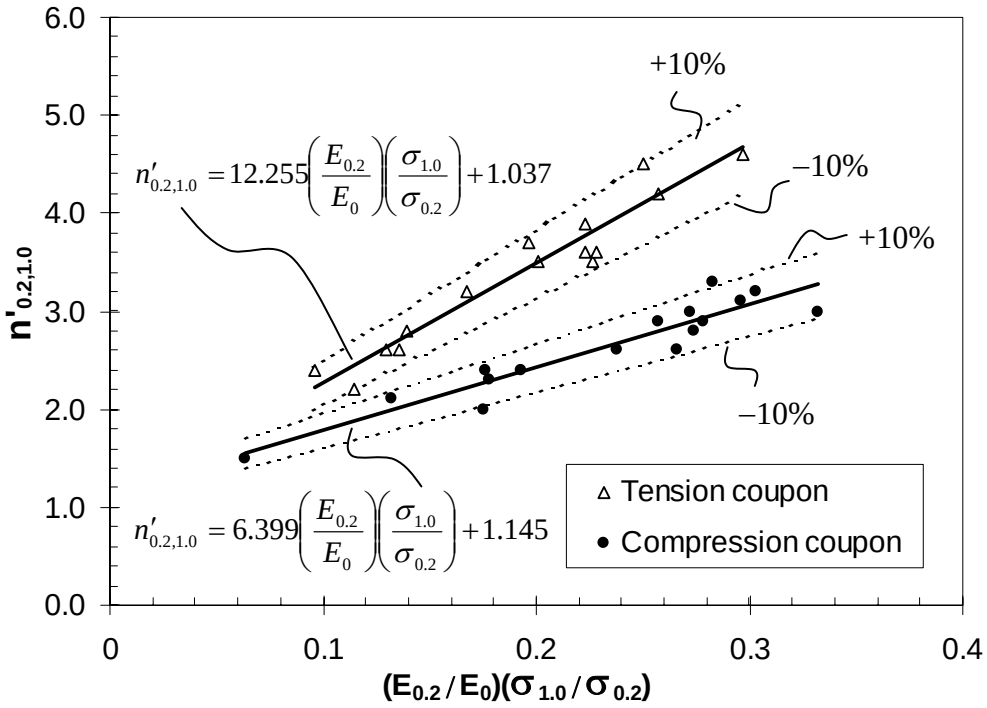

Figure 3.9 Relationship between $n'_{0.2,1.0}$ and $(E_{0.2}/E_0)(\sigma_{1.0}/\sigma_{0.2})$.

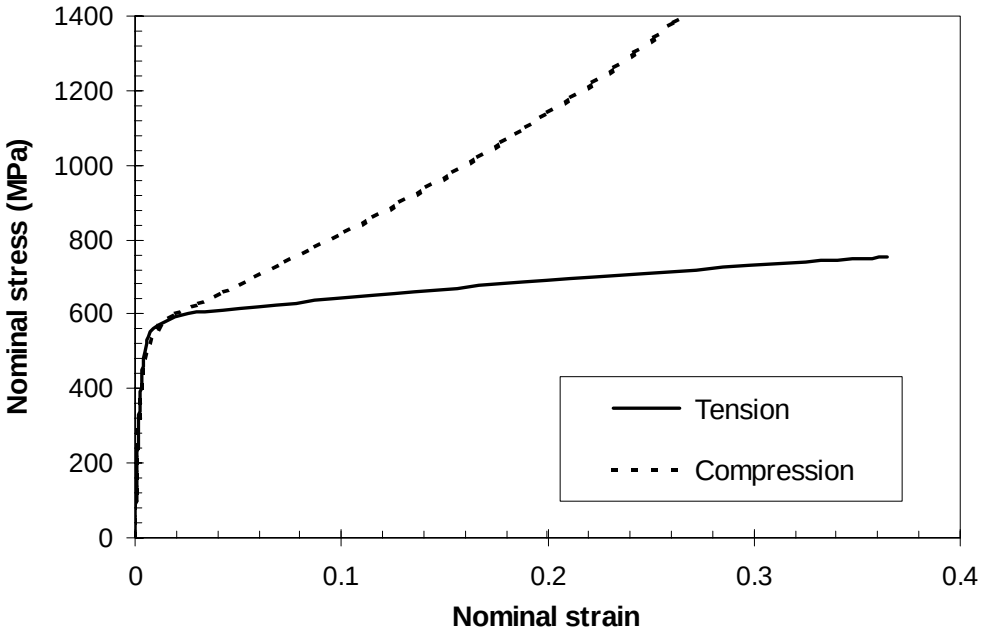

(a) Full stress-strain curves

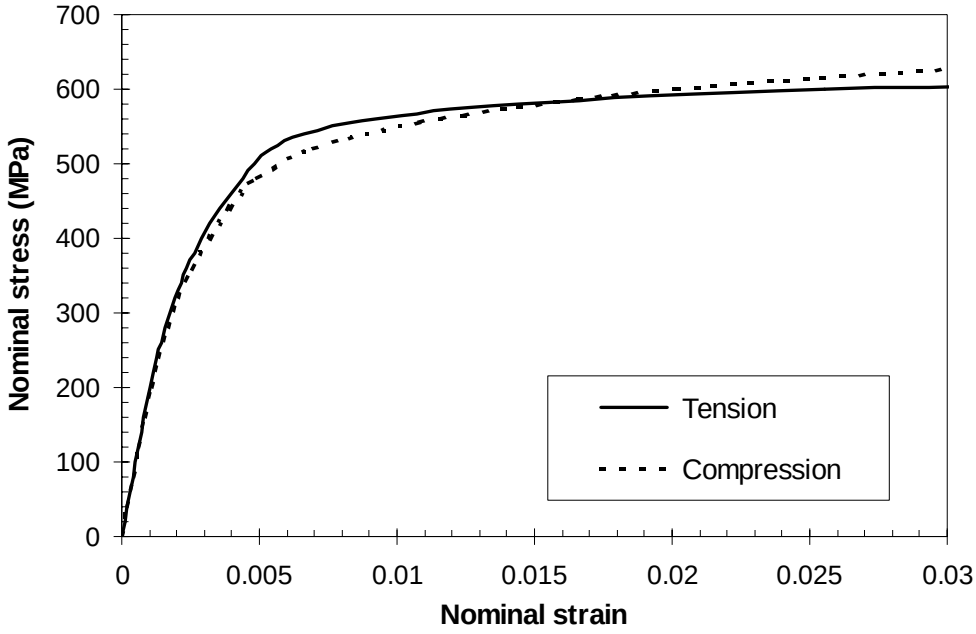

(b) Initial stress-strain curves

Figure 3.10 Typical nominal stress-strain curves for stainless steel defined by the 3-stage full-range stress-strain model.

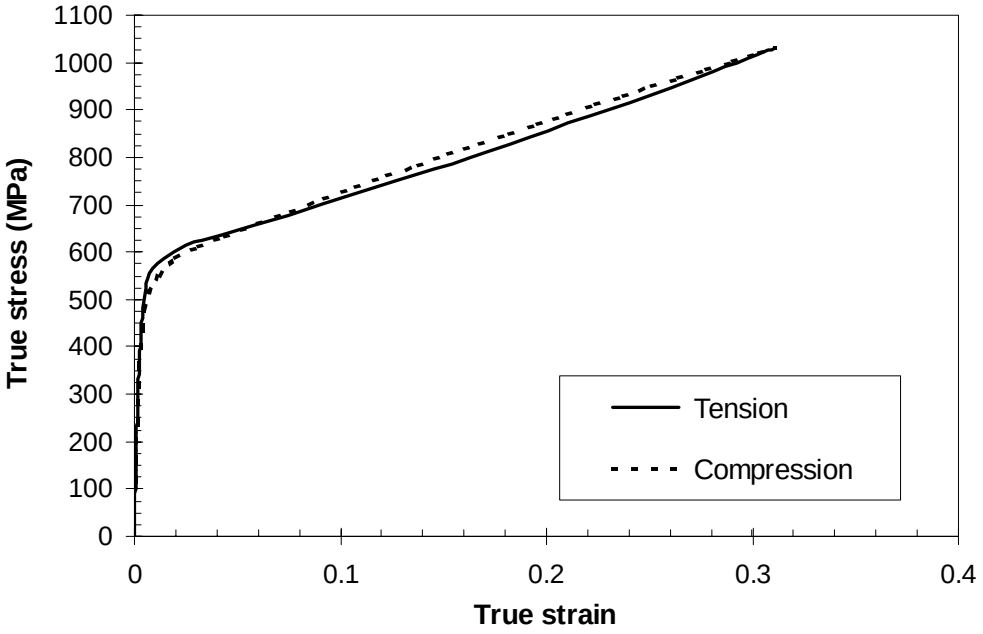

(a) Full stress-strain curves

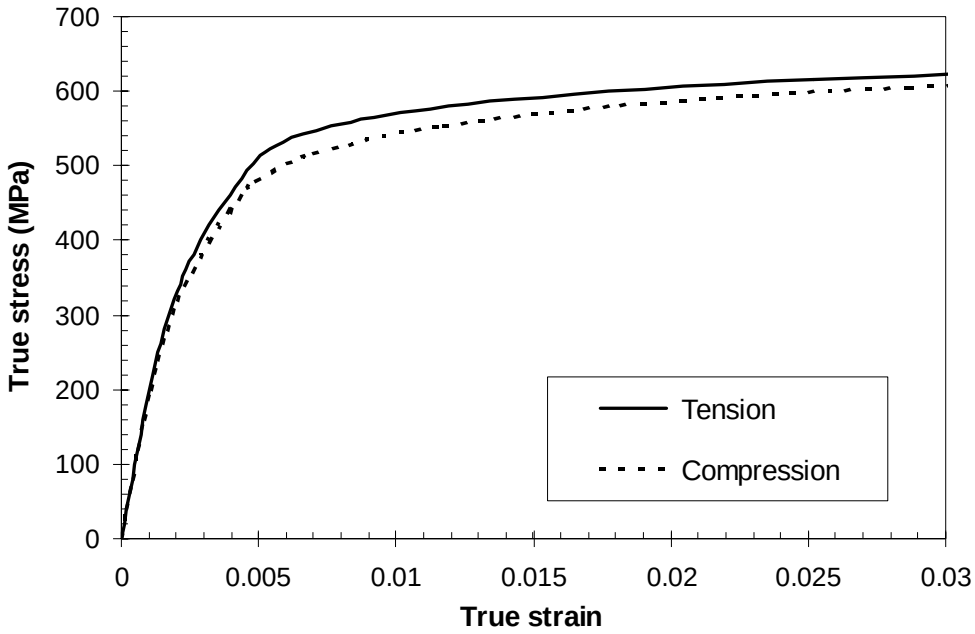

(b) Initial stress-strain curves

Figure 3.11 Typical true stress-strain curves for stainless steel defined by the 3-stage full-range stress-strain model.

Chapter 4

ANALYTICAL SOLUTION FOR RESIDUAL STRESSES IN STEEL SHEETS DUE TO COILING AND UNCOILING

4.1 INTRODUCTION

The manufacturing process of cold-formed sections induces residual stresses. Existing experimental studies on residual stresses in cold-formed sections have been reviewed in Chapter 2. As shown in the review, in most of these experimental studies, only surface residual stresses were measured with the variations across the plate thickness being assumed to be linear. Due to the thinness of cold-formed sections, real variations of residual stresses across the plate thickness generally cannot be obtained. Moreover, clear relationships between residual stresses and various steps of the manufacturing process cannot be established by an examination of the measurement results. Because of these limitations of laboratory measurements, accurate theoretical predictions of residual stresses in cold-formed sections are needed and can be obtained by the modelling of the manufacturing process.

As explained in Chapters 1 and 2, the fabrication of cold-formed sections is a two-stage process which consists of the coiling-uncoiling stage and the cold-forming stage (either roll forming or press braking). These two stages involve plane strain pure

bending of a steel sheet with different amounts of straining in the two orthogonal directions respectively. This chapter is concerned only with the first stage by presenting a general analytical solution for the plane strain pure bending of steel sheets. Based on this general analytical solution, separate solutions were formulated for four common types of sheet steels: (1) elastic-perfectly plastic steels, (2) elastic-linear strain-hardening steels, (3) elastic-nonlinear strain-hardening steels, and (4) nonlinear strain-hardening steels, such as stainless steel alloys with negligible material anisotropy. To facilitate the application of this analytical solution in the subsequent finite element simulation of the cold-forming process and in the buckling analysis of cold-formed members, the prediction of equivalent plastic strains is also addressed in addition to residual stresses in both the longitudinal and transverse directions.

4.2 TERMINOLOGY

Before proceeding further, the terminology adopted in this chapter in referring to stresses in various directions should be noted first. The direction of bending is referred to as the longitudinal direction (z direction) and the width direction of the plate is referred to as the transverse direction (x direction), while the direction normal to the plate is referred to as the through-thickness direction (y direction). The present terminology has the advantage that the longitudinal direction of a steel sheet remains the longitudinal direction of a cold-formed member produced from the sheet after the coiling and uncoiling process being discussed here, and is consistent with the terminology used in the subsequent chapters. It should also be noted that, in the

manufacturing process of a press-braked lipped channel section (see Figure 1.2 in Chapter 1), the outer surface of a coiled sheet becomes the inner surface of the lipped channel section produced from the sheet.

4.3 GENERAL ANALYTICAL SOLUTION

4.3.1 Assumptions

In the present study, it is assumed that any residual stresses due to cold rolling have been removed in the annealing furnace. That is, the flat steel sheet is assumed to be free from residual stresses before it is coiled for storage. Furthermore, as the effect of cold work is deemed to have been removed in the annealing furnace, a steel sheet before coiling can be assumed to possess a stress-strain curve of the virgin material (e.g. a stress-strain curve of the shape-yielding type for carbon steel sheets). The virgin material of the steel sheet can be assumed to possess an elastic-plastic strain-hardening stress-strain curve, and obey the von Mises yield criterion with the isotropic hardening rule and the Prandtl-Reuss flow rule. The stress-strain curve of the sheet material can be obtained from uniaxial tests and generally defined by a function:

$$\sigma = F(\varepsilon) \quad \text{or} \quad \varepsilon = f(\sigma) \tag{4.1}$$

where σ and ε are the stress and strain, respectively, from the uniaxial stress-strain curve. The coiling of a steel sheet into a curvature κ_c and its subsequently uncoiling and flattening can thus be modelled as plane strain pure bending in the y-z plane (see

Figure 1.2 in Chapter 1). This section presents an analytical solution for this elastic-plastic bending problem.

4.3.2 Coiling

During the coiling of the steel sheet, an arbitrary point in the sheet undergoes elastic or elastic-plastic deformation, depending on the given coiling curvature κ_c and its location y away from the neutral axis of the section. For elastic material points across the thickness, under a plane strain condition in the width direction (x direction) and a plane stress condition in the through-thickness direction (y direction), the in-plane strains are given by

$$\varepsilon_{z,c} = \frac{\left(\sigma_{z,c} - \nu\sigma_{x,c}\right)}{E_0} \tag{4.2a}$$

$$\varepsilon_{x,c} = \frac{\left(\sigma_{x,c} - \nu\sigma_{z,c}\right)}{E_0} = 0 \tag{4.2b}$$

where E_0 is the initial elastic modulus, ν is the Poisson's ratio, $\sigma_{x,c}$ and $\sigma_{z,c}$ are the stresses in the x and z directions, respectively, due to coiling, while $\varepsilon_{x,c}$ and $\varepsilon_{z,c}$ are the corresponding strains.

The elastic coiling stresses at any arbitrary location y from the neutral axis of the section are then related to the longitudinal strain $\varepsilon_{z,c}$ due to bending by

$$\sigma_{z,c} = \frac{E_0}{\left(1-\nu^2\right)}\varepsilon_{z,c} \tag{4.3a}$$

$$\sigma_{x,c} = \frac{\nu E_0}{\left(1-\nu^2\right)}\varepsilon_{z,c} \tag{4.3b}$$

with

$$\varepsilon_{z,c} = \kappa_c y \tag{4.3c}$$

The above relationships are valid only for points under elastic straining. For material points undergoing plastic straining, the von Mises yield criterion is satisfied:

$$\overline{\sigma} = \sigma_{yc} \tag{4.4}$$

in which σ_{yc} is the instantaneous yield stress reached at the end of coiling, and $\overline{\sigma}$ is the equivalent stress, for the plane stress condition in the through-thickness direction, given by

$$\overline{\sigma} = \sqrt{\sigma_{z,c}^2 + \sigma_{x,c}^2 - \sigma_{x,c}\sigma_{z,c}} \tag{4.5}$$

For a material point at the onset of yielding (i.e. $\sigma_{yc} = \sigma_{y0}$, where σ_{y0} is the initial yield stress), the von Mises yield criterion can thus be stated as

$$\sqrt{\sigma_{z,c}^2 + \sigma_{x,c}^2 - \sigma_{x,c}\sigma_{z,c}} = \sigma_{y0} \tag{4.6}$$

By substituting Eq. (4.3) into Eq. (4.6), the longitudinal strain at which a material point starts to yield (such as point E in Figure 4.1) is found to be

$$\varepsilon_{z,cy} = \pm\sigma_{y0}\left(1-\nu^2\right)\Big/\left(E_0\sqrt{1-\nu+\nu^2}\right) \tag{4.7}$$

in which $\varepsilon_{z,cy} > 0$ if the strain is tensile (i.e. $y > 0$). Under a coiling curvature κ_c, the central core of material of the section remains elastic and the size of this central core is twice the value given by the following expression:

$$y_{cy} = \sigma_{y0}\left(1-\nu^2\right)\Big/\left(E_0\kappa_c\sqrt{1-\nu+\nu^2}\right) \tag{4.8}$$

Therefore, for $|y| \le y_{cy}$, the stresses are given by Eq. (4.3). Points located at $|y| > y_{cy}$ are in plastic flow and the stresses obey the von Mises yield criterion. By defining the following stress ratio:

$$\omega_c = \sigma_{x,c}\big/\sigma_{z,c} \tag{4.9}$$

and combining it with Eqs. (4.4) and (4.5), the coiling stresses of any point undergoing plastic straining (such as point P in Figure 4.1) can then be obtained as

$$\sigma_{z,c} = \pm\frac{\sigma_{yc}}{\sqrt{1-\omega_c+\omega_c^2}} \tag{4.10a}$$

$$\sigma_{x,c} = \pm\frac{\omega_c\sigma_{yc}}{\sqrt{1-\omega_c+\omega_c^2}} \tag{4.10b}$$

in which $\sigma_{x,c}$ and $\sigma_{z,c} \geq 0$ (i.e. tensile stresses) when $y \geq 0$.

For isotropic materials, the relationship between equivalent stress $\bar{\sigma}$ and equivalent plastic strain $\bar{\varepsilon}_p$ is assumed to be the same as the uniaxial stress-plastic strain curve (Ragab and Bayoumi 1998) for which the corresponding uniaxial stress-strain curve is now defined by the function $\sigma = F(\varepsilon)$ or $\varepsilon = f(\sigma)$ (see Eq. (4.1)). That is,

$$\bar{\sigma} = \sigma, \text{ when } \bar{\varepsilon}_p = \varepsilon_p \tag{4.11a}$$

and

$$d\bar{\sigma} = d\sigma, \text{ when } d\bar{\varepsilon}_p = d\varepsilon_p \tag{4.11b}$$

in which ε_p and $d\varepsilon_p$ are the plastic strain and its increment respectively, and the plastic strain is given by

$$\varepsilon_p = \varepsilon - \frac{\sigma}{E_0} \tag{4.12}$$

From Eqs. (4.11) and (4.12), the equivalent plastic strain $\bar{\varepsilon}_{p,c}$ due to the applied coiling curvature κ_c can be determined as

$$\bar{\varepsilon}_{p,c} = \varepsilon_{p,c} = \varepsilon_{yc} - \frac{\sigma_{yc}}{E_0} \tag{4.13}$$

in which the subscript c refers to the coiling stage, and σ_{yc} and ε_{yc} are the instantaneous yield stress and the corresponding strain reached at the end of coiling with their relationship defined by the function $\sigma = F(\varepsilon)$ or $\varepsilon = f(\sigma)$ (see Eq. (4.1)). Therefore, once σ_{yc} is known, ε_{yc} can be determined from the stress-strain curve of the material (see Eq. (4.1)) and the equivalent plastic strain $\bar{\varepsilon}_{p,c}$ due to coiling can then be calculated from Eq. (4.13).

It is worth noting that there exists a limit value κ_{cy} for the coiling curvature at which the extreme surfaces of the thin sheet start to yield (shown as point E in Figure 4.1), and this limit is found by substituting $\varepsilon_{z,c} = \kappa_{cy}\, t/2$ into Eq. (4.7):

$$\kappa_{cy} = 2\sigma_{y0}\left(1-\nu^2\right)\Big/\left(E_0 t\sqrt{1-\nu+\nu^2}\right) \tag{4.14}$$

The value of κ_{cy} depends only on the material properties of the sheet material. Obviously, if the coiling curvature $\kappa_c < \kappa_{cy}$, no plastic bending is involved during coiling and hence no residual stresses exist following uncoiling. When $\kappa_c \geq \kappa_{cy}$, yielding of material due to coiling will result in the development of residual stresses at the end of the coiling-uncoiling process.

In order to determine the coiling stresses and the equivalent plastic strain due to coiling at any location y for a given coiling curvature κ_c, it is necessary to first calculate the values of σ_{yc} and ω_c numerically for each value of y. The determination of σ_{yc} and ω_c is discussed in the next subsection.

4.3.3 Determination of σ_{yc} and ω_c

For elastic-perfectly plastic materials, the value of the instantaneous yield stress σ_{yc} is independent of the amount of plastic straining and the value of the stress ratio ω_c, and is thus treated as a constant. As a result, the stress ratio ω_c can be directly related to the value of y and a closed-form analytical solution can be established for elastic-perfectly plastic materials. Such closed-form analytical solution will be presented later in this chapter. For strain-hardening materials, σ_{yc} and ω_c are related to each other. To establish their relationship, the stress ratio ω_c and its increment $d\omega_c$ can be expressed in terms of the stress σ and the stress increment $d\sigma$ from the uniaxial stress-strain curve. Due to the strain-hardening material properties, it is difficult to obtain closed-form analytical expressions for σ_{yc} and ω_c. Instead, their values can be determined numerically, using their inter-relationship and the known boundary values.

For material points under plastic straining, the slope of the equivalent stress-equivalent plastic strain relation H' is equal to the corresponding slope of the uniaxial stress-plastic strain curve:

$$H' = \frac{d\bar{\sigma}}{d\bar{\varepsilon}_p} = \frac{d\sigma}{d\varepsilon_p} = \left(\frac{d\varepsilon}{d\sigma} - \frac{1}{E_0} \right)^{-1} \tag{4.15}$$

in which $d\varepsilon/d\sigma$ can be obtained by differentiating Eq. (4.1) and can be expressed in terms of σ. Eq. (4.15) is valid for both the coiling and the uncoiling stages.

During coiling, the incremental relations for stresses and strains are given by

$$\begin{Bmatrix} d\sigma_{z,c} \\ d\sigma_{x,c} \end{Bmatrix} = \frac{E_0}{S_c} \begin{bmatrix} s_{x,c}^2 + 2p & 2\nu p - s_{x,c}s_{z,c} \\ 2\nu p - s_{x,c}s_{z,c} & s_{z,c}^2 + 2p \end{bmatrix} \begin{Bmatrix} d\varepsilon_{z,c} \\ d\varepsilon_{x,c} \end{Bmatrix} \tag{4.16}$$

in which the subscript c refers to the coiling stage, $d\varepsilon_{z,c}$ and $d\varepsilon_{x,c}$ are the longitudinal and transverse strain increments, $s_{z,c}$ and $s_{x,c}$ are the deviatoric stresses given by

$$s_{z,c} = \left(2\sigma_{z,c} - \sigma_{x,c}\right)/3 \tag{4.17a}$$

$$s_{x,c} = \left(2\sigma_{x,c} - \sigma_{z,c}\right)/3 \tag{4.17b}$$

and S_c is given by

$$S_c = 2p\left(1-\nu^2\right) + s_{x,c}^2 + s_{x,c}^2 + 2\nu\ s_{x,c}s_{z,c} \tag{4.18a}$$

with

$$p = \frac{2\overline{\sigma}^2 H'}{9E_0} \tag{4.18b}$$

Due to the plane strain condition, the transverse coiling strain increment is zero:

$$d\varepsilon_{x,c} = d\varepsilon_{ex,c} + d\varepsilon_{px,c} = 0 \tag{4.19}$$

By defining the following ratio of stress increments:

$$\Omega_c = d\sigma_{x,c} / d\sigma_{z,c} \tag{4.20}$$

and making use of Eqs. (4.9), (4.16) and (4.19), the ratio of stress increments is obtained as

$$\Omega_c = \frac{4\nu H'\left(1-\omega_c+\omega_c^2\right) - E_0\left(2-\omega_c\right)\left(2\omega_c-1\right)}{E_0\left(2\omega_c-1\right)^2 + 4H'\left(1-\omega_c+\omega_c^2\right)} \tag{4.21}$$

in which H' is given by Eq. (4.15). As H' is expressed in terms of σ, the ratio Ω_c given by Eq. (4.21) becomes a function of ω_c and σ.

Differentiations of Eqs. (4.5) and (4.9) lead to

$$\frac{d\sigma_{x,c}}{d\sigma_{z,c}} = \frac{\bar{\sigma}\left(2-\omega_c\right)d\omega_c + 2\omega_c\left(1-\omega_c+\omega_c^2\right)d\bar{\sigma}}{\bar{\sigma}\left(1-2\omega_c\right)d\omega_c + 2\left(1-\omega_c+\omega_c^2\right)d\bar{\sigma}} \tag{4.22}$$

By combining Eq. (4.20) with Eq. (4.22) and making use of Eq. (4.11), the following equation is obtained:

$$d\omega_c = \frac{2\left(1-\omega_c+\omega_c^2\right)\left(\Omega_c-\omega_c\right)}{\sigma\left[\left(2-\omega_c\right)+\Omega_c\left(2\omega_c-1\right)\right]}d\sigma \tag{4.23}$$

in which Ω_c is given by Eq. (4.21). Eq. (4.23) can then be used to solve numerically for the value of σ_{yc} and the corresponding stress ratio ω_c at each location y.

On the other hand, the Prandtl-Reuss flow rule is given by

$$\begin{Bmatrix} d\varepsilon_{pz,c} \\ d\varepsilon_{px,c} \end{Bmatrix} = d\bar{\varepsilon}_{p,c} \frac{3}{2\sqrt{\sigma_{z,c}^2 + \sigma_{x,c}^2 - \sigma_{x,c}\sigma_{z,c}}} \begin{Bmatrix} s_{z,c} \\ s_{x,c} \end{Bmatrix} \tag{4.24}$$

in which the subscript c refers to the coiling stage, $d\varepsilon_{pz,c}$ and $d\varepsilon_{px,c}$ are the longitudinal and transverse plastic strain increments, $d\bar{\varepsilon}_{p,c}$ is the equivalent plastic strain increment, and $s_{z,c}$ and $s_{x,c}$ are the deviatoric stresses and are given by Eq. (4.17).

Eqs. (4.17) and (4.24) imply that

$$\frac{d\varepsilon_{pz,c}}{d\varepsilon_{px,c}} = \frac{s_{z,c}}{s_{x,c}} = \frac{2\sigma_{z,c} - \sigma_{x,c}}{2\sigma_{x,c} - \sigma_{z,c}} \tag{4.25}$$

By substituting Eq. (4.9) into Eq. (4.25), the following equation is obtained:

$$\frac{d\varepsilon_{pz,c}}{d\varepsilon_{px,c}} = \frac{2 - \omega_c}{2\omega_c - 1} \tag{4.26}$$

The longitudinal coiling strain increment $d\varepsilon_{z,c}$ consists of an elastic strain increment $d\varepsilon_{ez,c}$ and a plastic strain increment $d\varepsilon_{pz,c}$:

$$d\varepsilon_{z,c} = d\varepsilon_{ez,c} + d\varepsilon_{pz,c} \tag{4.27}$$

Substitution of Eqs. (4.19) and (4.26) into Eq. (4.27) leads to

$$d\varepsilon_{z,c} = d\varepsilon_{ez,c} - \left(\frac{2-\omega_c}{2\omega_c - 1}\right) d\varepsilon_{ex,c} \tag{4.28}$$

The incremental elastic strains are given by

$$\begin{Bmatrix} d\varepsilon_{ez,c} \\ d\varepsilon_{ex,c} \end{Bmatrix} = \frac{1}{E_0}\begin{bmatrix} 1 & -\nu \\ -\nu & 1 \end{bmatrix}\begin{Bmatrix} d\sigma_{z,c} \\ d\sigma_{x,c} \end{Bmatrix} \tag{4.29}$$

Eq. (4.29) is then substituted into Eq. (4.28) to arrive at

$$d\varepsilon_{z,c} = \left[1 + \nu\left(\frac{2-\omega_c}{2\omega_c - 1}\right)\right]\frac{d\sigma_{z,c}}{E_0} - \left[\nu + \left(\frac{2-\omega_c}{2\omega_c - 1}\right)\right]\frac{d\sigma_{x,c}}{E_0} \tag{4.30}$$

By substituting Eq. (4.22) into Eq. (4.30) and making use of Eqs. (4.5), (4.9) and (4.11), the following equation can be obtained:

$$d\varepsilon_{z,c} = \pm\left\{\begin{array}{l} \dfrac{\left[(1-2\omega_c)^2 - 2\nu(1-2\omega_c)(2-\omega_c)+(2-\omega_c)^2\right]\sigma}{2E_0(1-2\omega_c)\left(1-\omega_c+\omega_c^2\right)^{3/2}}d\omega_c \\ +\dfrac{(1-\omega_c^2)(1-2\nu)}{E_0(1-2\omega_c)\left(1-\omega_c+\omega_c^2\right)^{1/2}}d\sigma \end{array}\right\} \qquad (4.31)$$

where the right-hand side of Eq. (4.31) assumes the positive sign when y ≥ 0.

Integrating the left-hand side of Eq. (4.31) from the onset yield strain $\varepsilon_{z,cy}$ (see Eq. (4.7)) to an arbitrary longitudinal coiling strain $\varepsilon_{z,c}$ and the right-hand side from the initial yield stress σ_{y0} to the instantaneous yield stress σ_{yc} due to coiling for $d\sigma$ and from Poisson's ratio ν to the stress ratio ω_c corresponding to $\varepsilon_{z,c}$ for $d\omega_c$ results in

$$\varepsilon_{z,c} - \varepsilon_{z,cy} = \pm\left\{\begin{array}{l} \displaystyle\int_{\nu}^{\omega_c} \frac{\left[(1-2\omega_c)^2 - 2\nu(1-2\omega_c)(2-\omega_c)+(2-\omega_c)^2\right]\sigma}{2E_0(1-2\omega_c)\left(1-\omega_c+\omega_c^2\right)^{3/2}}d\omega_c \\ +\displaystyle\int_{\sigma_{y0}}^{\sigma_{yc}} \frac{(1-\omega_c^2)(1-2\nu)}{E_0(1-2\omega_c)\left(1-\omega_c+\omega_c^2\right)^{1/2}}d\sigma \end{array}\right\} \qquad (4.32)$$

In Eq. (4.32), as the values of $\varepsilon_{z,c}$ and $\varepsilon_{z,cy}$ can be computed by Eqs. (4.3c) and (4.7) respectively, the integration can be performed numerically by the Euler forward method. The lower limits (i.e. ν for $d\omega_c$ and σ_{y0} for $d\sigma$) of the integration in Eq. (4.32) are treated as initial conditions. Starting with these initial conditions, the value of $d\omega_c$ can be calculated from Eq. (4.23) for a small assigned value of $d\sigma$, and the values of ω_c and σ can then be updated for each step. After the numerical integration (see Eq. (4.32)) is done, the values of σ_{yc} and the corresponding stress ratio ω_c, which are the upper limits of the integration, can be determined.

4.3.4 Uncoiling including flattening

It should be noted that, when $\kappa_c \geq \kappa_{cy}$ (see Eq. (4.14)), the natural uncoiling of a coiled sheet leads to a sheet with a small residual curvature, but in practice this curvature is removed either before cold forming by the imposition of necessary restraints or during cold forming as a result of the out-of-plane stiffness associated with a fold. In the present study, flattening, corresponding to the imposition of necessary restraints, is assumed to take place before cold forming, and implemented by the application of a curvature equal in magnitude but opposite in direction to the coiling curvature. That is, the uncoiling curvature κ_u satisfies the following condition:

$$\kappa_u = -\kappa_c \tag{4.33}$$

After such uncoiling (including flattening), the total stresses of any point can be found by adding the uncoiling stresses to the coiling stresses (point UP in Figure 4.1):

$$\sigma_{z,r} = \sigma_{z,c} + \sigma_{z,u} \tag{4.34a}$$

$$\sigma_{x,r} = \sigma_{x,c} + \sigma_{x,u} \tag{4.34b}$$

The unloading stresses are elastic, until the reverse bending curvature exceeds a threshold curvature value. The elastic uncoiling stresses are given by

$$\sigma_{z,u} = \frac{E_0}{(1-\nu^2)} \kappa_u y$$

$$\sigma_{x,u} = \frac{\nu E_0}{(1-\nu^2)} \kappa_u y$$

An uncoiling curvature limit κ_{uy}, beyond which uncoiling stresses are no elastic, can be defined to indicate the onset of reverse yielding. If reverse y occurs at the limit κ_{uy} as a result of uncoiling, then the yield surface shou again to expand from the preceding one developed at the end of coiling and tl stresses should also obey the von Mises yield criterion. That is,

$$\sigma_{z,r}^2 + \sigma_{x,r}^2 - \sigma_{x,r}\sigma_{z,r} = \sigma_{yc}^2$$

Hence, such an uncoiling curvature limit κ_{uy} can be determined by substitutir (4.10), (4.34) and (4.35) into Eq. (4.36) as

$$\kappa_{uy} = -\frac{\sigma_{yc}(1-\nu^2)[2-\nu+(2\nu-1)\omega_c]}{E_0|y|(1-\nu+\nu^2)\sqrt{1-\omega_c+\omega_c^2}}$$

The total longitudinal strain of any point at the onset of reverse yielding (sh point UE in Figure 4.1) during uncoiling is then

$$\varepsilon_{z,uy} = (\kappa_c + \kappa_{uy})y$$

The corresponding uncoiling stresses are

$$\sigma_{z,uy} = \frac{E_0}{\left(1-\nu^2\right)}\kappa_{uy} y \tag{4.39a}$$

$$\sigma_{x,uy} = \frac{\nu E_0}{\left(1-\nu^2\right)}\kappa_{uy} y \tag{4.39b}$$

and the corresponding stress ratio is

$$\omega_{uy} = \frac{\sigma_{x,c} + \sigma_{x,uy}}{\sigma_{z,c} + \sigma_{z,uy}} \tag{4.40}$$

Making use of Eqs. (4.10), (4.37) and (4.39), Eq. (4.40) can be re-written as

$$\omega_{uy} = \frac{\left[\left(1-\nu^2\right)\omega_c - \nu\left(2-\nu\right)\right]}{\left[\left(1-2\nu\right)\omega_c - \left(1-\nu^2\right)\right]} \tag{4.41}$$

Therefore, when $\kappa_c \le \left|\kappa_{uy}\right|$,

$$\sigma_{z,u} = -\frac{E_0}{\left(1-\nu^2\right)}\kappa_c y \tag{4.42a}$$

$$\sigma_{x,u} = -\frac{\nu E_0}{\left(1-\nu^2\right)}\kappa_c y \tag{4.42b}$$

When $\kappa_c > \left|\kappa_{uy}\right|$, reverse yielding occurs. The total stresses after uncoiling (including flattening) are constrained by the von Mises yield criterion:

$$\sigma_{z,r}^2 + \sigma_{x,r}^2 - \sigma_{x,r}\sigma_{z,r} = \sigma_{yr}^2 \tag{4.43}$$

in which σ_{yr} is the instantaneous yield stress reached after uncoiling (including flattening).

From Eq. (4.43), the total stresses after uncoiling (such as point UP in Figure 4.1) can be obtained as

$$\sigma_{z,r} = \mp \frac{\sigma_{yr}}{\sqrt{1-\omega_u+\omega_u^2}} \tag{4.44a}$$

$$\sigma_{x,r} = \mp \frac{\omega_u \sigma_{yr}}{\sqrt{1-\omega_u+\omega_u^2}} \tag{4.44b}$$

with

$$\omega_u = \sigma_{x,r}/\sigma_{z,r} = \left(\sigma_{x,c}+\sigma_{x,u}\right)/\left(\sigma_{z,c}+\sigma_{z,u}\right) \tag{4.44c}$$

in which $\sigma_{x,r}$ and $\sigma_{z,r} \le 0$ (i.e. compressive stresses) when $y \ge 0$. Hence, from Eqs. (4.10), (4.34) and (4.44), the uncoiling stresses for $\kappa_c > \left|\kappa_{uy}\right|$ are calculated as

$$\sigma_{z,u} = \mp\left(\frac{\sigma_{yc}}{\sqrt{1-\omega_c+\omega_c^2}} + \frac{\sigma_{yr}}{\sqrt{1-\omega_u+\omega_u^2}}\right) \tag{4.45a}$$

$$\sigma_{x,u} = \mp\left(\frac{\omega_c\sigma_{yc}}{\sqrt{1-\omega_c+\omega_c^2}} + \frac{\omega_u\sigma_{yr}}{\sqrt{1-\omega_u+\omega_u^2}}\right) \tag{4.45b}$$

where $\sigma_{x,u}$ and $\sigma_{z,u} \le 0$ (i.e. compressive stresses) when $y \ge 0$.

Similar to Eq. (4.13), the total equivalent plastic strain after uncoiling can be determined as

$$\bar{\varepsilon}_{p,r} = \varepsilon_{p,r} = \varepsilon_{yr} - \frac{\sigma_{yr}}{E_0} \tag{4.46}$$

in which the subscript r refers to the end of the uncoiling stage, and σ_{yr} and ε_{yr} are the instantaneous yield stress and the corresponding strain reached at the end of flattening with their relationship defined by the function $\sigma = F(\varepsilon)$ or $\varepsilon = f(\sigma)$ (see Eq. (4.1)). Therefore, once σ_{yr} is known, ε_{yr} can be determined from the stress-strain curve of the material (see Eq. (4.1)) and the total equivalent plastic strain $\bar{\varepsilon}_{p,r}$ after uncoiling can then be calculated from Eq. (4.46).

In order to determine the uncoiling stresses, the total stresses and the total equivalent plastic strain after uncoiling at any location y, it is again necessary to first calculate the values of σ_{yc}, σ_{yr}, ω_c and ω_u numerically for each value of y. The values of σ_{yc} and ω_c can be determined from Eqs. (4.23) and (4.32) given in the previous subsection. The determination of σ_{yr} and ω_u is discussed in the next subsection.

4.3.5 Determination of σ_{yr} and ω_u

Following the same procedure explained in Subsection 4.3.3 (see Eqs. (4.16)~(4.31)), the equation for the increment of the stress ratio during uncoiling can be obtained as

$$d\omega_u = \frac{2\left(1-\omega_u+\omega_u^2\right)\left(\Omega_u-\omega_u\right)}{\sigma\left[\left(2-\omega_u\right)+\Omega_u\left(2\omega_u-1\right)\right]}d\sigma \tag{4.47}$$

in which H' is given by Eq. (4.15), and Ω_u is the ratio of stress increments $d\sigma_{x,r}/d\sigma_{z,r}$ given by

$$\Omega_u = \frac{4\nu H'\left(1-\omega_u+\omega_u^2\right)-E_0\left(2-\omega_u\right)\left(2\omega_u-1\right)}{E_0\left(2\omega_u-1\right)^2+4H'\left(1-\omega_u+\omega_u^2\right)} \tag{4.48}$$

The equation for longitudinal strain increment during uncoiling can also be obtained as

$$d\varepsilon_{z,u} = \pm\left\{\begin{array}{l} -\dfrac{\left[\left(1-2\omega_u\right)^2-2\nu\left(1-2\omega_u\right)\left(2-\omega_u\right)+\left(2-\omega_u\right)^2\right]\sigma}{2E_0\left(1-2\omega_u\right)\left(1-\omega_u+\omega_u^2\right)^{3/2}}d\omega_u \\ -\dfrac{\left(1-\omega_u^2\right)\left(1-2\nu\right)}{E_0\left(1-2\omega_u\right)\left(1-\omega_u+\omega_u^2\right)^{1/2}}d\sigma \end{array}\right\} \tag{4.49}$$

in which the right-hand side of Eq. (4.49) assumes the positive sign when y ≥ 0. Eq. (4.49) is the same as Eq. (4.31), except for a change in the sign since uncoiling causes material yielding in the opposite direction and a different subscript u to refer to the uncoiling stage.

Integrating the left-hand side of Eq. (4.49) from the longitudinal strain $\varepsilon_{z,uy}$ at the onset of reverse yielding to the final longitudinal strain $\varepsilon_{z,r}$ and the right-hand side from the instantaneous yield stress σ_{yc} due to coiling to the instantaneous yield stress σ_{yr} after uncoiling for $d\sigma$ and from the stress ratio ω_{uy} at the onset of reverse yielding to the stress ratio ω_u corresponding to $\varepsilon_{z,r}$ for $d\omega_u$ results in

$$\varepsilon_{z,r} - \varepsilon_{z,uy} = \pm \left\{ \begin{array}{l} \displaystyle\int_{\omega_{uy}}^{\omega_u} \frac{\left[(1-2\omega_u)^2 - 2\nu(1-2\omega_u)(2-\omega_u) + (2-\omega_u)^2\right]\sigma}{2E_0(2\omega_u - 1)\left(1-\omega_u+\omega_u^2\right)^{3/2}} d\omega_u \\ \displaystyle + \int_{\sigma_{yc}}^{\sigma_{yr}} \frac{(1-\omega_u^2)(1-2\nu)}{E_0(2\omega_u - 1)\left(1-\omega_u+\omega_u^2\right)^{1/2}} d\sigma \end{array} \right\} \tag{4.50}$$

Uncoiling including flattening enforces the final longitudinal strain $\varepsilon_{z,r}$ to become zero at the end of the process. That is,

$$\varepsilon_{z,r} = 0 \tag{4.51}$$

After σ_{yc} and ω_c are determined from the numerical integration of Eq. (4.32) for the coiling stage, the value of ω_{uy} can be calculated by Eq. (4.41). In Eq. (4.50), as the values of $\varepsilon_{z,uy}$ and $\varepsilon_{z,r}$ can be determined from Eqs. (4.38) and (4.51) respectively, the integration can be performed numerically again by the Euler forward method. The lower limits (i.e. ω_{uy} for $d\omega_u$ and σ_{yc} for $d\sigma$) of the integration in Eq. (4.50) are treated as initial conditions. Starting with these initial conditions, the value of $d\omega_u$ can be calculated from Eq. (4.47) for a small assigned value of $d\sigma$, and then the

values of ω_u and σ can be updated for each step. After the numerical integration (see Eq. (4.50)) is done, the values of σ_{yr} and the corresponding stress ratio ω_u, which are the upper limits of the integration, can be determined.

4.4 SOLUTION FOR ELASTIC-PERFECTLY PLASTIC SHEETS

4.4.1 Residual stresses

Previous section has presented a general analytical solution for a strain-hardening material, in which the values of the parameters σ_{yc}, σ_{yr}, ω_c and ω_u need to be determined numerically. For an elastic-perfectly plastic sheet subjected to the coiling and uncoiling, the value of the instantaneous yield stress is independent of the amount of plastic straining, and is treated as a constant. Therefore, when the analytical solution is applied to the coiling and uncoiling of elastic-perfectly plastic sheets, the initial yield stress σ_{y0} and the instantaneous yield stresses σ_{yc} and σ_{yr} are all equal in magnitudes and can be replaced by a single constant yield stress σ_y in those equations presented in Section 4.3. That is,

$$\sigma_{yr} = \sigma_{yc} = \sigma_{y0} = \sigma_y \tag{4.52}$$

The initial elastic modulus E_0 is now simply referred to as the elastic modulus E for the elastic-perfectly plastic material discussed in this section. The stress-strain relationship of this material can be defined by the following equation:

$$\sigma = \begin{cases} E\varepsilon, & \varepsilon \le \sigma_y / E \\ \sigma_y, & \varepsilon > \sigma_y / E \end{cases} \tag{4.53}$$

Hence, Eq. (4.53) is now used to define the function $\sigma = F(\varepsilon)$ (see Eq. (4.1)) in the general analytical solution. As a result of the constant yield stress, the stress ratios ω_c and ω_u can be directly related to the value of y for a given coiling curvature κ_c and a closed-form analytical solution for residual stresses can be established as detailed below.

As $\sigma = \sigma_y$ for material points in plastic flow, Eq. (4.32) can be reduced to

$$\varepsilon_{z,c} = \varepsilon_{z,cy} \pm \frac{\sigma_y}{E}\left[\frac{\omega_c(1-2\nu)}{\sqrt{1-\omega_c+\omega_c^2}} + \frac{\sqrt{3}}{2}\coth^{-1}\left(\sqrt{\frac{4\left(1-\omega_c+\omega_c^2\right)}{3}}\right)\right]_{\nu}^{\omega_c} \tag{4.54}$$

By substituting Eqs. (4.3c) and (4.7) into Eq. (4.54), the following expression is obtained:

$$|y| = \frac{\sigma_y\left(1-\nu^2\right)}{E\kappa_c\sqrt{1-\nu+\nu^2}} + \frac{\sigma_y}{E\kappa_c}\left[\frac{\omega_c(1-2\nu)}{\sqrt{1-\omega_c+\omega_c^2}} + \frac{\sqrt{3}}{2}\coth^{-1}\left(\sqrt{\frac{4\left(1-\omega_c+\omega_c^2\right)}{3}}\right)\right]_{\nu}^{\omega_c} \tag{4.55}$$

which relates the stress ratio ω_c to the value of y. Therefore, for a given coiling curvature κ_c, the stress ratio ω_c can be determined from Eq. (4.55) at each location

of $|y| > y_{cy}$, and then the corresponding inelastic coiling stresses can be determined from Eq. (4.10). For $|y| \le y_{cy}$, coiling stresses in the elastic core can still be calculated by Eq. (4.3).

Similarly, with $\sigma = \sigma_y$ for points in plastic flow, Eq. (4.50) can also be reduced to

$$\varepsilon_{z,r} = \varepsilon_{z,uy} \pm \frac{\sigma_y}{E}\left[\frac{-\omega_u(1-2\nu)}{\sqrt{1-\omega_u+\omega_u^2}} - \frac{\sqrt{3}}{2}\coth^{-1}\left(\sqrt{\frac{4\left(1-\omega_u+\omega_u^2\right)}{3}}\right)\right]_{\omega_{uy}}^{\omega_u} \tag{4.56}$$

Substitution of Eqs. (4.38) and (4.51) into Eq. (4.56) yields

$$|y| = \frac{\sigma_y}{E\left(\kappa_c + \kappa_{uy}\right)}\left[\frac{\omega_u(1-2\nu)}{\sqrt{1-\omega_u+\omega_u^2}} + \frac{\sqrt{3}}{2}\coth^{-1}\left(\sqrt{\frac{4\left(1-\omega_u+\omega_u^2\right)}{3}}\right)\right]_{\omega_{uy}}^{\omega_u} \tag{4.57}$$

where the values of κ_{uy} and ω_{uy} can be determined from Eqs. (4.37) and (4.41) respectively. With Eq. (4.57), the stress ratio ω_u can be determined at any location y for $\kappa_c > |\kappa_{uy}|$, and then the corresponding uncoiling stresses and total residual stresses can be determined from Eqs. (4.45) and (4.34) respectively. When $\kappa_c \le |\kappa_{uy}|$, elastic uncoiling stresses can still be determined from Eq. (4.42).

4.4.2 Equivalent plastic strains

Apart from residual stresses, the equivalent plastic strain is another quantity of interest as it reflects the total deformation state of a point. Since the yield stress becomes constant for elastic-perfectly plastic material points undergoing plastic straining (i.e. $\sigma = \sigma_y$ for $\varepsilon > \sigma_y / E$), the equivalent plastic strains $\bar{\varepsilon}_{p,c}$ and $\bar{\varepsilon}_{p,r}$ cannot be determined from Eqs. (4.13) and (4.46) respectively. However, they can be derived from the equivalent plastic strain increment $d\bar{\varepsilon}_p$. During the coiling stage, the equivalent plastic strain increment $d\bar{\varepsilon}_{p,c}$ is given by

$$d\bar{\varepsilon}_{p,c} = \frac{2\sigma_y \left(s_{z,c} + \nu s_{x,c}\right)}{3\left(s_{x,c}^2 + s_{z,c}^2 + 2\nu s_{x,c} s_{z,c}\right)} d\varepsilon_{z,c} \tag{4.58}$$

where $s_{z,c}$ and $s_{x,c}$ are the deviatoric stresses given by Eq. (4.17), and $d\varepsilon_{z,c}$ is the longitudinal coiling strain increment given by Eq. (4.31). As $\sigma = \sigma_y$ for material points in plastic flow, Eq. (4.31) can be reduced to

$$d\varepsilon_{z,c} = \pm \frac{\sigma_y \left[\left(1-2\omega_c\right)^2 - 2\nu\left(2-\omega_c\right)\left(1-2\omega_c\right) + \left(2-\omega_c\right)^2\right]}{2E\left(1-2\omega_c\right)\left(1-\omega_c+\omega_c^2\right)^{3/2}} d\omega_c \tag{4.59}$$

By substituting Eqs. (4.17) and (4.59) into Eq. (4.58), one obtains

$$d\bar{\varepsilon}_{p,c} = \frac{\sigma_y \left[\left(2-\omega_c\right) + \nu\left(2\omega_c - 1\right)\right]}{E\left(1-\omega_c+\omega_c^2\right)\left(1-2\omega_c\right)} d\omega_c \tag{4.60}$$

Integrating the left-hand side from zero to the corresponding equivalent plastic strain $\bar{\varepsilon}_{p,c}$ experienced during coiling and the right-hand side of Eq. (4.60) from Poisson's ratio ν to the stress ratio ω_c results in

$$\bar{\varepsilon}_{p,c} = \frac{\sigma_y}{E}\left[\ln\left(\frac{\left(1-\omega_c+\omega_c^2\right)^{1/2}}{2\omega_c-1}\right)+(1-2\nu)\frac{\sqrt{3}}{3}\tan^{-1}\left(\frac{\sqrt{3}(2\omega_c-1)}{3}\right)\right]_{\nu}^{\omega_c} \tag{4.61}$$

Similarly, the equivalent plastic strain increment $d\bar{\varepsilon}_{p,u}$ during the uncoiling stage can be obtained as

$$d\bar{\varepsilon}_{p,u} = \frac{\sigma_y\left[(2-\omega_u)+\nu(2\omega_u-1)\right]}{E\left(1-\omega_u+\omega_u^2\right)(1-2\omega_u)}d\omega_u \tag{4.62}$$

Integrating the left-hand side of Eq. (4.62) from the equivalent plastic strain $\bar{\varepsilon}_{p,c}$ at the end of coiling to the total equivalent plastic strain $\bar{\varepsilon}_{p,r}$ after flattening, and the right-hand side from the stress ratio ω_{uy} at the onset of reverse yielding to the stress ratio ω_u corresponding to $\varepsilon_{z,r}$ or $\bar{\varepsilon}_{p,r}$, results in

$$\bar{\varepsilon}_{p,r} = \bar{\varepsilon}_{p,c} + \frac{\sigma_y}{E}\left[\ln\left(\frac{\left(1-\omega_u+\omega_u^2\right)^{1/2}}{2\omega_u-1}\right)+(1-2\nu)\frac{\sqrt{3}}{3}\tan^{-1}\left(\frac{\sqrt{3}(2\omega_u-1)}{3}\right)\right]_{\omega_{uy}}^{\omega_u} \tag{4.63}$$

With the stress ratios ω_c and ω_u determined at each location y from Eqs. (4.55) and (4.57), the equivalent plastic strains due to the coiling and the uncoiling can be calculated from Eqs. (4.61) and (4.63) respectively.

It is worth noting that the closed-form analytical solution presented in this section can be used to predict residual stresses and equivalent plastic strains in carbon steel sheets due to the coiling-uncoiling process. For a carbon steel sheet possessing a stress-strain curve of the sharp-yielding type (i.e. a yield plateau exists before strain hardening), the strains induced by the coiling-uncoiling process are relatively small, so it is reasonable to assume that strain hardening is not involved. That is, the carbon steel can be assumed to possess an elastic-perfectly plastic stress-strain curve, and thus the closed-form analytical solution can be employed for the prediction.

4.5 SOLUTION FOR ELASTIC-LINEAR STRAIN-HARDENING SHEETS

The analytical solution presented in Section 4.3 can be applied to the coiling and uncoiling of elastic-linear strain-hardening sheets. The stress-strain curve of an elastic-linear strain-hardening material can be defined by the following equation:

$$\sigma = \begin{cases} E_0 \varepsilon, & \varepsilon \le \sigma_{y0} / E_0 \\ \sigma_{y0} + E_{st}\left(\varepsilon - \dfrac{\sigma_{y0}}{E_0} \right), & \varepsilon > \sigma_{y0} / E_0 \end{cases} \tag{4.64a}$$

or

$$\varepsilon = \begin{cases} \dfrac{\sigma}{E_0}, & \sigma \le \sigma_{y0} \\ \dfrac{\sigma_{y0}}{E_0} + \dfrac{\left(\sigma - \sigma_{y0}\right)}{E_{st}}, & \sigma > \sigma_{y0} \end{cases} \tag{4.64b}$$

where E_{st} is the slope of the stress-strain curve in the strain-hardening stage. Eq. (4.2) is now used to define the function $\sigma = F(\varepsilon)$ or $\varepsilon = f(\sigma)$ (see Eq. (4.1)) in the general analytical solution.

By substituting Eq. (4.64) after differentiation into Eq. (4.15), the slope of the equivalent stress-equivalent plastic strain relation H' for $\sigma > \sigma_{y0}$ becomes

$$H' = \frac{E_0 E_{st}}{E_0 - E_{st}} \tag{4.65}$$

By substituting Eq. (4.64) into Eqs. (4.13) and (4.46), the equivalent plastic strains $\bar{\varepsilon}_{p,c}$ and $\bar{\varepsilon}_{p,r}$ can be obtained as:

$$\bar{\varepsilon}_{p,c} = \left(\sigma_{yc} - \sigma_{y0}\right)\left[\frac{E_0 - E_{st}}{E_0 E_{st}}\right] \tag{4.66}$$

and

$$\bar{\varepsilon}_{p,r} = \left(\sigma_{yr} - \sigma_{y0}\right)\left[\frac{E_0 - E_{st}}{E_0 E_{st}}\right] \tag{4.67}$$

Hence, residual stresses and equivalent plastic strains in an elastic-linear strain-hardening sheet due to the coiling-uncoiling process can be obtained by replacing

Eqs. (4.1), (4.13), (4.15) and (4.46) with Eqs. (4.64)~(4.67), and then following the procedure explained in Section 4.3 (see Eqs. (4.1)~(4.51)).

4.6 SOLUTION FOR ELASTIC-NONLINEAR STRAIN-HARDENING SHEETS

The analytical solution presented in Section 4.3 is now applied to the coiling and uncoiling of elastic-nonlinear strain-hardening sheets. This can be achieved by defining the stress-strain relationship of an elastic nonlinear strain-hardening material to replace Eq. (4.1). The stress-strain curve of this material can be defined by the modified Ludwik equation (Chakrabarty 2000) given below:

$$\sigma = \begin{cases} E_0\varepsilon, & \varepsilon \le \sigma_{y0}/E_0 \\ \sigma_{y0}\left(\dfrac{E_0\varepsilon}{\sigma_{y0}}\right)^{n_s}, & \varepsilon > \sigma_{y0}/E_0 \end{cases} \tag{4.68a}$$

or

$$\varepsilon = \begin{cases} \dfrac{\sigma}{E_0}, & \sigma \le \sigma_{y0} \\ \dfrac{\sigma_{y0}}{E_0}\left(\dfrac{\sigma}{\sigma_{y0}}\right)^{1/n_s}, & \sigma > \sigma_{y0} \end{cases} \tag{4.68b}$$

where n_s is the strain-hardening exponent.

By substituting Eq. (4.68) after differentiation into Eq. (4.15), the slope H' for $\sigma > \sigma_{y0}$ becomes

$$H' = \frac{n_s E_0}{\left(\sigma / \sigma_{y0}\right)^{(1-n_s)/n_s} - n_s} \tag{4.69}$$

By substituting Eq. (4.68) into Eqs. (4.13) and (4.46), the equivalent plastic strains $\bar{\varepsilon}_{p,c}$ and $\bar{\varepsilon}_{p,r}$ can be obtained as:

$$\bar{\varepsilon}_{p,c} = \frac{\sigma_{y0}}{E_0}\left(\frac{\sigma_{yc}}{\sigma_{y0}}\right)^{1/n_s} - \frac{\sigma_{yc}}{E_0} \tag{4.70}$$

and

$$\bar{\varepsilon}_{p,r} = \frac{\sigma_{y0}}{E_0}\left(\frac{\sigma_{yr}}{\sigma_{y0}}\right)^{1/n_s} - \frac{\sigma_{yr}}{E_0} \tag{4.71}$$

Hence, residual stresses and equivalent plastic strains in an elastic nonlinear strain-hardening sheet due to the coiling-uncoiling process can be obtained by replacing Eqs. (4.1), (4.13), (4.15) and (4.46) with Eqs. (4.68)~(4.71), and then following the procedure explained in Section 4.3 (see Eqs. (4.1)~(4.51)).

4.7 SOLUTION FOR NONLINEAR STRAIN-HARDENING SHEETS —— STAINLESS STEEL SHEETS

The analytical solution presented in Section 4.3 can also be applied to the coiling and uncoiling of nonlinear strain-hardening sheets such as stainless steel sheets discussed in this section. To achieve this, the stress-strain relationship of stainless steel alloys

needs to be defined first. Stainless steel alloys are characterized by a low proportional limit, an extended strain-hardening capability and material anisotropy. The effect of material anisotropy on yielding can be ignored for certain alloys, such as austenitic alloys (Johansson and Olsson 2000). Therefore, the analytical solution presented in Section 4.3 is applicable to sheets made of these stainless steel alloys by assuming that the alloys possess isotropic material properties.

The nonlinear stress-strain behaviour of stainless steel alloys is generally described by the Ramberg-Osgood relationship which can closely approximate measured stress-strain curves up to the 0.2% proof stress $\sigma_{0.2}$, but inaccuracy may arise for strains exceeding the total strain $\varepsilon_{0.2}$ at the 0.2% proof stress (the so-called 0.2% total strain). In view of this, a new stress-strain model, namely the 3-stage full-range stress-strain model presented in Chapter 3, has been developed for stainless steel alloys over full ranges of both tensile and compressive strains. Even in the coiling-uncoiling process, strains caused by the larger coiling curvatures can be well beyond the 0.2% total strain $\varepsilon_{0.2}$. For this reason, instead of using the Ramberg-Osgood expression, the 3-stage full-range stress-strain relationship given by Eq. (3.6) is employed in the present study.

Due to the “roundhouse” type material behaviour, no purely elastic straining is involved during coiling and the initial yield point coincides with the origin of the stress-strain curve. The size $(2y_{cy})$ of the elastic core in a thin sheet thus becomes zero, and the limit value κ_{cy} of the coiling curvature at which the extreme surfaces of the thin sheet start to yield also becomes zero (point E coincides with point O in Figure 4.1). That is,

$$\sigma_{y0} = 0 \tag{4.72}$$

$$y_{cy} = 0 \tag{4.73}$$

and

$$\kappa_{cy} = 0 \tag{4.74}$$

Therefore, except the point at the neutral axis ($y = 0$), all material points across the thickness experience inelastic straining right from the beginning.

By substituting Eq. (3.6) after differentiation into Eq. (4.15), H' becomes

$$H' = \begin{cases} \dfrac{\sigma_{0.2}^{n}}{0.002 n \sigma^{n-1}}, & \sigma \le \sigma_{0.2} \\ \left\{ \dfrac{1}{E_{0.2}} - \dfrac{1}{E_0} + n'_{0.2,1.0} \left[0.008 + \left(\sigma_{1.0} - \sigma_{0.2}\right) \left(\dfrac{1}{E_0} - \dfrac{1}{E_{0.2}} \right) \right] \dfrac{\left(\sigma - \sigma_{0.2}\right)^{n'_{0.2,1.0}-1}}{\left(\sigma_{1.0} - \sigma_{0.2}\right)^{n'_{0.2,1.0}}} \right\}^{-1}, & \\ & \sigma_{0.2} < \sigma \le \sigma_{2.0} \\ \left[\dfrac{\left(b \mp \sigma\right) \pm \left(\sigma - a\right)}{\left(b \mp \sigma\right)^2} - \dfrac{1}{E_0} \right]^{-1}, & \sigma > \sigma_{2.0} \end{cases} \tag{4.75}$$

where the upper sign corresponds to tension, and the lower sign corresponds to compression. The parameters $E_{0.2}$, $\varepsilon_{0.2}$, $\sigma_{1.0}$, $\sigma_{2.0}$, a and b in Eq. (4.75) have been defined in Chapter 3 in terms of the basic Ramberg-Osgood parameters (E_0, $\sigma_{0.2}$ and n).

The equivalent plastic strains $\bar{\varepsilon}_{p,c}$ and $\bar{\varepsilon}_{p,r}$ are still given by Eqs. (4.13) and (4.46). In Eqs. (4.13) and (4.46), ε_{yc} and ε_{yr} are the strains corresponding to the instantaneous yield stresses σ_{yc} and σ_{yr} respectively, and can be calculated from the 3-stage full-range stress-strain relationship given by Eq. (3.6). Hence, residual stresses and equivalent plastic strains in a stainless steel sheet due to the coiling-uncoiling process can be obtained by replacing Eqs. (4.1), (4.8), (4.14) and (4.15) with Eqs. (3.6), (4.73)~(4.75) and then following the procedure explained in Section 4.3 (see Eqs. (4.1)~(4.51)).

4.8 FINITE ELEMENT SIMULATION

4.8.1 General

In order to verify the analytical solutions presented in the preceding sections, the coiling and uncoiling process of steel sheets was also simulated using the finite element package ABAQUS (2002). A carbon steel sheet and an austenitic stainless steel sheet were studied here, and these two sheets had the thickness of 2 mm. For both materials (i.e. the carbon steel and the austenitic stainless steel), a flat strip of 60 mm in length, was modelled with one end fixed and the other end free (see Figure 4.2). Both geometrical and material nonlinearities were considered. The mechanical properties of the carbon steel sheet and the stainless steel sheet as well as the modelling of their material behaviour are given in the next subsection.

Twenty four layers of CPE4R elements, which are 2-D plane strain 4-node elements with reduced integration and hourglass control, were employed to capture the through-thickness variations of stresses. Two steps were required to simulate the whole coiling-uncoiling process: coiling was simulated as pure bending of the cantilever steel strip to a coil radius r $(= D/2)$ of 250 mm, and uncoiling including flattening was simulated as reverse bending of the strip to the initial zero curvature. The steps involved are summarized in Figure 4.3.

At the fixed end, all nodes were constrained in the longitudinal direction. In addition, the node at the mid-depth was constrained also in the through-thickness direction. By means of kinematic coupling, the longitudinal displacements of all nodes at the free end were constrained to the rigid body motion of the reference node located at the mid-depth on the free end, to ensure that the plane section remained plane. Both coiling and uncoiling were achieved by specifying the desired amounts of translation and rotation of the reference node at the free end, corresponding to the desired coiling curvature and final zero curvature respectively.

4.8.2 Material modelling

Carbon steel sheets possess the stress-strain curve of the sharp-yielding type. As discussed in Section 4.4, the strains induced by the coiling-uncoiling process are relatively small, so it is reasonable to assume that strain hardening is not involved in carbon steel sheets. Therefore, the carbon steel used for the verification was assumed

to be elastic-perfectly plastic with the following properties: yield stress σ_y = 250 MPa, elastic modulus E = 200 GPa and Poisson's ratio ν = 0.3.

Austenitic alloys are the most common stainless steel grades used in structures. Austenitic grade 304 alloy (equivalent to grade UNS30400 in accordance with ASTM E527-83 (ASTM 2003)) was used for the verification and was assumed to be an isotropic nonlinear strain-hardening material with the following mechanical properties for longitudinal tension given in Appendix B of AS/NZS 4673 Standard (AS/NZS 2001): 0.2% proof stress $\sigma_{0.2}$ = 205.0 MPa, initial elastic modulus E_0 = 195.0 GPa, exponent n = 7.5 and Poisson's ratio ν = 0.3. In this case, the non-dimensional 0.2% proof stress $e = \sigma_{0.2}/E_0$ is 0.00105.

To describe the stress-strain behaviour of the austenitic stainless steel, the 3-stage full-range stress-strain model (see Eq. (3.6)) presented in Chapter 3 was incorporated into the finite element analysis to provide the nominal stress-strain data over the whole range of strains up to the ultimate strain. Instead of using the more general expression (see Eq. (3.13b)) for the ultimate stress σ_u^{ten}, Eq. (3.13a) was used to provide a more accurate prediction of σ_u^{ten} for the austenitic alloys studied in this section.

The ABAQUS metal plasticity model is characterized by the von Mises yield criterion and associated flow rule with isotropic hardening. The modelling of material nonlinearity required the definition of a true stress-logarithmic plastic strain (or the so-called true plastic strain) relationship up to the ultimate point, which was converted

from the nominal stress-strain data. The nominal stress-strain curve, the true stress-strain curve and the true stress-logarithmic plastic strain curve for the austenitic stainless steel are shown in Figure 4.4.

4.8.3 Comparison between analytical predictions and finite element results

Residual stresses predicted by the finite element model are uniform along the whole length of the strip, so only the stress distributions at the fixed end are compared in Figures 4.5~4.8 with the predictions of the analytical solutions. The analytical predictions for the carbon steel sheet are determined by the closed-form analytical solution presented in Section 4.4, while the predictions for the stainless steel sheet are determined by the analytical solution presented in Section 4.7.

The longitudinal and transverse residual stresses as well as the equivalent plastic strains predicted by both the analytical solution and the finite element simulation are seen to be in very close agreement, which demonstrates the validity and accuracy of both approaches. The results in Figures 4.5~4.8 also show that the residual stresses are not linearly distributed across the thickness. Therefore, the assumption of a linear residual stress distribution adopted in existing experimentally-based residual stress studies is not appropriate.

4.9 STRESS PATH OF THE COILING-UNCOILING PROCESS

4.9.1 Carbon steel

Using the predictions from the analytical solution presented and verified above, the carbon steel sheet described in the preceding section is examined here to illustrate the development of stresses at different stages of the coiling-uncoiling process. The development process of stresses in the stainless steel sheet will be examined in the next subsection.

Figure 4.9 shows the stress path of the extreme tensile fibre of the carbon steel sheet during the entire coiling-uncoiling process, while Figures 4.10 and 4.11 present the distributions of stresses and equivalent plastic strains, respectively, corresponding to different deformation states. In Figure 4.9, the path O-E represents elastic coiling, with point E being reached (attainment of yielding) when the applied curvature reaches the limit value κ_{cy} which is 0.00128 mm^{-1}. During this stage, the through-thickness distributions of both the longitudinal and transverse stresses are linear (Figure 4.10(a)). With further loading, the stress path of the extreme fibre is represented by E-P in Figure 4.9, with point P denoting the end of the coiling stage. In this stage, the through-thickness stress distributions become nonlinear and the equivalent plastic strain $\bar{\varepsilon}_{p,c}$ starts to accumulate (see Figures 4.10(b) and 4.11). At the end of the coiling stage, two plastic zones are developed near the top and bottom surfaces of the sheet with an elastic core in the middle (Figure 4.10(b)). The maximum longitudinal and transverse coiling stresses are $1.154\sigma_y$ and $0.557\sigma_y$ respectively.

Elastic uncoiling is represented by the stress path P-UE in Figure 4.9. During elastic uncoiling, no additional plastic strains are induced. The stress distributions at the onset of reverse yielding are shown in Figure 4.10(c). The next stage, involving reverse yielding, is represented by stress path UE-UP in Figure 4.9. During this stage, plastic strains are induced. At the end of this stage, the residual stresses are as shown in Figure 4.10(d), while the distribution of the equivalent plastic strain is shown in Figure 4.11. The maximum longitudinal and transverse residual stresses are $1.145\sigma_y$ and $0.444\sigma_y$ respectively. It is seen that, due to the zero curvature after flattening, no residual stresses are found in the elastic core. Two zones of high tensile and compressive longitudinal residual stresses, with magnitudes greater than σ_y, are located near the inner and outer surfaces of the flattened sheet respectively, and each has a size larger than $0.25t$.

On the surfaces of the carbon steel sheet, the stress ratio ω_c after coiling is 0.482 while the stress ratio ω_u after flattening is 0.387. Because elastic strains are considered in the present analysis, the stress ratios ω_c and ω_u will never reach the value of 0.5 for rigid-plastic bending. However, from Eqs. (4.54) and (4.56), it can be observed that, as the longitudinal coiling strain $\varepsilon_{z,c}$ and the final strain after flattening $\varepsilon_{z,r}$ approach infinity, the stress ratios ω_c and ω_u will approach 0.5. This means that the point UL on the yield envelope (Figure 4.9) can only be approached but can never be reached.

4.9.2 Stainless steel

Using the predictions from the analytical solution verified in the preceding section, the development process of stresses in the stainless steel sheet due to the coiling and uncoiling is examined here. Figure 4.1 shows the general stress development process of the extreme tensile fibre of a strain-hardening steel sheet during the entire coiling-uncoiling process, such as the present stainless steel strip. Figures 4.12 and 4.13 present the distributions of stresses and equivalent plastic strains respectively corresponding to different deformation states of the stainless steel sheet.

In Figure 4.1, for the stainless steel sheet, point E coincides with point O due to the "roundhouse" type material behaviour, and thus the path O-E vanishes to become a single point O. The stress path of the extreme fibre undergoing inelastic coiling is represented by O-P in Figure 4.1, with point P denoting the end of the coiling stage. During this stage, the material points across whole thickness are subjected to inelastic straining and the yield envelope of each material point expands gradually. As a result, the distributions of coiling stresses and the equivalent plastic strain $\bar{\varepsilon}_{p,c}$ over the thickness become nonlinear (Figures 4.12(a) and 4.13), and two inelastic zones are developed respectively in the upper and lower halves of the thickness. The coiling stresses and equivalent plastic strain have their maximum magnitudes at the sheet surfaces, and gradually decrease to zero at the middle of the thickness (Figure 4.12(a)). At the end of the coiling stage, the maximum longitudinal and transverse coiling stresses at the sheet surfaces are $1.206\sigma_{0.2}$ and $0.584\sigma_{0.2}$ respectively.

Elastic uncoiling which follows inelastic coiling is represented by the stress path P-UE in Figure 4.1. During elastic uncoiling, no additional plastic strains are induced. The stress distributions at the onset of reverse yielding are shown in Figure 4.12(b). The next stage, involving reverse yielding, is represented by stress path UE-UP in Figure 4.1. During this stage, plastic strains are induced again and the yield envelope starts to expand further. At the end of this stage, the residual stresses are as shown in Figure 4.12(c), while the distribution of the equivalent plastic strain is shown in Figure 4.13. The maximum longitudinal and transverse residual stresses are $1.244\sigma_{0.2}$ and $0.529\sigma_{0.2}$ respectively. Two zones of high tensile and compressive longitudinal residual stresses, with magnitudes greater than $\sigma_{0.2}$, are located within the lower and upper halves of the sheet thickness respectively.

On the surfaces of the stainless steel sheet, the stress ratio ω_c after coiling is 0.484 while the stress ratio ω_u after flattening is 0.425. Similar to the coiling and uncoiling of the carbon steel sheet, because some elastic deformation is involved, the stress ratios ω_c and ω_u can never reach the value of 0.5 for rigid-plastic bending. This means that the point UL on the yield envelope (Figure 4.1) can only be approached but can never be reached.

4.10 CONCLUSIONS

Residual stresses in cold-formed sections are in general due to both the cold-forming process (press braking or cold rolling) and the prior coiling-uncoiling process. In both processes, residual stresses are induced as a result of plastic bending. This chapter has

been concerned with the accurate prediction of residual stresses resulting from the coiling-uncoiling process, as such predictions are a necessary starting point for the prediction of residual stresses from the process of cold forming.

In this chapter, a general analytical solution for the residual stresses from the coiling-uncoiling process has been presented in which coiling, uncoiling and flattening are all taken into account in a plane strain pure elastic-plastic bending model. This general analytical solution was then specialized for four common types of sheet steels by incorporating their specific stress-strain relationships: (1) elastic-perfectly plastic steels, (2) elastic-linear strain-hardening steels, (3) elastic-nonlinear strain-hardening steels, and (4) nonlinear strain-hardening steels, such as stainless steel alloys. A finite element simulation of the same problem has also been presented. The analytical predictions have been shown to agree closely with finite element results, demonstrating the validity of both approaches. Results from both methods showed that through-thickness variations of residual stresses are nonlinear.

The analytical solution was employed to generate numerical results to illustrate the development process of residual stresses. The analytical solution provides accurate residual stresses and equivalent plastic strains which can be specified as the initial state in a finite element simulation of the cold-forming process. Such exploitation of the present analytical solution will be reported in Chapter 5.

It should be noted that the analytical solution presented in this paper is based on the plane strain assumption which is invalid for a narrow zone along each longitudinal edge of a wide plate of finite width. As a result, the solution is unlikely to give

satisfactory predictions if applied to the coiling of a rather narrow strip (e.g. a width-to-thickness ratio below 50). The validity and limitation of this plane strain assumption used for modelling the coiling-uncoiling process and its subsequent effect on the structural behaviour of cold-formed members are explored and discussed in Appendices B and C. Finally, it is also worth noting that although the present solution has been presented in the context of cold-formed steel sections, it can be applied to any other situations where a wide steel plate is bent into a cylindrical surface.

4.11 REFERENCES

ABAQUS (2002). *Standard User's Manual, V6.3*, Hibbitt, Karlsson and Sorensen, Inc., United States.

AS/NZS (2001). *Cold-Formed Stainless Steel Structures, AS/NZS 4673:2001*, Australian/New Zealand Standard, Standards Australia, Sydney.

ASTM (2003). *Standard Practice for Numbering Metals and Alloys (UNS), ASTM E527-83*, American Society for Testing and Materials, United States.

Chakrabarty, J. (2000). *Applied Plasticity*, Springer-Verlag, Inc., New York.

Johansson, B. and Olsson, A. (2000). Current design practice and research on stainless steel structures in Sweden. *Journal of Constructional Steel Research*, **54**, 3-29.

Ragab, A. R. and Bayoumi, S. E. (1998). *Engineering Solid Mechanics: Fundamentals and Applications*, CRC press, United States.

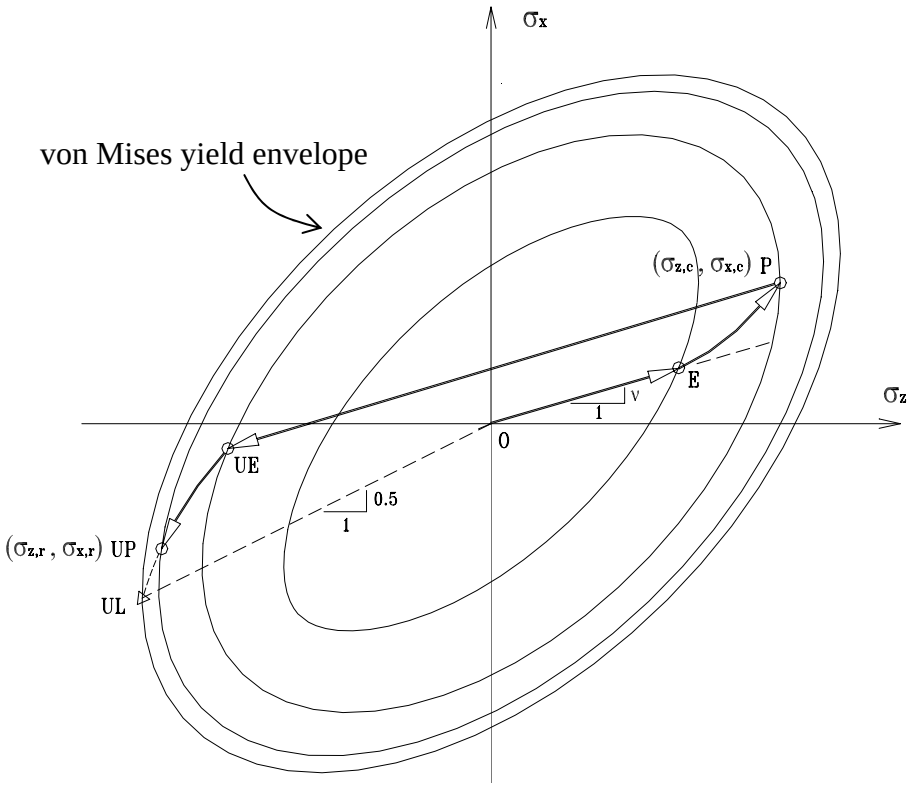

Figure 4.1 Stress path of a surface point of a strain-hardening steel strip during the coiling-uncoiling process.

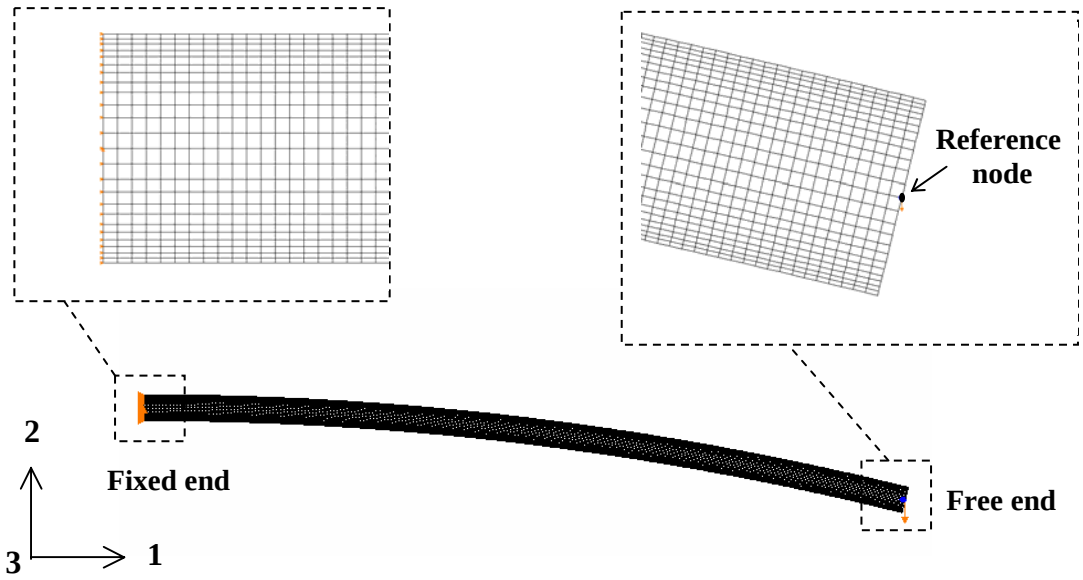

Figure 4.2 Mesh and boundary conditions.

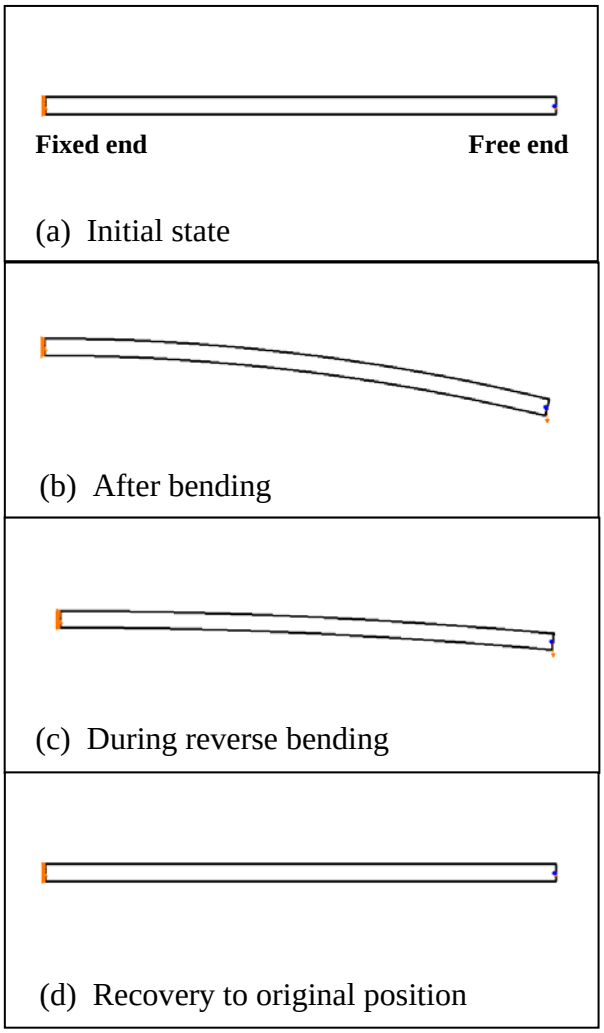

Figure 4.3 Pure bending of a flat strip.

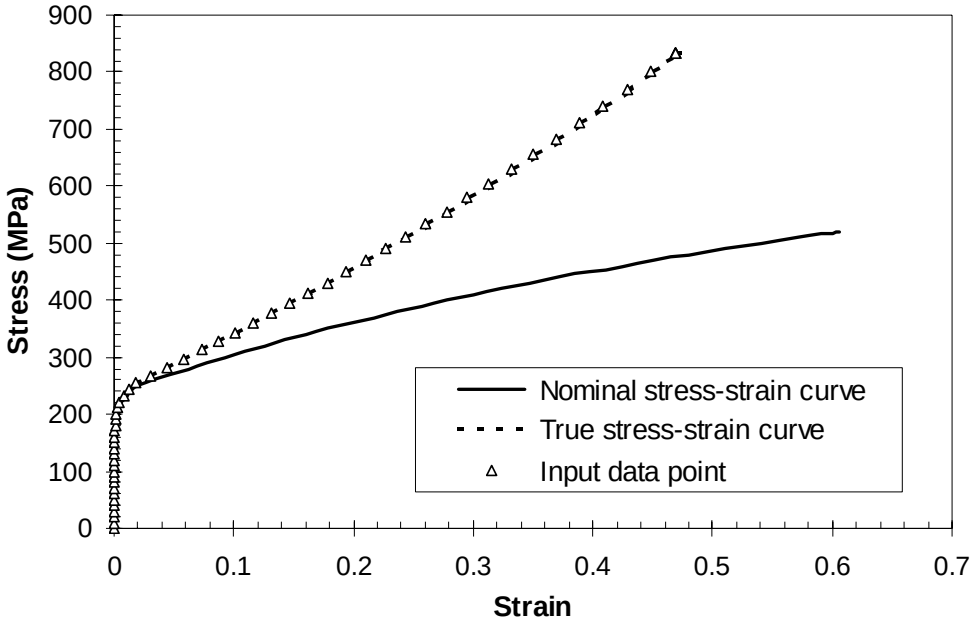

(a) Full stress-strain curves

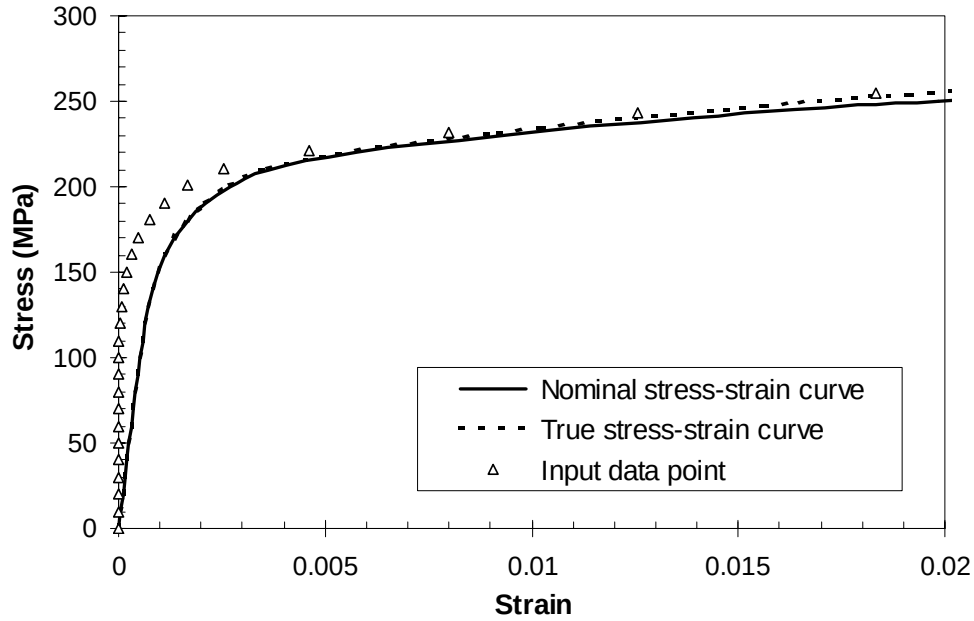

(b) Initial stress-strain curves

Figure 4.4 Stress-strain curves for the longitudinal tension of the austenitic stainless steel.

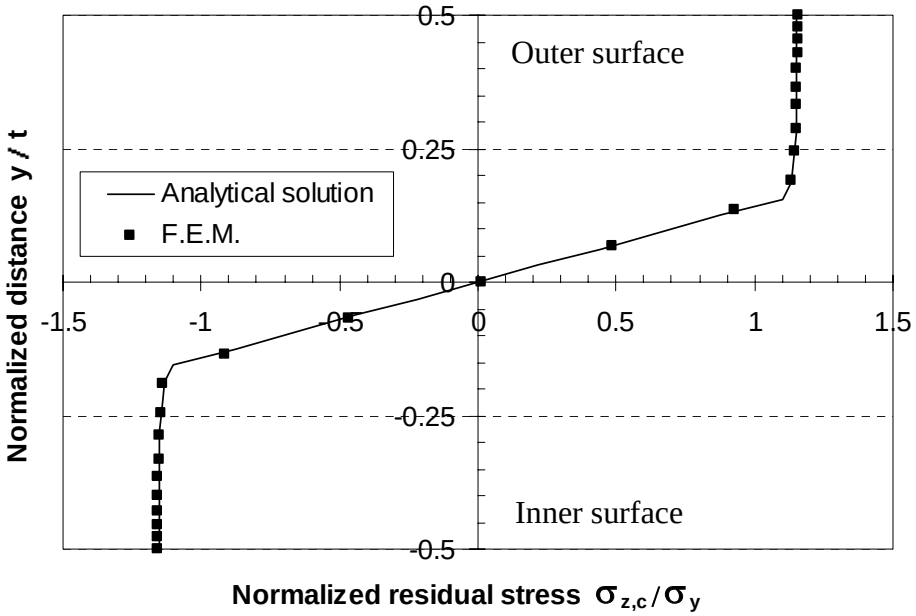

(a) Longitudinal coiling stress

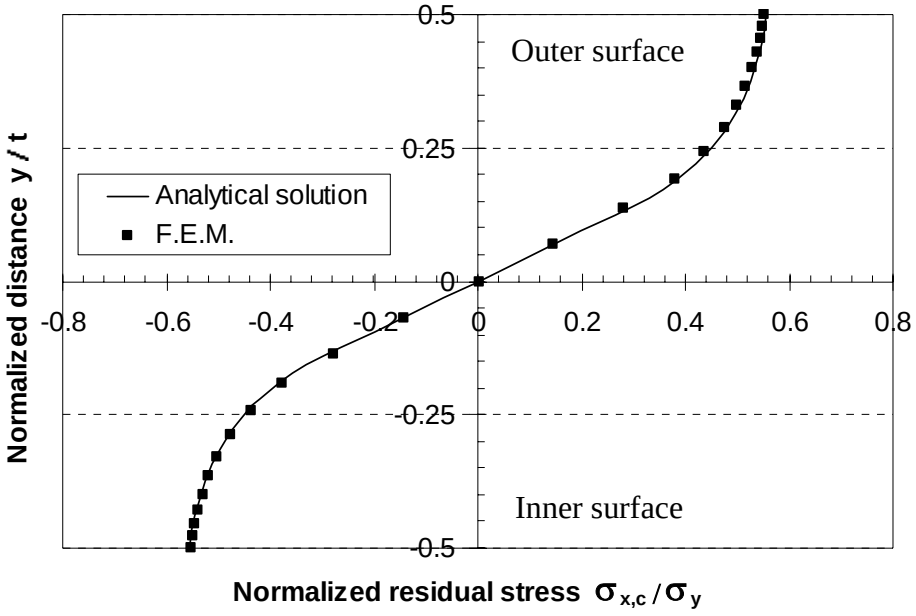

(b) Transverse coiling stress

Figure 4.5 Comparison of residual stresses between the analytical solution and finite element analysis for the carbon steel sheet.

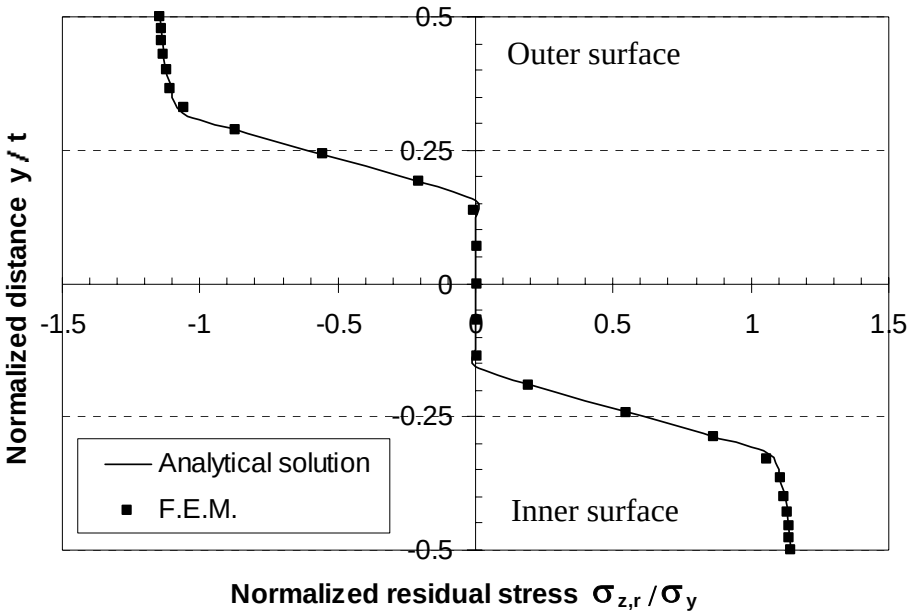

(c) Final longitudinal residual stress

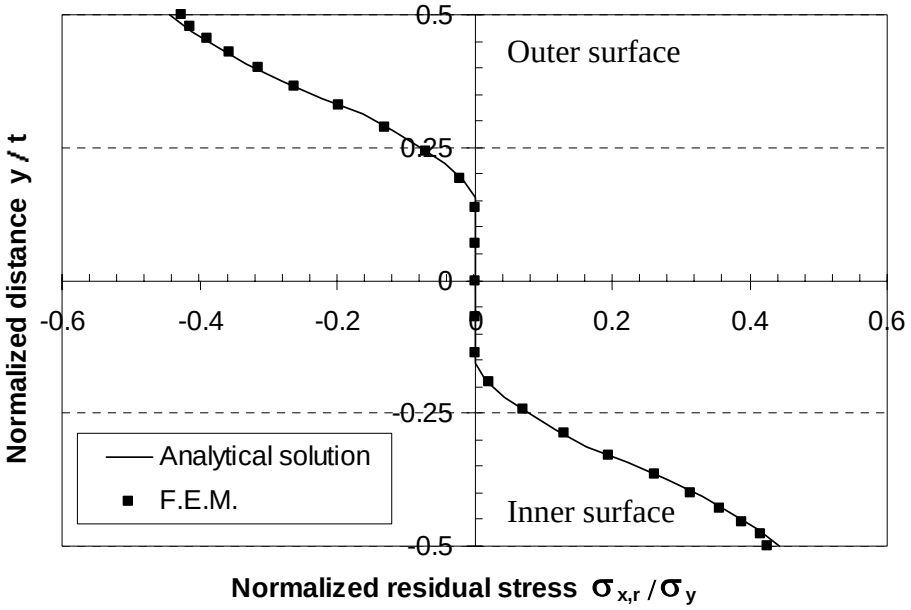

(d) Final transverse residual stress

Figure 4.5 Comparison of residual stresses between the analytical solution and finite element analysis for the carbon steel sheet (continued).

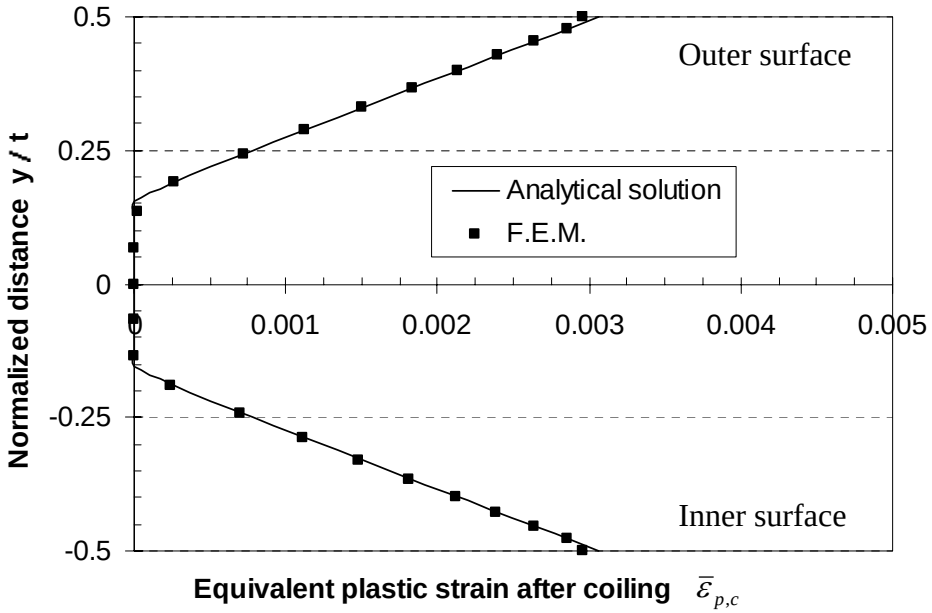

(a) After coiling

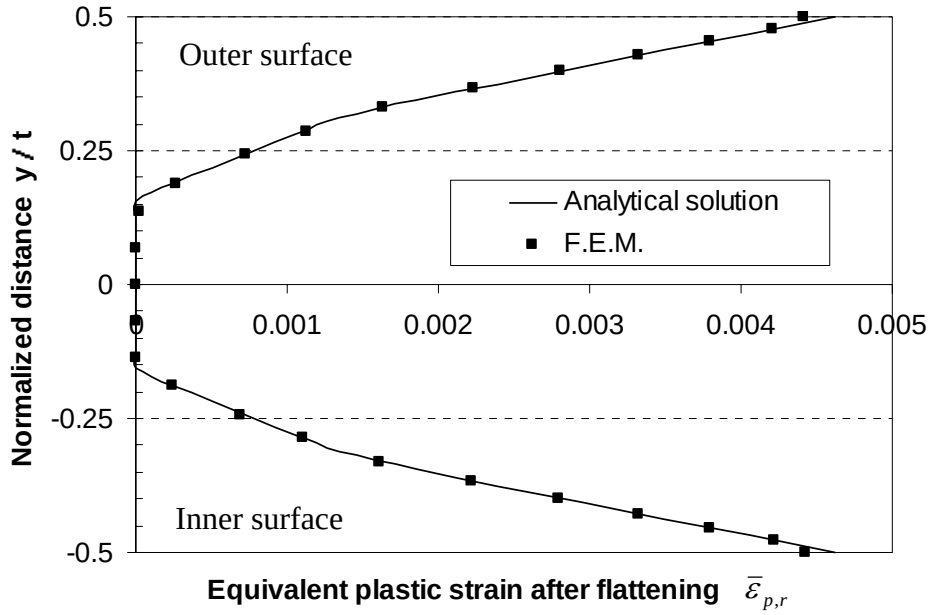

(b) After flattening

Figure 4.6 Comparison of equivalent plastic strains between the analytical solution and finite element analysis for the carbon steel sheet.

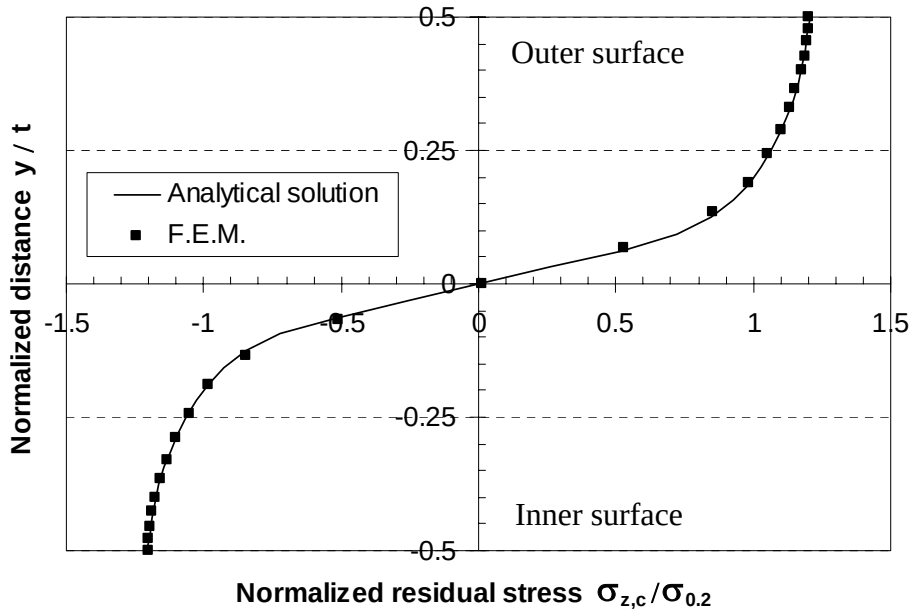

(a) Longitudinal coiling stress

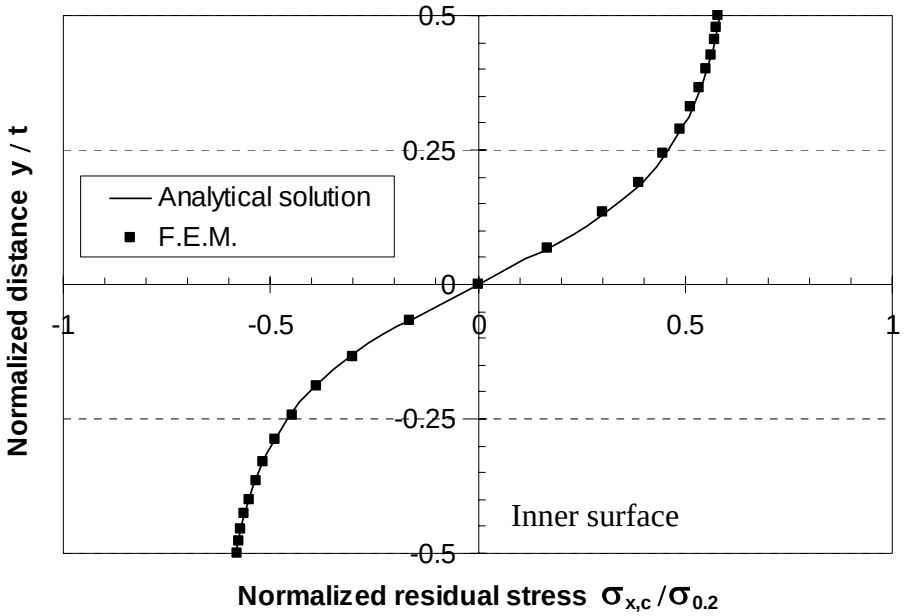

(b) Transverse coiling stress

Figure 4.7 Comparison of residual stresses between the analytical solution and finite element analysis for the austenitic stainless steel sheet.

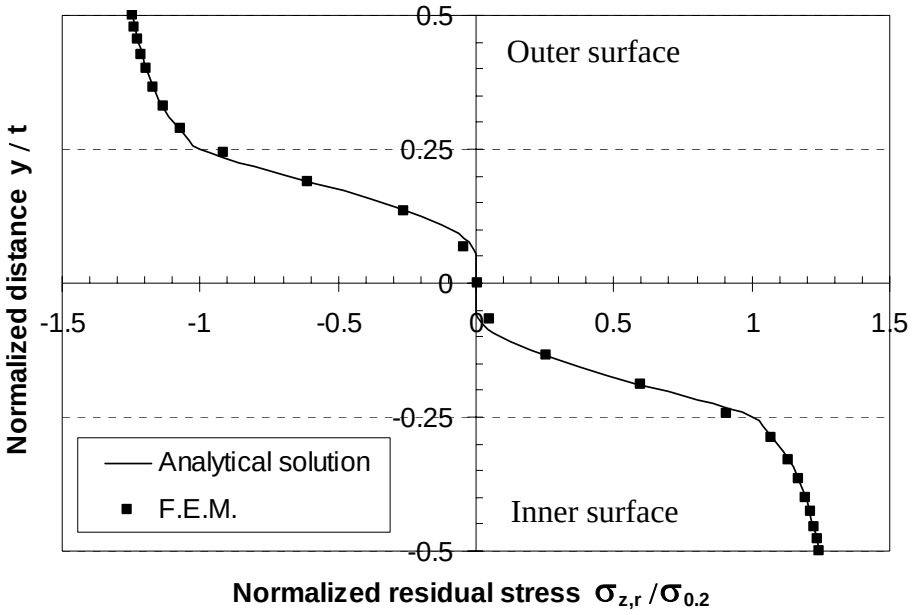

(c) Final longitudinal residual stress

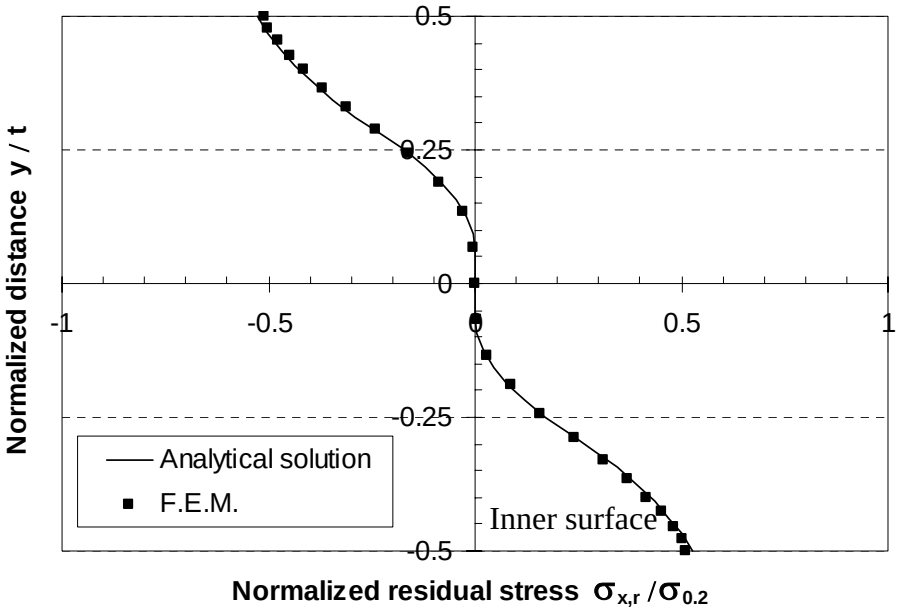

(d) Final transverse residual stress

Figure 4.7 Comparison of residual stresses between the analytical solution and finite element analysis for the austenitic stainless steel sheet (continued).

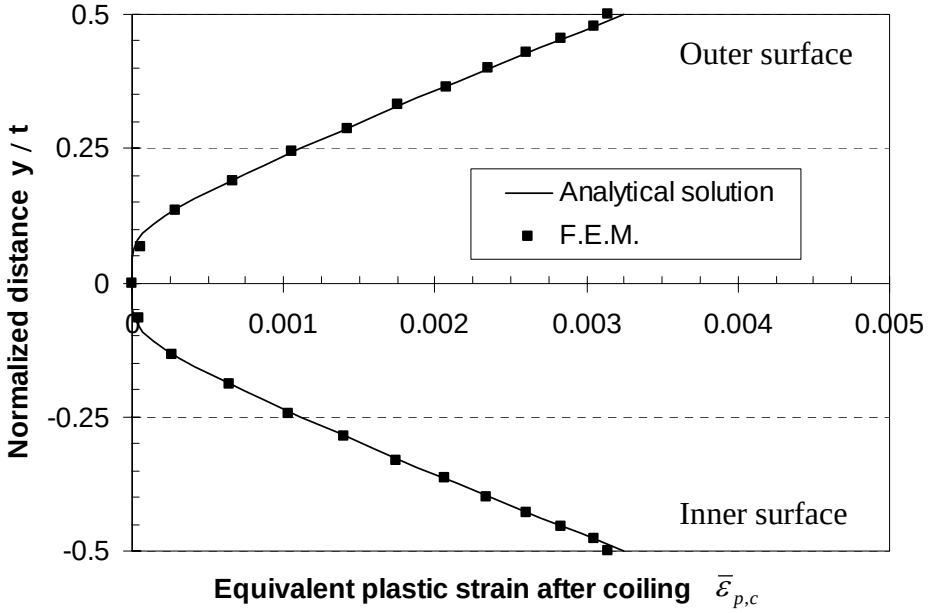

(a) After coiling

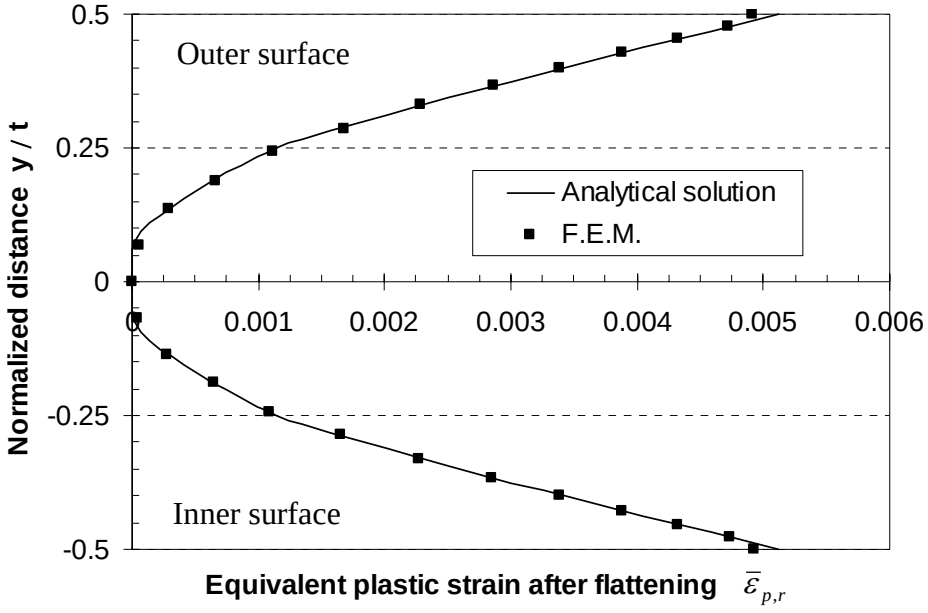

(b) After flattening

Figure 4.8 Comparison of equivalent plastic strains between the analytical solution and finite element analysis for the austenitic stainless steel sheet.

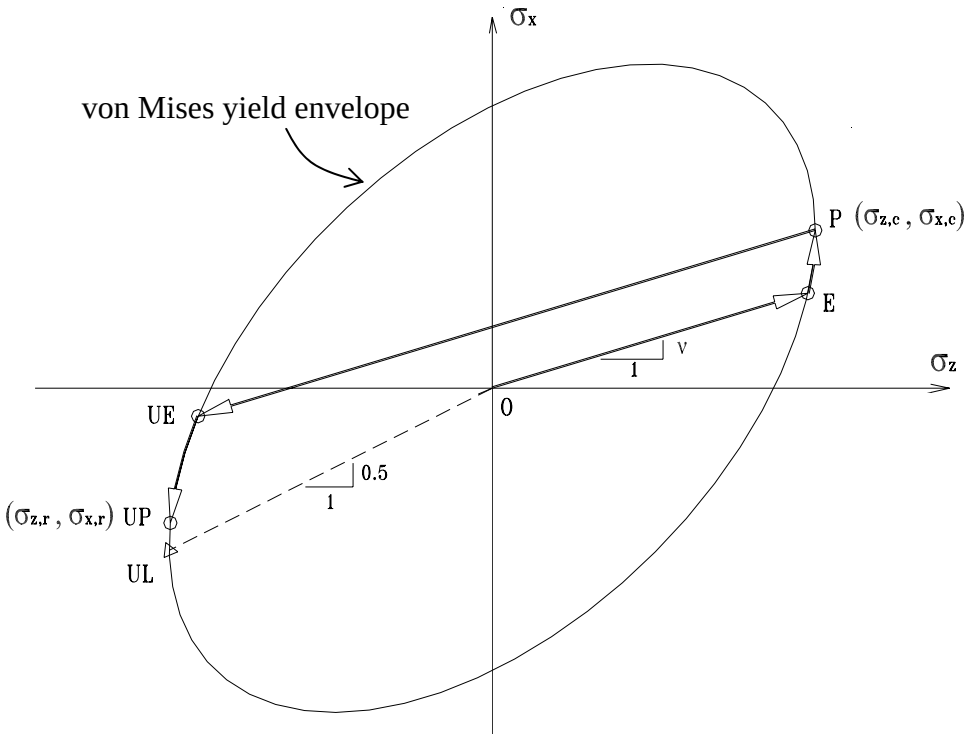

Figure 4.9 Stress path of a surface point of a carbon steel strip during the coiling-uncoiling process.

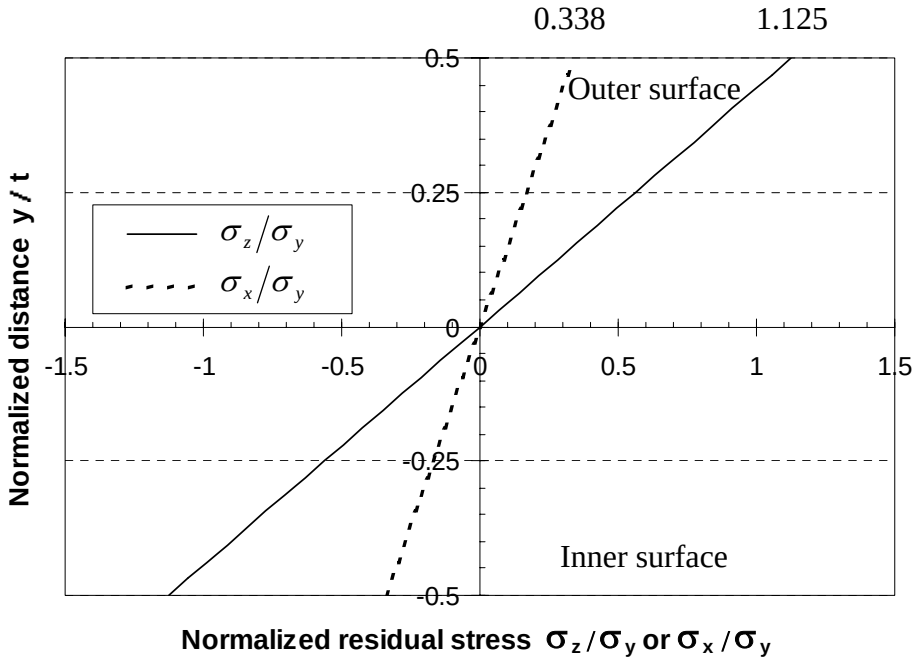

(a) Onset of surface yielding

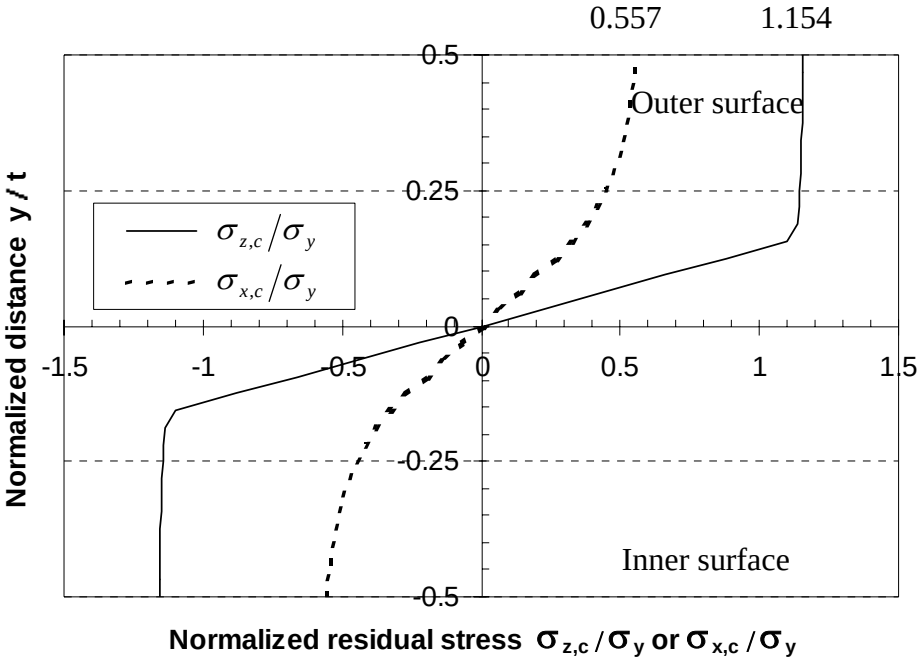

(b) End of coiling

Figure 4.10 Residual stresses in the carbon steel sheet during the coiling-uncoiling process.

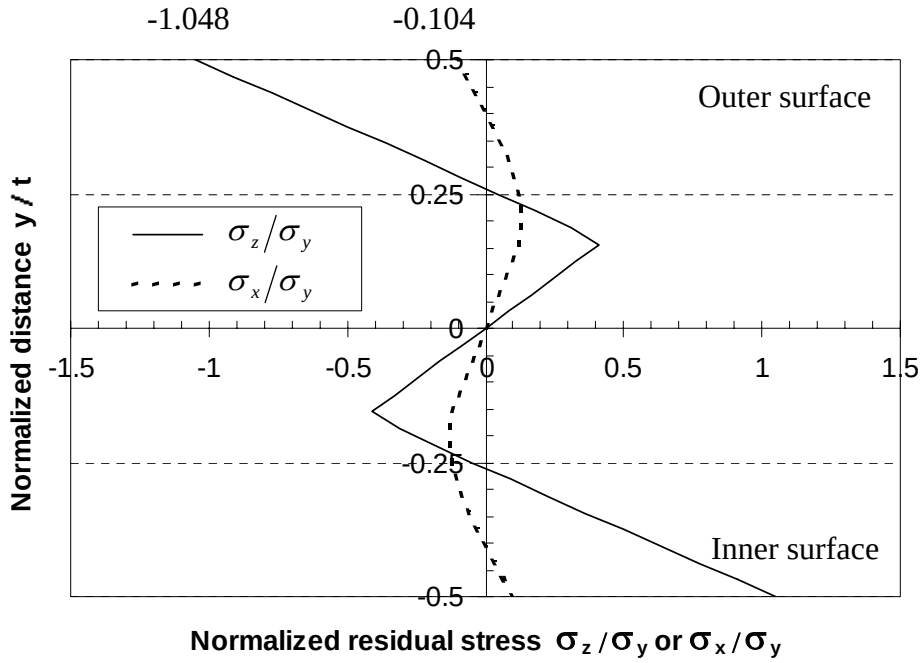

(c) Onset of reverse surface yielding

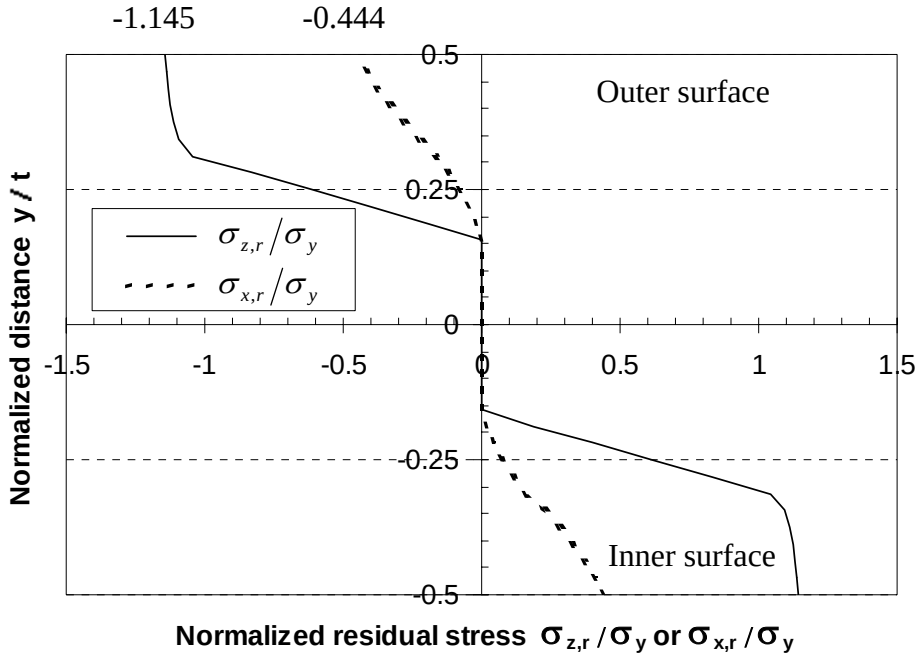

(d) After flattening

Figure 4.10 Residual stresses in the carbon steel sheet during the coiling-uncoiling process (continued).

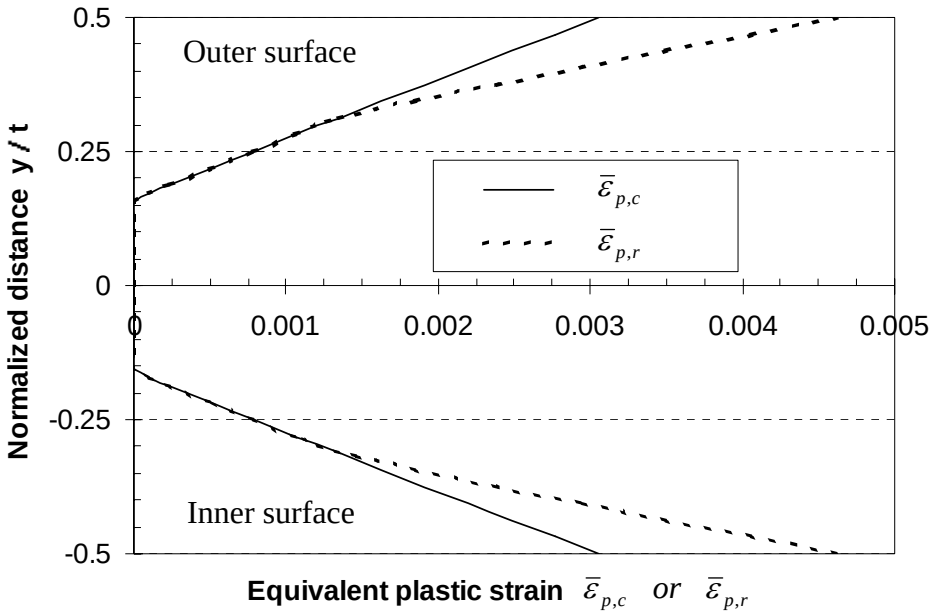

Figure 4.11 Equivalent plastic strain distributions in the carbon steel sheet.

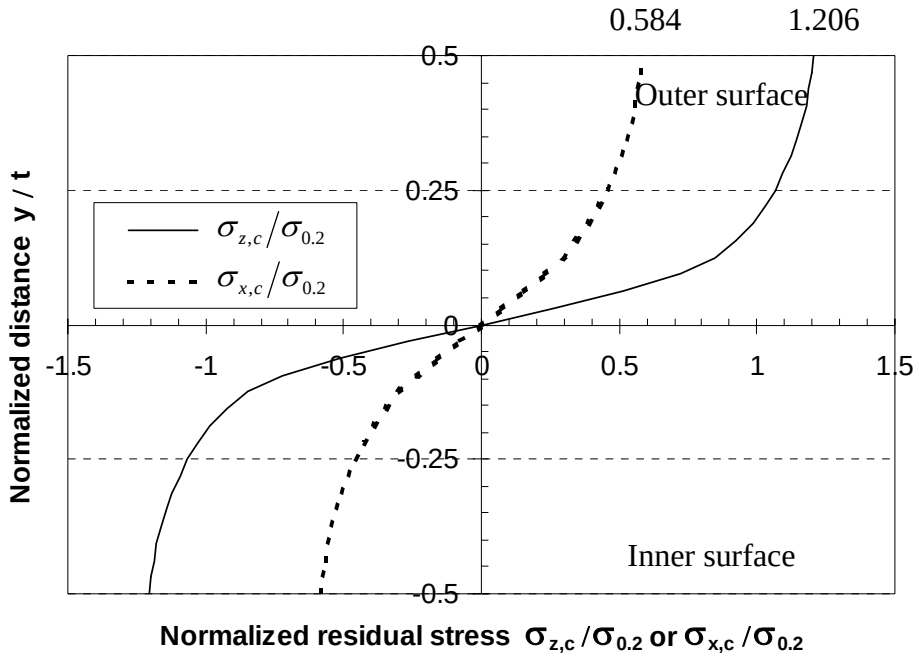

(a) End of coiling

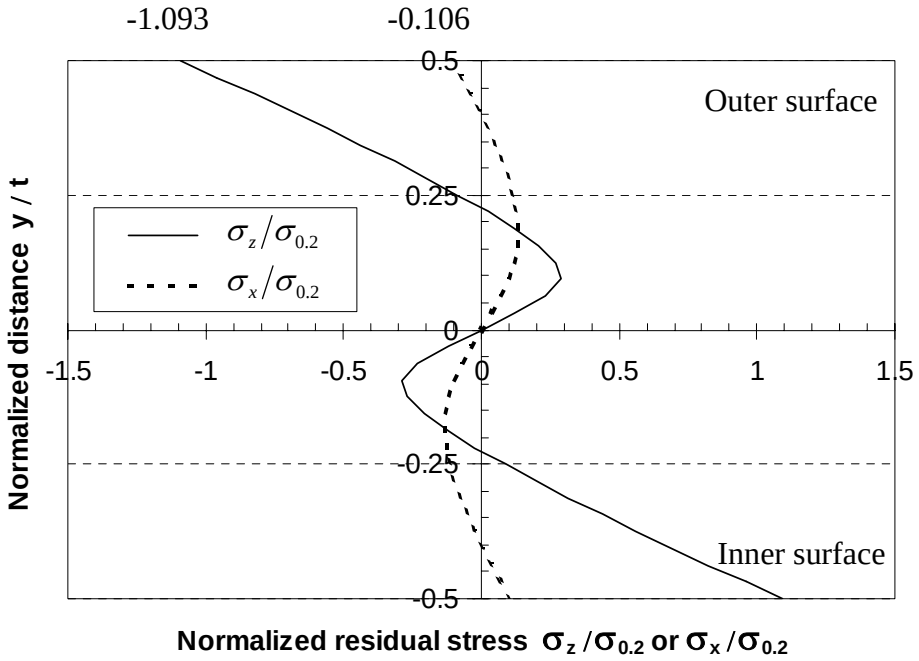

(b) Onset of reverse surface yielding

Figure 4.12 Residual stresses in the austenitic stainless steel sheet during the coiling-uncoiling process.

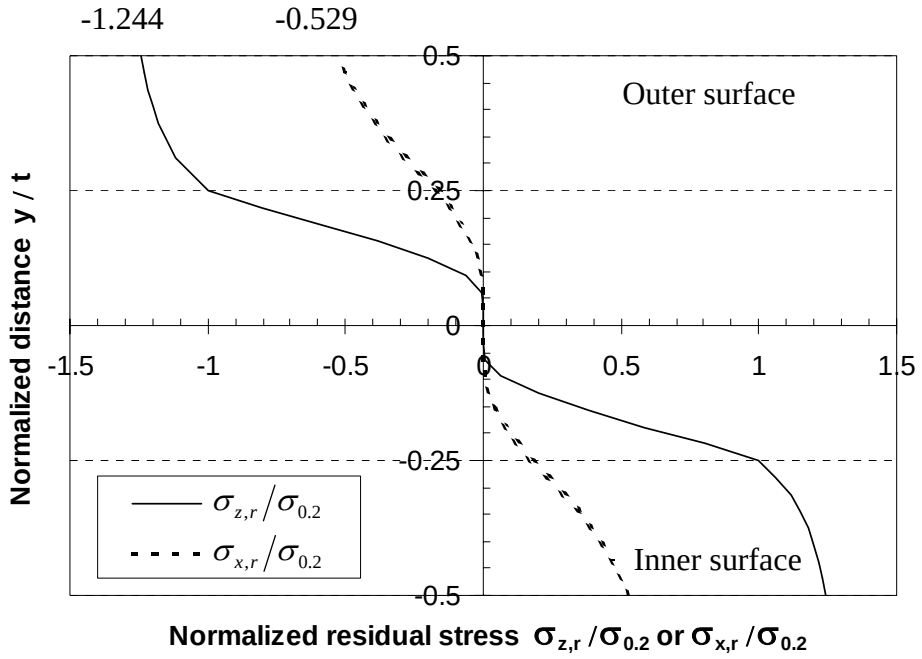

(c) After flattening

Figure 4.12 Residual stresses in the austenitic stainless steel sheet during the coiling-uncoiling process (continued).

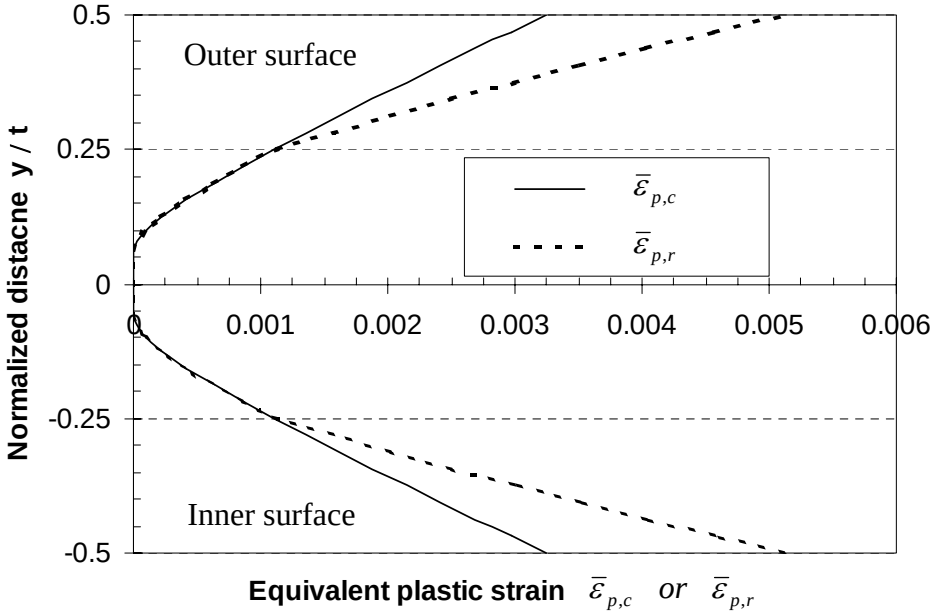

Figure 4.13 Equivalent plastic strain distributions in the austenitic stainless steel sheet.

Chapter 5

NUMERICAL SIMULATION OF THE PRESS-BRAKING PROCESS

5.1 INTRODUCTION

As seen from the literature review in Chapter 2, laboratory measurements of residual stresses in cold-formed sections are not only time-consuming but also of limited accuracy. For example, due to the thinness of cold-formed sections, through-thickness variations of residual stresses are difficult to examine experimentally and only surface residual stresses were measured in most experimental studies. Accurate predictions of residual stresses in cold-formed sections require the modelling of the cold-forming process and are not yet available. This chapter therefore explores a finite element-based method for predicting residual stresses in cold-formed sections, which overcomes these difficulties. The method can provide residual stress distributions over the cross section as well as across the thickness.

Cold-formed members are usually manufactured by either roll forming or press braking. Only press braking is considered in the present study. As summarized in Chapter 1, in a press-braking operation, short lengths of strips cut from a coil are fed into a press brake and a complete fold is produced along the full length of a section. As discussed in Chapter 4, a flat steel strip can be assumed to be free from residual stresses before it is coiled for storage, since any residual stress in the strip prior to the

coiling have been removed in the annealing furnace. Therefore, the residual stresses in a press-braked section are derived from two distinct sources: the coiling-uncoiling process and the cold bending of press-braking operations. In the proposed finite element-based method, the effects of coiling and uncoiling are accounted for analytically, with the resulting residual stresses and equivalent plastic strains specified as the initial state in a subsequent finite element simulation of cold bending. The method offers a powerful tool for exploring the effect of different forming parameters on the magnitude and distribution of residual stresses so that these forming parameters can be optimized.

Before proceeding further, it should be noted that the same terminology adopted in Chapter 4 in referring to stresses in various directions is also used in this chapter. It should also be noted that, in the manufacturing process of a press-braked lipped channel section (see Figure 1.2 in Chapter 1), the outer surface of a coiled sheet becomes the inner surface of the lipped channel section produced from the sheet.

5.2 RESIDUAL STRESSES BEFORE COLD BENDING

The residual stresses in steel sheets due to the coiling-uncoiling process have been studied in Chapter 4 by presenting a general analytical solution and verifying its accuracy using results from a finite element simulation. A detailed derivation of the equations for this analytical solution is given in Chapter 4. This analytical solution can provide the prediction of the stress state in a steel sheet before the cold bending is applied in the press-braking operation. Therefore, in the finite element-based method,

the residual stresses and equivalent plastic strains in a steel sheet due to coiling and uncoiling are first calculated using this analytical solution, and are then specified as the initial state in a subsequent finite element simulation of cold bending. Such finite element simulation is discussed in the next section.

5.3 FINITE ELEMENT SIMULATION OF COLD BENDING

The finite element code ABAQUS (2001) was employed to simulate cold bending in press-braking operations. Two sets of existing experiments were selected for finite element simulation, as these experimental results provide the necessary data for the verification of the finite element model. These include Weng and Peköz's (1990) experiments in which residual stresses in press-braked carbon steel channel sections were measured in detail and Weng and White's (1990a, 1990b) experiments on cold-bent thick steel plates. The latter experiments provided through-thickness residual stress distributions not available from the former, and were therefore first simulated for verification of the finite element model.

Both sets of experiments were modelled with the CPE4R element, which is a 2-D plane strain 4-node element with reduced integration and hourglass control, while the die and punch were modelled with analytical rigid surfaces. The interaction between the steel section and the die/punch was simulated by defining contact pairs with the hard contact model and finite sliding formulation available in ABAQUS (2001). Both geometrical and material nonlinearities were considered. This element is capable of handling large strains and large rotations, so it is suitable for use in cold bending

simulations. The modelling of material nonlinearity required the definition of a true stress-logarithmic plastic strain relationship up to the ultimate point (ABAQUS 2001), which was converted from the nominal stress-strain data. The nominal stress-strain curves, true stress-strain curves and true stress-logarithmic plastic strain curves are shown in Figure 5.1 for these two sets of experiments.

The carbon steels used for the press-braked channel sections (specimens PBC14 and P16) studied by Weng and Peköz (1990) had a pronounced yield point as indicated by tensile tests on coupons cut from the flat portions but the complete stress-strain curves for these two specimens are not available in the paper by Weng and Peköz (1990). In the present study, the stress-strain curves employed for these two specimens are defined by the use of the power function given by Eq. (4.68a) (see Chapter 4) for elastic-nonlinear strain-hardening materials. The initial yield stress σ_{y0} and initial elastic modulus E_0 in Eq. (4.68a) are now referred to simply as the yield stress σ_y and elastic modulus E respectively in this chapter. The value of the strain-hardening exponent n_s in Eq. (4.68a) is found by fitting a nominal stress-strain curve through the measured values of yield stress σ_y, yield strain ε_y, ultimate stress σ_u and ultimate strain ε_u (Table 5.1). This approach implies the assumption that the cold work of the manufacturing process had little effect on the properties of the steel in the flat portions. This assumption is consistent with existing experimental evidence for press-braked sections (Karren and Winter 1967).

In this power function form, the yield plateau is ignored. The exclusion of this transition region between elastic behaviour and strain hardening leads to little error when the strain under consideration is greater than 4% (Hosford and Caddell 1993). It

may be noted that surface strains in the corner regions of the channel sections studied here exceed 16%.

In simulating the press-braking process of channel sections, only half of the section was modelled with the condition of symmetry properly imposed in the half-section model (Figure 5.2). Twelve steps were required to achieve the whole press-braking process of channel sections, while four steps were needed for the cold bending of thick plates. Some of the steps were used to reposition the steel sheet after a press-braking operation, to deactivate and reactivate the contact pairs after a press-braking operation and before the next operation. The six key steps required for numerically forming a channel section are summarized in Figure 5.3.

Since the strains induced by the coiling-uncoiling process are relatively small, it is reasonable to assume that strain hardening is not involved in the coiling and uncoiling of the carbon steel sheets used for the channel sections (specimens PBC14 and P16). That is, the carbon steels can be assumed to possess elastic-perfectly plastic stress-strain behaviour during the coiling-uncoiling process. Thus, the longitudinal and transverse residual stresses together with the equivalent plastic strain due to the coiling-uncoiling process were calculated using the closed-form analytical solution for elastic-perfectly plastic materials presented in Section 4.4 of Chapter 4. The resulting residual stresses and equivalent plastic strains were then specified as the initial state in the finite element model. It should be noted that a plane strain finite element model with such initial stresses does not satisfy equilibrium, as the sheet is now bent in a direction perpendicular to that of coiling. Consequently, in the nonlinear finite element analysis, the first step was used for the restoration of

equilibrium, which involved deformations of the steel sheet. In the subsequent steps, cold-bending operations were simulated, during which the section had to be rotated. During these rotations, the symmetric boundary condition along the line of symmetry in the half-section model was retained by constraining the intermediate nodes to a line defined by the two end nodes on the boundary, allowing the possibility of movement along the line of symmetry. In the final step during which spring-back took place, the symmetric boundary condition was again assigned along the line of symmetry.

For accurate predictions, a mesh convergence study as summarized in Tables 5.2~5.4 was carried out to obtain the final meshes used in the present study (Figures 5.2 and 5.4). In the mesh convergence study, the surface residual stresses were monitored as only these surface residual stresses are commonly obtained from laboratory measurements. In addition, peak compressive residual stresses in both the longitudinal and transverse directions were monitored as these compressive stresses may lower the buckling strength. In order to compare different meshes of the same physical model, residual stresses at the following sections were monitored: (a) mid-corner section of the 1-in. thick cold-bent HY-80 steel plate with an inner bending radius $R = 1.5$ in. and a bend angle of 90º; and (b) mid-corner section of the lip-flange corner and mid-web section of channel section PBC14 with a coil diameter $D = 200\,t$. In Tables 5.2~5.4 and in the figures of this chapter, tensile residual stresses are taken to be positive.

In Tables 5.2~5.4, the results found with meshes consisting of 20 layers of elements provide the reference values to check the accuracy of other meshes. For the cold-bent thick plate, the adopted mesh with 16 layers of elements in the corner region (i.e.

curved portion) and the adjacent areas and eight layers of elements in the flat portions is seen to produce results that differ from the reference values by no more than 0.8 %. For the channel section, the adopted mesh shown in Figure 5.2, which consists of 16 layers of elements throughout the section and narrower elements near the corners, led to results which differ from the reference values by no more 4.8 %. This 4.8 % difference is taken to be satisfactory.

5.4 WENG AND WHITE'S EXPERIMENTS

In their experiments, four 1-in. thick HY-80 steel plates were bent by 90º with four different inner bending radii (1.5, 2.5, 3.5 and 5.5 in.). The yield stress of the steel is 593 MPa. Both the surface longitudinal residual stresses and the through-thickness variation of transverse residual stresses were measured. For the dimensions of the plates, punches and dies, readers can refer to Weng and White (1990a, 1990b). For all four inner bending radii, the variations of residual stresses across section A-A (see Figure 5.5) predicted by the finite element method are in close agreement with their experimental results (Figure 5.6), although the experimental measurements did not capture the residual stress peaks. This comparison indicates that the finite element model can provide accurate predictions of residual stresses due to cold bending.

Figure 5.5 shows the contours of residual stresses in one of the cold-bent plates with an inner bending radius R = 2.5 in. It is seen that the inner half-thickness is mainly under compressive residual stresses, while the outer half-thickness is mainly under tensile residual stresses, in both the longitudinal and transverse directions (also refer

to Figure 5.6). Figure 5.6 shows that both the maximum longitudinal and maximum transverse compressive residual stresses occur near the quarter surfaces of the plate. The maximum longitudinal tensile residual stress and a transverse tensile residual stress peak are located near the middle surface of the plate, where their values are about $0.4\sigma_y$ and $0.8\sigma_y$ respectively. The maximum longitudinal compressive residual stress ranges from $0.6\sigma_y$ to σ_y, while the maximum transverse compressive residual stress ranges from $1.1\sigma_y$ to $1.5\sigma_y$.

5.5 WENG AND PEKÖZ'S EXPERIMENTS

As mentioned earlier, residual stresses in cold-formed sections consist of two components: those due to the coiling-uncoiling process and those due to cold bending. This observation is consistent with experimental evidence. For example, Young and Rasmussen (1995) found negligible residual stresses in the flat portions of their lipped channels, while Weng and Peköz (1990) found residual strains on the flat portions of their press-braked sections to be up to about 40% of the yield strain. This difference in residual stresses in the flat portions may be attributed to the different residual stresses from the coiling-uncoiling process. Young and Rasmussen's specimens might have been made from flat steel sheets uncoiled from a state of small curvature, while those tested by Weng and Peköz uncoiled from a state of a larger curvature. Obviously, whether and how much residual stresses are induced by the coiling-uncoiling process depend on two factors: the coil diameter-to-sheet thickness ratio and the yield stress (see Chapter 4 and Chapter 8).

In the numerical simulations of Weng and Peköz's press-braked channels, the residual stresses and equivalent plastic strains over the thickness, resulting from coiling and uncoiling were calculated using the closed-form analytical solution presented in Section 4.4 (also see Figures 5.7 and 5.8), and then imposed in the finite element model to define the initial state for the subsequent finite element analysis. Altogether, three press-braked specimens were tested by Weng and Peköz (1990). Two of these specimens, PBC14 and P16, are considered here. Numerical simulation of the third specimen (specimen P11) failed to converge, so it is excluded from the discussion here. By trial and error, it was found that a coil diameter D of 1100 mm for Weng and Peköz's press-braked channels led to the closest match between finite element predictions and measured residual strains for both specimens PBC14 and P16. Figure 5.9 shows that the longitudinal residual strains from finite element analysis provide a close prediction of the test results for both specimens PBC14 and P16, except for the local strain peaks found from the tests on the inner surface, which are believed to be due to local concentration of contact pressure during braking.

Figures 5.10~5.12 show that the through-thickness variations of residual stresses in the lip-flange corner (the curved portion) and the web. The through-thickness variations at three different locations in the lip-flange corner (Figure 5.10) are shown in Figure 5.11. It can be seen that within the corner, both the longitudinal and transverse residual stresses are fairly uniform, and both tensile and compressive residual stresses are present over different parts of the thickness, with their peak values being generally near the middle surface and quarter surface of the plate respectively. For example, at section A-A (Figures 5.10 and 5.11), the maximum longitudinal compressive residual stress is about $0.9\sigma_y$ and the maximum transverse

compressive residual stress is about $1.4\sigma_y$. The peak longitudinal and transverse tensile residual stresses, which are found near the middle surface, are about $0.5\sigma_y$ and $0.8\sigma_y$ respectively. Near the ends of the corner region, such as at section C-C (Figures 5.10 and 5.11), both the maximum transverse tensile and compressive residual stresses, which are approximately equal to $0.9\sigma_y$ and $1.1\sigma_y$ respectively, are located near the middle surface.

It is seen that the residual stresses consist of not only a membrane component and a flexural component as conventionally idealized for channel sections, but also a layering component. Decomposition of these variations shows that the magnitude of the layering component may be even greater than those of the other two components. This layering component results from the coiling-uncoiling process and the press-braking operations, with contributions also from spring-back. The distributions of residual stresses in flat portions are highly affected by the coiling curvature, and will be discussed in Section 8.2 of Chapter 8.

5.6 CONCLUSIONS

A finite element method for the prediction of residual stresses in cold-formed steel sections produced by press-braking operations has been presented. In this method, the effects of coiling and uncoiling are accounted for analytically, with the resulting residual stresses and equivalent plastic strains specified as the initial state in a subsequent finite element simulation of cold bending. Numerical results from this method have been shown to agree closely with laboratory measurements,

demonstrating the validity and accuracy of the method. The method can therefore be applied in the future in parametric studies to gain further insight into the causes and nature of residual stresses in press-braked sections and to optimise various forming parameters such as corner radii adopted in cold bending. Numerical results presented in the chapter also allow the following conclusions to be made:

(a) Residual stresses in press-braked sections consist of not only a membrane component and a flexural component as conventionally idealized for channel sections, but also a layering component. The magnitude of the layering component may be even greater than those of the other two components. This layering component results from the coiling-uncoiling process and press braking, with contributions also from spring-back.

(b) The maximum residual stresses in a press-braked section generally occur in the corner region and away from the surfaces, and their values can be much higher than those at the surfaces. This means that the conventional method of measuring the surface residual stresses in the laboratory and assuming a linear variation across the plate thickness may greatly underestimate the real residual stresses. The implication of this underestimation should be investigated in future research.

5.7 REFERENCES

ABAQUS (2001). *Standard User's Manual, V6.2,* Hibbitt, Karlsson and Sorensen, Inc., United States.

Hosford, W. F. and Caddell, R. M. (1993). *Metal Forming: Mechanics and Metallurgy*, Prentice Hall, New York.

Karren, K. W. and Winter, G. (1967). Effects of cold-forming on light-gage steel members. *Journal of the Structural Division, ASCE Proceedings*, **93:ST1**, 433-469.

Weng, C. C. and Peköz, T. (1990). Residual stresses in cold-formed steel members. *Journal of Structural Engineering, ASCE*, **116:6**, 1611-1625.

Weng, C. C. and White, R. N. (1990a). Residual stresses in cold-bent thick steel plates. *Journal of Structural Engineering, ASCE*, **116:1**, 24-39.

Weng, C. C. and White, R. N. (1990b). Cold-bending of thick high-strength steel plates. *Journal of Structural Engineering, ASCE*, **116:1**, 40-54.

Young, B. and Rasmussen, K. J. R. (1995). *Compression Tests of Fixed-Ended and Pin-Ended Cold-Formed Lipped Channels, Research Report No. R715*, School of Civil and Mining Engineering, University of Sydney, Australia.

Table 5.1 Dimensions and material properties of press-braked lipped channel sections.

Specimen	$t^{\#}$ (mm)	$a^{\#}$ (mm)	$b^{\#}$ (mm)	$c^{\#}$ (mm)	$R^{\#}$ (mm)	σ_y (MPa)	σ_u (MPa)	ε_y ($\times 10^{-6}$)	E (GPa)	n_s ($\times 10^{-2}$)	ε_u * (%)
PBC14	1.80	76.23	41.45	15.37	3.96	250.1	345.0	1230	203.3	9.56	33
P16	1.63	67.18	34.98	15.82	2.39	220.9	310.7	1090	202.7	9.74	32

Note: # As defined in Figure 5.2.
* Percentage elongation in 2 in. gauge length.

Table 5.2 Comparison of residual stresses at the mid-corner section predicted with different finite element meshes for a 1-in. thick cold-bent HY-80 steel plate with an inner bending radius R = 1.5 in. and a bend angle of 90º.

Mesh	No. of elements	Outer surface stress				Peak compressive stress			
		σ_z (MPa)	Relative change (%)	σ_x (MPa)	Relative change (%)	σ_z (MPa)	Relative change (%)	σ_x (MPa)	Relative change (%)
8×142	1136	127.4	4.0	-222.7	9.1	-428.3	26.4	-583.8	34.7
12×212	2544	132.5	8.2	-205.7	16.0	-623.1	7.1	-993.7	11.2
16×286	4576	122.2	0.3	-246.6	0.6	-580.1	0.2	-886.6	0.8
Adopted mesh 16×74+8×94	1936	122.0	0.4	-247.0	0.8	-579.9	0.3	-886.6	0.8
20×356	7120	122.5	0.0	-245.0	0.0	-581.6	0.0	-893.3	0.0

Table 5.3 Comparison of residual stresses at the mid-corner section predicted with different finite element meshes for specimen PBC14 with D/t = 200.

Mesh	No. of elements	Outer surface stress				Peak compressive stress			
		σ_z (MPa)	Relative change (%)	σ_x (MPa)	Relative change (%)	σ_z (MPa)	Relative change (%)	σ_x (MPa)	Relative change (%)
8×224	1792	61.6	1.5	-107.5	3.9	-187.6	10.9	-297.7	9.5
12×339	4068	65.2	4.3	-100.6	10.0	-187.7	10.8	-237.0	28.0
Adopted mesh 16×320	5120	62.1	0.8	-112.4	0.5	-218.8	3.9	-345.0	4.8
20×569	11380	62.6	0.0	-111.8	0.0	-210.5	0.0	-329.1	0.0

Table 5.4 Comparison of residual stresses at the mid-web section predicted with different finite element meshes for specimen PBC14 with $D/t = 200$.

Mesh	No. of elements	Outer surface stress				Peak compressive stress			
		σ_z (MPa)	Relative change (%)	σ_x (MPa)	Relative change (%)	σ_z (MPa)	Relative change (%)	σ_x (MPa)	Relative change (%)
8×224	1792	255.4	0.8	13.7	13.4	-255.7	0.8	-21.8	28.3
12×339	4068	254.4	0.4	13.2	9.4	-256.5	0.5	-27.8	8.6
Adopted mesh 16×320	5120	253.8	0.1	12.5	3.5	-257.4	0.1	-29.5	3.1
20×569	11380	253.4	0.0	12.1	0.0	-257.7	0.0	-30.4	0.0

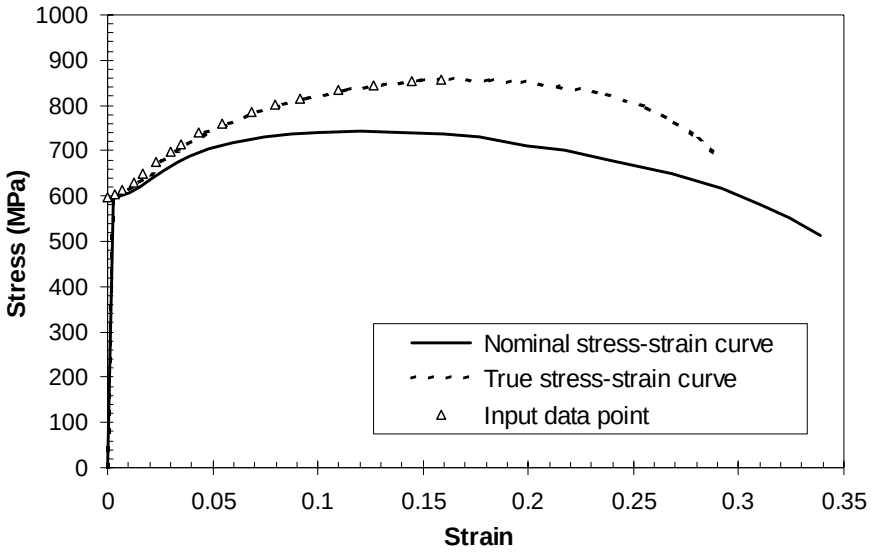

(a) Weng and White's HY-80 thick steel plates

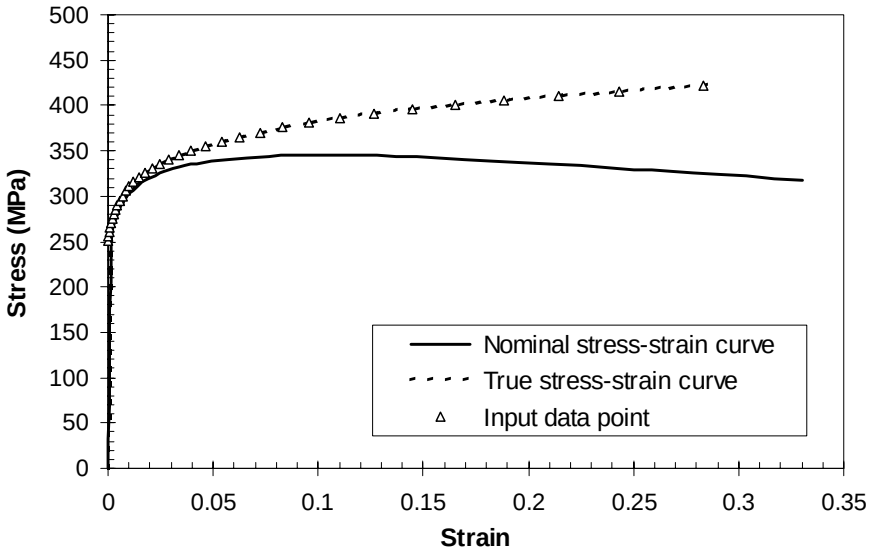

(b) Weng and Peköz's lipped channel section specimen PBC14

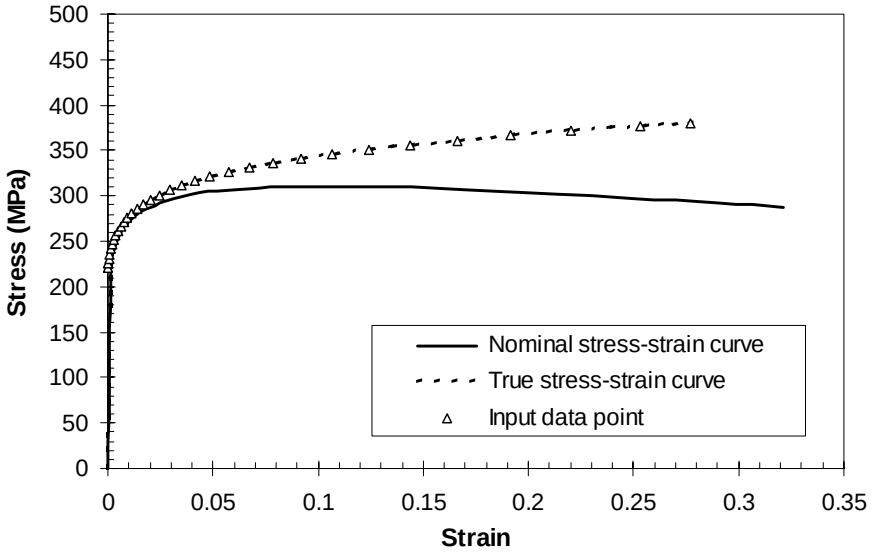

(c) Weng and Peköz's lipped channel section specimen P16

Figure 5.1 Stress-strain curves.

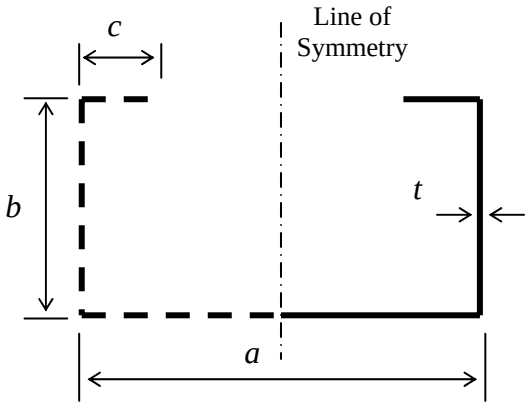

(a) Half-section model

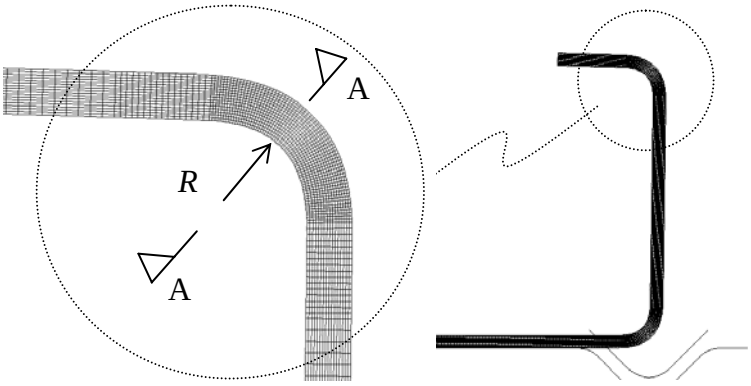

(b) Mesh of the final deformed half-section model after spring-back

Figure 5.2 Finite element model of a channel section.

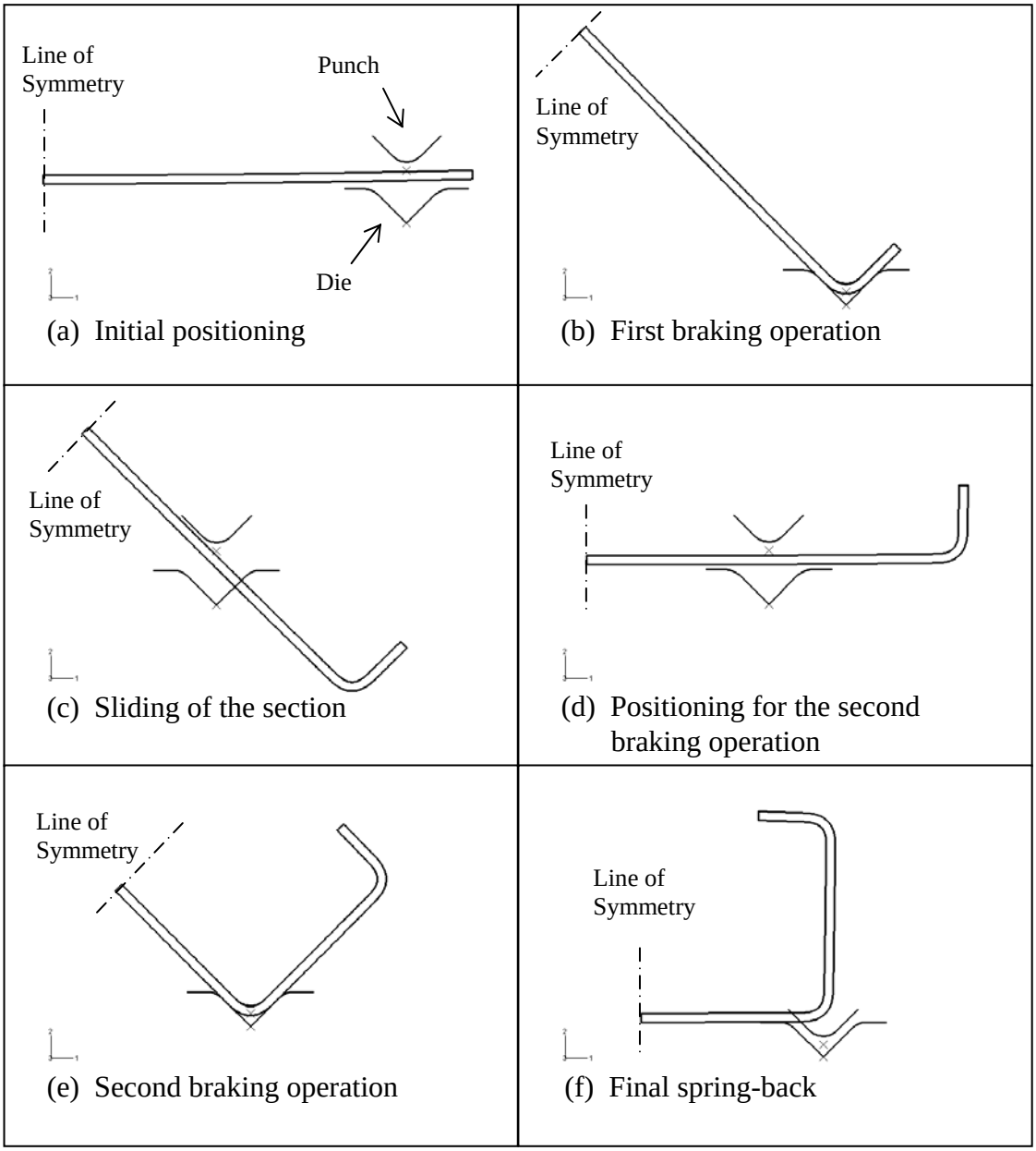

Figure 5.3 Schematic representation of the press-braking process for a channel section.

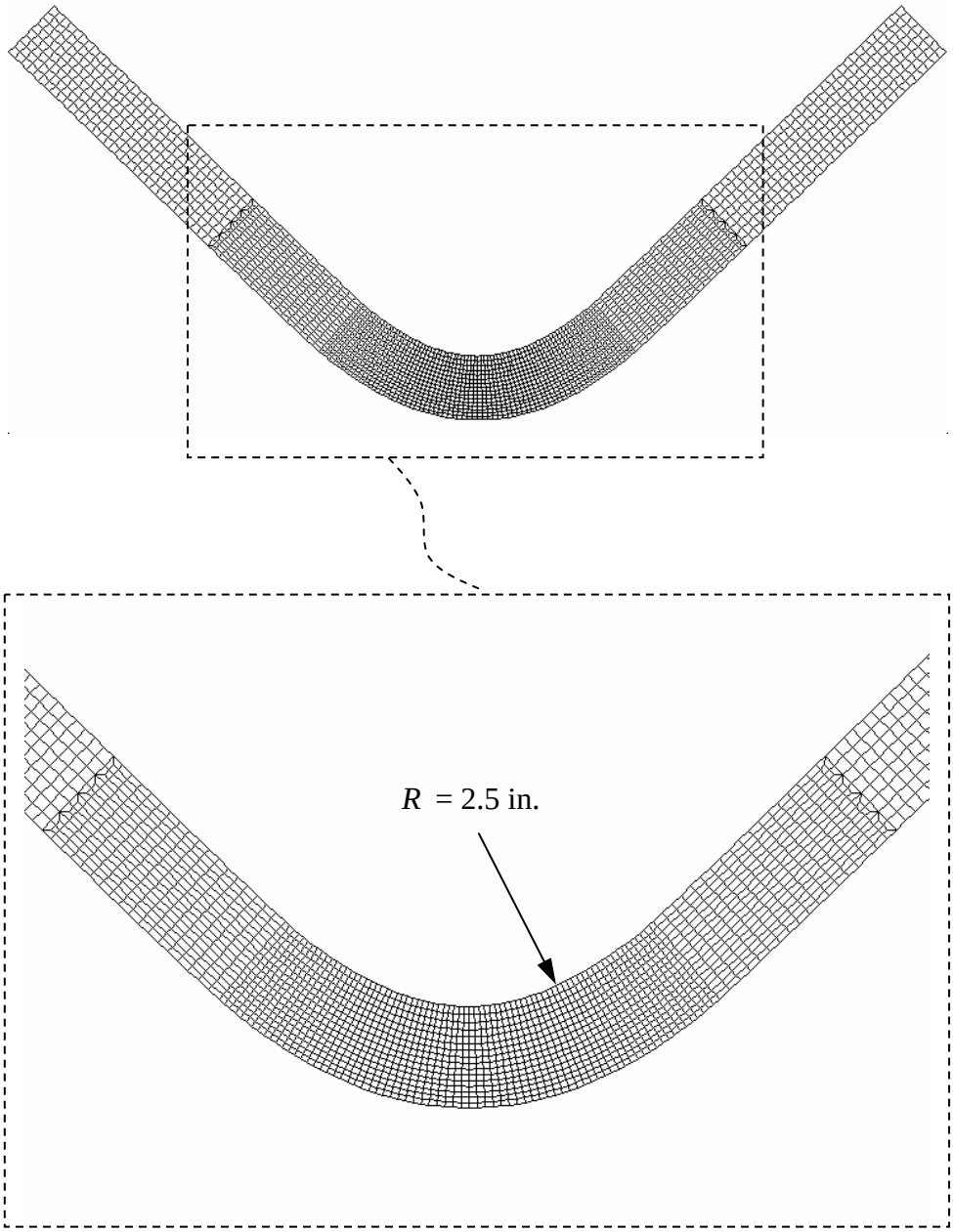

Figure 5.4 Deformed mesh for a 1-in. thick 90º cold-bent HY-80 steel plate.

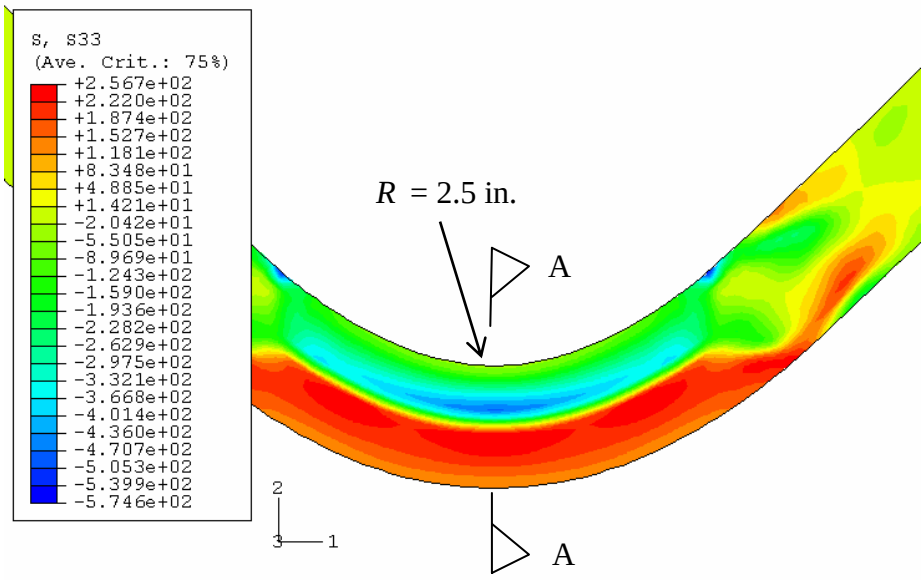

(a) Longitudinal residual stress

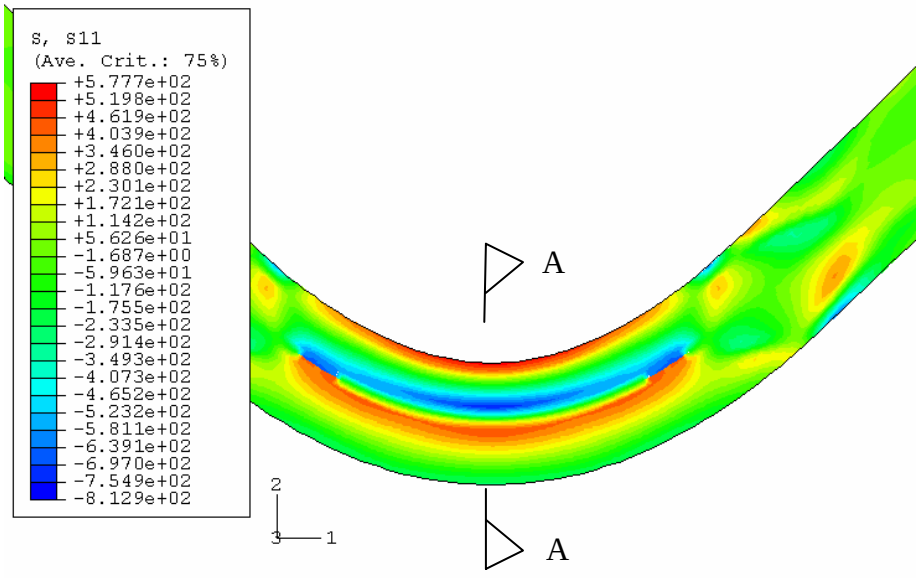

(b) Transverse residual stress

Figure 5.5 Stress contours in a 1-in. thick 90º cold-bent HY-80 steel plate.

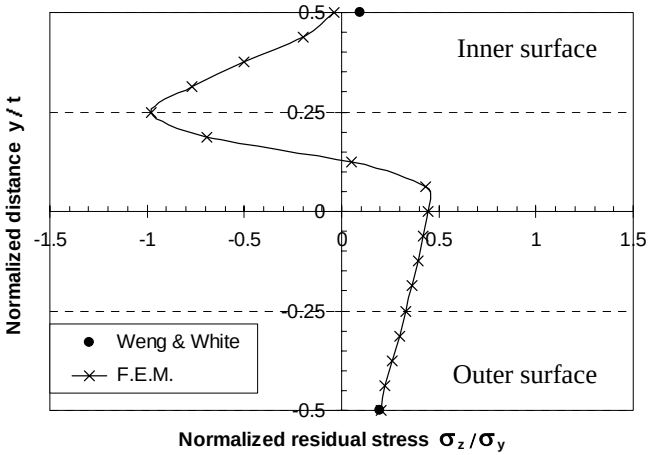

(a) Longitudinal residual stress, R = 1.5 in.

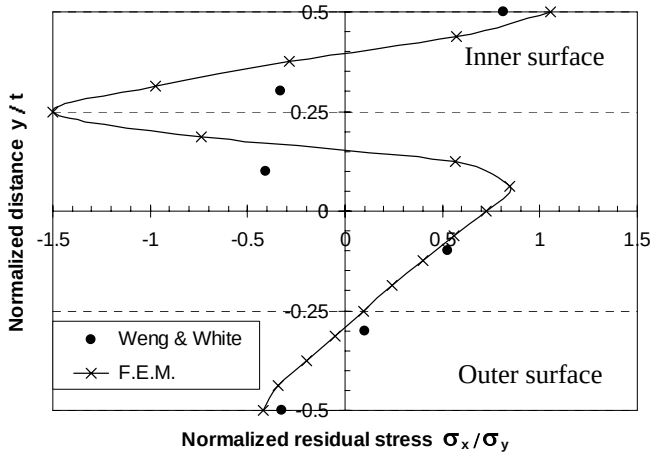

(b) Transverse residual stress, R = 1.5 in.

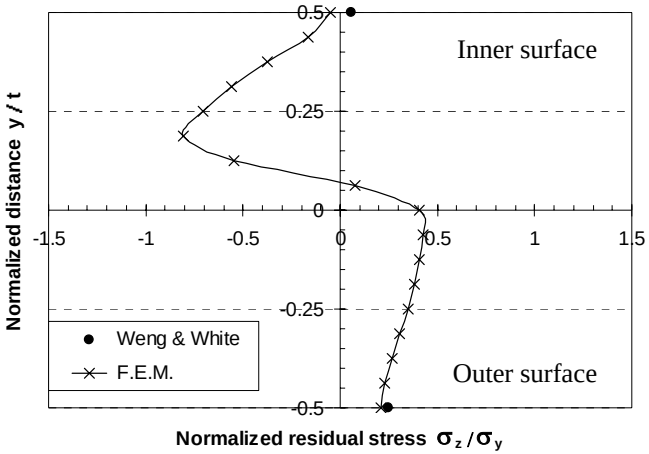

(c) Longitudinal residual stress, R = 2.5 in.

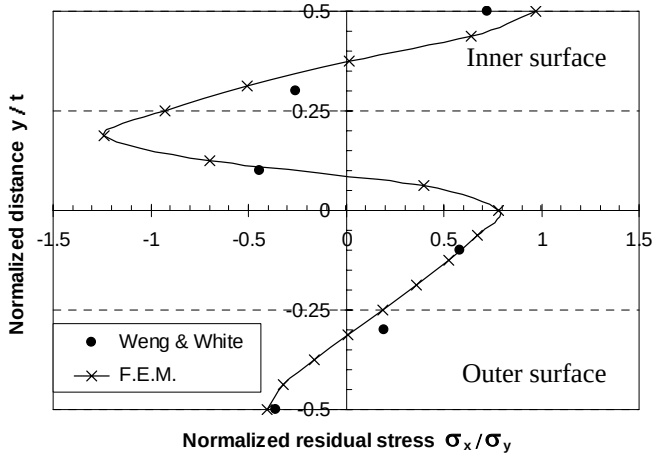

(d) Transverse residual stress, R = 2.5 in.

Figure 5.6 Comparison of finite element results with experimental results from Weng and White.

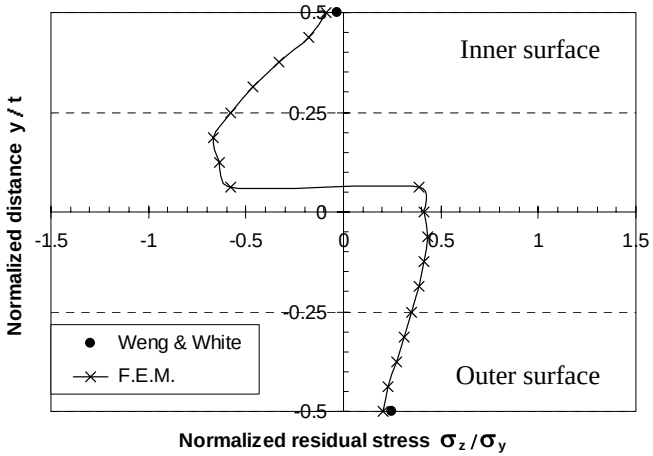

(a) Longitudinal residual stress, R = 3.5 in.

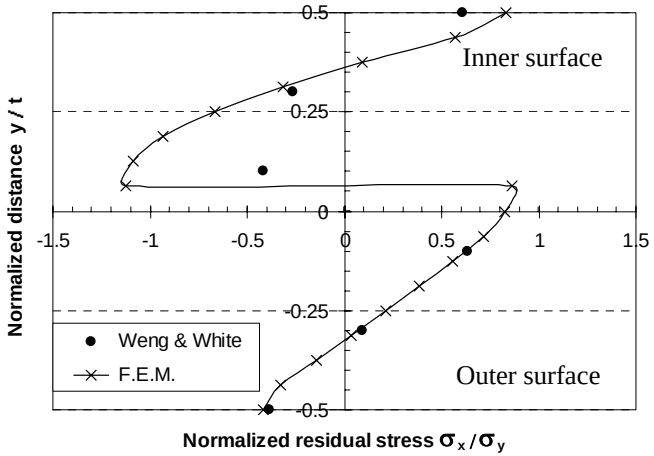

(b) Transverse residual stress, R = 3.5 in.

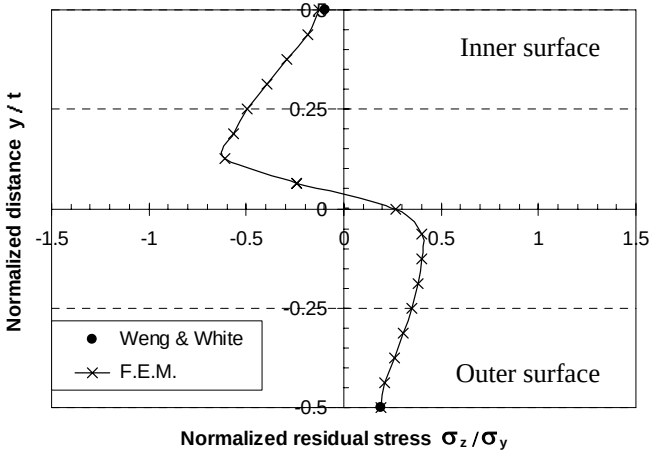

(c) Longitudinal residual stress, R = 5.5 in.

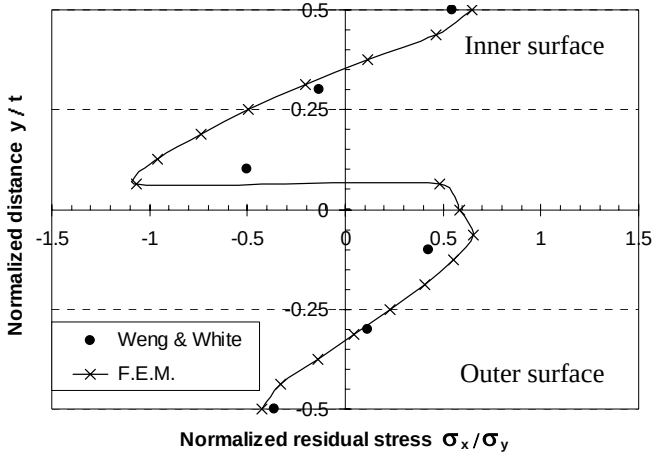

(d) Transverse residual stress, R = 5.5 in.

Figure 5.6 Comparison of finite element results with experimental results from Weng and White (continued).

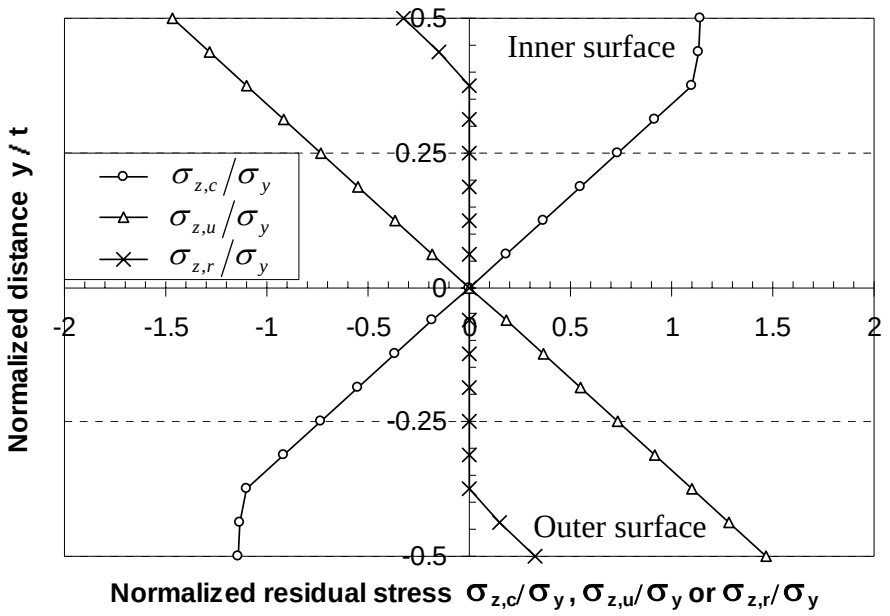

(a) Longitudinal residual stress

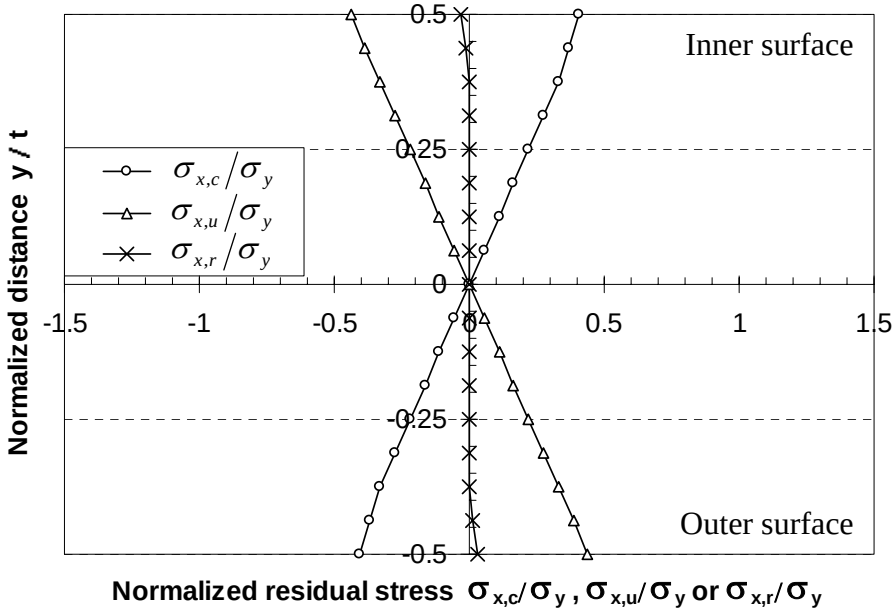

(b) Transverse residual stress

Figure 5.7 Residual stresses due to coiling and uncoiling in specimen PBC14 with D = 1100 mm.

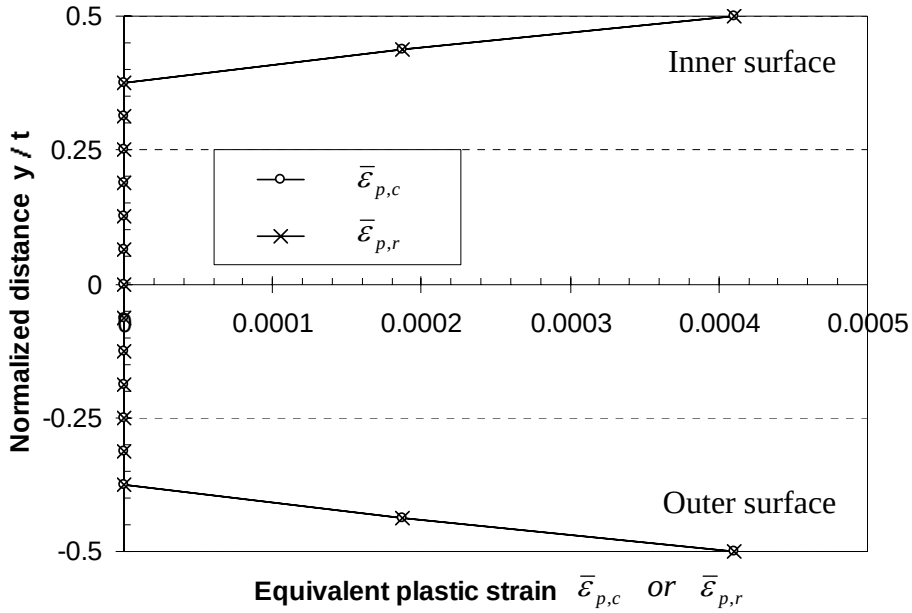

Figure 5.8 Equivalent plastic strains due to coiling and uncoiling in specimen PBC14 with D = 1100 mm.

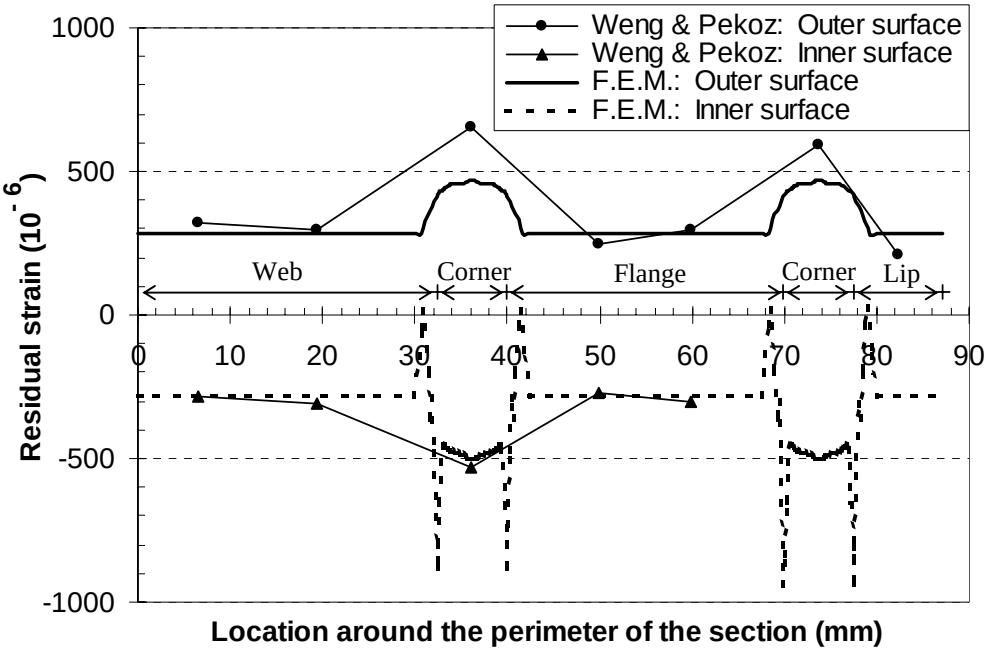

(a) Specimen PBC14

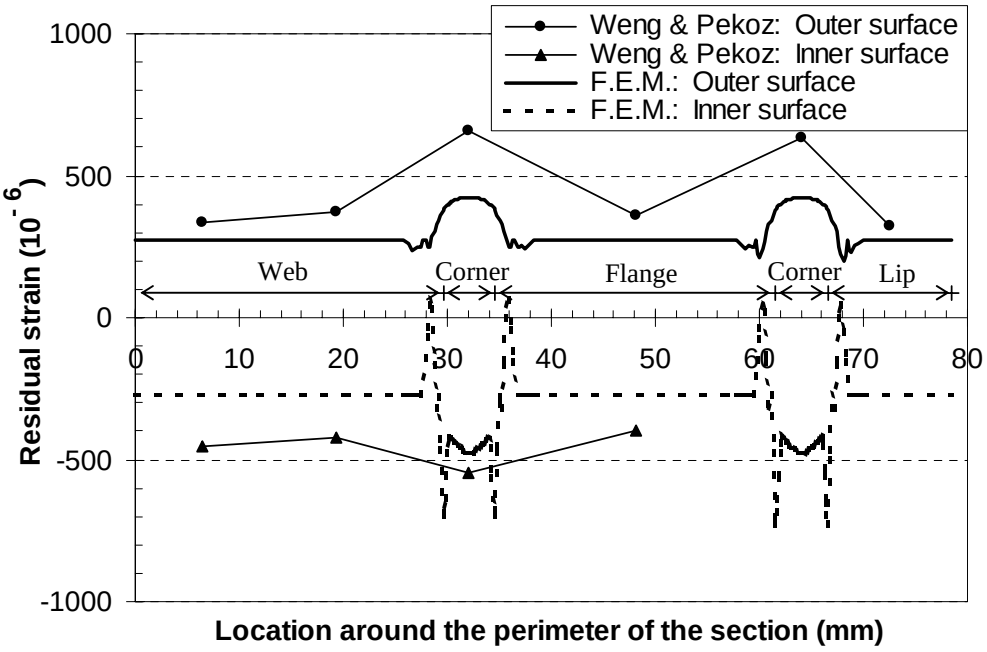

(b) Specimen P16

Figure 5.9 Longitudinal surface residual strain distributions in Weng and Peköz's sections with D = 1100 mm.

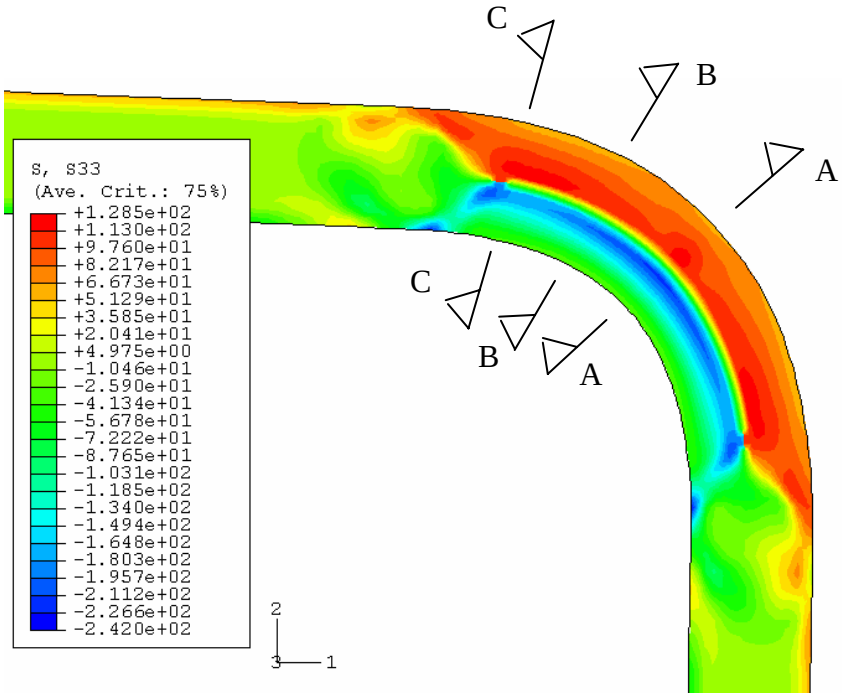

(a) Longitudinal residual stress

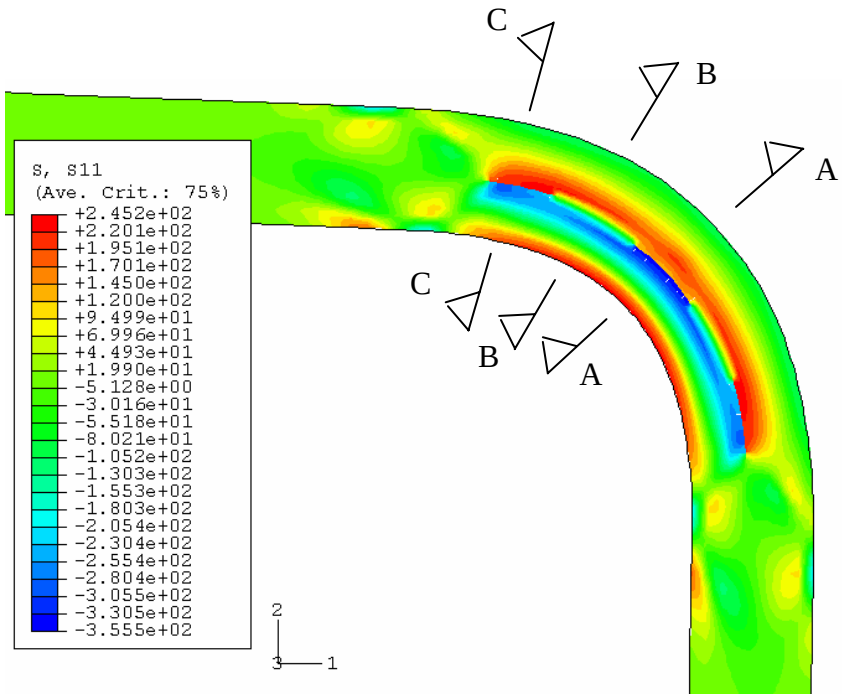

(b) Transverse residual stress

Figure 5.10 Stress contours in the lip-flange corner of specimen PBC14 with D = 1100 mm.

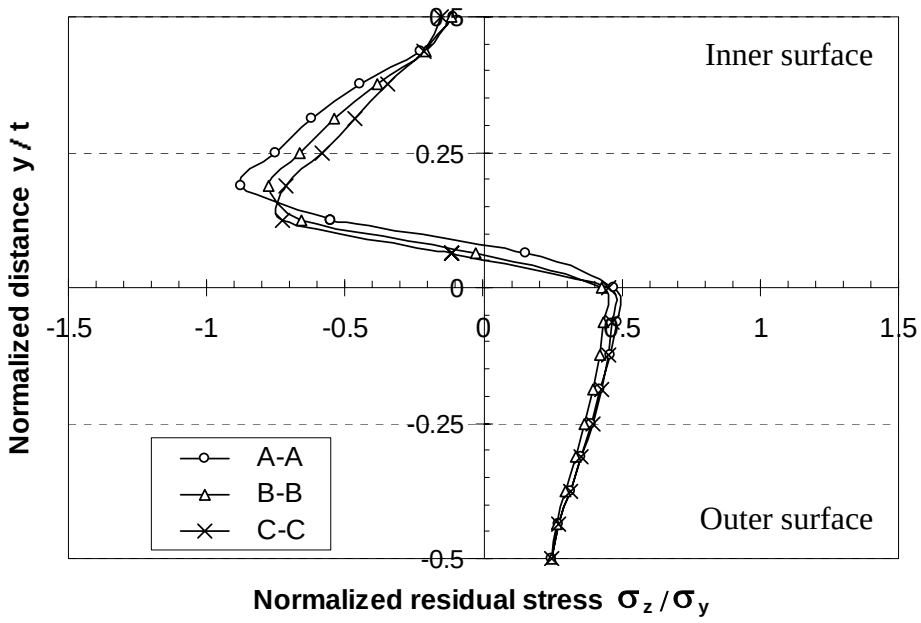

(a) Longitudinal residual stress

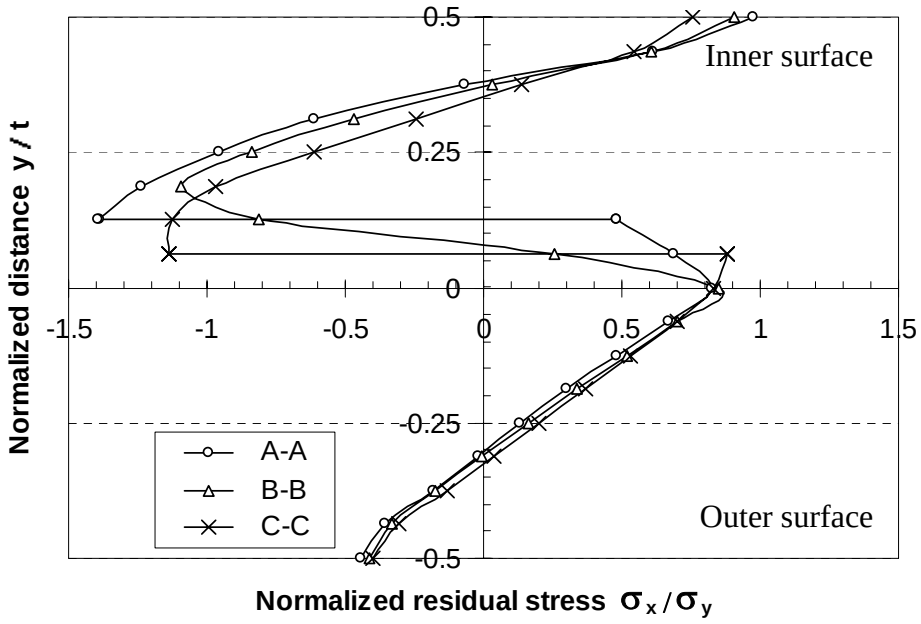

(b) Transverse residual stress

Figure 5.11 Through-thickness variations of residual stresses at different locations in the lip-flange corner of specimen PBC14.

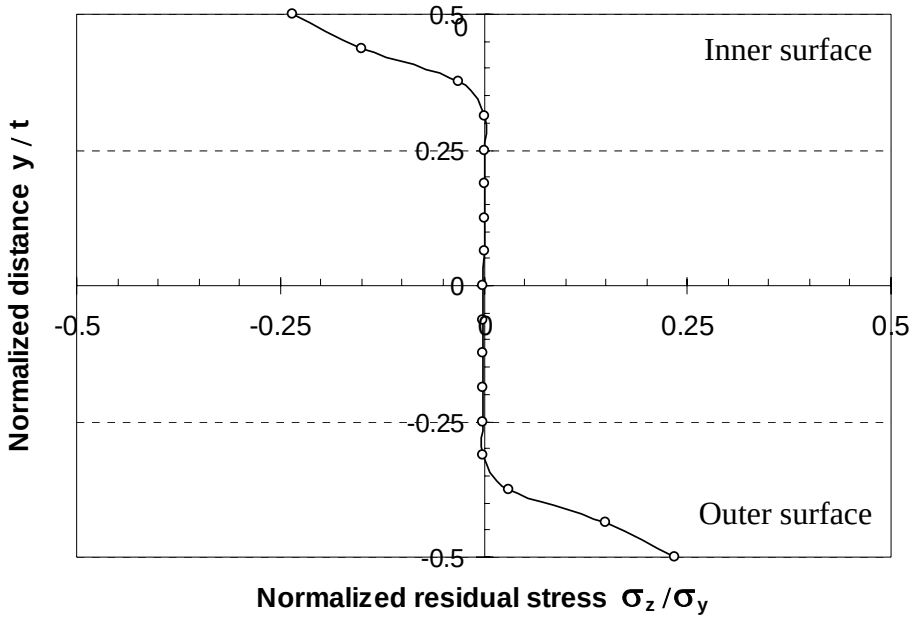

(a) Longitudinal residual stress

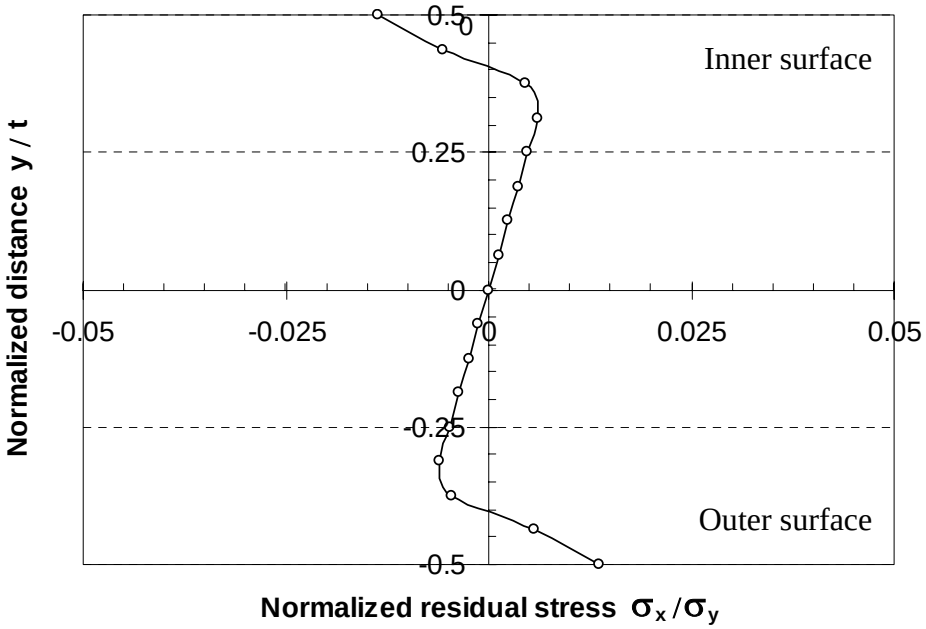

(b) Transverse residual stress

Figure 5.12 Through-thickness variations of residual stresses at the mid-web section of specimen PBC14 with D = 1100 mm.

Chapter 6

ANALYTICAL SOLUTION FOR RESIDUAL STRESSES IN CORNER REGIONS DUE TO COLD BENDING

6.1 INTRODUCTION

The residual stresses in press-braked sections have been studied in Chapter 5 by presenting a finite element-based method and demonstrating its validity and accuracy using results from laboratory measurements. In the finite element-based method, while the effects of coiling and uncoiling are accounted for analytically, the cold bending of press-braking operations is simulated using the finite element method. To have a more efficient method, it is desirable that each stage of this two-stage fabrication process (i.e. the coiling-uncoiling process and the cold bending of press-braking operations) is modelled analytically.

Similar to the coiling and uncoiling of steel sheets, the cold bending of an uncoiled sheet into the corners of a press-braked section can also be modelled as a problem of plane strain pure bending of a sheet into a large curvature. This chapter is concerned with the prediction of residual stresses from the cold bending of press-braking operations by presenting a general analytical solution for the plane strain bending of steel sheets into a large curvature. Based on this general analytical solution, separate solutions were also formulated for three common types of strain-hardening steels: (1) elastic-linear strain-hardening steels, (2) elastic-nonlinear strain-hardening steels, and

(3) nonlinear strain-hardening steels – stainless steel alloys with negligible material anisotropy. To facilitate the application of this analytical solution in the subsequent buckling analysis of cold-formed members, the prediction of equivalent plastic strains is also addressed in addition to residual stresses.

Before proceeding further, it should be noted that the same terminology adopted in Chapters 4 and 5 in referring to stresses in various directions and to surfaces of coiled sheets and press-braked lipped channel sections is also used in this chapter.

6.2 GENERAL ANALYTICAL SOLUTION

6.2.1 Assumptions

Results (Figure 5.10 in Chapter 5) of the finite element-based method presented in Chapter 5 show that press-braking operations induce cold work locally at the corner regions of a press-braked section and basically do not affect the stress state in the flat portions. This means that the residual stresses in the flat portions are mainly derived from the coiling and uncoiling of the steel sheet and can be determined by means of the analytical solution for the coiling-uncoiling process. The verification of this simple method for the modelling of residual stresses in the flat portions is presented later in Section 8.2 of Chapter 8. Furthermore, as shown in Chapter 5, the residual stresses within a corner of a cold-formed section vary across the thickness but are fairly uniform around the perimeter of the bent corner. Since the bending curvature of a corner is usually much larger than the coiling curvature, the residual stresses in the

corner regions of a cold-formed section are not significantly affected by the coiling-uncoiling process. This can be observed later in detail from the parametric study presented in Section 8.2 of Chapter 8. Hence, the cold bending of an uncoiled sheet into the corners of a cold-formed section can also be modelled as a problem of plane strain pure bending of a sheet into a large curvature in the transverse direction with the preceding deformation history of the coiling-uncoiling process ignored. The analytical solution for the coiling of steel sheets presented in Chapter 4 is extended in this chapter to model residual stresses due to the cold bending of a steel sheet into the corners of a press-braked section, and thus most equations presented in Chapter 4 can still be used in this chapter with some modification to develop the analytical solution for cold bending.

Before proceeding further for the model development, it is necessary to first understand the difference between the coiling of sheets and the cold bending of sheets into corners, in terms of both the physical process and theoretical modelling. Although both the coiling and the cold bending can be modelled as a problem of plane strain pure bending, the magnitudes of the bending curvatures involved in these two processes are different. According to the dimensions of the representative cold-formed open sections listed in AISI Cold-Formed Steel Specification (AISI 1996), the centre-line radius R_c of corners ranges from $2t$ to $6t$ (where t is the plate thickness). These bending curvature of corners are much greater than those involved in the coiling-uncoiling process. As indicated by Yu and Zhang (1996), for pure bending of wide plates with the centre-line bending radius $R_c \geq 10t$, adopting engineering strain and adopting logarithmic strain (or the so-called true strain) cause a difference of less than 2.5% in the calculation of the maximum bending strain, and the engineering

strain can used to provide results with sufficient accuracy. Otherwise, for greater bending curvatures (i.e. $R_c < 10t$), the logarithmic strain should be adopted. Therefore, while the engineering strain has been adopted in the analytical solution for the coiling-uncoiling process, the logarithmic strain should be used in the analytical solution for the cold bending of a sheet into a corner.

Following Hill's general theory of sheet bending (Hill 1950), in which the strains due to plane strain pure bending are of any magnitude, the neutral surface of a wide plate initially coincides with the middle surface, but moves towards the inner surface during the bending process. At some intermediate stage, the fibres overtaken by the neutral surface are first strained in compression and are elongated afterwards as the bending deformation proceeds. Such strain reversal happens over a zone bounded by the neutral surface and the deformed location of the original middle surface. Within this zone, there is a surface which is compressed and then extended by the same amount. This is known as the un-stretched surface where the final strain is zero. Hill's general theory is applicable to the pure bending of wide plates into both small and large curvatures. For bending into a small curvature such as $R_c \geq 10t$ (Yu and Zhang 1996), the zone of strain reversal is so small that it can be neglected, and the neutral surface can be assumed to coincide with the middle surface.

To extend the analytical solution for the coiling of a steel sheet to model the cold bending of a sheet to form corners of large curvatures, the following simplifying assumptions are made for the large-curvature bending involved: (1) the sheet thickness is assumed to remain unchanged after bending, (2) through-thickness stresses are ignored, and (3) the strain reversal during the movement of the neutral

surface is ignored. These simplifying assumptions are consistent with the basic assumptions in deriving the analytical solution for the coiling of steel sheets. Although the strain reversal during the movement of the neutral surface is not considered in the analytical solution for cold bending, the neutral surface will not always coincide with the current middle surface after cold bending. The location of the neutral surface can be found by means of the equilibrium condition.

In the later proposed analytical solution, the strains are defined based on the deformed plate with the unchanged thickness. For metal sheets under pure bending, the plate thickness should reduce as the bending curvature increases. The study on a mild steel plate by Zhang and Yu (1988) has shown that the change of the plate thickness is about 5% for R_c/t = 1. As indicated earlier, the ratio R_c/t for the corners of cold-formed open sections usually ranges from 2 to 6. Thus, for cold-formed sections, the reduction in the plate thickness of corners will most likely be bounded by 5%. The 5% reduction in the plate thickness of corners will result in negligible errors in the calculation of strains in corners.

The through-thickness stress is negligible for bending of small curvatures (i.e. $R_c \geq 10t$), such as the coiling of sheets, but its magnitude increases as the curvature increases. Since residual stresses calculated for a press-braked section are eventually incorporated into a finite element model composed of shell elements for non-linear buckling analysis, in which only in-plane residual stresses can be accommodated, through-thickness residual stresses are thus unimportant for such a finite element model and are not considered in modelling the cold bending of a sheet into a corner. The omission of through-thickness stresses in corner regions will lead to higher errors

in the in-plane residual stresses near the neutral surface where the through-thickness stress is the highest. The effect of these simplifying assumptions will be examined by comparing analytical predictions with finite element results, as shown in Chapter 7 for stainless steel sheets where material anisotropy is also taken into account.

6.2.2 Cold bending

In the present study, a steel sheet is supposed to possess an elastic-plastic strain-hardening stress-strain curve defined by a general function $\sigma = F(\varepsilon)$ (or $\varepsilon = f(\sigma)$). During the cold bending of the sheet into a corner (see Figure 1.2(c) in Chapter 1 and Figure 6.1), an arbitrary point in the sheet undergoes transverse straining with the amount depending on its location y away from the current middle surface of the sheet, the distance s between the neutral surface and the current middle surface, and the given bending curvature κ_b (where $\kappa_b = 1/R_c$, and R_c is the current centre-line radius of the corner). By the assumption of zero strains at the neutral surface, the true transverse strain due to cold bending can be obtained as

$$\varepsilon_{x,b} = \ln\left(1 + \left(\frac{s - y}{R_c - s}\right)\right) \tag{6.1}$$

As the through-thickness stresses are ignored, only the in-plane stresses are taken into account for both elastic and inelastic material points across the thickness. Thus, for material points undergoing plastic straining, the von Mises yield criterion is still given by Eqs. (4.4) and (4.5) in Chapter 4, except that the stress components $\sigma_{x,c}$ and $\sigma_{z,c}$

are now replaced by $\sigma_{z,b}$ and $\sigma_{x,b}$ respectively in which the subscript b is used to refer to cold bending.

For elastic material points, the longitudinal and transverse stresses are given by

$$\sigma_{z,b} = \frac{\nu E_0}{\left(1-\nu^2\right)}\varepsilon_{x,b} \tag{6.2a}$$

$$\sigma_{x,b} = \frac{E_0}{\left(1-\nu^2\right)}\varepsilon_{x,b} \tag{6.2b}$$

By analogy with Eq. (4.7), the transverse strain at which a material point starts to yield is given by

$$\varepsilon_{x,by} = \pm\sigma_{y0}\left(1-\nu^2\right)\Big/\left(E_0\sqrt{1-\nu+\nu^2}\right) \tag{6.3}$$

in which $\varepsilon_{x,by} > 0$ if the strain is tensile (i.e. $y < s$). Under the bending curvature $\kappa_b = 1/R_c$, a zone near the centre of the thickness remains elastic, and its extent, which can be determined by combining Eq. (6.3) with Eq. (6.1), is found to be

$$s-\left(R_c-s\right)\left[\exp\left(\frac{\sigma_{y0}\left(1-\nu^2\right)}{E_0\sqrt{1-\nu+\nu^2}}\right)-1\right] < y < s-\left(R_c-s\right)\left[\exp\left(\frac{-\sigma_{y0}\left(1-\nu^2\right)}{E_0\sqrt{1-\nu+\nu^2}}\right)-1\right] \tag{6.4}$$

Therefore, for the elastic zone defined by Eq. (6.4), the stresses are given by Eq. (6.2). The material points outside this elastic zone are subjected to plastic straining. By defining the following stress ratio:

$$\omega_b = \sigma_{z,b} \big/ \sigma_{x,b} \tag{6.5}$$

and combining it with the von Mises yield criterion (see Eqs. (4.4) and (4.5)), the stresses of any point undergoing plastic straining due to cold bending can be obtained as

$$\sigma_{z,b} = \pm \frac{\omega_b \sigma_{yb}}{\sqrt{1 - \omega_b + \omega_b^2}} \tag{6.6a}$$

$$\sigma_{x,b} = \pm \frac{\sigma_{yb}}{\sqrt{1 - \omega_b + \omega_b^2}} \tag{6.6b}$$

in which $\sigma_{x,b}$ and $\sigma_{z,b} \leq 0$ (i.e. compressive stresses) when $y \geq s$ (see Figure 6.1), and σ_{yb} is the instantaneous yield stress reached at the end of cold bending.

Similar to Eq. (4.13), the equivalent plastic strain due to cold bending can be given by

$$\bar{\varepsilon}_{p,b} = \varepsilon_{yb} - \frac{\sigma_{yb}}{E_0} \tag{6.7}$$

in which the subscript b is used to refer to cold bending, σ_{yb} and ε_{yb} are the instantaneous yield stress and the corresponding strain reached at the end of cold bending with their relationship defined by the function $\sigma = F(\varepsilon)$ (or $\varepsilon = f(\sigma)$). Therefore, once σ_{yb} is obtained, ε_{yb} can be determined from the stress-strain

relationship $\sigma = F(\varepsilon)$ (or $\varepsilon = f(\sigma)$), and the equivalent plastic strain $\bar{\varepsilon}_{p,b}$ due to cold bending can then be calculated from Eq. (6.7).

For pure bending, the stress equilibrium in the bending direction is given by

$$\sum F = \int_{-t/2}^{t/2} \sigma_{x,b} dy = 0 \tag{6.8}$$

If the bending curvature is small, the transverse bending stresses are anti-symmetrically distributed across the thickness, and the equilibrium condition of Eq. (6.8) is naturally satisfied. At large bending curvatures, the neutral surface shifts toward the inner surface of the bent sheet, and the distribution of bending stresses becomes non-antisymmetrical. Thus, the equilibrium condition of Eq. (6.8) has to be imposed to ensure a condition of pure bending. By trial and error, the value of s, which is the distance between the neutral surface and the current middle surface, can be determined such that the equilibrium condition of Eq. (6.8) is satisfied.

In order to determine the stresses and the equivalent plastic strain due to cold bending at any location y for a given bending curvature κ_b and a trial value of s, it is necessary to first calculate the values of σ_{yb} and ω_b numerically for each value of y. The determination of σ_{yb} and ω_b is discussed in the next subsection.

6.2.3 Determination of σ_{yb} and ω_b

Since σ_{yb} and ω_b are related to each other for strain-hardening materials, their values are determined numerically using their inter-relationship and the known boundary values. By defining the following ratio of stress increments:

$$\Omega_b = d\sigma_{z,b} / d\sigma_{x,b} \tag{6.9}$$

for inelastic material points and following a procedure similar to that given in Section 4.3, the increment of stress ratio is obtained as:

$$d\omega_b = \frac{2\left(1-\omega_b+\omega_b^2\right)\left(\Omega_b-\omega_b\right)}{\sigma\left[\left(2-\omega_b\right)+\Omega_b\left(2\omega_b-1\right)\right]} d\sigma \tag{6.10}$$

in which H' is given by Eq. (4.15), and Ω_b is given by

$$\Omega_b = \frac{4\nu H'\left(1-\omega_b+\omega_b^2\right)-E_0\left(2-\omega_b\right)\left(2\omega_b-1\right)}{E_0\left(2\omega_b-1\right)^2+4H'\left(1-\omega_b+\omega_b^2\right)} \tag{6.11}$$

The increment $d\omega_b$ given by Eq. (6.10) is a function of ω_b and σ. Eq. (6.10) can then be used to solve numerically for the values of σ_{yb} and the corresponding stress ratio ω_b for each location y.

In analogy with Eq. (4.32), the transverse bending strain $\varepsilon_{x,b}$ at an arbitrary location y can be expressed as a function of ω_b and σ through the following integral:

$$\varepsilon_{x,b} = \varepsilon_{x,by} \pm \left\{ \begin{array}{l} \displaystyle\int_{\nu}^{\omega_b} \frac{\left[(1-2\omega_b)^2 - 2\nu(1-2\omega_b)(2-\omega_b) + (2-\omega_b)^2\right]\sigma}{2E_0(2\omega_b - 1)\left(1-\omega_b+\omega_b^2\right)^{3/2}} d\omega_b \\ \displaystyle + \int_{\sigma_{y0}}^{\sigma_{yb}} \frac{\left(1-\omega_b^2\right)(1-2\nu)}{E_0(2\omega_b - 1)\left(1-\omega_b+\omega_b^2\right)^{1/2}} d\sigma \end{array} \right\} \qquad (6.12)$$

in which the +ve sign of "±" applies when $y \geq s$, and $\varepsilon_{x,b}$ and $\varepsilon_{x,by}$ are given by Eq. (6.1) and (6.3) respectively.

For a trial value of the distance s, the values of $\varepsilon_{x,b}$ and $\varepsilon_{x,by}$ can be calculated by Eqs. (6.1) and (6.3) respectively. The integration in Eq. (6.12) can be performed numerically by the Euler forward method. The lower limits (i.e. ν for $d\omega_b$ and σ_{y0} for $d\sigma$) of the integration are treated as initial conditions. Starting with these initial conditions, the value of $d\omega_b$ can be calculated from Eq. (6.10) for a small assigned value of $d\sigma$, and the values of ω_b and σ can then be updated for each step. After the numerical integration (see Eq. (6.12)) is done, the values of σ_{yb} and the corresponding stress ratio ω_b, which are the upper limits of the integration, can be determined.

After the values of σ_{yb} and ω_b are determined for each trial value of s, the stresses and the equivalent plastic strain of any inelastic material point due to cold bending can be calculated from Eqs. (6.6) and (6.7). Then the equilibrium condition of Eq.

(6.8) is checked, and the value of the distance s is adjusted for the next trial until the condition given by Eq. (6.8) is satisfied.

6.3 SOLUTION FOR ELASTIC-LINEAR STRAIN-HARDENING SHEETS

The stress-strain relationship $\sigma = F(\varepsilon)$ (or $\varepsilon = f(\sigma)$) in the general analytical solution presented in the preceding section is now defined by Eq. (4.64) for elastic-linear strain-hardening materials. By substituting Eq. (4.64) into Eq. (6.7), the equivalent plastic strain due to cold bending can be obtained as

$$\bar{\varepsilon}_{p,b} = \left(\sigma_{yb} - \sigma_{y0}\right)\left[\frac{E_0 - E_{st}}{E_0 E_{st}}\right] \tag{6.13}$$

Hence, stresses and equivalent plastic strains due to the cold bending of an elastic-linear strain-hardening steel sheet into a corner can be obtained by defining the stress-strain relationship $\sigma = F(\varepsilon)$ (or $\varepsilon = f(\sigma)$) with Eq. (4.64) and replacing Eqs. (4.15) and (6.7) with Eq. (4.65) and (6.13), and then following the procedure explained in Section 6.2 (see Eqs. (6.1)~(6.12)).

6.4 SOLUTION FOR ELASTIC-NONLINEAR STRAIN-HARDENING SHEETS

The stress-strain relationship $\sigma = F(\varepsilon)$ (or $\varepsilon = f(\sigma)$) in the general analytical solution presented in Section 6.2 can be defined by the power function given by Eq. (4.68) for elastic-nonlinear strain-hardening materials. By substituting Eq. (4.68) into Eq. (6.7), the equivalent plastic strain due to cold bending can be obtained as

$$\bar{\varepsilon}_{p,b} = \frac{\sigma_{y0}}{E_0}\left(\frac{\sigma_{yb}}{\sigma_{y0}}\right)^{1/n_s} - \frac{\sigma_{yb}}{E_0} \tag{6.14}$$

Hence, stresses and equivalent plastic strains due to the cold bending of an elastic-nonlinear strain-hardening steel sheet into a corner can be obtained by defining the stress-strain relationship $\sigma = F(\varepsilon)$ (or $\varepsilon = f(\sigma)$) with Eq. (4.68) and replacing Eqs. (4.15) and (6.7) with Eq. (4.69) and (6.14), and then following the procedure explained in Section 6.2 (see Eqs. (6.1)~(6.12)).

It is worth noting that the specialized analytical solution presented above can be used to predict stresses and equivalent plastic strains in corner regions of press-braked carbon steel sections. For a carbon steel sheet possessing a stress-strain curve of the sharp-yielding type (i.e. a yield plateau exists before strain hardening), the yield plateau can be ignored for large straining. As explained in Chapter 5, the exclusion of this transition region between elastic behaviour and strain hardening leads to little error when the strain under consideration is greater than 4% (Hosford and Caddell 1993), while surface strains in corners of a press-braked section are usually much

greater than this amount. That is, if residual stresses in corner regions are concerned, the carbon steel can be assumed to possess an elastic-nonlinear strain-hardening stress-strain curve defined by the power function (see Eq. (4.68)), and the specialized analytical solution presented in this section can be employed for the prediction.

6.5 SOLUTION FOR NONLINEAR STRAIN-HARDENING SHEETS —— STAINLESS STEEL SHEETS

The general analytical solution presented in Section 6.2 can be applied to the cold bending of nonlinear strain-hardening sheets such as stainless steel sheets discussed in this section. To achieve this, the stress-strain relationship of stainless steel alloys needs to be defined first. The nominal stress-strain relationship of stainless steel alloys can be easily defined by the 3-stage full-range stress-strain model (Eq. (3.6)) presented in Chapter 3. However, the stress-strain behaviour of the material at large strains such as those involve in the cold bending cannot be accurately described by the nominal stress-strain relationship.

Nominal stress-strain curves obtained from coupon tests can accurately describe the stress-strain behaviour of materials at small and intermediate strain levels, such as that involved in the coiling-uncoiling process. At larger strains, the nominal stress-strain relationship deviates from the “real” stress-strain response due to the fact that the nominal stress-strain curve does not take into account the changes of cross sections of test coupons. In this case, the true stress-strain relationship should be used to represent the “real” stress-strain response of the material. Therefore, for large

curvatures involved in the cold bending at corners, the stress-strain relationship $\sigma = F(\varepsilon)$ (or $\varepsilon = f(\sigma)$) of the material should be represented by the relationship between the true stress σ_t and the true strain ε_t. That is,

$$\sigma = \sigma_t \quad \text{and} \quad \varepsilon = \varepsilon_t \tag{6.15}$$

The true stress σ_t, the true strain ε_t and the true plastic strain ε_{tp} can be converted from the nominal stress σ_n and the nominal strain ε_n by the following equations:

$$\sigma_t = \sigma_n(1 \pm \varepsilon_n) \tag{6.16a}$$

$$\varepsilon_t = \pm \ln(1 \pm \varepsilon_n) \tag{6.16b}$$

$$\varepsilon_{tp} = \varepsilon_t - \frac{\sigma_t}{E_0} = \pm \ln(1 \pm \varepsilon_n) - \frac{\sigma_n(1 \pm \varepsilon_n)}{E_0} \tag{6.16c}$$

where the upper sign corresponds to tension, the lower sign corresponds to compression, and σ_n, ε_n, σ_t, ε_t and ε_{tp} are absolute values for both tension and compression coupon tests.

As the stress-strain relationship $\sigma = F(\varepsilon)$ (or $\varepsilon = f(\sigma)$) of the material is described by the true stress-strain relationship for large straining (see Eq. (6.15)), the slope of the equivalent stress-equivalent plastic strain relation H' for inelastic material points can still be given by Eq. (4.15) but the strain rate $d\varepsilon/d\sigma$ in Eq. (4.15) should be replaced by the strain rate $d\varepsilon_t/d\sigma_t$ of the true stress-strain curve. The strain rate

$d\varepsilon/d\sigma$ in Eq. (4.15) can be expressed in terms of the nominal stress σ_n and the nominal strain ε_n as follows:

$$\frac{d\varepsilon}{d\sigma}=\frac{d\varepsilon_t}{d\sigma_t}=\frac{d\varepsilon_n/d\sigma_n}{(1\pm\varepsilon_n)\left[(1\pm\varepsilon_n)\pm\sigma_n(d\varepsilon_n/d\sigma_n)\right]} \tag{6.17}$$

By substituting Eq. (6.17) into Eq. (4.15), the slope of the equivalent stress-equivalent plastic strain relation H' can be determined as

$$H'=\frac{d\bar{\sigma}}{d\bar{\varepsilon}_p}=\left[\frac{d\varepsilon_n/d\sigma_n}{(1\pm\varepsilon_n)\left[(1\pm\varepsilon_n)\pm\sigma_n(d\varepsilon_n/d\sigma_n)\right]}-\frac{1}{E_0}\right]^{-1} \tag{6.18}$$

in which $d\varepsilon_n/d\sigma_n$ is the strain rate of the nominal stress-strain curve. For stainless steel alloys, the strain rate $d\varepsilon_n/d\sigma_n$ can be found by the differentiation of the 3-stage full-range stress-strain relationship (see Eq. (3.6) in Chapter 3):

$$\frac{d\varepsilon_n}{d\sigma_n}=\begin{cases}\dfrac{1}{E_0}+0.002n\dfrac{\sigma_n^{n-1}}{\sigma_{0.2}^{n}}, & \sigma_n\le\sigma_{0.2}\\[2ex] \dfrac{1}{E_{0.2}}+n'_{0.2,1.0}\left[0.008+(\sigma_{1.0}-\sigma_{0.2})\left(\dfrac{1}{E_0}-\dfrac{1}{E_{0.2}}\right)\right]\dfrac{(\sigma_n-\sigma_{0.2})^{n'_{0.2,1.0}-1}}{(\sigma_{1.0}-\sigma_{0.2})^{n'_{0.2,1.0}}}, & \sigma_{0.2}<\sigma_n\le\sigma_{2.0}\\[2ex] \dfrac{(b\mp\sigma_n)\pm(\sigma_n-a)}{(b\mp\sigma_n)^2}, & \sigma_n>\sigma_{2.0}\end{cases} \tag{6.19}$$

where the upper sign corresponds to tension, and the lower sign corresponds to compression.

If the nominal stress-strain relationship of the material is known, the stress increment $d\sigma$ in Eq. (6.10) can be calculated from the nominal stress σ_n and its increment $d\sigma_n$. By combining Eqs. (6.15) and (6.16a) after differentiation with Eqs. (3.6) and (6.19), the stress increment $d\sigma$ for stainless steel alloys can be obtained as

$$\frac{d\sigma}{d\sigma_n}=\frac{d\sigma_t}{d\sigma_n}=\begin{cases}1\pm\left[\dfrac{2\sigma_n}{E_0}+0.002(n+1)\left(\dfrac{\sigma_n}{\sigma_{0.2}}\right)^n\right], & \sigma_n\le\sigma_{0.2}\\[2ex] 1\pm\left\{\begin{array}{l}\varepsilon_{0.2}+\dfrac{(2\sigma_n-\sigma_{0.2})}{E_{0.2}}+\left[(n'_{0.2,1.0}+1)\sigma_n-\sigma_{0.2}\right]\cdot\\ \left[0.008+(\sigma_{1.0}-\sigma_{0.2})\left(\dfrac{1}{E_0}-\dfrac{1}{E_{0.2}}\right)\right]\dfrac{(\sigma_n-\sigma_{0.2})^{n'_{0.2,1.0}-1}}{(\sigma_{1.0}-\sigma_{0.2})^{n'_{0.2,1.0}}}\end{array}\right\}, & \sigma_{0.2}<\sigma_n\le\sigma_{2.0}\\[2ex] 1\pm\dfrac{(2\sigma_n-a)(b\mp\sigma_n)\pm\sigma_n(\sigma_n-a)}{(b\mp\sigma_n)^2}, & \sigma_n>\sigma_{2.0}\end{cases} \tag{6.20}$$

Eq. (6.10) together with Eq. (6.20) can then be used to solve numerically for the values of σ_{yb} and the corresponding stress ratio ω_b at each location y.

For stainless steel sheets, due to the nonlinear material behaviour, the initial yield point coincides with the origin of the stress-strain curve (i.e. $\sigma_{y0}=0$) and inelastic straining takes place across the whole thickness. The elastic zone defined by Eq. (6.4) thus vanishes and the onset yield strain $\varepsilon_{x,by}$ becomes zero:

$$\varepsilon_{x,by}=0 \tag{6.21}$$

To calculate the stresses and equivalent plastic strains due to the cold bending of an isotropic stainless steel sheet into a corner, a procedure similar to that explained in Section 6.2 (see Eqs. (6.1)~(6.12)) should be followed by noting that $\sigma_{y0} = 0$ and $\varepsilon_{x,by} = 0$, but the value of $d\omega_b$ is no longer calculated directly from an assigned value of $d\sigma$ using Eq. (6.10). Instead, for each step, the value of $d\sigma$ is first calculated from a small assigned value of $d\sigma_n$ using Eq. (6.20), and the value of $d\omega_b$ can then be calculated from the resulting stress increment $d\sigma$ using Eqs. (6.10) and (6.18). In such a way, the values of σ_n, σ and ω_b can be updated for each step.

6.6 CONCLUSIONS

Residual stresses in press-braked sections are derived from two distinct sources: the coiling-uncoiling process and the cold bending of press-braking operations. The latter induces residual stresses in the corners of a press-braked section. This chapter has been concerned with the analytical prediction of residual stresses in corner regions resulting from the cold bending of press-braking operations.

In this chapter, a general analytical solution for residual stresses in corner regions has been presented in which the cold bending of press-braking operations is taken into account in a plane strain large-curvature pure bending model. This general analytical solution was then specialized for three common types of strain-hardening steels by incorporating their specific stress-strain relationships: (1) elastic-linear strain-hardening steels, (2) elastic-nonlinear strain-hardening steels, and (3) nonlinear strain-hardening steels, such as stainless steel alloys. This analytical solution has been

developed based on some simplifying assumptions. The effect of these simplifying assumptions and the verification of the analytical solution will be examined in Chapter 7 by comparing analytical predictions with finite element results, for stainless steel sheets where material anisotropy is also taken into account.

The analytical solution presented in this chapter can provide predictions of residual stresses in corner regions of press-braked sections with good accuracy. This analytical solution for cold bending together with the analytical solution for the coiling-uncoiling process presented in Chapter 4 can lead to a complete analytical model for residual stresses in press-braked sections. Such complete analytical model can provide accurate residual stresses and equivalent plastic strains, in different parts of a press-braked section due to the whole two-stage manufacturing process, which can be specified as the initial state in a finite element model of the cold-formed member for the subsequent nonlinear bucking analysis. Such exploitation of the present analytical solution is reported in Chapters 7 and 9.

6.7 REFERENCES

AISI (1996). *Cold-Formed Steel Design Manual*, 1996 edition, American Iron and Steel Institute, Washington, D.C.

Hill, R. (1950). *The Mathematical Theory of Plasticity*, Oxford University Press, United States.

Hosford, W. F. and Caddell, R. M. (1993). *Metal Forming: Mechanics and Metallurgy*, Prentice Hall, New York.

Yu, T. X. and Zhang, L. C. (1996). *Plastic Bending: Theory and Applications*, World Scientific Publishing Co., New Jersey.

Zhang, L. C. and Yu, T. X. (1988). A refined theory of elastic-plastic pure bending of wide plates. *Journal of Peking University (Natural Sciences edition),* **24,** 65-72.

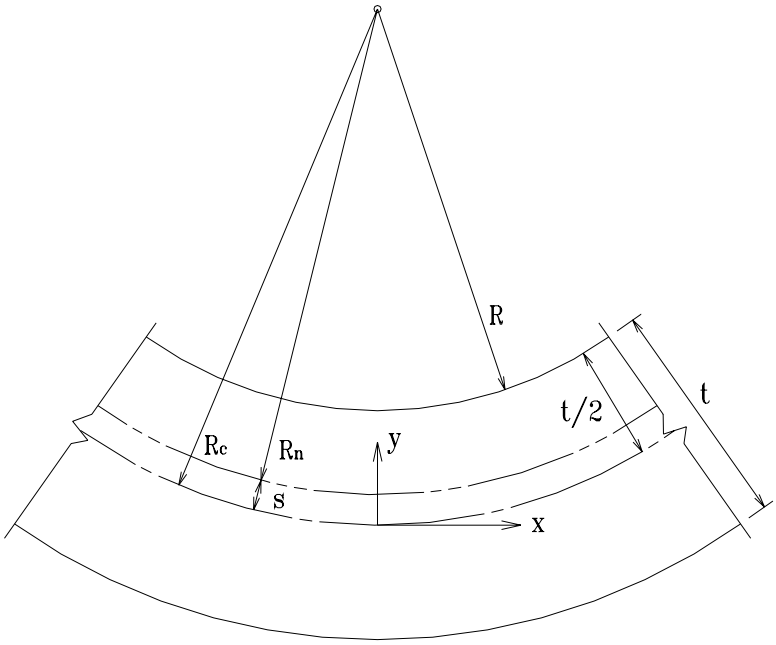

Figure 6.1 Schematic diagram of a sheet under pure bending with a large curvature.

Chapter 7

ANALYTICAL SOLUTIONS FOR RESIDUAL STRESSES IN PRESS-BRAKED STAINLESS STEEL SECTIONS CONSIDERING THE EFFECT OF MATERIAL ANISOTROPY

7.1 INTRODUCTION

In order to predict residual stresses in press-braked sections, two distinct stages of the manufacturing process (which are the coiling-uncoiling process and the press-braking operation respectively) have been modelled by presenting two general analytical solutions in Chapters 4 and 6 respectively. Based on these general analytical solutions, separate analytical solutions have also been formulated for residual stresses in press-braked sections made of different types of isotropic materials, which include stainless steel alloys with negligible material anisotropy, such as austenitic alloys.

For other stainless steel alloys with a greater degree of material anisotropy, such as duplex alloys, the effect of material anisotropy on residual stresses should be considered. Thus, improved analytical solutions are needed for residual stresses in stainless steel sections for which material anisotropy is important. Therefore, this chapter is concerned with the analytical prediction of residual stresses in press-braked stainless steel sections with the material anisotropy of the sheet material taken into

account. In this chapter, two distinct analytical solutions are presented for the coiling-uncoiling process and the press-braking operation respectively which are again modelled as plane strain pure bending problems. On the basis of these two analytical solutions, a complete analytical model is proposed to predict residual stresses in press-braked sections. The prediction of equivalent plastic strains is also addressed in addition to residual stresses.

Before proceeding further, it should be noted first that the same terminology adopted in Chapters 4 and 5 in referring to stresses in various directions and to surfaces of coiled sheets and press-braked lipped channel sections is also used in this chapter.

7.2 ANALYTICAL SOLUTION FOR THE COILING-UNCOILING PROCESS

7.2.1 Assumptions

Stainless steel alloys are characterized by a nonlinear stress-strain relationship and material anisotropy, and have different properties in tension and compression and different properties in the longitudinal and the transverse directions. Although the effect of material anisotropy on yielding can be ignored for austenitic alloys, it is more pronounced for other stainless steel alloys, such as duplex and ferritic alloys. A flat stainless steel sheet can be assumed to possess a stress-strain curve of the virgin material before it is coiled for storage, since the effect of cold work prior to the coiling has been removed in the annealing furnace. In the present analytical solution,

the state of anisotropy is described by Hill's anisotropic yield criterion, while nonlinear strain hardening is modelled by incorporating the stress-strain relationship of the virgin material in the longitudinal direction, which can generally be defined by a function:

$$\sigma_{yL} = F\left(\varepsilon_{yL}\right) \text{ or } \varepsilon_{yL} = f\left(\sigma_{yL}\right) \tag{7.1}$$

where σ_{yL} and ε_{yL} are the instantaneous yield stress and the corresponding strain in the longitudinal direction.

The stress-strain relationship of Eq. (7.1) can represent the Ramberg-Osgood curve for small strains or the 3-stage full-range stress-strain relationship (see Eq. (3.6)) presented in Chapter 3 for a full range of strains. The coiling of a stainless steel sheet into a curvature κ_c and its subsequently uncoiling and flattening can be modelled as plane strain pure bending in the y-z plane (see Figure 1.2 in Chapter 1). This section presents the analytical solution for this inelastic bending problem.

7.2.2 Coiling

Due to the "roundhouse" type of material behaviour of stainless steel alloys, purely elastic straining does not occur during the coiling process, so no elastic core exists. During the coiling of a stainless steel sheet, an arbitrary point in the sheet undergoes inelastic straining, and the amount of strains depends on the given coiling curvature κ_c and its location y away from the neutral axis of the section. For material points

across the thickness, under a plane strain condition in the transverse direction (x direction) and a plane stress condition in the through-thickness direction (y direction), Hill's anisotropic yield criterion (Hill 1950) is given by

$$F\sigma_{z,c}^2 + G\left(\sigma_{z,c} - \sigma_{x,c}\right)^2 + H\sigma_{x,c}^2 = 1 \tag{7.2a}$$

$$F = \frac{1}{2}\left[\frac{1}{\sigma_{0N}^2} + \frac{1}{\sigma_{0L}^2} - \frac{1}{\sigma_{0T}^2}\right] \tag{7.2b}$$

$$G = \frac{1}{2}\left[\frac{1}{\sigma_{0T}^2} + \frac{1}{\sigma_{0L}^2} - \frac{1}{\sigma_{0N}^2}\right] \tag{7.2c}$$

$$H = \frac{1}{2}\left[\frac{1}{\sigma_{0T}^2} + \frac{1}{\sigma_{0N}^2} - \frac{1}{\sigma_{0L}^2}\right] \tag{7.2d}$$

where $\sigma_{x,c}$ and $\sigma_{z,c}$ are the stresses in the x and z directions respectively due to coiling at an arbitrary location y from the neutral axis of the section; F, G and H are the anisotropy parameters; σ_{0L}, σ_{0T} and σ_{0N} are the initial yield stresses (taken as 0.2% proof stresses) in the longitudinal (z), transverse (x), and through-thickness (y) directions respectively.

By taking the initial yield stress σ_{0L} in the longitudinal direction as the reference yield stress and multiplying both sides of Eq. (7.2) by σ_{0L}, Hill's anisotropic yield criterion can be written as

$$\overline{F}\sigma_{z,c}^2 + \overline{G}\left(\sigma_{z,c} - \sigma_{x,c}\right)^2 + \overline{H}\sigma_{x,c}^2 = \sigma_{0L}^2 \tag{7.3a}$$

$$\overline{F} = F\sigma_{0L}^2 = \frac{1}{2}\left[\left(\frac{\sigma_{0L}}{\sigma_{0N}}\right)^2 + \left(\frac{\sigma_{0L}}{\sigma_{0L}}\right)^2 - \left(\frac{\sigma_{0L}}{\sigma_{0T}}\right)^2\right] \tag{7.3b}$$

$$\overline{G} = G\sigma_{0L}^2 = \frac{1}{2}\left[\left(\frac{\sigma_{0L}}{\sigma_{0T}}\right)^2 + \left(\frac{\sigma_{0L}}{\sigma_{0L}}\right)^2 - \left(\frac{\sigma_{0L}}{\sigma_{0N}}\right)^2\right] \tag{7.3c}$$

$$\overline{H} = H\sigma_{0L}^2 = \frac{1}{2}\left[\left(\frac{\sigma_{0L}}{\sigma_{0T}}\right)^2 + \left(\frac{\sigma_{0L}}{\sigma_{0N}}\right)^2 - \left(\frac{\sigma_{0L}}{\sigma_{0L}}\right)^2\right] \tag{7.3d}$$

in which $\overline{F}$, $\overline{G}$ and $\overline{H}$ are the dimensionless anisotropy parameters which are defined by the ratios of the yield stresses in the principal directions of anisotropy. Hill's anisotropic yield criterion given by Eq. (7.3) can be applied to anisotropic nonlinearly hardening materials, as long as the dimensionless anisotropy parameters remain nearly unchanged over the considered range of strains and the change in the state of anisotropy is negligible. Hence, Eq. (7.3a) can be rewritten in a more general manner

$$\overline{F}\sigma_{z,c}^2 + \overline{G}\left(\sigma_{z,c} - \sigma_{x,c}\right)^2 + \overline{H}\sigma_{x,c}^2 = \sigma_{yL}^2 \tag{7.4}$$

where σ_{yL} is the instantaneous yield stress in the longitudinal direction. The nonlinear strain hardening of the material can then be described by the stress-strain relationship $\sigma_{yL} = F\left(\varepsilon_{yL}\right)$ or $\varepsilon_{yL} = f\left(\sigma_{yL}\right)$ (see Eq. (7.1)) in the longitudinal direction.

Using the stress ratio ω_c (where $\omega_c = \sigma_{x,c}/\sigma_{z,c}$) defined by Eq. (4.9) in Chapter 4 and combining it with Eq. (7.4), the coiling stresses of any material point (such as point P in Figure 7.1) at the end of coiling can then be obtained as

$$\sigma_{z,c} = \pm \frac{\sigma_{yLc}}{\sqrt{\left(\overline{F}+\overline{G}\right) - 2\overline{G}\,\omega_c + \left(\overline{G}+\overline{H}\right)\omega_c^2}} \tag{7.5a}$$

$$\sigma_{x,c} = \pm \frac{\omega_c \sigma_{yLc}}{\sqrt{\left(\overline{F}+\overline{G}\right) - 2\overline{G}\,\omega_c + \left(\overline{G}+\overline{H}\right)\omega_c^2}} \tag{7.5b}$$

in which $\sigma_{x,c}$ and $\sigma_{z,c} \geq 0$ (i.e. tensile stresses) when $y \geq 0$, and σ_{yLc} is the instantaneous yield stress in the longitudinal direction at the end of coiling.

According to the hypothesis of work equivalence, when the principal axes of stresses are coincident with the axes of anisotropy, the equivalent plastic strain increment is given by (Hill 1950)

$$d\bar{\varepsilon}_p = \sqrt{\frac{2}{3}\left(\overline{F}+\overline{G}+\overline{H}\right)\left[\begin{array}{l}\overline{F}\left(\dfrac{\overline{G}\,d\varepsilon_{py} - \overline{H}\,d\varepsilon_{pz}}{\overline{FG}+\overline{GH}+\overline{HF}}\right)^2 + \overline{G}\left(\dfrac{\overline{H}\,d\varepsilon_{pz} - \overline{F}\,d\varepsilon_{px}}{\overline{FG}+\overline{GH}+\overline{HF}}\right)^2 \\ + \overline{H}\left(\dfrac{\overline{F}\,d\varepsilon_{px} - \overline{G}\,d\varepsilon_{py}}{\overline{FG}+\overline{GH}+\overline{HF}}\right)^2\end{array}\right]^{1/2}} \tag{7.6}$$

where $d\varepsilon_{px}$, $d\varepsilon_{py}$ and $d\varepsilon_{pz}$ are the principal plastic strain increments along the x, y and z directions respectively.

For the case of a uniaxial stress in the longitudinal direction only, the ratios among the three principal plastic strain increments are given by

$$d\varepsilon_{px} : d\varepsilon_{py} : d\varepsilon_{pz} = -\overline{G} : -\overline{F} : \overline{G}+\overline{F} \tag{7.7}$$

In Eq. (7.7), the principal plastic strain increment $d\varepsilon_{pz}$ in the longitudinal (z) direction represents the plastic strain increment $d\varepsilon_{pL}$ from the stress-strain curve in the longitudinal direction. That is,

$$d\varepsilon_{pz} = d\varepsilon_{pL} \tag{7.8}$$

Using Eqs. (7.6), (7.7) and (7.8), the equivalent plastic strain increment $d\bar{\varepsilon}_p$ can be directly related to the plastic strain increment $d\varepsilon_{pL}$ from the stress-strain curve in the longitudinal direction:

$$d\bar{\varepsilon}_p = \sqrt{\frac{2}{3}\left(\frac{\bar{F}+\bar{G}+\bar{H}}{\bar{F}+\bar{G}}\right)}d\varepsilon_{pL} \tag{7.9}$$

Integration of Eq. (7.9) leads to

$$\bar{\varepsilon}_p = \sqrt{\frac{2}{3}\left(\frac{\bar{F}+\bar{G}+\bar{H}}{\bar{F}+\bar{G}}\right)}\varepsilon_{pL} \tag{7.10a}$$

with

$$\varepsilon_{pL} = \varepsilon_{yL} - \frac{\sigma_{yL}}{E_{0z}} \tag{7.10b}$$

where $\bar{\varepsilon}_p$ is the equivalent plastic strain, ε_{pL} is the plastic strain from the stress-strain curve in the longitudinal direction, E_{0z} is the initial elastic modulus in the longitudinal direction.

Hence, the equivalent plastic strain due to the applied coiling curvature κ_c is given by

$$\bar{\varepsilon}_{p,c} = \sqrt{\frac{2}{3}\left(\frac{\bar{F}+\bar{G}+\bar{H}}{\bar{F}+\bar{G}}\right)}\varepsilon_{pL,c} \tag{7.11a}$$

with

$$\varepsilon_{pL,c} = \varepsilon_{yLc} - \frac{\sigma_{yLc}}{E_{0z}} \tag{7.11b}$$

in which the subscript c refers to the coiling stage, $\varepsilon_{pL,c}$ is the plastic strain from the stress-strain curve in the longitudinal direction at the end of coiling, and σ_{yLc} and ε_{yLc} are the instantaneous yield stress and the corresponding strain in the longitudinal direction at the end of coiling. The relationship between σ_{yLc} and ε_{yLc} is given by Eq. (7.1). Therefore, once σ_{yLc} is known, ε_{yLc} can be determined from Eq. (7.1) and the equivalent plastic strain $\bar{\varepsilon}_{p,c}$ due to coiling can then be calculated from Eq. (7.11).

To determine $\sigma_{x,c}$, $\sigma_{z,c}$ and $\bar{\varepsilon}_{p,c}$ (see Eqs. (7.5) and (7.11)) at any location y for a given coiling curvature κ_c, the values of σ_{yLc} and ω_c need to be calculated

numerically for each value of y. The determination of σ_{yLc} and ω_c is discussed in the next subsection.

7.2.3 Determination of σ_{yLc} and ω_c

σ_{yLc} and ω_c are related to each other. To establish their relationship, the stress ratio ω_c and its increment $d\omega_c$ can be related to the instantaneous yield stress σ_{yL} and the stress increment $d\sigma_{yL}$. Due to the nonlinear material properties, it is difficult to obtain closed-form analytical expressions for σ_{yLc} and ω_c. Instead, their values can be determined numerically, using their inter-relationship and the known boundary values.

When the principal axes of stresses are coincident with the axes of anisotropy, the equivalent stress is given by (Hill 1950)

$$\overline{\sigma} = \sqrt{\frac{3}{2}\left(\frac{\overline{F}\left(\sigma_y - \sigma_z\right)^2 + \overline{G}\left(\sigma_z - \sigma_x\right)^2 + \overline{H}\left(\sigma_x - \sigma_y\right)^2}{\overline{F} + \overline{G} + \overline{H}} \right)} \tag{7.12}$$

For the state of uniaxial stresses in the longitudinal (z) direction, $\sigma_x = 0$, $\sigma_y = 0$ and $\sigma_z = \sigma_{yL}$. With these conditions, Eq. (7.12) becomes

$$\overline{\sigma} = \sqrt{\frac{3}{2}\left(\frac{\overline{F} + \overline{G}}{\overline{F} + \overline{G} + \overline{H}} \right)}\sigma_{yL} \tag{7.13}$$

By combining the differentiation of Eq. (7.13) with Eq. (7.9), the slope of the equivalent stress-equivalent plastic strain relation H' can be determined as

$$H' = \frac{d\bar{\sigma}}{d\bar{\varepsilon}_p} = \frac{3\left(\bar{F}+\bar{G}\right)}{2\left(\bar{F}+\bar{G}+\bar{H}\right)}\frac{d\sigma_{yL}}{d\varepsilon_{pL}} \tag{7.14}$$

By differentiating Eq. (7.10b) and then combining it with Eq. (7.14), the slope H' is found to be

$$H' = \frac{3\left(\bar{F}+\bar{G}\right)}{2\left(\bar{F}+\bar{G}+\bar{H}\right)}\left[\frac{d\varepsilon_{yL}}{d\sigma_{yL}} - \frac{1}{E_{0z}}\right]^{-1} \tag{7.15}$$

in which $d\varepsilon_{yL}/d\sigma_{yL}$ can be obtained by differentiating Eq. (7.1) and can be expressed in terms of σ_{yL}. Eq. (7.15) is applicable to both the coiling and the uncoiling stages.

Under planar stresses (in the x-z plane) along the principal axes of anisotropy, the yield surface for an anisotropic material with isotropic strain-hardening behaviour is given by a single equation as

$$f(\{\sigma\},k) = \bar{\sigma} - \sqrt{\frac{3}{2\left(\bar{F}+\bar{G}+\bar{H}\right)}}\sigma_{yL} = 0 \tag{7.16a}$$

with

$$\bar{\sigma} = \sqrt{\frac{3}{2}\left(\frac{\bar{F}\sigma_z^2 + \bar{G}(\sigma_z - \sigma_x)^2 + \bar{H}\sigma_x^2}{\bar{F} + \bar{G} + \bar{H}}\right)} \tag{7.16b}$$

in which $\{\sigma\}$ is the stress vector representing the state of stresses, and k is the hardening parameter.

During coiling, the incremental relations for stresses and strains are

$$\begin{Bmatrix} d\sigma_{z,c} \\ d\sigma_{x,c} \end{Bmatrix} = \left[[D_e] - [D_p]\right] \begin{Bmatrix} d\varepsilon_{z,c} \\ d\varepsilon_{x,c} \end{Bmatrix} \tag{7.17a}$$

with

$$[D_e] = \begin{bmatrix} E_{0z}/(1-\nu_{xz}\nu_{zx}) & \nu_{xz}E_{0z}/(1-\nu_{xz}\nu_{zx}) \\ \nu_{xz}E_{0z}/(1-\nu_{xz}\nu_{zx}) & E_{0x}/(1-\nu_{xz}\nu_{zx}) \end{bmatrix} \tag{7.17b}$$

$$[D_p] = \frac{[D_e]\left\{\frac{\partial f}{\partial\{\sigma\}}\right\}\left\{\frac{\partial f}{\partial\{\sigma\}}\right\}^T[D_e]}{H' + \left\{\frac{\partial f}{\partial\{\sigma\}}\right\}^T[D_e]\left\{\frac{\partial f}{\partial\{\sigma\}}\right\}} \tag{7.17c}$$

$$\nu_{zx} = \nu_{xz}\, E_{0z}/E_{0x} \tag{7.17d}$$

in which the subscript c refers to the coiling stage; $d\sigma_{z,c}$ and $d\sigma_{x,c}$ are the longitudinal and transverse stress increments, and $d\varepsilon_{z,c}$ and $d\varepsilon_{x,c}$ are the longitudinal and transverse strain increments; ν_{xz} is the Poisson's ratio for a strain caused in the z direction due to a uniaxial stress in the x direction; and E_{0z} and E_{0x} are the initial elastic moduli for the longitudinal and transverse directions respectively.

By substituting Eq. (7.16) after differentiation into Eq. (7.17), the incremental relations can be rewritten as

$$\begin{Bmatrix} d\sigma_{z,c} \\ d\sigma_{x,c} \end{Bmatrix} = \frac{E_{0z}}{\left(1-\nu_{xz}\nu_{zx}\right)} \begin{bmatrix} 1-S_1^2/S_3 & \nu_{xz}-S_1S_2/S_3 \\ \nu_{xz}-S_1S_2/S_3 & E_{0x}/E_{0z}-S_2^2/S_3 \end{bmatrix} \begin{Bmatrix} d\varepsilon_{z,c} \\ d\varepsilon_{x,c} \end{Bmatrix} \tag{7.18a}$$

with

$$S_1 = \frac{2\overline{\sigma}}{3}\left(\nu_{xz}\frac{\partial f}{\partial \sigma_x} + \frac{\partial f}{\partial \sigma_z}\right) \tag{7.18b}$$

$$S_2 = \frac{2\overline{\sigma}}{3}\left(\frac{E_{0x}}{E_{0z}}\frac{\partial f}{\partial \sigma_x} + \nu_{xz}\frac{\partial f}{\partial \sigma_z}\right) \tag{7.18c}$$

$$S_3 = \frac{4H'\overline{\sigma}^2}{9E_{0z}}\left(1-\nu_{xz}\nu_{zx}\right) + \frac{4\overline{\sigma}^2}{9}\left[\frac{E_{0x}}{E_{0z}}\left(\frac{\partial f}{\partial \sigma_x}\right)^2 + 2\nu_{xz}\frac{\partial f}{\partial \sigma_x}\frac{\partial f}{\partial \sigma_z} + \left(\frac{\partial f}{\partial \sigma_z}\right)^2\right] \tag{7.18d}$$

$$\frac{\partial f}{\partial \sigma_x} = \frac{3}{2\overline{\sigma}}\left[\frac{\overline{H}\sigma_{x,c} + \overline{G}\left(\sigma_{x,c}-\sigma_{z,c}\right)}{\overline{F}+\overline{G}+\overline{H}}\right] \tag{7.18e}$$

$$\frac{\partial f}{\partial \sigma_z} = \frac{3}{2\overline{\sigma}}\left[\frac{\overline{F}\sigma_{z,c} + \overline{G}\left(\sigma_{z,c}-\sigma_{x,c}\right)}{\overline{F}+\overline{G}+\overline{H}}\right] \tag{7.18f}$$

in which $\sigma_{z,c}$ and $\sigma_{x,c}$ are the longitudinal and transverse stresses during the coiling stage.

Due to the plane strain condition, the transverse coiling strain increment is zero. This leads to the condition (i.e. $d\varepsilon_{x,c} = d\varepsilon_{ex,c} + d\varepsilon_{px,c} = 0$) given by Eq. 4.19 in Chapter 4.

Using Eqs. (4.9), (4.19) and (7.18), the ratio of stress increments Ω_c (where $\Omega_c = d\sigma_{x,c}/d\sigma_{z,c}$) defined by Eq. 4.20 is now obtained as

$$\Omega_c = \frac{\begin{array}{l} 2H'\nu_{xz}\left(E_{0z}/E_{0x}\right)\left(\overline{F}+\overline{G}+\overline{H}\right)\left[\overline{F}+\overline{G}-2\overline{G}\,\omega_c+\left(\overline{G}+\overline{H}\right)\omega_c^2\right] \\ -3E_{0z}\left(\overline{F}+\overline{G}-\overline{G}\,\omega_c\right)\left[\left(\overline{G}+\overline{H}\right)\omega_c-\overline{G}\right] \end{array}}{2H'\left(E_{0z}/E_{0x}\right)\left(\overline{F}+\overline{G}+\overline{H}\right)\left[\overline{F}+\overline{G}-2\overline{G}\,\omega_c+\left(\overline{G}+\overline{H}\right)\omega_c^2\right]+3E_{0z}\left[\left(\overline{G}+\overline{H}\right)\omega_c-\overline{G}\right]^2} \tag{7.19}$$

in which H' is given by Eq. (7.15). As H' is given in terms of σ_{yL}, the ratio Ω_c given by Eq. (7.19) becomes a function of ω_c and σ_{yL}.

Differentiations of Eqs. (4.9) and (7.4) lead to

$$\frac{d\sigma_{x,c}}{d\sigma_{z,c}} = \frac{\left(\overline{F}+\overline{G}-\overline{G}\,\omega_c\right)d\omega_c\sigma_{yL}+\left[\overline{F}+\overline{G}-2\overline{G}\,\omega_c+\left(\overline{G}+\overline{H}\right)\omega_c^2\right]\omega_c d\sigma_{yL}}{\left[\overline{G}-\left(\overline{G}+\overline{H}\right)\omega_c\right]d\omega_c\sigma_{yL}+\left[\overline{F}+\overline{G}-2\overline{G}\,\omega_c+\left(\overline{G}+\overline{H}\right)\omega_c^2\right]d\sigma_{yL}} \tag{7.20}$$

By combining Eqs. (4.20) and (7.20), the following equation is obtained:

$$d\omega_c = \frac{\left[\overline{F}+\overline{G}-2\overline{G}\,\omega_c+\left(\overline{G}+\overline{H}\right)\omega_c^2\right]\left(\Omega_c-\omega_c\right)}{\sigma_{yL}\left\{\left(\overline{F}+\overline{G}-\overline{G}\,\omega_c\right)+\Omega_c\left[\left(\overline{G}+\overline{H}\right)\omega_c-\overline{G}\right]\right\}}d\sigma_{yL} \tag{7.21}$$

in which Ω_c is given by Eq. (7.19). Eq. (7.21) can then be used to solve numerically for the values of σ_{yLc} and the corresponding stress ratio ω_c at each location y.

Furthermore, the flow rule is given by

$$\begin{Bmatrix} d\varepsilon_{pz,c} \\ d\varepsilon_{px,c} \end{Bmatrix} = d\lambda \begin{Bmatrix} \overline{F}\sigma_{z,c}+\overline{G}\left(\sigma_{z,c}-\sigma_{x,c}\right) \\ \overline{G}\left(\sigma_{x,c}-\sigma_{z,c}\right)+\overline{H}\sigma_{x,c} \end{Bmatrix} \tag{7.22}$$

in which the subscript c refers to the coiling stage, and $d\varepsilon_{pz,c}$ and $d\varepsilon_{px,c}$ are the longitudinal and transverse plastic strain increments respectively.

Substituting Eq. (4.9) into Eq. (7.22) yields

$$\frac{d\varepsilon_{pz,c}}{d\varepsilon_{px,c}} = \frac{\overline{F} + \overline{G} - \overline{G}\,\omega_c}{\left(\overline{G} + \overline{H}\right)\omega_c - \overline{G}} \tag{7.23}$$

The longitudinal coiling strain increment $d\varepsilon_{z,c}$ consists of an elastic strain increment $d\varepsilon_{ez,c}$ and a plastic strain increment $d\varepsilon_{pz,c}$. This leads to the condition (i.e. $d\varepsilon_{z,c} = d\varepsilon_{ez,c} + d\varepsilon_{pz,c}$) given by Eq. (4.27) in Chapter 4.

Substitution of Eqs. (4.19) and (7.23) into Eq. (4.27) leads to

$$d\varepsilon_{z,c} = d\varepsilon_{ez,c} - \left[\frac{\overline{F} + \overline{G} - \overline{G}\,\omega_c}{\left(\overline{G} + \overline{H}\right)\omega_c - \overline{G}}\right] d\varepsilon_{ex,c} \tag{7.24}$$

The incremental elastic strains are given by

$$\begin{Bmatrix} d\varepsilon_{ez,c} \\ d\varepsilon_{ex,c} \end{Bmatrix} = \begin{bmatrix} 1/E_{0z} & -\nu_{xz}/E_{0x} \\ -\nu_{zx}/E_{0z} & 1/E_{0x} \end{bmatrix} \begin{Bmatrix} d\sigma_{z,c} \\ d\sigma_{x,c} \end{Bmatrix} \tag{7.25}$$

Eq. (7.25) is then substituted into Eq. (7.24) to arrive at

$$d\varepsilon_{z,c} = \left\{1+\nu_{xz}\frac{E_{0z}}{E_{0x}}\left[\frac{\overline{F}+\overline{G}-\overline{G}\,\omega_c}{\left(\overline{G}+\overline{H}\right)\omega_c-\overline{G}}\right]\right\}\frac{d\sigma_{z,c}}{E_{0z}} - \left[\nu_{xz}+\frac{\overline{F}+\overline{G}-\overline{G}\,\omega_c}{\left(\overline{G}+\overline{H}\right)\omega_c-\overline{G}}\right]\frac{d\sigma_{x,c}}{E_{0x}} \quad (7.26)$$

By substituting Eqs. (4.9) and (7.4) after differentiation into Eq. (7.26), the following equation can be obtained:

$$d\varepsilon_{z,c} = \pm\left\{\begin{array}{l} \dfrac{\left\{\begin{array}{l}\dfrac{E_{0z}}{E_{0x}}\left(\overline{F}+\overline{G}-\overline{G}\,\omega_c\right)^2+\left[\overline{G}-\left(\overline{G}+\overline{H}\right)\omega_c\right]^2 \\ -2\nu_{xz}\dfrac{E_{0z}}{E_{0x}}\left(\overline{F}+\overline{G}-\overline{G}\,\omega_c\right)\left[\overline{G}-\left(\overline{G}+\overline{H}\right)\omega_c\right]\end{array}\right\}\sigma_{yL}}{E_{0z}\left[\overline{G}-\left(\overline{G}+\overline{H}\right)\omega_c\right]\left[\overline{F}+\overline{G}-2\overline{G}\,\omega_c+\left(\overline{G}+\overline{H}\right)\omega_c^2\right]^{3/2}}d\omega_c \\ +\dfrac{\left\{\begin{array}{l}\left(1-\omega_c\nu_{xz}\dfrac{E_{0z}}{E_{0x}}\right)\left[\overline{G}-\left(\overline{G}+\overline{H}\right)\omega_c\right] \\ +\dfrac{E_{0z}}{E_{0x}}\left(\omega_c-\nu_{xz}\right)\left(\overline{F}+\overline{G}-\overline{G}\,\omega_c\right)\end{array}\right\}}{E_{0z}\left[\overline{G}-\left(\overline{G}+\overline{H}\right)\omega_c\right]\left[\overline{F}+\overline{G}-2\overline{G}\,\omega_c+\left(\overline{G}+\overline{H}\right)\omega_c^2\right]^{1/2}}d\sigma_{yL}\end{array}\right\} \quad (7.27)$$

where the +ve sign of "±" applies when $y \geq 0$.

Integrating the left-hand side of Eq. (7.27) from zero to the longitudinal coiling strain $\varepsilon_{z,c}$ (where $\varepsilon_{z,c} = \kappa_c y$ as given by Eq. (4.3c) in Chapter 4) and the right-hand side from zero to the instantaneous yield stress σ_{yLc} due to coiling for $d\sigma_{yL}$ and from Poisson's ratio ν_{xz} to the stress ratio ω_c corresponding to $\varepsilon_{z,c}$ for $d\omega_c$ results in

$$\varepsilon_{z,c} = \pm \left\{ \begin{array}{l} \displaystyle\int_{\nu_{xz}}^{\omega_c} \frac{\left\{ \begin{array}{l} \dfrac{E_{0z}}{E_{0x}}\left(\overline{F}+\overline{G}-\overline{G}\,\omega_c\right)^2 + \left[\overline{G}-\left(\overline{G}+\overline{H}\right)\omega_c\right]^2 \\ -2\nu_{xz}\dfrac{E_{0z}}{E_{0x}}\left(\overline{F}+\overline{G}-\overline{G}\,\omega_c\right)\left[\overline{G}-\left(\overline{G}+\overline{H}\right)\omega_c\right] \end{array} \right\}\sigma_{yL}}{E_{0z}\left[\overline{G}-\left(\overline{G}+\overline{H}\right)\omega_c\right]\left[\overline{F}+\overline{G}-2\overline{G}\,\omega_c+\left(\overline{G}+\overline{H}\right)\omega_c^2\right]^{3/2}} d\omega_c \\ + \displaystyle\int_0^{\sigma_{yLc}} \frac{\left\{ \begin{array}{l} \left(1-\omega_c\nu_{xz}\dfrac{E_{0z}}{E_{0x}}\right)\left[\overline{G}-\left(\overline{G}+\overline{H}\right)\omega_c\right] \\ +\dfrac{E_{0z}}{E_{0x}}\left(\omega_c-\nu_{xz}\right)\left(\overline{F}+\overline{G}-\overline{G}\,\omega_c\right) \end{array} \right\}}{E_{0z}\left[\overline{G}-\left(\overline{G}+\overline{H}\right)\omega_c\right]\left[\overline{F}+\overline{G}-2\overline{G}\,\omega_c+\left(\overline{G}+\overline{H}\right)\omega_c^2\right]^{1/2}} d\sigma_{yL} \end{array} \right\} \quad (7.28)$$

In Eq. (7.28), as the value of $\varepsilon_{z,c}$ is known and equal to $\kappa_c y$ (see Eq. (4.3c) in chapter 4) at any arbitrary location y, the integration can be performed numerically by the Euler forward method. The lower limits (i.e. ν_{xz} for $d\omega_c$ and zero for $d\sigma_{yL}$) of the integration in Eq. (7.28) are treated as initial conditions. Starting with these initial conditions, the value of $d\omega_c$ can be calculated from Eq. (7.21) for a small assigned value of $d\sigma_{yL}$, and the values of ω_c and σ_{yL} can then be updated for each step. After the numerical integration (see Eq. (7.28)) is done, the values of σ_{yLc} and the corresponding stress ratio ω_c, which are the upper limits of the integration, can be determined.

7.2.4 Uncoiling including flattening

As explained in Chapter 4, uncoiling including flattening is assumed to take place before cold forming, and implemented by the application of an uncoiling curvature

κ_u equal in magnitude but opposite in direction to the coiling curvature κ_c. That is, $\kappa_u = -\kappa_c$ which has been given by Eq. (4.33) in Chapter 4.

After such uncoiling, the total stresses $\sigma_{z,r}$ and $\sigma_{x,r}$ of any point can be found by adding the uncoiling stresses to the coiling stresses (point UP in Figure 7.1). This leads to $\sigma_{z,r} = \sigma_{z,c} + \sigma_{z,u}$ and $\sigma_{x,r} = \sigma_{x,c} + \sigma_{x,u}$ as already given by Eq. (4.34) in Chapter 4.

The unloading stresses are elastic, until the reverse bending curvature exceeds a threshold curvature value. The elastic uncoiling stresses are given by

$$\sigma_{z,u} = \frac{E_{0z}}{\left(1-\nu_{xz}\nu_{zx}\right)}\kappa_u y = \frac{E_{0z}}{\left(1-\nu_{xz}^2\, E_{0z}/E_{0x}\right)}\kappa_u y \tag{7.29a}$$

$$\sigma_{x,u} = \frac{\nu_{zx}E_{0x}}{\left(1-\nu_{xz}\nu_{zx}\right)}\kappa_u y = \frac{\nu_{xz}E_{0z}}{\left(1-\nu_{xz}^2\, E_{0z}/E_{0x}\right)}\kappa_u y \tag{7.29b}$$

An uncoiling curvature limit κ_{uy}, beyond which uncoiling stresses are no longer elastic, can be defined to indicate the onset of reverse yielding. If reverse yielding occurs at the limit κ_{uy} as a result of uncoiling, then the yield surface should start again to expand from the preceding one developed at the end of coiling and the total stresses should also obey Hill's anisotropic yield criterion. That is,

$$\overline{F}\sigma_{z,r}^2 + \overline{G}\left(\sigma_{z,r}^2 - \sigma_{x,r}^2\right) + \overline{H}\sigma_{x,r}^2 = \sigma_{yLc}^2 \tag{7.30}$$

Hence, such an uncoiling curvature limit κ_{uy} can be determined by substituting Eqs. (4.34), (7.5) and (7.29) into Eq. (7.30) as

$$\kappa_{uy} = -\frac{2\sigma_{yLc}\left(1-\nu_{xz}^2 E_{0z}/E_{0x}\right)\left\{\overline{F}+\overline{G}-\overline{G}\,\nu_{xz}+\left[\left(\overline{H}+\overline{G}\right)\nu_{xz}-\overline{G}\right]\omega_c\right\}}{E_{0z}|y|\left[\overline{F}+\overline{G}-2\overline{G}\,\nu_{xz}+\left(\overline{G}+\overline{H}\right)\nu_{xz}^2\right]\sqrt{\overline{F}+\overline{G}-2\overline{G}\,\omega_c+\left(\overline{G}+\overline{H}\right)\omega_c^2}} \tag{7.31}$$

Similar to the uncoiling of isotropic sheets presented in Chapter 4, the total longitudinal strain of any point in the anisotropic stainless steel sheet at the onset of reverse yielding during uncoiling can still be given by Eq. (4.38) (i.e. $\varepsilon_{z,uy} = \left(\kappa_c + \kappa_{uy}\right)y$) in Chapter 4, but the value of κ_{uy} in Eq. (4.38) is now calculated from Eq. (7.31).

The corresponding uncoiling stresses are

$$\sigma_{z,uy} = \frac{E_{0z}}{\left(1-\nu_{xz}^2 E_{0z}/E_{0x}\right)}\kappa_{uy} y \tag{7.32a}$$

$$\sigma_{x,uy} = \frac{\nu_{xz} E_{0z}}{\left(1-\nu_{xz}^2 E_{0z}/E_{0x}\right)}\kappa_{uy} y \tag{7.32b}$$

and the corresponding stress ratio ω_{uy} is still given by Eq. (4.40) (i.e. $\omega_{uy} = \left(\sigma_{x,c} + \sigma_{x,uy}\right)/\left(\sigma_{z,c} + \sigma_{z,uy}\right)$) in chapter 4.

Making use of Eqs. (7.5), (7.31) and (7.32), Eq. (4.40) can be re-written as

$$\omega_{uy} = \frac{\left[\overline{F} + \overline{G} - \left(\overline{H} + \overline{G}\right)\nu_{xz}^2\right]\omega_c - 2\left(\overline{F} + \overline{G} - \overline{G}\,\nu_{xz}\right)\nu_{xz}}{2\left[\overline{G} - \left(\overline{H} + \overline{G}\right)\nu_{xz}\right]\omega_c - \left[\overline{F} + \overline{G} - \left(\overline{H} + \overline{G}\right)\nu_{xz}^2\right]} \tag{7.33}$$

Therefore, when $\kappa_c \le \left|\kappa_{uy}\right|$,

$$\sigma_{z,u} = -\frac{E_{0z}}{\left(1 - \nu_{xz}^2\, E_{0z}/E_{0x}\right)}\kappa_c y \tag{7.34a}$$

$$\sigma_{x,u} = -\frac{\nu_{xz} E_{0z}}{\left(1 - \nu_{xz}^2\, E_{0z}/E_{0x}\right)}\kappa_c y \tag{7.34b}$$

When $\kappa_c > \left|\kappa_{uy}\right|$, reverse yielding occurs. The total stresses after uncoiling (including flattening) are constrained by Hill's anisotropic yield criterion:

$$\overline{F}\sigma_{z,r}^2 + \overline{G}\left(\sigma_{z,r}^2 - \sigma_{x,r}^2\right) + \overline{H}\sigma_{x,r}^2 = \sigma_{yLr}^2 \tag{7.35}$$

in which σ_{yLr} is the instantaneous yield stress in the longitudinal direction after uncoiling (including flattening).

From Eq. (7.30), the total stresses after uncoiling (such as point UP in Figure 7.1) can be obtained as

$$\sigma_{z,r} = \mp\frac{\sigma_{yLr}}{\sqrt{\left(\overline{F} + \overline{G}\right) - 2\overline{G}\,\omega_u + \left(\overline{G} + \overline{H}\right)\omega_u^2}} \tag{7.36a}$$

$$\sigma_{x,r} = \mp\frac{\omega_u \sigma_{yLr}}{\sqrt{\left(\overline{F} + \overline{G}\right) - 2\overline{G}\,\omega_u + \left(\overline{G} + \overline{H}\right)\omega_u^2}} \tag{7.36b}$$

with

$$\omega_u = \sigma_{x,r} / \sigma_{z,r} = \left(\sigma_{x,c} + \sigma_{x,u}\right) / \left(\sigma_{z,c} + \sigma_{z,u}\right) \tag{7.36c}$$

in which $\sigma_{x,r}$ and $\sigma_{z,r} \le 0$ (i.e. compressive stresses) when $y \ge 0$. Hence, from Eqs. (4.34), (7.5) and (7.36), the uncoiling stresses for $\kappa_c > \left|\kappa_{uy}\right|$ are calculated as

$$\sigma_{z,u} = \mp\left[\frac{\sigma_{yLc}}{\sqrt{\left(\overline{F}+\overline{G}\right) - 2\overline{G}\,\omega_c + \left(\overline{G}+\overline{H}\right)\omega_c^2}} + \frac{\sigma_{yLr}}{\sqrt{\left(\overline{F}+\overline{G}\right) - 2\overline{G}\,\omega_u + \left(\overline{G}+\overline{H}\right)\omega_u^2}}\right] \tag{7.37a}$$

$$\sigma_{x,u} = \mp\left[\frac{\omega_c\sigma_{yLc}}{\sqrt{\left(\overline{F}+\overline{G}\right) - 2\overline{G}\,\omega_c + \left(\overline{G}+\overline{H}\right)\omega_c^2}} + \frac{\omega_u\sigma_{yLr}}{\sqrt{\left(\overline{F}+\overline{G}\right) - 2\overline{G}\,\omega_u + \left(\overline{G}+\overline{H}\right)\omega_u^2}}\right] \tag{7.37b}$$

where $\sigma_{x,u}$ and $\sigma_{z,u} \le 0$ (i.e. compressive stresses) when $y \ge 0$.

Similar to Eq. (7.11), the total equivalent plastic strain after uncoiling can be determined as

$$\overline{\varepsilon}_{p,r} = \sqrt{\frac{2}{3}\left(\frac{\overline{F}+\overline{G}+\overline{H}}{\overline{F}+\overline{G}}\right)}\varepsilon_{pL,r} \tag{7.38a}$$

with

$$\varepsilon_{pL,r} = \varepsilon_{yLr} - \frac{\sigma_{yLr}}{E_{0z}} \tag{7.38b}$$

in which the subscript r refers to the end of the uncoiling stage, $\varepsilon_{pL,r}$ is the plastic strain from the stress-strain curve in the longitudinal direction at the end of flattening,

and σ_{yLr} and ε_{yLr} are the instantaneous yield stress and the corresponding strain in the longitudinal direction at the end of flattening. The relationship between σ_{yLr} and ε_{yLr} is given by Eq. (7.1). Therefore, once σ_{yLr} is obtained, ε_{yLr} can be determined from Eq. (7.1) and the total equivalent plastic strain $\bar{\varepsilon}_{p,c}$ after uncoiling can then be calculated from Eq. (7.38).

In order to determine the uncoiling stresses, the total residual stresses and the total equivalent plastic strain (see Eqs. (7.36)~(7.38)) at any location y, the values of σ_{yLc}, σ_{yLr}, ω_c and ω_u need to be calculated numerically for each value of y. The values of σ_{yLc} and ω_c can be determined numerically from Eqs. (7.21) and (7.28) given in the previous subsection. The determination of σ_{yLr} and ω_u is discussed in the next subsection.

7.2.5 Determination of σ_{yLr} and ω_u

Following the same procedure explained in Subsection 7.2.3 (see Eqs. (7.17)~(7.27)), the equation for the increment of the stress ratio during uncoiling can be obtained as

$$d\omega_u = \frac{\left[\overline{F}+\overline{G}-2\overline{G}\,\omega_u+\left(\overline{G}+\overline{H}\right)\omega_u^2\right]\left(\Omega_u-\omega_u\right)}{\sigma_{yL}\left\{\left(\overline{F}+\overline{G}-\overline{G}\,\omega_u\right)+\Omega_u\left[\left(\overline{G}+\overline{H}\right)\omega_u-\overline{G}\right]\right\}}d\sigma_{yL} \tag{7.39}$$

in which H' is given by Eq. (7.15), and Ω_u is the ratio of stress increments $d\sigma_{x,r}/d\sigma_{z,r}$ given by

$$\Omega_u = \frac{\begin{array}{l} 2H'\nu_{xz}\left(E_{0z}/E_{0x}\right)\left(\overline{F}+\overline{G}+\overline{H}\right)\left[\overline{F}+\overline{G}-2\overline{G}\,\omega_u+\left(\overline{G}+\overline{H}\right)\omega_u^2\right] \\ -3E_{0z}\left(\overline{F}+\overline{G}-\overline{G}\,\omega_u\right)\left[\left(\overline{G}+\overline{H}\right)\omega_u-\overline{G}\right] \end{array}}{2H'\left(E_{0z}/E_{0x}\right)\left(\overline{F}+\overline{G}+\overline{H}\right)\left[\overline{F}+\overline{G}-2\overline{G}\,\omega_u+\left(\overline{G}+\overline{H}\right)\omega_u^2\right]+3E_{0z}\left[\left(\overline{G}+\overline{H}\right)\omega_u-\overline{G}\right]^2} \tag{7.40}$$

The equation for longitudinal strain increment during uncoiling can also be obtained as

$$d\varepsilon_{z,u} = \pm\left\{\begin{array}{l} -\dfrac{\left\{\begin{array}{l}\dfrac{E_{0z}}{E_{0x}}\left(\overline{F}+\overline{G}-\overline{G}\,\omega_u\right)^2+\left[\overline{G}-\left(\overline{G}+\overline{H}\right)\omega_u\right]^2 \\ -2\nu_{xz}\dfrac{E_{0z}}{E_{0x}}\left(\overline{F}+\overline{G}-\overline{G}\,\omega_u\right)\left[\overline{G}-\left(\overline{G}+\overline{H}\right)\omega_u\right]\end{array}\right\}\sigma_{yL}}{E_{0z}\left[\overline{G}-\left(\overline{G}+\overline{H}\right)\omega_u\right]\left[\overline{F}+\overline{G}-2\overline{G}\,\omega_u+\left(\overline{G}+\overline{H}\right)\omega_u^2\right]^{3/2}}d\omega_u \\ -\dfrac{\left\{\begin{array}{l}\left(1-\omega_u\nu_{xz}\dfrac{E_{0z}}{E_{0x}}\right)\left[\overline{G}-\left(\overline{G}+\overline{H}\right)\omega_u\right] \\ +\dfrac{E_{0z}}{E_{0x}}\left(\omega_u-\nu_{xz}\right)\left(\overline{F}+\overline{G}-\overline{G}\,\omega_u\right)\end{array}\right\}}{E_{0z}\left[\overline{G}-\left(\overline{G}+\overline{H}\right)\omega_u\right]\left[\overline{F}+\overline{G}-2\overline{G}\,\omega_u+\left(\overline{G}+\overline{H}\right)\omega_u^2\right]^{1/2}}d\sigma_{yL} \end{array}\right\} \tag{7.41}$$

where the +ve sign of "±" applies when $y \geq 0$. Eq. (7.41) is the same as Eq. (7.27), except for a change in sign since uncoiling causes material yielding in the opposite direction and a different subscript u to refer to the uncoiling stage.

Integrating the left-hand side of Eq. (7.41) from the longitudinal strain $\varepsilon_{z,uy}$ at the onset of reverse yielding to the final longitudinal strain $\varepsilon_{z,r}$ and the right-hand side from the instantaneous yield stress σ_{yLc} due to coiling to the instantaneous yield

stress σ_{yLr} after uncoiling for $d\sigma_{yL}$ and from the stress ratio ω_{uy} at the onset of reverse yielding to the stress ratio ω_u corresponding to $\varepsilon_{z,r}$ for $d\omega_u$ results in

$$\varepsilon_{z,r}-\varepsilon_{z,uy}=\pm\left\{\begin{array}{l}\displaystyle\int_{\omega_{uy}}^{\omega_u}\frac{\left\{\begin{array}{l}\dfrac{E_{0z}}{E_{0x}}\left(\overline{F}+\overline{G}-\overline{G}\,\omega_u\right)^2+\left[\overline{G}-\left(\overline{G}+\overline{H}\right)\omega_u\right]^2\\ -2\nu_{xz}\dfrac{E_{0z}}{E_{0x}}\left(\overline{F}+\overline{G}-\overline{G}\,\omega_u\right)\left[\overline{G}-\left(\overline{G}+\overline{H}\right)\omega_u\right]\end{array}\right\}\sigma_{yL}}{E_{0z}\left[\left(\overline{G}+\overline{H}\right)\omega_u-\overline{G}\right]\left[\overline{F}+\overline{G}-2\overline{G}\,\omega_u+\left(\overline{G}+\overline{H}\right)\omega_u^2\right]^{3/2}}d\omega_u\\ +\displaystyle\int_{\sigma_{yLc}}^{\sigma_{yLr}}\frac{\left\{\begin{array}{l}\left(1-\omega_u\nu_{xz}\dfrac{E_{0z}}{E_{0x}}\right)\left[\overline{G}-\left(\overline{G}+\overline{H}\right)\omega_u\right]\\ +\dfrac{E_{0z}}{E_{0x}}\left(\omega_u-\nu_{xz}\right)\left(\overline{F}+\overline{G}-\overline{G}\,\omega_u\right)\end{array}\right\}}{E_{0z}\left[\left(\overline{G}+\overline{H}\right)\omega_u-\overline{G}\right]\left[\overline{F}+\overline{G}-2\overline{G}\,\omega_u+\left(\overline{G}+\overline{H}\right)\omega_u^2\right]^{1/2}}d\sigma_{yL}\end{array}\right\}$$

(7.42)

In Eq. (7.42), $\varepsilon_{z,r}=0$ (see Eq. (4.51) in Chapter 4), since uncoiling including flattening enforces the final longitudinal strain $\varepsilon_{z,r}$ to become zero at the end of the process.

After σ_{yLc} and ω_c are determined from the numerical integration of Eq. (7.28) for the coiling stage, the value of ω_{uy} can be calculated by Eq. (7.33). In Eq. (7.42), as the value of $\varepsilon_{z,uy}$ is given by Eq. (4.38) and the value of $\varepsilon_{z,r}$ is equal to zero, the integration can be performed numerically again by the Euler forward method. The lower limits (i.e. ω_{uy} for $d\omega_u$ and σ_{yLc} for $d\sigma_{yL}$) of the integration in Eq. (7.42) are treated as initial conditions. Starting with these initial conditions, the value of $d\omega_u$ can be calculated from Eq. (7.39) for a small assigned value of $d\sigma_{yL}$, and the values

of ω_u and σ_{yL} can then be updated for each step. After the numerical integration (see Eq. (7.42)) is done, the values of σ_{yLr} and the corresponding stress ratio ω_u, which are the upper limits of the integration, can be determined.

7.2.6 Description of stress-strain behaviour

For the application of the above analytical solution to a specific stainless steel alloy, the general representation of the stress-strain relationship for stainless steel alloys (Eq. (7.1)) needs to be replaced by a specific stress-strain relationship. Several stress-strain relationships to describe the nonlinear strain-hardening behaviour of stainless steel alloys exists, as discussed previously in Chapter 3, but each of them has its own limitations. A new improved stress-strain relationship, the so-called 3-stage full-range stress-strain model (Eq. (3.6)), has been presented in Chapter 3 for stainless steel alloys. This new stress-strain relationship is now adopted to describe the stress-strain behaviour in the longitudinal direction in this analytical solution. The initial elastic modulus E_0 in Eq. (3.6) is now replaced by E_{0z} with the subscript z referring to the longitudinal (z) direction, and the stress σ from the stress-strain curve (Eq. (3.6)) in the longitudinal direction is replaced by the instantaneous yield stress σ_{yL}.

By substituting Eq. (3.6) after differentiation into Eq. (7.15), the slope of the equivalent stress-equivalent plastic strain relation H' become:

$$H' = \begin{cases} \dfrac{3\left(\overline{F}+\overline{G}\right)}{2\left(\overline{F}+\overline{G}+\overline{H}\right)}\left(\dfrac{\sigma_{0.2}^{n}}{0.002n\sigma_{yL}^{n-1}}\right), & \sigma_{yL} \le \sigma_{0.2} \\ \dfrac{3\left(\overline{F}+\overline{G}\right)}{2\left(\overline{F}+\overline{G}+\overline{H}\right)}\left\{\begin{array}{l} \dfrac{1}{E_{0.2}}-\dfrac{1}{E_{0z}} \\ +n'_{0.2,1.0}\left[\begin{array}{l} 0.008 \\ +\left(\sigma_{1.0}-\sigma_{0.2}\right)\left(\dfrac{1}{E_{0z}}-\dfrac{1}{E_{0.2}}\right) \end{array}\right]\dfrac{\left(\sigma_{yL}-\sigma_{0.2}\right)^{n'_{0.2,1.0}-1}}{\left(\sigma_{1.0}-\sigma_{0.2}\right)^{n'_{0.2,1.0}}} \end{array}\right\}^{-1}, & \sigma_{0.2} < \sigma_{yL} \le \sigma_{2.0} \\ \dfrac{3\left(\overline{F}+\overline{G}\right)}{2\left(\overline{F}+\overline{G}+\overline{H}\right)}\left[\dfrac{\left(b \mp \sigma_{yL}\right) \pm \left(\sigma_{yL}-a\right)}{\left(b \mp \sigma_{yL}\right)^{2}}-\dfrac{1}{E_{0z}}\right]^{-1}, & \sigma_{yL} > \sigma_{2.0} \end{cases} \tag{7.43}$$

where the upper sign corresponds to tension, and the lower sign corresponds to compression. The parameters $E_{0.2}$, $\varepsilon_{0.2}$, $\sigma_{1.0}$, $\sigma_{2.0}$, a and b in Eq. (7.43) are the material parameters in the longitudinal direction and are described in terms of the basic Ramberg-Osgood parameters (E_{0z}, $\sigma_{0.2}$ and n). The expressions for these parameters can be found in Chapter 3.

The residual stresses and equivalent plastic strains due to the coiling-uncoiling process can be obtained by replacing Eqs. (7.1) and (7.15) with Eqs. (3.6) and (7.43) and then following the procedure explained throughout the preceding subsections (Subsections 7.2.1~7.2.5).

7.2.7 Yield strength in the through-thickness direction

To define the material anisotropy of stainless steels, the initial yield stresses (0.2% proof stresses) in the three principal directions of anisotropy should be used. The

initial yield stresses in the longitudinal and transverse directions can be taken as 0.2% proof stresses determined from coupon tests for both directions. The initial yield stress in the through-thickness direction cannot be easily determined and is generally not available. Hence, it is necessary to relate the through-thickness yield stress to the yield stresses in the two other directions on the plane, so that its value can be determined.

If a stainless steel sheet is subject to stresses in its plane (x-z plane), the only nonzero stress components are σ_x, σ_z and τ_{xz}, and the yield criterion (Hill 1950) is given by

$$F\sigma_z^2 + G(\sigma_z - \sigma_x)^2 + H\sigma_x^2 + 2M\tau_{xz}^2 = 1 \tag{7.44a}$$

with

$$M = 1/2\tau_{0XZ}^2 \tag{7.44b}$$

in which τ_{0XZ} is the initial shear yield stress (0.2% proof stress) for the x-z plane, and F, G and H are given by Eqs. (7.2b)~(7.2d). For a uniaxial stress σ applied in a direction making a counter clockwise angle α with the longitudinal direction (z direction), the stress components corresponding to the uniaxial stress σ are

$$\sigma_z = \sigma\cos^2\alpha \tag{7.45a}$$

$$\sigma_x = \sigma\sin^2\alpha \tag{7.45b}$$

$$\tau_{xz} = \sigma\sin\alpha\cos\alpha \tag{7.45c}$$

When the uniaxial stress σ is applied in the diagonal direction ($\alpha = 45°$) and reaches the diagonal initial yield stress σ_{0D}, that is $\sigma = \sigma_{0D}$, the through-thickness initial yield stress σ_{0N} can be then determined by substituting Eqs. (7.2b)~(7.2d) and (7.45) into Eq. (7.44), as

$$\sigma_{0N} = \frac{1}{2}\left(\frac{1}{\sigma_{0D}^2} - \frac{1}{4\tau_{0XZ}^2}\right)^{-1/2} \tag{7.46}$$

The initial shear yield stress τ_{0XZ} can be approximated by the following relationship (Rasmussen *et al*. 2003):

$$\tau_{0XZ} \cong \sigma_{0D} / \sqrt{3} \tag{7.47}$$

Substitution of Eq. (7.47) into Eq. (7.46) leads to the following approximation:

$$\sigma_{0N} \cong \sigma_{0D} \cong \sqrt{3}\tau_{0XZ} \tag{7.48}$$

Therefore, the initial yield stress σ_{0N} in the through-thickness direction can be determined either from the diagonal initial yield stress σ_{0D} or from the initial shear yield stress τ_{0XZ}.

7.3 ANALYTICAL SOLUTION FOR COLD BENDING

7.3.1 Assumptions

An analytical solution has been presented in Chapter 6 for residual stresses in the corners of press-braked sections which are made of isotropic materials. In this section, an improved analytical solution of the same problem is presented for stainless steel sections which are made of stainless steel alloys with material anisotropy. As discussed in Chapter 6, based on the results from the finite element-based method (see Chapters 5 and 8), it can be concluded that the cold bending of an uncoiled sheet into the corners of a cold-formed section can be modelled as a problem of plane strain pure bending of a sheet into a large curvature in the transverse direction with the preceding deformation history of the coiling-uncoiling process ignored. Therefore, the analytical solution for the coiling of stainless steel sheets presented in the preceding section is extended in this section to model residual stresses due to the cold bending of a stainless steel sheet into the corners of a press-braked section. The simplifying assumptions made in Chapter 6 are adopted in this section for the present analytical solution for cold bending. The validity of these simplifying assumptions has been preliminarily discussed in Chapter 6. The effect of these simplifying assumptions will be examined by comparing analytical predictions with finite element results, as shown in Section 7.5 of this chapter and Appendix C.

For consistency, it is necessary to keep the coordinate system unchanged and to use the stress-strain curve in the same direction to describe the nonlinear strain-hardening behaviour throughout the modelling of the whole two-stage manufacturing process of

press-braked sections. Therefore, in the modelling of the cold bending of press-braking operations, the initial yield stress σ_{0L} in the longitudinal direction is also used as the reference yield stress and the stress-strain curve (Eq. (7.1)) in the longitudinal direction is also incorporated to describe the nonlinear strain-hardening behaviour. It should be noted that, although the reference yield stress in the same direction is used for both stages, the direction of bending (the transverse direction) involved in the cold bending of a stainless sheet into the corners of a press-braked section is not coincident with, and is orthogonal to the direction of the sheet coiling (longitudinal direction).

7.3.2 Cold bending

During the cold bending of a stainless steel sheet into the corners of a press-braked section, an arbitrary point in the sheet undergoes transverse straining. The true transverse bending strain in a corner can be given by Eq. (6.1) in Chapter 6. As through-thickness stresses are ignored, Hill's anisotropic yield criterion (Hill 1950) is still given by Eqs. (7.2)~(7.4), but the stress components $\sigma_{x,c}$ and $\sigma_{z,c}$ are now replaced by $\sigma_{z,b}$ and $\sigma_{x,b}$ respectively in which the subscript *b* is used to refer to bending.

Using the stress ratio ω_b (where $\omega_b = \sigma_{z,b} / \sigma_{x,b}$) defined by Eq. (6.5) in Chapter 6 and combining it with Hill's anisotropic yield criterion (see Eq. (7.4)), the stresses of any point across the thickness due to cold bending can be obtained as

$$\sigma_{z,b} = \pm \frac{\omega_b \sigma_{yLb}}{\sqrt{\left(\overline{G} + \overline{H}\right) - 2\overline{G}\,\omega_b + \left(\overline{F} + \overline{G}\right)\omega_b^2}} \tag{7.49a}$$

$$\sigma_{x,b} = \pm \frac{\sigma_{yLb}}{\sqrt{\left(\overline{G} + \overline{H}\right) - 2\overline{G}\,\omega_b + \left(\overline{F} + \overline{G}\right)\omega_b^2}} \tag{7.49b}$$

in which $\sigma_{x,b}$ and $\sigma_{z,b} \le 0$ (i.e. compressive stresses) when $y \ge s$ (see Figure 6.1 in Chapter 6), and σ_{yLb} is the instantaneous yield stress in the longitudinal direction at the end of cold bending.

Similar to Eq. (7.11), the equivalent plastic strain due to cold bending can be given by

$$\overline{\varepsilon}_{p,b} = \sqrt{\frac{2}{3}\left(\frac{\overline{F} + \overline{G} + \overline{H}}{\overline{F} + \overline{G}}\right)}\varepsilon_{pL,b} \tag{7.50a}$$

with

$$\varepsilon_{pL,b} = \varepsilon_{yLb} - \frac{\sigma_{yLb}}{E_{0z}} \tag{7.50b}$$

in which the subscript *b* is used to refer to cold bending, $\varepsilon_{pL,b}$ is the plastic strain from the stress-strain curve in the longitudinal direction at the end of cold bending, and σ_{yLb} and ε_{yLb} are the instantaneous yield stress and the corresponding strain in the longitudinal direction at the end of cold bending. The relationship between σ_{yLb} and ε_{yLb} is given by Eq. (7.1). Therefore, once σ_{yLb} is obtained, ε_{yLb} can be determined from Eq. (7.1) and the equivalent plastic strain $\overline{\varepsilon}_{p,b}$ due to cold bending can then be calculated from Eq. (7.50).

For pure bending, the stress equilibrium condition in the bending direction is given by Eq. (6.8) as shown in Chapter 6. As explained in Chapter 6, at large bending curvatures, this equilibrium condition (Eq. (6.8)) has to be imposed to ensure a condition of pure bending. By trial and error, the value of s, which is the distance between the neutral surface and the current middle surface after cold bending, can be determined such that the equilibrium condition of Eq. (6.8) is satisfied.

To determine $\sigma_{x,b}$, $\sigma_{z,b}$ and $\bar{\varepsilon}_{p,b}$ from Eqs. (7.49) and (7.50) at any location y for a given bending curvature κ_b and a trial value of s, the values of σ_{yLb} and ω_b are first found numerically for each value of y. The determination of σ_{yLb} and ω_b is discussed in the next subsection.

7.3.3 Determination of σ_{yLb} and ω_b

As discussed in Section 6.5 of Chapter 6, nominal stress-strain curves obtained from coupon tests can accurately describe the stress-strain behaviour of materials at small and intermediate strains. At larger strains, the "real" stress-strain response of the material should be represented by the true stress-strain relationship. Therefore, for large curvatures involved in the cold bending at corners, the stress-strain curve $\sigma_{yL} = F\left(\varepsilon_{yL}\right)$ (see Eq. (7.1)) in the longitudinal direction should be described by the true stress-strain relationship. That is,

$$\sigma_{yL} = \sigma_t \quad \text{and} \quad \varepsilon_{yL} = \varepsilon_t \tag{7.51}$$

where σ_t and ε_t are the true stress and true strain respectively, from the stress-strain curve in the longitudinal direction. The true stress σ_t, the true strain ε_t and the true plastic strain ε_{tp} can be converted from the nominal stress σ_n and the nominal strain ε_n by Eq. (6.16) in Chapter 6. The nominal stress-strain relationship in the longitudinal direction can be given by the 3-stage full-range stress-strain model (see Eq. (3.6)).

As the stress-strain relationship $\sigma_{yL} = F(\varepsilon_{yL})$ (Eq. (7.1)) in the longitudinal direction is described by the true stress-strain relationship for large straining, the slope of the equivalent stress-equivalent plastic strain relation H' can still be given by Eq. (7.15) but the strain rate $d\varepsilon_{yL}/d\sigma_{yL}$ in Eq. (7.15) should be represented by the strain rate $d\varepsilon_t/d\sigma_t$ of the true stress-strain curve. From Eqs. (6.16) and (7.51), the strain rate $d\varepsilon_{yL}/d\sigma_{yL}$ in Eq. (7.15) can be expressed in terms of the nominal stress σ_n and the nominal strain ε_n as follows:

$$\frac{d\varepsilon_{yL}}{d\sigma_{yL}} = \frac{d\varepsilon_t}{d\sigma_t} = \frac{d\varepsilon_n/d\sigma_n}{(1\pm\varepsilon_n)\left[(1\pm\varepsilon_n)\pm\sigma_n(d\varepsilon_n/d\sigma_n)\right]} \tag{7.52}$$

By substituting Eq. (7.52) into Eq. (7.15), H' can then be determined as

$$H' = \frac{d\bar{\sigma}}{d\bar{\varepsilon}_p} = \frac{3(\bar{F}+\bar{G})}{2(\bar{F}+\bar{G}+\bar{H})}\left[\frac{d\varepsilon_n/d\sigma_n}{(1\pm\varepsilon_n)\left[(1\pm\varepsilon_n)\pm\sigma_n(d\varepsilon_n/d\sigma_n)\right]} - \frac{1}{E_{0z}}\right]^{-1} \tag{7.53}$$

in which $d\varepsilon_n/d\sigma_n$ is the strain rate of the nominal stress-strain curve in the longitudinal direction and is given by Eq. (6.19) for the 3-stage full-range stress-strain relationship (Eq. (3.6)).

Following a procedure similar to that given in the preceding section, the increment of stress ratio is obtained as:

$$d\omega_b = \frac{\left[\overline{G} + \overline{H} - 2\overline{G}\,\omega_b + \left(\overline{F} + \overline{G}\right)\omega_b^2\right]\left(\Omega_b - \omega_b\right)}{\sigma_{yL}\left\{\left(\overline{G} + \overline{H} - \overline{G}\,\omega_b\right) + \Omega_b\left[\left(\overline{F} + \overline{G}\right)\omega_b - \overline{G}\right]\right\}} d\sigma_{yL} \tag{7.55}$$

in which H' is given by Eq. (7.53), and Ω_b is the ratio of stress increments $d\sigma_{z,b}/d\sigma_{x,b}$ given by

$$\Omega_b = \frac{\begin{array}{l} 2H'\nu_{zx}\left(E_{0x}/E_{0z}\right)\left(\overline{F} + \overline{G} + \overline{H}\right)\left[\overline{G} + \overline{H} - 2\overline{G}\,\omega_b + \left(\overline{F} + \overline{G}\right)\omega_b^2\right] \\ -3E_{0x}\left(\overline{G} + \overline{H} - \overline{G}\,\omega_b\right)\left[\left(\overline{F} + \overline{G}\right)\omega_b - \overline{G}\right] \end{array}}{2H'\left(E_{0x}/E_{0z}\right)\left(\overline{F} + \overline{G} + \overline{H}\right)\left[\overline{G} + \overline{H} - 2\overline{G}\,\omega_b + \left(\overline{F} + \overline{G}\right)\omega_b^2\right] + 3E_{0x}\left[\left(\overline{F} + \overline{G}\right)\omega_b - \overline{G}\right]^2} \tag{7.54}$$

In Eq. (7.55), the stress increment $d\sigma_{yL}$ can be calculated from the nominal stress σ_n and its increment $d\sigma_n$. By combining the differentiations of Eqs. (7.51) and (6.16a) with Eqs. (3.6) and (6.19), the stress increment $d\sigma_{yL}$ can be obtained as

$$\frac{d\sigma_{yL}}{d\sigma_n}=\frac{d\sigma_t}{d\sigma_n}=\begin{cases}1\pm\left[\dfrac{2\sigma_n}{E_{0z}}+0.002(n+1)\left(\dfrac{\sigma_n}{\sigma_{0.2}}\right)^n\right], & \sigma_n\le\sigma_{0.2}\\[2ex] 1\pm\left\{\begin{array}{l}\varepsilon_{0.2}+\dfrac{(2\sigma_n-\sigma_{0.2})}{E_{0.2}}+\left[(n'_{0.2,1.0}+1)\sigma_n-\sigma_{0.2}\right]\dfrac{(\sigma_n-\sigma_{0.2})^{n'_{0.2,1.0}-1}}{(\sigma_{1.0}-\sigma_{0.2})^{n'_{0.2,1.0}}}\\ \cdot\left[0.008+(\sigma_{1.0}-\sigma_{0.2})\left(\dfrac{1}{E_{0z}}-\dfrac{1}{E_{0.2}}\right)\right]\end{array}\right\}, & \sigma_{0.2}<\sigma_n\le\sigma_{2.0}\\[2ex] 1\pm\dfrac{(2\sigma_n-a)(b\mp\sigma_n)\pm\sigma_n(\sigma_n-a)}{(b\mp\sigma_n)^2}, & \sigma_n>\sigma_{2.0}\end{cases} \quad (7.56)$$

Eqs. (7.55) and (7.56) can then be used to solve numerically for the values of σ_{yLb} and the corresponding stress ratio ω_b at each location y.

In analogy with Eq. (7.28), the transverse bending strain $\varepsilon_{x,b}$ at an arbitrary location y can be expressed as a function of ω_b and σ through the following integral:

$$\varepsilon_{x,b}=\pm\left\{\begin{array}{l}\displaystyle\int_{\nu_{zx}}^{\omega_b}\frac{\left\{\begin{array}{l}\dfrac{E_{0x}}{E_{0z}}\left(\overline{G}+\overline{H}-\overline{G}\,\omega_b\right)^2+\left[\overline{G}-\left(\overline{F}+\overline{G}\right)\omega_b\right]^2\\ -2\nu_{zx}\dfrac{E_{0x}}{E_{0z}}\left(\overline{G}+\overline{H}-\overline{G}\,\omega_b\right)\left[\overline{G}-\left(\overline{F}+\overline{G}\right)\omega_b\right]\end{array}\right\}\sigma_{yL}}{E_{0x}\left[\left(\overline{F}+\overline{G}\right)\omega_b-\overline{G}\right]\left[\overline{G}+\overline{H}-2\overline{G}\,\omega_b+\left(\overline{F}+\overline{G}\right)\omega_b^2\right]^{3/2}}d\omega_b\\[2ex] +\displaystyle\int_0^{\sigma_{yLb}}\frac{\left\{\begin{array}{l}\left(1-\omega_b\nu_{zx}\dfrac{E_{0x}}{E_{0z}}\right)\left[\overline{G}-\left(\overline{F}+\overline{G}\right)\omega_b\right]\\ +\dfrac{E_{0x}}{E_{0z}}\left(\omega_b-\nu_{zx}\right)\left(\overline{G}+\overline{H}-\overline{G}\,\omega_b\right)\end{array}\right\}}{E_{0x}\left[\left(\overline{F}+\overline{G}\right)\omega_b-\overline{G}\right]\left[\overline{G}+\overline{H}-2\overline{G}\,\omega_b+\left(\overline{F}+\overline{G}\right)\omega_b^2\right]^{1/2}}d\sigma_{yL}\end{array}\right\} \quad (7.57)$$

where the +ve sign of "±" applies when $y\ge s$, and $\varepsilon_{x,b}$ is given by Eq. (6.1).

For a trial value of the distance s (see Figure 6.1 in Chapter 6), the value of $\varepsilon_{x,b}$ can be calculated by Eq. (6.1). The integration in Eq. (7.57) can be performed numerically by the Euler forward method. The lower limits (i.e. ν_{zx} for $d\omega_b$ and zero for $d\sigma_{yL}$) of the integration are treated as initial conditions. Starting with these initial conditions, the value of $d\sigma_{yL}$ is calculated from a small assigned value of $d\sigma_n$ using Eq. (7.56), and the value of $d\omega_b$ can then be calculated from the resulting stress increment $d\sigma_{yL}$ using Eq. (7.55). In such a way, the values of σ_n, σ_{yL} and ω_b can be updated for each step. After the numerical integration (see Eq. (7.57)) is done, the values of σ_{yLb} and the corresponding stress ratio ω_b, which are the upper limits of the integration, can be determined.

After the values of σ_{yLb} and ω_b are determined for each trial value of s, the stresses and equivalent plastic strain due to cold bending can be calculated from Eqs. (7.49) and (7.50) and the 3-stage stress-strain model (Eq. (3.6)). Then the equilibrium condition of Eq. (6.8) is checked, and the value of the distance s is adjusted for the next trial until the condition given by Eq. (6.8) is satisfied.

7.4 FINITE ELEMENT SIMULATION OF COILING AND UNCOILING

7.4.1 General

In order to verify the analytical solution for the coiling-uncoiling process presented in Section 7.2, the coiling-uncoiling process of stainless steel sheets was also simulated

using the finite element package ABAQUS (2002a). A duplex stainless steel strip of 60 mm in length, having a thickness of 2mm, was modelled with one end fixed and the other end free (see Figure 4.2 in Chapter 4). Both geometrical and material nonlinearities were considered. Coiling was simulated as pure bending of the cantilever steel strip to a coil radius r $(= D/2)$ of 100 mm, and uncoiling including flattening was simulated as reverse bending of the strip to the initial zero curvature. The finite element modelling of the process can be found in detail in Section 4.8 of Chapter 4.

To define the material anisotropy of the duplex stainless steel strip in both the analytical solution and the finite element model, the through-thickness initial yield stress σ_{0N} is needed and it can be approximated by the initial yield stresses σ_{0D} in the diagonal direction (Eq. (7.48)). Tensile and compressive yield stresses in the diagonal direction of stainless steel sheets are generally not available in most existing literatures and design codes, but can be found in Rasmussen *et al*. (2003). Rasmussen and his researchers (Rasmussen *et al*. 2003) carried out tension and compression tests of coupons cut in the longitudinal, transverse and diagonal directions to obtain the material properties of a duplex stainless steel plate (grade UNS31803 duplex alloy), as shown in Table 7.1. Hence, the material properties of the duplex stainless steel plate tested by Rasmussen *et al*. (2003) were adopted in the present study, and the anisotropic material properties based on the compression coupons (LC, TC and DC) were used for the verification. Poisson's ratio ν_{xz} (or ν_{31}) was assumed to be 0.3. The material modelling of the duplex stainless steel strip is given in the next two subsections.

7.4.2 Nonlinear strain hardening

In the finite element analysis, the stress-strain curve for longitudinal compression (LC) was incorporated to describe the material hardening behaviour. To consider that strains caused by large coiling curvatures can be well beyond the 0.2% total strain, the 3-stage full-range stress-strain model (Eq. (3.6)) was used to define the nominal stress-strain relationship over the whole range of compressive strains in the longitudinal direction.

The modelling of the nonlinear hardening behaviour for anisotropic metals requires the definition of an equivalent stress $\bar{\sigma}$ and equivalent plastic strain $\bar{\varepsilon}_p$ relationship (ABAQUS 2002b) as input data. In the present study, the equivalent stress $\bar{\sigma}$ and the equivalent plastic strain $\bar{\varepsilon}_p$ were converted from the true stress σ_t and true plastic strain ε_{tp} for longitudinal compression (LC) by the following equation (Hill 1950):

$$\bar{\sigma} = \sqrt{\frac{3}{2}\left(\frac{F+G}{F+G+H}\right)}\sigma_t \tag{7.58a}$$

$$\bar{\varepsilon}_p = \sqrt{\frac{2}{3}\left(\frac{F+G+H}{F+G}\right)}\varepsilon_{tp} \tag{7.58b}$$

In order to determine the equivalent stress $\bar{\sigma}$ and the equivalent plastic strain $\bar{\varepsilon}_p$ from Eq. (7.58), the true stress σ_t and the true plastic strain ε_{tp} were first converted from the nominal stress-strain data for longitudinal compression (LC), which were defined by the 3-stage full-range stress-strain model (Eq. (3.6)), using Eq. (6.16). The

nominal stress-strain curve and the true stress-strain curve for longitudinal compression, and the equivalent stress-equivalent plastic strain curve are shown in Figure 7.2. It is worth noting that, for isotropic materials, $F = G = H$ and Eq. (7.58) leads to $\overline{\sigma} = \sigma_t$ and $\overline{\varepsilon}_p = \varepsilon_{tp}$. Thus, for isotropic materials, the true stress-true plastic strain relationship is required as input data.

7.4.3 Material anisotropy

To model the material anisotropy in the finite element model, a local coordinate system was used to define the material directions of each plane strain element, and initially coincided with the global coordinate system. The material directions of each element rotated as the stainless steel strip was deformed during the finite element simulation. In this local coordinate system, the 1-direction is referred to as the longitudinal direction, the 2-direction is referred to as the through-thickness direction and the 3-direction is referred to as the transverse direction. The anisotropic material properties were thus defined on the basis of this local coordinate system.

In the finite element analysis, the material anisotropy is described by the orthotropic elasticity model and the anisotropic metal plasticity model. The orthotropic elasticity model is defined by the following engineering constants: elastic moduli E_1, E_2, E_3; Poisson's ratios ν_{12}, ν_{13}, ν_{23}; and shear moduli G_{12}, G_{13} and G_{23}. For these engineering constants, the subscripts 1, 2 and 3 are used to refer to the local 1-, 2- and 3-directions respectively for each plane strain element.

The moduli E_1 and E_3 were taken as the initial elastic moduli E_{0z} and E_{0x} for longitudinal compression (LC) and transverse compression (TC) respectively. Since the modulus E_2 is the initial elastic modulus E_{0y} in the through-thickness direction, which is not available and inconsequential, the values of the modulus E_2 was assumed to be the same as the initial elastic modulus E_3 (i.e. E_{0x}). The Poisson's ratios ν_{12} and ν_{23} were assumed to be 0.3. As the Poisson's ratio ν_{31} has also been assumed to be 0.3, the Poisson's ratio ν_{13} can be calculated as 0.26 by Eq. (7.17d). The shear moduli G_{12}, G_{13} and G_{23} were taken as the initial shear elastic modulus of grade UNS31803 duplex alloy given in Appendix B of AS/NZS 4673 Standard (AS/NZS 2001). It should be noted that the values of ν_{12}, ν_{23}, G_{12}, G_{13} and G_{23} are inconsequential even they have been assumed with reasonable values from different sources. Hence, these engineering constants were calculated as

$$E_1 = E_{0z} = 181.65 \text{ GPa};\ \ E_2 = E_{0y} = 210.00 \text{ GPa};\ \ E_3 = E_{0x} = 210.00 \text{ GPa};$$

$$\nu_{12} = 0.30;\ \ \nu_{13} = \nu_{31} E_1 / E_3 = 0.26;\ \ \nu_{23} = 0.30; \tag{7.59}$$

$$G_{12} = 75.00 \text{ GPa};\ \ G_{13} = 75.00 \text{ GPa};\ \ G_{23} = 75.00 \text{ GPa}$$

The ABAQUS anisotropic metal plasticity model is characterized by Hill's yield criterion for anisotropic materials and the flow rule with isotropic hardening. While the nonlinear strain hardening is modelled by specifying a "reference" stress-strain curve, the state of the plastic anisotropy is defined in ABAQUS by means of six yield stress ratios R_{ij}. The six yield stress ratios are defined as

$$R_{11}=\frac{\sigma_{0,11}}{\sigma_0};\ R_{22}=\frac{\sigma_{0,22}}{\sigma_0};\ R_{33}=\frac{\sigma_{0,33}}{\sigma_0};\ R_{12}=\frac{\tau_{0,12}}{\tau_0};\ R_{13}=\frac{\tau_{0,13}}{\tau_0};\ R_{23}=\frac{\tau_{0,23}}{\tau_0} \quad (7.60)$$

where $\sigma_{0,ii}$ is the measured initial yield stress in the i-direction, $\tau_{0,ij}$ is the measured initial shear yield stress for the i - j plane, σ_0 is the reference yield stress and $\tau_0=\sigma_0/\sqrt{3}$.

The initial yield stresses $\sigma_{0,ii}$ were taken as the compressive 0.2% proof stresses in the three principal directions (see Table 7.1), in which the through-thickness 0.2% proof stress σ_{0N} (i.e. $\sigma_{0,22}$) was approximated by the diagonal 0.2% proof stress σ_{0D} (see Eq. (7.48)). That is,

$$\sigma_{0,11}=\sigma_{0L}=527 \text{ MPa};\ \ \sigma_{0,22}=\sigma_{0N}=610 \text{ MPa};\ \ \sigma_{0,33}=\sigma_{0T}=617 \text{ MPa} \quad (7.61)$$

The values of shear yield stresses $\tau_{0,ij}$ are inconsequential for this plane strain bending problem. Nevertheless, the shear yield stress $\tau_{0,13}$, which is τ_{0XZ}, was approximated by $\sigma_{0D}/\sqrt{3}$ (see Eq. (7.47)). Both $\tau_{0,12}$ and $\tau_{0,23}$ were taken as τ_0 such that $R_{12}=1$ and $R_{23}=1$. That is,

$$\tau_{0,12}=\tau_0;\ \ \tau_{0,13}=\tau_{0XZ}=610/\sqrt{3} \text{ MPa};\ \ \tau_{0,23}=\tau_0 \quad (7.62)$$

In the present study, the stress-strain curve for longitudinal compression (LC) was incorporated to describe the material hardening behaviour. Thus, the equivalent stress-

equivalent plastic strain relationship converted from the stress-strain curve for longitudinal compression (LC) was used to define the "reference" stress-strain curve. As the reference yield stress σ_0 is the yield stress of the "reference" stress-strain curve, the reference yield stress σ_0 was taken as the equivalent stress $\overline{\sigma}$ converted from the compressive 0.2% proof stress σ_{0L} in the longitudinal direction, and hence given by

$$\sigma_0 = \sqrt{\frac{3}{2}\left(\frac{F+G}{F+G+H}\right)}\sigma_{0L} \tag{7.63}$$

where F, G and H are the anisotropy parameters defined by Eqs. (7.2b)~(7.2d). Its value was thus calculated as $\sigma_0 = 580$ MPa.

7.4.4 Comparison between analytical predictions and finite element results

Since the residual stresses predicted by the finite element model are uniform along the whole length of the stainless steel strip, only the stress distributions at the fixed end are compared with the predictions of the analytical solution. The longitudinal and transverse residual stresses as well as the equivalent plastic strains predicted by both the analytical solution and the finite element simulation are shown in Figures 7.3 and 7.4. The analytical predictions are shown to agree closely with the finite element results, which demonstrates the validity and accuracy of both approaches. The results in Figures 7.3 and 7.4 show that the residual stresses are not linearly distributed across

the thickness. The similar observation has also been made in Chapter 4 where residual stresses in a carbon steel sheet and an austenitic stainless steel sheet has been studied.

7.5 VALIDATION OF ANALYTICAL SOLUTIONS FOR LARGE-CURVATURE TRANSVERSE BENDING

An analytical solution has been presented in Section 7.3 for residual stresses in the corners of press-braked stainless steel sections. This analytical solution has been developed based on the large-strain formulation and was extended from the analytical solution for the coiling of stainless steel sheets with the proper modification to deal with large straining due to the large-curvature cold bending in the transverse direction. Obviously, the small-strain formulation used in the analytical solution for the coiling of sheets may be used to provide accurate predictions of residual stresses in corner regions, if the corner radius is large enough. Thus, it is necessary to address the limitation of the small-strain formulation and the validity of the large-strain formation, when these two formulations are used to predict residual stresses due to large-curvature bending. To achieve this, the analytical predictions obtained from both formulations for the same problem need to be compared. Due to the effect of material anisotropy, the analytical solution for the coiling of stainless steel sheets cannot be directly used to provide predictions for the small-strain formulation. Instead, an analytical solution based on the small-strain formulation for transverse bending is needed for the comparison.

For the large-strain formulation used in the analytical solution for transverse cold bending presented in Section 7.3, the transverse bending strain is described by the true strain and the stress-strain curve of the material is described by the true stress-strain relationship. To obtain the analytical solution based on the small-strain formulation for transverse bending, the nominal stress-strain relationship should be used to describe the stress-strain behaviour of the material (see Eq. (7.1)) and the "true" transverse bending strain (see Eq. (6.1)) used in the large-strain formulation should be replaced by the "engineering" transverse bending strain which is

$$\varepsilon_{x,b} = -\kappa_b y = -y/R_c \tag{7.64}$$

Furthermore, due to small straining, the distance *s* between the neutral surface and the current middle surface becomes zero. Therefore, similar to the analytical solution for the coiling of stainless steel sheets, the instantaneous yield stress σ_{yL} and the corresponding strain ε_{yL} in the longitudinal direction are defined by the 3-stage full-range stress-strain model (Eq. (3.6)) for stainless steel alloys. The value of H' is thus given by Eq. (7.43) instead of Eq. (7.53).

To examine the validity of the analytical solution for large-curvature cold bending in which the large-strain formulation is used and to address the limitation of the small-strain formulation, analyses have been carried out for residual stresses due to the transverse bending with three different curvatures (or R_c/t ratios). Three different values (50, 25, and 2.5) of the R_c/t ratio have been considered, and the ratio of 2.5 represents the typical value for the corners of a press-braked section. The material properties of the duplex stainless steel plate tested by Rasmussen *et al*. (2003) were

adopted again, and the anisotropic material properties based on the compression coupons (LC, TC and DC) were used (see Table 7.1). The analytical predictions obtained from both the large-strain formulation and the small-strain formulation, are compared with finite element results as shown in Figures 7.5 and 7.6.

In both Figures 7.5 and 7.6, the letters “T” and “N” enclosed by the parentheses in legends are used to refer to the “true” strain used in the large-strain formulation, and the “nominal” strain used in the small-strain formulation respectively. It can be seen that, for R_c/t = 50, residual stresses and equivalent plastic strains determined from both the large-strain formulation and the small-strain formulation are in excellent agreement with finite element results. For a smaller R_c/t ratio of 25, the analytical predictions based on the large-strain formulation are still in close agreement with finite element results, and the predictions based on the small-strain formulation slightly deviate from finite element results at the sheet surfaces, which demonstrates the accuracy of both formulations up to this limit of the R_c/t ratio.

When the R_c/t ratio decreases to 2.5, residual stresses calculated from the small-strain formulation deviate from finite element results significantly, but the analytical predictions based on the large-strain formulation are generally in good agreement with finite element results except for a larger deviation in the longitudinal residual stress $\sigma_{z,b}$ near the central core (see Figures 7.5 and 7.6). It demonstrates the invalidity and limitation of the small-strain formulation used for large-curvature bending. For results from the large-strain formulation, the error in residual stresses near the central core of the sheet is mainly due to the omission of through-thickness stresses. Such omission reduces the accuracy of results for large bending curvatures,

but has an advantage of simplifying the formulation of the analytical solution. Although the omission of through-thickness stresses causes a larger error in the longitudinal residual stress $\sigma_{z,b}$ near the central core at large bending curvatures (e.g. R_c/t = 2.5), its effect on the accuracy of both the transverse residual stress $\sigma_{x,b}$ and the equivalent plastic strain $\bar{\varepsilon}_{p,b}$ is quite small. Moreover, this local deviation of longitudinal residual stresses will generally cause a negligible error in the prediction of the load-carrying capacity of a press-braked stainless steel section. This effect on the prediction of the structural behaviour of press-braked members will be examined in Appendix C. Hence, the analytical solution based on the large-strain formulation is considered to be suitable for the modelling of residual stresses in the corners of a press-braked section.

7.6 COMPLETE ANALYTICAL MODEL FOR RESIDUAL STRESSES IN PRESS-BRAKED SECTIONS

As mentioned earlier, residual stresses in press-braked sections consist of two components: those due to the coiling-uncoiling process and those due to the cold bending of press-braking operations. The modelling of residual stresses in a press-braked section can be achieved by either the finite element-based method or the analytical solutions obtained from the theoretical modelling of the manufacturing process.

In the finite element-based method, residual stresses and equivalent plastic strains due to the coiling and uncoiling of stainless steel sheets can be pre-determined from the

analytical solution presented in Section 7.2 and then be specified as the initial state in a subsequent finite element simulation of the press-braking process (see Figures 5.2 and 5.3). In the finite element-based method, several steps are required for the numerical forming of a channel section, and the numerical difficulty will be encountered during the simulation of the contact between the uncoiled sheet and the die or punch, especially for the section with the corners of small inner radius. The implementation of this method for press-braked carbon steel channels has been given in detail in Chapter 5.

Alternatively, residual stresses and equivalent plastic strains in the flat portions and the corner regions of a press-braked section can be determined from the analytical solutions for the coiling-uncoiling process and the press-braking operation respectively. This method provides a simply way to obtain accurate predictions and is regarded as a complete analytical model. To implement this complete analytical model to predict residual stresses in press-braked stainless steel sections, the analytical solutions presented in Sections 7.2 and 7.3 can be used.

In order to verify the validity of this complete analytical model, simulations on an identical press-braked stainless steel lipped channel section were carried out using both the finite element-based method and the complete analytical model, and the results from both methods were compared. The finite element package ABAQUS (2002a) was employed for both simulations. Material anisotropy, and both material and geometrical nonlinearities were considered. The stainless steel sheet was assumed to possess the same material properties as the duplex stainless steel plate (grade UNS31803 duplex alloy) tested by Rasmussen *et al*. (2003), and the anisotropic

material properties based on the compression coupons (LC, TC and DC) were assumed (see Table 7.1). The channel section studied here was assumed to have the same dimensions as the press-braked carbon steel channel, specimen PBC14, tested by Weng and Peköz (1990). The overall dimensions of the channel section selected for this comparative study have been summarized and shown in Table 5.1 and Figure 5.2 in Chapter 5. The coil diameter-to-thickness ratio D/t (= $2r/t$) was assumed to be 200, which is the lowest possible value for a coil.

Under the plane strain condition, only half of the channel section was modelled with the condition of symmetry properly imposed into the half-section finite element models shown in Figures 7.7 and 7.8 for the two methods respectively. The stainless steel sheet and the press-braked stainless steel section were modelled with the plane strain element (CPE4R), and the mesh convergence study has been carried out to obtain the final meshes used in this study (see Figure 5.2). In the finite element-based method, the punch and die were modelled with analytical rigid surfaces, and the interaction between the stainless steel sheet and the die/punch was simulated by defining contact pairs with hard contact model and finite sliding formulation. As several steps were required for the finite element-based method to numerically form the channel, only the initial state and final step are shown in Figure 7.7. The complete analytical model predicted the residual stresses and equivalent plastic strains in the channel section at the state just before transverse spring-back, and its predictions were then specified as the initial state in a finite element simulation of the transverse spring-back of the whole channel section to restore the equilibrium (see Figure 7.8). In comparison with the finite element-based method, by incorporating the complete analytical model, only one step was required for the finite element simulation to

obtain the final stress state in the press-braked section after the transverse spring-back (see Figure 7.8).

The comparison of the results from both methods is shown in Figures 7.9~7.11. Figure 7.9 shows the distribution of longitudinal residual stresses in the lip-flange corner of the channel section. Figures 7.10 and 7.11 show the through-thickness variations of residual stresses and equivalent plastic strains in both the lip-flange corner and the web of the channel section. It can be seen that both methods can provide identical results of both residual stresses and equivalent plastic strains in the flat portion (i.e. the web). In the corner, results obtained from the complete analytical model are generally in good agreement with results from the finite element-based method. It demonstrates the validity of the complete analytical model for the prediction of residual stresses in press-braked sections.

Results obtained from both methods show that residual stresses in the channel section consist of different components and their variations across the plate thickness are highly nonlinear. Similar observation has also been made in the study of the carbon steel channel section presented in Chapter 5.

7.7 CONCLUSIONS

This chapter has been concerned with the accurate prediction of residual stresses and equivalent plastic strains resulting from the manufacturing process of press-braked stainless steel sections for which the effect of material anisotropy on residual stresses

is considered. In this chapter, two distinct analytical solutions for residual stresses due to two different stages of the manufacturing process have been presented and verified, in which the coiling-uncoiling process and the cold bending of press-braking operations are taken into account in two plane strain pure bending models respectively. On the basis of these two analytical solutions, a complete analytical model has been presented to predict residual stresses in press-braked sections. A finite element-based simulation of the same problem has also been presented. The predictions of the complete analytical model have been in good agreement with the predictions of the finite element-based method, demonstrating the validity and accuracy of both methods. The effect of the simplifying assumptions used in the analytical solution for the cold bending of press-braking operations, on the accuracy of its predictions, has also been examined in detail.

Both the complete analytical model and the finite element-based method can provide accurate residual stresses and equivalent plastic strains in different parts of a press-braked section, which can be specified as the initial state in a finite element model of the press-braked member for the subsequent nonlinear buckling analysis. As residual stresses and equivalent plastic strains are two defining parameters of the effect of cold work, the change of the load-carrying capacity of a cold-formed member due to the manufacturing process can be examined. Such exploitation of the present analytical approach will be reported in Chapter 9.

7.8 REFERENCES

ABAQUS (2002a). *Standard User's Manual, V6.3,* Hibbitt, Karlsson and Sorensen, Inc., United States.

ABAQUS (2002b). *Theory Manual, V6.3,* Hibbitt, Karlsson and Sorensen, Inc., United States.

AS/NZS (2001). *Cold-Formed Stainless Steel Structures, AS/NZS 4673:2001,* Australian/New Zealand Standard, Standards Australia, Sydney.

Hill, R. (1950). *The Mathematical Theory of Plasticity*, Oxford University Press, United States.

Rasmussen, K. J. R., Burns, T., Bezkorovainy, P. and Bambach, M. R. (2003). Numerical modelling of stainless steel plates in compression. *Journal of Constructional Steel Research*, **59**, 1345-1362.

Weng, C. C. and Peköz, T. (1990). Residual stresses in cold-formed steel members. *Journal of Structural Engineering, ASCE*, **116:6,** 1611-1625.

Table 7.1 Mechanical properties of grade UNS31803 duplex stainless steel alloy tested by Rasmussen *et al*. (2003).

Specimen	E_0 (GPa)	$\sigma_{0.01}$ (MPa)	$\sigma_{0.2}$ (MPa)	$e\,(=\sigma_{0.2}/E_0)$	n
LT	200.00	310	575	0.00288	4.8
TT	215.25	430	635	0.00295	7.7
DT	195.00	376	565	0.00290	7.4
LC	181.65	275	527	0.00290	4.6
TC	210.00	380	617	0.00294	6.2
DC	205.00	460	610	0.00298	10.6
LT = Longitudinal Tension coupon TT = Transverse Tension coupon DT = Diagonal Tension coupon			LC = Longitudinal Compression coupon TC = Transverse Compression coupon DC = Diagonal Compression coupon		

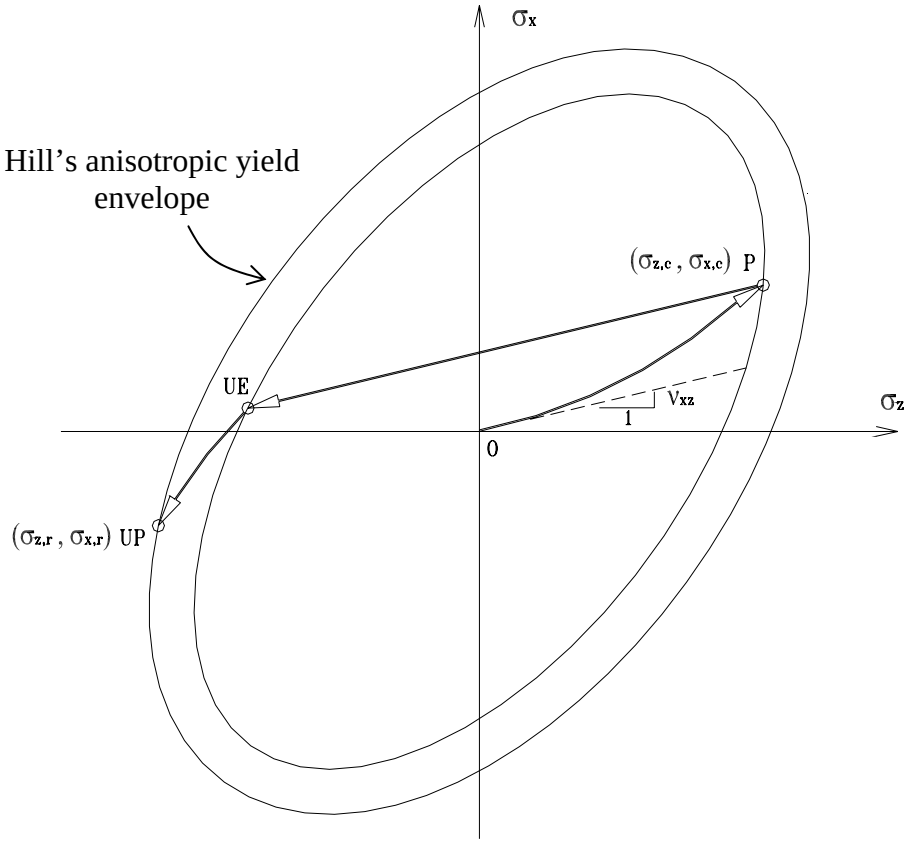

Figure 7.1 Stress path of a surface point of a stainless steel strip during the coiling-uncoiling process.

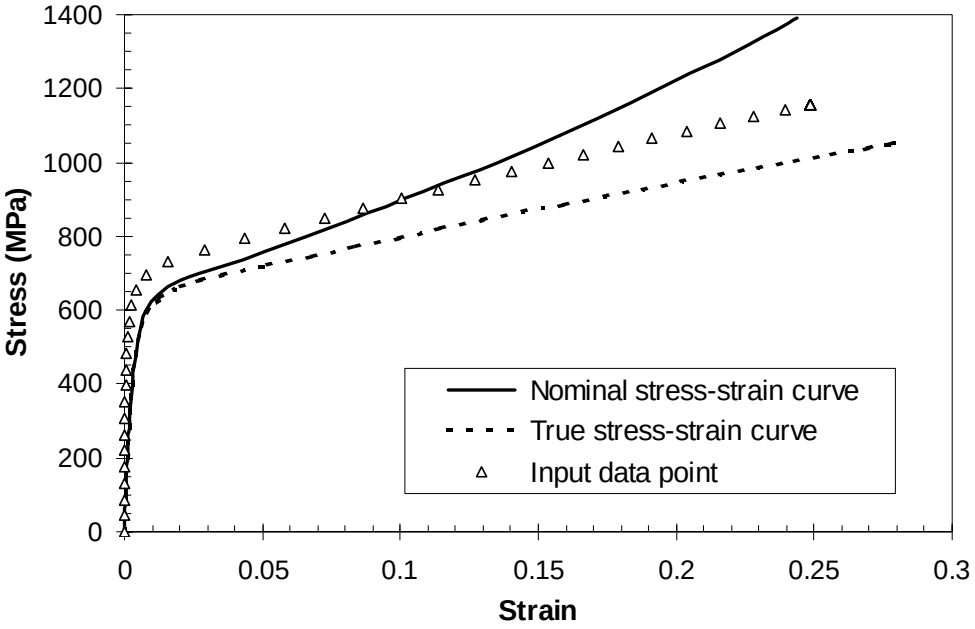

(a) Full stress-strain curves

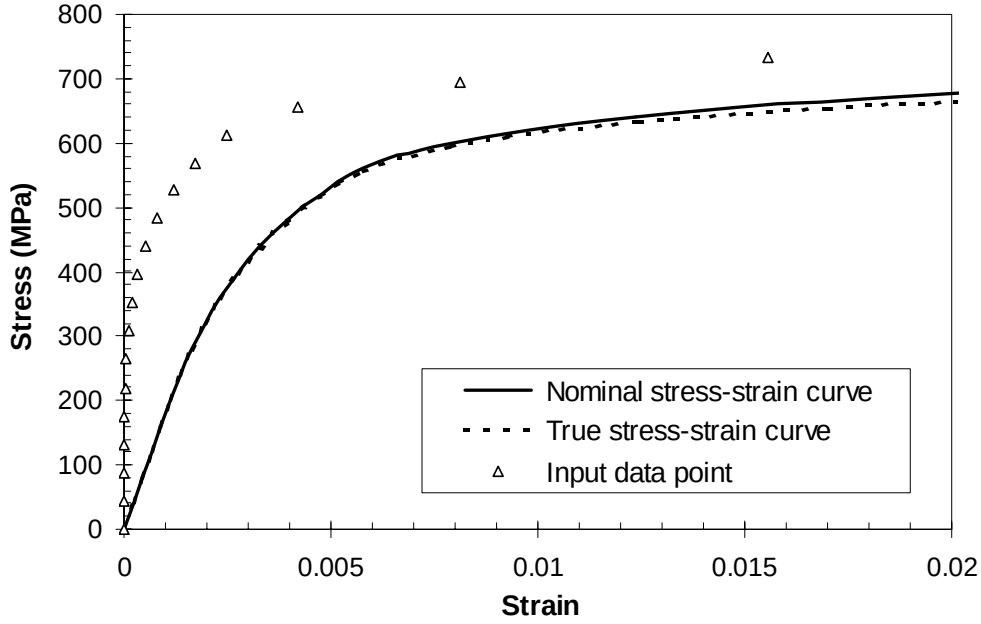

(b) Initial stress-strain curves

Figure 7.2 Stress-strain curves for longitudinal compression.

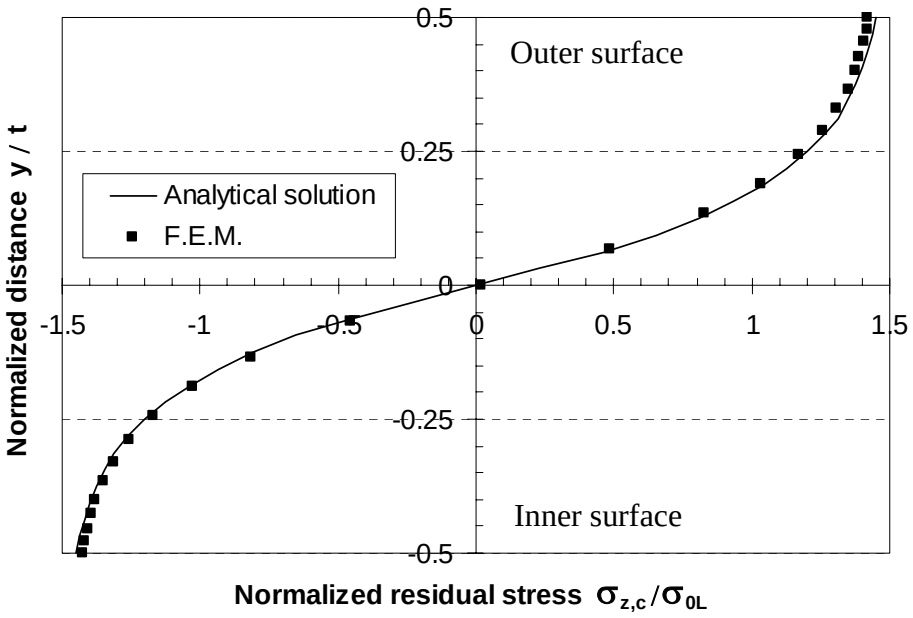

(a) Longitudinal coiling stress

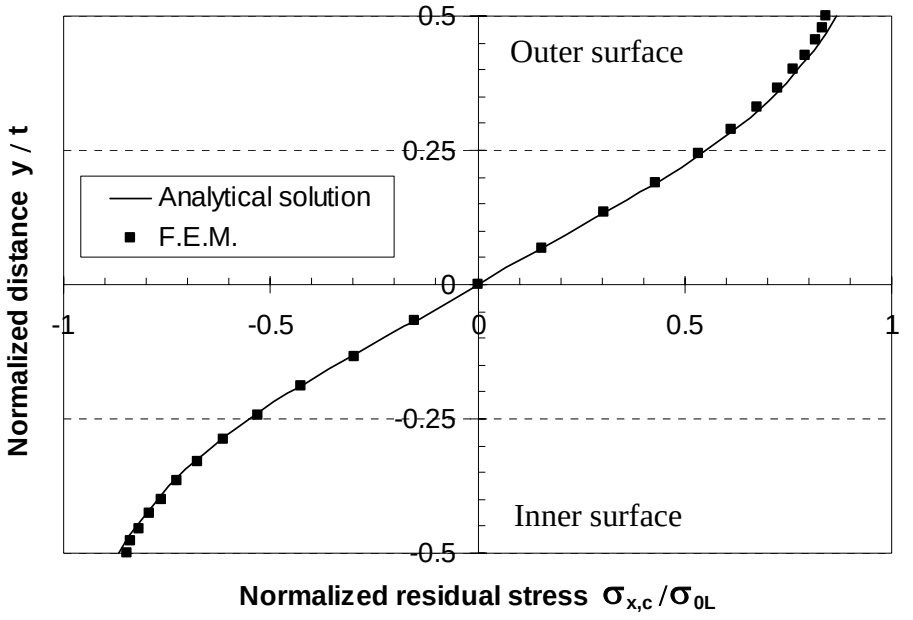

(b) Transverse coiling stress

Figure 7.3 Comparison of residual stresses between the analytical solution and finite element analysis.

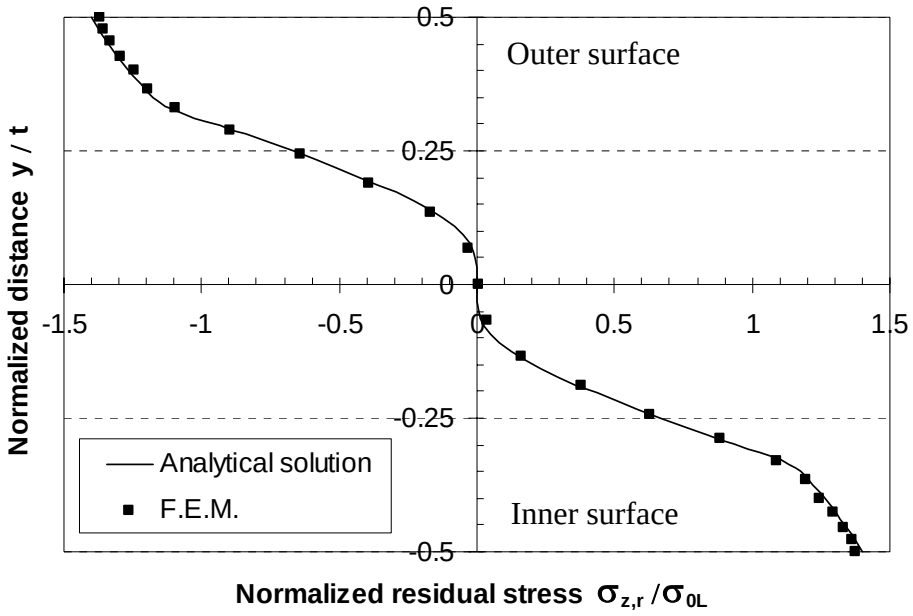

(c) Final longitudinal residual stress

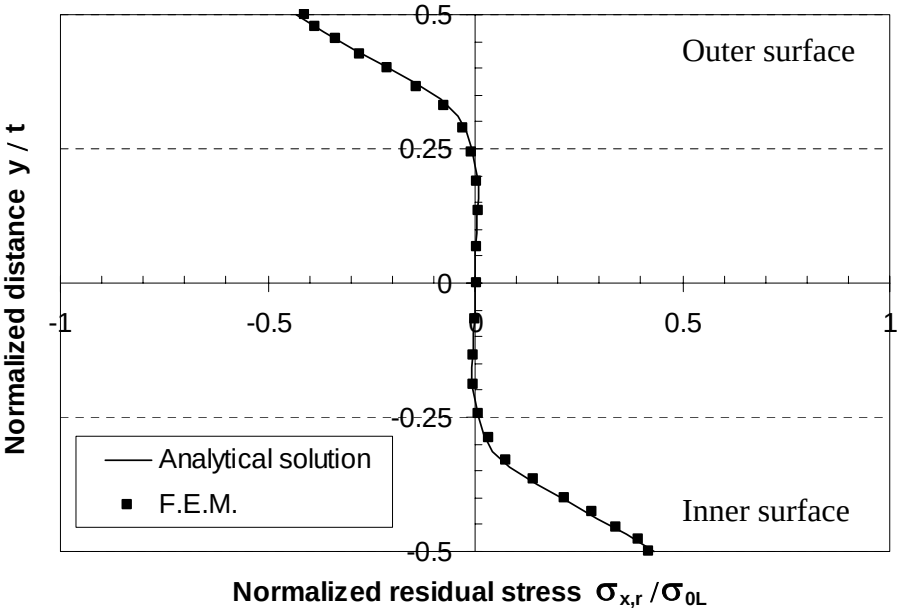

(d) Final transverse residual stress

Figure 7.3 Comparison of residual stresses between the analytical solution and finite element analysis (continued).

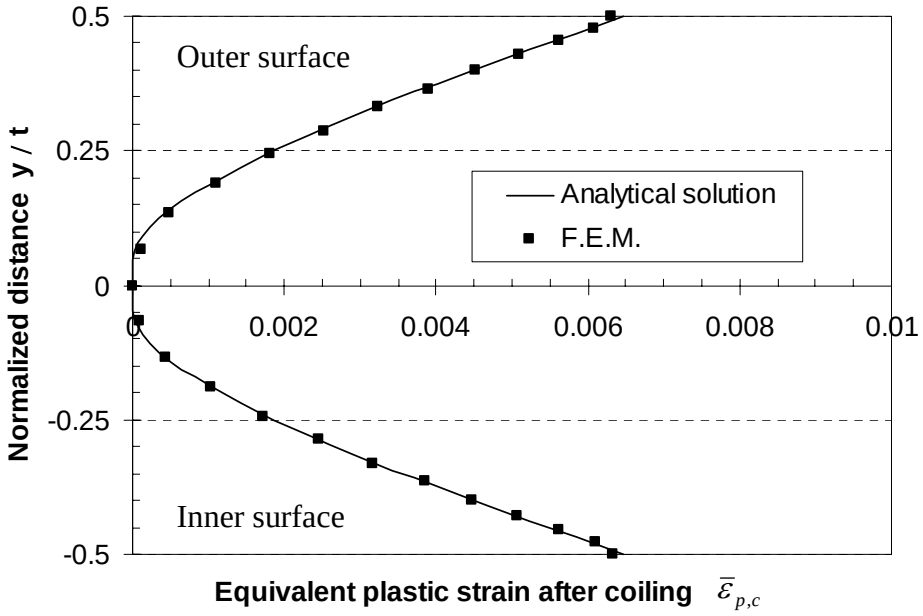

(a) After coiling

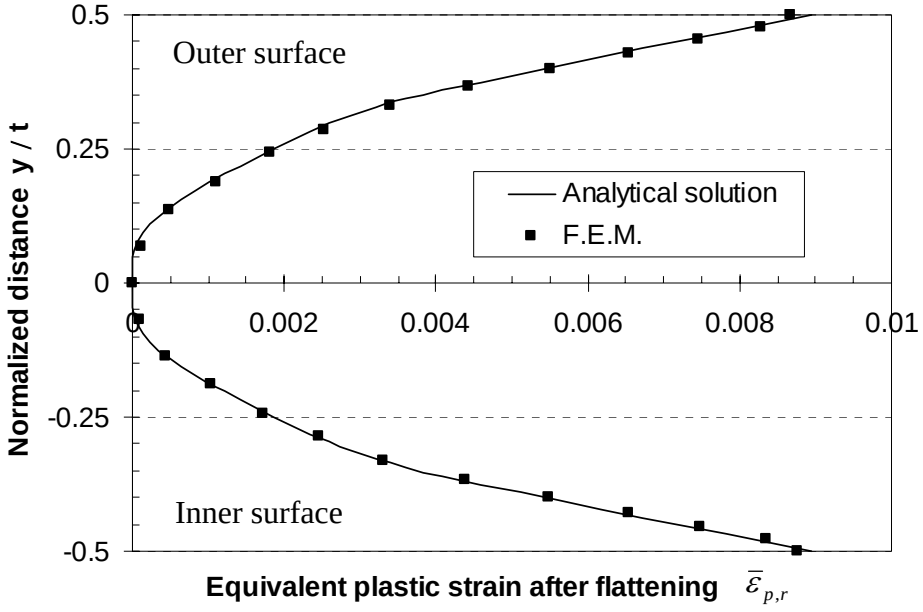

(b) After flattening

Figure 7.4 Comparison of equivalent plastic strains between the analytical solution and finite element analysis.

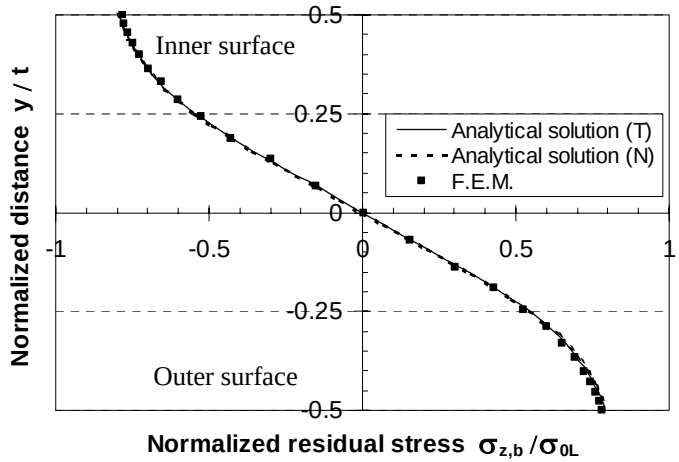

(a) Longitudinal residual stress, R_c/t = 50

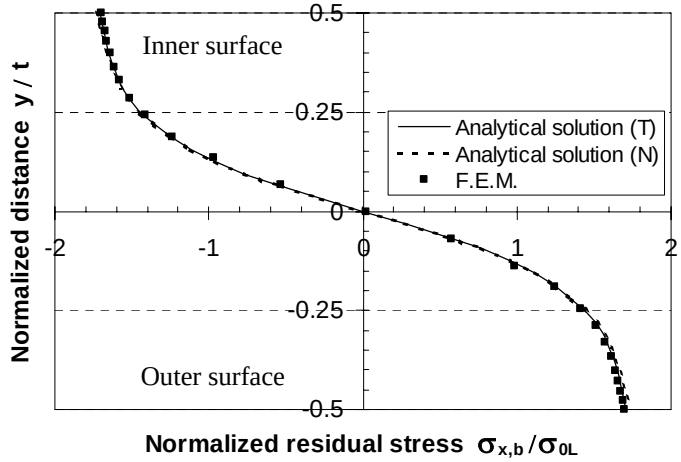

(b) Transverse residual stress, R_c/t = 50

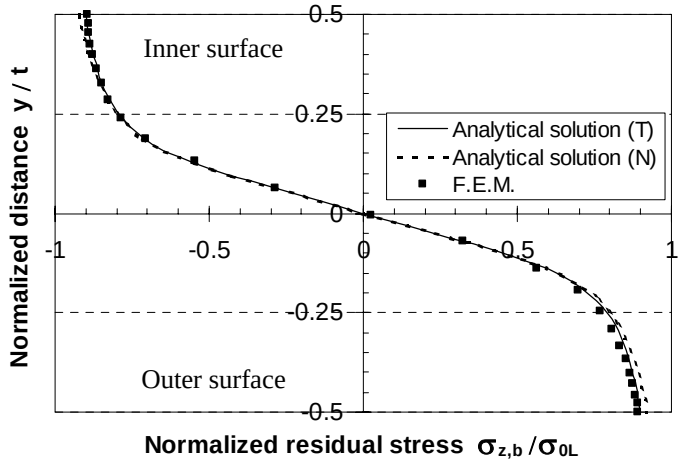

(c) Longitudinal residual stress, R_c/t = 25

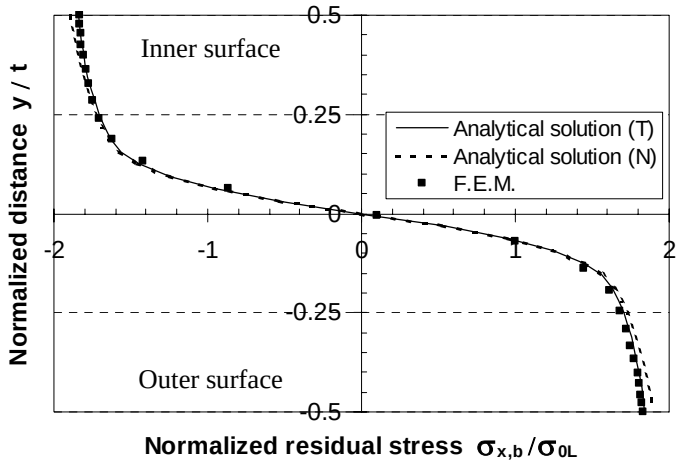

(d) Transverse residual stress, R_c/t = 25

Figure 7.5 Comparison of residual stresses between the analytical solution and finite element analysis, for different R_c/t ratios.

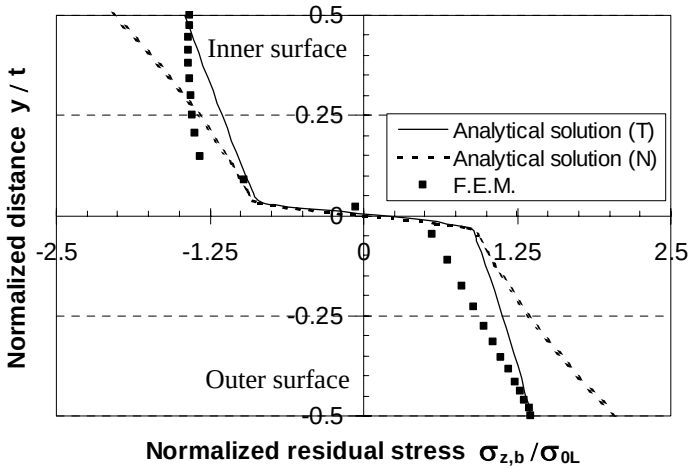

(e) Longitudinal residual stress, R_c/t = 2.5

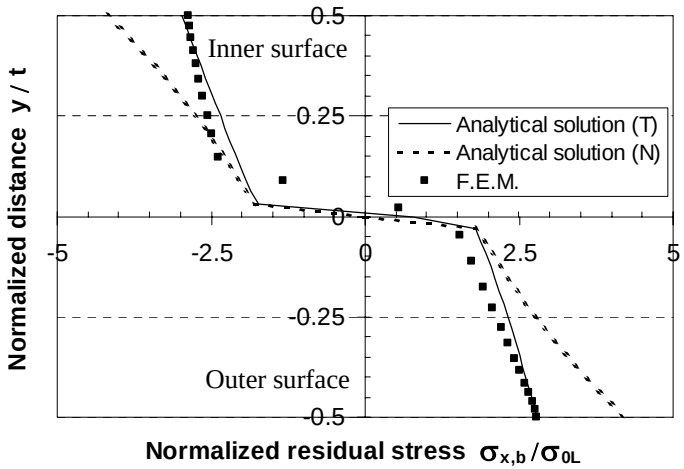

(f) Transverse residual stress, R_c/t = 2.5

Figure 7.5 Comparison of residual stresses between the analytical solution and finite element analysis, for different R_c/t ratios (continued).

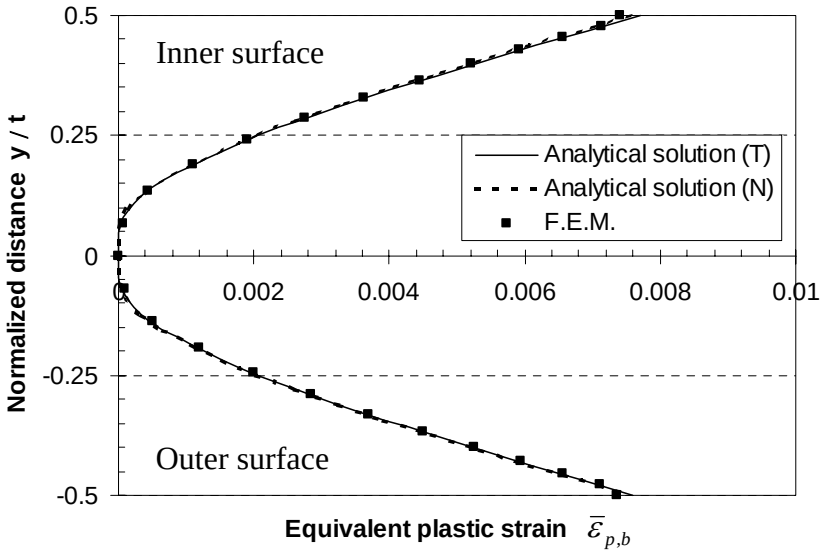

(a) R_c/t = 50

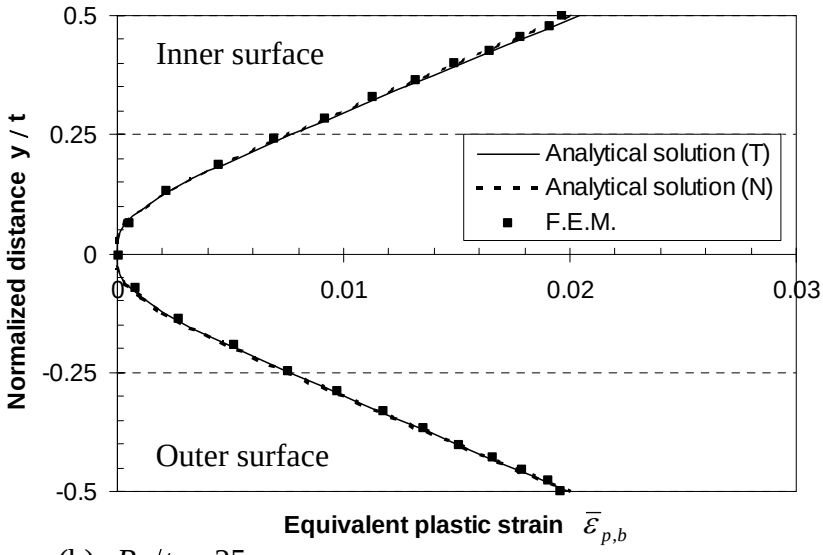

(b) R_c/t = 25

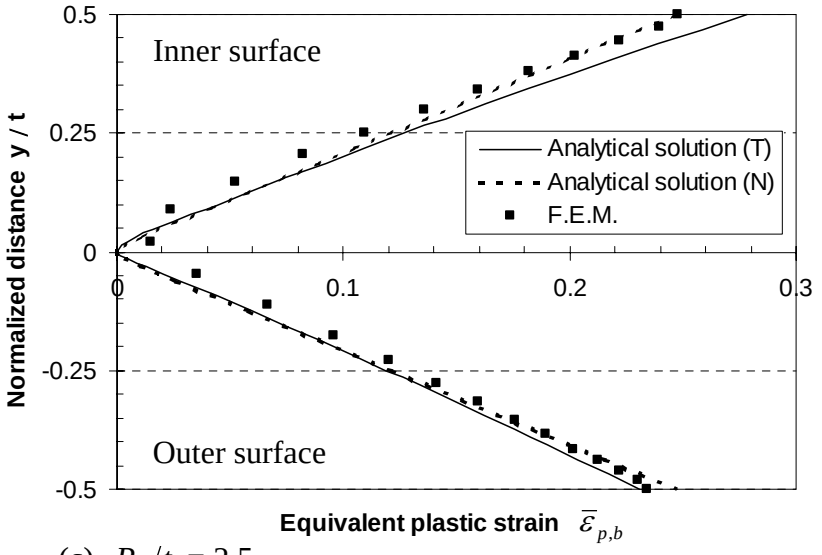

(c) R_c/t = 2.5

Figure 7.6 Comparison of equivalent plastic strains between the analytical solution and finite element analysis, for different R_c/t ratios.

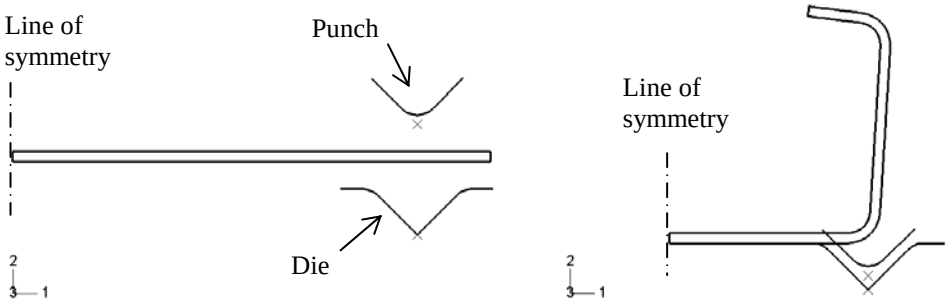

(a) Initial positioning (b) Final spring-back

Figure 7.7 Finite element-based simulation of the press-braking process for a channel section.

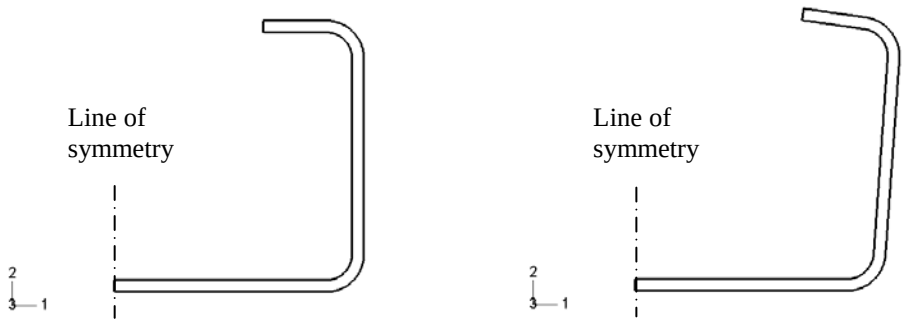

(a) Initial state (b) Final spring-back

Figure 7.8 Simulation of the manufacturing process of a press-braked channel section by incorporating the complete analytical model.

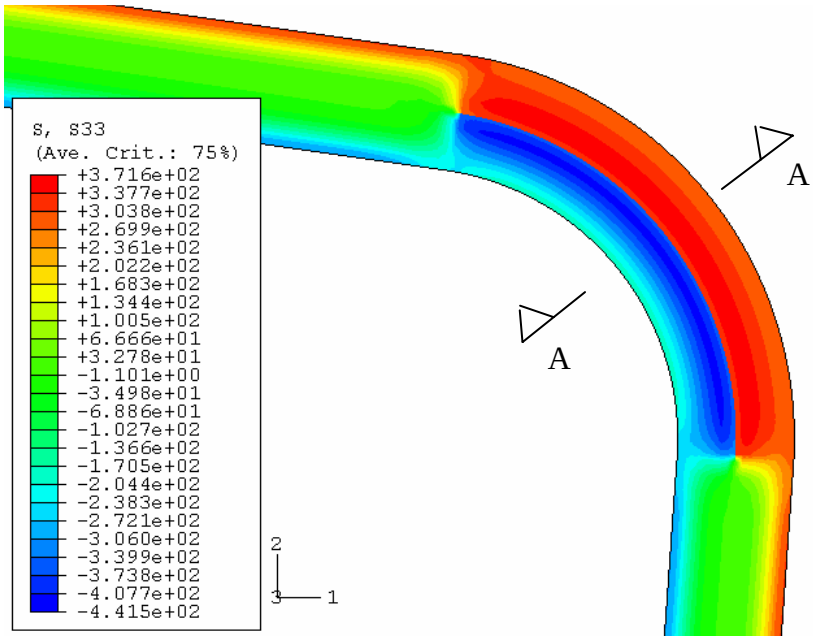

(a) Complete analytical model

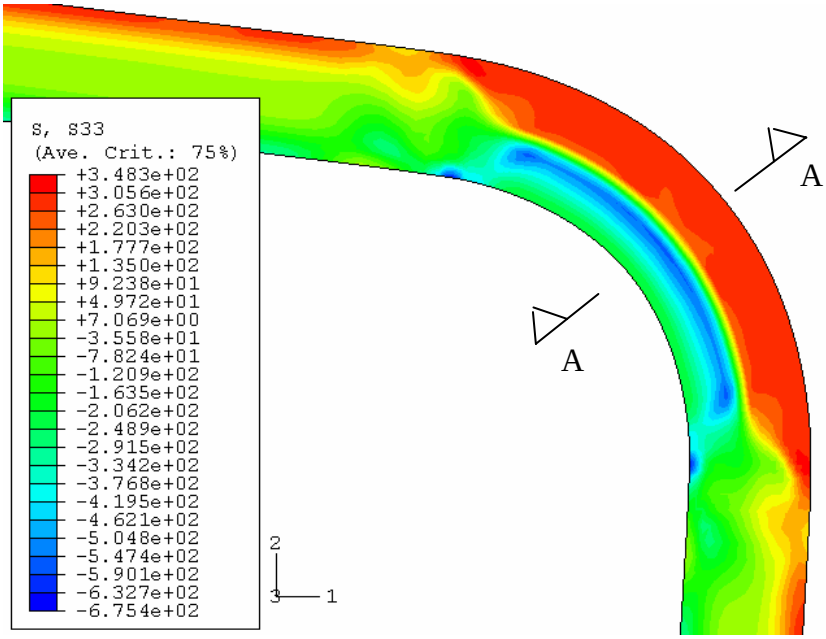

(b) Finite element-based method

Figure 7.9 Longitudinal stress contours in the lip-flange corner of the lipped channel with $D/t = 200$:
comparison between the complete analytical model and the finite element-based method.

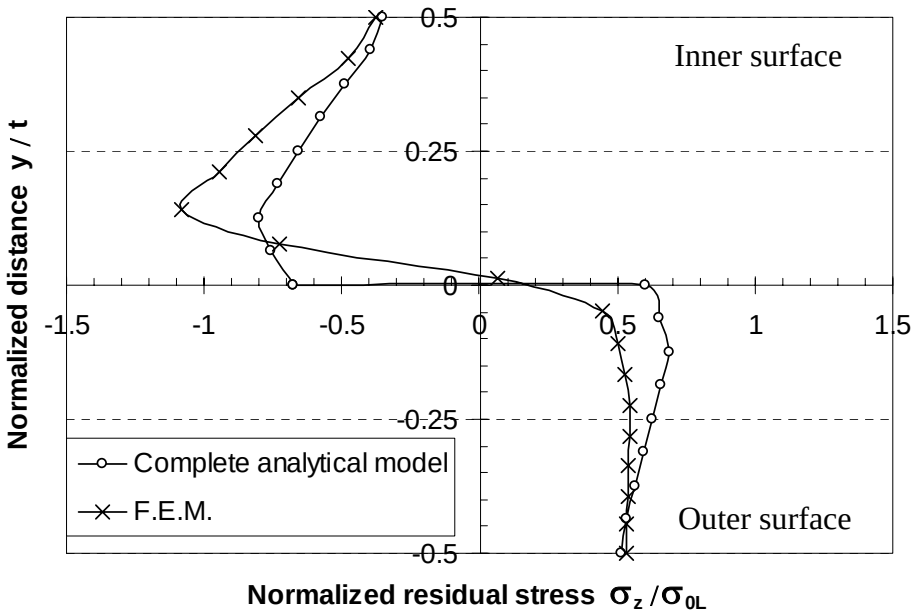

(a) Longitudinal residual stress at the center of the lip-flange corner (section A-A)

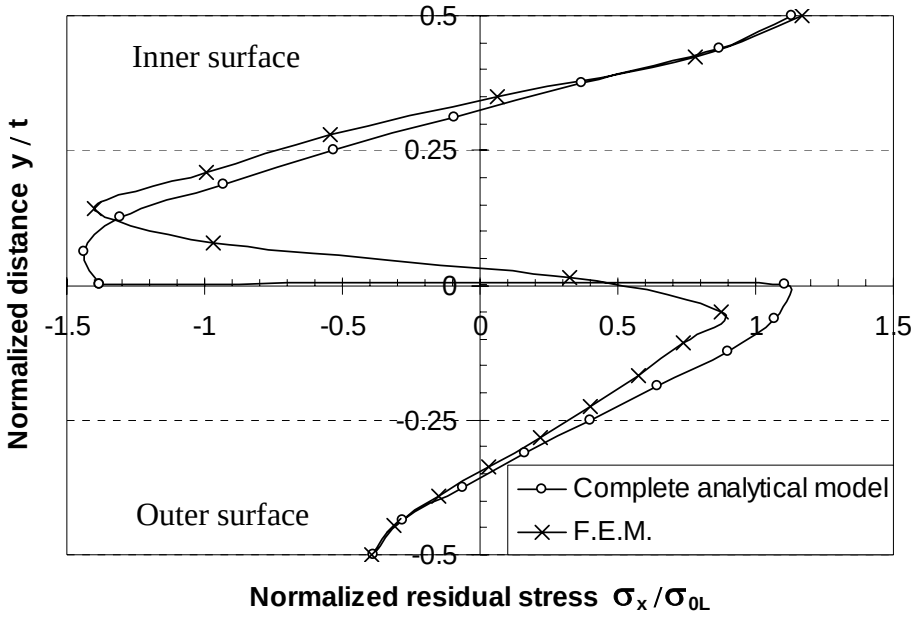

(b) Transverse residual stress at the center of the lip-flange corner (section A-A)

Figure 7.10 Through-thickness variations of residual stresses in the lipped channel with $D/t = 200$:
comparison between the complete analytical model and the finite element-based method.

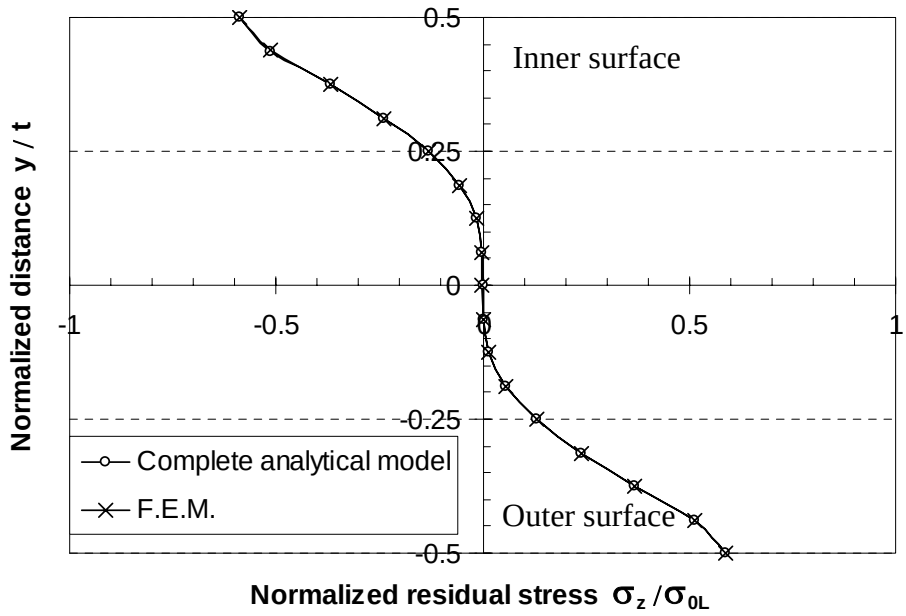

(c) Longitudinal residual stress at the mid-web section

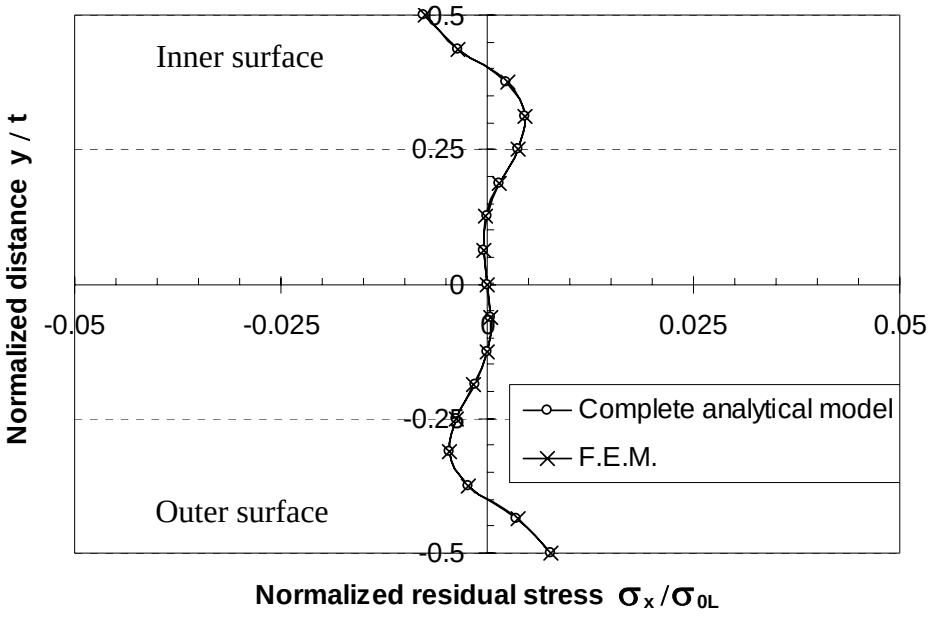

(d) Transverse residual stress at the mid-web section

Figure 7.10 Through-thickness variations of residual stresses in the lipped channel with $D/t = 200$:
comparison between the complete analytical model and the finite element-based method (continued).

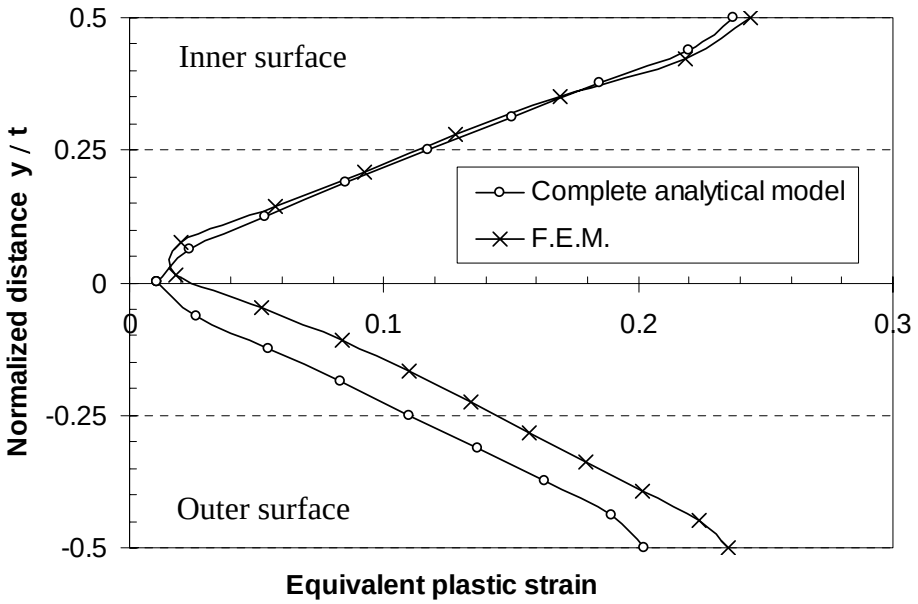

(a) At the center of the lip-flange corner (section A-A)

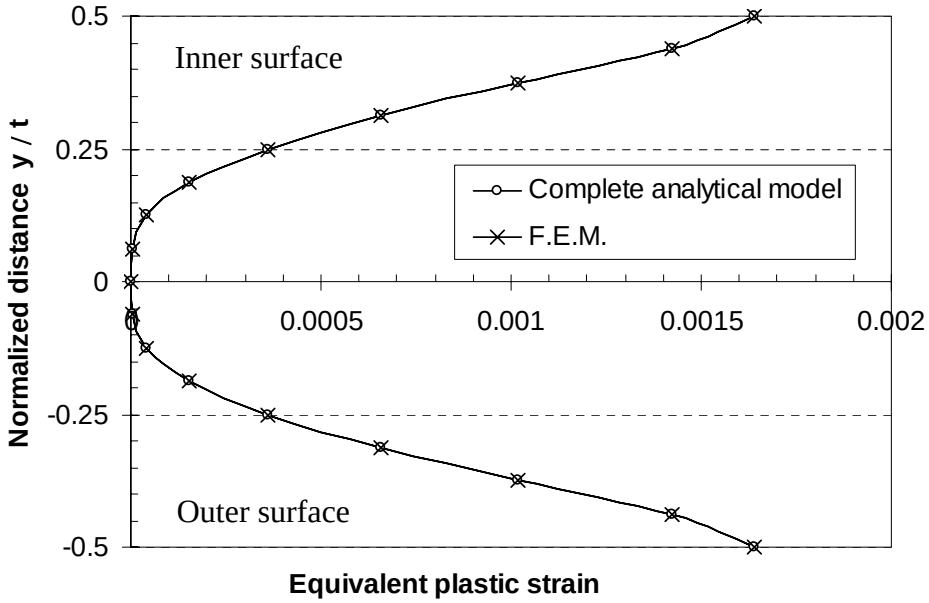

(b) At the mid-web section

Figure 7.11 Through-thickness variations of equivalent plastic strains in the lipped channel with D/t = 200:
comparison between the complete analytical model and the finite element-based method.

Chapter 8

PARAMETRIC STUDY ON RESIDUAL STRESSES IN PRESS-BRAKED SECTIONS

8.1 INTRODUCTION

In a two-stage manufacturing process of press-braked sections, residual stresses already exist in steel sheets before the press-braking operation is applied and are due to the coiling-uncoiling process. After press braking, different amounts of residual stresses exist in different parts of the press-braked section, and result from both the coiling-uncoiling process and the press-braking process. Thus, the predictions of residual stresses can be separated into two tasks: (1) the prediction of residual stresses due to the coiling-uncoiling process, and (2) the prediction of residual stresses from the press-braking process.

To gain insight into the cause and nature of residual stresses induced by each stage of the manufacturing process, a parametric study of residual stresses before and after press-braking operations was carried out and is presented in this chapter. In the present parametric study, both press-braked carbon steel sections and stainless steel sections are concerned. In this study, residual stresses in steel sheets due to the coiling-uncoiling process were calculated using the analytical solution presented in Chapter 4 for carbon steel sheets and the analytical solutions in Chapters 4 and 7 for stainless steel sheets. Residual stresses in press-braked sections were predicted by the

finite element-based method illustrated in Chapter 5, with the aforementioned analytical solutions for the coiling-uncoiling process to provide the initial state in the finite element model. The parameters of influence studied here for their effects on residual stresses are: coiling curvature, press-brake size and mechanical properties of virgin sheet materials. The effect of material anisotropy on residual stresses is also considered for stainless steel sheets and press-braked stainless steel sections. In addition to residual stresses, the deviation of the cross-sectional geometry, which is attributed to the press-brake size, is also addressed in this chapter.

Before proceeding further, it should be noted that the same terminology adopted in Chapter 4 in referring to stresses in various directions is also used in this chapter. It should also be noted that, in the manufacturing process of a press-braked lipped channel section (see Figure 1.2 in Chapter 1), the outer surface of a coiled sheet becomes the inner surface of the lipped channel section produced from the sheet.

8.2 CARBON STEEL SECTIONS

8.2.1 Effect of coiling curvature

8.2.1.1 Before press braking

Before press braking, residual stresses already exist in steel sheets and are due to the coiling-uncoiling process. As seen from the formulation of the analytical solution presented in Chapter 4, residual stresses in carbon steel sheets resulting from the

coiling-uncoiling process depend on the coiling curvature (or coil radius r), so in this section, the effect of the coiling curvature on residual stresses is explored for coil radii r ranging from 200 mm to 700 mm for carbon steel sheets of 2 mm in thickness. The closed-form analytical solution presented in Section 4.4 of Chapter 4 was employed for the investigation presented in this section. The carbon steel was assumed to have the following properties: elastic modulus E = 200 GPa and Poisson's ratio ν = 0.3, except that three different yield stresses are considered in this section (σ_y = 250, 350 and 450 MPa). The range of radii was chosen to cover the lower values of a practical range as a coil radius greater than 781 mm will not lead to any residual stresses.

Figure 8.1 shows that the magnitudes of residual stresses and the sizes of affected zones are quite sensitive to the coiling curvature. It is of interest to note that the coiling curvature limit κ_{cy}, which signifies the onset of yielding on sheet surfaces, depends on the material properties and the sheet thickness (refer to Eq. (4.14)). The uncoiling curvature limit κ_{uy}, which signifies the onset of reverse yielding, depends not only on the material properties, but also on the bending history and the through-thickness location concerned (refer to Eq. (4.37)). Although the value of κ_{uy} depends on the bending history, which is related to the applied coiling curvature κ_c, a change of the r/t ratio from 100 to 350 leads only to a change of $|\kappa_{uy}|$ value on the sheet surfaces from 0.00250 to 0.00256 mm^{-1} for yield stress σ_y = 250 MPa. This change in κ_{uy}, which is greater than changes elsewhere across the thickness, is less than 3%. This indicates that the uncoiling curvature limit κ_{uy} at which the carbon steel starts to experience reverse yielding is not sensitive to the applied coiling curvature κ_c.

As shown in Figure 8.1 (also see Table 8.1), as the r/t ratio decreases, the maximum surface residual stresses initially increase rapidly until the r/t ratio is small enough for reverse yielding to occur during uncoiling. With further decreases in the r/t ratio, the maximum surface residual stresses become stable as required by the von Mises yield criterion, but the residual stress zones continuously expand. The total thickness of the two residual stress zones referred to in Table 8.1 is given by $\left(t-2y_{cy}\right)$, where y_{cy} is half the thickness of the central elastic core.

Table 9.1 summarizes the magnitudes of maximum surface residual stresses and the total thickness of the residual stress zones. In addition to the r/t ratio, the effect of yield strength is also illustrated in Table 8.1, where results for three different yield stresses (σ_y = 250, 350 and 450 MPa) are shown. As expected, as the r/t ratio and the yield stress increase, the residual stresses reduce in both value and extent. At r/t =100, more than half of the sheet thickness experiences plastic bending and develops residual stresses for all three yield strengths. On the other hand, at r/t =350, residual stresses are only induced when the yield stress is 250 MPa, and these residual stresses are small. Obviously, at high values of both the r/t ratio and the yield strength σ_y, the coiling curvature $\kappa_c < \kappa_{cy}$ and no plastic bending is involved.

8.2.1.2 After press braking

After press braking, different amounts of residual stresses exist in different parts of a press-braked section, and results from both the coiling-uncoiling process and the

press-braking process. In this section, the effect of the coiling curvature (or the coil diameter) on residual stresses in a press-braked carbon steel channel section is investigated. The finite element-based method illustrated in Chapter 5 was adopted to simulate the manufacturing process, in which the effect of the coiling-uncoiling process was accounted for using the closed-form analytical solution presented in Section 4.4. The carbon steel section was assumed to possess the same material properties, cross-sectional geometry and thickness (see Table 5.1 and Figure 5.1(b)) as the press-braked carbon steel channel, specimen PBC14, tested by Weng and Peköz (1990).

Residual stresses in the flat portions and corner regions of the press-braked carbon steel channel were determined for three different values of coil diameter-to-thickness ratio (D/t = 200, 500 and 800). The results are shown in Figure 8.2. It can be observed that the coil diameter does not affect residual stress distributions across the thickness in the corner, but it does influence those in the flat portions. When the coil diameter-to-thickness ratio (D/t) is equal to 800, no residual stresses arise in the flat portions during the coiling-uncoiling process, because in this case the coiling curvature κ_c is less than the limit value κ_{cy} which signifies the onset of yielding on sheet surfaces. When the D/t ratio is reduced to 200, the magnitudes of the longitudinal and transverse residual stresses in the flat portions reach approximately $1.0\sigma_y$ and $0.1\sigma_y$ respectively. The residual stresses in the flat portions also have a layering profile across the thickness. Based on these results, it may be concluded that the different residual stresses in flat portions of otherwise identical cold-formed sections reported in the literature are due to differences in the coiling curvature and that these differences are responsible for the significant scatter in experimental load-

carrying capacities of cold-formed sections. This is an important aspect worthy of further attention in the future.

The residual stresses at the mid-web section of the carbon steel channel before and after press braking are compared in Figure 8.3. It is seen that the residual stresses in the flat portions are independent of the braking process, except small areas adjacent to the corners (see Figures 5.9 and 5.10). This observation provides a simple method for the modelling of residual stresses in the flat portions of a press-braked section: the residual stresses in the flat portions can be taken to be identical to those in an uncoiled steel strip before press braking.

8.2.2 Effect of die size

The dimensions of the die and punch can affect the location and extent of contact areas between the steel sheet and the press-brake device, and consequently affect the direction and amount of the elastic spring-back of the cross section after press braking. To form a 90° bent corner of a press-braked section, the basic geometrical requirement on the die opening W_d (see Figure 8.4) is

$$W_d \geq \sqrt{2}(R+t) \cong 1.414(R+t) \tag{9.1}$$

where R is the bending radius of the corner, and t is the sheet thickness. For the finite element simulation presented in Chapter 5, the die opening and the radius of the die support was taken as $W_d = 2.5(R+t)$, and $R_d = R$ respectively. The width of the

punch W_p was kept to be a bit greater than the die opening W_d and was taken as $W_p = W_d + 2R_d(1-\cos 45°)$.

In order to explore the effect of die size on the final cross-sectional geometry, the numerical press braking of the carbon steel channel section presented in the preceding subsection was carried out for different values of the $W_d/(R+t)$ ratio with the values of R and t kept constant. Since the sectional deviations from the nominal cross-sectional geometry can be characterized by the quantities D_{lip}, $D_{f\lg}$ and D_{web} as shown in Figure 8.5(a), those quantities were monitored against the $W_d/(R+t)$ ratio for a wide range of coil diameters.

From Figure 8.5, it can be seen that the normalized deviation of the flange $D_{f\lg}/t$ is generally larger than the other two sectional deviations. The value of the $D_{f\lg}/t$ ratio can increase up to about 6.0 for D/t = 200, when the $W_d/(R+t)$ ratio reduces to the limit value $\sqrt{2}$ (≅ 1.414). Obviously, the effect of the die size on the deviations D_{lip} and $D_{f\lg}$ has overridden the influence of the coiling curvature for small values of the $W_d/(R+t)$ ratio, while the deviation of the web D_{web} is more dependent on the coiling curvature than on the $W_d/(R+t)$ ratio. In general, as the $W_d/(R+t)$ ratio increases, all the sectional deviations decrease rapidly until the value of the $W_d/(R+t)$ ratio reaches about 2.0. When the $W_d/(R+t)$ ratio increases further, the sectional deviations decline gently and the amounts of these deviations become more dependent on the coiling curvature. It should be noted that an excessive value of the

$W_d/(R+t)$ ratio is not practical, since the width of a steel strip can no longer span over the two supports of the die when a small lip of a channel section is to be formed.

The contrast between the rapid increase of sectional deviations at small values of the $W_d/(R+t)$ ratio and the gentle decline of these deviations at large $W_d/(R+t)$ ratios is due to the different deformation modes experienced by the sheet bent at different $W_d/(R+t)$ ratios. It can be understood by observing the span action of the sheet in the die and the location of the contact between the sheet and the die/punch during the deformation process. Figures 8.6 and 8.7 indicate the positions of loading points due to the contact between the sheet and the press-brake device, and show the change of their contract locations during the deformation caused by press braking. Since the positions of loading points can be clearly reflected by the longitudinal stress contour; the deformed strip on the die is shown together with the stress contour in these two figures, in order to visualize the interaction between the strip and the die/punch.

For a small value of the $W_d/(R+t)$ ratio (i.e. $\sqrt{2}$), a 3-point bending happens at the beginning of the corner braking (see Figures 8.6). As the deformation progresses, the mid-point of the strip separates from the punch pole, and results in the 4-point bending. The two contact points between the strip and the punch move away from the punch pole, while the other two contact points between the strip and die get closer to each other until the end of corner braking. For a large $W_d/(R+t)$ ratio (i.e. 5.0), a 3-point bending also happens at the beginning and the contact area extends as deformation progresses (see Figures 8.7). As the mid-point of the strip separates from the punch pole, the side ends of the punch contact with the strip and this lead to the reverse bending adjacent to the corner (refer to step (c) in Figure 8.7). Such reverse

bending causes negative spring-back after the punch is released. When the $W_d/(R+t)$ ratio is small, the reverse bending is unlikely to occur through the contact between the strip and the side ends of the punch, and thus the size of the punch does not affect sectional deviations in this case. Therefore, the punch width may influence sectional deviations, only when the $W_d/(R+t)$ ratio becomes larger.

Generally speaking, a smaller $W_d/(R+t)$ ratio causes plastic bending over smaller area around the corner, and thus results in a larger deviation in the cross-sectional geometry. Nevertheless, in practice, sectional deviations are not allowed to have excessive magnitudes and should be limited by fabrication tolerances, such as those specified by the Metal Building Manufacturers Association (MBMA). According to MBMA, angular tolerances for the flange and the lip of a lipped channel section are: $|\theta_1| \leq 3°$ and $|\theta_2| \leq = 5°$ respectively (Yu 2000). These angular tolerances can be related to the sectional deviations by the following approximation:

$$\theta_1 \cong \tan^{-1}\left(D_{f\lg}/b\right) \quad \text{and} \quad \theta_2 \cong \tan^{-1}\left(D_{lip}/c\right) \tag{9.2}$$

in which b and c are the overall dimensions of the flange and the lip respectively.

From Eq. (9.2) and these angular tolerances, it can be found that the magnitudes of the deviations $D_{f\lg}$ and D_{lip} for a channel section should be limited by $1.20t$ and $0.75t$ respectively. By mapping these two upper bound values of $D_{f\lg}$ and D_{lip} on Figure 8.5, the minimum allowable value of the $W_d/(R+t)$ ratio can be found and varies approximately from 1.75 to 2.0 depending on the D/t ratio. This minimum allowable

$W_d/(R+t)$ ratio would be used as a guide to control the dimensions of the press-brake device, in order to limit the cross-sectional deviations within fabrication tolerances.

The sectional deviations D_{web}, $D_{f\lg}$ and D_{lip} may serve as the initial sectional imperfection which remains uniform throughout the length of the press-braked member. Nevertheless, the structural behaviour of the press-braked member would not be significantly affected by these uniform sectional deviations. It is because the structural behaviour of cold-formed members is sensitive to the sectional imperfection differentially varying along the length, rather than to this uniform sectional imperfection. Moreover, the magnitudes of these uniform sectional deviations of a cold-formed section are limited by the fabrication tolerance. Thus their effect on the structural behaviour is also very limited. It should be noted that additional sectional distortion may happen locally at the ends of the cold-formed member, as a result of the stress release near the ends of the member. The magnitude of this additional local distortion should be dependent on the amount of residual stresses released.

The effect of the press-bake size on residual stresses is also concerned in this chapter. Figure 8.8 shows that the die size has negligible effect on the longitudinal and transverse residual stresses in the corner. On the other hand, as already indicated in the preceding subsection (see Figure 8.3), the press-braking operation does not affect residual stresses in the flat portions except for a small area adjacent to the corner where the reverse bending and local contact have taken place. Therefore, the press-brake size has only negligible effect on the residual stresses in press-braked sections.

8.3 STAINLESS STEEL SECTIONS

8.3.1 Effect of coiling curvature

8.3.1.1 Before press braking

Before press braking, residual stresses in stainless steel sheets are derived from the coiling-uncoiling process. The effect of coiling curvature on residual stresses is explored for coil radii r ranging from 200 mm to 700 mm for stainless steel sheets of 2 mm in thickness. The range of radii r was chosen to cover the lower values of a practical range as a coil radius greater than 700 mm will generally lead to negligible amount of residual stresses.

The effect of mechanical properties is also investigated, but the effect of material anisotropy has been ignored in the study presented in this section. The analytical solution presented in Section 4.7 of Chapter 4 was employed for this study. Since the normalized residual stresses $\sigma_{z,r}/\sigma_{0.2}$ and $\sigma_{x,r}/\sigma_{0.2}$ have been found to be dependent on only two non-dimensional parameters ($e = \sigma_{0.2}/E_0$ and n) rather than all three Ramberg-Osgood parameters (E_0, $\sigma_{0.2}$ and n), different values of the non-dimensional 0.2% proof stress e (0.001, 0.002 and 0.003) and the parameter n (3, 5, and 10) are considered. Poisson's ratio ν was assumed to be 0.3 for all the cases. To account for the effect of the parameter n, the general expression of the ultimate stress σ_u^{ten} given by Eq. (3.13b) (refer to Chapter 3) was employed in this section.

Table 9.2 summarizes the predicted magnitudes of maximum surface residual stresses in terms of the 0.2% proof stress $\sigma_{0.2}$. The effects of both the r/t ratio and mechanical properties are illustrated in Table 8.2, where results for all the combinations of the non-dimensional parameters e and n are shown. As expected, the residual stresses reduce as the values of the r/t ratio, e and n increase. However, it can be found that the magnitudes of the residual stresses are quite sensitive to the coiling curvature and the non-dimensional 0.2 % proof stress e, but the effect of the parameter n is relatively small.

The magnitude and extent of residual stresses depends on the size of a zone, near each sheet surface, subjected to reverse yielding during uncoiling. It is of interest to note that the uncoiling curvature limit κ_{uy}, which signifies the onset of reverse yielding, depends not only on the material properties, but also on the bending history and the through-thickness location concerned (refer to Eq. (4.37)). The uncoiling curvature limit κ_{uy} is found to be more sensitive to the applied coiling curvature κ_c and the non-dimensional 0.2% proof stress e, than to the parameter n. For instance, with the same value of n equal to 3, a change of the r/t ratio from 100 to 350 can lead to a change of $|\kappa_{uy}|$ value on the sheet surfaces from 0.00232 to 0.00147 mm^{-1} for the alloy with a lower value of e equal to 0.001, and a change from 0.00618 to 0.00258 mm^{-1} for the alloy with a higher value of e equal to 0.003. These changes in κ_{uy}, which are less than changes elsewhere across the thickness, are already about 37% and 58% for e = 0.001 and 0.003 respectively. However, with the same value of e equal to 0.001, a change of n value from 3 to 10 leads to only 9% change of the κ_{uy}

value on the sheet surfaces at a low r/t ratio of 100 and 22% change at a high r/t ratio of 350.

Figure 8.9 shows the influence of the r/t ratio for the stainless steel sheet with mechanical properties of (e = 0.001, n = 3). It can be seen that both the magnitude and extent of residual stresses increase as the coiling curvature increases. As the r/t ratio decreases, the maximum surface residual stresses initially increase rapidly until the r/t ratio is small enough for reverse yielding to occur during uncoiling. With further decreases in the r/t ratio, the surface residual stresses develop gradually, two residual stress zones continuously expand, and each zone occupies half the sheet thickness. For stainless steel alloys with high non-dimensional 0.2 % proof stresses e, it is likely to have $\kappa_{uy} > \kappa_c$ on the sheet surfaces, and so reverse yielding will not occur in such case.

8.3.1.2 After press braking

In this section, the effect of the coiling curvature on residual stresses in a press-braked austenitic stainless steel section and a press-braked duplex stainless steel section is investigated. Both stainless steel sections were assumed to possess the same cross-sectional geometry (see Table 5.1 and Figure 5.2(a)) as the press-braked channel section, specimen PBC14, tested by Weng and Peköz (1990), but different virgin material properties. The finite element-based method illustrated in Chapter 5 was again adopted to simulate the manufacturing process, in which the effect of the coiling-uncoiling process is accounted for using the analytical solution given in

Section 4.7 for the austenitic stainless steel sheet and the analytical solution presented in Section 7.2 for the duplex stainless steel sheet.

Austenitic grade 304 alloy (equivalent to grade UNS30400 in accordance with ASTM E527-83 (ASTM 2003)) was assumed to be the virgin material of the austenitic stainless steel section, possessing the following mechanical properties for longitudinal tension given in Appendix B of AS/NZS 4673 Standard (AS/NZS 2001): 0.2% proof stress $\sigma_{0.2}$ = 205.0 MPa, initial elastic modulus E_0 = 195.0 GPa, exponent n = 7.5 and Poisson's ratio ν = 0.3. The stress-strain curve of the material was defined by the 3-stage full-range stress-strain model (see Eq. (3.6) in Chapter 3). The material anisotropy for the austenitic grade 304 alloy is negligible and thus has not been considered for this stainless steel grade.

The duplex stainless steel section was assumed to possess the same virgin material properties as the duplex stainless steel plate (grade UNS31803) tested by Rasmussen *et al.* (2003) as shown in Table 7.1 in Chapter 7. Moreover, the anisotropic material properties based on the compression coupons (LC, TC and DC) were assumed. Again, the 3-stage full-range stress-strain model (see Eq. (3.6)) was used to describe the stress-strain curve in the longitudinal direction.

The residual stresses in the flat portions and corner regions of both stainless steel sections were determined for three different values of coil diameter-to-thickness ratio (D/t = 200, 500 and 800). The results are shown in Figures 8.10 and 8.11. It can be seen that, for both stainless steel sections, the coiling curvature does not affect the residual stresses in the corners, but it does influence those in the flat portions. Based

on the results shown in Figures 8.10 and 8.11, it can also be concluded that, different residual stresses in the flat portions of otherwise identical cold-formed stainless steel sections are resulted from differences in the coiling curvature. The same observation and conclusion have also been made on the carbon steel section studied in the preceding section.

In the corner region, the through-thickness variations of residual stresses for both stainless steel sections are quite similar to that for the carbon steel section (see Figure 8.2), except for the location of the maximum longitudinal tensile residual stress. While the maximum longitudinal tensile residual stress in the corner of the carbon steel section is near the middle surface (see Figure 8.2), the longitudinal tensile residual stresses in the corners of both stainless steel sections are fairly uniform across the outer half of the thickness (see Figures 8.10(a) and 8.11(a)).

Although both stainless steel sections have the similar through-thickness variations of residual stresses in corners, the normalized magnitudes of the residual stresses in the corner of the duplex stainless steel section are generally greater than those in the corner of the austenitic stainless steel section. For residual stresses in the mostly concerned direction which is the longitudinal direction, the maximum longitudinal compressive residual stress in the corner, which is found near the quarter surface of the plate, are equal to $0.84\sigma_{0.2}$ ($\sigma_{0.2}$ is the 0.2% proof stress) for the austenitic section and $1.08\sigma_{0L}$ (σ_{0L} is the 0.2% proof stress for longitudinal compression) for the duplex section. The longitudinal tensile residual stress across the outer half of the corner thickness is approximately equal to $0.4\sigma_{0.2}$ for the austenitic section and $0.5\sigma_{0L}$ for the duplex section (see Figures 8.10(a) and 8.11(a)).

Residual stresses in the flat portion can also be studied from Figures 8.10 and 8.11. It is observed that the magnitudes of transverse residual stresses in the flat portion become negligible as a result of transverse spring-back, but longitudinal residual stresses in the flat portion can have considerable magnitudes depending on the coiling curvature. Under the same coiling curvature (e.g. $D/t = 200$), longitudinal residual stresses in the flat portion of the austenitic section generally have greater normalized magnitudes and greater extent than those in the flat portion of the duplex section. It is due to the fact that the virgin material of the austenitic section has smaller 0.2% proof stress than that of the duplex section, and hence it causes greater extent of residual stresses throughout the thickness of the uncoiled austenitic sheet when the sheet is subjected to reverse yielding during uncoiling.

If an uncoiled sheet has more through-thickness material points subjected to reverse yielding during uncoiling, the greater extent of residual stresses can be found in the flat portions of a press-braked section produced from the sheet. For example, at $D/t = 200$, there are a large amount of material points across more than half of the thickness subjected to reverse yielding in the uncoiled austenitic sheet, but there is no reverse yielding taking place in the uncoiled duplex sheet during uncoiling. Therefore, the normalized magnitudes and extent of residual stress in the flat portions of the austenitic section are greater than those in the flat portions of the duplex section.

This nature of residual stresses in flat portions can be further understood by the relation between reverse yielding and virgin material properties. Reverse yielding of a material point will occur, only when the magnitude of uncoiling curvature κ_u (which

is equal to the coiling curvature κ_c in magnitude, but opposite in sign) is greater than the uncoiling curvature limit κ_{uy} corresponding to this material point (refer to Chapters 4 and 7). The magnitude of the uncoiling curvature limit κ_{uy} increases as the 0.2% proof stress of the sheet material increases. As a result, it becomes more difficult for a sheet with a higher 0.2% proof stress to experience reverse yielding during uncoiling.

8.3.2 Effect of material behaviour of stainless steel

8.3.2.1 Before press braking

Residual stresses in stainless steel sheets before press braking are due to the coiling-uncoiling process. Their development is dependent on the applied coiling curvature and material properties. Material anisotropy, nonlinear strain-hardening capability, and different stress-strain relationships in tension and compression characterize the material behaviour of stainless steel alloys. In this section, the effect of material anisotropy is explored through the comparison of the results obtained from four different material models (two models for tension, two models for compression):

(1) isotropic nonlinearly hardening model for longitudinal tension (LT),

(2) isotropic nonlinearly hardening model for longitudinal compression (LC),

(3) anisotropic nonlinearly hardening model for tension (LT, TT, DT), and

(4) anisotropic nonlinearly hardening model for compression (LC, TC, DC).

The material properties of the duplex plate (grade UNS31803 alloy) tested by Rasmussen *et al*. (2003) were adopted for this investigation (see Table 7.1). The 3-stage full-range stress-strain model (see Eq. (3.6)) was used to describe the stress-strain relationship in the longitudinal direction, and the coil radius r of 100 mm and sheet thickness of 2 mm were assumed. For these anisotropic material models, the through-thickness initial yield stress σ_{0N} was approximated by the diagonal 0.2% proof stress σ_{0D} (see Eq. (7.48)). As the major straining in the coiled stainless steel sheet is the bending of the sheet in longitudinal direction, isotropic material models for both transverse tension and compression are not considered in this study. The results presented in this section were predicted by the analytical solution presented in Section 4.7 for the isotropic material models (i.e. LT and LC), and the analytical solutions developed in Section 7.2 for the anisotropic material models (i.e. (LT, TT, DT) and (LC, TC, DC)).

In order to show the whole picture about the effect of material anisotropy, in addition to residual stresses, equivalent plastic strains are also addressed. The residual stresses and equivalent plastic strains calculated for these four different material models are shown in Figures 8.12 and 8.13 respectively. The results of residual stresses are normalized by the uniaxial 0.2% proof stress σ_{0LC} for longitudinal compression, in which the subscript LC is especially used in this investigation to refer to as longitudinal compression.

As shown in Figures 8.12 and 8.13, if material anisotropy is not taken into account, the difference in the mechanical properties between longitudinal tension (LT) and longitudinal compression (LC) can only cause minor effect on the predictions of

residual stresses and equivalent plastic strains. The difference in residual stresses between the isotropic tension material model (LT) and the isotropic compression material model (LC) is generally around 10%, and the difference in equivalent plastic strains between these two isotropic material models is even less than 4%.

If material anisotropy is taken into account, the difference in the anisotropic material properties between tension (LT, TT, DT) and compression (LC, TC, DC) can cause more pronounced effect on the results. The difference in total residual stresses between the anisotropic tension (LT, TT, DT) and compression (LC, TC, DC) material models is more than 100% and the difference in total equivalent plastic strains between these two anisotropic material models is up to 17%.

By comparing the results for the anisotropic tension material model (LT, TT, DT) with those for the isotropic tension material model (LT), it can be found that the material anisotropy for tension has small effect on the predictions of residual stresses, with the maximum discrepancies normally occurring on the sheet surface and varying from about 3% to 9% (Figure 8.12). The effect of material anisotropy for tension on total equivalent plastic strains predicted is even small to become negligible. A small difference in the results between the isotropic tension material model (LT) and the anisotropic tension material model (LT, TT, DT) suggests that the effect of material anisotropy may be ignored in modelling the duplex stainless steel plates in tension.

The effect of material anisotropy on residual stresses is more obvious for the compressive material behaviour (i.e. (LC, TC, DC) and (LC)). The maximum discrepancies due to the material anisotropy for compression are found either on the

sheet surfaces or near the quarter surfaces of the sheet, and range from about 7% to 76% (see Figure 8.12). Although the material anisotropy for compression has obvious effect on residual stresses, it can only cause a limited effect on the total equivalent plastic strain for which the maximum difference of about 13% occurs on the sheet surfaces (see Figure 8.13). The clear difference in the results between the isotropic compression material model (LC) and the anisotropic compression material model (LC, TC, DC) suggests that it is necessary to consider the effect of material anisotropy in modelling the duplex stainless steel plates in compression.

The material anisotropy depends on the ratios among dimensionless anisotropic parameters $\overline{F}:\overline{G}:\overline{H}$ and the multiplication factor $3\left(\overline{F}+\overline{G}\right)/2\left(\overline{F}+\overline{G}+\overline{H}\right)$ which describes how the material anisotropy influences the slope of equivalent stress-equivalent plastic strain relation H' of a material (see Eq. (7.14)). As the factor $3\left(\overline{F}+\overline{G}\right)/2\left(\overline{F}+\overline{G}+\overline{H}\right)$ approaches to unit, the effect of material anisotropy becomes smaller. For isotropic materials, the multiplication factor is reduced to unit. For the duplex alloy used in this study, the factor $3\left(\overline{F}+\overline{G}\right)/2\left(\overline{F}+\overline{G}+\overline{H}\right)$ for the anisotropic tension material model (LT, TT, DT) is equal to 1.05, while the factor for the anisotropic compression material model (LC, TC, DC) is 1.21. It can be seen that the multiplication factor for the anisotropic tension material model is close to unit, and hence the effect of material anisotropy may be ignored in the modelling of the stainless steel plate in tension. By contrast, the multiplication factor for the anisotropic compression material model is greater than unit by about 20%, and the effect of material anisotropy should thus be considered in the modelling of the stainless steel plate in compression. Similarly, the effect of material anisotropy for

plates made of other stainless steel alloys can also be assessed by means of this multiplication factor

8.3.2.2 After press braking

In this section, the effect of material anisotropy on residual stresses in a press-braked duplex stainless steel section is explored through the comparison of the results based on four different material models: 1. LT; 2. LC; 3. (LT, TT, DT); and 4. (LC, TC, DC). The duplex stainless steel section was assumed to possess the same cross-sectional geometry (see Table 5.1 and Figure 5.2(a)) as specimen PBC14 tested by Weng and Peköz (1990), and the same virgin material properties as the duplex plate (grade UNS31803 alloy) tested by Rasmussen *et al*. (2003) as shown in Table 7.1. These four material models needed for the comparison were established based on the virgin material properties of the duplex grade UNS31803 alloy (see Table 7.1). The duplex stainless steel sheet for producing this duplex channel section was assumed to experience the coil diameter $D = 200t$ during the coiling-uncoiling process.

The finite element-based method illustrated in Chapter 5 was adopted to simulate the manufacturing process, in which the effect of the coiling-uncoiling process is account for using the analytical solution presented in Section 4.7 for the isotropic material models LT and LC and using the analytical solution presented in Section 7.2 for the anisotropic material models (LT, TT, DT) and (LC, TC, DC).

In addition to residual stresses, equivalent plastic strains are also addressed. Residual stresses and equivalent plastic strains in the duplex channel section were calculated

for these four different material models and they are shown in Figures 8.14 and 8.15 respectively. The results of residual stresses are normalized by the compressive 0.2% proof stress σ_{0LC} in the longitudinal direction, in which the subscript *LC* is especially used in this investigation to refer to as longitudinal compression.

In corner regions, the material anisotropy and the difference in mechanical properties between tension and compression have negligible effect on transverse residual stresses and equivalent plastic strains, but can cause significant influence on longitudinal residual stresses. As shown in Figure 8.14(a), the effect of material anisotropy on longitudinal residual stresses in the corner is remarkable. When the material anisotropy is not taken into account, the isotropic tension (LT) and compression (LC) material models provide nearly the same predictions of longitudinal residual stresses in the corner. If material anisotropy is taken into account, the difference in the anisotropic material properties between tension (LT, TT, DT) and compression (LC, TC, DC) can cause more pronounced effect on the predictions of longitudinal residual stresses in corners. The difference in longitudinal residual stresses between the anisotropic tension (LT, TT, DT) and compression (LC, TC, DC) material models can be greater than 100% .

In flat portions, the material anisotropy and the difference in mechanical properties between tension and compression have pronounced effect on transverse residual stresses. However, transverse residual stresses have negligible magnitudes as a result of the stress re-distribution due to the transverse spring-back. As shown in Figure 8.14(c), the effect of material anisotropy on longitudinal residual stresses in the flat portion is negligible, but the difference in mechanical properties between tension and

compression can cause greater effect. From Figure 8.15(b), it can be seen that the isotropic tension (LT) and compression (LC) material models as well as the anisotropic tension material model (LT, TT, DT) provide nearly the same prediction of equivalent plastic strains in the flat portions, while the anisotropic compression material model (LC, TC, DC) provides the prediction which is lower than those obtained from the other three material models.

Based on the results presented in this section, it can be concluded that material anisotropy causes greater effect on residual stresses in corner regions than those in flat portions. It has been observed that the material anisotropy has more pronounced effect on stresses perpendicular to the bending direction in which the press-braked section is cold-bent in the manufacturing process. That can be illustrated by the pronounced effect on the longitudinal residual stress in the corner region and the transverse residual stress in the flat portion, as a result of that the corner has been subjected to cold bending in the transverse direction due to press braking and the flat portion has been subjected to the preceding coiling and uncoiling in the longitudinal direction. Once again, these results further suggest that it is necessary to consider the effect of material anisotropy in the modelling of stainless steel plates in compression.

8.3.3 Effect of die size

As shown in Subsection 8.2.2 for the carbon steel section, the die size has negligible effect on the through-thickness variations of residual stresses in corners, but does influence the cross-sectional geometry. Hence, in this section, only its effect on the

cross-sectional geometries of stainless steel sections is considered. Additionally the effect of coiling curvature on cross-sectional deviations is also investigated.

Similar to Subsection 8.3.1.2, a press-braked austenitic stainless steel channel section and a press-braked duplex stainless steel channel section were studied. These two stainless steel section were assumed to possess the same nominal cross-sectional geometry (see Table 5.1 and Figure 5.2(a)) and the same material properties as the stainless steel sections presented in Subsection 8.3.1.2. Thus, the austenitic stainless steel section was assumed to possess the isotropic material properties and the duplex stainless steel section was assumed to posses the anisotropic material properties.

The numerical press braking of these stainless steel channel sections was carried out for different values of the $W_d/(R+t)$ ratio. Since sectional deviations from the nominal cross-sectional geometry can be characterized by the quantities D_{lip}, $D_{f\lg}$ and D_{web} as indicated in Figures 8.16(a) and 8.17(a), those quantities were monitored against the $W_d/(R+t)$ ratio for a wide range of coil diameters (i.e. D = $200t$, $500t$ and $800t$). The finite element-based method illustrated in Chapter 5 was adopted to simulate the manufacturing process, in which the effect of the coiling-uncoiling process is accounted for using the analytical solution given in Section 4.7 for the austenitic stainless steel sheet and the analytical solution presented in Section 7.2 for the duplex stainless steel sheet.

Numerical results for the austenitic channel section are plotted in Figure 8.16. For the austenitic section, the effect of the die size on the deviations D_{lip} and $D_{f\lg}$ has

overridden the influence of the coiling curvature for small value of the $W_d/(R+t)$ ratio. The deviation of the web D_{web} is more dependent on the coiling curvature than on the $W_d/(R+t)$ ratio. As the $W_d/(R+t)$ ratio increases, all the sectional deviations decrease rapidly until the value of $W_d/(R+t)$ ratio reaches about 2.0. When the $W_d/(R+t)$ ratio increases further, the effect of the die size becomes negligible, and the sectional deviations becomes near constants with their magnitudes depending on the coiling curvature.

Figure 8.17 shows the results for the duplex channel section. It can be seen that the effect of coiling curvature on sectional deviations is negligible. That is due to the high yield strength possessed by the duplex alloy. It causes a smaller amount of transverse residual stresses developed in the uncoiled duplex sheet, so that the amount of the transverse spring-back is greatly reduced. These sectional deviations are mainly affected by die size. Similar to the observation made on the carbon steel channel and the austenitic stainless steel channel, these sectional deviations decrease rapidly as the $W_d/(R+t)$ ratio increases, until the value of the $W_d/(R+t)$ ratio reaches about 2.0. When the $W_d/(R+t)$ ratio increases further, these sectional deviations start to decline in a more gent and linear manner.

In practice, sectional deviations should be limited by fabrication tolerances which are related to cross-sectional dimensions. Similar to the carbon steel channel studied in Subsection 8.2.2, by following the fabrication tolerances specified by the Metal Building Manufacturers Association (MBMA), the magnitudes of the deviations $D_{f\lg}$ and D_{lip} for both stainless steel channels are found to be limited by $1.20t$ and $0.75t$

respectively. By mapping these upper bound values of $D_{f\,\mathrm{lg}}$ and D_{lip} on the Figure 8.16, the minimum allowable value of the $W_d/(R+t)$ ratio for the austenitic channel section is found to vary approximately from 1.75 to 1.9 depending on the D/t ratio. By mapping the upper bound values of $D_{f\,\mathrm{lg}}$ and D_{lip} on the Figure 8.17, the minimum allowable $W_d/(R+t)$ ratio for the duplex channel section is found to be about 2.8. Again, this minimum allowable $W_d/(R+t)$ ratio would be used as a guide to control the dimensions of the press-brake device, in order to limit the cross-sectional deviations within the fabrication tolerances. Based on the results presented in this section, it may also be concluded that the cross-sectional distortion depends not only on the forming parameters, such as coiling curvature and press-brake size, but also on the mechanical properties of sheet materials.

8.4 CONCLUSIONS

A parametric study of residual stresses in press-braked carbon steel sections and stainless steel sections due to the manufacturing process have been presented. Residual stresses in press-braked sections were predicted by the finite element-based method in which the effect of coiling and uncoiling was accounted for analytically. The parameters of influence, such as the coiling curvature, press-brake size and material properties, have been studied for their effects on residual stresses. The effect of material anisotropy has also been illustrated for press-braked stainless steel sections. In addition to the concern of residual stresses, the cross-sectional distortion

due to press braking has also addressed in this chapter. Numerical results presented in this chapter allow the following conclusions to be made:

(a) The magnitude and extent of residual stresses in uncoiled sheets are sensitive to the coil radius and the basis material parameters, such as the yield stress for carbon steel sheets and the Ramberg-Osgood parameters ($e = \sigma_{0.2}/E_0$ and n) for stainless steel sheets.

(b) The distributions of residual stresses in flat portions are highly dependent on the initial coil diameter, so very different residual stresses can arise in the flat portions of otherwise identical cold-formed sections as a result of different initial coil diameters, which are unknown to designers and users of these sections. This may have been responsible for the significant scatter in test load capacities of cold-formed members.

(c) Residual stresses in the flat portions are independent of the press-braking operation, except small areas adjacent to the corners, and thus can be taken to be identical to those in an uncoiled steel strip before press braking.

(d) The effect of material anisotropy for stainless steel sheets can be assessed by means of the multiplication factor $3\left(\overline{F}+\overline{G}\right)/2\left(\overline{F}+\overline{G}+\overline{H}\right)$. As the factor approaches to unit, the effect of material anisotropy becomes smaller.

(e) Material anisotropy causes greater effect on residual stresses in the corner regions than those in the flat portions of a press-braked duplex stainless steel section. The material anisotropy has more pronounced effect on stresses perpendicular to the

bending direction in which the press-braked section is cold-bent in the manufacturing process. That can be illustrated by the pronounced effect on the longitudinal residual stress in the corner regions and the transverse residual stress in the flat portions.

(f) The cross-sectional distortion of a press-braked section due to the manufacturing process is dependent not only on the forming parameters, such as the coiling curvature and the press-brake size, but also on the mechanical properties of the sheet material. Such cross-sectional distortion may serve as the initial sectional imperfection which remains uniform throughout the length of the press-braked member. Nevertheless, this uniform sectional imperfection would not affect the structural behaviour of press-braked members significantly, as long as the cross-sectional deviations are limited by the fabrication tolerance.

(g) The minimum allowable $W_d/(R+t)$ ratio can be calculated for each sheet material and the practical range of coil diameters. It would be used as a guide to control the dimensions of the press-brake device, in order to limit cross-sectional deviations within fabrication tolerances.

8.5 REFERENCES

AS/NZS (2001). *Cold-Formed Stainless Steel Structures, AS/NZS 4673:2001,* Australian/New Zealand Standard, Standards Australia, Sydney.

ASTM (2003). *Standard Practice for Numbering Metals and Alloys (UNS), ASTM E527-83*, American Society for Testing and Materials, United States.

Rasmussen, K. J. R., Burns, T., Bezkorovainy, P. and Bambach, M. R. (2003). Numerical modelling of stainless steel plates in compression. *Journal of Constructional Steel Research*, **59**, 1345-1362.

Weng, C. C. and Peköz, T. (1990). Residual stresses in cold-formed steel members. *Journal of Structural Engineering, ASCE*, **116:6**, 1611-1625.

Yu, W. W. (2000). *Cold-Formed Steel Design*, 3rd. edition, John Wiley & Sons, United States.

Table 8.1 Effect of r/t ratio and yield strength on the magnitudes of maximum surface residual stresses and the size of residual stress zones.

r/t	σ_y (MPa)	Total thickness of residual stress zones over sheet thickness $(t-2y_{cy})/t$	Maximum $\sigma_{z,r}/\sigma_y$	Maximum $\sigma_{x,r}/\sigma_y$
100	250	0.74	1.153	0.522
	350	0.64	1.136	0.386
	450	0.54	1.095	0.230
150	250	0.62	1.127	0.347
	350	0.46	0.943	0.141
	450	0.31	0.485	0.056
200	250	0.49	1.047	0.163
	350	0.28	0.428	0.048
	450	0.08	0.091	0.007
250	250	0.36	0.612	0.077
	350	0.10	0.124	0.010
	450	N.A.*	N.A.	N.A.
300	250	0.23	0.326	0.033
	350	N.A.	N.A.	N.A.
	450	N.A.	N.A.	N.A.
350	250	0.10	0.124	0.010
	350	N.A.	N.A.	N.A.
	450	N.A.	N.A.	N.A.

* N.A.: No value is available, since no plastic bending is involved.

Table 8.2 Effect of r/t ratio and parameters (e, n) on the magnitudes of maximum surface residual stresses.

r/t	e	Maximum $\sigma_{z,r}/\sigma_{0.2}$			Maximum $\sigma_{x,r}/\sigma_{0.2}$		
		n = 3	n = 5	n = 10	n = 3	n = 5	n = 10
100	0.001	1.402	1.325	1.268	0.647	0.623	0.603
	0.002	1.259	1.211	1.172	0.268	0.284	0.296
	0.003	0.672	0.676	0.679	0.093	0.092	0.091
150	0.001	1.297	1.239	1.198	0.480	0.474	0.470
	0.002	0.770	0.744	0.718	0.117	0.107	0.099
	0.003	0.320	0.268	0.208	0.037	0.028	0.020
200	0.001	1.160	1.140	1.127	0.336	0.325	0.316
	0.002	0.473	0.412	0.345	0.063	0.050	0.038
	0.003	0.178	0.115	0.047	0.018	0.010	0.004
250	0.001	0.997	1.011	1.032	0.234	0.211	0.189
	0.002	0.315	0.239	0.155	0.038	0.025	0.014
	0.003	0.108	0.052	0.008	0.010	0.004	0.001
300	0.001	0.869	0.855	0.782	0.166	0.136	0.115
	0.002	0.221	0.143	0.061	0.025	0.013	0.005
	0.003	0.071	0.025	0.001	0.006	0.002	< 0.001
350	0.001	0.737	0.648	0.558	0.121	0.095	0.073
	0.002	0.161	0.087	0.020	0.017	0.007	0.001
	0.003	0.048	0.012	< 0.001	0.004	0.001	< 0.001

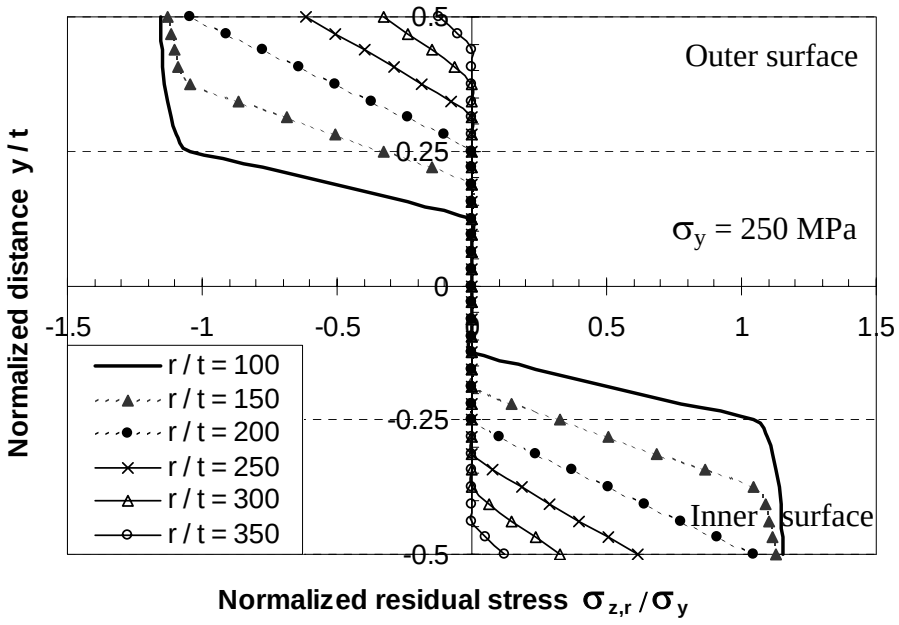

(a) Longitudinal residual stress

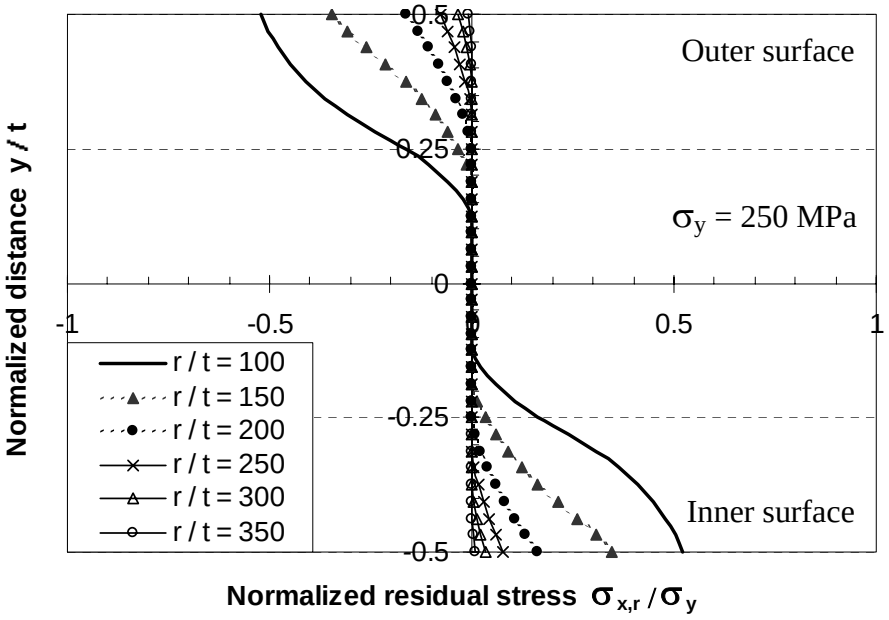

(b) Transverse residual stress

Figure 8.1 Through-thickness variations of residual stresses in a carbon steel sheet: effect of r/t ratio.

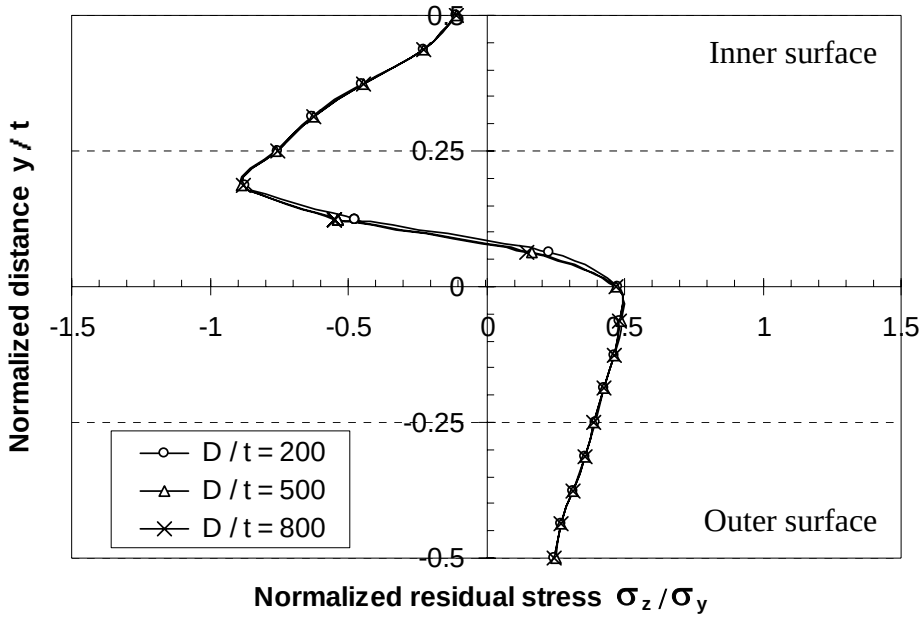

(a) Longitudinal residual stress at the centre of the lip-flange corner (section A-A in Figure 5.10)

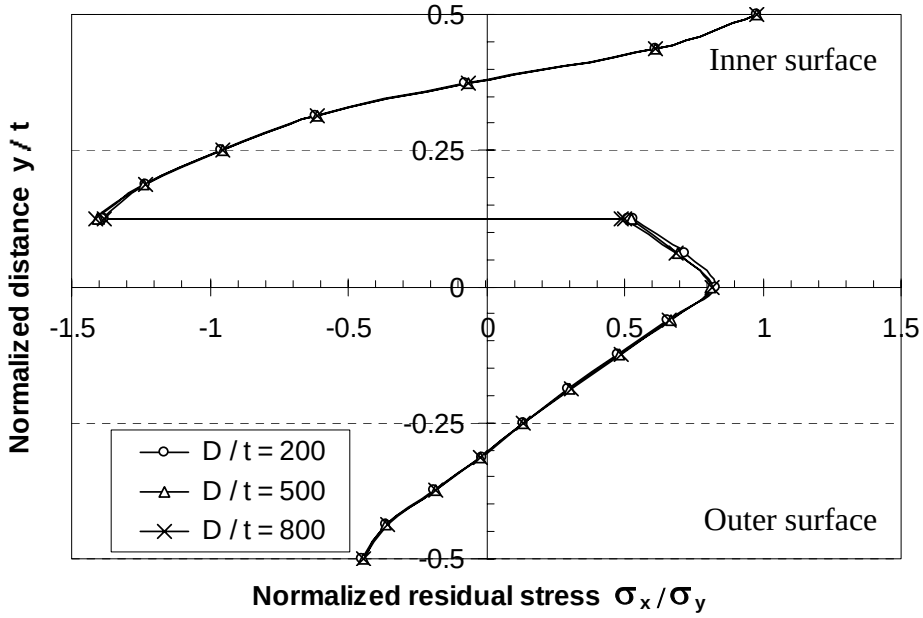

(b) Transverse residual stress at the centre of the lip-flange corner (section A-A in Figure 5.10)

Figure 8.2 Through-thickness variations of residual stresses in the carbon steel section: effect of coil diameter.

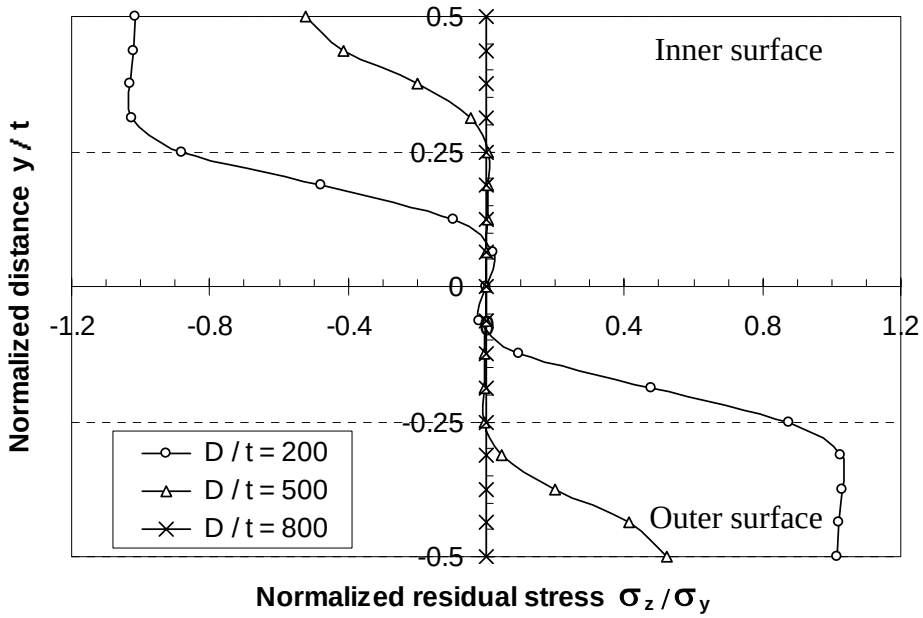

(c) Longitudinal residual stress at the mid-web section

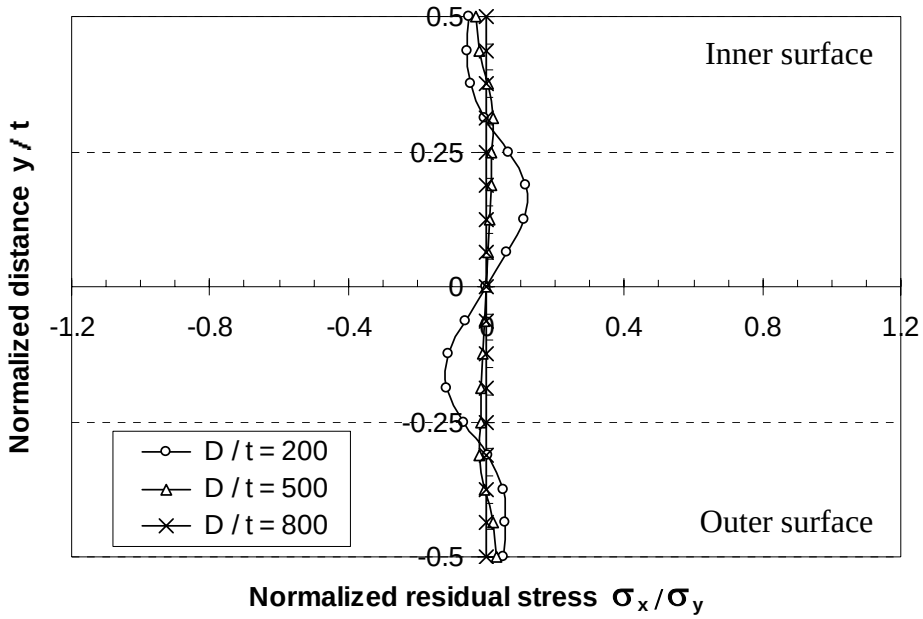

(d) Transverse residual stress at the mid-web section

Figure 8.2 Through-thickness variations of residual stresses in the carbon steel section: effect of coil diameter (continued).

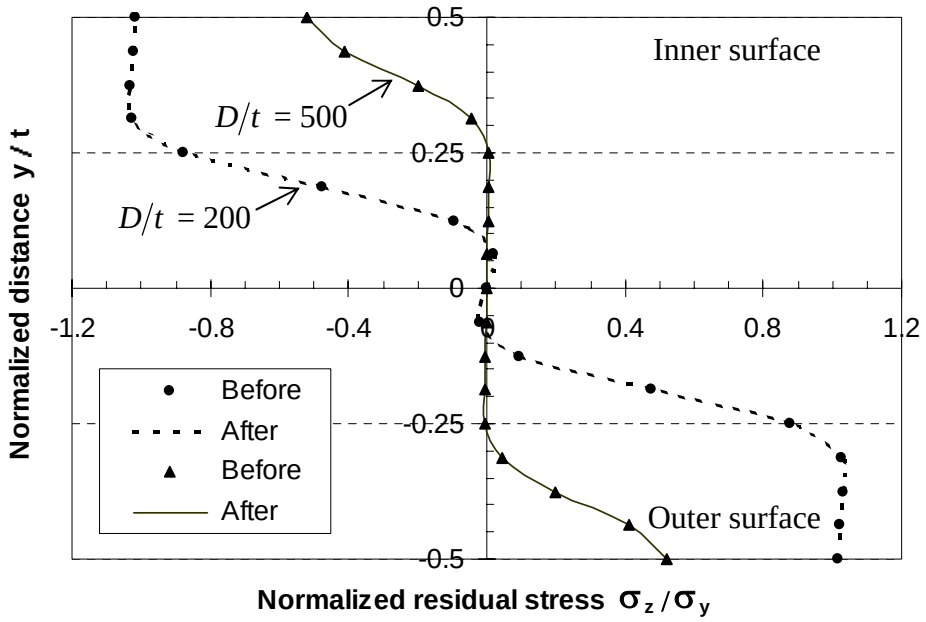

(a) Longitudinal residual stress

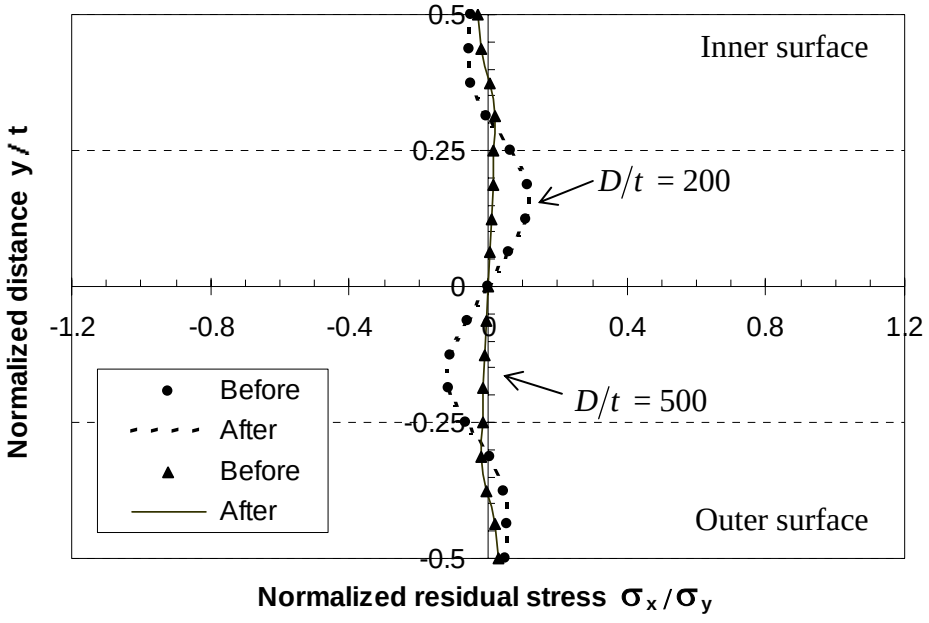

(b) Transverse residual stress

Figure 8.3 Residual stresses at the mid-web section of the carbon steel section before and after press braking.

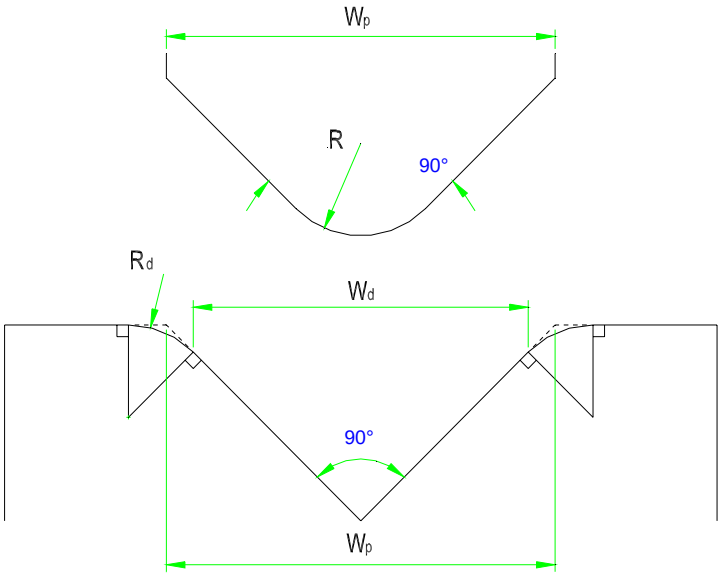

Figure 8.4 Dimensions of die and punch.

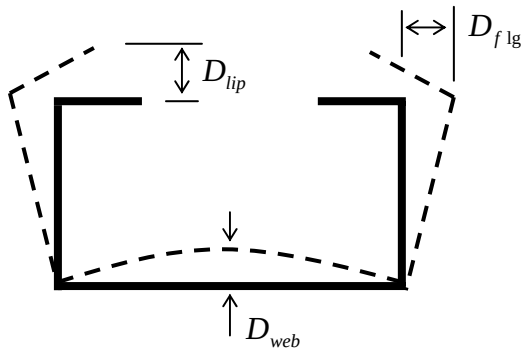

(a) Characterization of sectional derivations

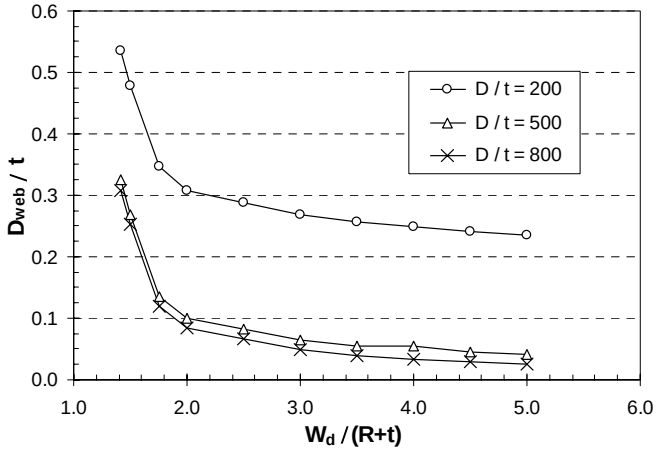

(b) Web

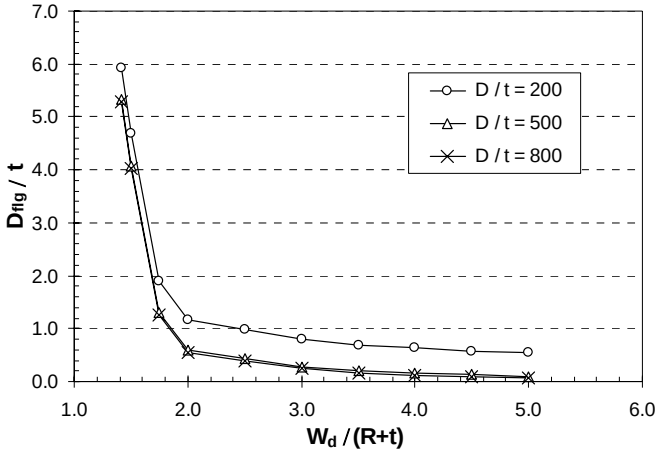

(c) Flange

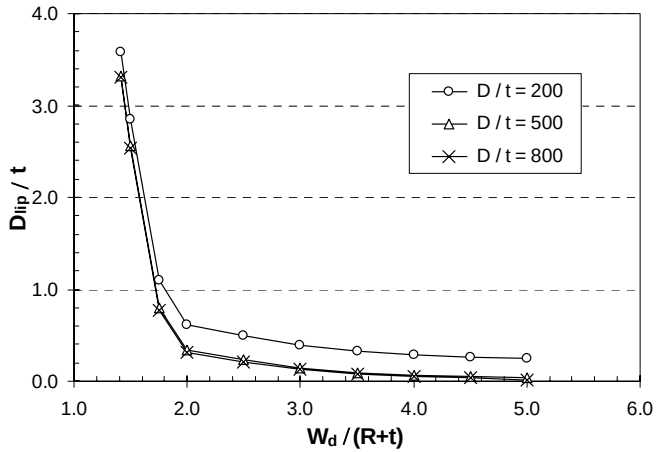

(d) Lip

Figure 8.5 Effect of die size and coiling curvature on cross-sectional deviations of the carbon steel section.

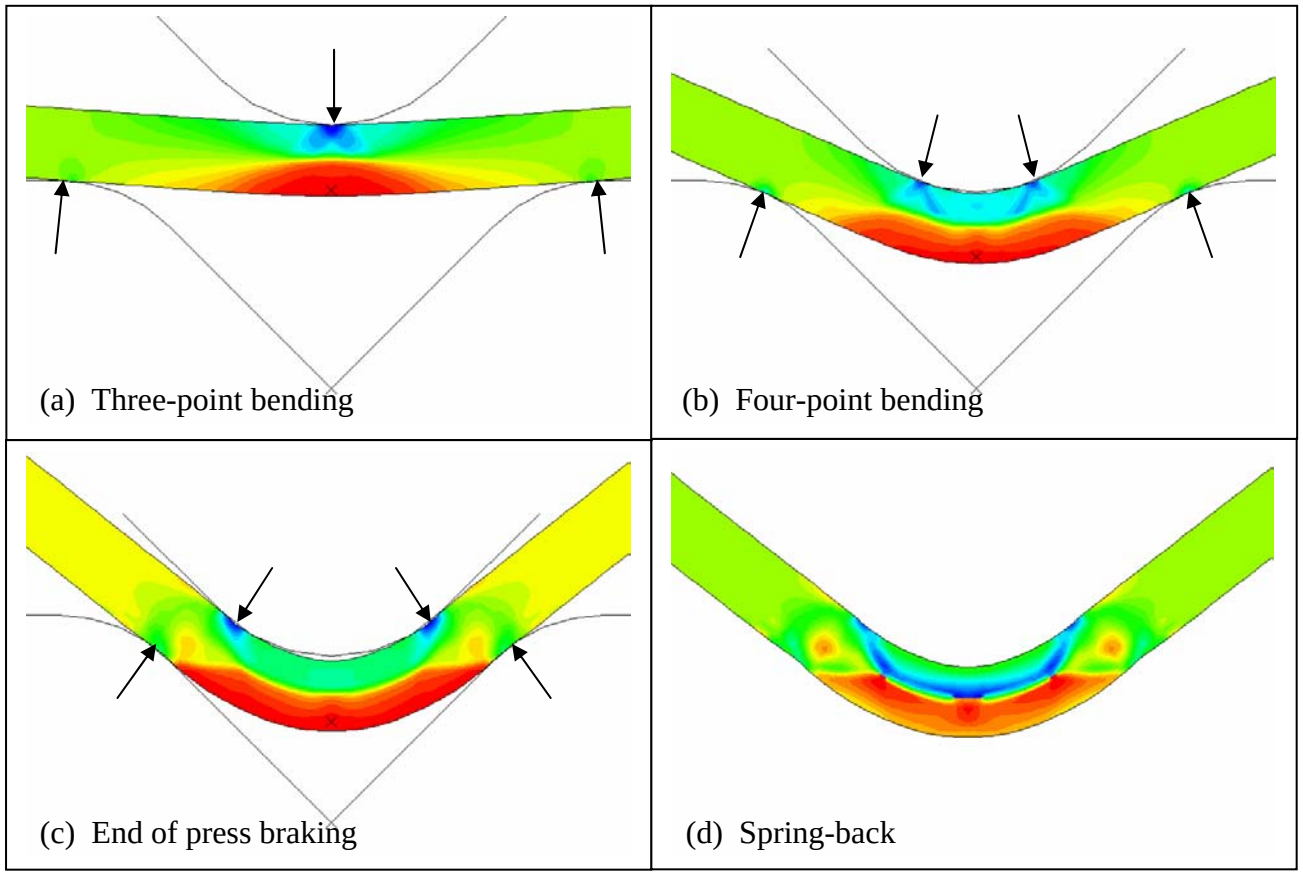

Figure 8.6 Deformation process and contact conditions of a 90° bent corner with a small die size ($W_d = \sqrt{2}(R+t)$).

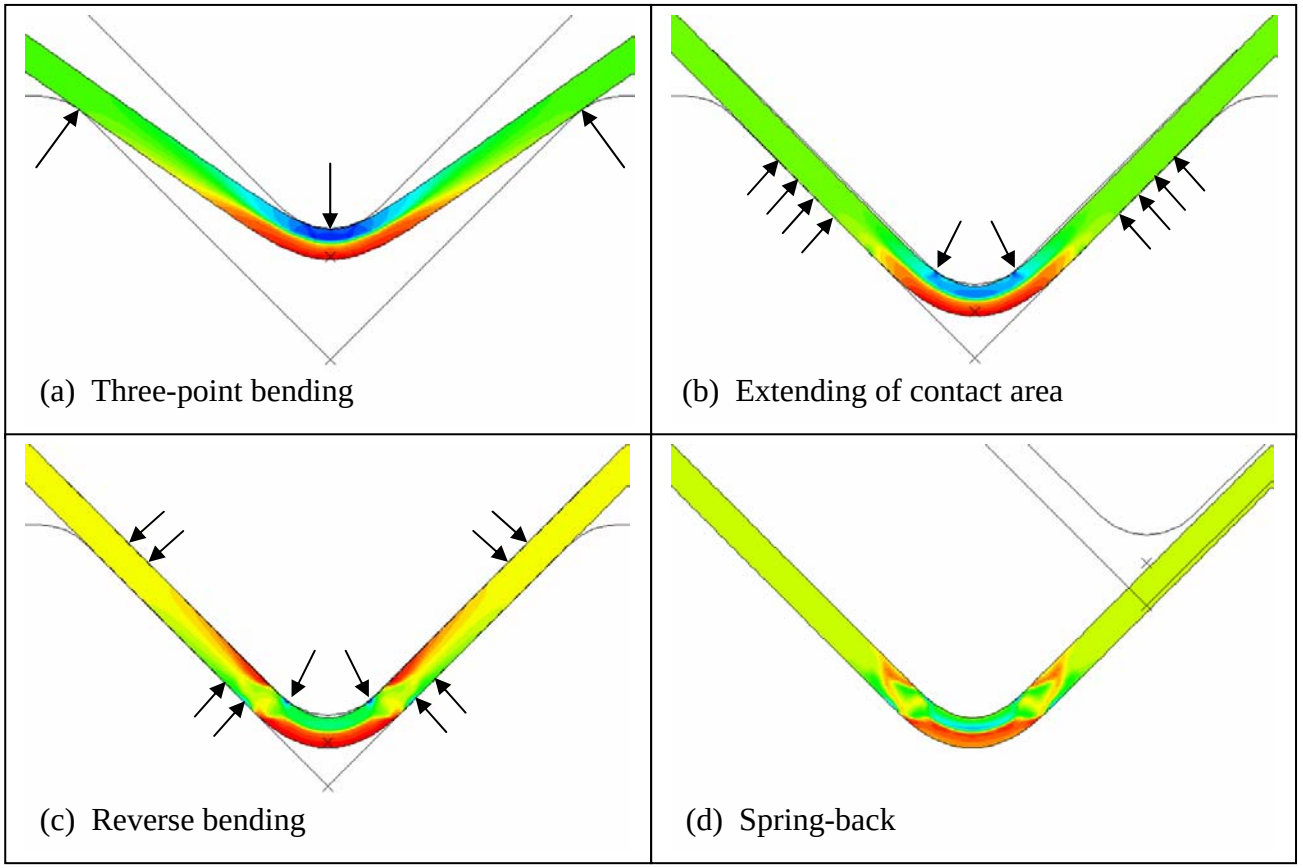

Figure 8.7 Deformation process and contact conditions of a 90° bent corner with a large die size ($W_d = 5(R+t)$).

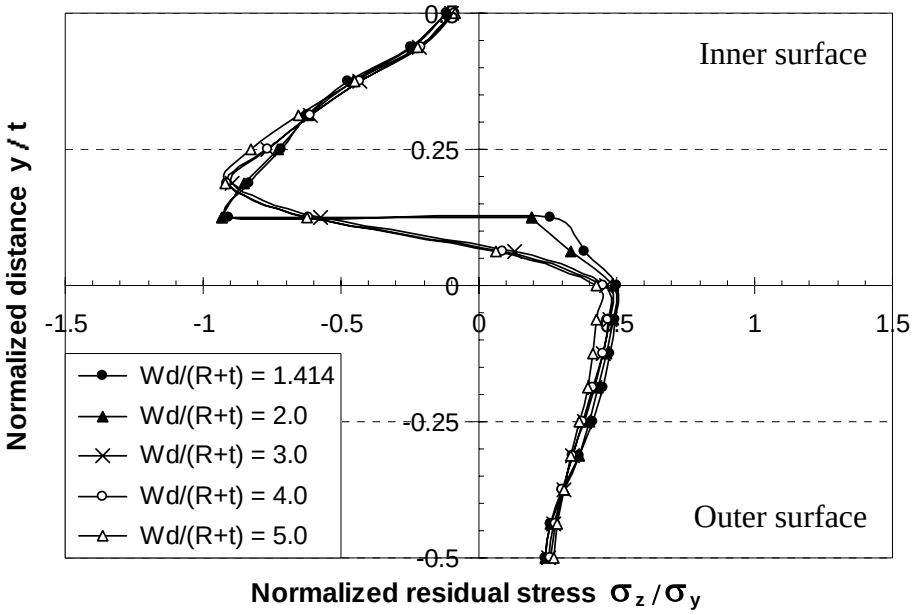

(a) Longitudinal residual stress (section A-A in Figure 5.10)

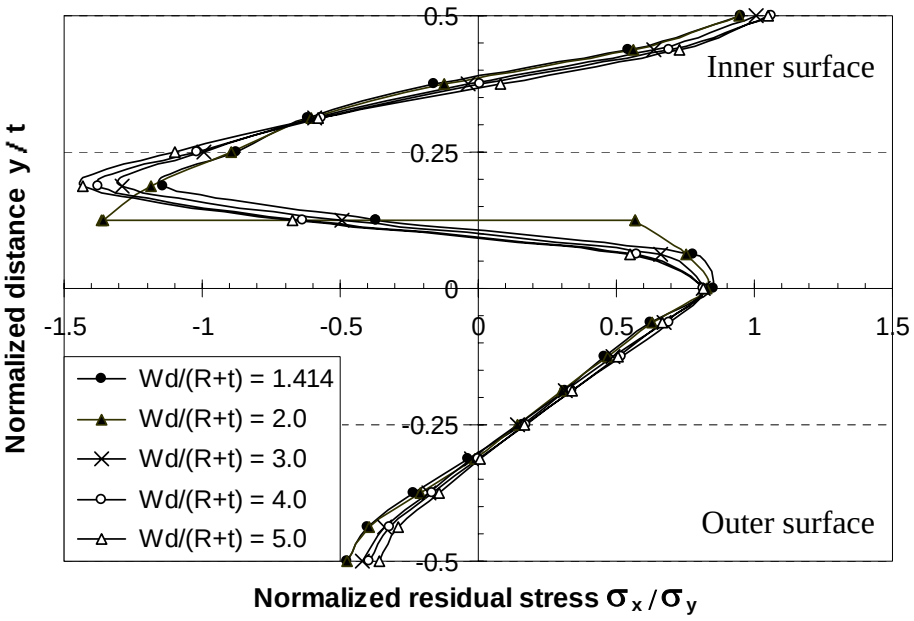

(b) Transverse residual stress (section A-A in Figure 5.10)

Figure 8.8 Effect of die size on residual stresses in a lip-flange corner of the carbon steel section.

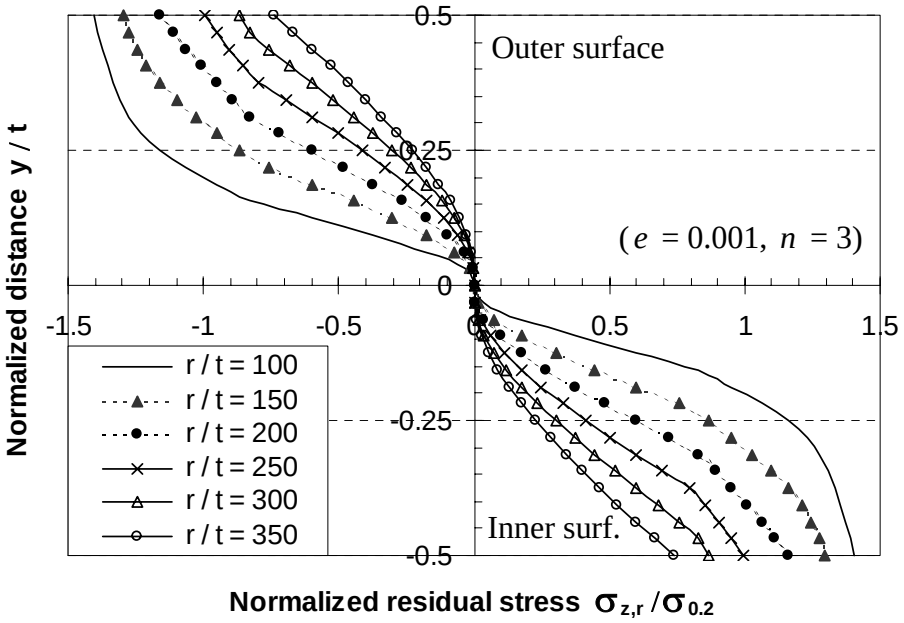

(a) Longitudinal residual stress

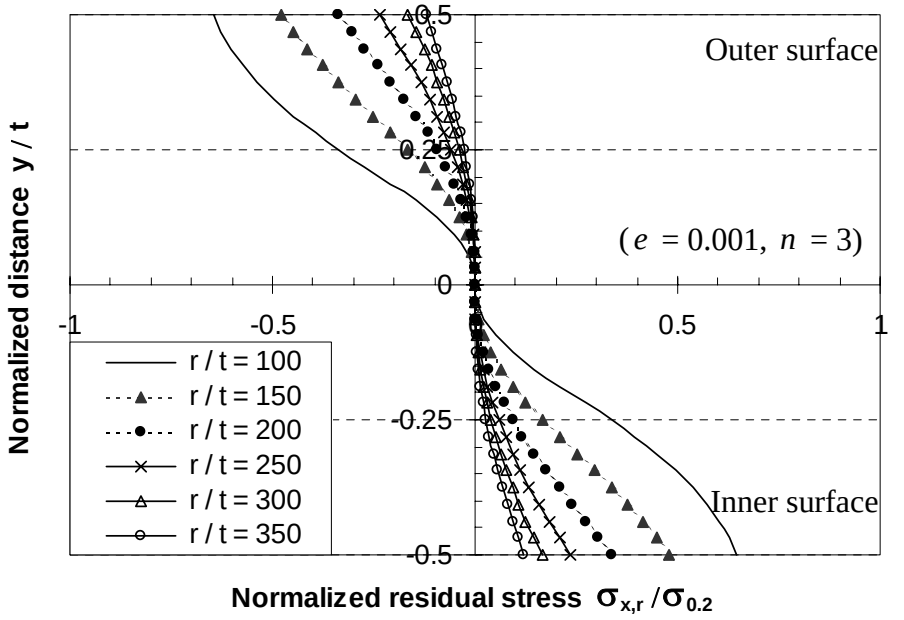

(b) Transverse residual stress

Figure 8.9 Through-thickness variations of residual stresses in a stainless steel sheet: effect of r/t ratio.

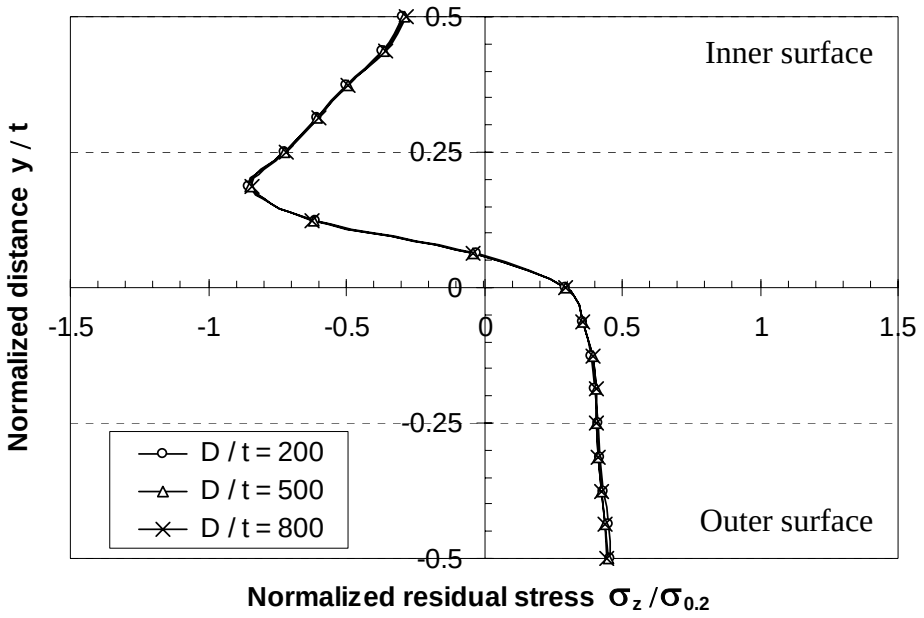

(a) Longitudinal residual stress at the centre of the lip-flange corner

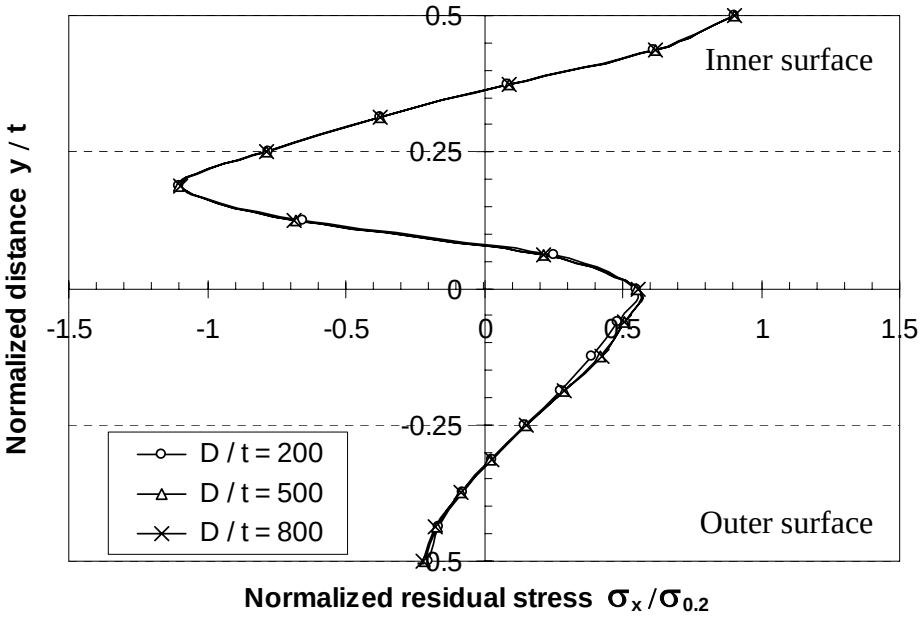

(b) Transverse residual stress at the centre of the lip-flange corner

Figure 8.10 Through-thickness variations of residual stresses in the austenitic stainless steel section: effect of coil diameter.

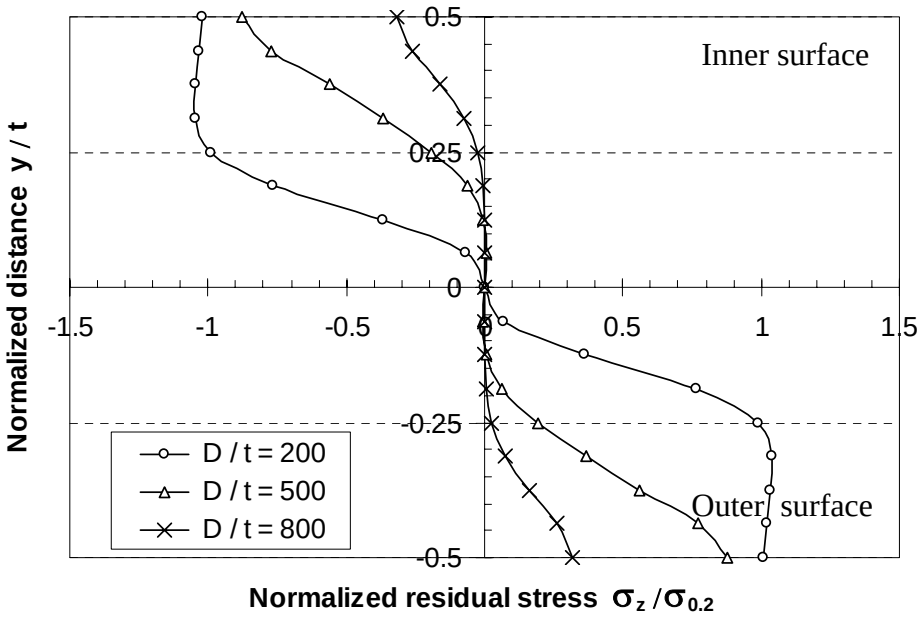

(c) Longitudinal residual stress at the mid-web section

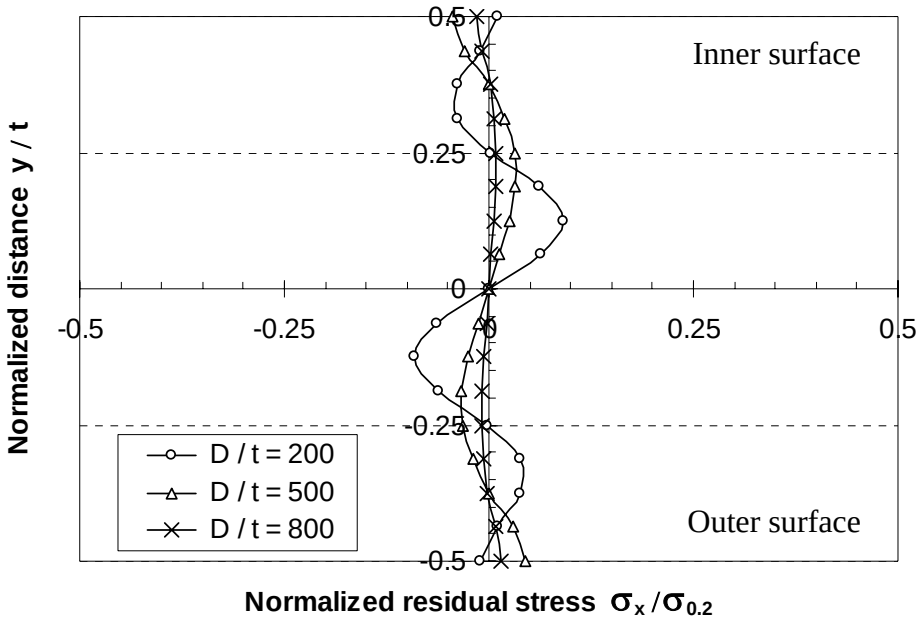

(d) Transverse residual stress at the mid-web section

Figure 8.10 Through-thickness variations of residual stresses in the austenitic stainless steel section: effect of coil diameter (continued).

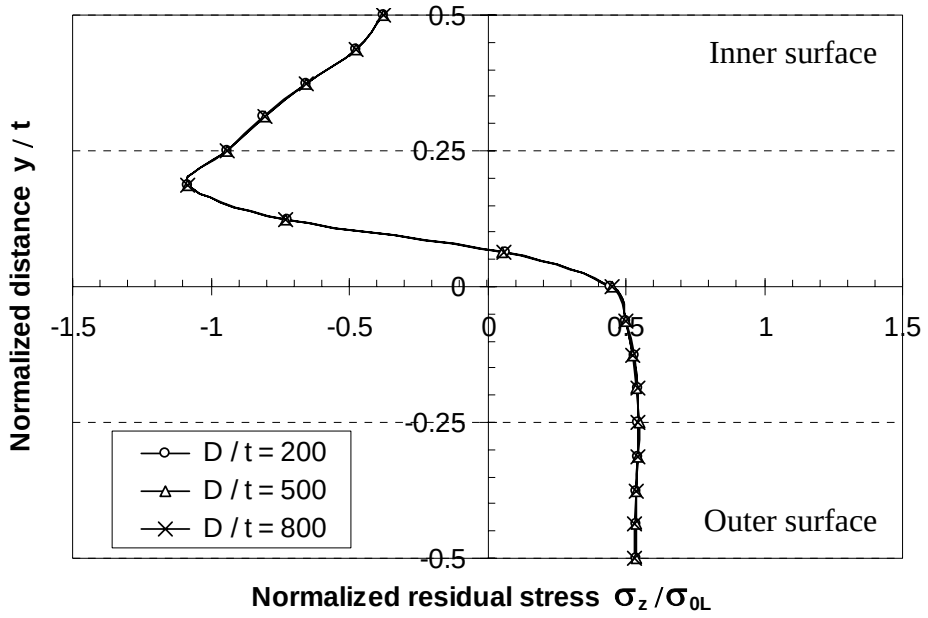

(a) Longitudinal residual stress at the centre of the lip-flange corner

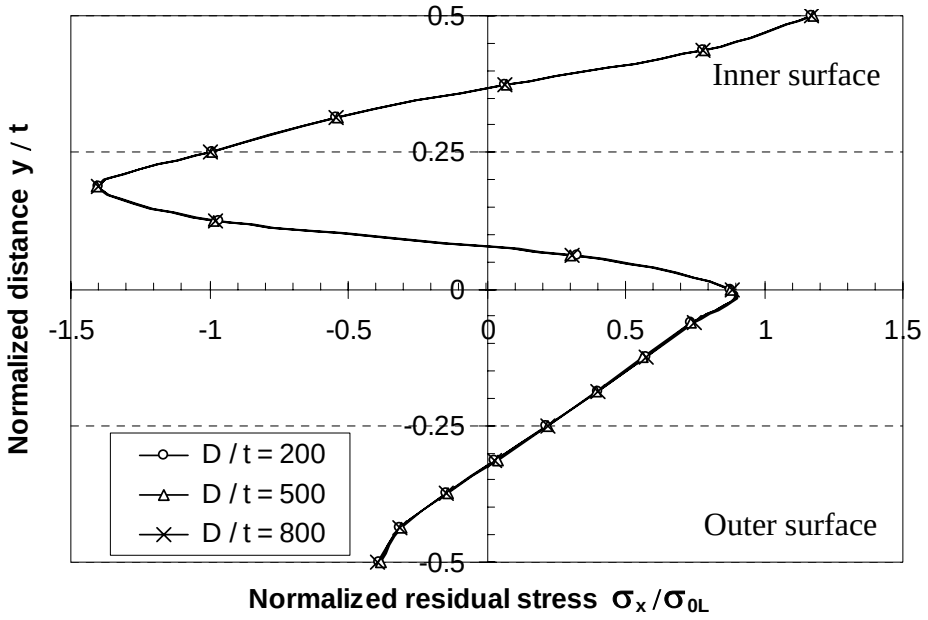

(b) Transverse residual stress at the centre of the lip-flange corner

Figure 8.11 Through-thickness variations of residual stresses in the duplex stainless steel section: effect of coil diameter.

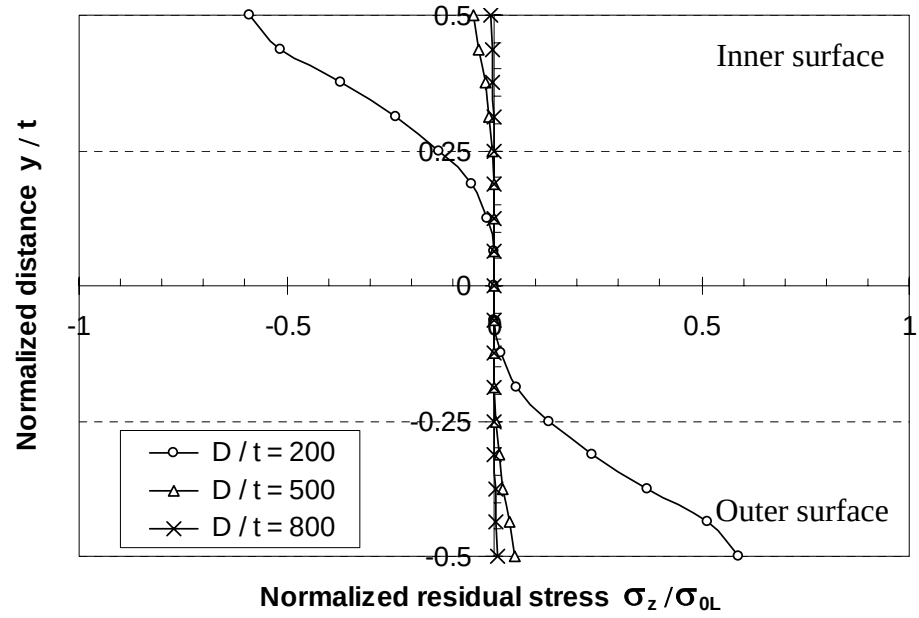

(c) Longitudinal residual stress at the mid-web section

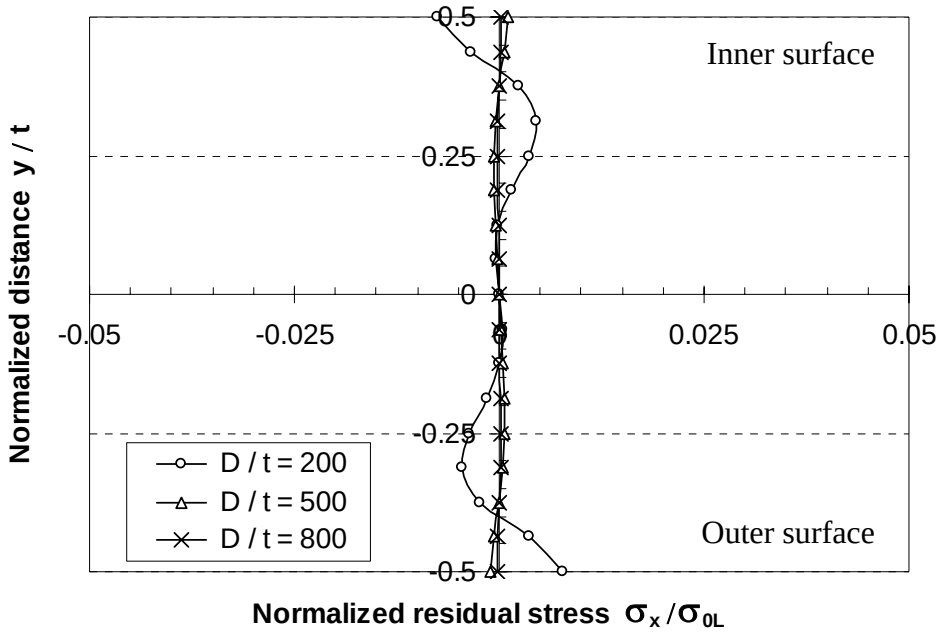

(d) Transverse residual stress at the mid-web section

Figure 8.11 Through-thickness variations of residual stresses in the duplex stainless steel section: effect of coil diameter (continued).

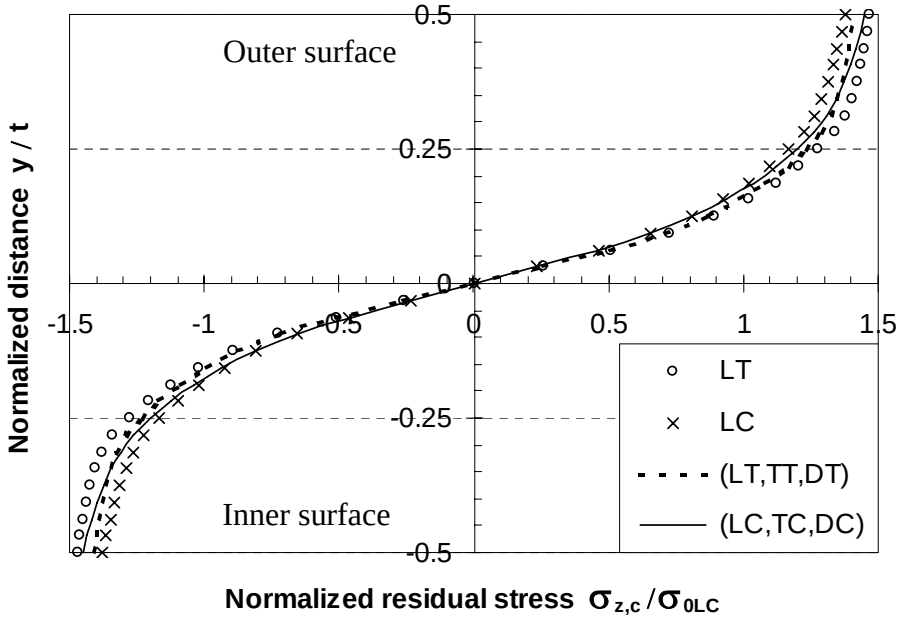

(a) Longitudinal coiling stress

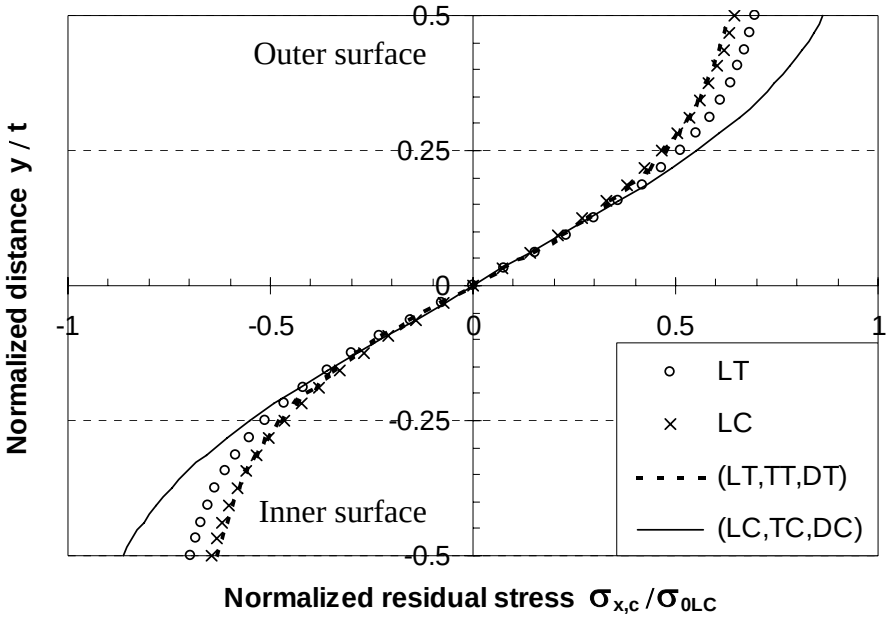

(b) Transverse coiling stress

Figure 8.12 Through-thickness variations of residual stresses in the duplex stainless steel sheet: effect of material anisotropy.

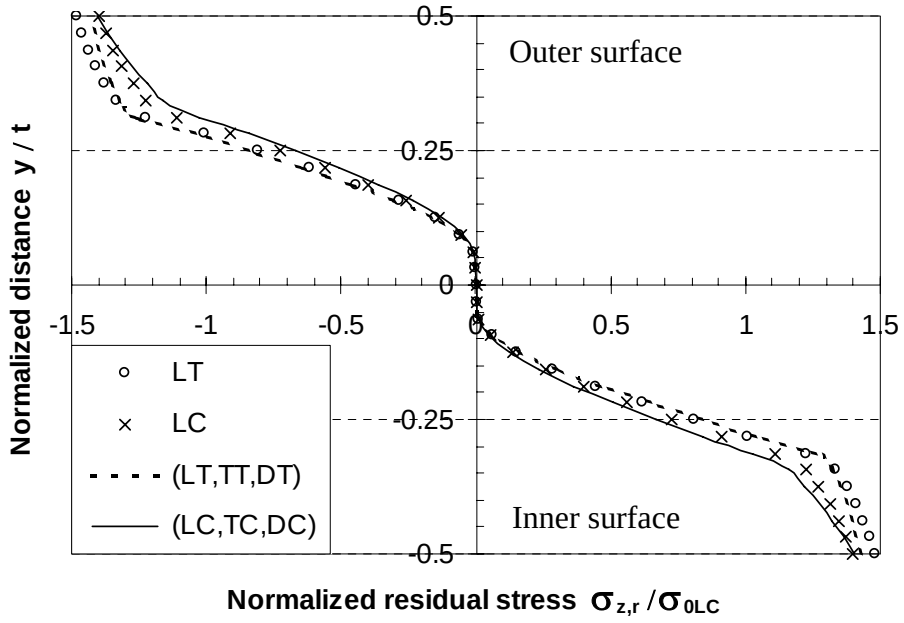

(c) Total longitudinal residual stress

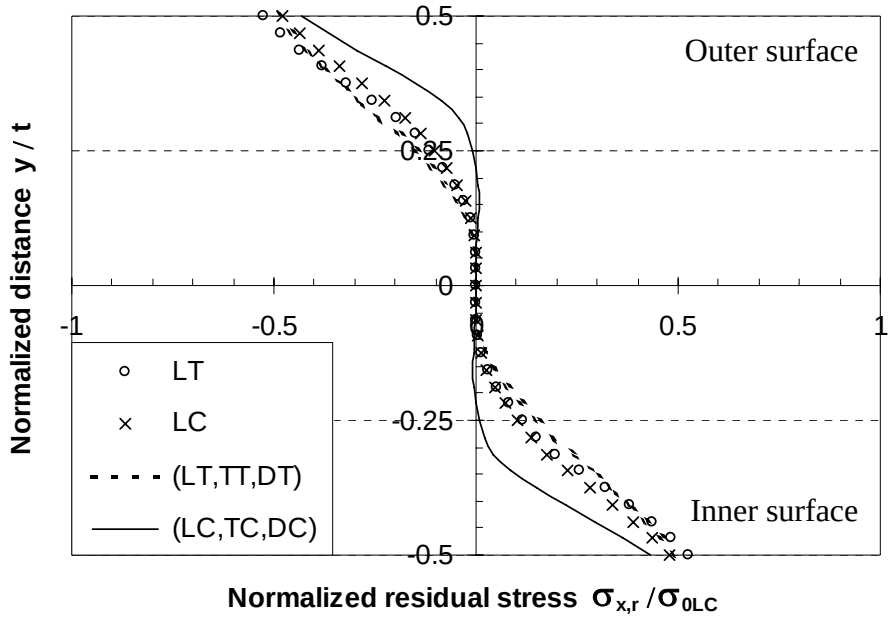

(d) Total transverse residual stress

Figure 8.12 Through-thickness variations of residual stresses in the duplex stainless steel sheet: effect of material anisotropy (continued).

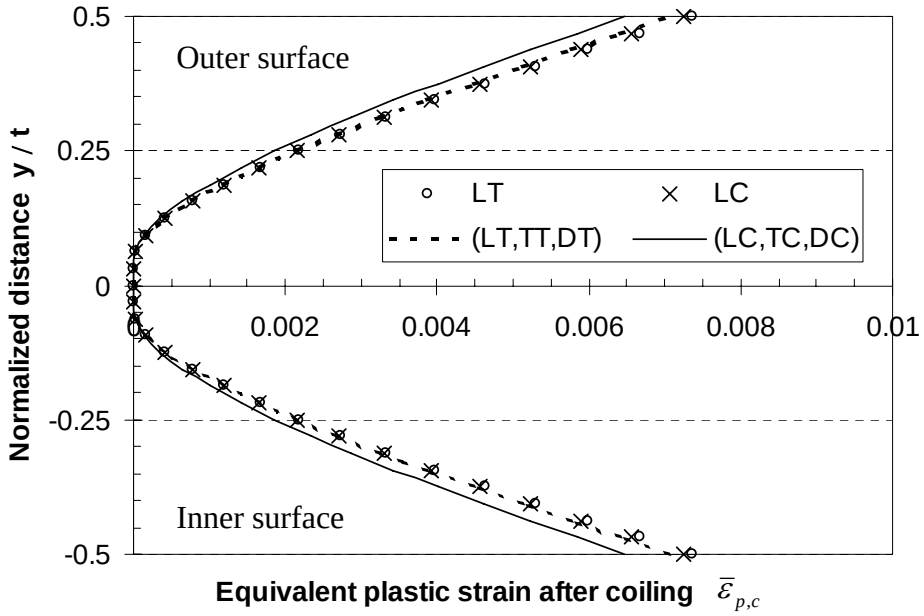

(a) After coiling

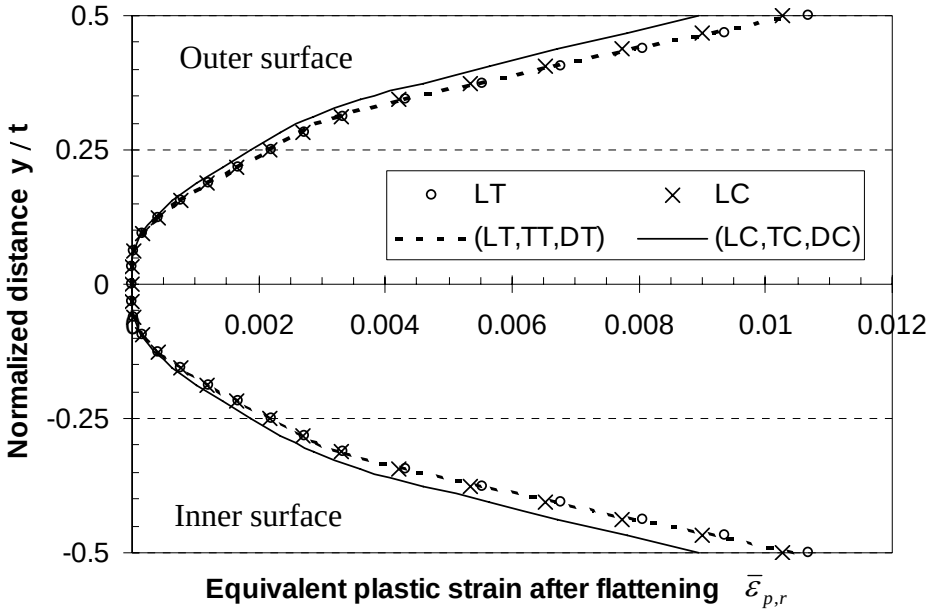

(b) After flattening

Figure 8.13 Through-thickness variations of equivalent plastic strains in the duplex stainless steel sheet: effect of material anisotropy.

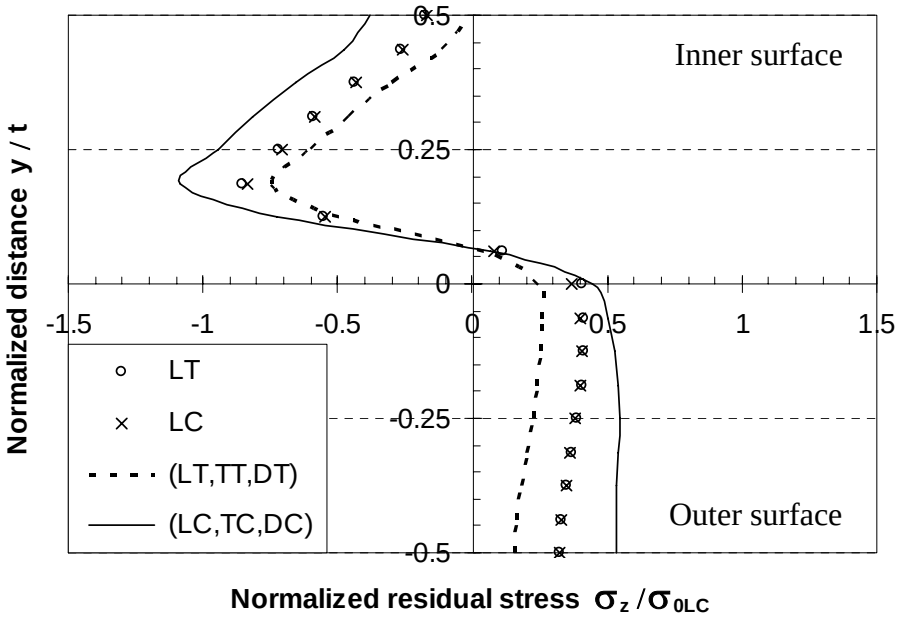

(a) Longitudinal residual stress at the centre of the lip-flange corner

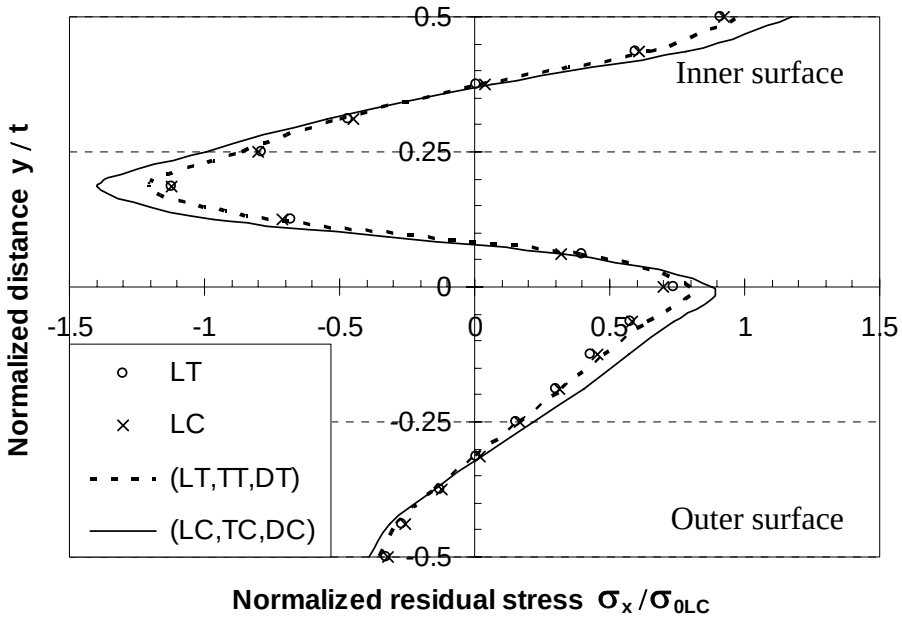

(b) Transverse residual stress at the centre of the lip-flange corner

Figure 8.14 Through-thickness variations of residual stresses in the duplex stainless steel section: effect of material anisotropy.

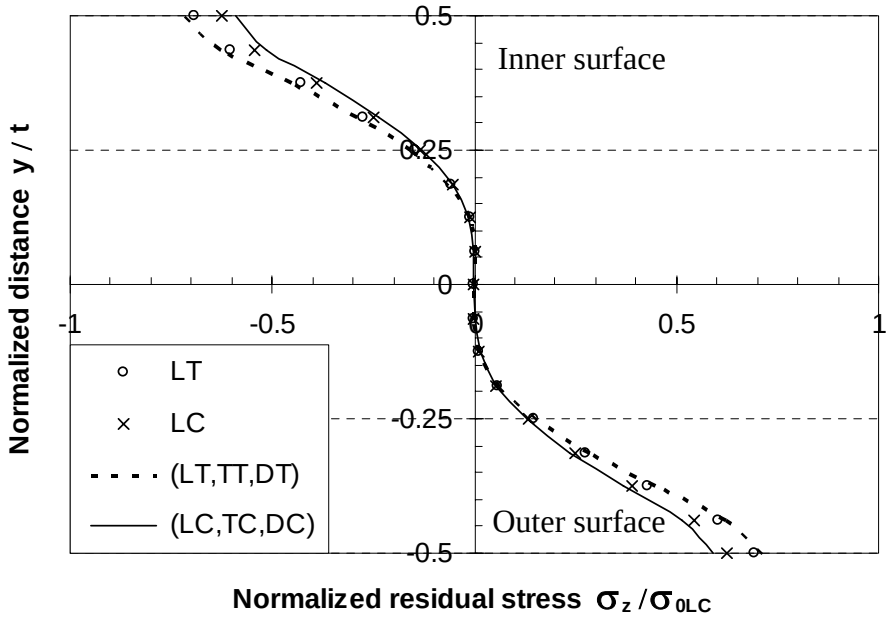

(c) Longitudinal residual stress at the mid-web section

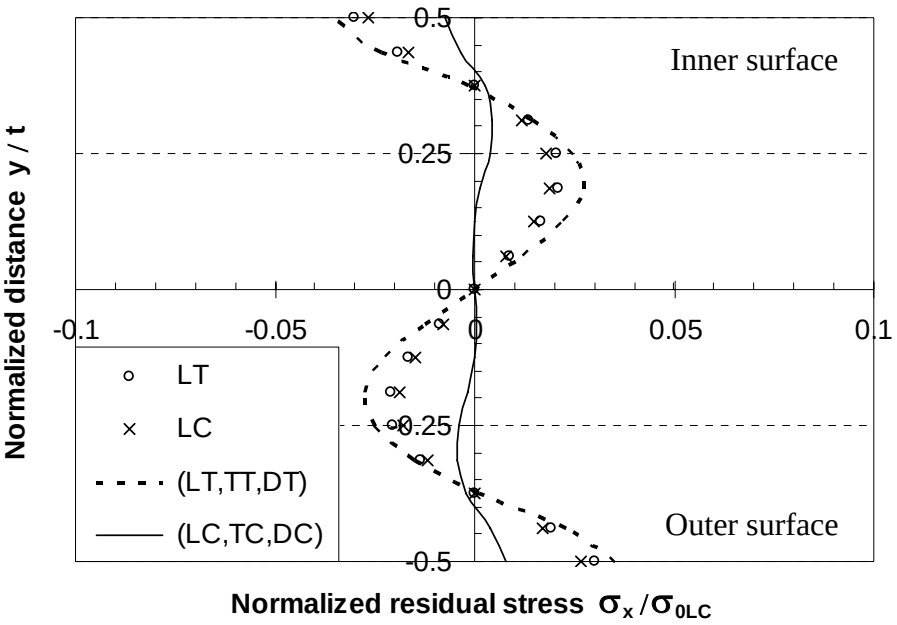

(d) Transverse residual stress at the mid-web section

Figure 8.14 Through-thickness variations of residual stresses in the duplex stainless steel section: effect of material anisotropy (continued).

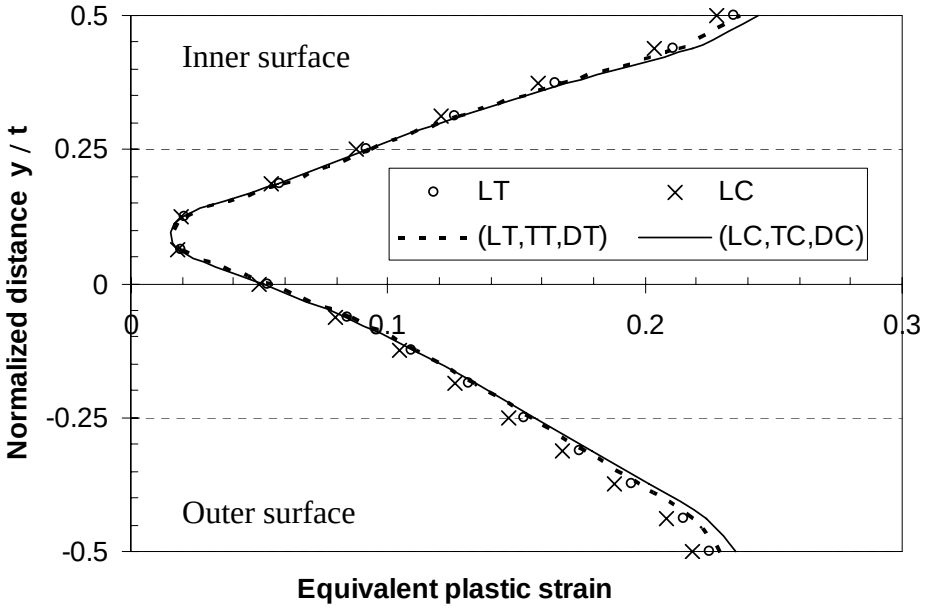

(a) At the centre of the lip-flange corner

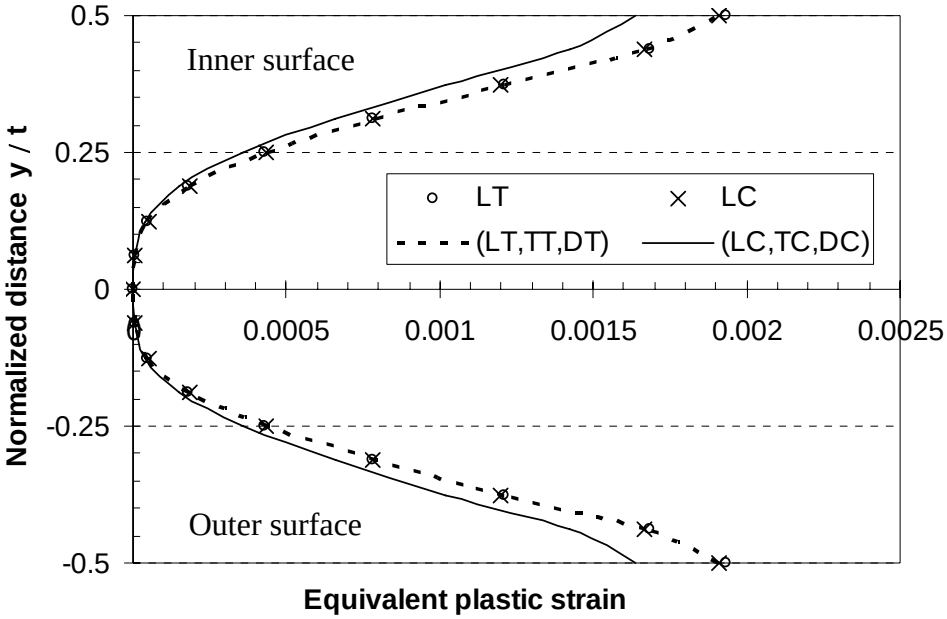

(b) At the mid-web section

Figure 8.15 Through-thickness variations of equivalent plastic strains in the duplex stainless steel section: effect of material anisotropy.

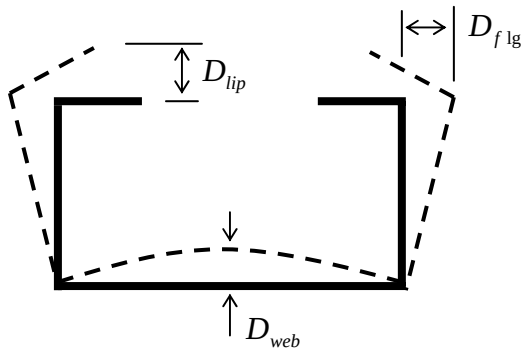

(a) Characterization of sectional derivations

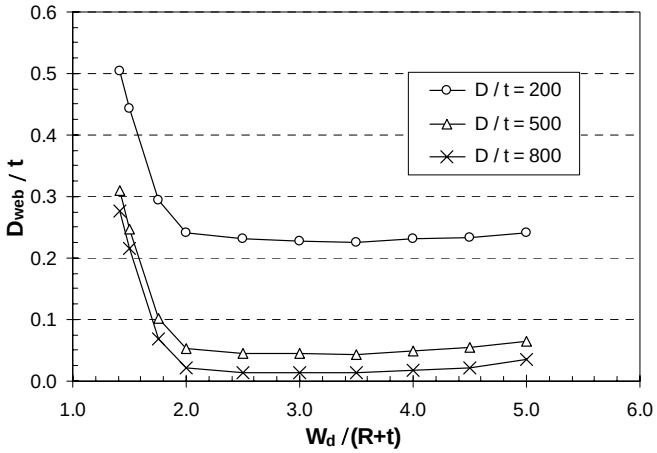

(b) Web

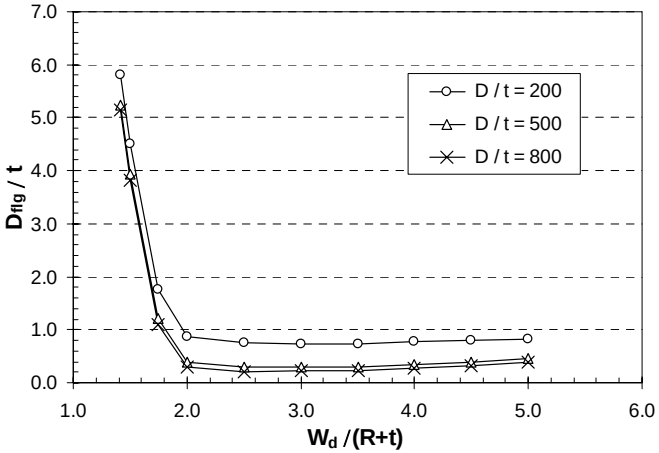

(c) Flange

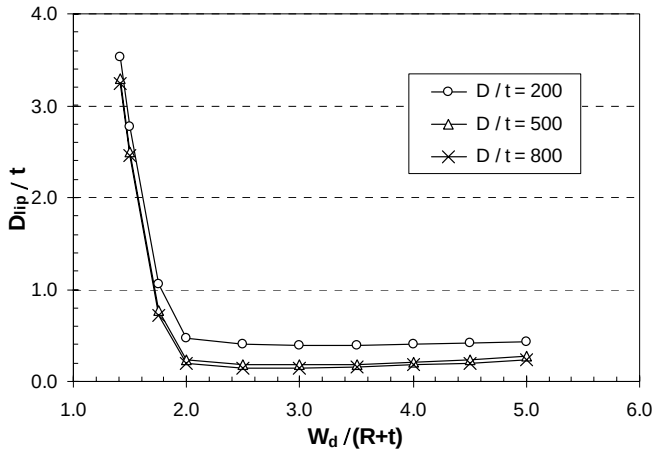

(d) Lip

Figure 8.16 Effects of the die size and coiling curvature on cross-sectional deviations of the austenitic stainless steel section.

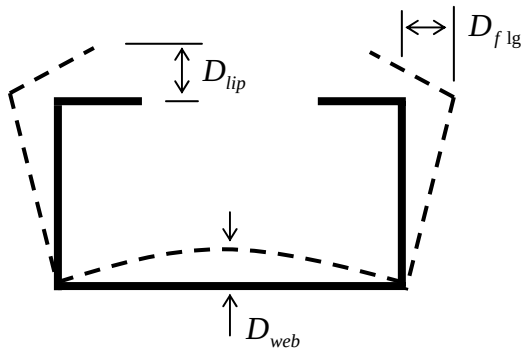

(a) Characterization of sectional derivations

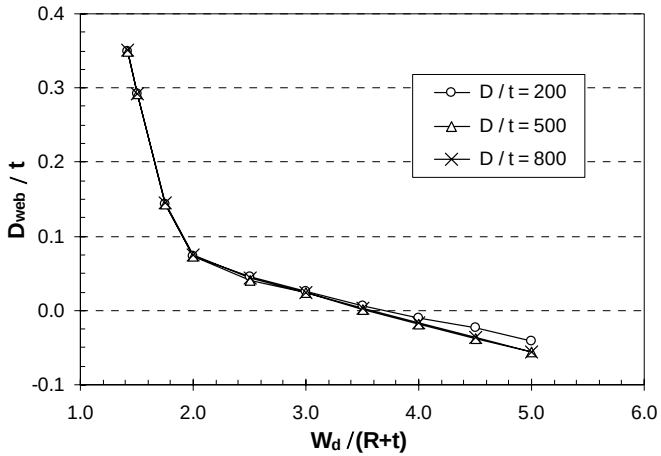

(b) Web

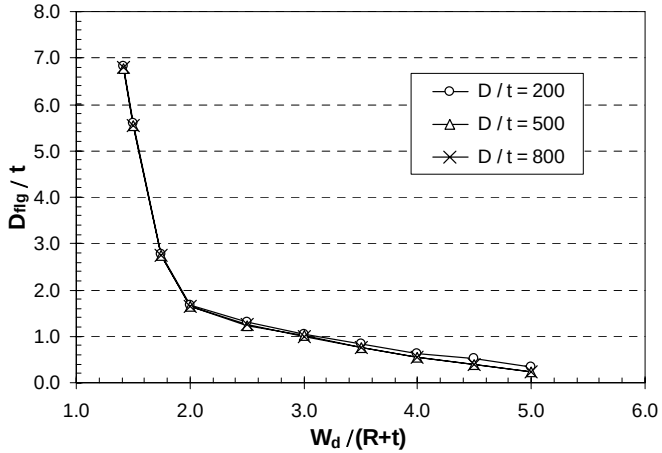

(c) Flange

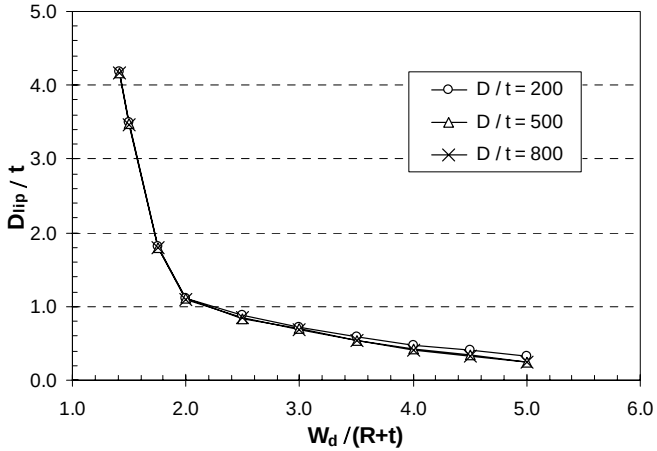

(d) Lip

Figure 8.17 Effects of the die size and coiling curvature on cross-sectional deviations of the duplex stainless steel section.

Chapter 9

NUMERICAL MODELLING OF THE STRUCTURAL BEHAVIOUR OF PRESS-BRAKED COLUMNS

9.1 INTRODUCTION

The load-carrying capacity of a cold-formed member is generally affected by geometrical and material imperfections. Material imperfections refer to residual stresses and different material properties for different parts of a cold-formed section. The cold work of the manufacturing process results in residual stresses and equivalent plastic strains in cold-formed members, and is responsible for this material imperfection.

The cold work of the manufacturing process may cause a positive effect (i.e. the strength enhancement) and a negative effect (i.e. the reduction of the load-carrying capacity) on a cold-formed member, as a result of the combined effect of the residual stresses and equivalent plastic strains in the member together with other factors. These residual stresses caused by cold forming do not exist alone and are always accompanied by corresponding equivalent plastic strains which are responsible for the definition of the work hardened state. In most existing studies on the numerical modelling of cold-formed members (see Chapter 2), only residual stresses were modelled without taking equivalent plastic strains into account and the flat portions and corner regions were assumed to possess different stress-strain curves. The use of

different stress-strain curves for different parts of a cold-formed section is an implicit way to deal with the effect of cold work in the corners. Since these stress-strain curves are obtained from the testing of coupons cut from members, the state of residual stresses and equivalent plastic strains in these coupons are expected to be different from the state in cold-formed members. Even though longitudinal residual stresses are usually reintroduced into coupons before tests by straightening, transverse residual stresses have already been released after coupons are cut from the members and thus lead to the redistribution of these longitudinal residual stresses. Hence, the effect of cold work on the structural performance of cold-formed members may have not been properly reflected in these previous studies.

To overcome the above shortcoming, a new advanced numerical approach has been developed to model the structural behaviour of cold-formed sections, in which the cold work effect of manufacturing process on the structural performance is taken into account in an explicit way. This chapter presents this new approach to the modelling of press-braked sections under compression. In this method, a single stress-strain curve of the virgin material is used for both flat portions and corner regions of a press-braked section. Residual stresses and equivalent plastic strains in different parts of the press-braked section resulting from the manufacturing process are pre-determined analytically and then imposed into a finite element model for nonlinear buckling analysis. The proposed method is illustrated through the study on the structural behaviour of a carbon steel section and a stainless steel section, and the effect of cold work in these sections on the column strength is also studied.

9.2 FINITE ELEMENT MODELLING

9.2.1 General

The advanced numerical approach was implemented using the finite element package ABAQUS (2002a), and was applied to study the structural behaviour of a carbon steel press-braked lipped channel section and a stainless steel press-braked lipped channel section subjected to axial compression. These two sections were assumed to possess the same cross-sectional geometry and the same thickness, but different material properties of virgin materials. The carbon steel section was assumed to possess the same material properties, cross-sectional geometry and thickness as the press-braked carbon steel lipped channel, specimen PBC14 (see Table 5.1 and Figure 5.1(b)), tested by Weng and Peköz (1990a). The stainless steel section was assumed to have the same cross-sectional geometry and thickness as specimen PBC14, but to possess the same material properties as the duplex stainless steel plate (grade UNS31803 duplex alloy) tested by Rasmussen *et al*. (2003) (see Table 7.1 and Figure 7.2). In the present finite element analysis, the material anisotropy of the stainless steel section was considered. For both of the carbon steel section and the stainless steel section, various column lengths with both pinned ends and fixed ends were studied.

In the finite element model, the material behaviour, initial geometrical imperfections as well as residual stresses and equivalent plastic strains due to the manufacturing process were all modelled. The finite element model was based on the centreline dimensions of the cross-section with rounded corners. Each column was modelled with the S4R shell element, which is a three-dimensional 4-node general-purpose

shell element with reduced integration and hourglass control. This element is capable of handling large strains and large rotations. Simpson's rule was used for the shell section integration, and 17 integration points were specified across the thickness of the shell element.

9.2.2 Finite element procedure

The advanced numerical approach to the modelling of the column behaviour consisted of three stages:

- In the first stage, an eigenvalue elastic buckling analysis was performed on the "perfect" column to establish probable buckling modes. Selected buckling modes were then scaled and superposed to give initial geometrical imperfections.

- In the second stage, initial geometrical imperfections and material imperfections were introduced into the finite element model in a nonlinear static analysis. Two analysis steps were required for the nonlinear static analysis. Both geometrical and material nonlinearities were considered. While initial geometrical imperfections were modelled as the superposition of scaled buckling modes obtained in the first stage, initial material imperfections were modelled by imposing residual stresses and equivalent plastic strains in the flat portions and corner regions of the press-braked section, resulting from the manufacturing process. These residual stresses and equivalent plastic strains were calculated using the analytical solutions presented in Section 4.4 of Chapter 4 (for the flat portions) and Section 6.4 of

Chapter 6 (for the corner regions) for the carbon steel section and those presented in Chapter 7 for the stainless steel section. The steps involved in the nonlinear static analysis of this second stage are summarized in Figure 9.1 for a carbon steel stub column.

In the first step of this nonlinear static analysis (i.e. the second stage of the advanced numerical approach), the above initial conditions were introduced into the finite element model, and all nodes of the model were restrained against all the degrees of freedom (DOF), except for the two translational degrees of freedom in the X and Y directions (the two directions on the cross-sectional plane) and the rotation about the Z direction (the longitudinal direction). Under these boundary conditions, the static equilibrium was achieved by allowing the cross-sectional deformation caused by the transverse spring-back. This transverse spring-back was contributed from the redistribution of transverse residual stresses under the plane strain condition just after press braking. This analysis step is necessary, because the analytical solutions presented in Chapters 4, 6 and 7 provide only the initial state before the transverse spring-back takes place.

After the transverse spring-back took place, the constraints at the translational degree of freedom in the Z direction (longitudinal direction) and the rotations about the X and Y directions were then removed for all nodes in the second analysis step, in order to simulate the release of residual stresses at both column ends due to the removal of the press-brake device from the press-braked section or due to cutting the full length of the press-braked section into the desired column

length. It led to the localized cross-sectional deformation happened at the ends of the press-braked member.

- In the third stage, the deformed mesh and its associated stress state and work hardened state resulting from the second stage were imported into a new nonlinear analysis. Both geometrical and material nonlinearities were incorporated. The nonlinear analysis on the “imperfect” column was carried out using the modified Riks method to obtain the ultimate load and the failure mode of the column.

  By means of kinematic coupling, all the degrees of freedom of the nodes at each end of a column was constrained to the rigid body motion of a reference node located at the centroid of the cross-section at the column end (see Figure 9.2). Boundary conditions at both ends of the column were then specified by restraining these two reference nodes. For fixed-ended columns, boundary conditions were modelled by restraining both reference nodes against all the degrees of freedom (DOF), except for the axial translation of the reference node at the top end. For pin-ended columns, the reference nodes at both ends were restrained against all the degrees of freedom, except for the axial translation of the reference node at the top end and the rotations of both reference nodes about the minor axis of the cross section. For both fixed-ended columns and pinned-ended columns, the axial compressive force was applied through the reference node at the top end.

Modelling of the material behaviour, initial geometrical imperfections, residual stresses and equivalent plastic strains are further discussed in the following sections.

9.2.3 Mesh convergence study

For accurate predictions, a mesh convergence study as summarized in Table 9.1 was carried out to obtain the final meshes used in the present study. In order to compare different meshes of the same physical model, the ultimate load of a 250-mm high steel stub column was monitored. The stub column was assumed to have the cross-sectional geometry and the virgin material properties of the press-braked steel channel section PBC14 (see Table 5.1) tested by Weng and Peköz (1990a). The channel section was assumed to be fabricated from a carbon steel sheet with the coil diameter $D = 200t$.

In Table 9.1, the result obtained from the finite element model consisting of 6 elements around each corner provides the reference value to check for the accuracy of other meshes. It can be seen that the use of fewer elements (varying from 2 to 6 elements) around the corner does not cause much difference in the ultimate load. To better approximate the corner curvature, the use of 4 elements around each corner is considered to be more appropriate. The adopted mesh shown in Figure 9.2 consists of 4 elements around each corner and larger elements in the flat portions, and the size of the element in the flat portions is approximately 5 mm × 5 mm. The adopted mesh produced the result that differs from the reference value by 0.1 %. This 0.1 % difference is taken to be satisfactory.

9.3 MATERIAL MODELLING

9.3.1 Carbon steel

The carbon steel section was assumed to possess the same virgin material properties as the press-braked steel channel section PBC14 (see Table 5.1) tested by Weng and Peköz (1990a). According to the measured surface residual strains of specimen PBC14 reported by Weng and Peköz (1990a), a finite element-based analysis has been carried out in Chapter 5 to predict the complete residual stress distribution in the section. The analysis showed that the carbon steel sheet forming this section most likely experienced the intermediate coil diameter D = 1100 mm during the coiling and uncoiling of the sheet in the manufacturing process, and this intermediate coiling curvature caused the strain hardening taking place over a small depth from the sheet surfaces. This finding implies that the cold work of the manufacturing process with this intermediate coiling curvature (i.e. D = 1100 mm) had little effect on the material properties of the steel in the flat portions. Moreover, the tensile test on the coupon cut from the flat portions of specimen PBC14 indicated that the carbon steel in the flat portions had a pronounced yield point (Weng and Peköz 1990a). This observation further suggests that the virgin material properties of specimen PBC14 can be approximated by the material properties of the steel from the flat portions (or the so-called flat material).

The complete tensile stress-strain curve of the flat material for specimen PBC14 is not available in Weng and Peköz (1990a and 1990b). Hence, in the present study, the stress-strain curve of the virgin material for the carbon steel section is defined by the

modified Ludwik equation (Chakrabarty 2000) (see Eq. (4.68a)) in which the value of the strain-hardening exponent n_s is found by fitting a nominal stress-strain curve through the measured values of the yield stress, the yield strain, the ultimate stress and the ultimate strain summarized in Table 5.1.

The modelling of material nonlinearity in ABAQUS requires the definition of a true stress-logarithmic plastic strain relationship as input data. Indeed, the stress-strain curve defined by Eq. (4.68) represents the true stress-strain relationship. Thus, the true stress σ_t and the true strain ε_t were given by Eq. (4.68) for each data point, and the corresponding logarithmic plastic strain ε_{tp} (or the so-called true plastic strain) was then calculated from the true stress σ_t and the true strain ε_t by Eq. (6.16c). The nominal stress-strain curve, the true stress-strain curve and the true stress-logarithmic plastic strain curve for the carbon steel section have been shown in Figure 5.1(b).

9.3.2 Stainless steel

The stainless steel section to be studied was assumed to possess the material properties of the grade UNS31803 duplex alloy (see Table 7.1), obtained from coupon tests done by Rasmussen *et al*. (2003). The longitudinal direction of the stainless steel section was assumed to coincide with the longitudinal direction of the duplex stainless steel plate tested by Rasmussen *et al*. (2003). The material anisotropy was considered, and the anisotropic material properties (see Table 7.1) based on the compression coupons (LC, TC and DC) were used for the material modelling. To define the material anisotropy, the initial yield stress σ_{0N} in the through-thickness direction is

also needed, but cannot be obtained from the coupon test. Thus, the initial yield stress σ_{0N} in the through-thickness direction was approximated by the diagonal initial yield stress σ_{0D} (i.e. $\sigma_{0N} \cong \sigma_{0D}$, see Eq. (7.48)).

9.3.2.1 Nonlinear strain hardening

The modelling of nonlinear hardening behaviour for anisotropic metals requires the definition of the equivalent stress-equivalent plastic strain relationship (ABAQUS 2002b) as input data. In this study, the equivalent stress $\overline{\sigma}$ and the equivalent plastic strain $\overline{\varepsilon}_p$ was converted from the true stress σ_t and true plastic strain ε_{tp} for longitudinal compression (LC) by Eq. (7.58). By following the procedure given in Subsection 7.4.2 of Chapter 7, the equivalent stress $\overline{\sigma}$ and equivalent plastic strain curve $\overline{\varepsilon}_p$ can be determined for each input data point over the full range of strains. The nominal stress-strain curve and the true stress-strain curve for longitudinal compression and the equivalent stress-equivalent plastic strain curve have been shown in Figure 7.2.

9.3.2.2 Material anisotropy

In order to define the material anisotropy in ABAQUS, the local coordinate system was defined for the material orientation of each shell element in the finite element model presented in this chapter. In this local coordinate system, the 1- and 2-directions for each element are on the plane of the shell element, and the 3-direction is referred to as the normal direction of the shell element. The local 1-direction of each element is tangent to the cross-sectional perimeter of the press-braked section. The

local 2-direction of each element coincides with the longitudinal direction of the press-braked member.

In the finite element analysis, the material anisotropy is described by the orthotropic elasticity model and the anisotropic metal plasticity model. These two material models are defined by specifying a set of engineering constants. These material models and the corresponding engineering constants have been introduced in Subsection 7.4.3 of Chapter 7.

To define the orthotropic elasticity model for the present finite element analysis, the moduli E_1 and E_2 were taken as the initial elastic moduli E_{0x} and E_{0z} for transverse compression (TC) and longitudinal compression (LC) respectively. Since the modulus E_3 is the initial elastic modulus E_{0y} in the through-thickness direction, which is not available and inconsequential, the value of E_3 was assumed to be the same as the initial elastic modulus E_1 (i.e. E_{0x}). The Poisson's ratios ν_{12}, ν_{13} and ν_{23} are ν_{xz}, ν_{xy} and ν_{zy} respectively and all of them were assumed to be 0.3. The shear moduli G_{12}, G_{13} and G_{23} were taken as the initial shear elastic modulus of grade UNS31803 duplex alloy given in Appendix B of AS/NZS 4673 (AS/NZS 2001). It should be noted that the values of ν_{12}, ν_{13}, ν_{23}, G_{12}, G_{13} and G_{23} are inconsequential even they have been assumed with reasonable values from different sources. Hence, these engineering constants were calculated as

$$E_1 = E_{0x} = 210.00 \text{ GPa}; \quad E_2 = E_{0z} = 181.65 \text{ GPa}; \quad E_3 = E_{0y} = 210.00 \text{ GPa};$$

$$\nu_{12} = 0.3; \quad \nu_{13} = 0.3; \quad \nu_{23} = 0.3; \tag{9.1}$$

$$G_{12} = 75 \text{ GPa};\ \ G_{13} = 75 \text{ GPa};\ \ G_{23} = 75 \text{ GPa}$$

For the ABAQUS anisotropic metal plasticity model defined in the present study, the state of plastic anisotropy is defined by the ratios of yield stresses in the three principal directions of anisotropy (see Eq. (7.60)). The initial yield stresses $\sigma_{0,ii}$ were taken as the compressive 0.2% proof stresses in the three principal directions (see Table 7.1), in which the through-thickness 0.2% proof stress σ_{0N} was approximated by the diagonal 0.2% proof stress σ_{0D} (i.e. $\sigma_{0N} \cong \sigma_{0D}$). The shear yield stresses $\tau_{0,12}$, which is τ_{0XZ}, was approximated by $\sigma_{0D}/\sqrt{3}$ (see Eq. (7.47)). Both $\tau_{0,13}$ and $\tau_{0,23}$ were taken as τ_0 such that $R_{13} = 1$ and $R_{23} = 1$. The initial yield stresses $\sigma_{0,ii}$ and the shear yield stresses $\tau_{0,ij}$ were thus determined as

$$\sigma_{0,11} = \sigma_{0T} = 617 \text{ MPa};\ \ \sigma_{0,22} = \sigma_{0L} = 527 \text{ MPa};\ \ \sigma_{0,33} = \sigma_{0N} = 610 \text{ MPa} \qquad (9.2)$$

and

$$\tau_{0,12} = \tau_{0XZ} = 610/\sqrt{3} \text{ MPa};\ \ \tau_{0,13} = \tau_0;\ \ \tau_{0,23} = \tau_0 \qquad (9.3)$$

In the ABAQUS anisotropic metal plasticity model, nonlinear strain hardening is modelled by specifying a “reference” stress-strain curve which is given by the equivalent stress-equivalent plastic strain relationship. Thus, the equivalent stress-equivalent plastic strain curve converted from the stress-strain curve for longitudinal compression (LC) was used as the “reference” stress-strain curve. As the reference

yield stress σ_0 is the yield stress of the "reference" stress-strain curve (see Eq. (7.58)), the reference yield stress σ_0 was taken as the equivalent stress $\overline{\sigma}$ converted from the compressive 0.2% proof stress σ_{0L} in the longitudinal direction, and thus given by Eq. (7.63). Therefore, its value was calculated as $\sigma_0 = 580$ MPa.

9.4 RESIDUAL STRESSES AND EQUIVALENT PLASTIC STRAINS

In this study, the complete analytical model illustrated in Chapter 7 was employed to predict the residual stresses and equivalent plastic strains in the carbon steel section and the stainless steel section. To achieve this, the analytical solution for the coiling-uncoiling process together with the solution for the cold bending of press-braking operations were used to provide the predictions of both residual stresses and equivalent plastic strains in the flat portions and the corner regions respectively.

The analytical solutions for residual stresses in steel sheets due to the coiling-uncoiling process have been presented in Chapter 4 and Section 7.2 of Chapter 7 for steel sheets with various material properties. The analytical solutions for residual stresses in the corner regions due to the cold bending of the press-braking operation have been presented in Chapter 6 and Section 7.3 of Chapter 7 for press-braked sections made of different types of materials. In the present study, residual stresses and equivalent plastic strains in the carbon steel section were calculated using the analytical solutions presented in Section 4.4 of Chapter 4 for the flat portions and Section 6.4 of Chapter 6 for the corner regions. For the stainless steel section, the effect of material anisotropy on residual stresses was considered. Residual stresses

and equivalent plastic strains in the stainless steel section were thus calculated using the analytical solutions presented in Section 7.2 of Chapter 7 for the flat portions and Section 7.3 for the corner regions.

These analytical predictions were imposed into the finite element model as the initial state using the *INITIAL CONDITIONS option in ABAQUS with TYPE=STRESS, USER parameter for residual stresses and with TYPE=HARDENING, USER parameter for equivalent plastic strains. These initial residual stresses and initial equivalent plastic strains were specified at 17 section points through the thickness of each shell element to define their through-thickness variations by means of the user subroutines SIGINI and HARDINI respectively.

9.5 GEOMETRICAL IMPERFECTIONS

9.5.1 Shape

Existing studies on the modelling of geometrical imperfection in cold-formed columns have been reviewed in Chapter 2. In most of these studies, the local imperfection was often assumed to be affine with the lowest local eigenmode, and the global imperfection was usually assumed to be the same as the scaled shape of the lowest global eigenmode. Therefore, in the present study, local and global imperfections were introduced into finite element models for both fixed-ended and pin-ended columns, and were modelled by scaling the lowest local eigenmode and the lowest global eigenmode respectively (see Figures 9.3 and 9.4 for the carbon steel

columns). By means of the eigenvalue elastic buckling analysis, required buckling modes were extracted from cold-formed members which were free from initial stresses and initial strain hardening due to the cold work of the manufacturing process.

For stub columns (column height L = 250 mm) and 500-mm high pin-ended columns, elastic global buckling loads were so large that difficulty was encountered in obtaining the corresponding lowest global eigenmode. Hence, only the lowest local eigenmode (the first eigenmode) was introduced into finite element models for stub columns and 500-mm high pin-ended columns as shown in Figures 9.5 and 9.6 respectively.

9.5.2 Amplitude

The global imperfection amplitude of a structural member is commonly given by the maximum initial out-of straightness which is limited by material delivery standards and is based on the member length (Bjorhovde 1992). The out-of-straightness used for carbon steel columns in limit states design codes is set as either the maximum allowable value of 1/1000 times the member length or the statistical mean of 1/1500 times the member length (Bjorhovde 1992). Therefore, besides the measured global imperfection magnitude (Yan and Young 2004) and the calibrated magnitude based on the best prediction of the member strength (Kaitila 2002, Young and Yan 2002a and 2002b; Gardner and Nethercot 2004), the maximum allowable out-of-straight (i.e.

L/1000, where L = the member length) were often used as the global imperfection amplitude in existing studies which has been reviewed in Chapter 2.

The local imperfection amplitude of a cold-formed member has been traditionally defined as a multiple of the plate thickness, and usually given by the imperfection magnitude determined for isolated plate elements. The modelling of the local imperfection amplitude for cold-formed sections has been reviewed in Chapter 2. As an early attempt, Dawson and Walker (1972) proposed three different forms to express the imperfection amplitude δ_o for simply supported steel plates. These three forms (see Eq. (2.14) in Chapter 2) are expressed in terms of the yield stress σ_y, the plate critical buckling stress σ_{cr}, the plate thickness t and three different calibrated constants α, β and γ for these three forms respectively. The values of these three constants α, β and γ were found to all be equal to 0.2 for providing the reasonably conservative fit to the test data for cold-rolled carbon steel sections.

In comparison with cold-formed carbon steel sections, only limited effort (Gardner and Nethercot 2004) has been made on the characterization of local imperfections for cold-formed stainless steel sections. To define local imperfection amplitudes for cold-rolled stainless steel rectangular hollow sections, Gardner and Nethercot (2004) recently adopted Dawson and Walker's expression $\delta_o = \gamma\left(\sigma_y / \sigma_{cr}\right) t$ (see Eq. (2.14c)), but proposed the use of a new value of γ = 0.023 to achieve the best fit to the measurement data of local imperfection magnitudes and replaced the yield stress σ_y in the expression with the 0.2% proof stress $\sigma_{0.2}$. On the other hand, they (Gardner and Nethercot 2004) used local imperfection amplitudes of $0.2t$ for stainless steel

circular hollow sections, in order to provide the best fit to test data. It can be seen that, different expressions of local imperfection amplitudes (i.e. $\delta_o = \alpha\, t$, $\delta_o = \beta\left(\sigma_y / \sigma_{cr}\right)^{0.5} t$ or $\delta_o = \gamma\left(\sigma_y / \sigma_{cr}\right) t$) and even different values of the calibrated constant (i.e. α, β or γ) may be needed for various cross-sectional geometries of cold-formed stainless steel sections. However, available measurement data of local imperfections for cold-formed stainless steel lipped channel sections were solely found. Therefore, the use of more complex expressions of local imperfection amplitudes for the stainless steel lipped channel section in the present study is not practical.

In the present study, Dawson and Walker's simply expression $\delta_o = 0.2t$ (see Eq. 2.14a) was used to specify local imperfection amplitudes for both the carbon steel and stainless steel lipped channel sections. The maximum allowable out-of-straight (L/1000) was used to specify global imperfection amplitudes for both sections. As Dawson and Walker (1972) showed that this simply expression $\delta_o = 0.2t$ of local imperfection amplitudes can provide an adequate conservative fit to test data on cold-formed steel sections, it should also be able to provide a reasonably conservative value for cold-formed stainless steel sections.

9.6 CURRENT DESIGN METHODS

9.6.1 General

For each press-braked column, the column strength determined by the advanced finite element approach described in the preceding sections is compared with the nominal strength predicted by design methods adopted in current American specifications. The direct strength method (DSM) detailed in the Appendix 1 (AISI 2004) of the North American Specification (NAS 2001) for the design of cold-formed steel structural members was used to predict the nominal axial strength $P_{n,DSM}$ of press-braked carbon steel columns. The effective width method adopted in the current American Society of Civil Engineers specification SEI/ASCE 8-02 (ASCE 2002) for the design of cold-formed stainless steel structural members was used to predict the nominal axial strength $P_{n,ASCE}$ of press-braked stainless steel columns.

9.6.2 Carbon steel columns

The direct strength method was initially proposed by Schafer and Peköz (1998) to determine the member resistance on the basis of gross cross-sectional properties and the limiting stress for laterally braced flexural steel members undergoing local and distortional buckling. The method was subsequently developed by Schafer (2002) to predict the strength of cold-formed steel columns undergoing local, distortional and global buckling. The direct strength method for column design was calibrated against the test data of concentrically loaded pin-ended steel columns with open cross-

sections. This method has been adopted as an alternative approach for column design in the NAS (2001) specification where the element based effective width method is conventionally used as a main design approach.

As detailed in Schafer (2002), the direct strength method for columns originally takes into account the effects of the local web/flange interaction, the interaction between local and global buckling as well as the interaction between distortional and global buckling. However, when this method is adopted for column design in the NAS (2001) specification, distortional buckling is considered alone and the interaction between distortional and global buckling is ignored. This presumes that distortional buckling failures are independent of the long-column behaviour, i.e., little if any distortional-global interaction exists (AISI 2004). Therefore, the nominal axial strength predicted by the direct strength method of the NAS (2001) specification is given by:

$$P_{n,DSM} = A_g f_{\min} \tag{9.4a}$$

with

$$f_{\min} = \min\left(f_{nl}, f_{nd}\right) \tag{9.4b}$$

$$f_{nl} = \begin{cases} f_n \ , & \lambda_l \le 0.776 \\ \left[1 - 0.15\left(\frac{f_{crl}}{f_n}\right)^{0.4}\right]\left(\frac{f_{crl}}{f_n}\right)^{0.4} f_n \ , & \lambda_l > 0.776 \end{cases} \tag{9.4c}$$

$$f_{nd} = \begin{cases} f_y \ , & \lambda_d \le 0.561 \\ \left[1 - 0.25\left(\frac{f_{crd}}{f_y}\right)^{0.6}\right]\left(\frac{f_{crd}}{f_y}\right)^{0.6} f_y \ , & \lambda_d > 0.561 \end{cases} \tag{9.4d}$$

$$f_n = \begin{cases} \left(0.658^{\lambda_c^2}\right) f_y , & \lambda_c \le 1.5 \\ \left(\frac{0.877}{\lambda_c^2}\right) f_y , & \lambda_c > 1.5 \end{cases} \qquad (9.4e)$$

in which

$$\lambda_l = \sqrt{\frac{f_n}{f_{crl}}}, \quad \lambda_d = \sqrt{\frac{f_y}{f_{crd}}} \quad \text{and} \quad \lambda_c = \sqrt{\frac{f_y}{f_{cre}}} \qquad (9.4f)$$

where A_g is the gross cross-sectional area; f_y is the yield stress; f_n is the critical global buckling stress; $f_{\min}$ is the minimum of two limiting stresses f_{nl} and f_{nd}; f_{nl} is the limiting stress for the interaction between local and global buckling; f_{nd} is the limiting stress for distortional buckling alone; f_{crl} is the critical elastic local buckling stress and its value can be calculated from Eqs. (2) and (4)~(6) of the paper by Schafer (2002); f_{crd} is the critical elastic distortional buckling stress and its value can be calculated from Eqs. (10)~(15) of the paper by Schafer (2002); and f_{cre} is the least of the critical elastic flexural, torsional and flexural-torsional buckling stresses determined according to Sections C4.1 through C4.4 of the NAS (2001) specification.

The nominal axial strength $P_{n,DSM}$ of press-braked carbon steel columns was calculated using Eq. (9.4) and the measured material properties shown in Table 5.1. The direct strength method used in the NAS (2001) specification was chosen for the present study, because this method can provide more accurate predictions than the conventional effective width method in the main specification (NAS 2001). In the effect width method of the specification (NAS 2001), the local web/flange interaction is ignored and distortional buckling is not explicitly considered.

9.6.3 Stainless steel columns

The direct strength method is currently limited to the design of cold-formed carbon steel members, and has not been further developed for cold-formed stainless steel members. The design of cold-formed stainless steel members still needs the use of effective width approach in current design specifications. The SEI/ASCE 8-02 specification (ASCE 2002) employs the effective width approach and adopts the Euler column strength to calculate the design stress. Due to the roundhouse type material properties of stainless steel alloys, the Euler column strength requires the calculation of tangent modulus to determine the design stress which involves an iterative procedure. The nominal axial strength is hence given by:

$$P_{n,ASCE} = A_e F_n \tag{9.5}$$

where A_e is the effective area at the stress F_n and can be calculated according to Sections 2.2 through 2.5 of the specification SEI/ASCE 8-02 (ASCE 2002); and F_n is the least of the flexural, torsional and flexural-torsional buckling stresses but is limited by the yield strength F_y, and can be determined according to Sections 3.4.1 through 3.4.4 of the specification (ASCE 2002).

The nominal axial strength $P_{n,ASCE}$ of stainless steel columns were calculated using Eq. (9.5) and the measured material properties of the longitudinal compression (LC) coupon shown in Table 7.1.

9.7 EFFECT OF MANUFACTURING PROCESS

9.7.1 General

For both the carbon steel section and the stainless steel section, various column lengths as shown in Tables 9.2 and 9.3 were chosen to investigate the effect of cold work on the column strength of fixed-ended lipped channels undergoing local buckling, global buckling, or the interaction between local and global modes. According to the suggestion from the AISI (1996) specification, the stub-column length was taken as 250 mm which is slightly greater than three times the greatest overall width of the lipped channel, but less than twenty times the minimum radius of gyration of the cross section.

In order to investigate the effect of boundary conditions on the variation of the column strength (the strength enhancement or the strength reduction) due to the cold work of the manufacturing process, a series of pin-ended columns were also studied. The column lengths of pin-ended channels (see Tables 9.2 and 9.3) were chosen to provide the same effective lengths as fixed-ended columns except for the stub column, and an additional 2000-mm high pined-ended column was also included in this study. The effective length L_e for minor axis flexural buckling was assumed to be equal to one-half of the column length L for fixed-ended columns ($L_e = L/2$) and equal to the column length L for pin-ended columns ($L_e = L$).

For each column (either the carbon steel section or the stainless steel section), three different cases of the cold work effect were considered, and each case refers to a

specific amount of cold work in the column due to the manufacturing process. The column was modelled by the advanced finite element approach (FEA) described in the preceding sections. The predicted column strength (P_{FEA}) for these three cases will then be compared with the nominal strength ($P_{n,DSM}$ for the carbon steel section or $P_{n,ASCE}$ for the stainless steel section) obtained from existing design methods. The three different amounts of cold work considered in the present study are:

1) No cold work (NC) — the cold work effect of the manufacturing process is completely ignored.
2) Cold work in corners (CC) — there is only cold work in the corner regions due to the cold bending of press-braking operations and no cold work in the flat portions; it means that the coiling curvature involved in the manufacturing process is zero.
3) Cold work in flats and corners (CFC) — there is cold work in both flat portions and corner regions due to the manufacturing process involving a coil diameter $D = 200t$, in which t is the sheet thickness.

Tables 9.4 and 9.5 summarize the comparison of the finite element results P_{FEA} for these three cases of the cold work effect, in order to indicate the variation of the column strength due to the effect of cold work. For the finite element results P_{FEA} presented in Table 9.4, the subscripts NC, CC, CFC are used to refer to the above three cases of the cold work effect respectively. For example, $P_{FEA,CFC}$ is the finite element prediction P_{FEA} of the column strength for the lipped channel with the cold work in both flat portions and corner regions due to the manufacturing process involving a coil diameter $D = 200t$.

9.7.2 Carbon steel columns

9.7.2.1 Comparison between finite element analysis and existing design methods

The finite element results P_{FEA} for three different amounts of cold work as well as the nominal column strength $P_{n,DSM}$ obtained from the direct strength method are summarized in Table 9.2, and Figures 9.7 and 9.8. It can be seen that the nominal strengths $P_{n,DSM}$ determined by the direct strength method (DSM) are generally matched closer to the column strength of channels with no cold work (NC), especially for the stub column strength. That is due to the fact that the nominal stub column strength $P_{n,DSM}$ and the finite element result $P_{FEA,NC}$ for the stub column with no cold work (NC) were both determined based on the material properties of virgin material.

When the effect of cold work in the corner regions (CC) was taken into account in the finite element analysis, the predicted strength $P_{FEA,CC}$ (= 82.6 kN) for the carbon steel stub column was found to agree closely with the average measured stub column strength (= 80.1 kN) of specimen PBC14 tested by Weng and Peköz (1990b). However, when the cold work in the flat portions was also considered in the finite element analysis, a larger difference was found between the finite element result $P_{FEA,CFC}$ and the measured stub column strength. That is due to the fact that; as discussed earlier in Subsection 9.3.1; the carbon steel sheet forming the steel channel section PBC14 most likely experienced the intermediate coil diameter (i.e. D = 1100 mm) which caused strain hardening taking place over a small depth from each sheet

surface, and had little effect on the material properties of the steel in the flat portions. Thus, the cold work in the steel channel section PBC14 should mainly take place in the corner regions. The finite element simulation also showed that the stub column failed in the local buckling mode with sectional distortion (L+D) (see Figure 9.9), which is different from the prediction obtained from the direct strength method used in NAS (2001). It is because that, in the direct strength method used in NAS (2001), the distortional mode is considered alone and the interaction between the distortional buckling mode and the other modes is ignored.

As shown in Figures 9.7 and 9.8, the design method can generally provide conservative results for columns without cold work (NC) or columns with cold work only in the corner regions (CC). However, it is seen that the use of the virgin material properties in the design calculation may result in un-conservative predictions ($P_{n,DSM}$) for longer columns (i.e. $L_e >$ 1000 mm) possessing the cold work in both flat portions and corner regions (CFC). From Table 9.2, it can be seen that failure modes predicted by the advanced finite element approach are generally agreed with predictions of the direct strength method, except for the 500-mm high pin-ended column with no cold work (NC) and the stub column. The typical post-failure deformed shape for the stub column is shown in Figure 9.9, and the typical post-failure deformed shapes for fixed-ended and pin-ended long columns are shown in Figures 9.10 and 9.11 respectively. The 500-mm high pin-ended column with no cold work (NC) failed under the interaction between distortional mode and flexural mode (D+F) as shown in Figure 9.12(a), while the same column with cold work (CC or CFC) was found to fail under the interaction between local mode and flexural mode (L+F) (see Figure 9.12(b)) which is the same failure mode predicted by the direct strength method. This

observation indicates that the cold work in cold-formed members may not only affect the ultimate load resistance but also the resultant failure mode.

9.7.2.2 Effect of cold work

The comparison shown in Table 9.4 reflects the cold work effect of the manufacturing process on the column strength. The ratio $P_{FEA,CC}/P_{FEA,NC}$ indicates the difference in the column strength due to cold work in the corner regions. The ratio $P_{FEA,CC}/P_{FEA,NC}$ varies from 1.00 for long columns (e.g. L_e = 1500 mm) to 1.06 for the stub column. It can be seen that the cold work in the corner regions always has positive effect on the column strength, and the load-carrying capacity of the stub column can be increased by 6%. The enhancement of the column strength due to the cold work in the corners decreases as the column length increases, and becomes negligible for longer columns (e.g. L_e = 1500 mm).

While the cold work in the corner regions can cause positive effect, the cold work in the flat portions may not always induce positive effect on the column strength. The effect of the cold work in the flat portions on the column strength can be indicated by the ratio $P_{FEA,CFC}/P_{FEA,CC}$, and the effect of the cold work in both flat portions and corner regions on the column strength is indicated by the ratio $P_{FEA,CFC}/P_{FEA,NC}$. For the stub column, the ratios $P_{FEA,CFC}/P_{FEA,CC}$ and $P_{FEA,CFC}/P_{FEA,NC}$ are 1.05 and 1.11 respectively. Both ratios decrease as the column length increases. The lowest values of the ratios $P_{FEA,CFC}/P_{FEA,CC}$ and $P_{FEA,CFC}/P_{FEA,NC}$ are found to be 0.83 and 0.84

respectively, and both values correspond to the longest (2000-mm long) pin-ended column.

It can be observed that the cold work in the flat portions can further enhance the strength of short columns, but reduce load-carrying capacities of columns with longer lengths (i.e. $L_e >$ 1000 mm). Under the effect of the cold work in both flat portions and corner regions, the stub column strength is increased by 11%, and the column strength for longer channels is reduced by 16%. The larger coiling curvature involved in the coiling-uncoiling process may result in a greater strength enhancement for short columns and a greater strength reduction for long columns. It is clear that the column strength is more sensitive to the cold work in the flat portions than the cold work in the corner regions. Further discussion about this observation can be found in next section (see Section 9.8).

Boundary conditions may also affect the variation of the column strength (the strength enhancement or the strength reduction) due to the cold work. Such influence of boundary conditions can be studied by comparing the strength of fixed-ended columns with the strength of pin-ended columns of the same effective lengths L_e. Table 9.4 shows that boundary conditions have greater effect on the strength reduction for the column of L_e = 1000 mm. For columns with other different effective lengths L_e, the effect of boundary conditions on the strength enhancement or strength reduction is negligible.

The cold work of the manufacturing process affects not only the column strength, but also the member stiffness. From Figures 9.13~9.15, it can be seen that the cold work

in the corner regions has negligible effect on the member stiffness, but the cold work in the flat portions can obviously reduce the member stiffness. Such reduction in the member stiffness can be observed from any carbon steel columns with different lengths and different boundary conditions considered in this study.

9.7.3 Stainless steel columns

9.7.3.1 Comparison between finite element analysis and existing design methods

Table 9.3, and Figures 9.16 and 9.17 summarize the finite element results P_{FEA} for three different amounts of cold work as well as the nominal column strength $P_{n,ASCE}$ obtained from the SEI/ASCE 8-02 specification (ASCE 2002). It can be seen that the nominal strength $P_{n,ASCE}$ is generally greater than the column strength determined for these three cases of the cold work effect, except for the stub column. The nominal strength $P_{n,ASCE}$ for the stub column agrees closely with the finite element result $P_{FEA,NC}$ of the stub column with no cold work (NC), but is less than the finite element result $P_{FEA,CC}$ or $P_{FEA,CFC}$ of the stub column with cold work (CC or CFC) in the section. It is due to the fact that the nominal stub column strength $P_{n,ASCE}$ was calculated based on the material properties of the virgin material, and thus the strength increase due to the cold work effect of forming is not utilized in the design prediction.

According to the SEI/ASCE 8-02 specification (ASCE 2002), the utilization of the strength increase due to the cold work effect of forming is applied only to fully

effective sections (i.e. the reduction factor $\rho = 1$ for each component elements), but the stainless steel section studied here is not fully effective. Nevertheless, the cold work in the corner regions (CC) can still enhance the stub column strength by 9% (see Tables 9.3 and 9.5). The strength enhancement of the stainless steel stub column due to the cold work in the corners is found to be greater than that of the carbon steel stub column. It is because that the duplex stainless steel alloy has greater extent of strain hardening than the carbon steel.

As shown in Table 9.3, failure modes predicted by the advanced finite element approach are generally agreed with those predicted by SEI/ASCE 8-02 (ASCE 2002), except for the stub column and long columns with effective lengths $L_e \geq 1500$ mm. For the stub column, the local buckling mode was predicted by SEI/ASCE 8-02, while the local buckling with sectional distortion (L+D) was observed in the finite element simulation. For long columns (i.e. $L_e \geq 1500$ mm), the global buckling mode (flexural buckling about minor axis for pin-ended columns, and flexural-torsional buckling mode for fixed-ended columns) was predicted by SEI/ASCE 8-02 (ASCE 2002), but the finite element simulation showed that the interaction between the local buckling mode and the global buckling mode was resulted.

9.7.3.2 Effect of cold work

Similar to those carbon steel columns, the cold work in the corner regions of the stainless steel section can also induce positive effect on the column strength, and the enhancement of the column strength tends to decrease as the column length increases. As seen from Table 9.5, the ratio $P_{FEA,CC} / P_{FEA,NC}$ varies from 1.01 to 1.09, and

increases as the column length decreases. As a result of the effect of the cold work in the corner regions, the stub column strength of the stainless steel section is increased by 9% ($P_{FEA,CC}/P_{FEA,NC}$ = 1.09), which is greater than that of the carbon steel section ($P_{FEA,CC}/P_{FEA,NC}$ = 1.06). The greater enhancement of the stub column strength for the stainless steel section than the carbon steel section is due to the fact that the stainless steel has greater extent of strain hardening than the carbon steel.

Concerning the effect of the cold work in the flat portions on the column strength, the ratio $P_{FEA,CFC}/P_{FEA,CC}$ is observed and its value ranges only from 1.01 to 1.03 for all the stainless steel columns summarized in Table 9.5. In comparison with the values (vary from 0.83 to 1.05) of the ratio $P_{FEA,CFC}/P_{FEA,CC}$ for those carbon steel columns (see Table 9.4), the cold work in the flat portions of stainless steel channels has only little effect on the column strength, even the effect is on the positive side. That is mainly due to the fact that the reverse yielding of the sheet material has not happened during the uncoiling of the stainless steel sheet in the manufacturing process. As the reverse yielding did not occur, equivalent plastic strains in the sheet cannot be increased by means of the uncoiling and thus the amounts of equivalent plastic strains in the flat portions were largely limited. This weakens the efficiency of the strength enhancement. Furthermore, without the reverse yielding taking place in the sheet, the amounts of residual stresses stored in the flat portions were also reduced due to the elastic uncoiling.

The effect of cold work on the member stiffness has also been studied. By comparing the load-axial displacement curves corresponding to three different cases of the cold work effect as shown in Figures 9.18~9.20, it can be seen that the cold work in the

corner regions has negligible effect on the overall member stiffness of columns. As the cold work in the flat portions is limited by the lack of the reverse yielding in the stainless steel sheet during uncoiling, its effect on the member stiffness thus also becomes negligible. Nevertheless, the cold work (CC and CFC) in the stub column was found to increase the tangent modulus of the load-displacement curve since at the middle load level (see Figure 9.18), while the cold work only modified the post-peak behaviour for longer columns (see Figures 9.19 and 9.20).

9.8 DISCUSSIONS

Results from the advanced finite element approach for the carbon steel lipped channel section have shown that the cold work in the corner regions can always enhance the column strength, and the amount of the strength enhancement is dependent on the column length. However, the cold work in the flat portions can further enhance the column strength for short steel columns, but it will reduce the column strength if the steel column is long enough. Such observation can be explained by the amounts of residual stresses and equivalent plastic strains pre-existing in the carbon steel channels of various lengths.

The cold work in a cold-formed section due to the manufacturing process can be quantified by the amounts of residual stresses and equivalent plastic strains in the member, and its effect on the column strength is thus a result of the interaction between these two influencing parameters. During the press-braking operation of a press-braked section, some of residual stresses in both flat portions and corner regions

are released due to the transverse spring-back of the cross section (see Figure 9.1(b)), and some are released locally near the column ends upon the removal of the press-brake device from the press-braked section or cutting the full length of the press-braked section into the desired column length (see Figure 9.1(c)). The first release of residual stresses due to the transverse spring-back results in the uniform residual stresses distribution along the column length. The final release of residual stresses at the column ends induces the non-uniform distribution of the stress state in the column, and this non-uniform stress state presents a type of imperfection in the column. However, the release of residual stresses generally does not cause any significant change in equivalent plastic strains previously caused by the fabrication process.

For short carbon steel columns (e.g. the stub column), the release of residual stresses near the column ends takes place over a larger proportion of the column length. The amounts of residual stresses stored in these short columns reduce after the stress release, but the amounts of the equivalent plastic strains remain nearly unchanged. The column strength can thus be enhanced for these short columns. As the column length increases; the release of residual stresses due to cutting or the removal of the press-brake device only takes place over a short length near each column end, and the residual stresses near the mid-height of the column are almost unaffected where the local buckling most likely happens. Therefore, for long carbon steel columns studied here, residual stresses govern the local buckling and the global buckling behaviour and reduce the ultimate load. It should be noted that whether the strength of a column can be enhanced or reduced is resulted from the balance between the amounts of the pre-existing residual stresses and equivalent plastic strains in the member, and such balance would vary depending on the material properties and the forming process.

Results from the advanced finite element approach for stainless steel columns have shown that the reverse yielding of the sheet material in uncoiling plays an important role in affecting the column strength. The reverse yielding will happen only when the magnitude of the uncoiling curvature κ_u ($=-2/D$, D is coil diameter) is greater than that of an uncoiling curvature limit κ_{uy} for the onset of reverse yielding (see Chapter 7). The magnitude of the uncoiling curvature limit κ_{uy} will increase as the yield strength (0.2% proof stress) of the sheet material increases. In this study, the duplex alloy of the stainless steel section possesses a high 0.2% proof stress, so that the magnitude of the limit κ_{uy} is too large for the stainless steel sheet to yield again during uncoiling. As a result, the cold work in the flat portions of the stainless steel section is greatly limited and its effect on the column strength is also small. However, the reverse yielding will still take place in the flat portions of the stainless steel section, if a greater initial coiling curvature is involved in the coiling-uncoiling process. On the other hand, for other stainless alloys with lower 0.2% proof stresses, such as austenitic alloys, the greater strength enhancement in both flat portions and corner regions could be expected, since the reverse yielding of the sheet can easily occur at small initial coiling curvatures.

As seen from the study on press-braked carbon steel channel sections presented in Chapters 5 and 8, residual stresses in the corner regions are mainly dependent on the inner corner radius, but the residual stresses in the flat portions are dependent on the initial coiling curvature which highly varies in the manufacturing process and is bounded by the maximum and minimum coil diameters of the steel coil. This is also valid for stainless steel press-baked sections. Therefore, the variation of initial coiling

curvatures is responsible for the significant scatter in the cold work in cold-formed sections, and so for the scatter in test load capacities of cold-formed members.

9.9 CONCLUSIONS

The cold work of the manufacturing process can alter the structural behaviour of cold-formed members. In this chapter, an advanced numerical approach to the modelling of the column behaviour of press-braked sections has been presented, in which the cold work effect of the manufacturing process on the structural behaviour of the press-braked members has been properly taken into account. In this approach, residual stresses and equivalent plastic strains in press-braked sections arising from the manufacturing process have been determined by incorporating the complete analytical model. This advanced numerical approach has been implemented using the finite element package ABAQUS (2002a), to analyze two series of press-braked columns: carbon steel lipped channels and stainless steel lipped channels. Numerical results presented in this chapter also allow for the following conclusions to be made:

(a) The cold work in a cold-formed member due to the manufacturing process can be quantified by the amounts of residual stresses and equivalent plastic strains in the member, and its effect on the member strength is basically dependent on the following factors: the corner radius, the initial coiling curvature, and the material properties of the virgin sheet material.

(b) Whether the column strength of a cold-formed member can be enhanced or reduced is a result of the balance between the amounts of pre-existing residual

stresses and equivalent plastic strains in the member, and such balance would vary depending on the material properties and the forming parameters of the manufacturing process.

(c) The cold work in corner regions can enhance the column strength with the amount of the strength enhancement decreasing as the column length increases. In general, the enhancement of the column strength for the stainless steel section is greater than that for the carbon steel section, since the stainless steel studied here has a greater extent of strain hardening than the carbon steel.

(d) For the carbon steel section, cold work in the flat portions can further enhance the strength of short columns, but will reduce the column strength if the column is long enough. For the stainless steel section, since the reverse yielding of the stainless steel sheet did not occur during uncoiling, the cold work in the flat portions was greatly limited and led to a minor effect on the column strength.

(e) The cold work in the corner regions has a negligible effect on the member stiffness, but the cold work in the flat portions can obviously reduce the member stiffness of carbon steel columns.

(f) The variation of the initial coiling curvature is responsible for the significant scatter in the cold work in cold-formed sections, and so for the scatter in the test load capacities of cold-formed members.

It is worth noting that, instead of using expensive laboratory tests, the new numerical approach presented in this chapter can provide a rapid and economical alterative

means to generate accurate numerical data for the structural performance of cold-formed members. The method allows the rapid development and improvement of design rules for new cold-formed members with innovative cross-sectional geometries and complex stiffeners.

9.10 REFERENCES

ABAQUS (2002a). *Standard User's Manual, V6.3*, Hibbitt, Karlsson and Sorensen, Inc., United States.

ABAQUS (2002b). *Theory Manual, V6.3*, Hibbitt, Karlsson and Sorensen, Inc., United States.

AISI (1996). *Cold-Formed Steel Design Manual*, 1996 edition, American Iron and Steel Institute, Washington, D.C.

AISI (2004). *Appendix 1: Design of Cold-Formed Steel Structural Members using the Direct Strength Method*, 2004 edition, American Iron and Steel Institute, Washington, D.C.

ASCE (2002). *Specification for the Design of Cold-Formed Stainless Steel Structural Members, SEI/ASCE 8-02*, American Society of Civil Engineers, New York.

AS/NZS (2001). *Cold-Formed Stainless Steel Structures, AS/NZS 4673:2001*, Australian/New Zealand Standard, Standards Australia, Sydney.

Bjorhovde, R. (1992). Compression members. *Constructional Steel Design: An International Guide*, edited by Dowling, P. J., Harding, J. E. and Bjorhovde, R., Elsevier Science Ltd., United Kingdom.

Chakrabarty, J. (2000). *Applied Plasticity*, Springer-Verlag, Inc., New York.

Dawson, R. G. and Walker, A. C. (1972). Post-buckling of geometrically imperfect plates. *Journal of the Structural Division, ASCE*, **98:ST1**, 75-94.

Gardner, L. and Nethercot, D. A. (2004). Numerical modelling of stainless steel structural components – A consistent approach. *Journal of Structural Engineering, ASCE*, **130:10,** 1586-1601.

Kaitila, O. (2002). Imperfection sensitivity analysis of lipped channel columns at high temperatures. *Journal of Constructional Steel Research*, **58**, 333-351.

NAS (2001). *North American Specification for the Design of Cold-Formed Steel Structural Members*, American Iron and Steel Institute, Washington, D.C.

Rasmussen, K. J. R., Burns, T., Bezkorovainy, P. and Bambach, M. R. (2003). Numerical modelling of stainless steel plates in compression. *Journal of Constructional Steel Research*, **59**, 1345-1362.

Schafer, B. W. (2002). Local, distortional and Euler buckling of thin-walled columns. *Journal of Structural Engineering, ASCE*, **128:3,** 289-299.

Schafer, B. W. and Peköz, T. (1998). Direct strength prediction of cold-formed steel members using numerical elastic buckling solutions. *Thin-Walled Structures - Research and Development, Proceedings of the Second International Conference on*

Thin-Walled Structures, Singapore, Dec. 1998, edited by Shanmugam, N. E., Liew, J. Y. R. and Thevendran, V., Elsevier Science, 137-144.

Weng, C. C. and Peköz, T. (1990a). Residual stresses in cold-formed steel members. *Journal of Structural Engineering, ASCE*, **116:6,** 1611-1625.

Weng, C. C. and Peköz, T. (1990b). Compression tests of cold-formed steel columns. *Journal of Structural Engineering, ASCE*, **116:5,** 1230-1246.

Yan, J. and Young, B. (2004), Numerical investigation of channel columns with complex stiffeners - Part I: Test verification. *Thin-Walled Structures,* **42:6,** 883-893.

Young, B. and Yan, J. (2002a). Finite element analysis and design of fixed-ended plain channel columns. *Finite Elements in Analysis and Design*, **38**, 549-566.

Young, B. and Yan, J. (2002b). Channel columns undergoing local, distortional, and overall buckling. *Journal of Structural Engineering, ASCE*, **128:6,** 728-736.

Table 9.1 Comparison of column strengths predicted with different finite element meshes for the carbon steel stub column with D/t = 200.

Mesh	No. of elements around a corner	No. of elements around the section	No. of elements along the length	Total no. of elements	Column strength (kN)	Relative change (%)
42×28	4	42	28	1176	87.5	1.3
Adopted mesh 58×56	4	58	56	3248	86.5	0.1
62×88	2	62	88	5456	86.1	0.3
70×88	4	70	88	6260	86.5	0.1
78×88	6	78	88	6864	86.4	0.0

Table 9.2 Comparison of column strengths between the advanced finite element approach (FEA) and the direct strength method (DSM) of the NAS (2001) specification for the carbon steel lipped channel section.

Boundary conditions	L (mm)	L_e (mm)	FEA			DSM		$\frac{P_{FEA}}{P_{n,DSM}}$
			Amount of cold work*	P_{FEA} (kN)	Failure mode**	$P_{n,DSM}$ (kN)	Failure mode**	
Fixed-ended	250	125	NC	77.8	L+D	78.2	L+FT	0.99
			CC	82.6	L+D			1.06
			CFC	86.5	L+D			1.11
	1000	500	NC	75.2	L+D+FT	72.0	L+FT	1.04
			CC	77.9	L+D+FT			1.08
			CFC	79.7	L+D+FT			1.11
	2000	1000	NC	61.3	L+FT	56.6	L+FT	1.08
			CC	61.6	L+FT			1.09
			CFC	52.9	L+FT			0.93
	3000	1500	NC	40.5	L+FT	40.3	L+FT	1.00
			CC	40.5	L+FT			1.00
			CFC	34.2	L+FT			0.85
Pin-ended	500	500	NC	77.6	D+F	74.6	L+F	1.04
			CC	78.4	L+F			1.05
			CFC	80.9	L+F			1.08
	1000	1000	NC	66.7	L+F	63.6	L+F	1.05
			CC	68.2	L+F			1.07
			CFC	63.7	L+F			1.00
	1500	1500	NC	50.8	L+F	48.7	L+F	1.04
			CC	51.0	L+F			1.05
			CFC	43.1	L+F			0.89
	2000	2000	NC	33.2	L+F	33.6	L+F	0.99
			CC	33.5	L+F			1.00
			CFC	27.9	L+F			0.83

* NC = No Cold work
CC = Cold work in Corners only
CFC = Cold work in both Flats and Corners due to a coil diameter $D = 200t$

** L = Local buckling mode
D = Distortional buckling mode
F = Flexural buckling mode
FT = Flexural-torsional buckling mode
\+ = Interaction between different modes

Table 9.3 Comparison of column strengths between the advanced finite element approach (FEA) and the effective width method of the SEI/ASCE 8-02 specification (ASCE 2002) for the stainless steel lipped channel section.

Boundary conditions	L (mm)	L_e (mm)	FEA			ASCE		$\frac{P_{FEA}}{P_{n,ASCE}}$
			Amount of cold work*	P_{FEA} (kN)	Failure mode**	$P_{n,ASCE}$ (kN)	Failure mode**	
Fixed-ended	250	125	NC	145.0	L+D	144.6	L	1.00
			CC	158.0	L+D			1.09
			CFC	159.0	L+D			1.10
	1000	500	NC	118.0	L+D+FT	125.8	L+FT	0.94
			CC	125.0	L+D+FT			0.99
			CFC	129.0	L+D+FT			1.03
	2000	1000	NC	64.8	L+FT	75.1	L+FT	0.86
			CC	65.5	L+FT			0.87
			CFC	67.2	L+FT			0.89
	3000	1500	NC	39.7	L+FT	42.9	FT	0.93
			CC	41.0	L+FT			0.96
			CFC	42.0	L+FT			0.98
Pin-ended	500	500	NC	120.0	L+F	139.2	L+F	0.86
			CC	130.0	L+F			0.93
			CFC	132.0	L+F			0.95
	1000	1000	NC	80.8	L+F	93.2	L+F	0.87
			CC	85.6	L+F			0.92
			CFC	87.3	L+F			0.94
	1500	1500	NC	48.9	L+F	57.5	F	0.85
			CC	50.3	L+F			0.87
			CFC	51.1	L+F			0.89
	2000	2000	NC	30.0	L+F	34.2	F	0.88
			CC	30.7	L+F			0.90
			CFC	31.2	L+F			0.91

* NC = No Cold work
CC = Cold work in Corners only
CFC = Cold work in both Flats and Corners due to a coil diameter $D = 200t$

** L = Local buckling mode
D = Distortional buckling mode
F = Flexural buckling mode
FT = Flexural-torsional buckling mode
\+ = Interaction between different modes

Table 9.4 Comparison of numerical column strengths P_{FEA} for the carbon steel lipped section possessing different amounts of cold work.

Boundary conditions	L (mm)	L_e (mm)	$\frac{P_{FEA,CFC}}{P_{FEA,NC}}$	$\frac{P_{FEA,CC}}{P_{FEA,NC}}$	$\frac{P_{FEA,CFC}}{P_{FEA,CC}}$
Fixed-ended	250	125	1.11	1.06	1.05
	1000	500	1.06	1.04	1.02
	2000	1000	0.86	1.00	0.86
	3000	1500	0.84	1.00	0.84
Pin-ended	500	500	1.04	1.01	1.03
	1000	1000	0.96	1.02	0.93
	1500	1500	0.85	1.00	0.85
	2000	2000	0.84	1.01	0.83

Note: The subscript NC is used to refer to the column with No Cold work.

The subscript CC is used to refer to the column with Cold work in Corners only.

The subscript CFC is used to refer to the column with Cold work in both Flats and Corners due to a coil diameter $D = 200t$.

Table 9.5 Comparison of numerical column strengths P_{FEA} for the stainless steel lipped section possessing different amounts of cold work.

Boundary conditions	L (mm)	L_e (mm)	$\frac{P_{FEA,CFC}}{P_{FEA,NC}}$	$\frac{P_{FEA,CC}}{P_{FEA,NC}}$	$\frac{P_{FEA,CFC}}{P_{FEA,CC}}$
Fixed-ended	250	125	1.10	1.09	1.01
	1000	500	1.09	1.06	1.03
	2000	1000	1.04	1.01	1.03
	3000	1500	1.06	1.03	1.02
Pin-ended	500	500	1.10	1.08	1.02
	1000	1000	1.08	1.06	1.02
	1500	1500	1.05	1.03	1.02
	2000	2000	1.04	1.02	1.02

Note: The subscript NC is used to refer to the column with No Cold work.

The subscript CC is used to refer to the column with Cold work in Corners only.

The subscript CFC is used to refer to the column with Cold work in both Flats and Corners due to a coil diameter $D = 200t$.

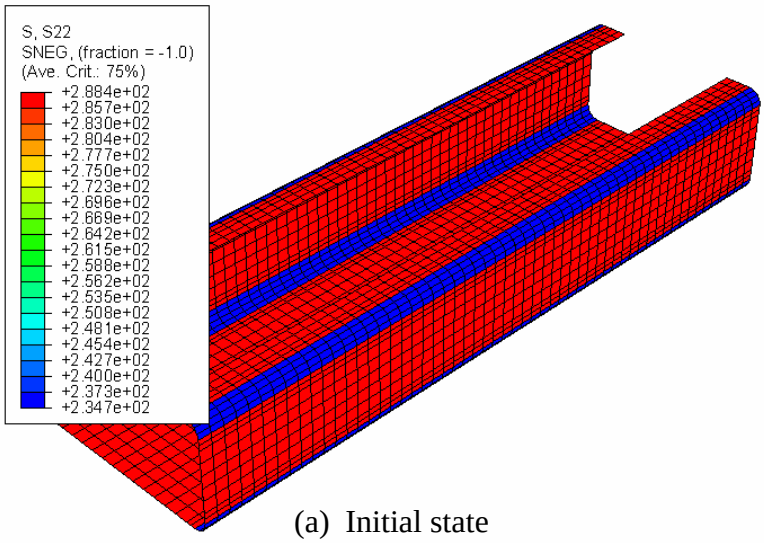

(a) Initial state

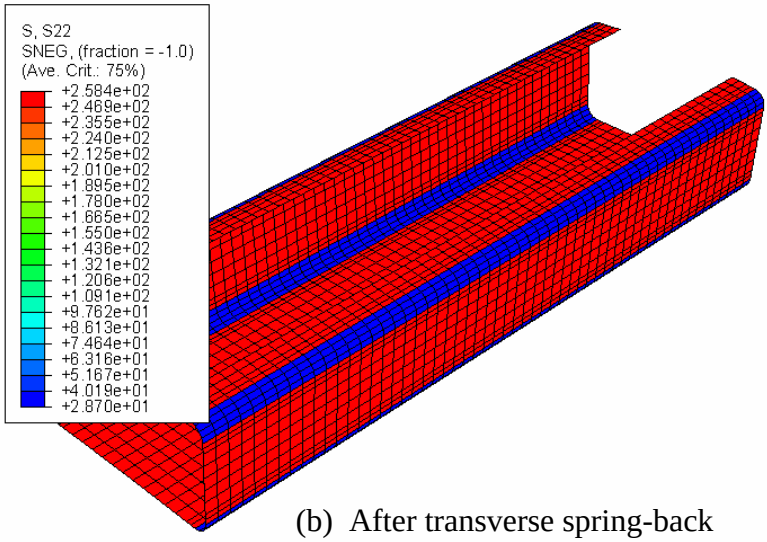

(b) After transverse spring-back

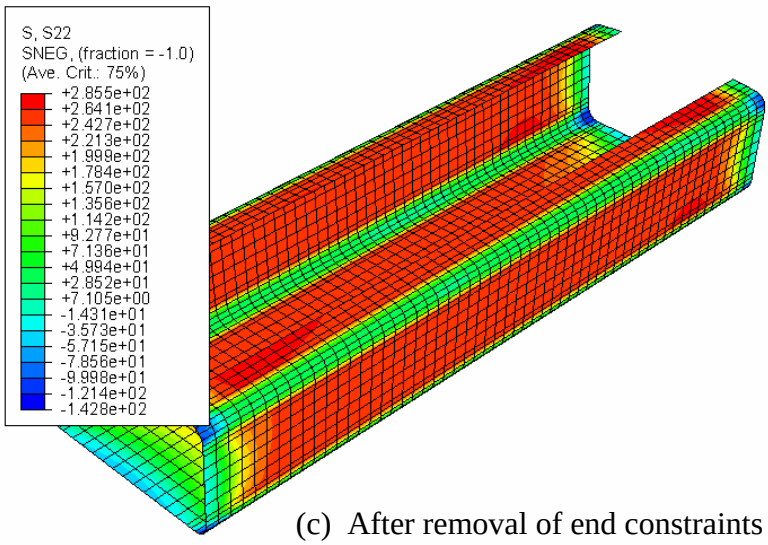

(c) After removal of end constraints

Figure 9.1 Longitudinal stress contours on the outer surface of the carbon steel stub column with D/t = 200 at different states of a nonlinear static analysis.

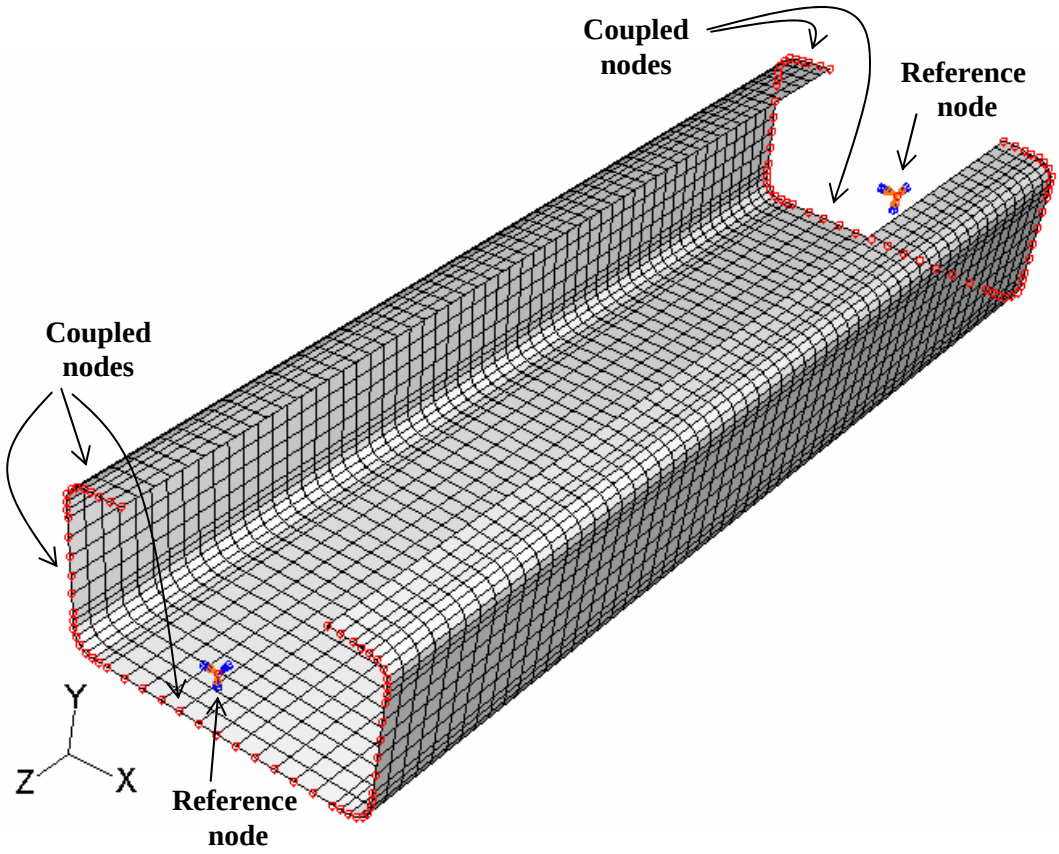

Figure 9.2 Finite element mesh and boundary conditions used in the nonlinear buckling analysis for the stub column.

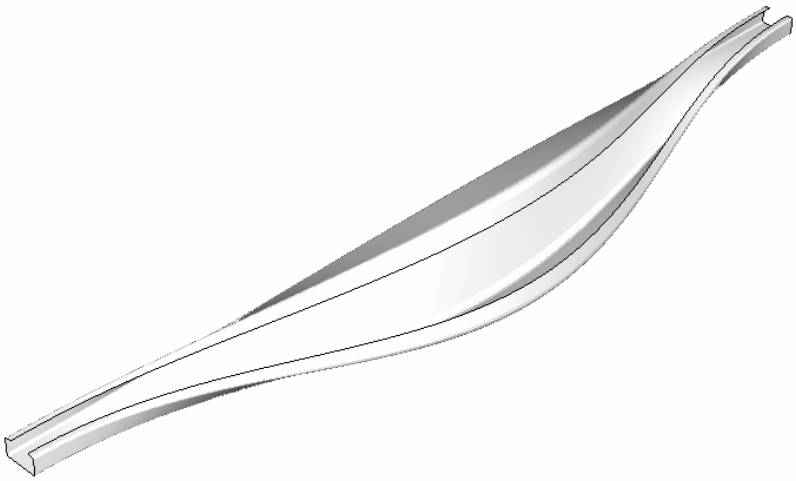

(a) The lowest global model (eigenmode 1)

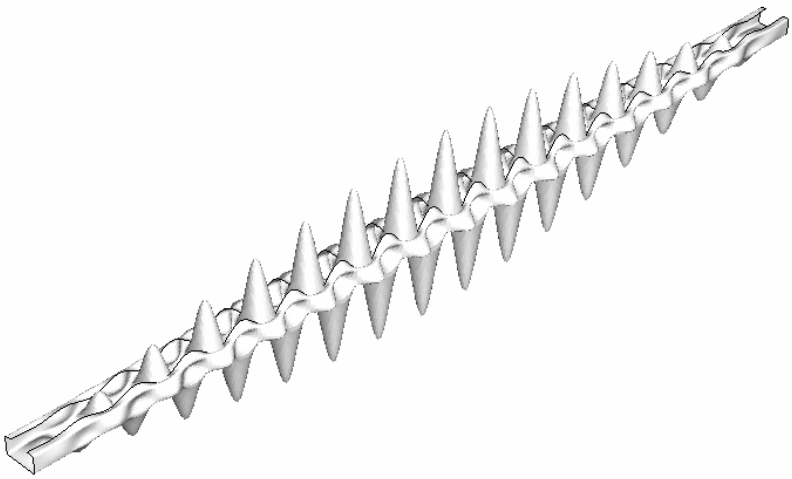

(b) The lowest local model (eigenmode 4)

Figure 9.3 Eigenmodes for the 2000-mm high fixed-ended carbon steel column.

(a) The lowest global model (eigenmode 1)

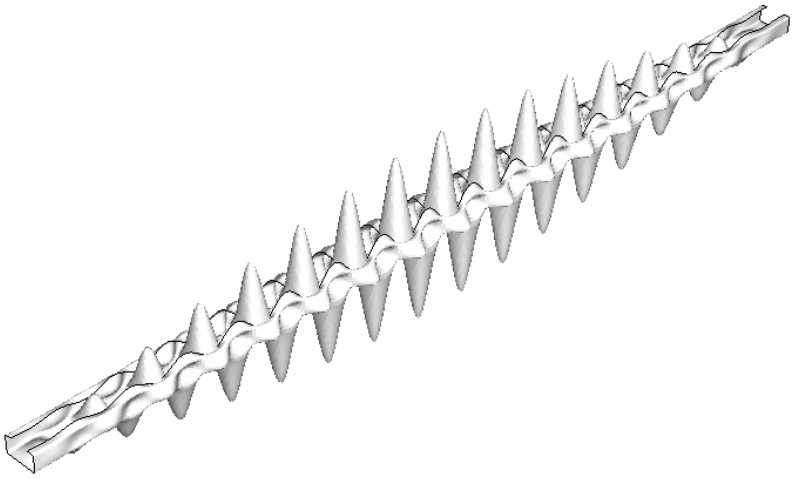

(b) The lowest local model (eigenmode 5)

Figure 9.4 Eigenmodes for the 2000-mm high pin-ended carbon steel column.

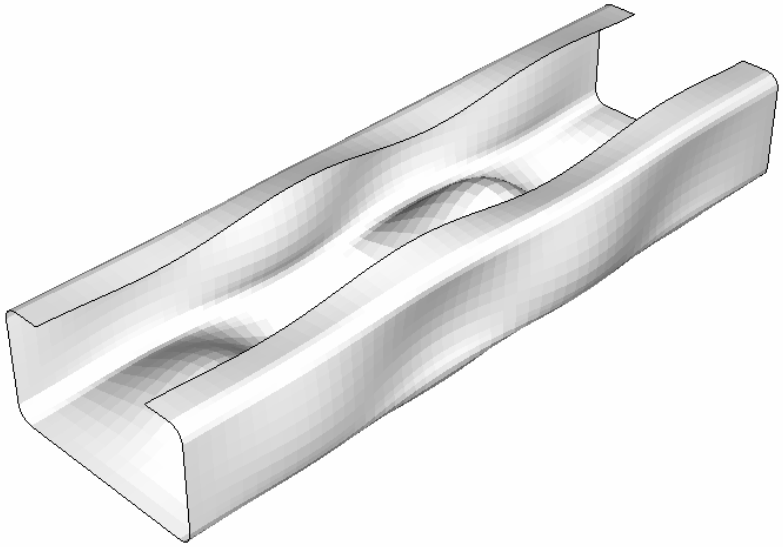

Figure 9.5 The first eigenmode for the carbon steel stub column.

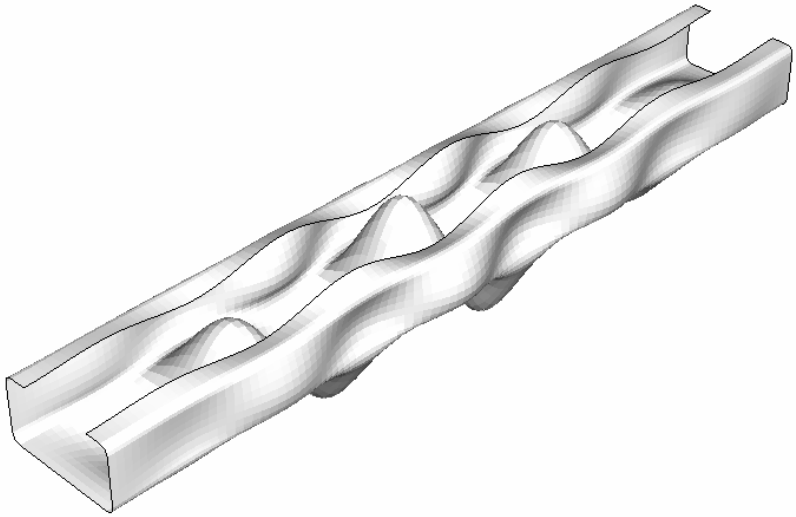

Figure 9.6 The first eigenmode for the 500-mm high pin-ended carbon steel column.

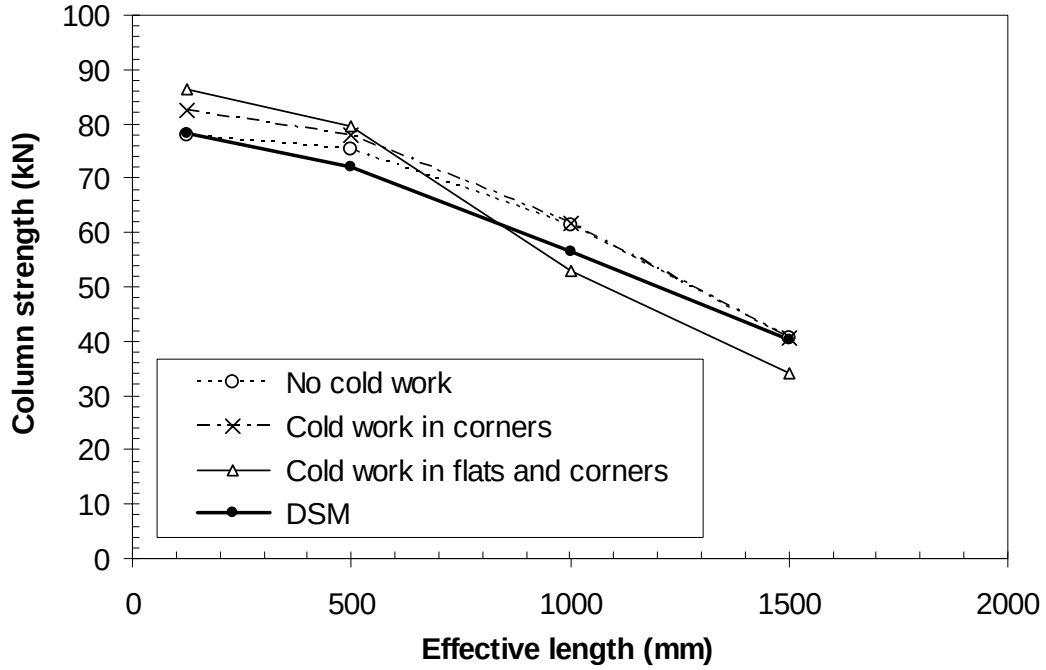

Figure 9.7 Comparison of column strengths between the advanced finite element approach (FEA) and the direct strength method (DSM) of the NAS (2001) specification for fixed-ended carbon steel columns.

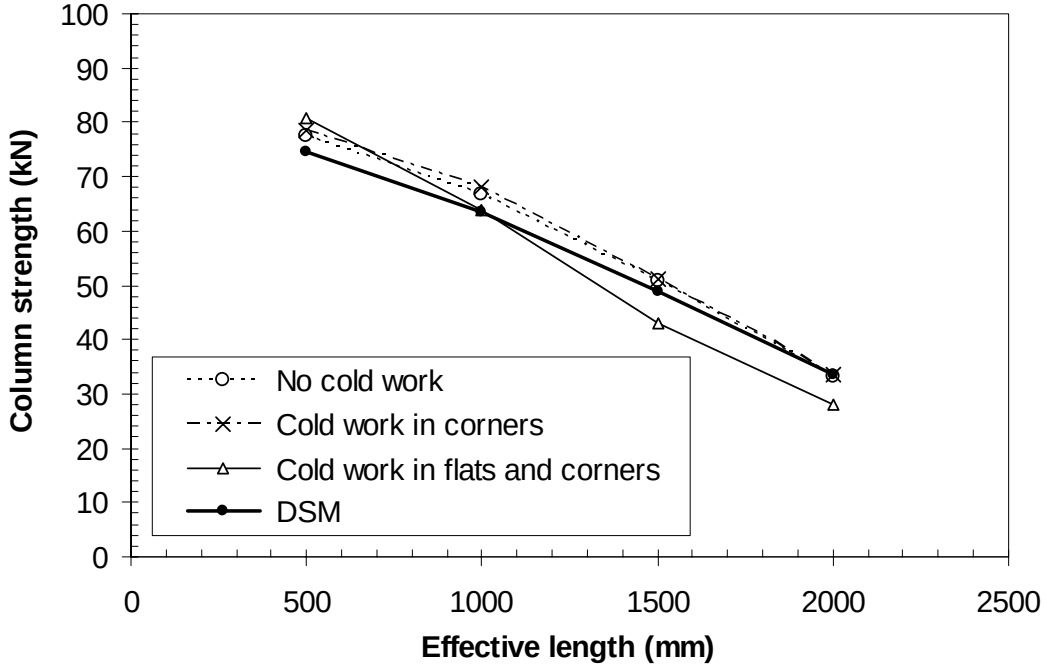

Figure 9.8 Comparison of column strengths between the advanced finite element approach (FEA) and the direct strength method (DSM) of the NAS (2001) specification for pin-ended carbon steel columns.

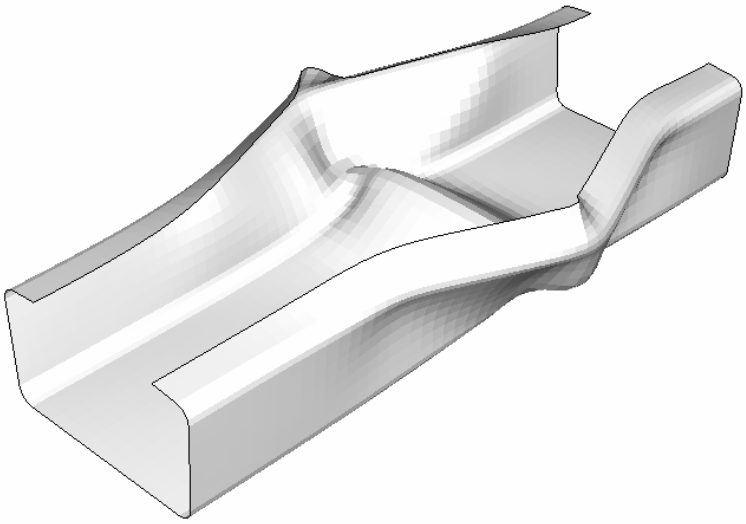

Figure 9.9 Post-failure deformed shape of the carbon steel stub column with D/t = 200.

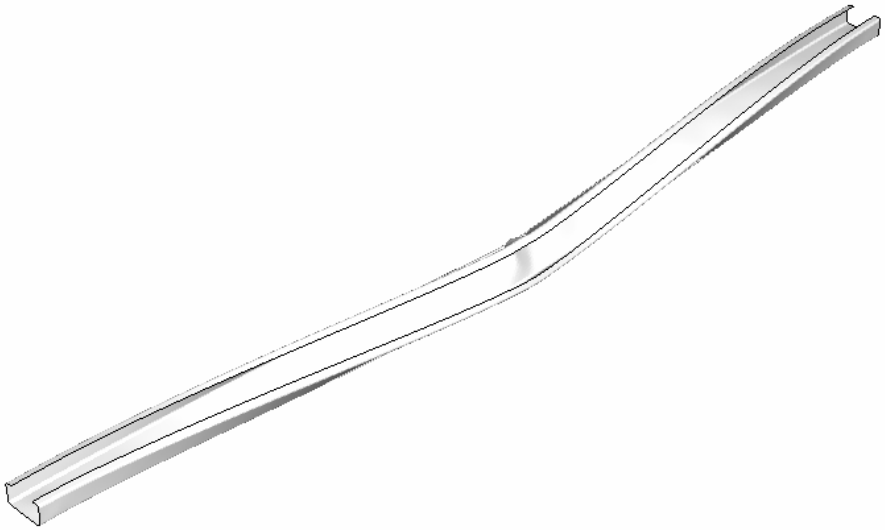

Figure 9.10 Post-failure deformed shape of the 2000-mm high fixed-ended carbon steel column with D/t = 200.

Figure 9.11 Post-failure deformed shape of the 2000-mm high pin-ended carbon steel column with D/t = 200.

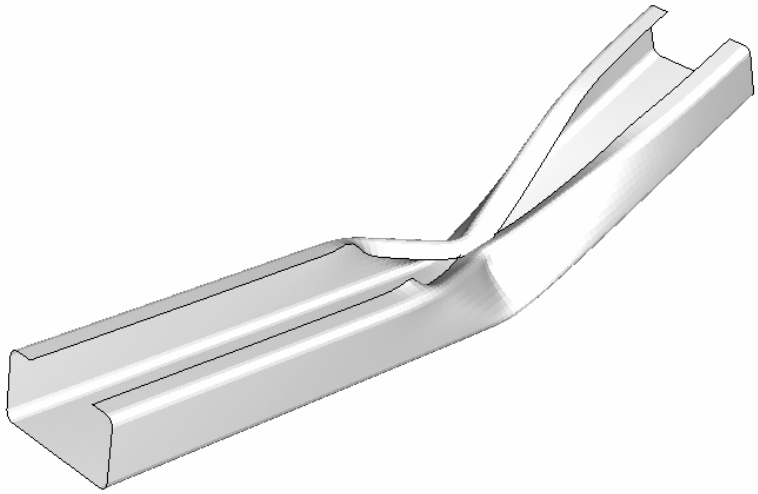

(a) Column with no cold work

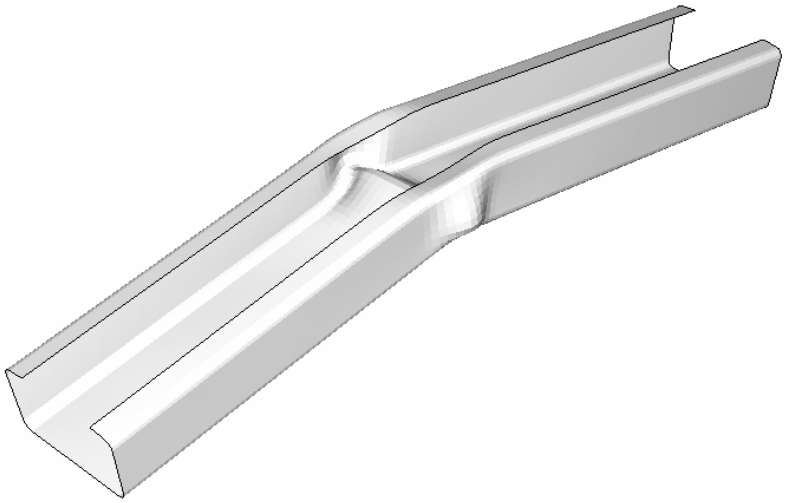

(b) Column with cold work in both flats and corners due to a coil diameter $D = 200\,t$

Figure 9.12 Post-failure deformed shape of the 500-mm high pin-ended carbon steel column.

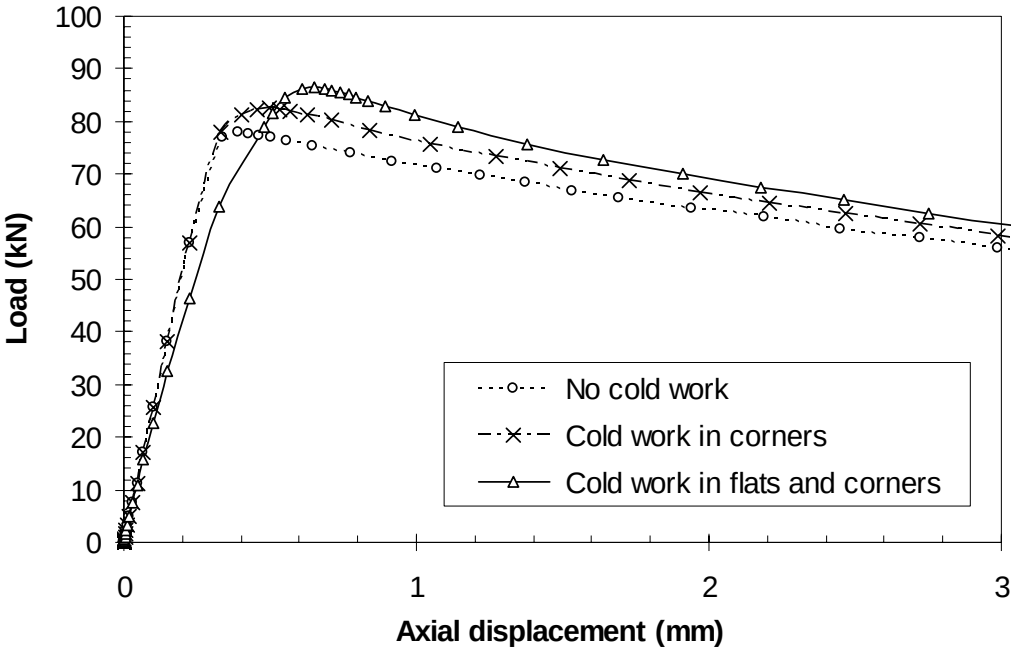

Figure 9.13 Load-axial displacement curves for the carbon steel stub column.

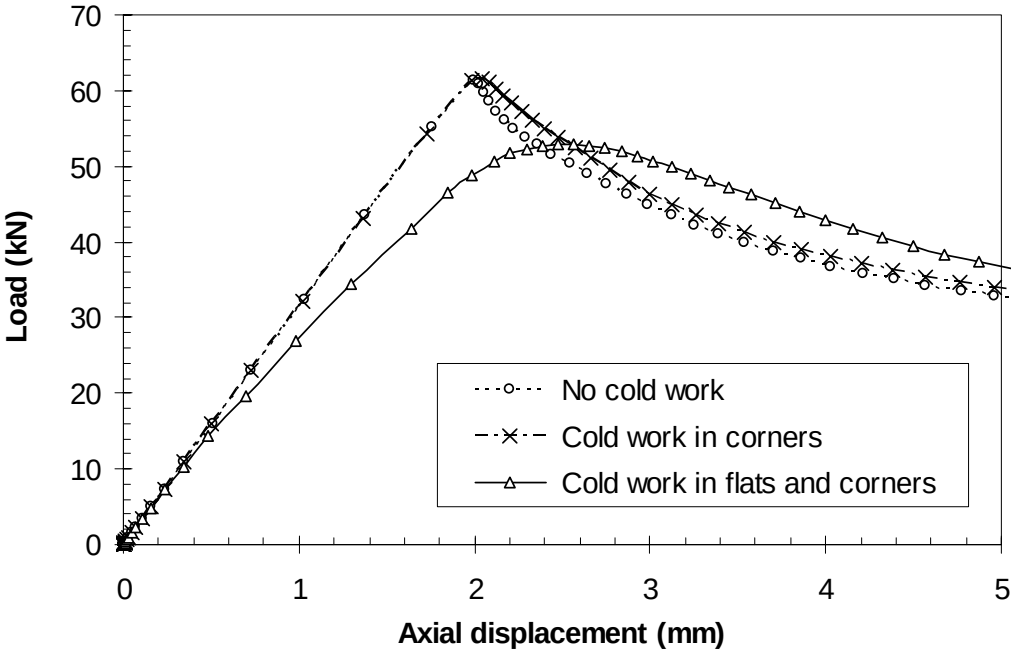

Figure 9.14 Load-axial displacement curves for the 2000-mm high fixed-ended carbon steel column.

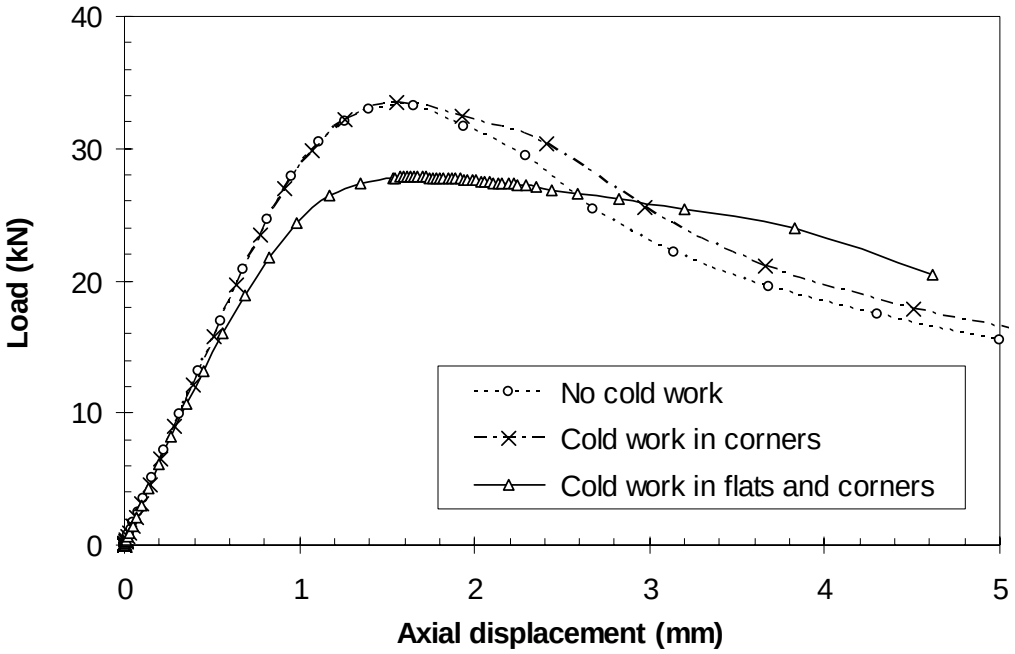

Figure 9.15 Load-axial displacement curves for the 2000-mm high pin-ended carbon steel column.

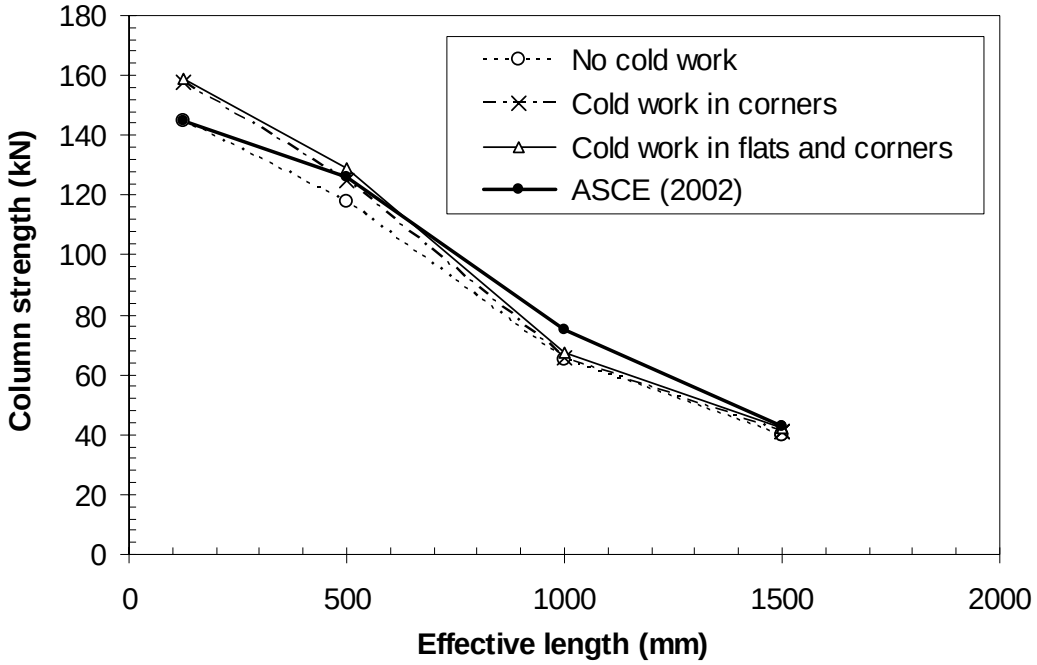

Figure 9.16 Comparison of column strengths between the advanced finite element approach (FEA) and the effective width method of the SEI/ASCE 8-02 specification (ASCE 2002) for fixed-ended stainless steel columns.

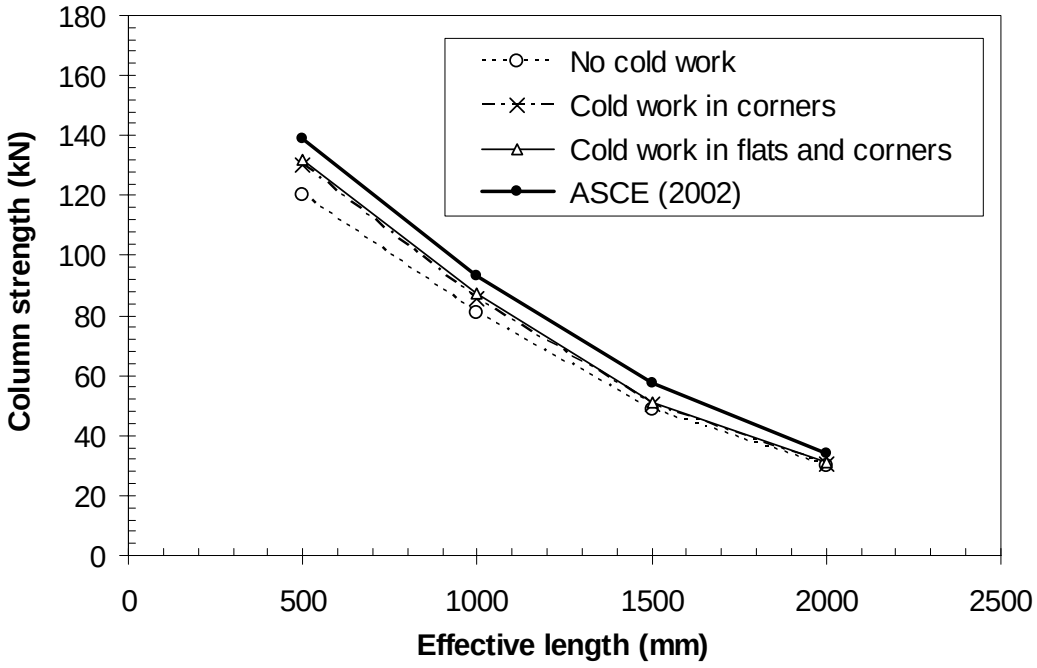

Figure 9.17 Comparison of column strengths between the advanced finite element approach (FEA) and the effective width method of the SEI/ASCE 8-02 specification (ASCE 2002) for pin-ended stainless steel columns.

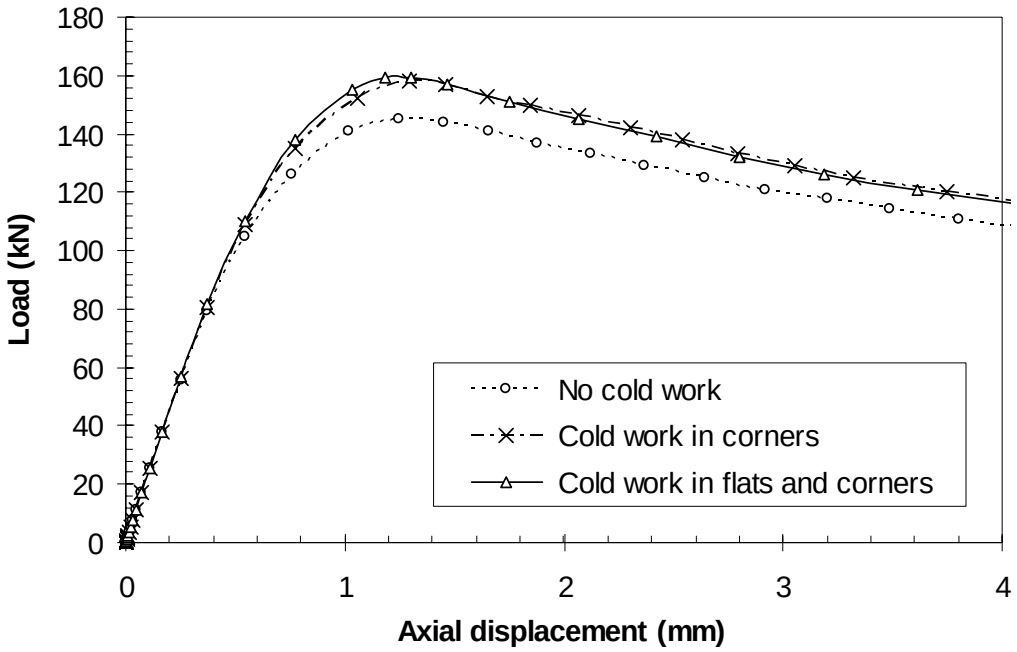

Figure 9.18 Load-axial displacement curves for the stainless steel stub column.

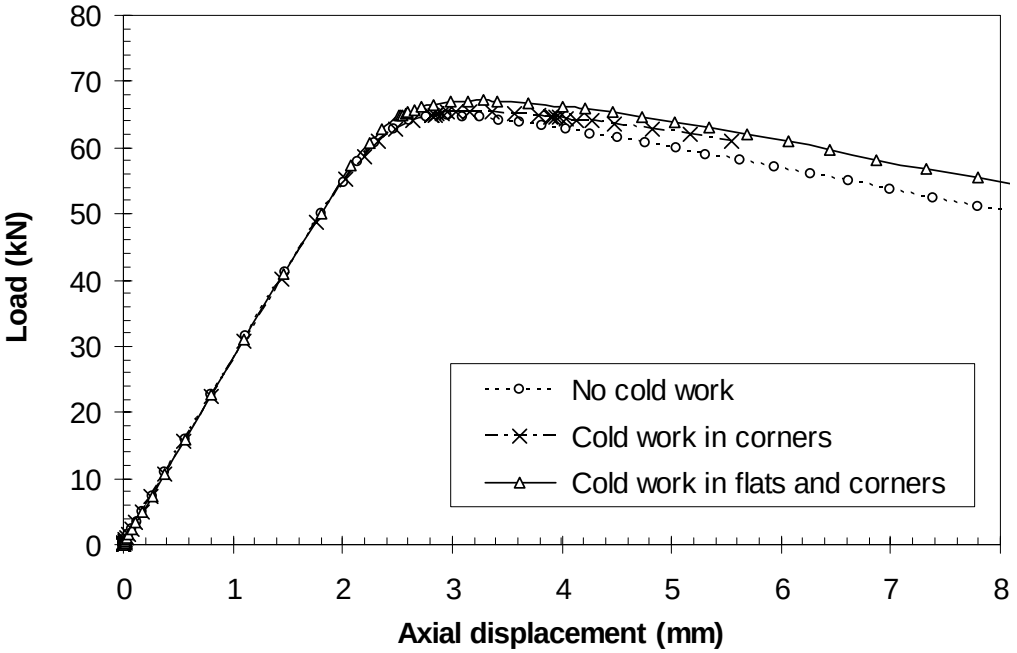

Figure 9.19 Load-axial displacement curves for the 2000-mm high fixed-ended stainless steel column.

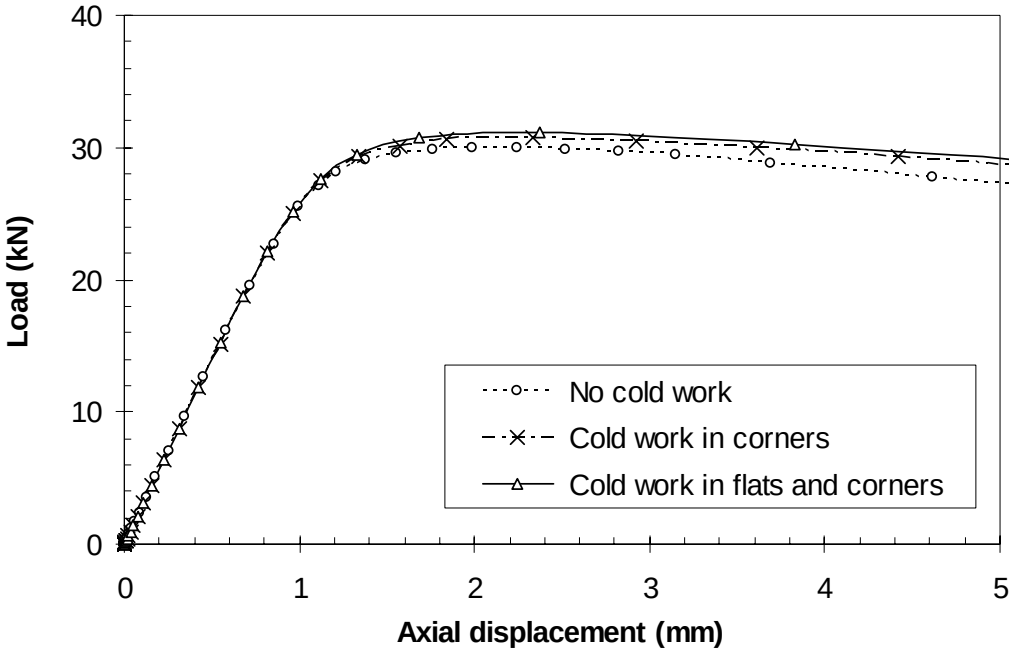

Figure 9.20 Load-axial displacement curves for the 2000-mm high pin-ended stainless steel column.

Chapter 10

CONCLUSIONS AND FUTURE WORK

10.1 INTRODUCTION

The manufacturing process of cold-formed steel members can cause residual stresses in and strain hardening of the material, and thus affects the structural behaviour of the members. To assess this effect accurately, the manufacturing process needs to be closely modelled. Cold-formed members are usually manufactured by either roll forming or press braking. In the present study, press braking has been considered. In the press-braking method, a virgin steel sheet is first coiled into a roll for storage, and subsequently uncoiled from the roll and forced to become a flat sheet before cold-forming forces are applied. Such a process prior to the press-braking operation is referred to simply as the coiling-uncoiling process. The manufacturing process of press-braked sections thus consists of two stages: the coiling-uncoiling process and the press-braking process. In this thesis, such a two-stage manufacturing process of press-braked carbon steel and stainless steel sections has been modelled to predict the resulting residual stresses and equivalent plastic strains, and its effect on the column behaviour of press-braked sections has been studied.

10.2 SUMMARY AND CONCLUSIONS

This section first summarizes the work presented in this thesis, and then presents the main observations and conclusions from the present study. More detailed conclusions and observations can be found at the end of each chapter.

This thesis has been concerned with the theoretical modelling of the manufacturing process of press-braked carbon and stainless steel sections for the prediction of the resulting residual stresses and equivalent plastic strains. The modelling of the manufacturing process requires the knowledge of the stress-strain behaviour of the sheet material over the full range of strains. Stainless steel alloys have different stress-strain responses in tension and compression, but the stress-strain curve over the full range of compressive strains cannot be obtained from tests of compression coupons. This leads to difficulty in modelling the material behaviour of stainless steel alloys. To overcome this problem, a new stress-strain model has been established and presented in Chapter 3 to describe the stress-strain relationship over full ranges of both tensile and compressive strains using the basic Ramberg-Osgood parameters (E_0, $\sigma_{0.2}$ and n).

For a two-stage manufacturing process of press-braked sections, the residual stresses and equivalent plastic strains in such sections are derived from two sources: the coiling-uncoiling process and the press-braking process. A series of analytical solutions have been presented in Chapters 4, 6 and 7 to predict the residual stresses and the associated equivalent plastic strains in steel sheets as a result of cold bending, covering both processes. These solutions have been verified using finite element

simulations of cold bending of steel sheets. As residual stresses and equivalent plastic strains are the two defining parameters of the effect of cold work, the cold work effect of the manufacturing process can be captured by these analytical solutions.

On the basis of these analytical solutions, two alternative approaches for the prediction of residual stresses and equivalent plastic strains in press-braked sections have been presented and verified in Chapters 5 and 7 respectively: (a) a finite element-based method in which a finite element simulation of the cold-forming process is carried out with its initial state being defined by an analytical solution for the coiling-uncoiling process; and (b) a complete analytical model in which the residual stresses and equivalent plastic strains from both processes are given by analytical solutions. The accuracy of both approaches has been demonstrated by comparing their predictions with existing laboratory measurements. A parametric study employing the finite element-based approach has been conducted and presented in Chapter 8 to study the effect of forming parameters on the resulting residual stresses in press-braked sections. The complete analytical model provides an attractive approach for defining the initial state of a section in a column nonlinear buckling analysis.

The thesis has also presented an advanced numerical approach to predict the buckling behaviour of cold-formed columns in which the effect of the manufacturing process is explicitly and accurately accounted for. In this approach, the complete analytical model for residual stresses and equivalent plastic strains has been employed together with an appropriate geometrical imperfection model. Using this advanced finite

element approach, the effect of cold work on the buckling behaviour of press-braked carbon and stainless steel columns has been examined and presented in Chapter 9.

The investigations and the results presented in this thesis allow the following observations and conclusions to be made:

- The through-thickness variations of residual stresses in cold-formed sections are nonlinear, and residual stresses in corner regions are different from those in flat portions. Residual stresses in a cold-formed section are dependent not only on the material properties but also on the forming parameters such as the corner radius and the coil diameter. Thus, the traditional assumption of linear variations of residual stresses with their magnitudes being proportional to the yield stress is inappropriate.

- If the coil diameter of the coiling-uncoiling process remains unchanged, press-braked sections with smaller yield stresses are subjected to residual stresses of greater magnitude and extent in the flat portions. This means that conventional idealized residual stress distributions may greatly underestimate the real residual stresses.

- The distributions of residual stresses in the flat portions are highly dependent on the initial coil diameter, so very different residual stresses can arise in the flat portions of otherwise identical cold-formed sections as a result of different initial coil diameters, which are unknown to designers and users of these sections. This

may have been responsible for the significant scatter in test load capacities of cold-formed members.

- Whether the column strength of a cold-formed member can be enhanced or reduced by cold work is a result of the combined effect of the pre-existing residual stresses and equivalent plastic strains in the member, and this combined effect varies depending on the initial material properties and the forming parameters.

- For a press-braked member under axial compression, the cold work in the corner regions and flat portions can enhance the column strength, and the amount of the strength enhancement decreases as the column length increases. With further increases in the column length, the effect of the cold work in the corner regions becomes negligible, and the cold work in the flat portions may cause reductions in the column strength.

- The cold work effect of the manufacturing process on the structural behaviour of cold-formed members has been traditionally assessed using idealized residual stress distributions based on limited laboratory measurements in conjunction with separate specifications of mechanical properties for the flat portions and the corner regions, or using the whole section mechanical properties obtained from stub column tests. These conventional approaches are highly empirical and do not provide an accurate description of the co-existent residual stresses and strain hardening of the material arising from the manufacturing process. For example, in these approaches, equivalent plastic strains are not addressed, which are needed to define the work hardened state due to the cold work from forming. Furthermore,

the mechanical properties obtained from coupon tests cannot properly reflect the initial work hardened state of a cold-formed member, since part of the residual stresses will be released when coupons are cut from the member. The use of whole section properties obtained from stub column tests may provide better predictions of the mechanical response of cold-formed sections, but the initial state in a stub column is quite different from that in a cold-formed member with another length. This has been demonstrated by the results presented in Chapter 9.

- In contrast with the aforementioned conventional approaches which require stub column tests or coupon tests of corner and flat materials to provide data for the modelling of the cold work effect, the proposed advanced numerical approach presented in the thesis allows the effect of cold work from forming to be assessed accurately in an explicit way, and requires only the basic forming parameters and the mechanical properties of virgin sheet materials as input data.

10.3 FUTURE WORK

The proposed analytical solutions for residual stresses and equivalent plastic strains arising from the manufacturing process of press-braked sections can be applied or further extended to other relevant research areas as follows:

- Cold work in cold-formed hollow sections due to the manufacturing process and its effect on the structural behaviour.

- The strength enhancement of cold-formed sections with complex stiffeners and multiple folds.

The structural behaviour of a cold-formed member is affected by geometrical and material imperfections. Material imperfections refer to the co-existent residual stresses and strain hardening of the material arising from the manufacturing process which has been accurately modelled in the present study. In order to enable the accurate prediction of the structural behaviour of cold-formed members, further research is needed on the following aspects:

- The modelling of critical geometrical imperfections.

- The interaction between residual stresses and critical geometrical imperfections.

With a more accurate geometrical imperfection model obtained from future research, the advanced numerical approach presented in this thesis can be further advanced and can provide more accurate predictions of the structural response of cold-formed members. Instead of using expensive laboratory tests, this advanced numerical approach can provide a rapid and economical alterative means to generate accurate numerical data for the structural performance of cold-formed members. The method allows the rapid development and improvement of design rules for new cold-formed members with innovative and complex cross-sectional geometries.

Appendix A

COMPARISON OF THE 3-STAGE FULL-RANGE STRESS-STRAIN MODEL WITH EXPERIMENTAL STRESS-STRAIN CURVES

A.1 GENERAL

In this appendix, stress-strain curves predicted by the proposed 3-stage full-range stress-strain model are compared with existing experimental stress-strain curves. Totally 39 experimental stress-strain curves available in existing literatures have been used to for the comparison. Test data include tension and compression coupon tests on different alloys: 31 tests on austenitic alloys, 4 tests on duplex alloys and 4 tests on ferritic alloys. The measured values of basic Ramberg-Osgood parameters for these 39 tests are summarized in Table 3.3 of Chapter 3.

Figures A.1 shows the comparison for the test by Macdonald *et al*. (2000). Figures A.2~A.31 show the comparison for tests by Gardner and Nethercot (2004). Figures A.32~A.35 show the comparison for tests by Rasmussen *et al*. (2002), and Figures A.36~A.39 show the comparison for tests by Korvink *et al*. (1995). Stress-strain curves predicted by the full-range stress-strain model proposed by Rasmussen (2003) are also included in these figures as references.

Gardner and Nethercot (2004) only reported the weighted average measured material properties for each hollow section that they tested, rather than complete stress-strain curves. In this appendix, Gardner and Nethercot's experimental stress-strain curves are re-generated by using their proposed stress-strain relationship (refer to the paper by Gardner and Nethercot (2004) or Eq. (2.13)) together with their weighted average test data. Because Gardner and Nethercot (2004) concluded that their proposed relationship can provide excellent agreement with test data up to approximately 10%, their proposed stress-strain relationship has been adopted to generate experimental stress-strain data only up to the strain at the 10% proof stress.

A.2 REFERENCES

Gardner, L. and Nethercot, D. A. (2004). Experiments on stainless steel hollow sections – Part 1: Material and cross-sectional behaviour. *Journal of Constructional Steel Research,* **60**, 1291-1318.

Korvink, S. A., Van den Berg, G. J. and Van der Merwe, P. (1995). Web crippling of stainless steel cold-formed beams. *Journal of Constructional Steel Research,* **34**, 225-248.

Macdonald, M., Rhodes, J. and Taylor, G. T. (2000). Mechanical properties of stainless steel lipped channels. *Proceedings of the Fifteenth International Specialty Conference on Cold-Formed Steel Structures*, St. Louis, Missouri, United States, 19-20 October, 673-686.

Rasmussen, K. J. R. (2003). Full-range stress-strain curves for stainless steel alloys. *Journal of Constructional Steel Research*, **59**, 47-61.

Rasmussen, K. J. R., Burns, T., Bezkorovainy, P. and Bambach, M. R. (2002). *Numerical Modelling of Stainless Steel Plates in Compression, Research Report No. R813*, March 2002, Department of Civil Engineering, University of Sydney, Sydney.

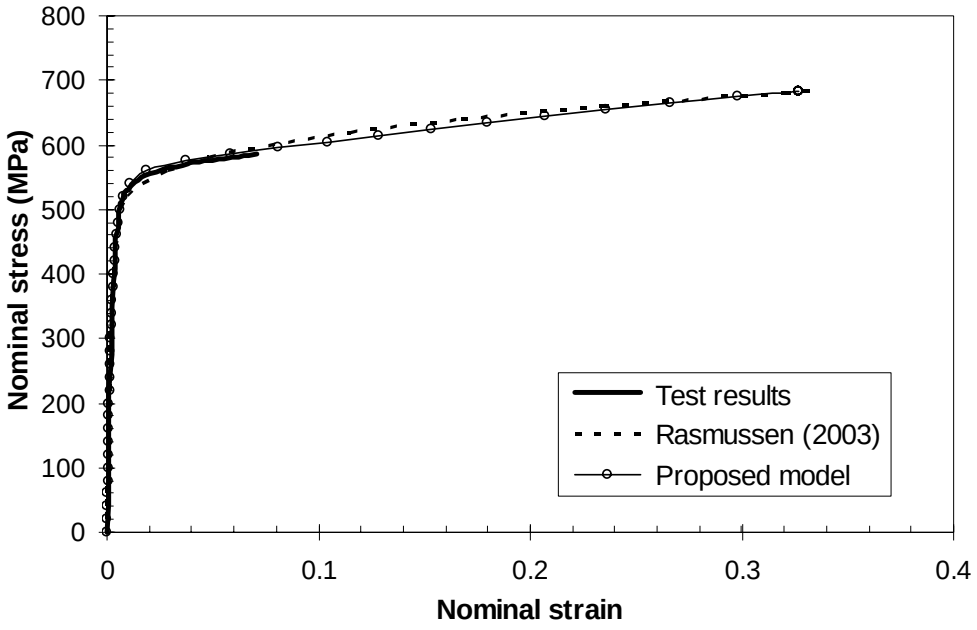

(a) Full stress-strain curves

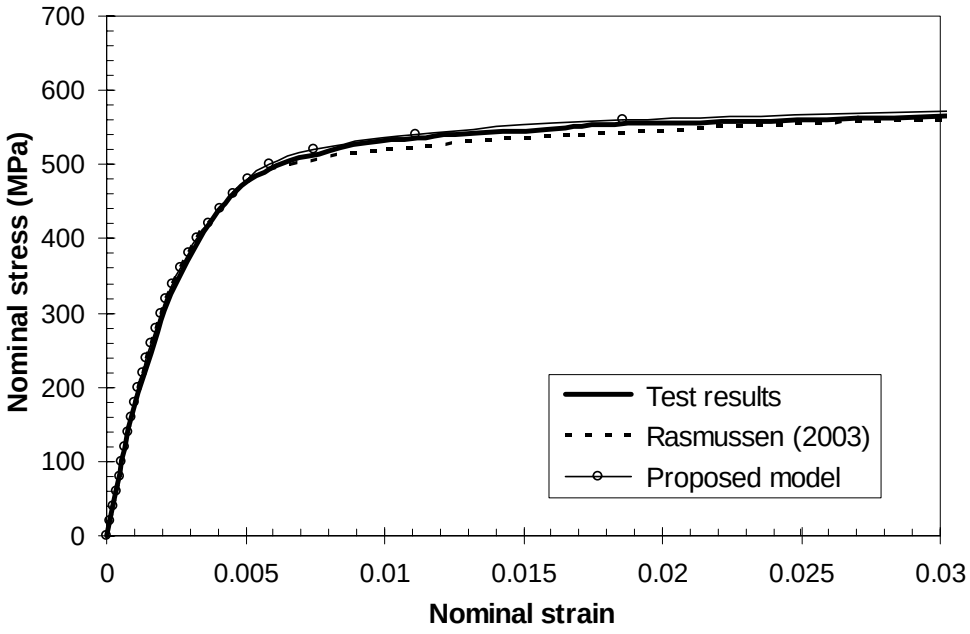

(b) Initial stress-strain curves

Figure A.1 Nominal stress-strain curves for the tension coupon cut from the thick lipped channel section tested by Macdonald *et al*. (2000).

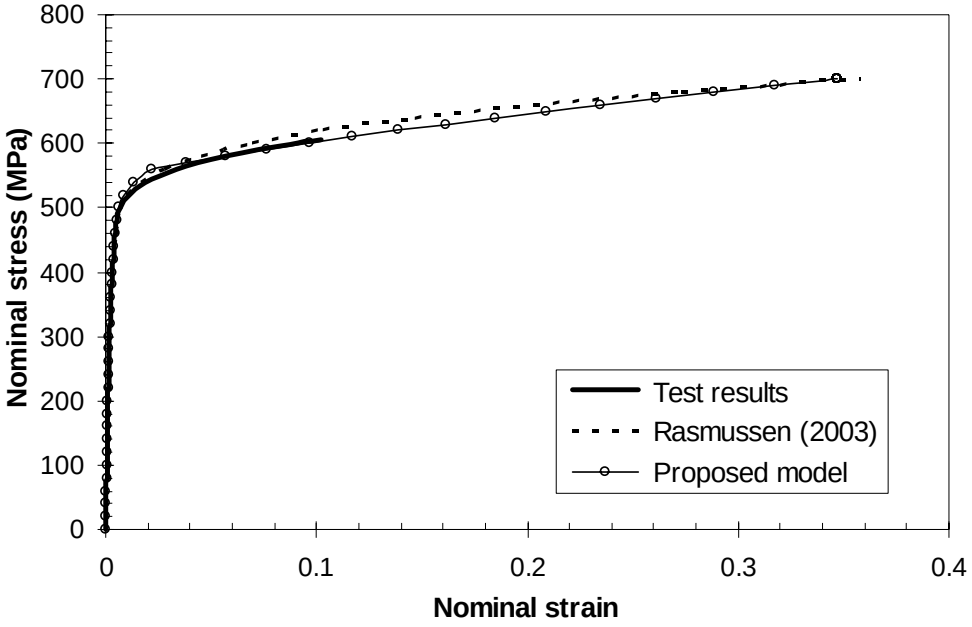

(a) Full stress-strain curves

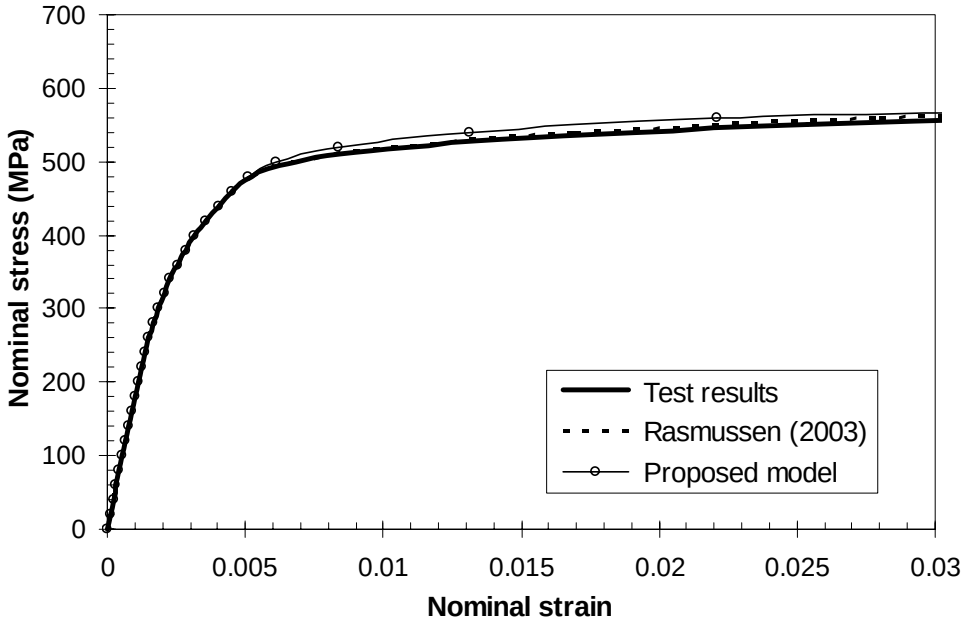

(b) Initial stress-strain curves

Figure A.2 Nominal stress-strain curves for the flat tension coupon cut from section SHS 80×80×4 tested by Gardner and Nethercot (2004).

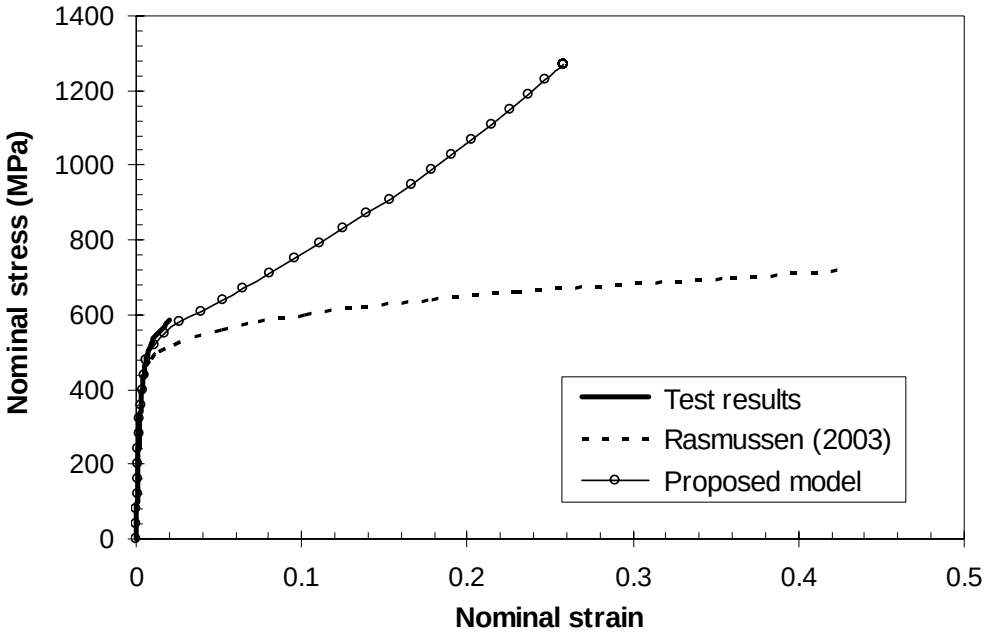

(a) Full stress-strain curves

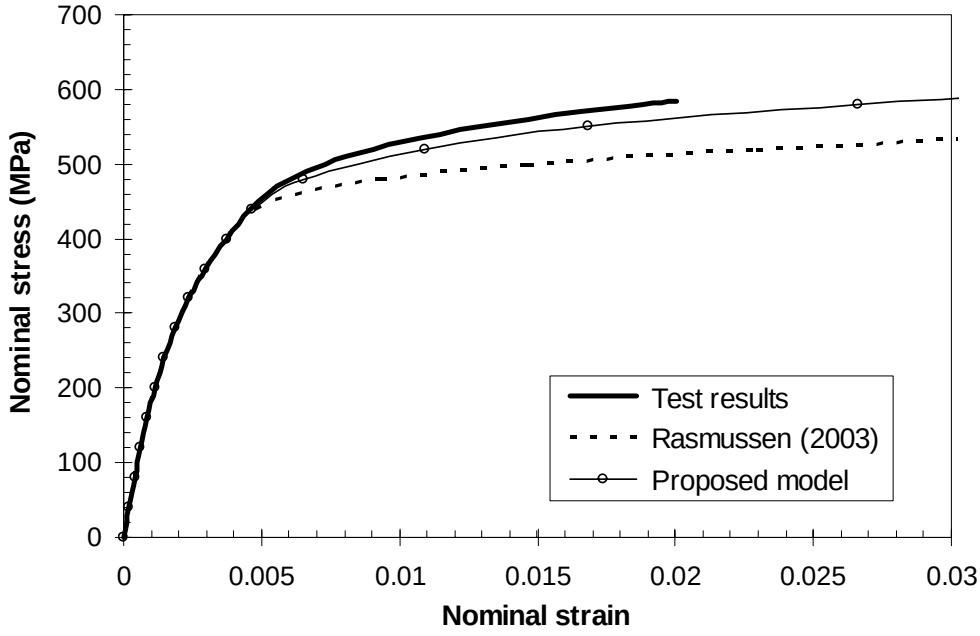

(b) Initial stress-strain curves

Figure A.3 Nominal stress-strain curves for the flat compression coupon cut from section SHS 80×80×4 tested by Gardner and Nethercot (2004).

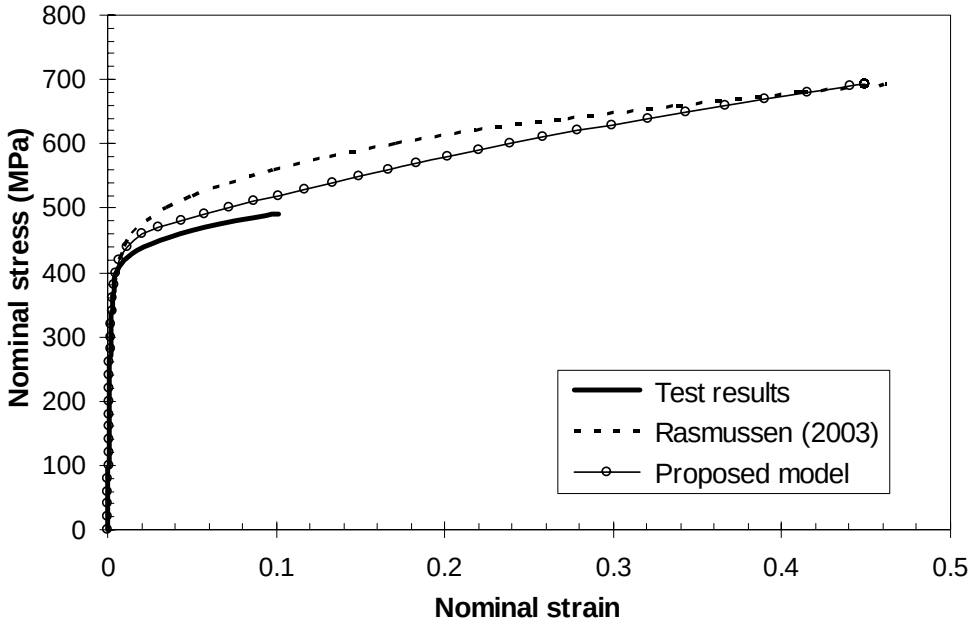

(a) Full stress-strain curves

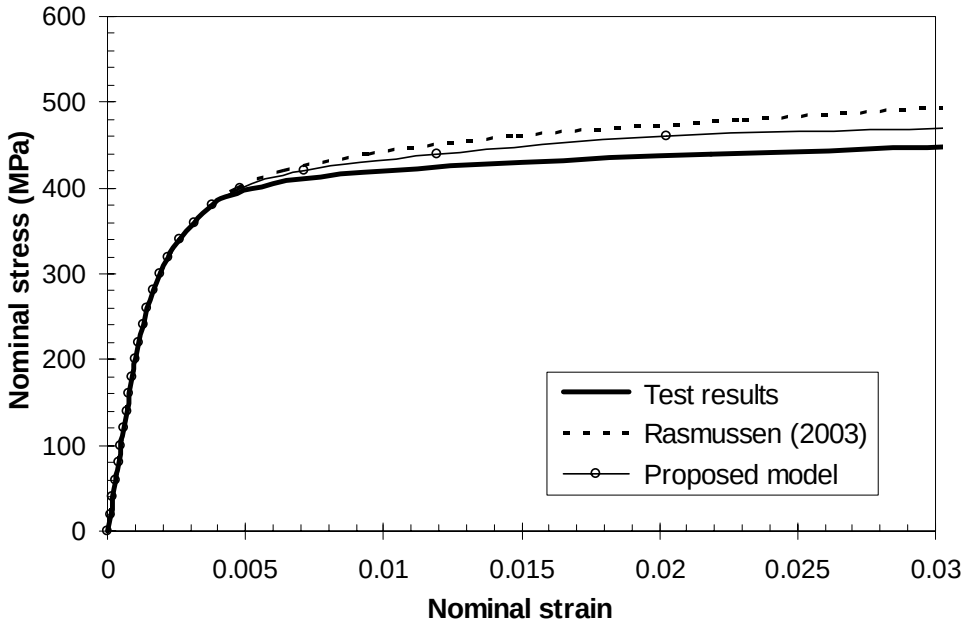

(b) Initial stress-strain curves

Figure A.4 Nominal stress-strain curves for the flat tension coupon cut from section SHS 100×100×2 tested by Gardner and Nethercot (2004).

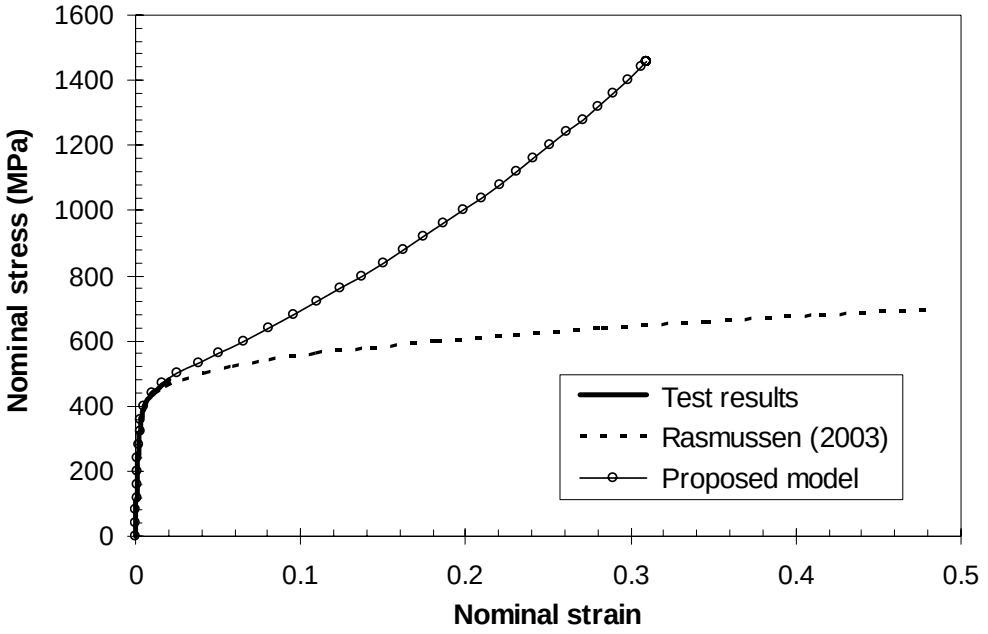

(a) Full stress-strain curves

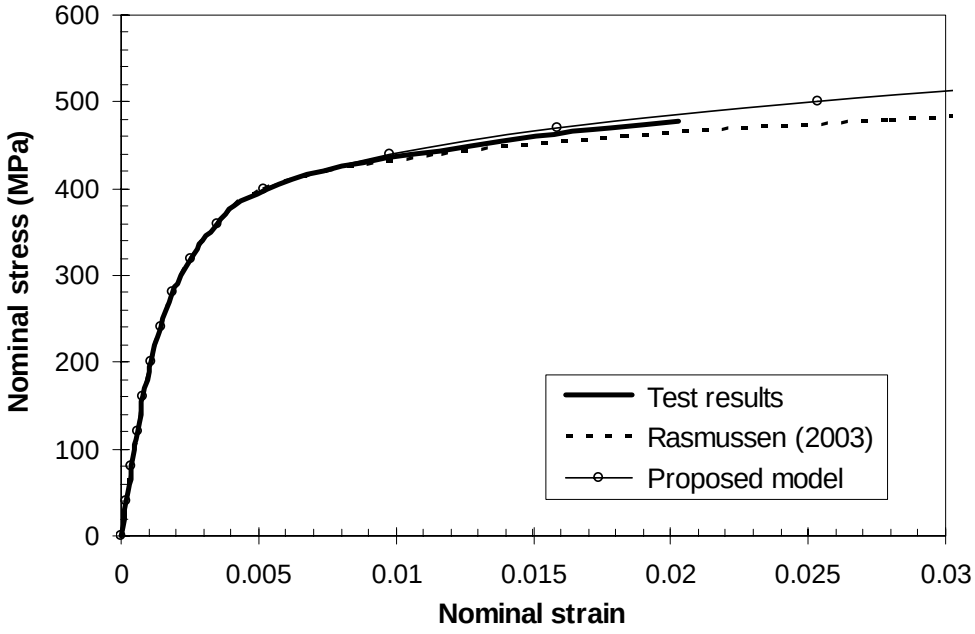

(b) Initial stress-strain curves

Figure A.5 Nominal stress-strain curves for the flat compression coupon cut from section SHS 100×100×2 tested by Gardner and Nethercot (2004).

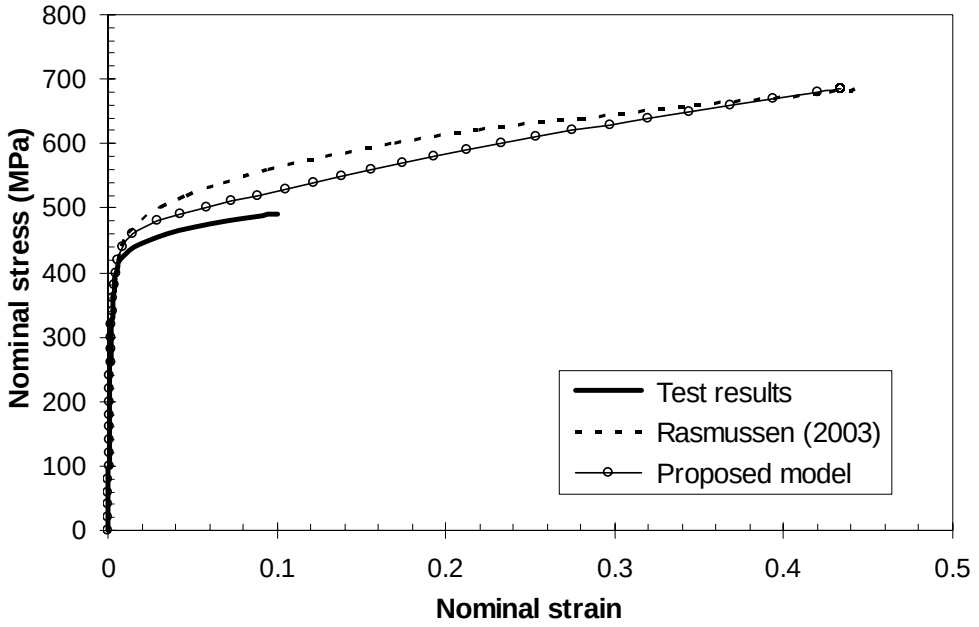

(a) Full stress-strain curves

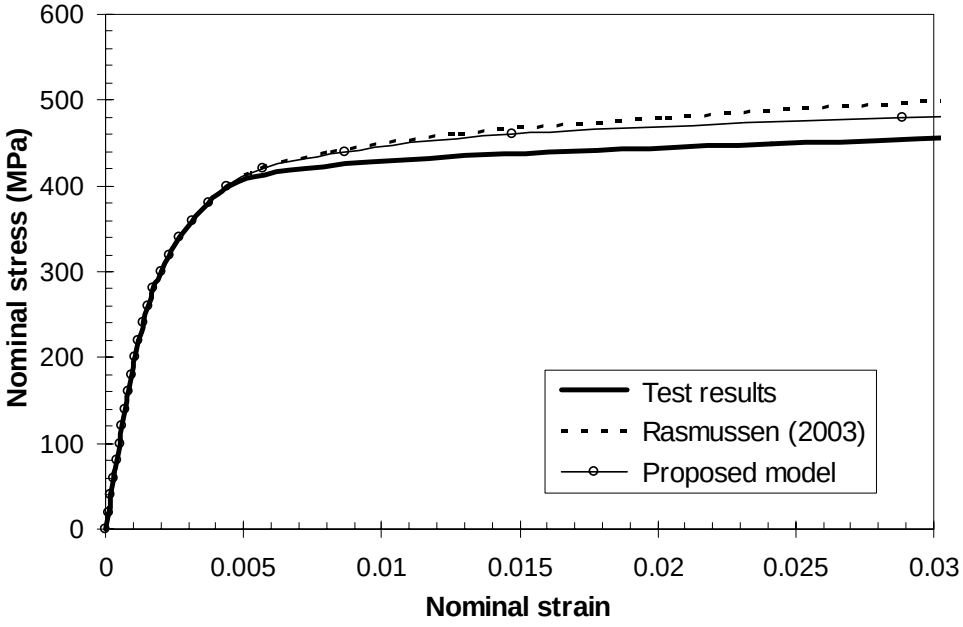

(b) Initial stress-strain curves

Figure A.6 Nominal stress-strain curves for the flat tension coupon cut from section SHS 100×100×3 tested by Gardner and Nethercot (2004).

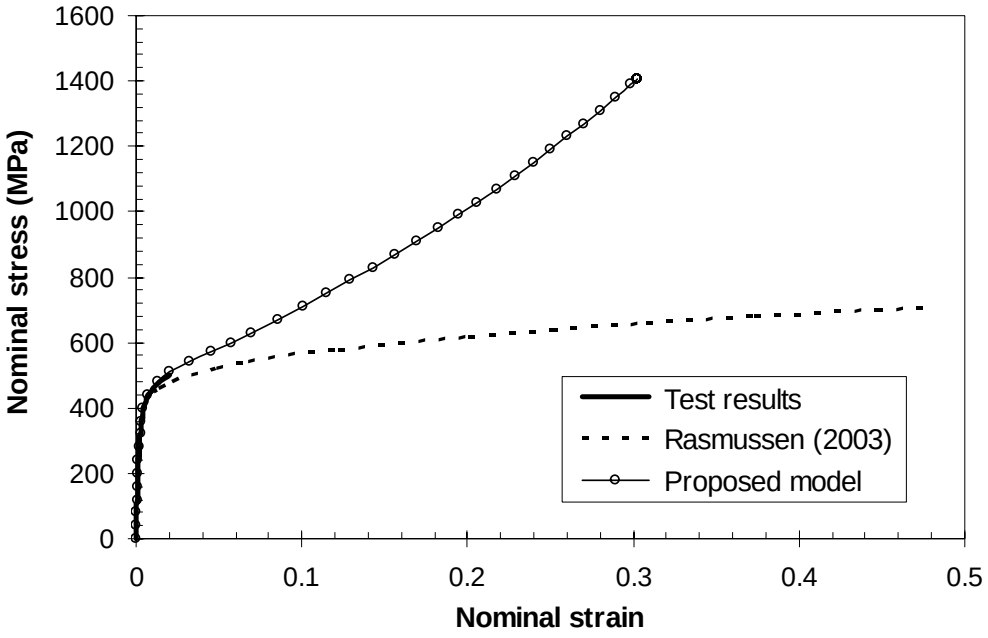

(a) Full stress-strain curves

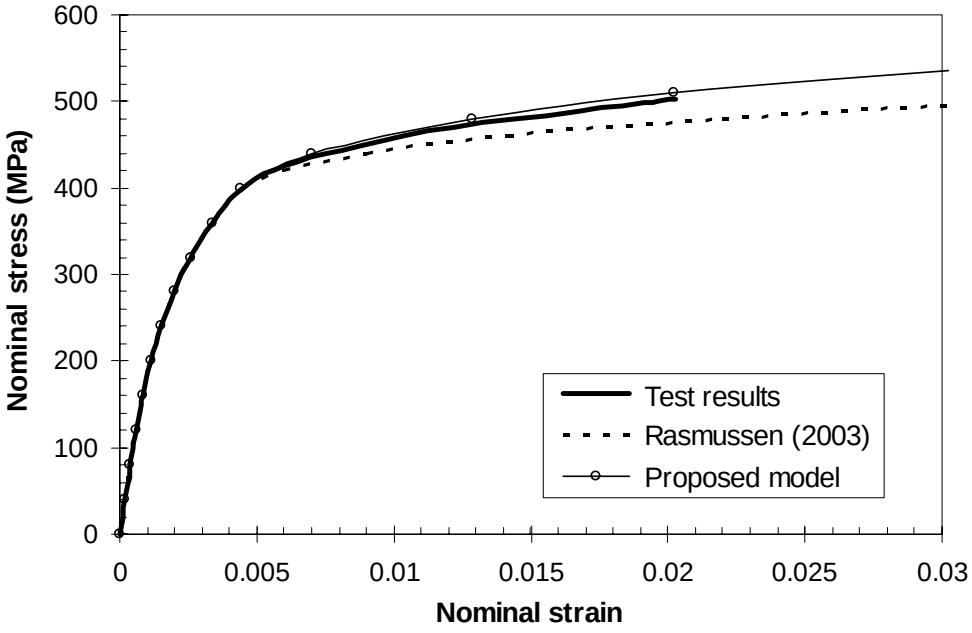

(b) Initial stress-strain curves

Figure A.7 Nominal stress-strain curves for the flat compression coupon cut from section SHS 100×100×3 tested by Gardner and Nethercot (2004).

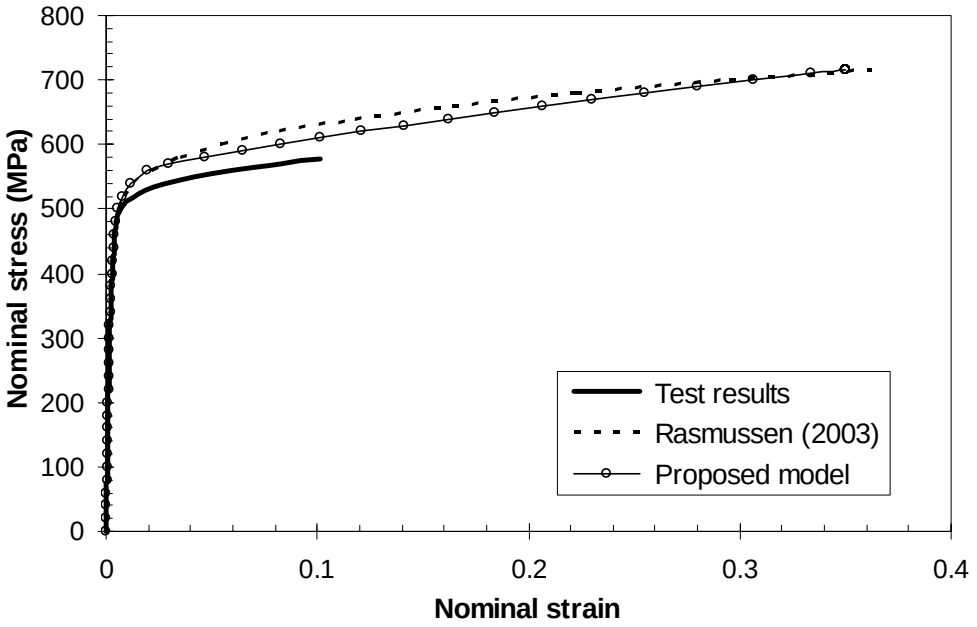

(a) Full stress-strain curves

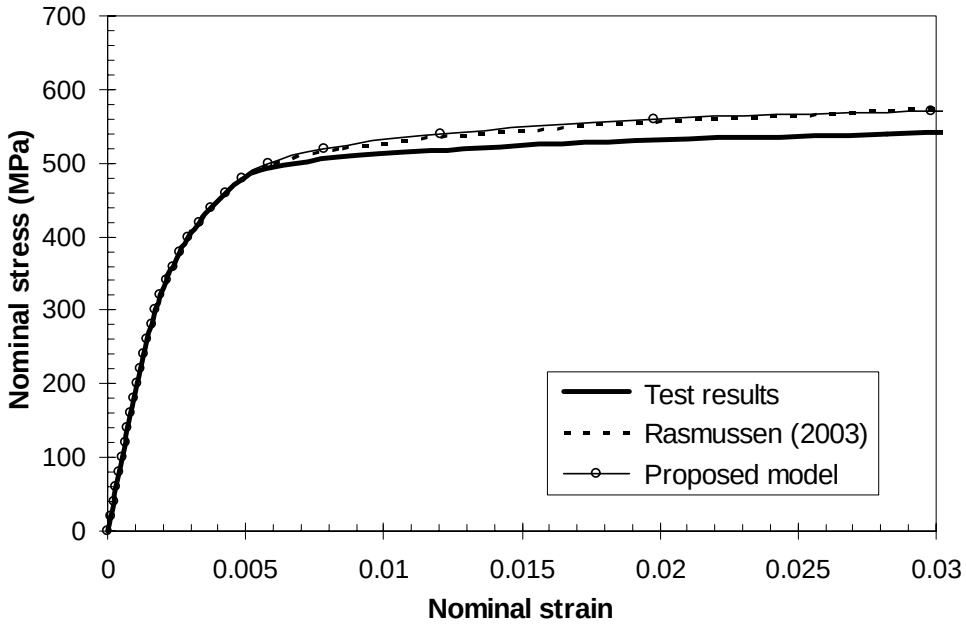

(b) Initial stress-strain curves

Figure A.8 Nominal stress-strain curves for the flat tension coupon cut from section SHS 100×100×4 tested by Gardner and Nethercot (2004).

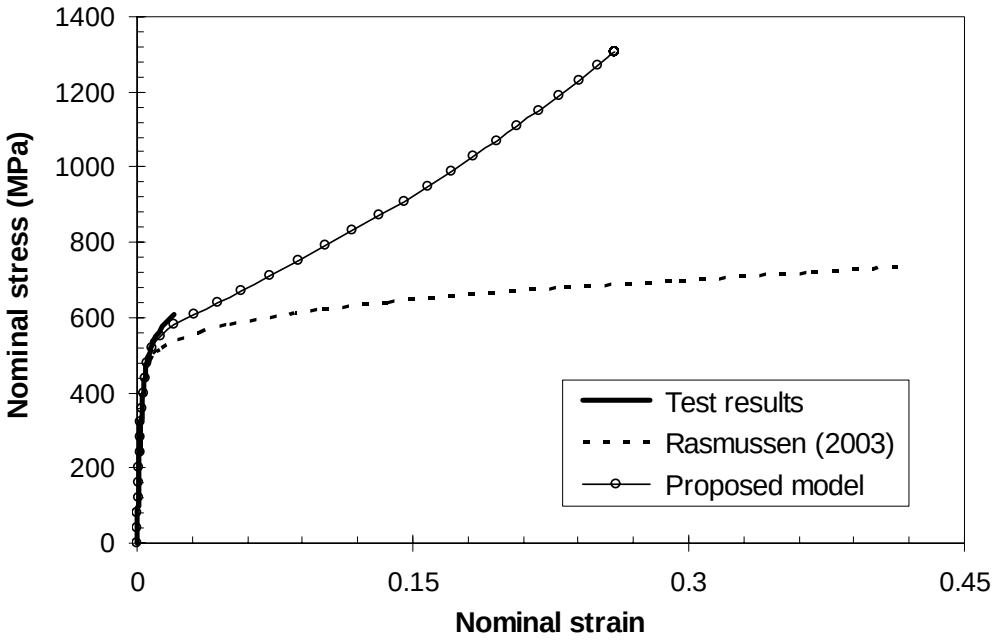

(a) Full stress-strain curves

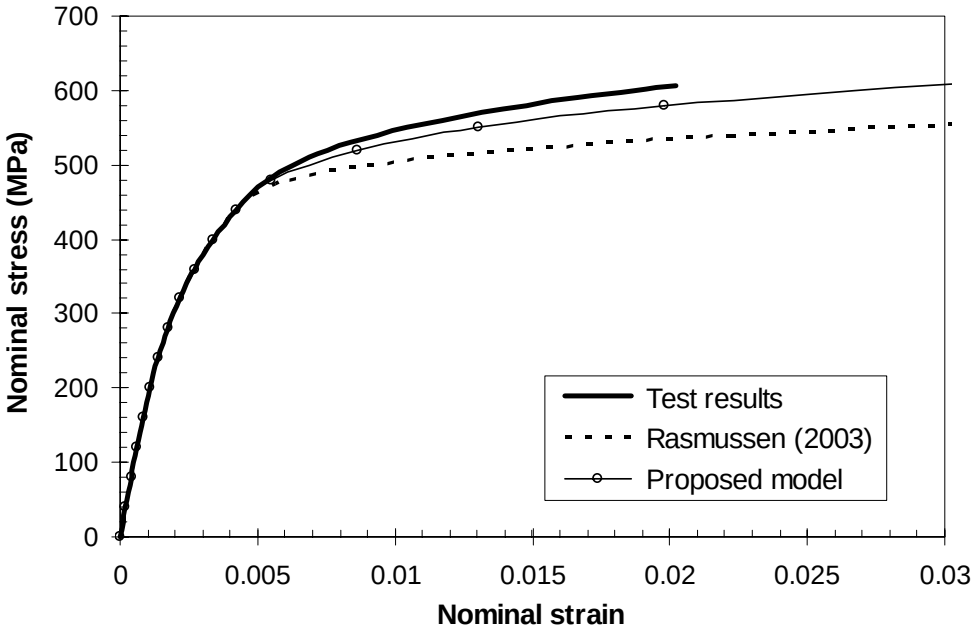

(b) Initial stress-strain curves

Figure A.9 Nominal stress-strain curves for the flat compression coupon cut from section SHS 100×100×4 tested by Gardner and Nethercot (2004).

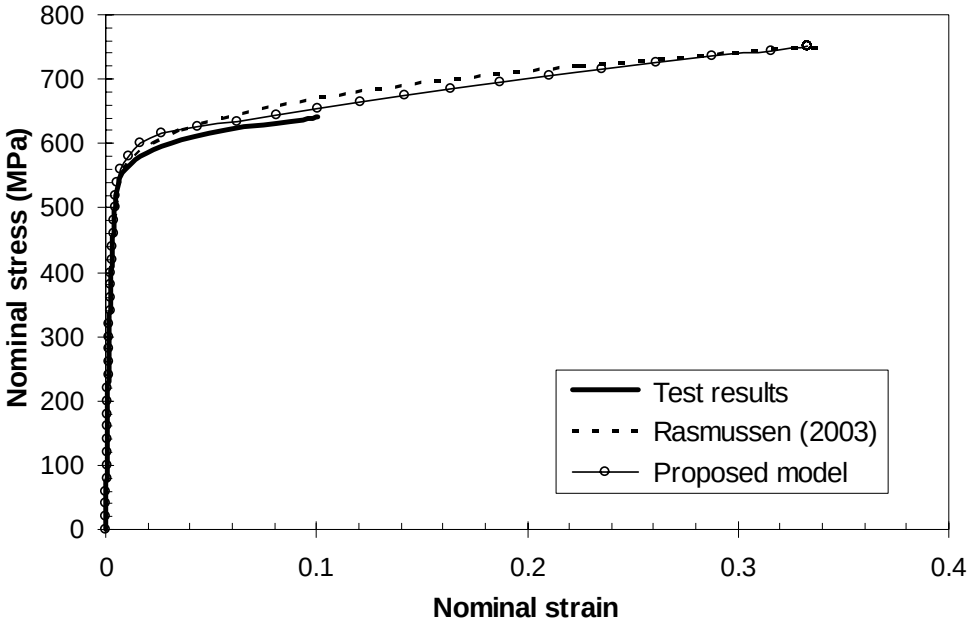

(a) Full stress-strain curves

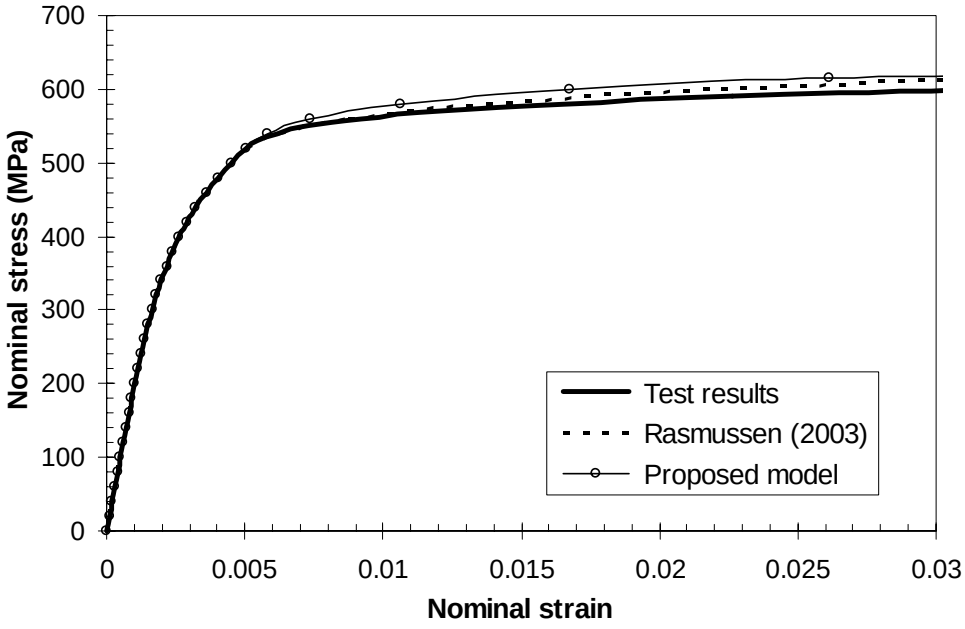

(b) Initial stress-strain curves

Figure A.10 Nominal stress-strain curves for the flat tension coupon cut from section SHS 100×100×6 tested by Gardner and Nethercot (2004).

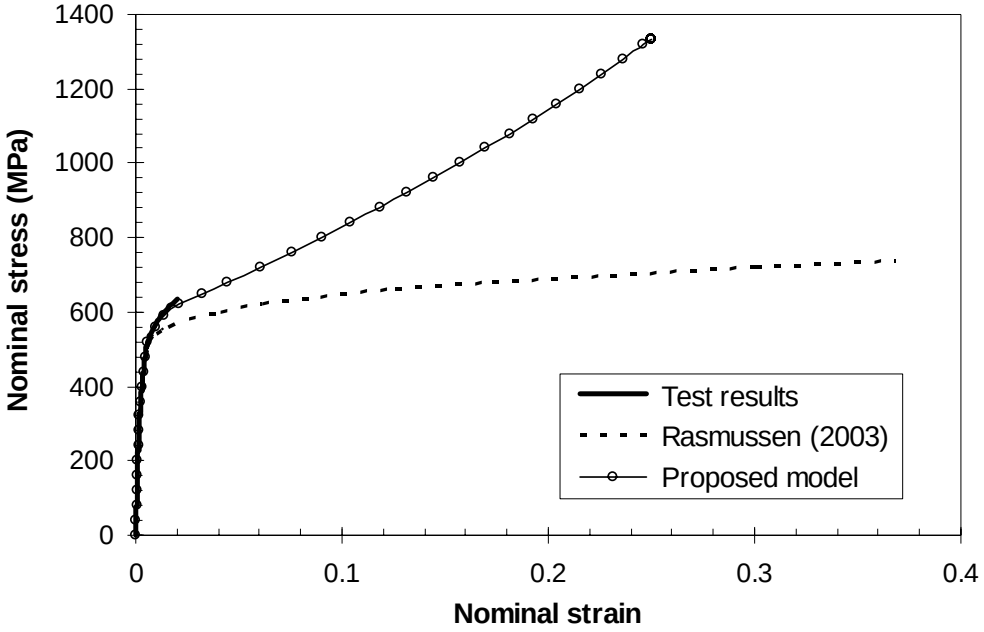

(a) Full stress-strain curves

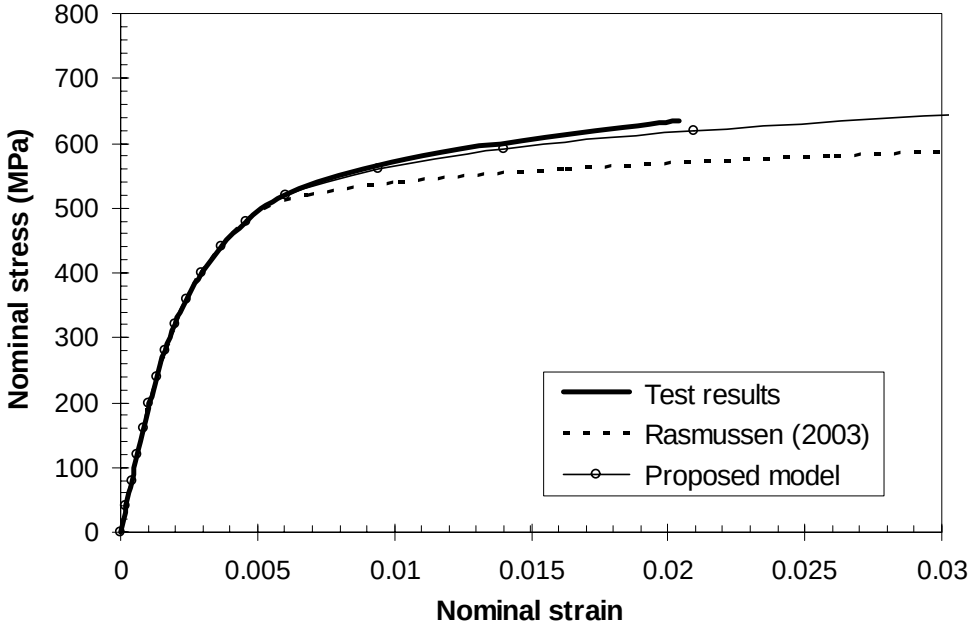

(b) Initial stress-strain curves

Figure A.11 Nominal stress-strain curves for the flat compression coupon cut from section SHS 100×100×6 tested by Gardner and Nethercot (2004).

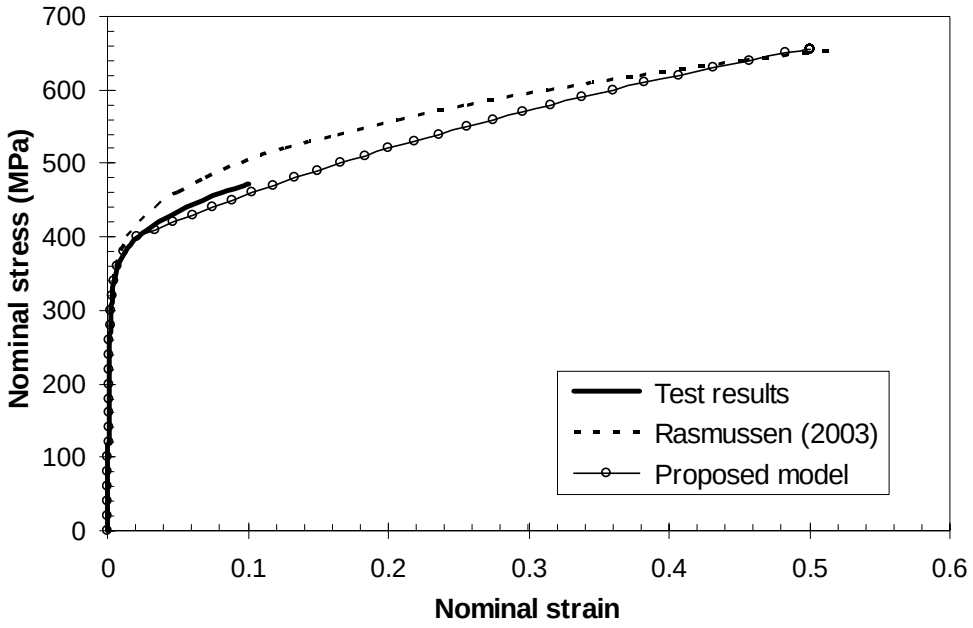

(a) Full stress-strain curves

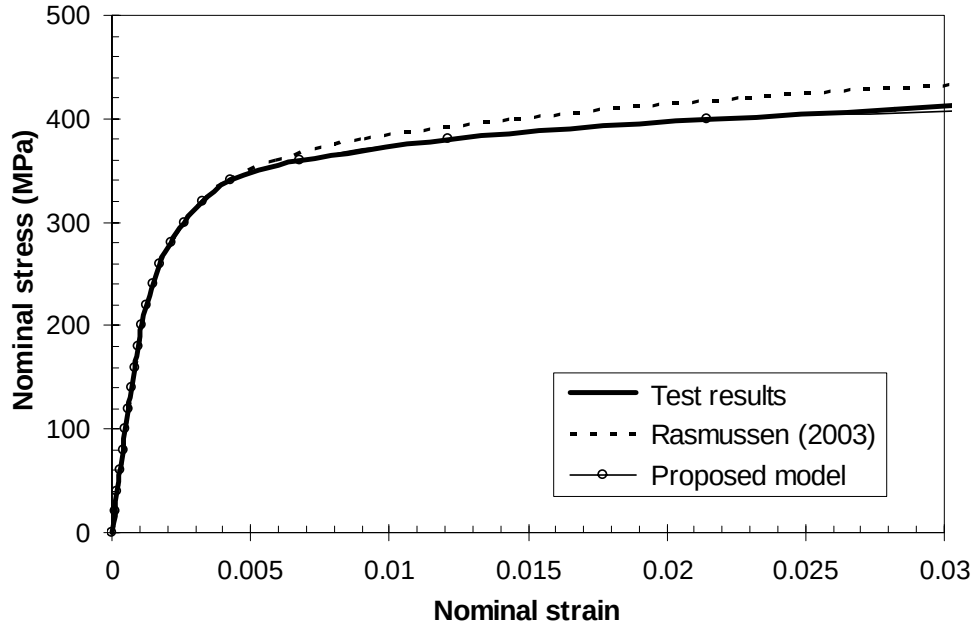

(b) Initial stress-strain curves

Figure A.12 Nominal stress-strain curves for the flat tension coupon cut from section SHS 100×100×8 tested by Gardner and Nethercot (2004).

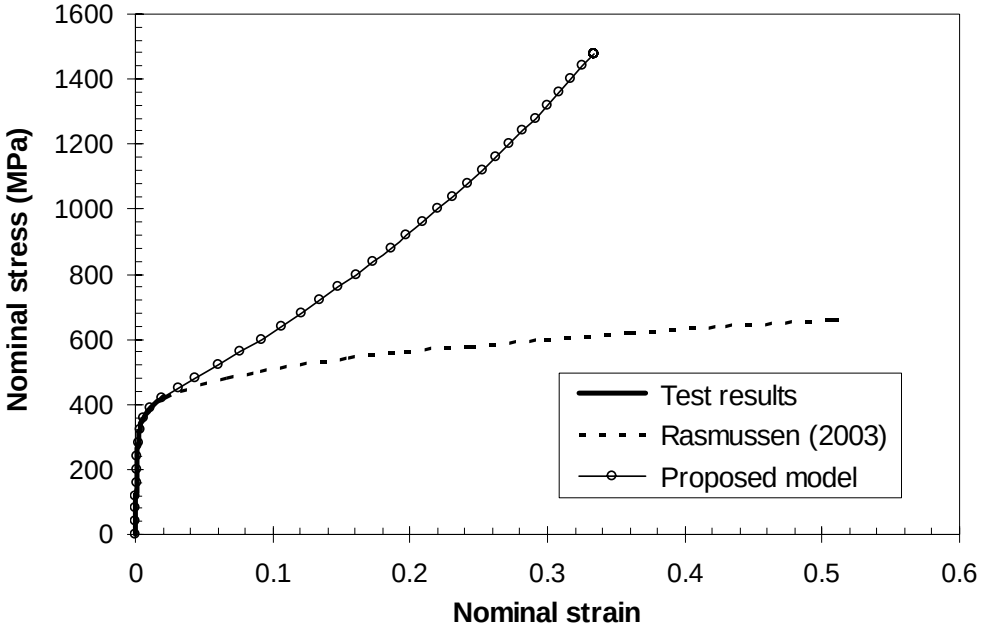

(a) Full stress-strain curves

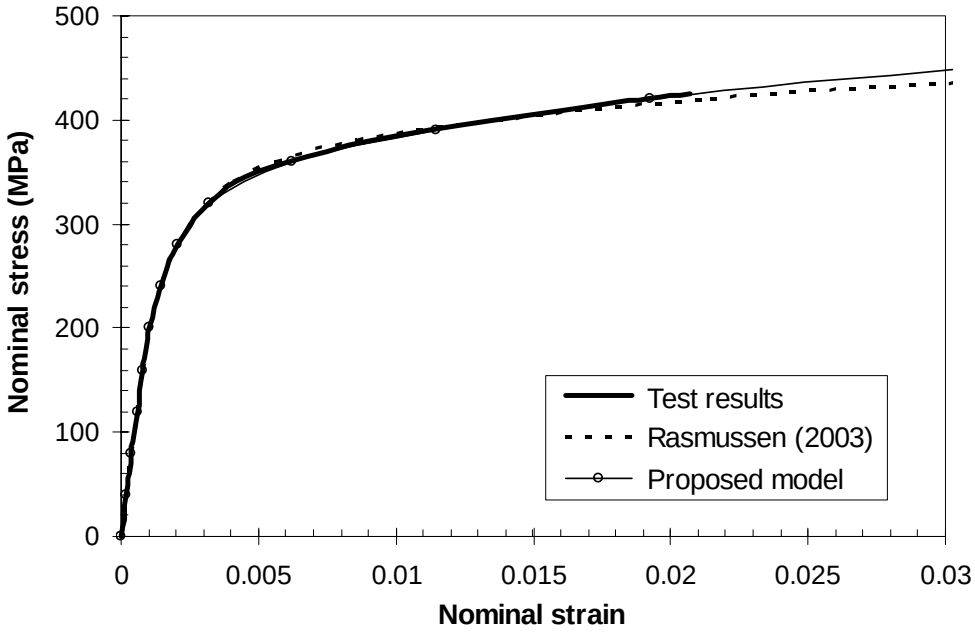

(b) Initial stress-strain curves

Figure A.13 Nominal stress-strain curves for the flat compression coupon cut from section SHS 100×100×8 tested by Gardner and Nethercot (2004).

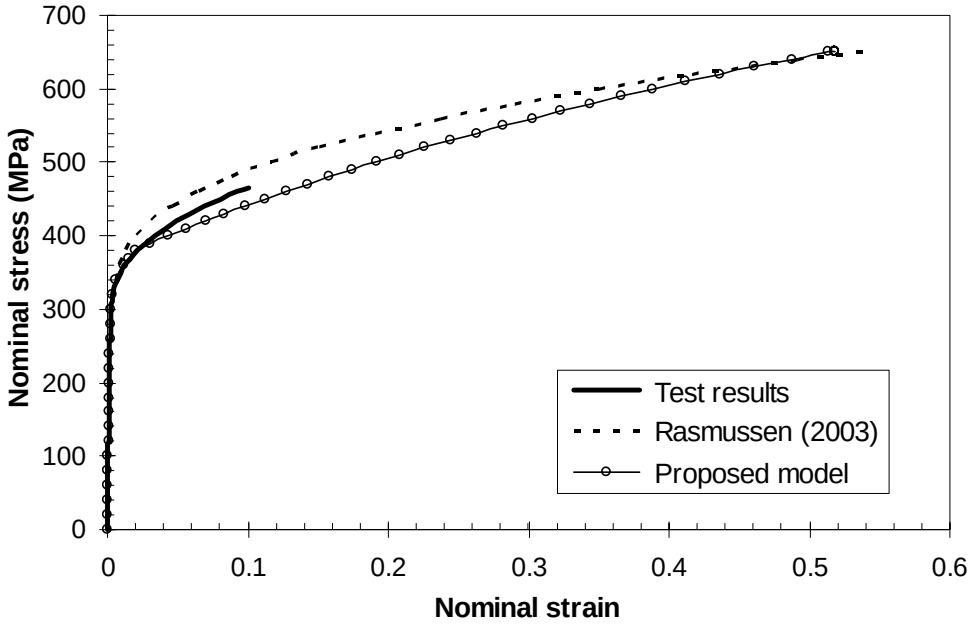

(a) Full stress-strain curves

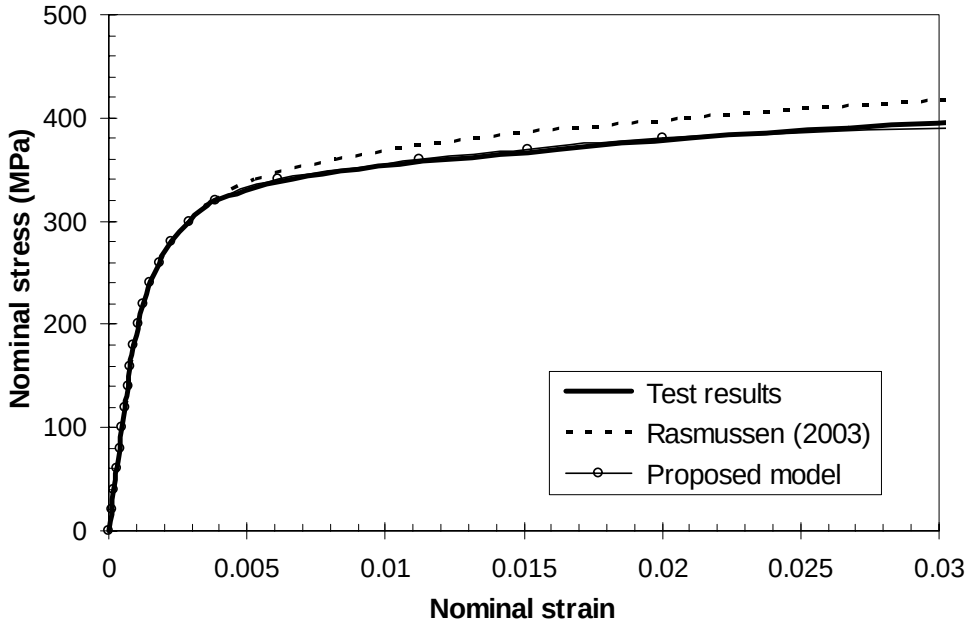

(b) Initial stress-strain curves

Figure A.14 Nominal stress-strain curves for the flat tension coupon cut from section SHS 150×150×4 tested by Gardner and Nethercot (2004).

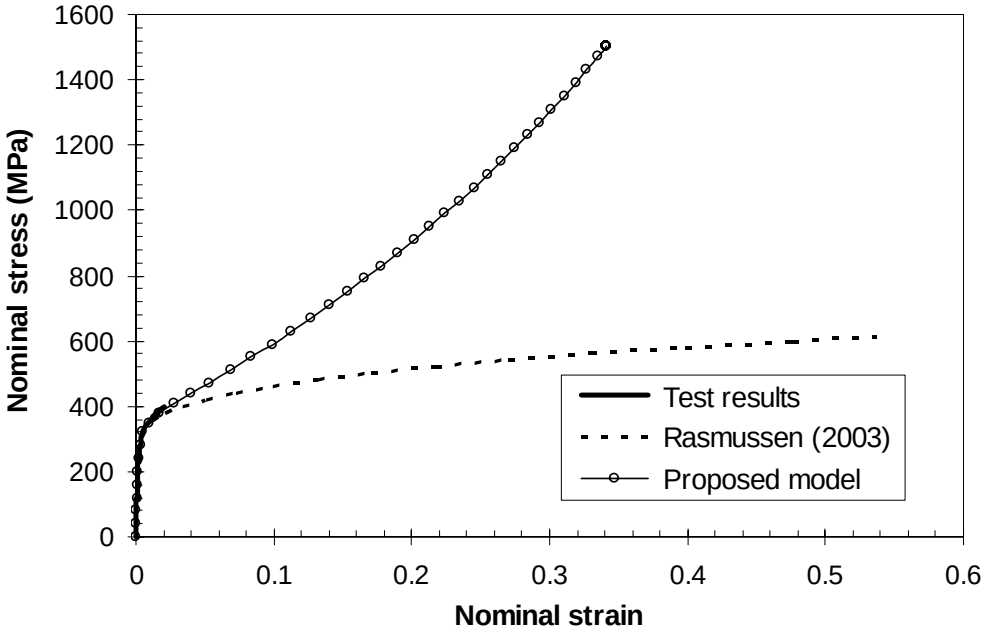

(a) Full stress-strain curves

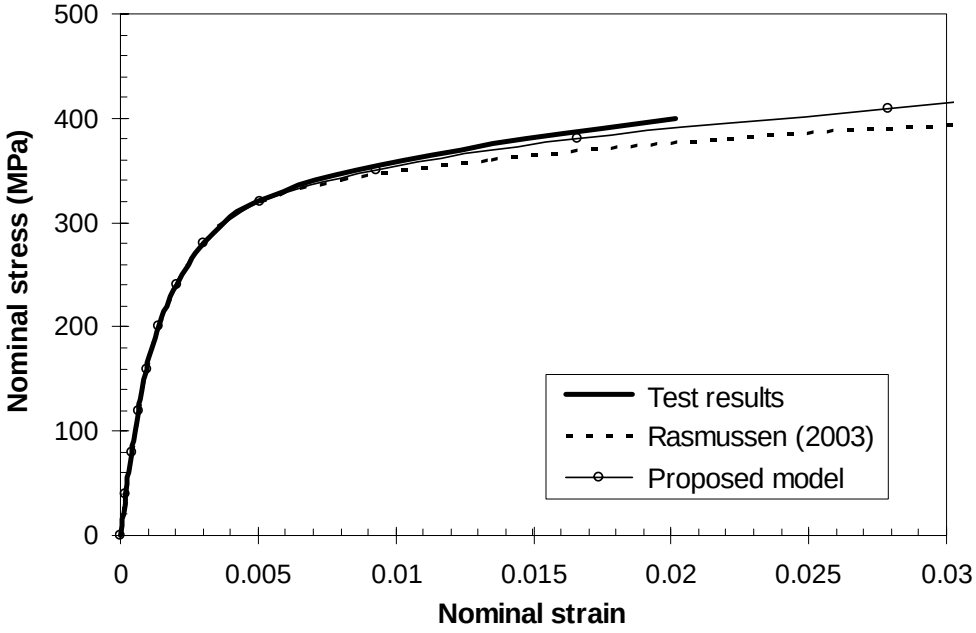

(b) Initial stress-strain curves

Figure A.15 Nominal stress-strain curves for the flat compression coupon cut from section SHS 150×150×4 tested by Gardner and Nethercot (2004).

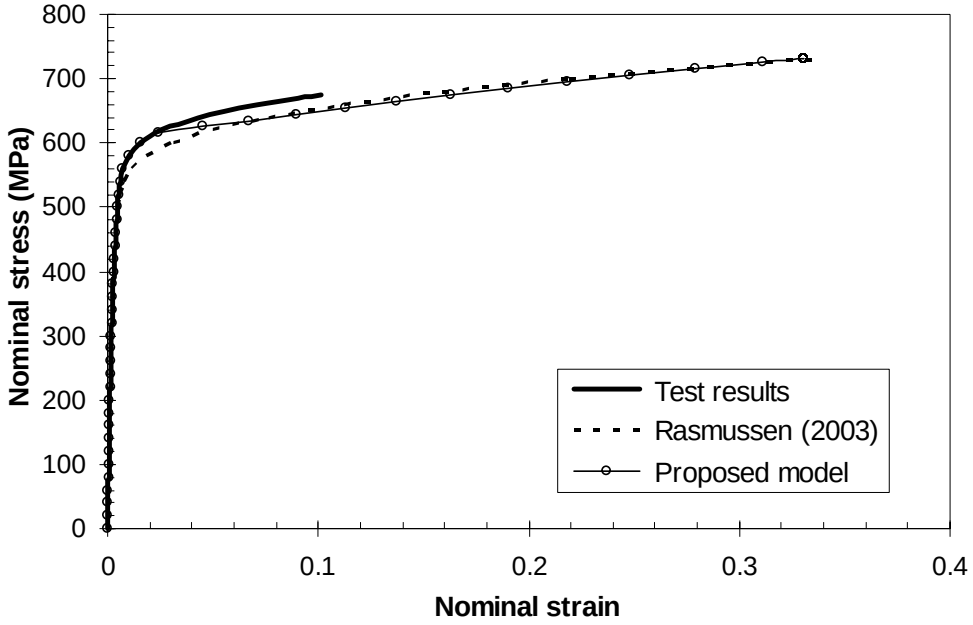

(a) Full stress-strain curves

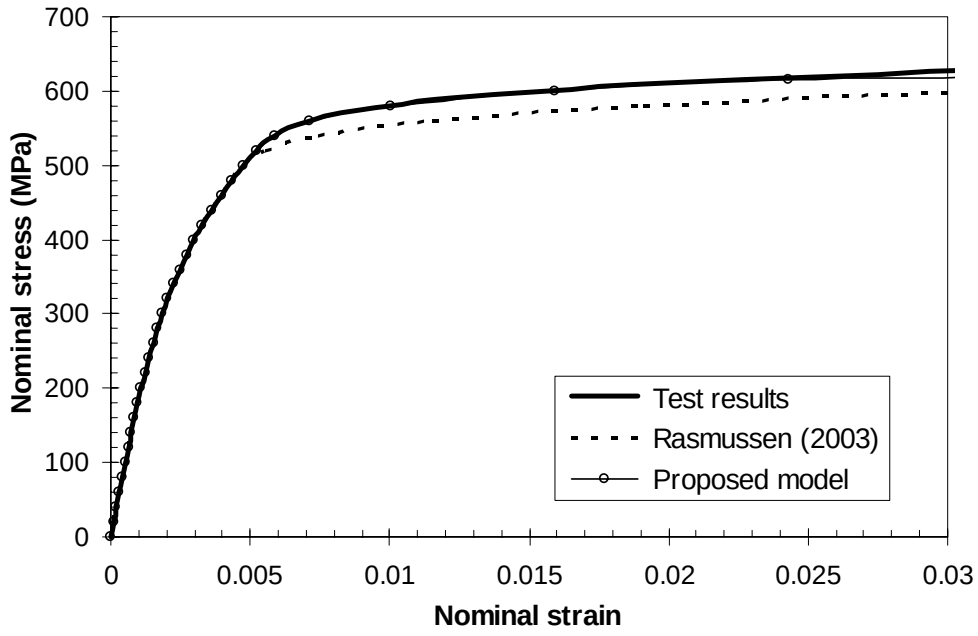

(b) Initial stress-strain curves

Figure A.16 Nominal stress-strain curves for the flat tension coupon cut from section RHS 60×40×4 tested by Gardner and Nethercot (2004).

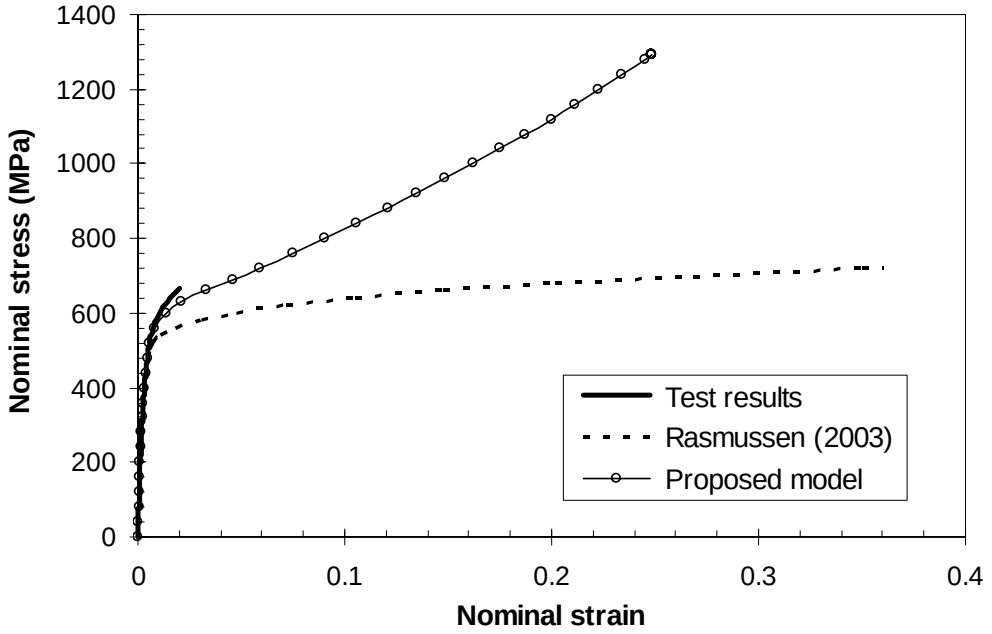

(a) Full stress-strain curves

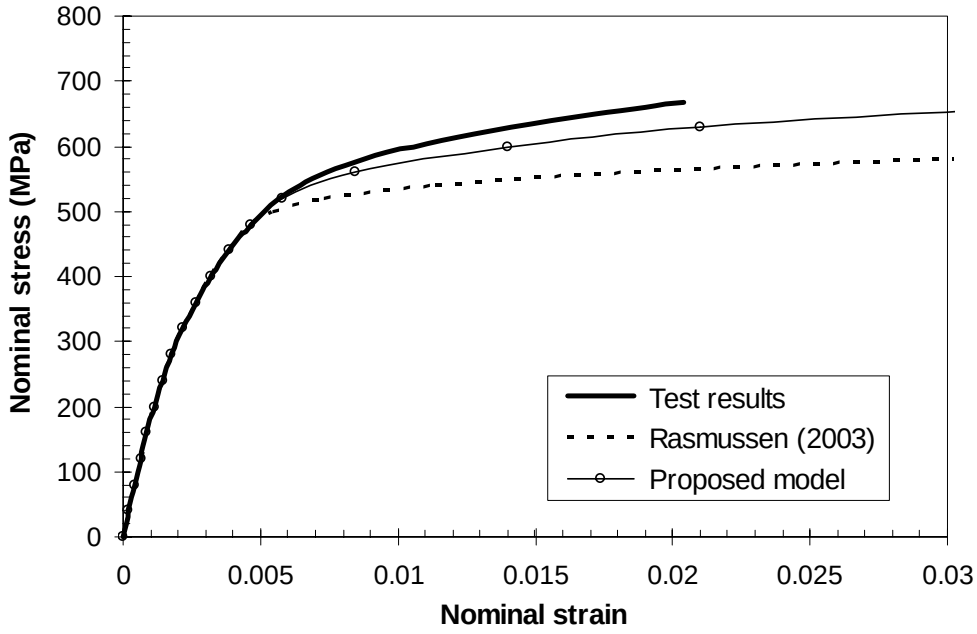

(b) Initial stress-strain curves

Figure A.17 Nominal stress-strain curves for the flat compression coupon cut from section RHS 60×40×4 tested by Gardner and Nethercot (2004).

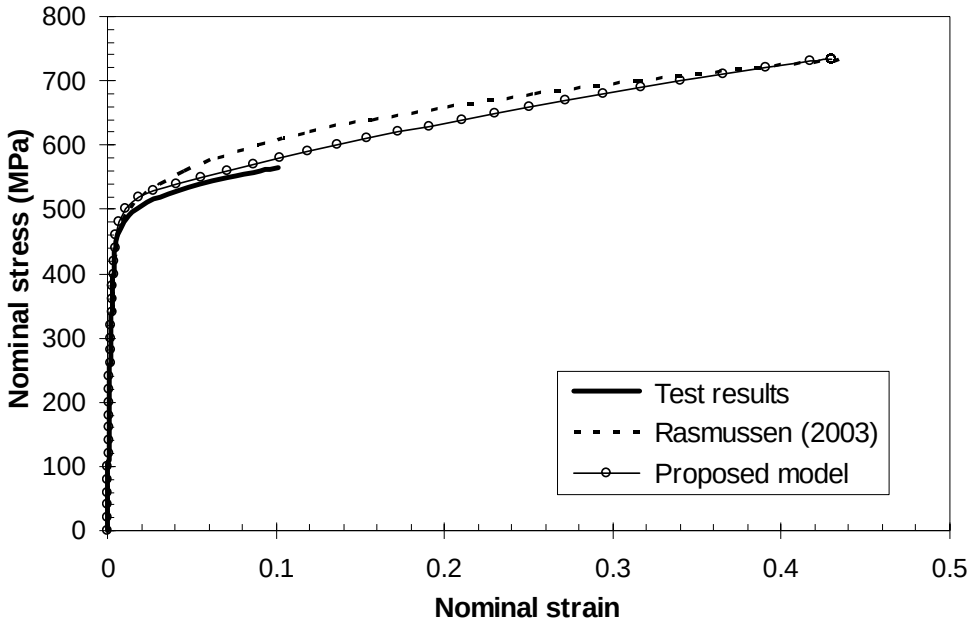

(a) Full stress-strain curves

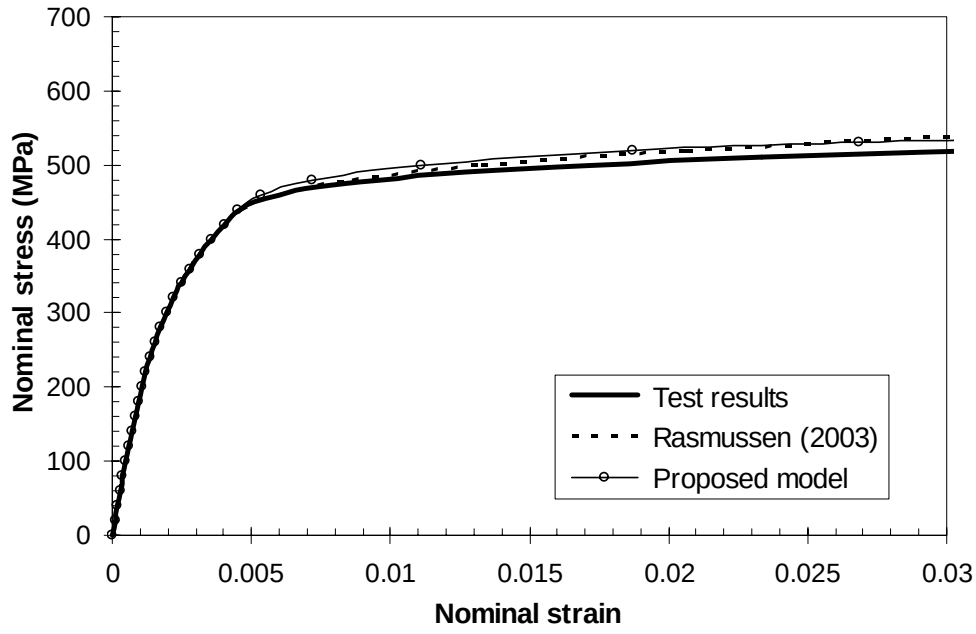

(b) Initial stress-strain curves

Figure A.18 Nominal stress-strain curves for the flat tension coupon cut from section RHS 120×80×3 tested by Gardner and Nethercot (2004).

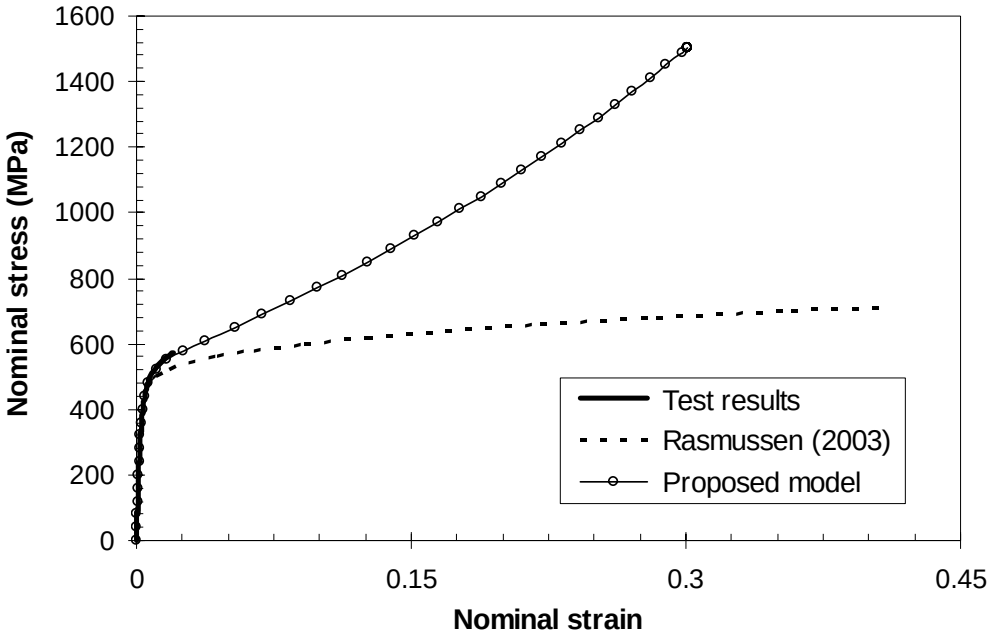

(a) Full stress-strain curves

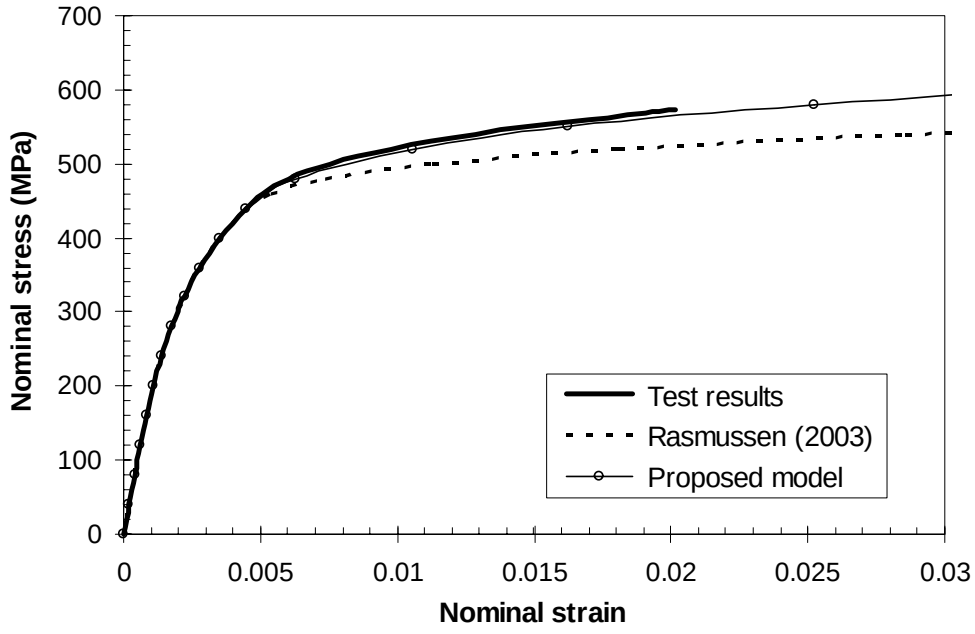

(b) Initial stress-strain curves

Figure A.19 Nominal stress-strain curves for the flat compression coupon cut from section RHS 120×80×3 tested by Gardner and Nethercot (2004).

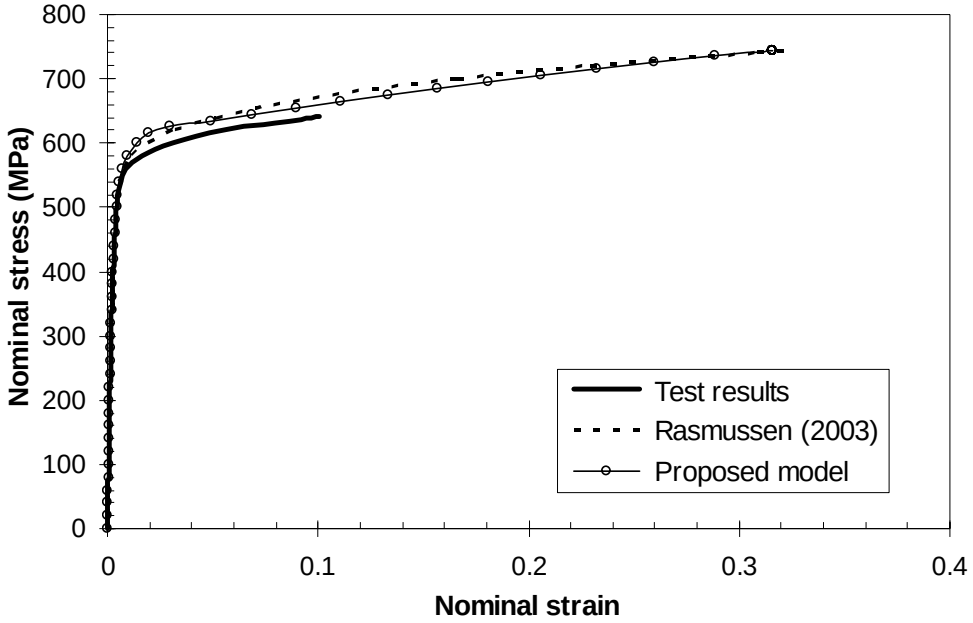

(a) Full stress-strain curves

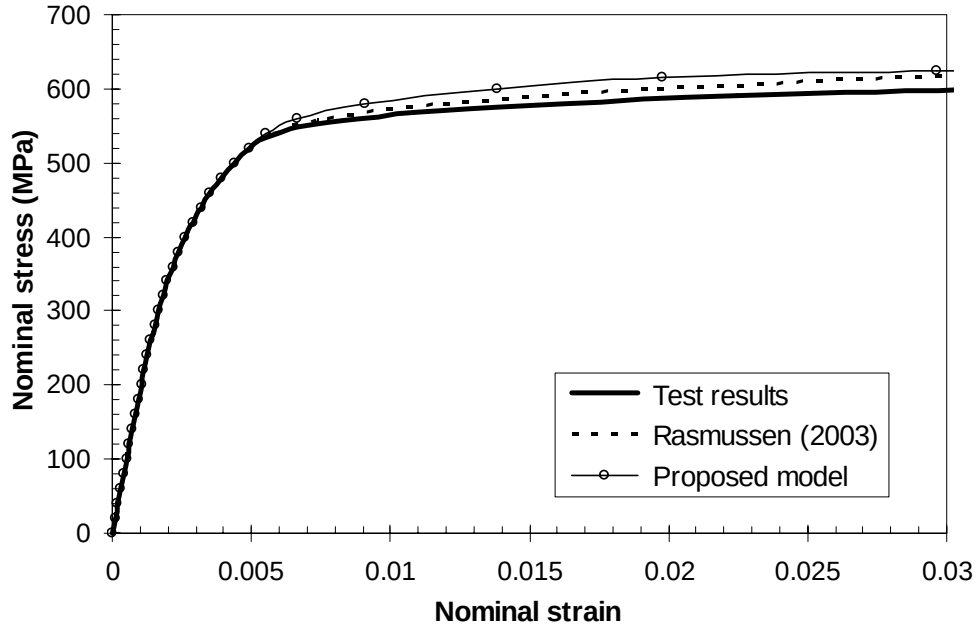

(b) Initial stress-strain curves

Figure A.20 Nominal stress-strain curves for the flat tension coupon cut from section RHS 120×80×6 tested by Gardner and Nethercot (2004).

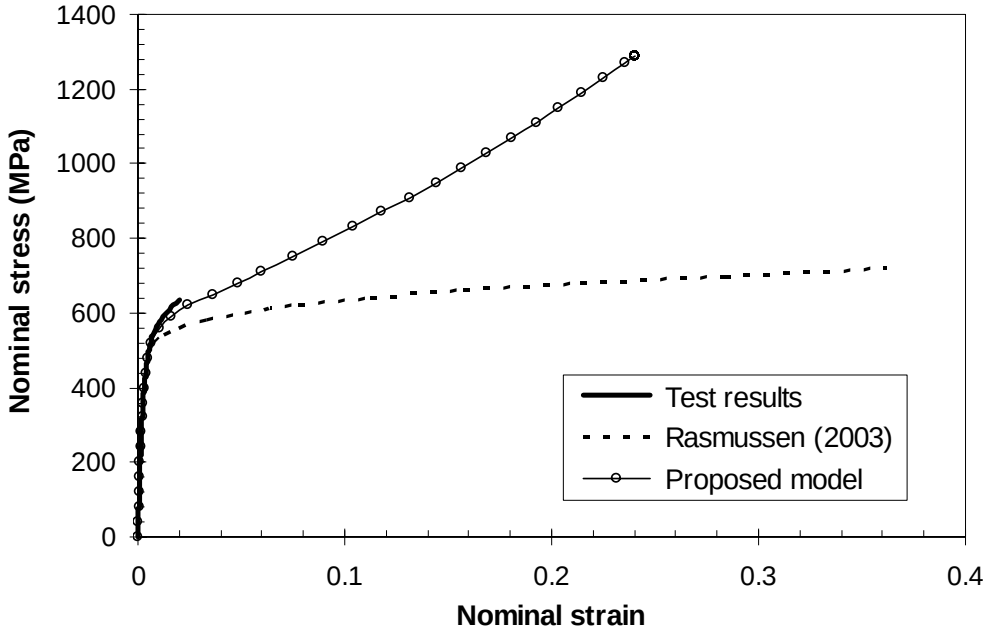

(a) Full stress-strain curves

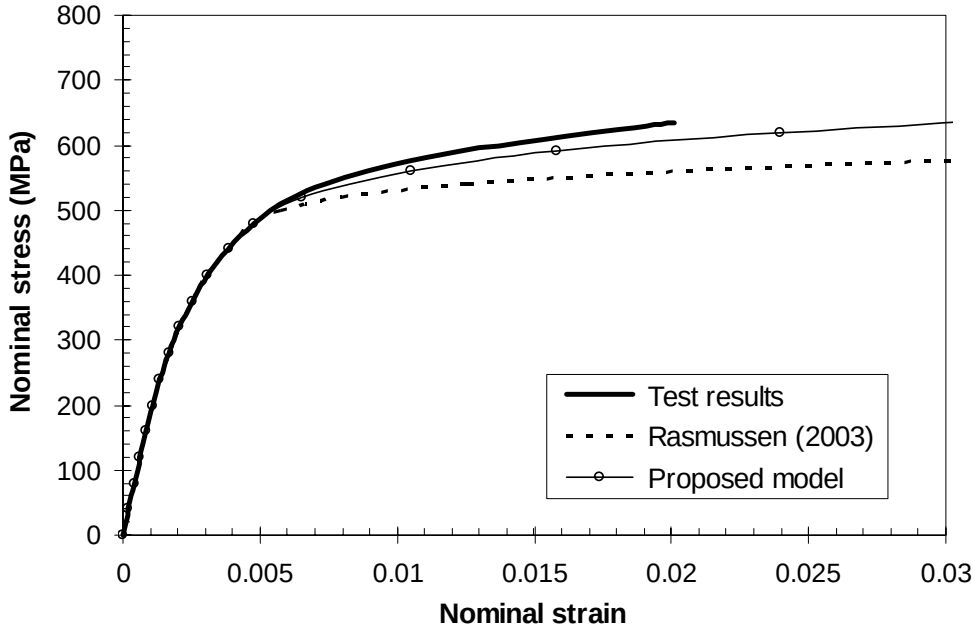

(b) Initial stress-strain curves

Figure A.21 Nominal stress-strain curves for the flat compression coupon cut from section RHS 120×80×6 tested by Gardner and Nethercot (2004).

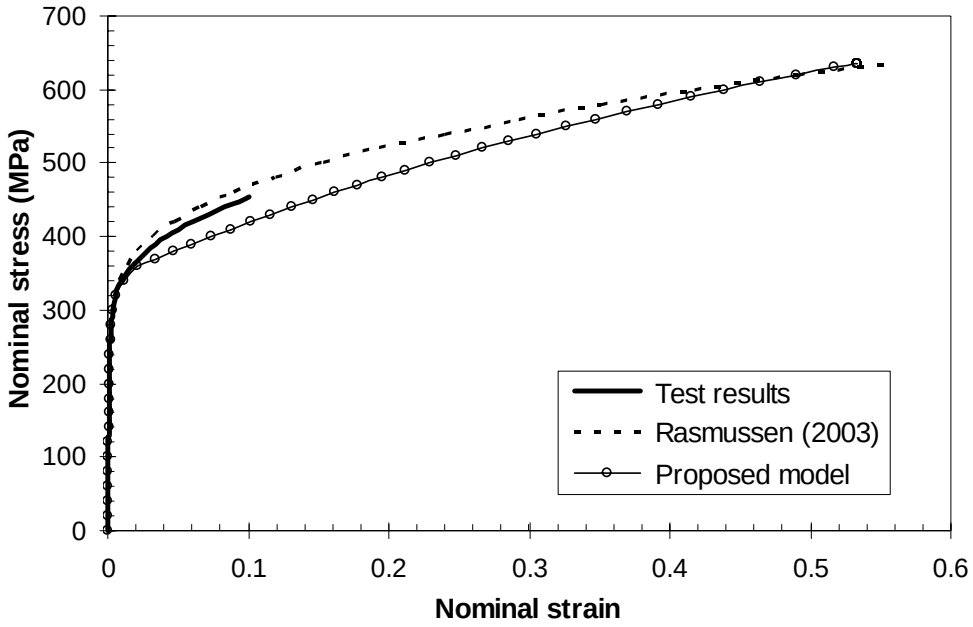

(a) Full stress-strain curves

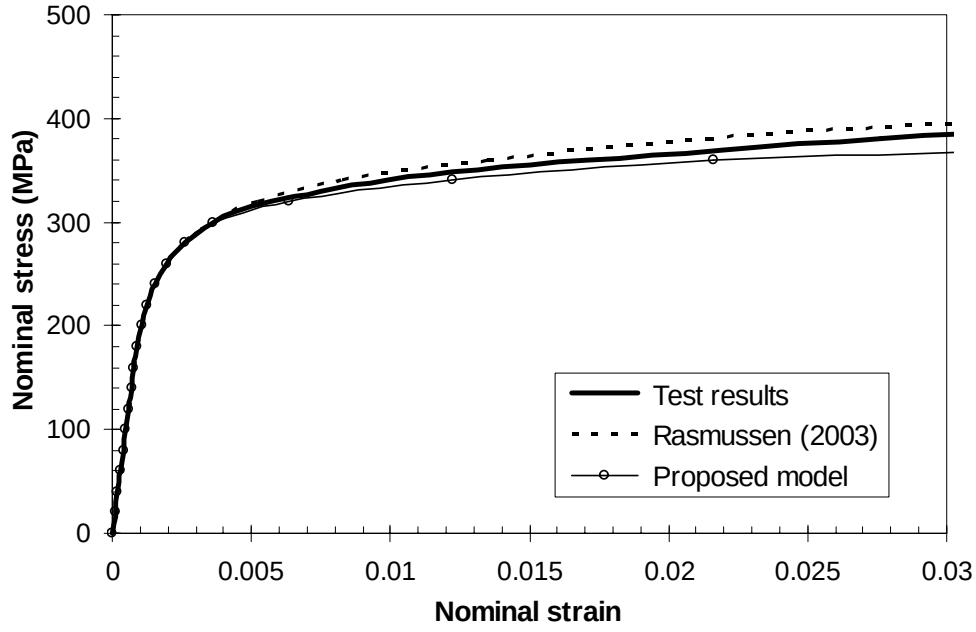

(b) Initial stress-strain curves

Figure A.22 Nominal stress-strain curves for the flat tension coupon cut from section RHS 150×100×4 tested by Gardner and Nethercot (2004).

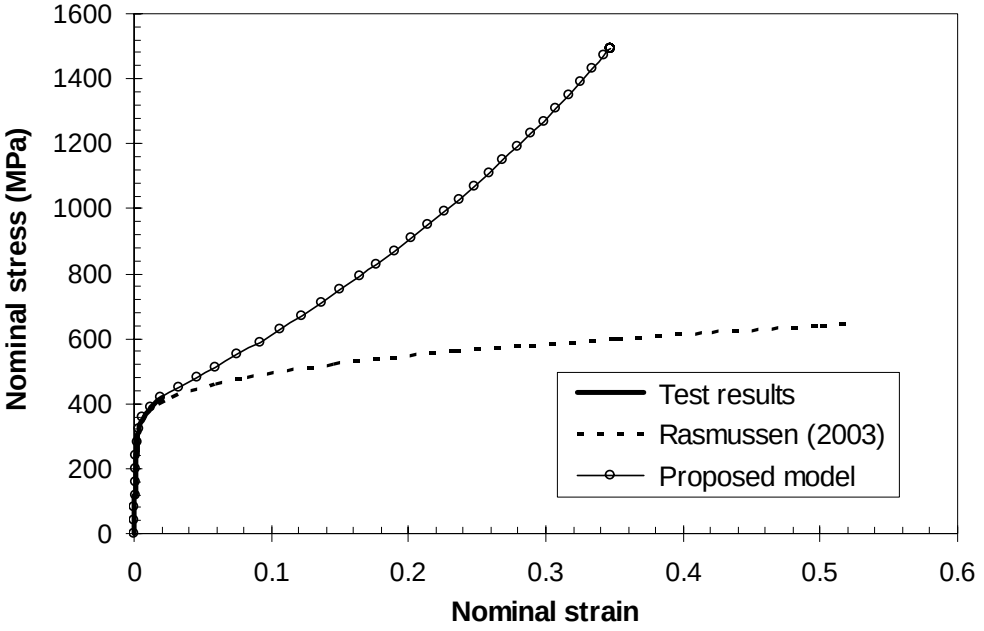

(a) Full stress-strain curves

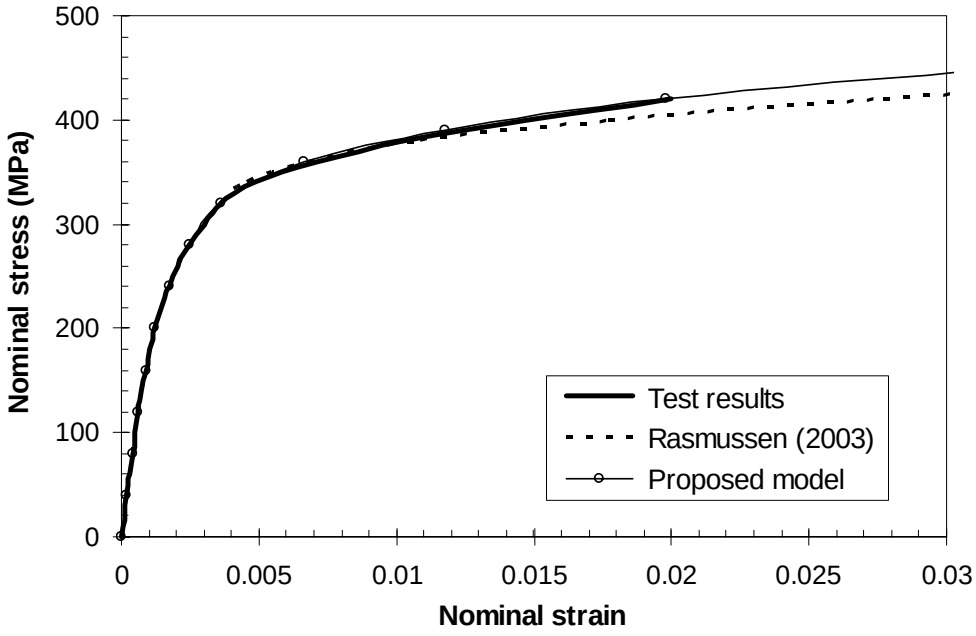

(b) Initial stress-strain curves

Figure A.23 Nominal stress-strain curves for the flat compression coupon cut from section RHS 150×100×4 tested by Gardner and Nethercot (2004).

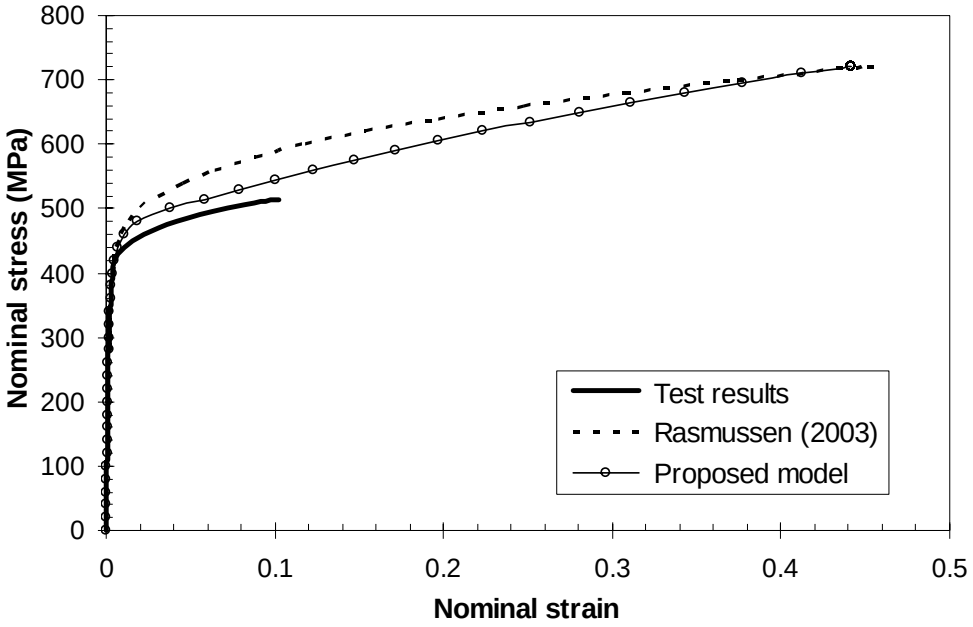

(a) Full stress-strain curves

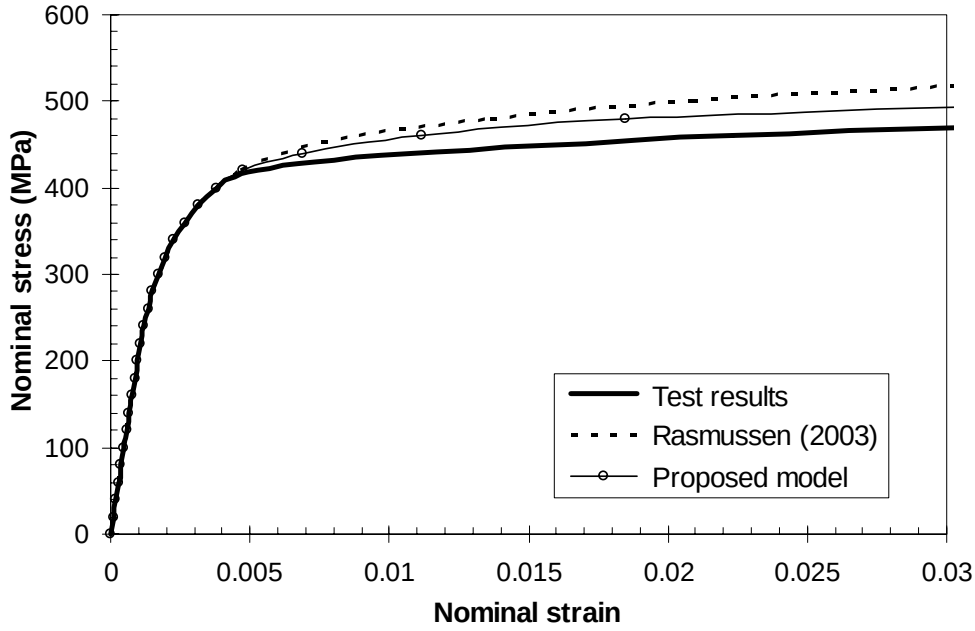

(b) Initial stress-strain curves

Figure A.24 Nominal stress-strain curves for the flat tension coupon cut from section RHS 100×50×2 tested by Gardner and Nethercot (2004).

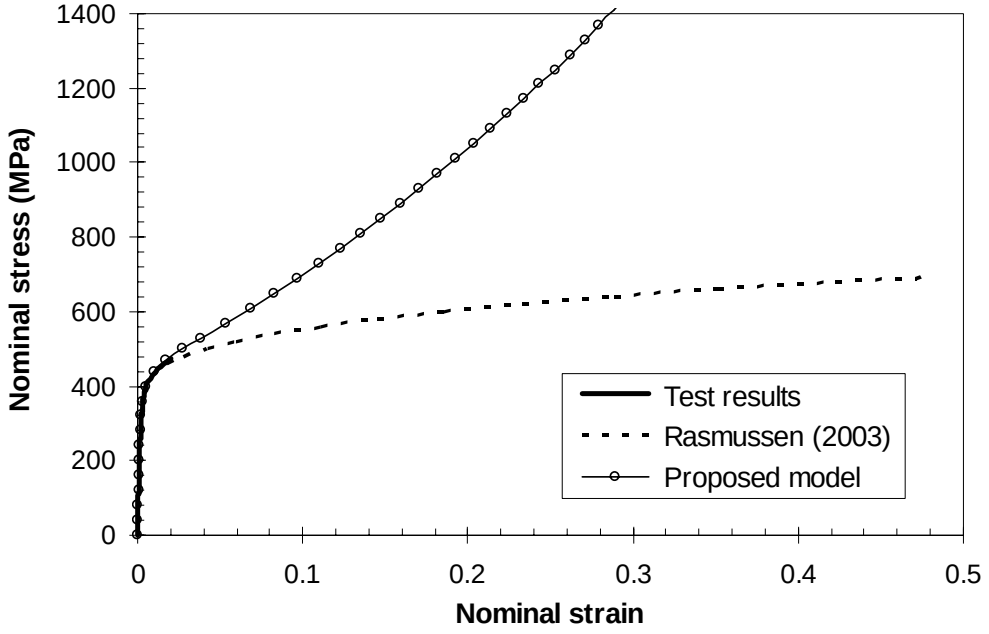

(a) Full stress-strain curves

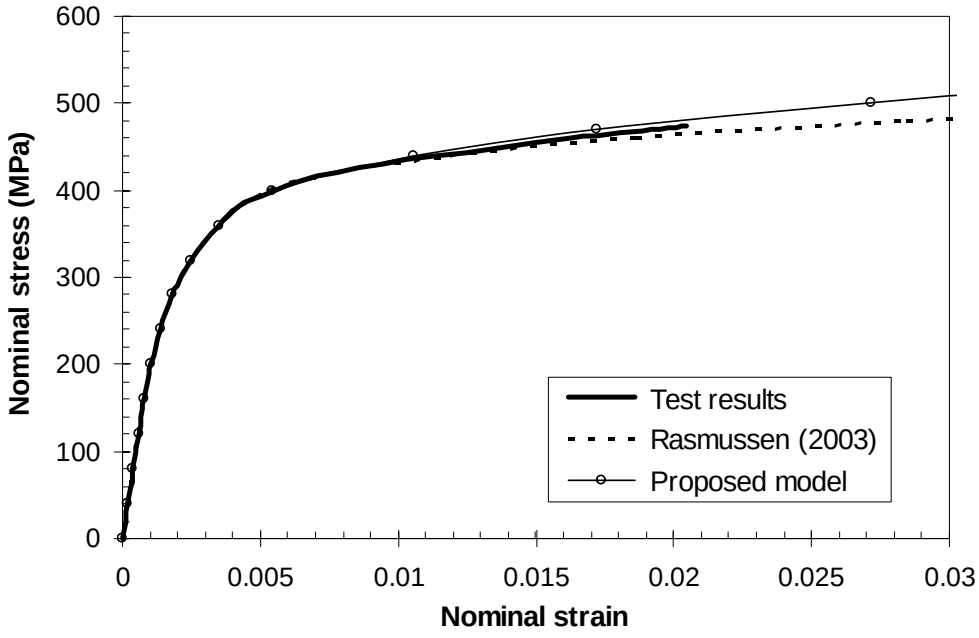

(b) Initial stress-strain curves

Figure A.25 Nominal stress-strain curves for the flat compression coupon cut from section RHS 100×50×2 tested by Gardner and Nethercot (2004).

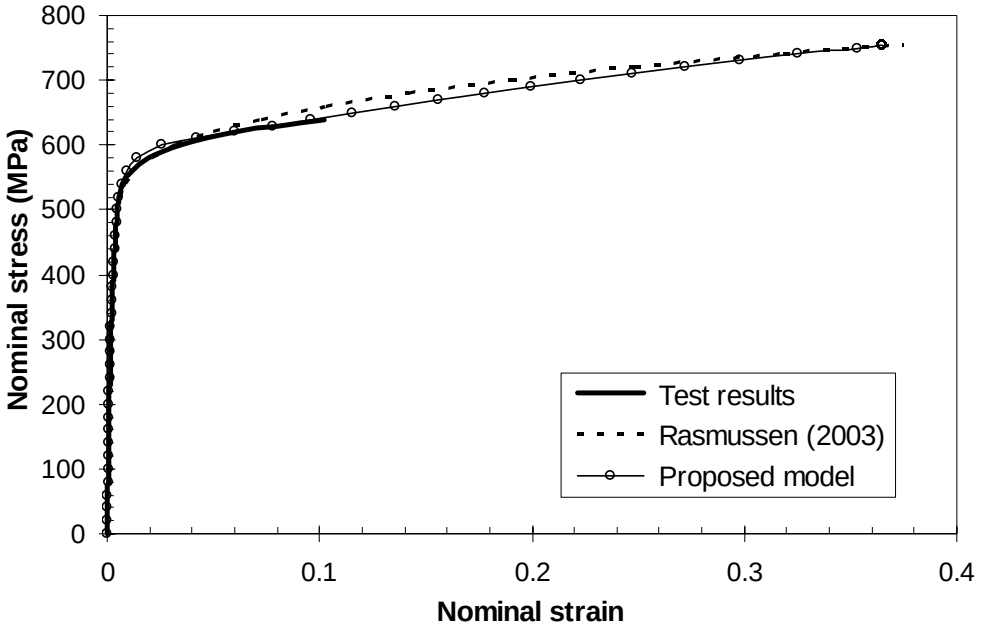

(a) Full stress-strain curves

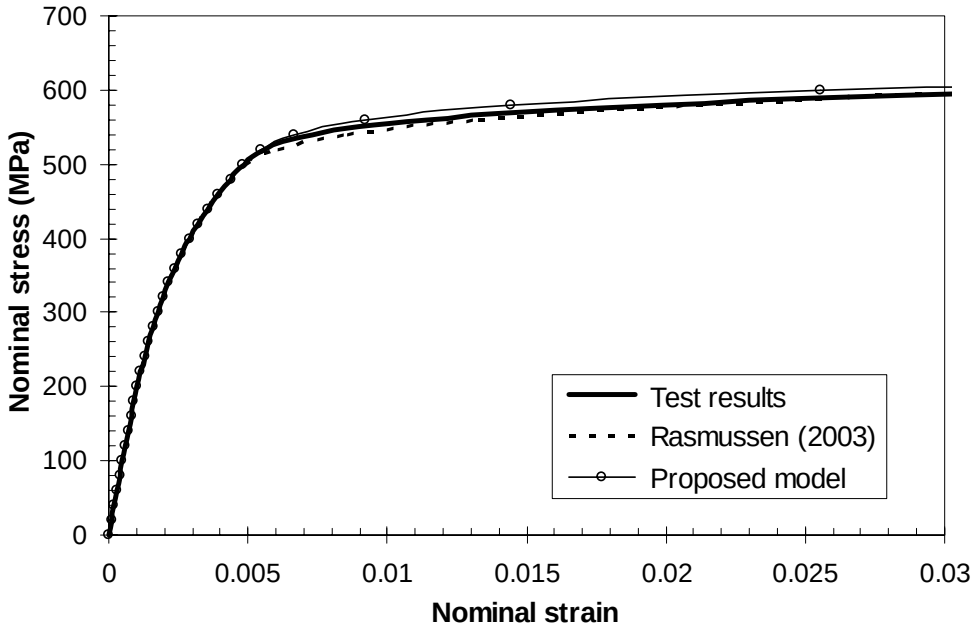

(b) Initial stress-strain curves

Figure A.26 Nominal stress-strain curves for the flat tension coupon cut from section RHS 100×50×3 tested by Gardner and Nethercot (2004).

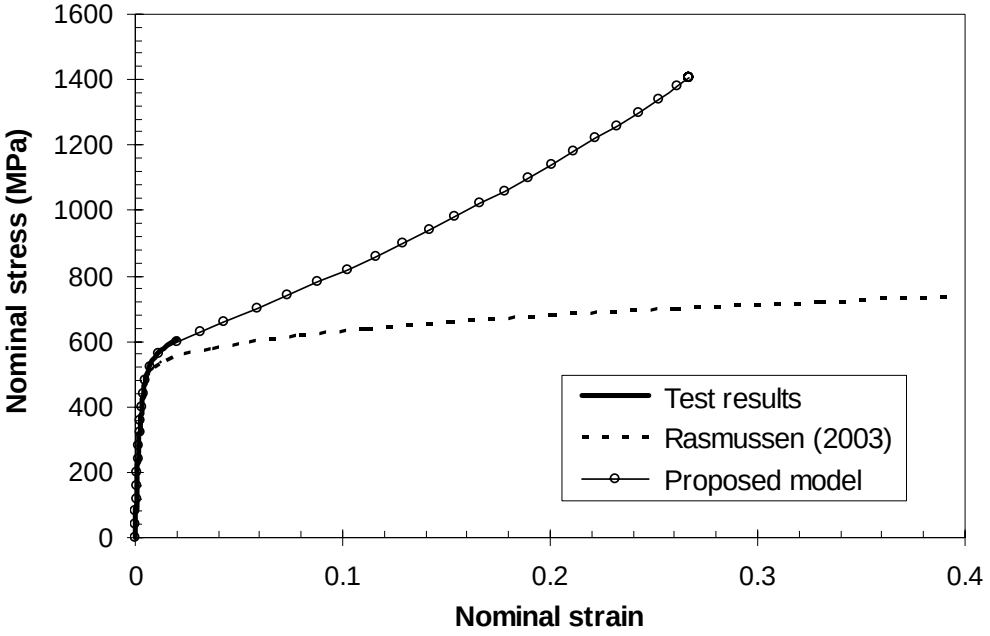

(a) Full stress-strain curves

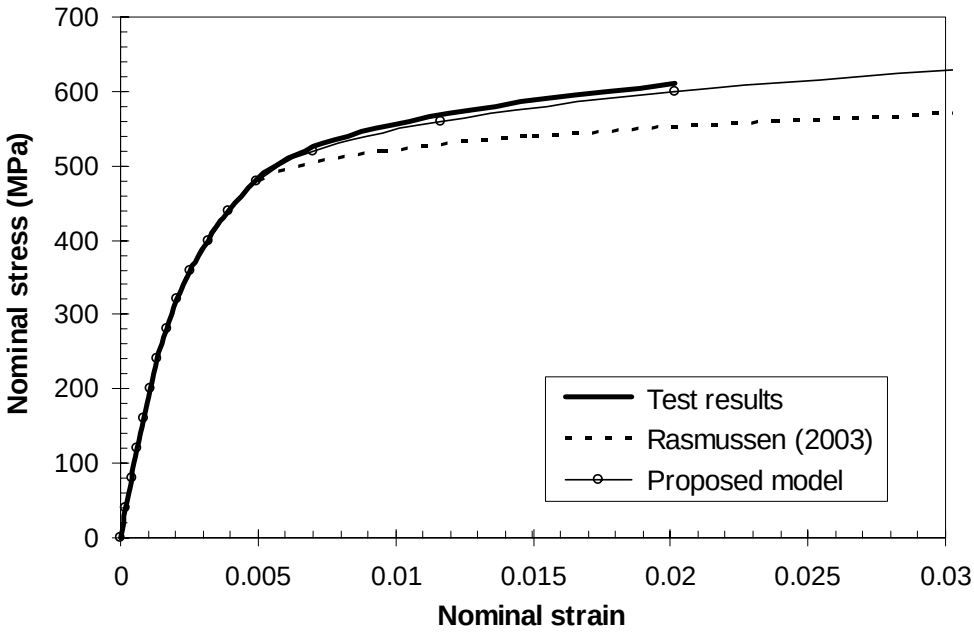

(b) Initial stress-strain curves

Figure A.27 Nominal stress-strain curves for the flat compression coupon cut from section RHS 100×50×3 tested by Gardner and Nethercot (2004).

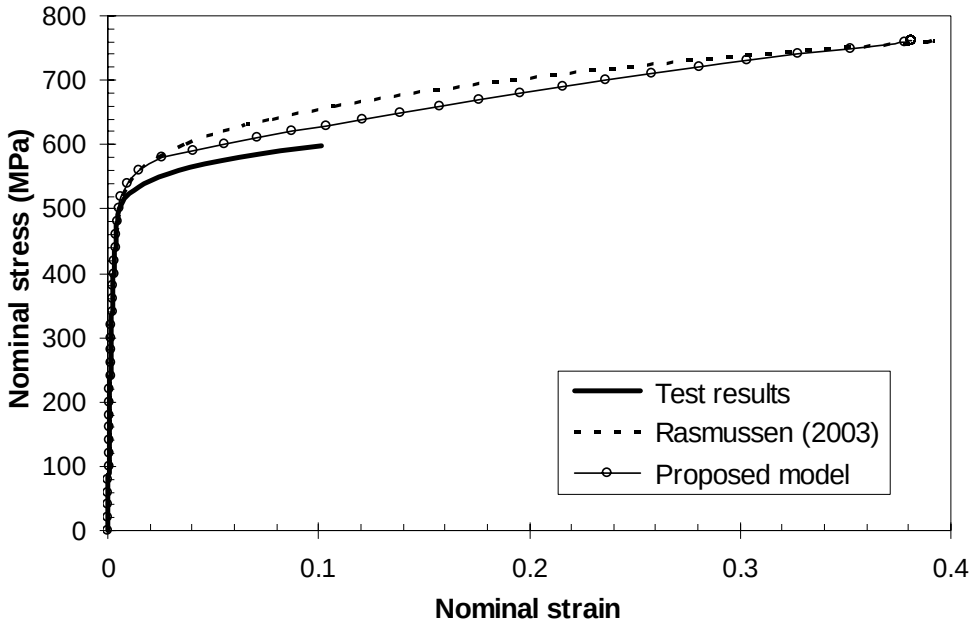

(a) Full stress-strain curves

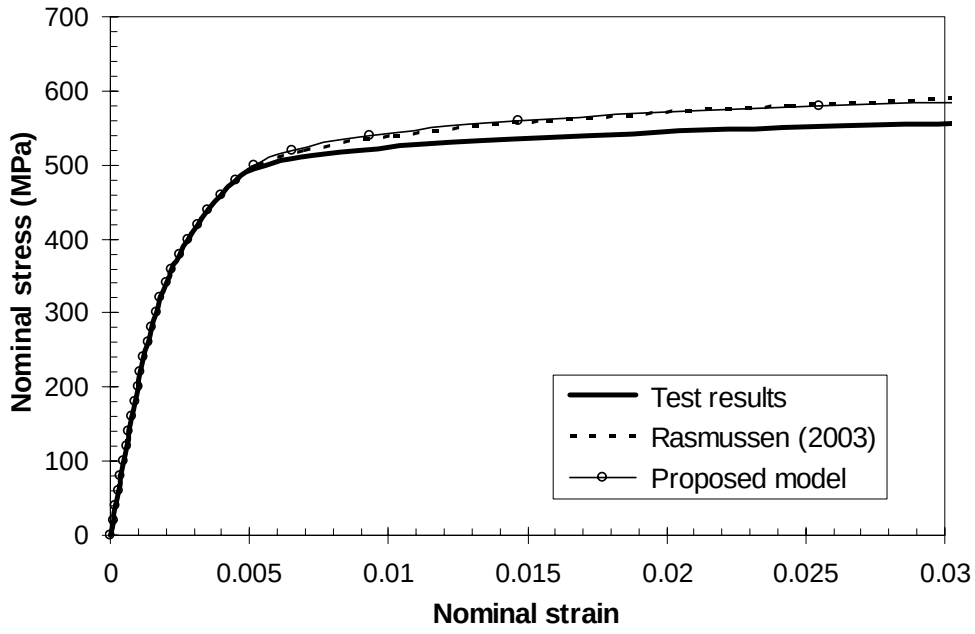

(b) Initial stress-strain curves

Figure A.28 Nominal stress-strain curves for the flat tension coupon cut from section RHS 100×50×4 tested by Gardner and Nethercot (2004).

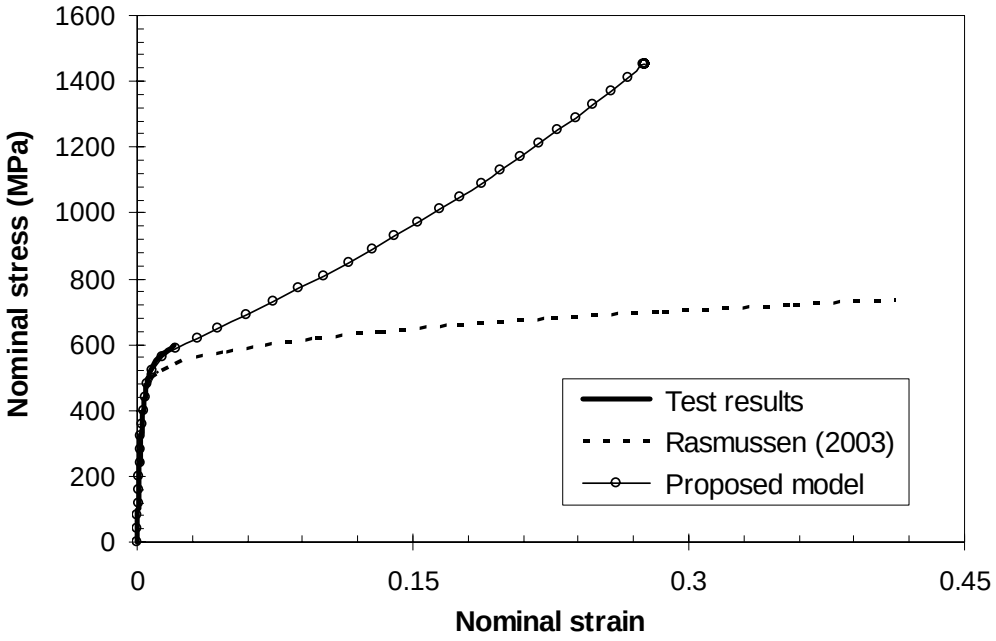

(a) Full stress-strain curves

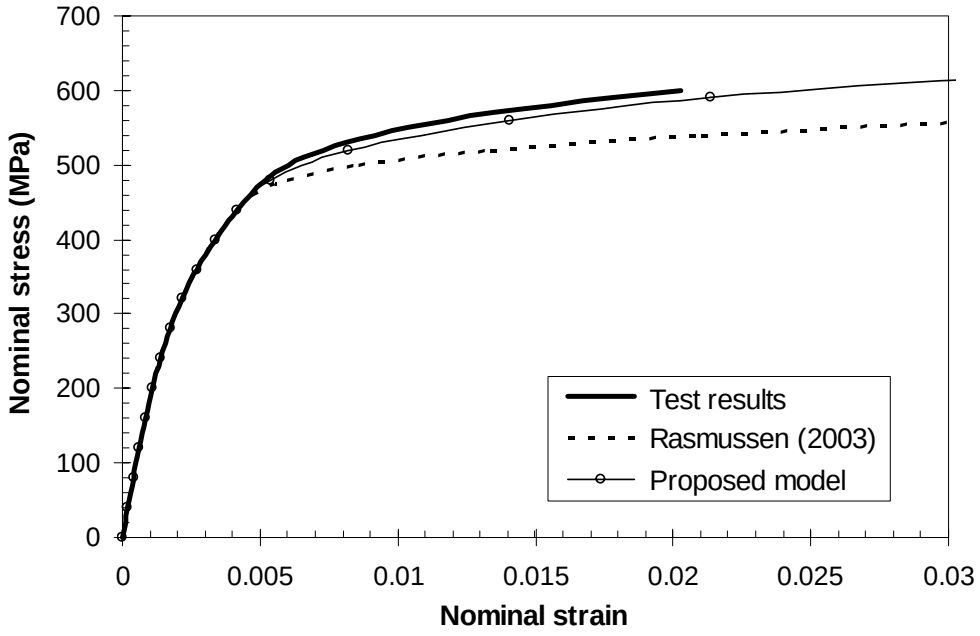

(b) Initial stress-strain curves

Figure A.29 Nominal stress-strain curves for the flat compression coupon cut from section RHS 100×50×4 tested by Gardner and Nethercot (2004).

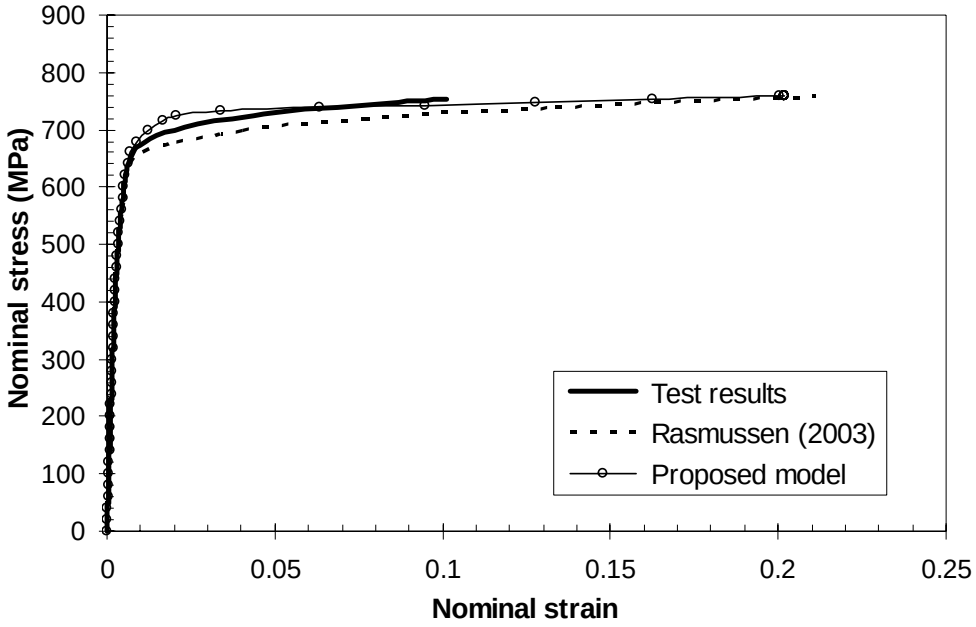

(a) Full stress-strain curves

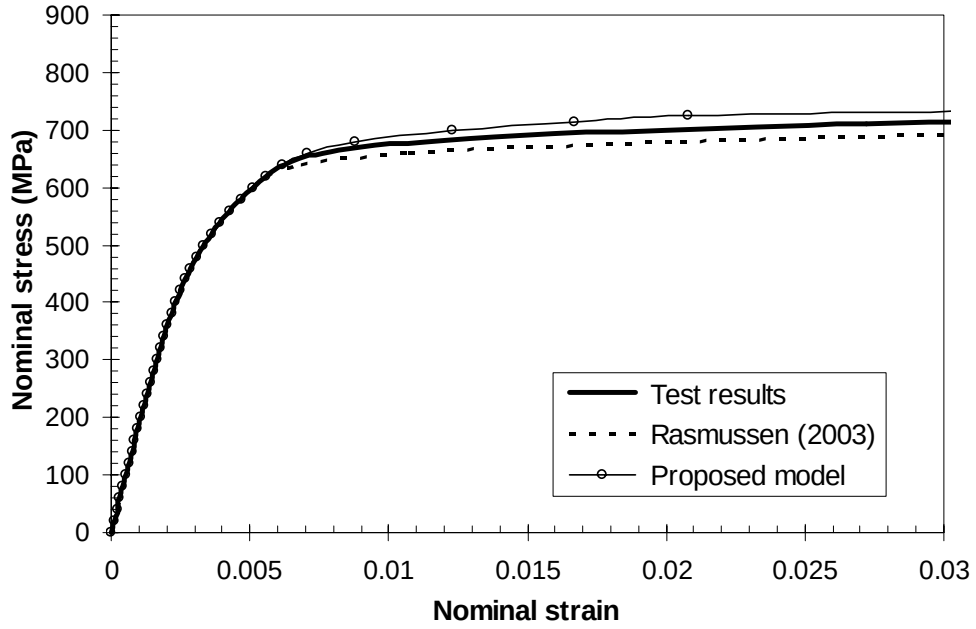

(b) Initial stress-strain curves

Figure A.30 Nominal stress-strain curves for the flat tension coupon cut from section RHS 100×50×6 tested by Gardner and Nethercot (2004).

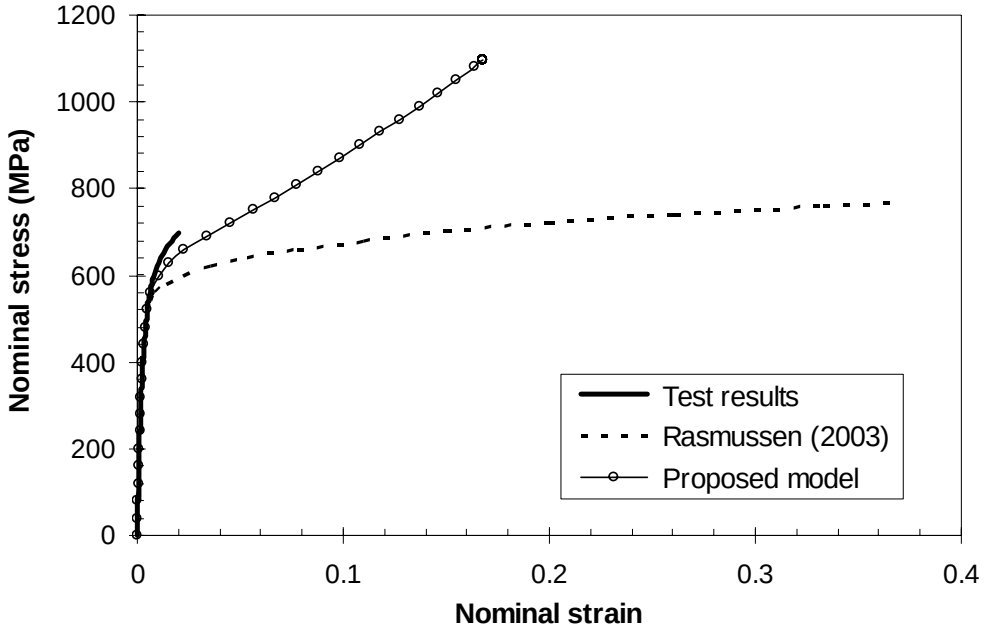

(a) Full stress-strain curves

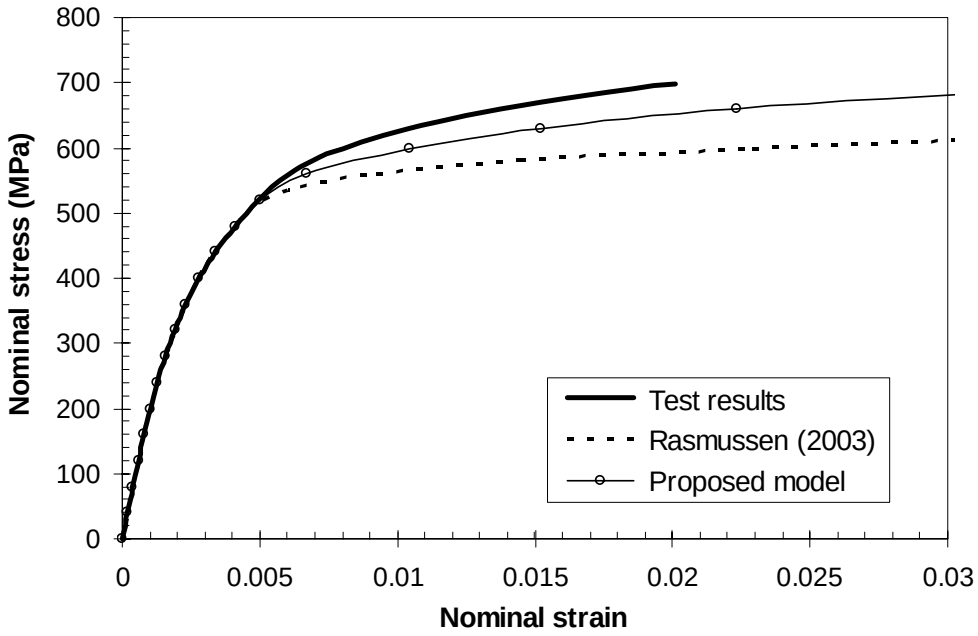

(b) Initial stress-strain curves

Figure A.31 Nominal stress-strain curves for the flat compression coupon cut from section RHS 100×50×6 tested by Gardner and Nethercot (2004).

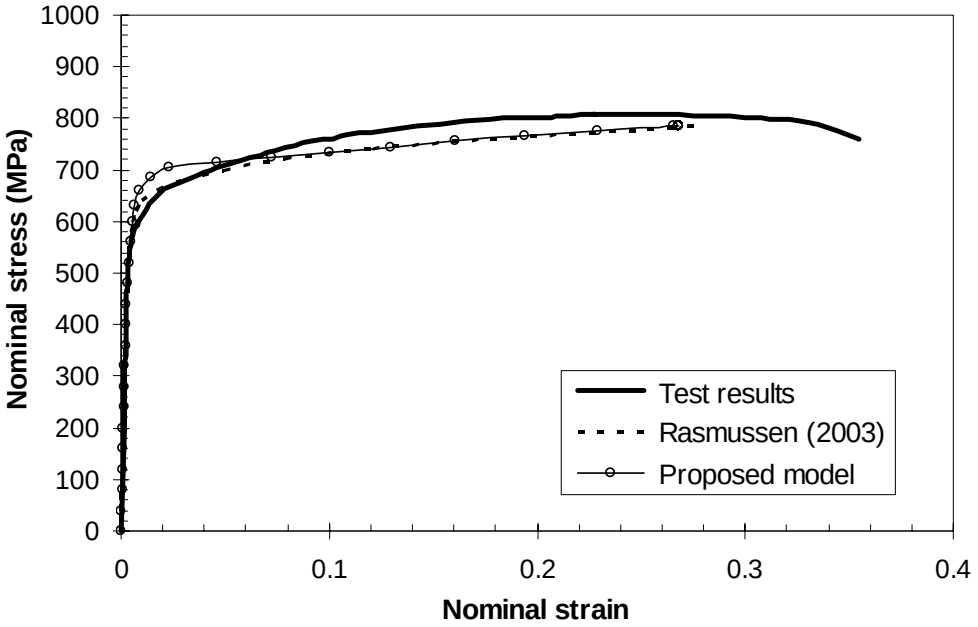

(a) Full stress-strain curves

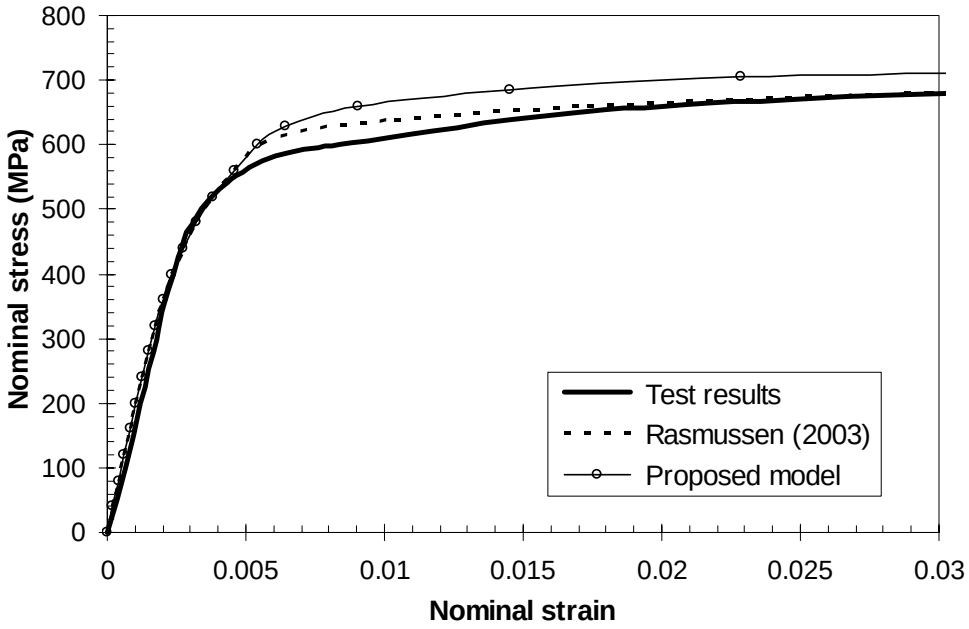

(b) Initial stress-strain curves

Figure A.32 Nominal stress-strain curves for the longitudinal tension coupon cut from the duplex stainless steel plate tested by Rasmussen *et al*. (2003).

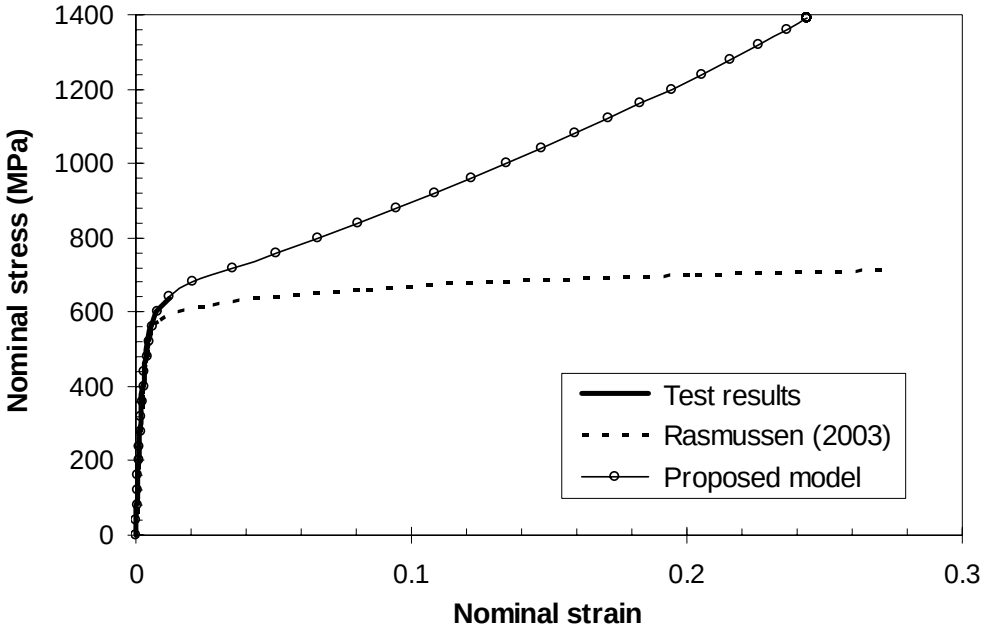

(a) Full stress-strain curves

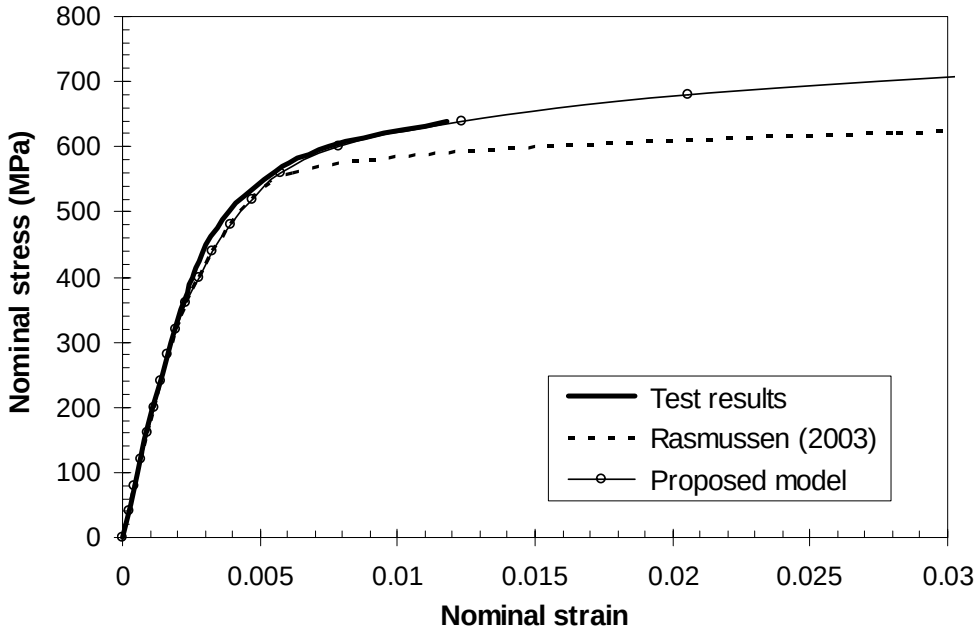

(b) Initial stress-strain curves

Figure A.33 Nominal stress-strain curves for the longitudinal compression coupon cut from the duplex stainless steel plate tested by Rasmussen *et al*. (2003).

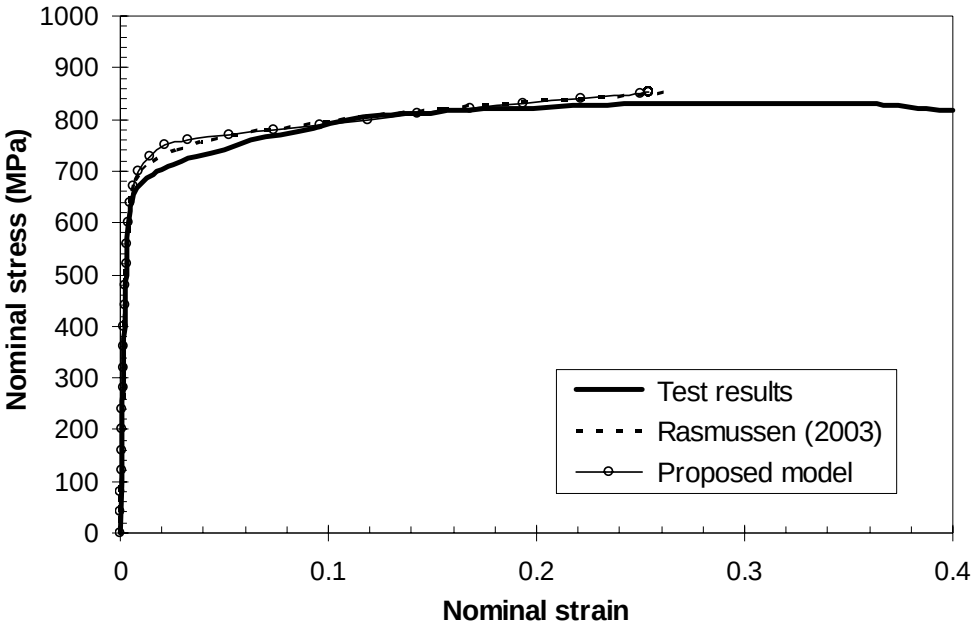

(a) Full stress-strain curves

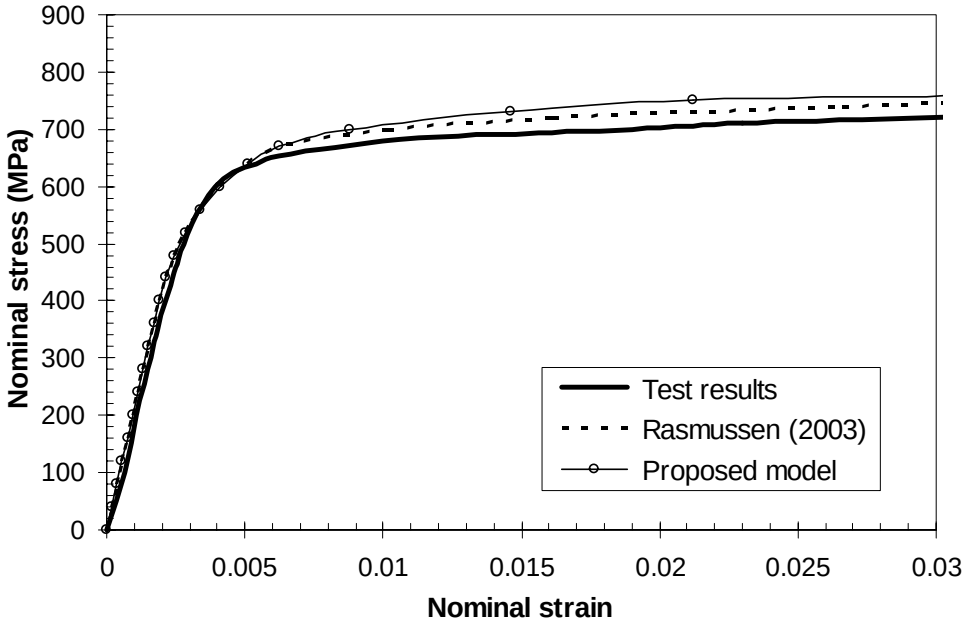

(b) Initial stress-strain curves

Figure A.34 Nominal stress-strain curves for the transverse tension coupon cut from the duplex stainless steel plate tested by Rasmussen *et al*. (2003).

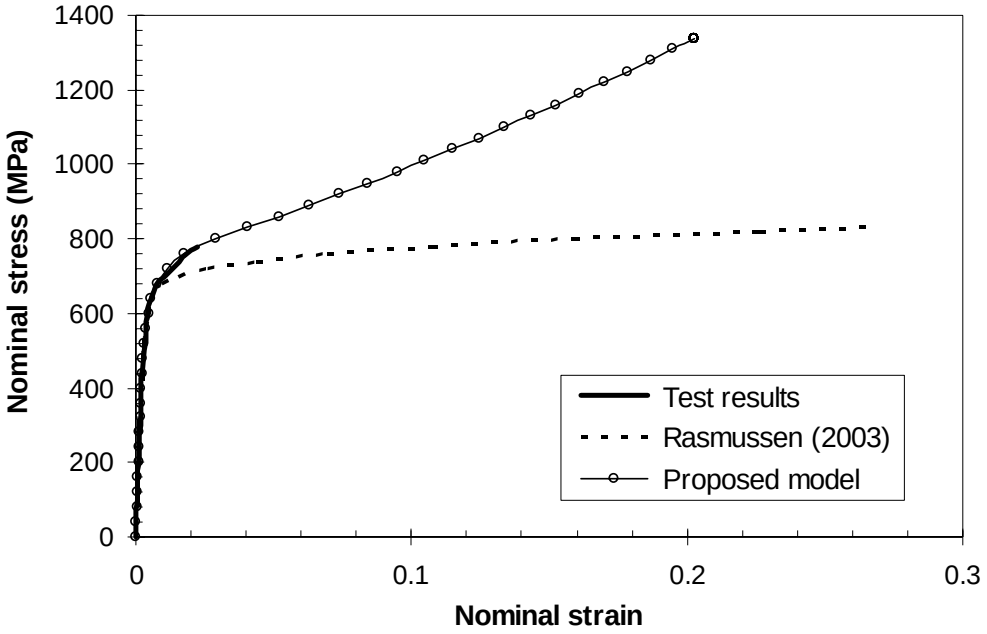

(a) Full stress-strain curves

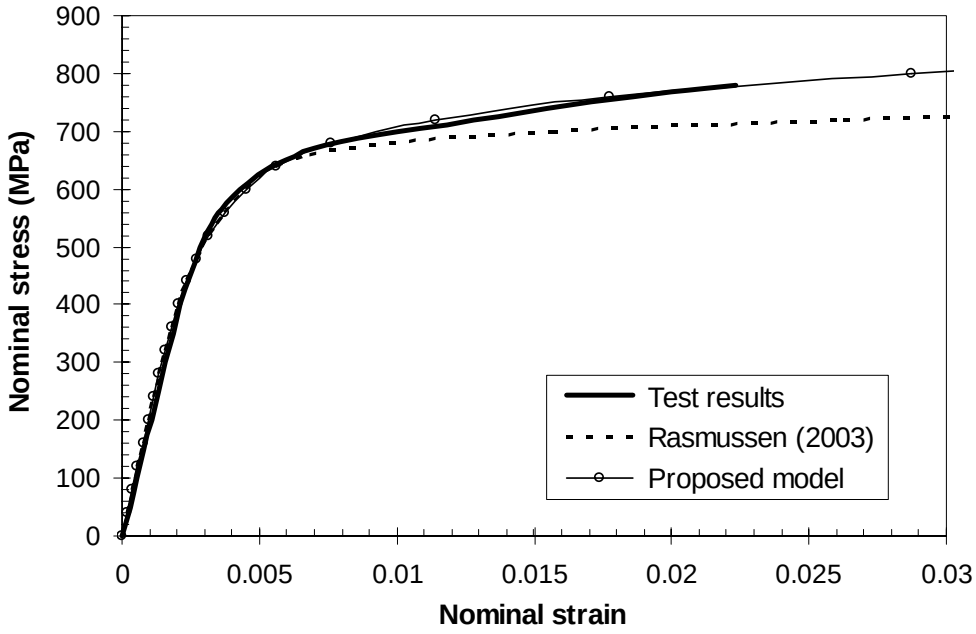

(b) Initial stress-strain curves

Figure A.35 Nominal stress-strain curves for the transverse compression coupon cut from the duplex stainless steel plate tested by Rasmussen *et al*. (2003).

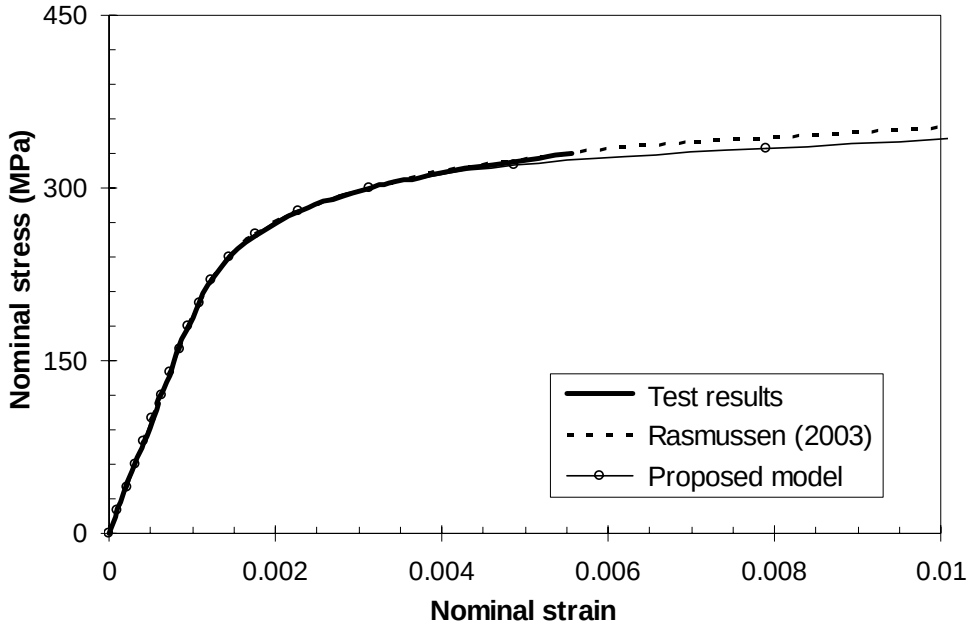

Figure A.36 Nominal stress-strain curves for the longitudinal tension coupon cut from the ferritic stainless steel plate tested by Korvink *et al*. (1995).

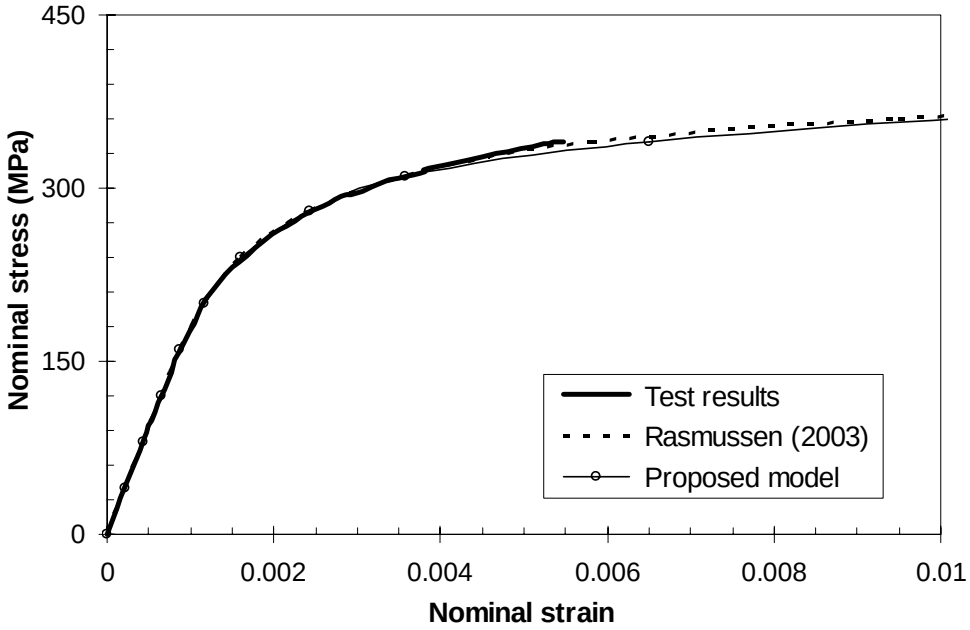

Figure A.37 Nominal stress-strain curves for the longitudinal compression coupon cut from the ferritic stainless steel plate tested by Korvink *et al*. (1995).

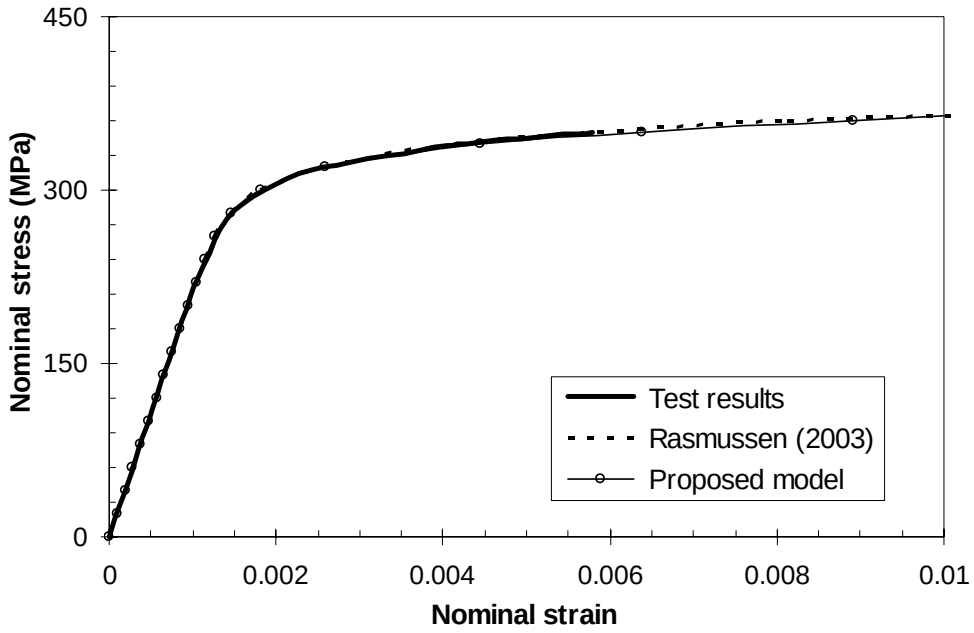

Figure A.38 Nominal stress-strain curves for the transverse tension coupon cut from the ferritic stainless steel plate tested by Korvink *et al*. (1995).

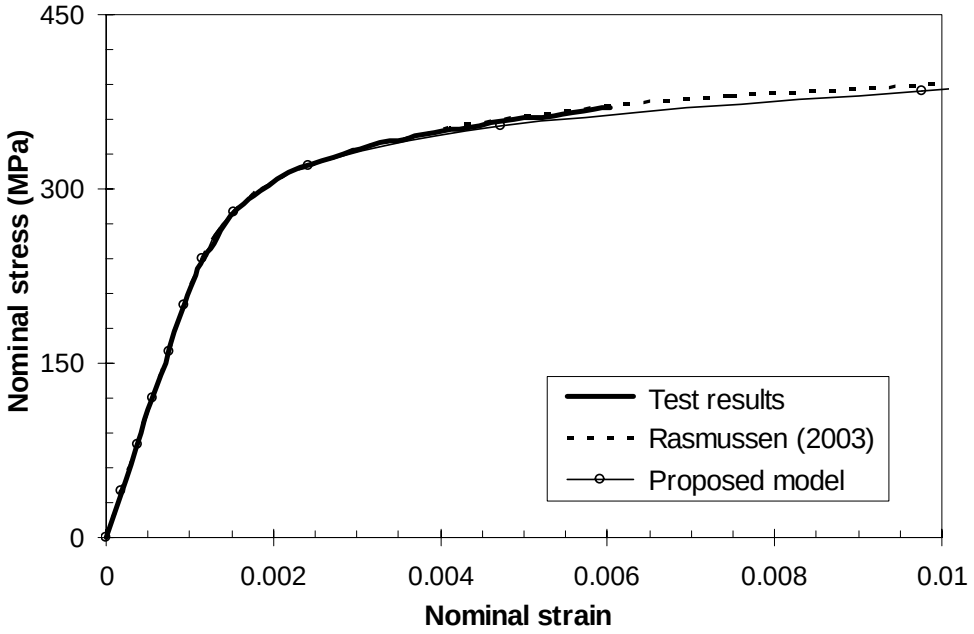

Figure A.39 Nominal stress-strain curves for the transverse compression coupon cut from the ferritic stainless steel plate tested by Korvink *et al*. (1995).

Appendix B

VALIDATION OF THE PLANE STRAIN ASSUMPTION FOR THE COILING AND UNCOILING OF WIDE PLATES

B.1 GENERAL

The analytical solutions for the coiling-uncoiling process presented in Chapters 4 and 7 are based on the plane strain assumption which is invalid for a narrow zone along each longitudinal edge of a wide plate of finite width. This appendix concerns the size of this edge zone for the plane strain assumption.

The coiling and uncoiling (including flattening) of four wide steel plates were simulated using the finite element package ABAQUS (2002). Each wide plate was subjected to the coiling curvature corresponding to the coil radius-to-thickness ratio r/t=100, and the direction of bending coincided with the longitudinal direction of the plate. The steel was assumed to possess an elastic-perfectly plastic stress-strain curve. Geometrical nonlinearity was considered. Each wide plate was modelled with the S4R shell element, which is a three-dimensional 4-node general-purpose shell element with reduced integration and hourglass control. This element is capable of handling large strains and large rotations. Each wide plate was constrained with one edge fixed and the opposite edge subjected to the prescribed displacement and rotation

corresponding to the desired coiling curvature. All the nodes along the fixed edge and the loading edge were free to translate in the width direction. All the nodes along the two longitudinal edges were free from any restraint.

Four wide plates with two different yield stresses (σ_y = 250 and 450 MPa) and two different plate thicknesses (t = 1 and 3 mm) were studied. Plate thicknesses chosen for this study cover the practical range (from 1 mm to 3.4 mm) of plate thicknesses for common cold-formed open sections presented in the AISI (1996) design manual. The widths of these wide plates were chosen such that each plate was wide enough to show the distinct edge effect and all the plates had the same width-to-thickness ratio (w/t = 200). The length of each plate was chosen to minimize the localized effect of the loading boundary on stresses near the mid-length of the plate. The material properties and dimensions of these wide steel plates are summarized in Table B.1.

B.2 RESULTS AND CONCLUSIONS

Figures B.1~B.3 show the variations of surface residual stresses and surface equivalent plastic strains along the width direction at the mid-length, for these four wide plates. In these figures, the surface residual stresses are normalized by the yield stress σ_y, equivalent plastic strains are normalized by the yield strain ε_y, and the distance x along the width direction measured from the longitudinal edge is normalized by the plate thickness t. The boundary of the edge zone is also indicated in each figure. It can be seen that, the size of the edge zone is only dependent on the plate thickness, while the magnitudes of residual stresses and equivalent plastic strains

are dependent on the yield stress of the sheet material. For the most important longitudinal residual stress, the size of this edge zone is about $15t$ from each free longitudinal edge of the plate.

B.3 REFERENCES

ABAQUS (2002). *Standard User's Manual, V6.3*, Hibbitt, Karlsson and Sorensen, Inc., United States.

AISI (1996). *Cold-Formed Steel Design Manual*, 1996 edition, American Iron and Steel Institute, Washington, D.C.

Table B.1 Dimensions and material properties.

Yield stress σ_y (MPa)	Young's modulus E (GPa)	Poisson's ratio ν	Thickness t (mm)	Length L (mm)	Width w (mm)	w/t
250	200	0.3	1	200	200	200
250	200	0.3	3	150	600	200
450	200	0.3	1	200	200	200
450	200	0.3	3	150	600	200

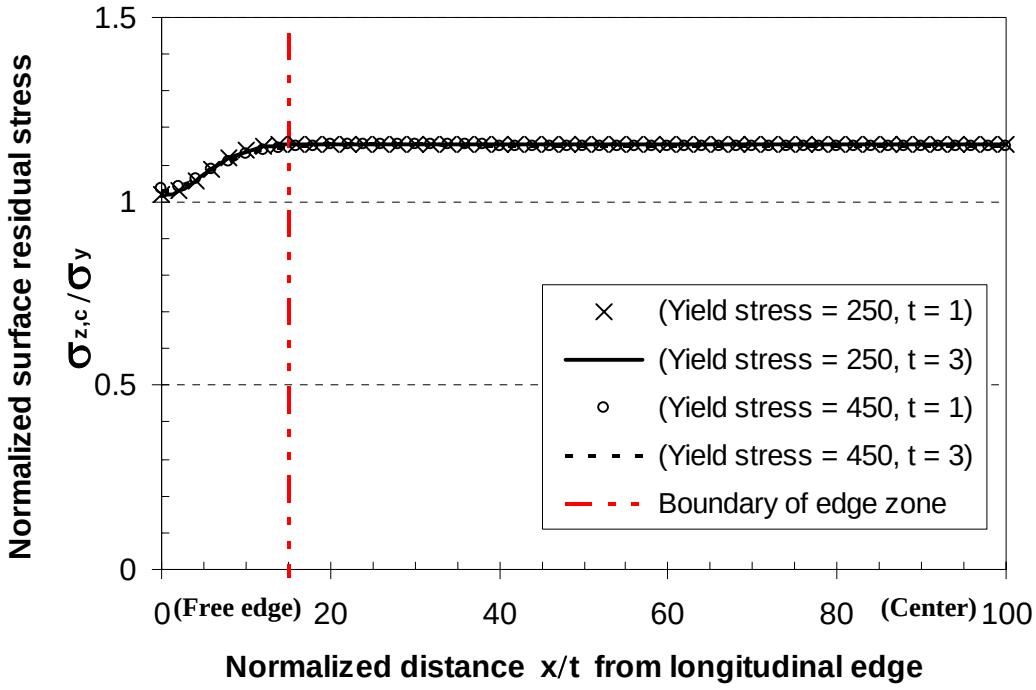

(a) Longitudinal coiling stress

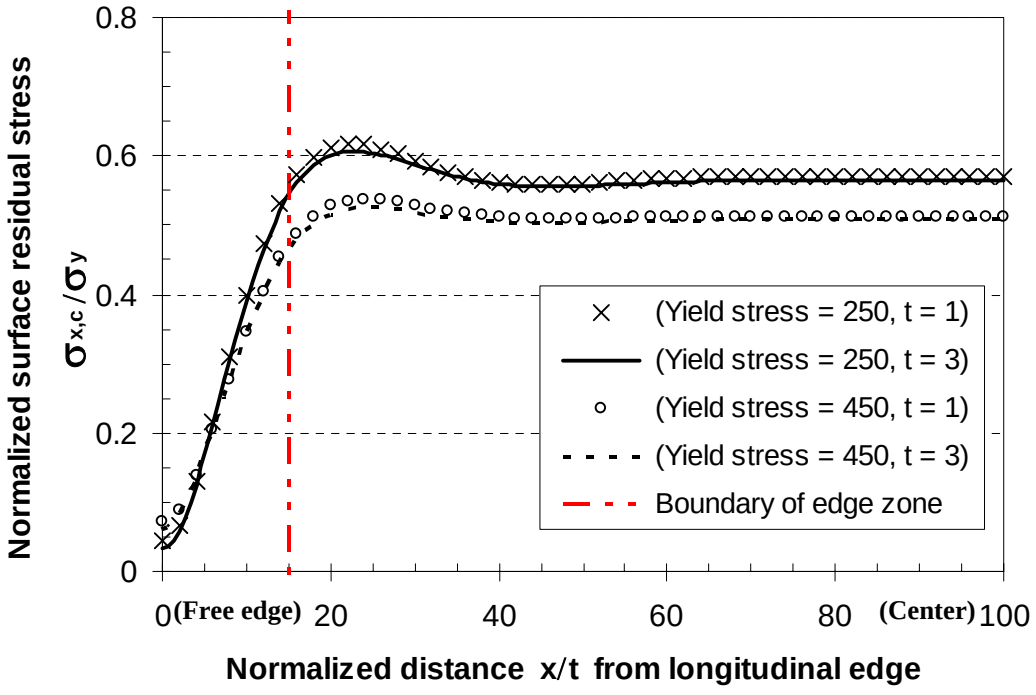

(b) Transverse coiling stress

Figure B.1 Residual stresses on the outer surface after coiling.

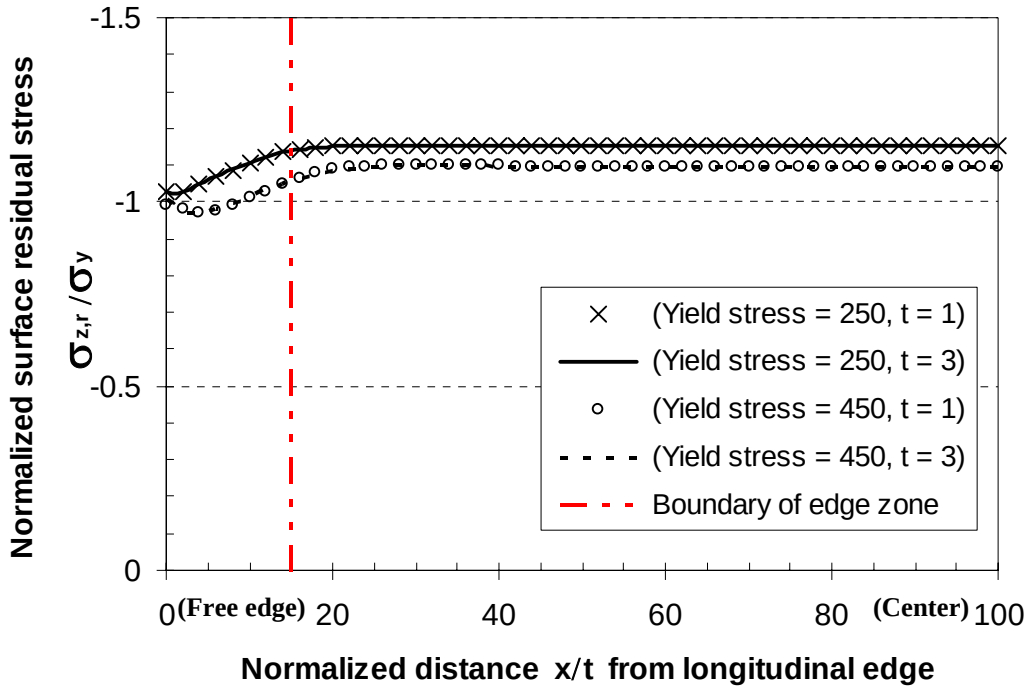

(a) Total longitudinal residual stress

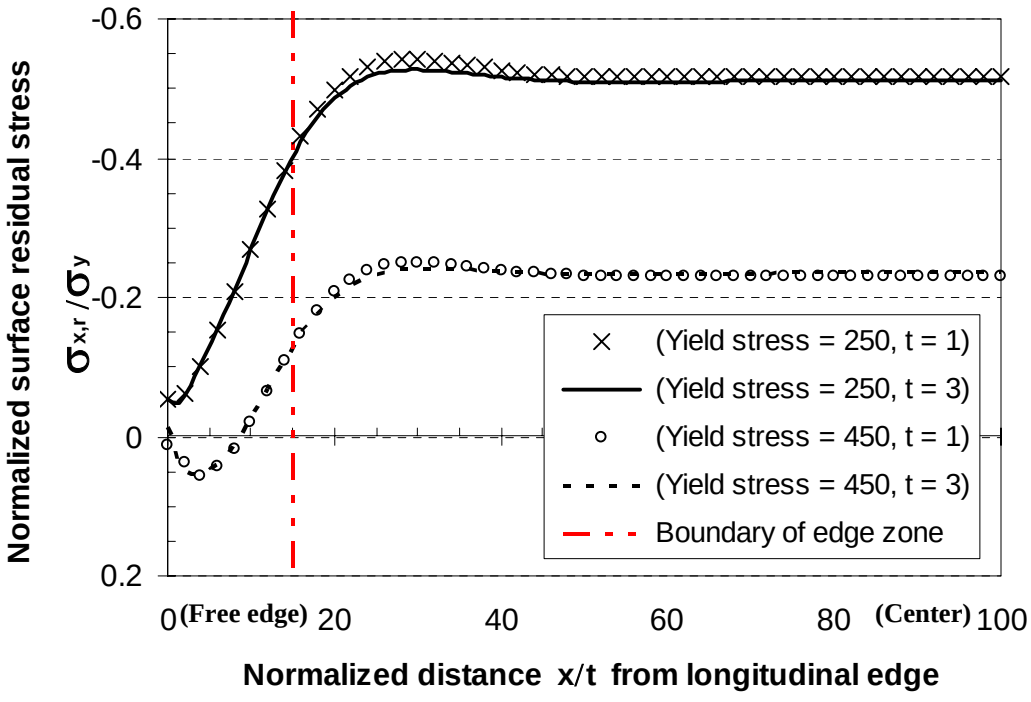

(b) Total transverse residual stress

Figure B.2 Residual stresses on the outer surface after flattening.

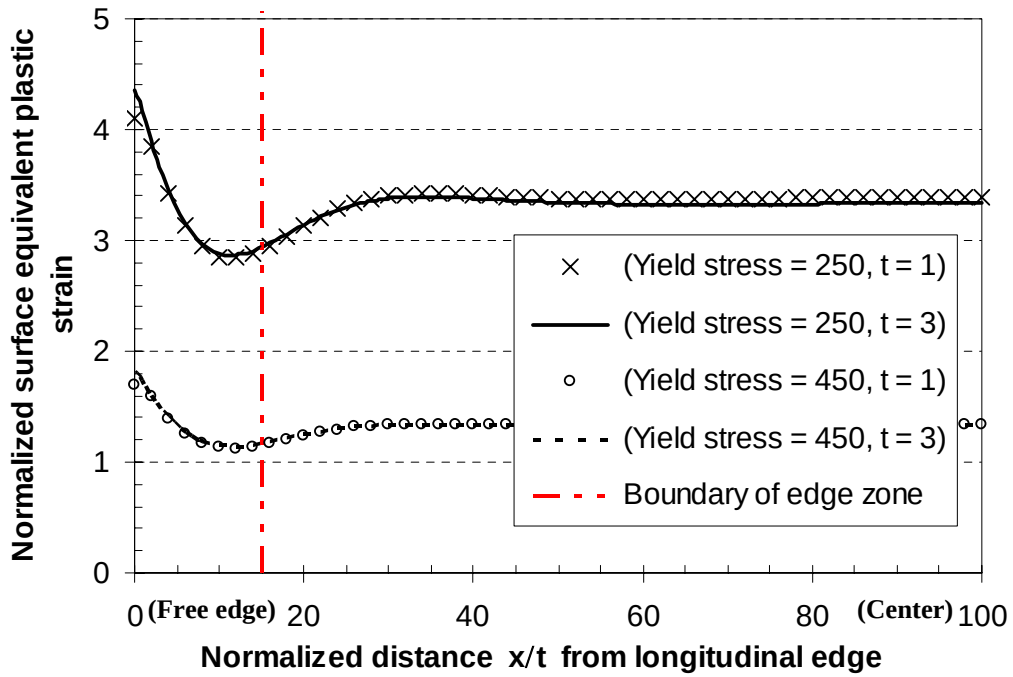

(a) After coiling

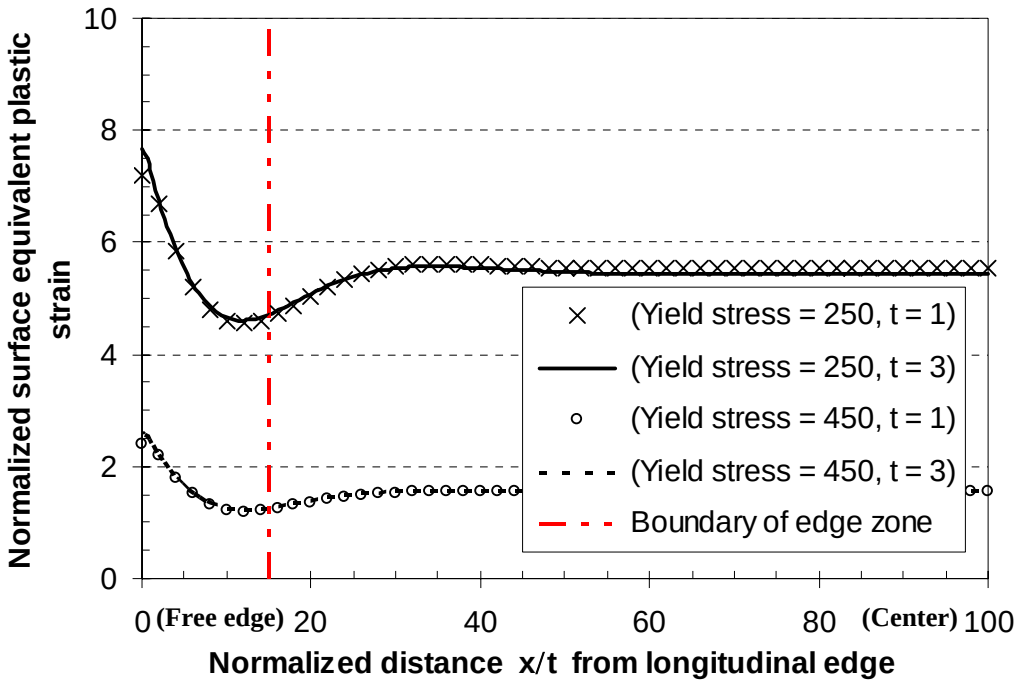

(b) After flattening

Figure B.3 Equivalent plastic strains on the outer surface due to coiling and uncoiling (including flattening).

Appendix C

ACCURACY OF THE PROPOSED ADVANCED FINITE ELEMENT APPROACH FOR COLUMN BEHAVIOUR

C.1 GENERAL

The advanced numerical approach presented in this thesis has been developed to predict the structural behaviour of press-braked columns, in which the cold work effect of the manufacturing process is taken into account. In this advanced numerical approach, residual stresses and equivalent plastic strains in press-braked sections, arising from the manufacturing process, can be modelled by incorporating either the finite element-based method or the complete analytical model.

In both the finite element-based method and the complete analytical model, the coiling and uncoiling of steel sheets have been modelled based on the plane strain assumption. However, this plane strain assumption is invalid for a narrow zone along each longitudinal edge of a steel sheet. In Appendix B, it has been shown that the size of this invalid zone is only dependent on the plate thickness t and is about $15t$ from each longitudinal edge of a wide steel plate. On the other hand, in the complete analytical model, simplifying assumptions have been made for the modelling of residual stresses in corner regions resulting from the large-curvature cold bending (see Chapters 6 and 7). As seen in Section 7.5 of Chapter 7, these simplifying assumptions reduce the accuracy of the predicted residual stresses near the central core of the

corner thickness. Therefore, the effect of all the aforementioned assumptions on the accuracy of the advanced numerical approach for column behaviour needs to be examined, and such an investigation is presented in this appendix.

In this investigation, a series of carbon steel lipped channel columns were studied. The structural behaviour of each column was simulated by three different column models: (1) full FE model, (2) analytical-FE model and (3) complete analytical model. These three column models are named after their respective three residual stress models. Column model (1) incorporates a full FE residual stress model in which residual stresses and equivalent plastic strains arising from both the coiling-uncoiling process and the cold bending of press-braking operations are modelled by finite element simulations. This column model is thus referred to as the full FE model in this appendix for ease of reference. Column model (2) incorporates the finite element-based method presented in Chapter 5 for the modelling of residual stresses and equivalent plastic strains in the press-braked channel section. This column model is thus referred to as the analytical-FE model in this appendix. Column model (3) incorporates the complete analytical model presented in Chapters 7 and 9 for the residual stresses and equivalent plastic strains in the channel section. This column model is thus simply referred to as the complete analytical model. These column models are described in detail in next sections.

Indeed, the analytical-FE column model and the complete analytical column model represent the advanced numerical approach incorporating two different residual stress models: (a) the finite element-based method and (b) the complete analytical model respectively. Since the full FE model takes into account the effect of the

manufacturing process accurately by finite element simulation, its predictions can provide accurate reference values. Therefore, the effect of the simplifying assumptions adopted for the analytical solutions presented in the thesis and the accuracy of the proposed advanced numerical approach can be assessed by comparing the predictions from the full FE model with the predictions from the other two column models.

All the columns studied here were assumed to have the same cross-sectional geometry (see Table 5.1 and Figure 5.2(a)) as the carbon steel channel, specimen PBC14, tested by Weng and Peköz (1990); and were assumed to possess a coil diameter $D = 200t$ in the manufacturing process. The virgin carbon steel sheet used for producing the press-braked section was assumed to have the same material properties as the flat material of specimen PBC14 (see Table 5.1 and Figure 5.1(b)). This carbon steel sheet was assumed to possess the elastic-perfectly plastic stress-strain behaviour during the coiling-uncoiling process, and to possess the elastic-nonlinear strain-hardening behaviour defined by the modified Ludwik equation (see Eq. (4.68)) during the cold bending of the sheet into the corners of a press-braked section. Various column lengths L and two different boundary conditions (i.e. fixed-ended and pin-ended) were considered (see Table C.1).

C.2 FULL FE MODEL

C.2.1 Coiling and uncoiling of plates of finite width

In the full FE model, residual stresses and equivalent plastic strains due to the coiling-uncoiling process were determined by the finite element simulation of the coiling and uncoiling process of a carbon steel sheet of finite width. The carbon steel sheet was 1.8-mm thick, 174.3-mm wide and 150.0-mm long. The width of this steel sheet was equal to the unfolded dimension of the channel section, and its thickness was the same as the plate thickness of the channel section. The length of the sheet was chosen to minimize the localized effect of the loading boundary on stresses near the mid-length of the sheet.

The wide carbon steel sheet was bent to a curvature corresponding to a coil diameter $D = 200t$, and was then forced to become flat. This was simulated using the finite element package ABAQUS (2002). Geometrical nonlinearity was considered. The wide sheet was modelled with the S4R shell element, which is a three-dimensional 4-node general-purpose shell element with reduced integration and hourglass control. This element is capable of handling large strains and large rotations. The wide sheet was fixed on one edge, while the opposite edge was subjected to the prescribed displacement and rotation corresponding to the desired coiling curvature. All the nodes along the fixed edge and loading edge were free to translate in the width direction. All the nodes along the two longitudinal edges were free from any restraint.

Results obtained from the above finite element simulation are shown in Figures C.1~C.4. Figure C.1 shows the stress contour for the uncoiled sheet. Figures C.2~C.4 show the through-thickness variations of residual stresses and equivalent plastic strains at different locations across the width (along the path from point P1042 to point P4942 in Figure C.1) of the uncoiled sheet. These residual stresses and equivalent plastic strains at the mid-length of the steel sheet were then specified as the initial state in a subsequent finite element simulation of press braking.

C.2.2 Numerical simulation of press braking

After the residual stresses and equivalent plastic strains due to the coiling and uncoiling of the wide carbon steel sheet were determined by the above finite element simulation, they were then specified as the initial state in a subsequent finite element simulation of press braking using the plane strain pure bending model on the plane of the cross section. The procedure for the finite element modelling of press-braking operations has been given in detail in Section 5.3 of Chapter 5.

The predicted longitudinal stress contour on the channel section is shown in Figure C.5(a). From Figures C.1~C.4, it can be seen that the edge zone of the wide sheet, in which the plane strain assumption for the coiling-uncoiling process is invalid, extends from the longitudinal edge (point P1042) to a location noted as point P13042. By mapping this edge zone onto the finite element mesh of the channel section shown in Figure C.5(a), the point P13042 is found to be located somewhere below the lip-flange corner. It means that the lip and the lip-flange corner are within the edge zone.

Nevertheless, other portions, such as the web, flanges and web-flange corners, are not affected.

C.3 ANALYTICAL-FE MODEL

In the analytical-FE model, the finite element-based method was employed to predict residual stresses and equivalent plastic strains in the channel section. The residual stresses and equivalent plastic strains resulting from the coiling-uncoiling process were determined by the analytical solution presented in Section 4.4 of Chapter 4. The residual stresses and equivalent plastic strains due to the cold bending of press-braking operations were determined by the finite element simulation of press braking. The predicted longitudinal stress contour on the channel section is shown in Figure C.5(b). The procedure of the finite element-based method has been given in detail in Chapter 5.

C.4 COMPLETE ANALYTICAL MODEL

In the complete analytical model, residual stresses and equivalent plastic strains arising from the coiling-uncoiling process were determined by the analytical solution presented in Section 4.4 of Chapter 4, and those due to the cold bending of press-braking operations were determined by the analytical solution presented in Section 6.4 of Chapter 6.

C.5 NONLINEAR BUCKLING ANALYSIS

The structural behaviour of each column was simulated using the above three column models respectively. Both residual stresses and equivalent plastic strains in each column, determined by the three residual stress models described in Sections C.2~C.4, were included respectively into the three finite element models as the initial state for the subsequent nonlinear buckling analysis. The nonlinear buckling analysis was carried out by employing the finite element package ABAQUS (2002) and using the modified Riks method. In the nonlinear bucking analysis, press-braked columns were modelled with the S4R shell element. Simpson's rule was used for the shell section integration, and 17 integration points were specified across the thickness of the shell element to allow for the specification of residual stresses and equivalent plastic strains. Both geometrical and material nonlinearities were considered.

Initial geometrical imperfections were also introduced into each finite element model. Both local and global imperfections were introduced into the finite element model of each column except for the stub column. For the stub column ($L = 250$ mm), only the local imperfection was introduced into the finite element model. The local and global imperfections were modelled by scaling the lowest local buckling mode and the lowest global buckling mode respectively. The local imperfection amplitude was assumed to be $0.2t$ and the global imperfection amplitude was taken as $L/1000$ for both fixed-ended and pin-ended columns.

The procedure for the numerical modelling of the column behaviour of the carbon steel channel section using the complete analytical model has been given in detail in

Section 9.2 of Chapter 9. The modelling of the column behaviour using the full FE model and the analytical-FE model was achieved by following the similar procedure given in Section 9.2, except that no analysis step was required to allow for the transverse spring-back of the channel section since the effect of the transverse spring-back had been taken into account in their residual stress models. Hence, in these two column models (i.e. the full FE model and the analytical-FE model), all the nodes at the column ends were initially restrained against longitudinal translations and rotations about the two principal directions on the cross-sectional plane (see Figure C.6(a)). After the initial state was introduced into the finite element model, residual stresses were then allowed to be released locally at the column ends by removing these end constraints (see Figure C.6(b)), in order to simulate the removal of end constraints after press braking or after cutting the full length of the member into the desired column length. The resulting deformed mesh and its associated stress state defined the “imperfect” column for the subsequent nonlinear buckling analysis.

C.6 RESULTS AND CONCLUSIONS

Comparisons of column strengths predicted by the three column models are summarized in Table C.1. Comparisons of load-axial displacement curves are shown in Figures C.7~C.11. As the full FE model has accurately taken into account the effect of the manufacturing process by the finite element simulation, its predictions are considered to be more accurate than those from the other two column models and are treated as reference values for comparison. It can be seen that column strengths and

load-displacement curves predicted by the analytical-FE model and the complete analytical model are in close agreement with those predicted by the full FE model.

The maximum difference in the column strength between the analytical-FE model and the full FE model is about 1% only. The maximum difference in the column strength between the complete analytical model and the full FE model is about 2% only. The difference in the column strength between the complete analytical model and the analytical-FE model indicates the net effect of the simplifying assumptions made for the large-curvature cold bending at corners. The maximum difference is about 3%. This 3% maximum difference is considered to be satisfactory. It demonstrates the accuracy of the advanced numerical approach. It also shows that the effect of the simplifying assumptions which have been made for the analytical solutions presented in this thesis is negligible.

C.7 REFERENCES

ABAQUS (2002). *Standard User's Manual, V6.3*, Hibbitt, Karlsson and Sorensen, Inc., United States.

Weng, C. C. and Peköz, T. (1990). Residual stresses in cold-formed steel members. *Journal of Structural Engineering, ASCE*, **116:6**, 1611-1625.

Table C.1 Comparison of column strengths.

Boundary conditions	Column length L (mm)	Column strength (kN)			(2)/(1)	(3)/(1)	(3)/(2)
		Full FE model (1)	Analytical-FE model (2)	Complete analytical model (3)			
Fixed-ended	250*	88.4	88.4	86.5	1.00	0.98	0.98
	1000	80.6	81.8	79.7	1.01	0.99	0.97
	2000	54.2	54.7	52.9	1.01	0.98	0.97
Pin-ended	1000	63.4	64.0	63.7	1.01	1.00	1.00
	2000	28.6	28.5	27.9	1.00	0.98	0.98

Note: * The length of the stub column.

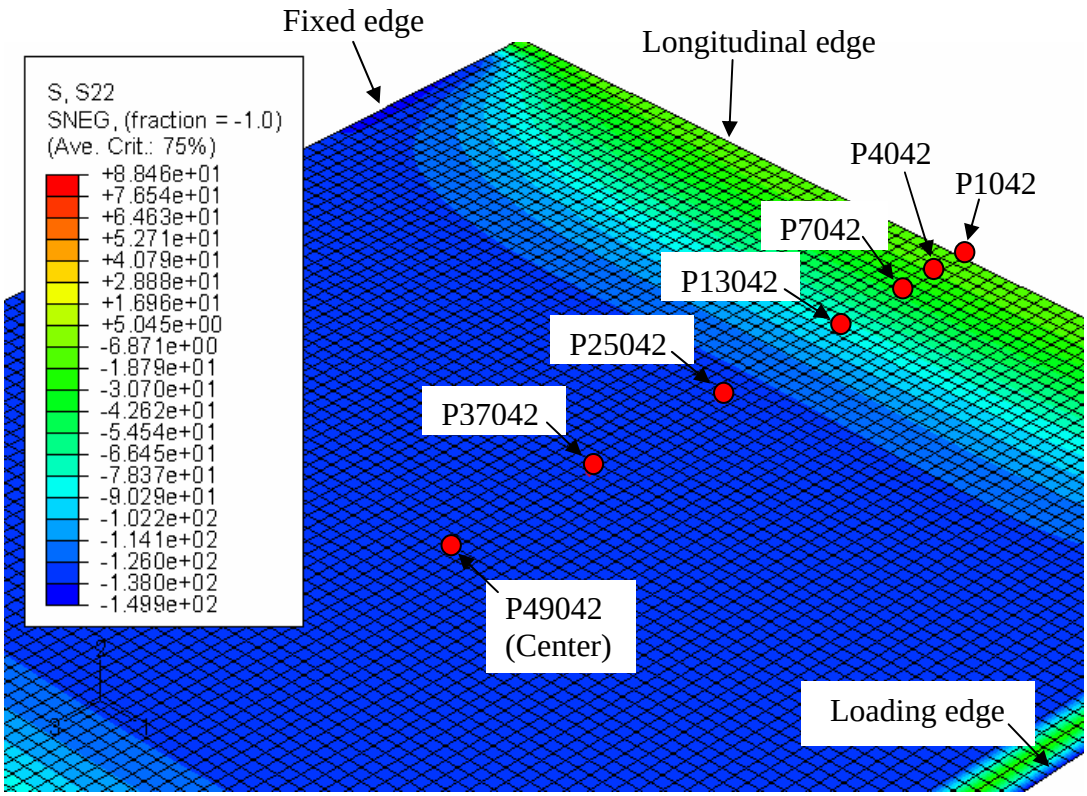

Figure C.1 Transverse stress contour on the outer surface of the uncoiled carbon steel sheet.

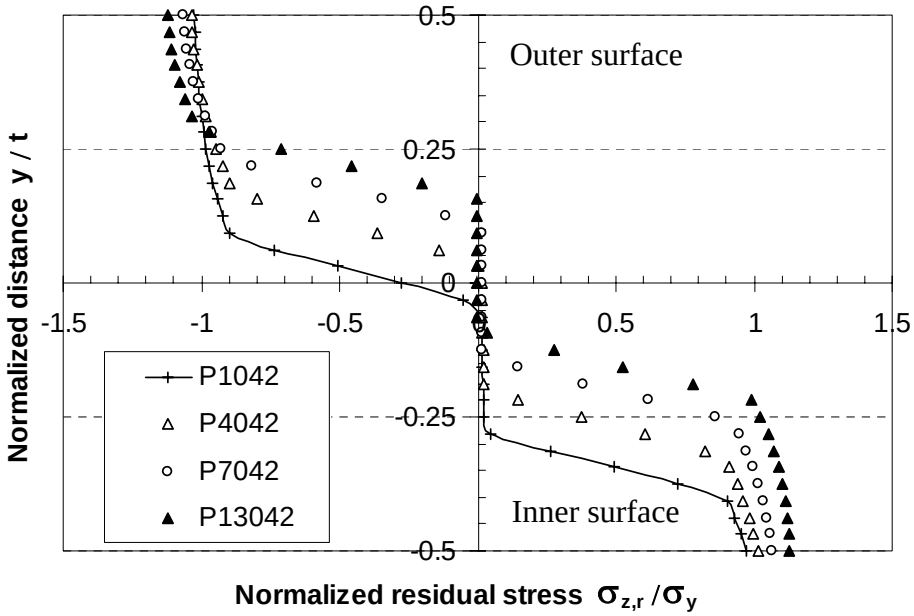

(a) Longitudinal residual stresses at points P1042 through P13042

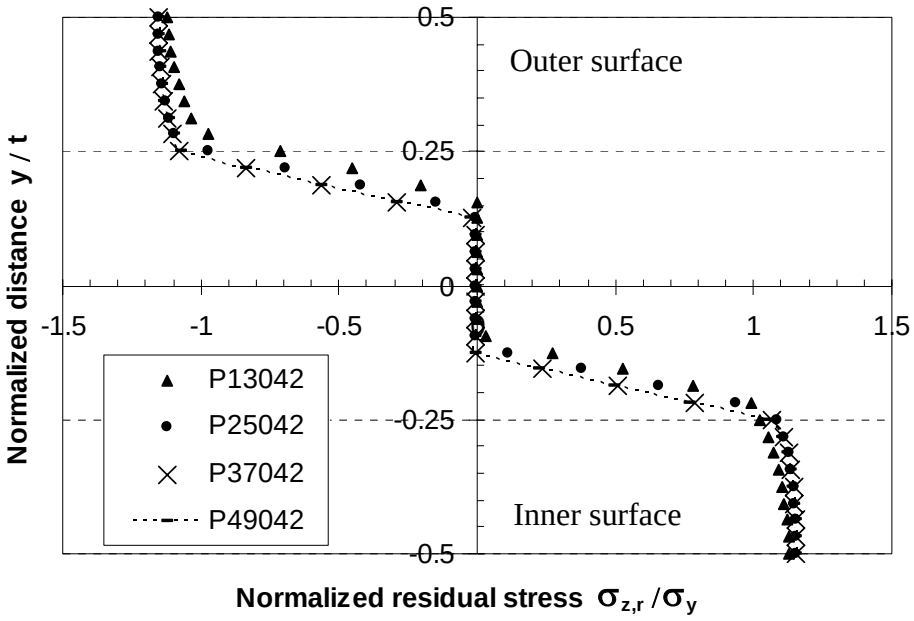

(b) Longitudinal residual stresses at points P13042 through P49042

Figure C.2 Through-thickness variations of longitudinal residual stresses at different locations on the uncoiled carbon steel sheet.

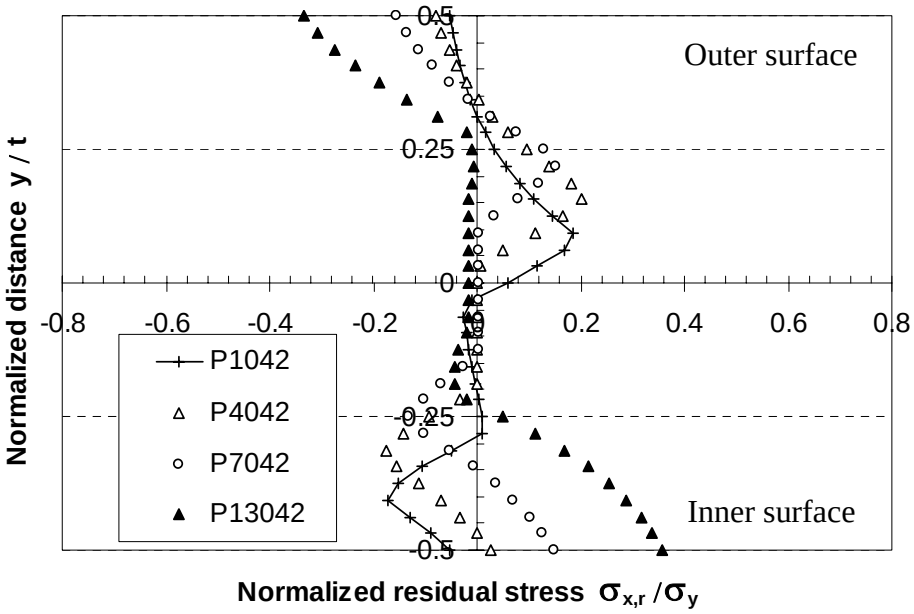

(a) Transverse residual stresses at points P1042 through P13042

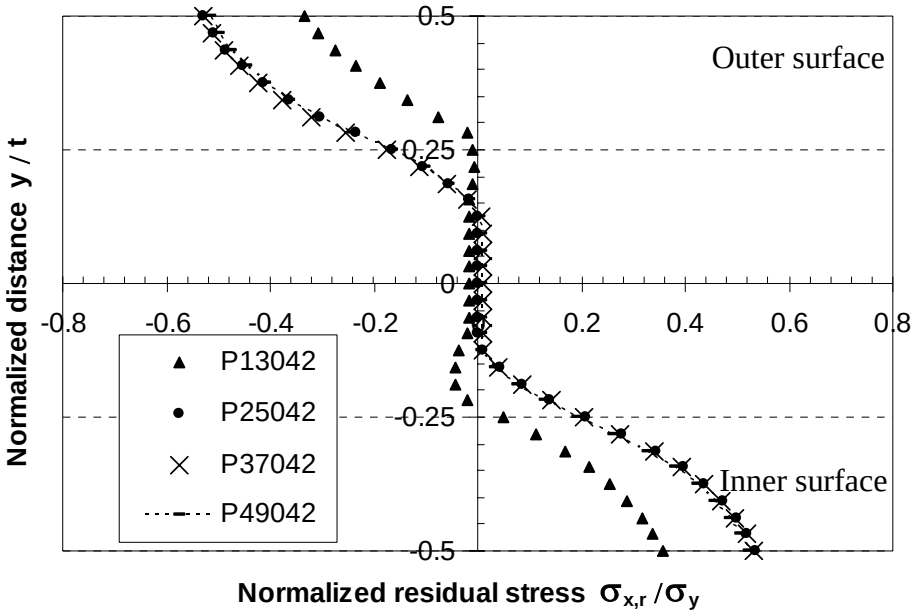

(b) Transverse residual stresses at points P13042 through P49042

Figure C.3 Through-thickness variations of transverse residual stresses at different locations on the uncoiled carbon steel sheet.

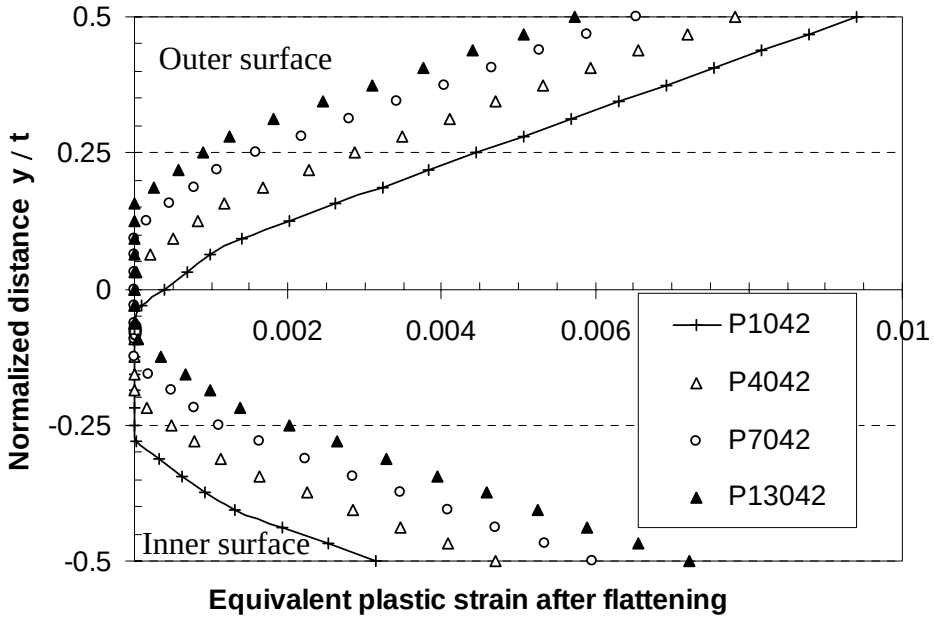

(a) Equivalent plastic strains at points P1042 through P13042

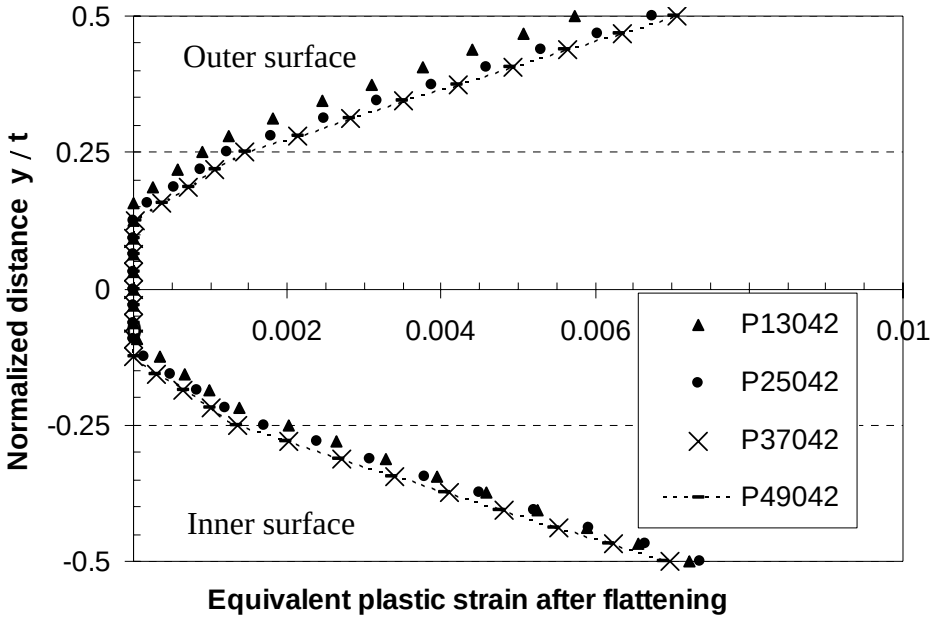

(b) Equivalent plastic strains at points P13042 through P49042

Figure C.4 Through-thickness variations of equivalent plastic strains at different locations on the uncoiled carbon steel sheet.

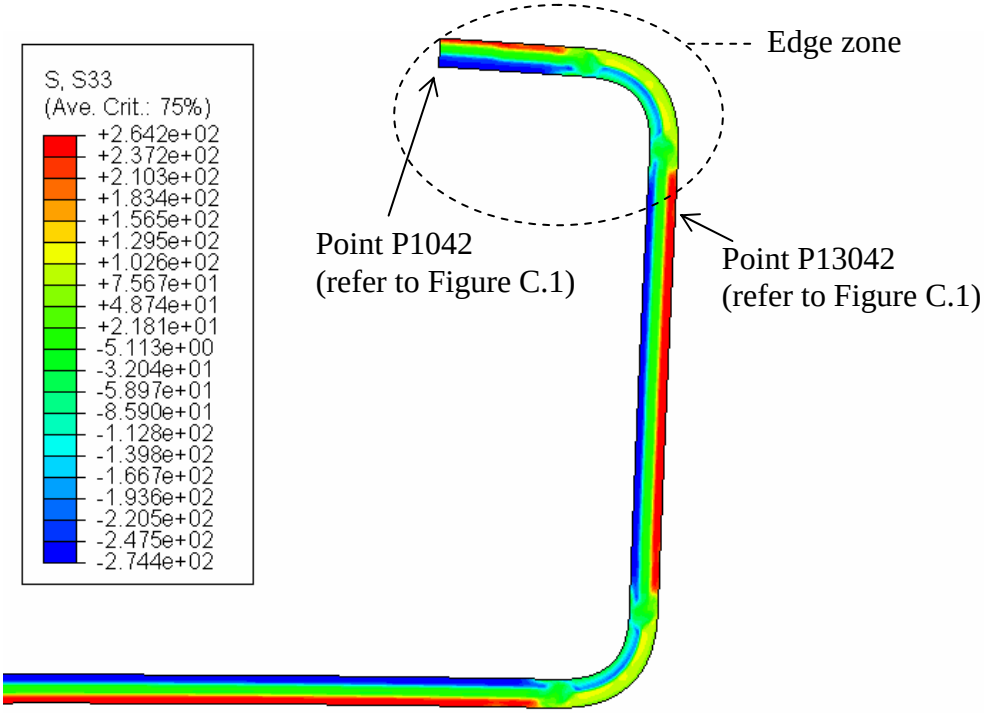

(a) Full FE model

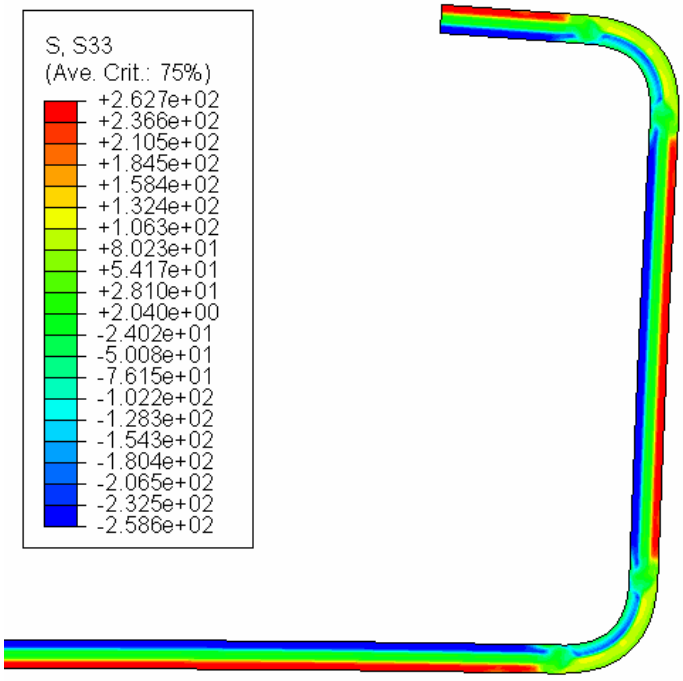

(b) Analytical-FE model

Figure C.5 Longitudinal stress contours on the lipped channel section.

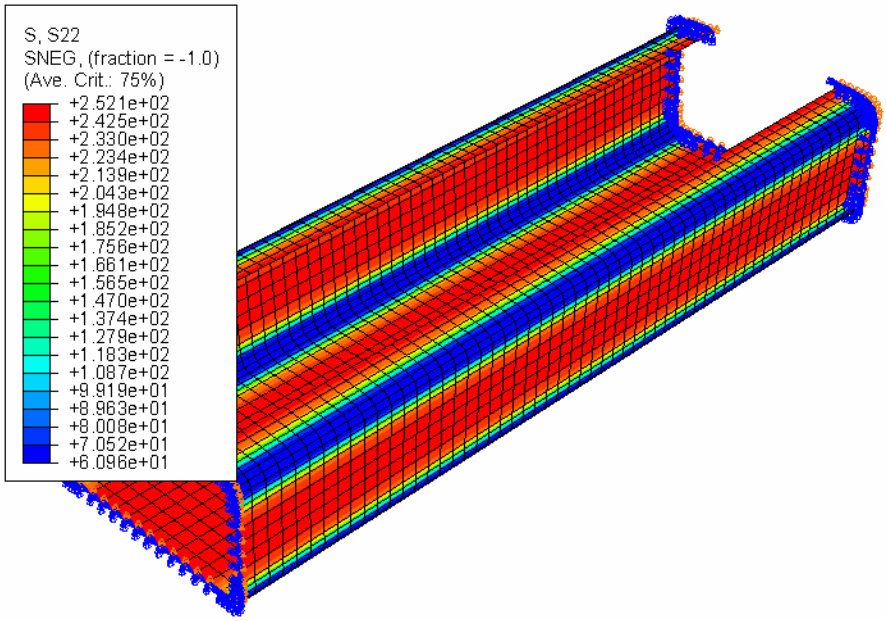

(a) Initial state

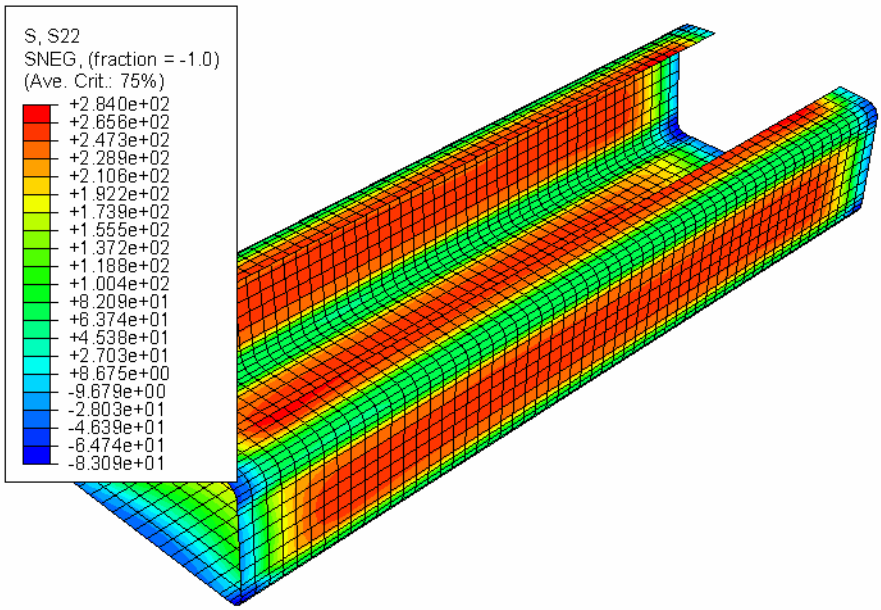

(b) After removal of end constraints

Figure C.6 Longitudinal stress contours on the outer surface of the stub column before and after the removal of end constraints.

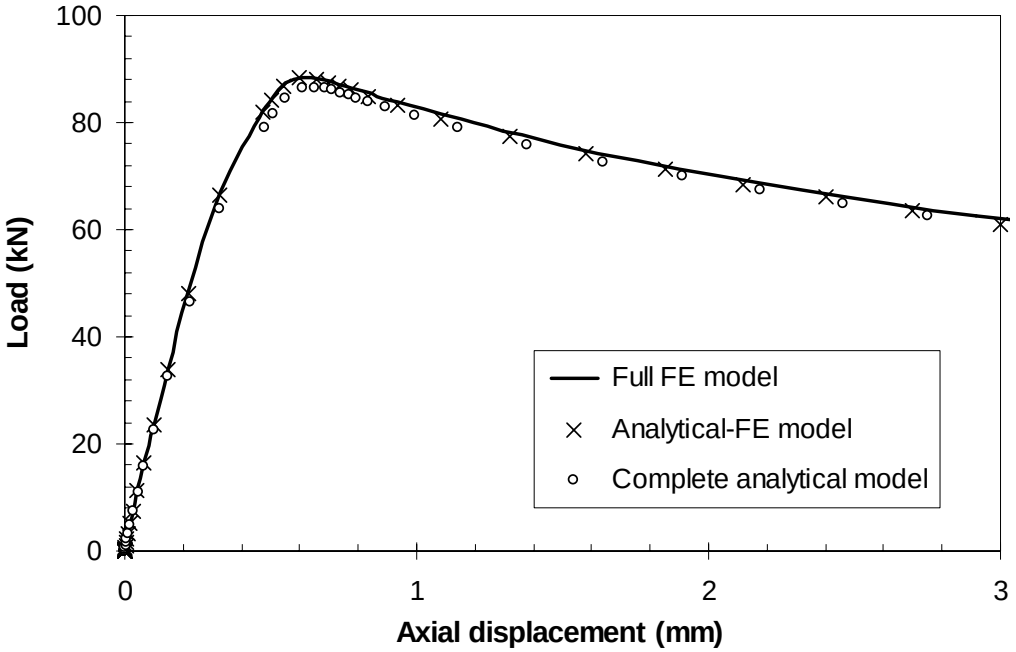

Figure C.7 Load-axial displacement curves for the stub column.

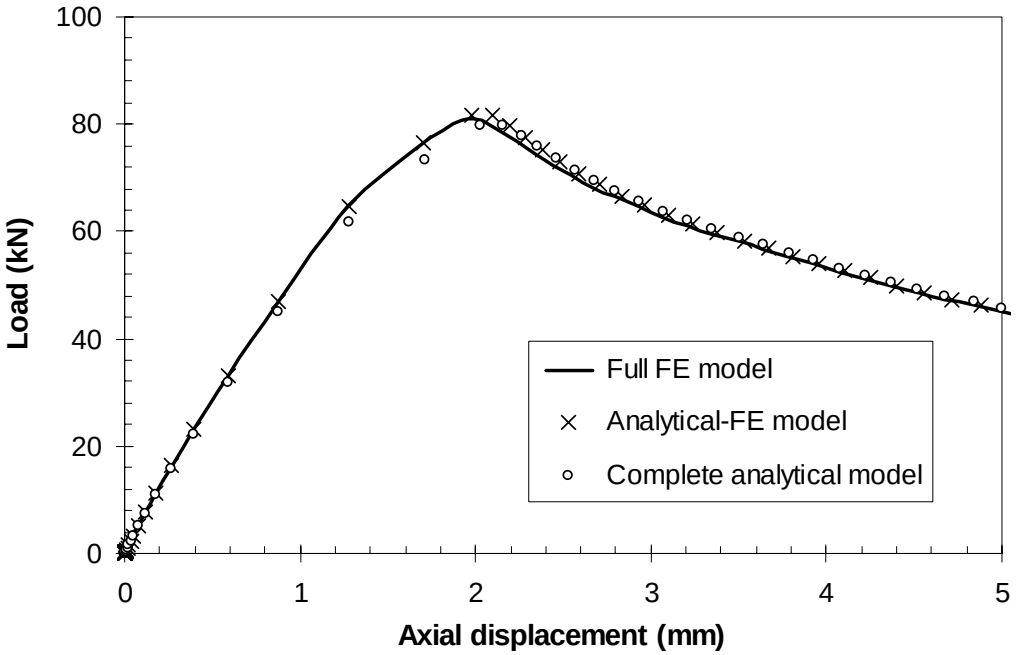

Figure C.8 Load-axial displacement curves for the 1000-mm high fixed-ended column.

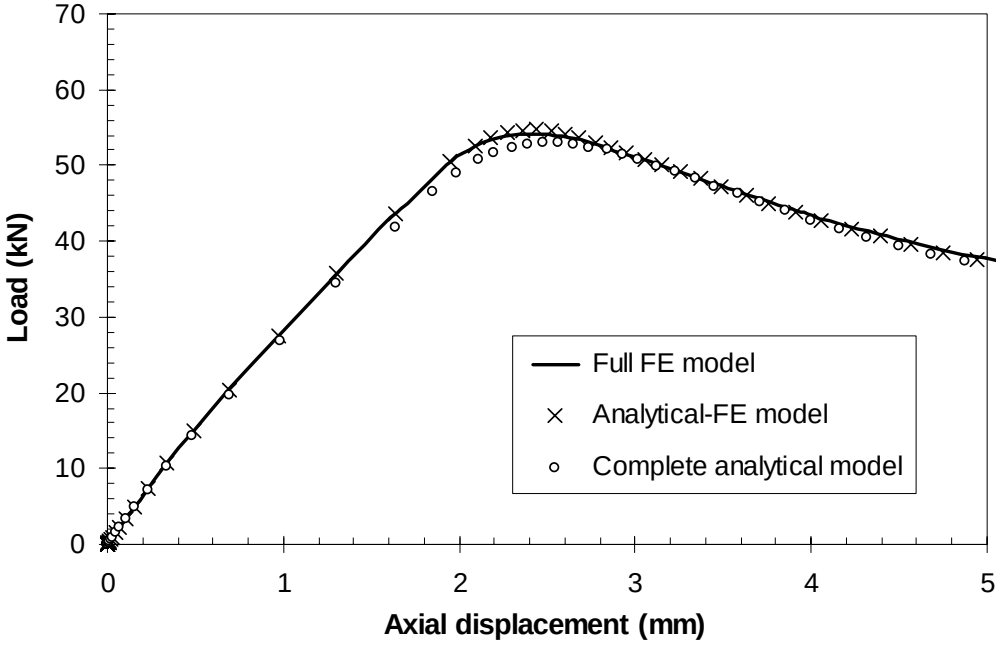

Figure C.9 Load-axial displacement curves for the 2000-mm high fixed-ended column.

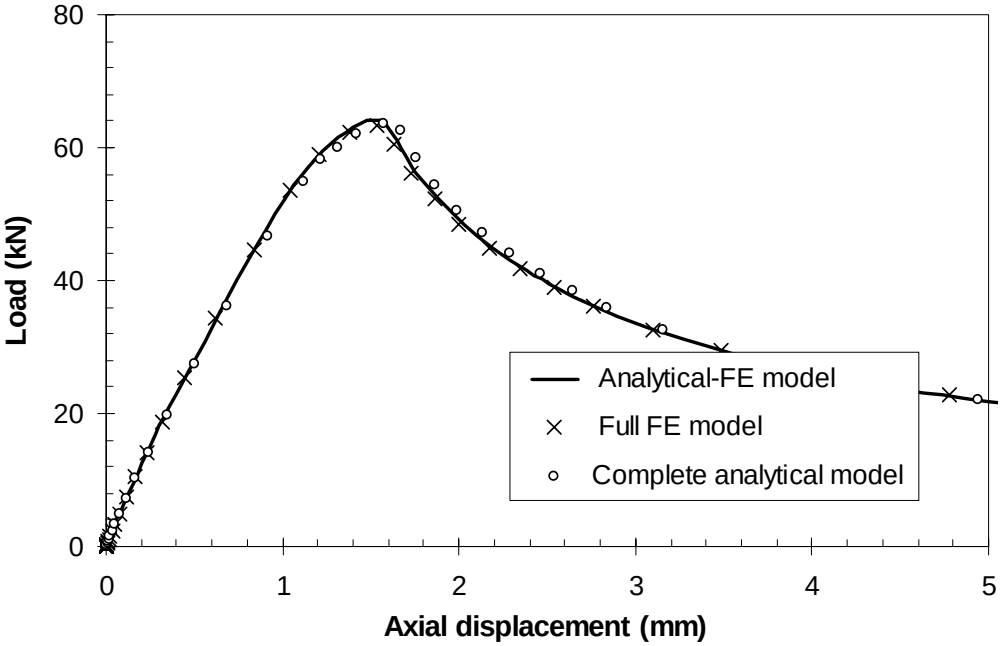

Figure C.10 Load-axial displacement curves for the 1000-mm high pin-ended column.

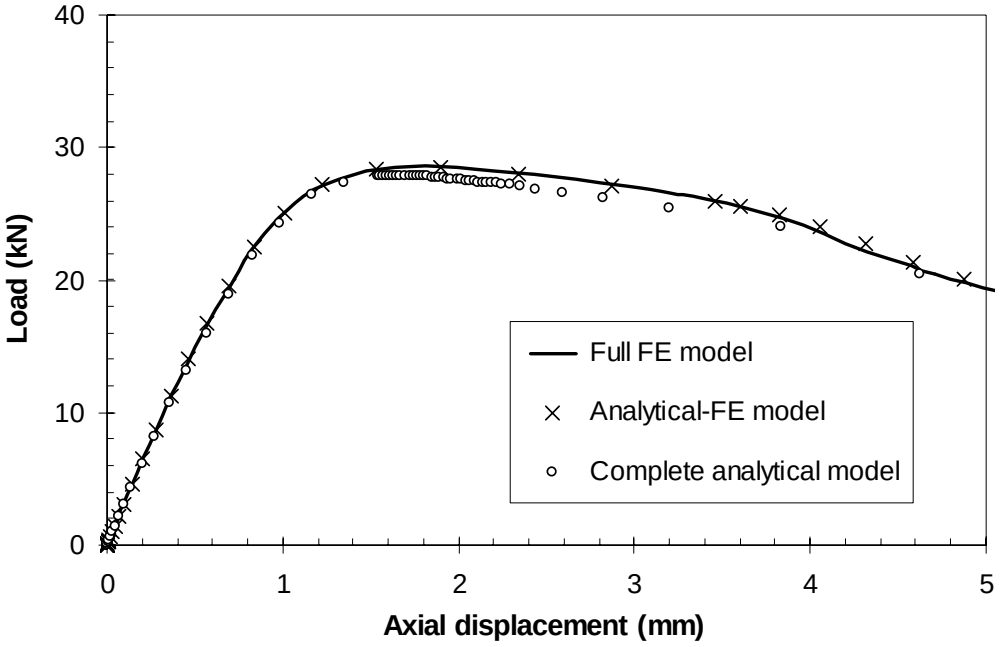

Figure C.11 Load-axial displacement curves for the 2000-mm high pin-ended column.